FATIGUE AND CORROSION FATIGUE CRACK GROWTH RESISTANCE OF RQT501 STEEL

BY

HAIYUN HU

A Dissertation Submitted to the University of Sheffield

for the Degree of Doctor of Philosophy in the

Faculty of Engineering

Structural Integrity Research Institute University of Sheffield

Department of Mechanical Engineering

August 1997

DEDICATED

TO

MY PARENTS

AND TO

MY HUSBAND, XIAOFAN

Whose patience and love have enabled me to complete this study

FATIGUE AND CORROSION FATIGUE CRACK GROWTH RESISTANCE OF RQT501 STEEL

H. HU

SUMMARY

This project is concerned with the fatigue response of roller quenched and tempered (RQT501) steels. Three closely related aspects are considered: (i) the relationship between the microstructure and fatigue properties, (ii) the influence of the environment on fatigue properties, (iii) theoretical modelling of fatigue crack growth.

The material used is an RQT501 grade steel. Two steels have been chosen: (A) without Mo and V additions, (B) with Mo and V additions. The second condition is chosen to evaluate the role of these elements, as hydrogen traps, on the resistance to corrosion fatigue crack growth. In order to evaluate these effects, tests have been carried out under freely corroding conditions and applied cathodic polarisation (-950 mV/SCE).

Metallographic examination has been carried out to evaluate grain size and inclusion distribution, size and morphology. To enable a comparison between short and long fatigue crack growth, smooth shallow hour-glass specimens have been used to study initiation and growth of short fatigue cracks, and compact tension specimens were used to monitor propagation of long fatigue cracks. The fatigue response ($S \sim N_f$ curve) and fatigue crack growth rate behaviour has been studied in air (5 ~ 10 Hz) and in 3.5%NaCl solution (0.2 Hz) or artificial seawater (0.2 Hz) with an applied stress ratio of 0.1 and sinusoidal waveform. The generation and growth behaviour of cracks from smooth hour-glass specimens has been investigated through successive observation using the plastic replication method. Long fatigue crack lengths were measured using a Direct Current Potential Drop (DCPD) technique and monitored via a chart recorder. Based upon the results of these tests a fatigue crack growth model was developed based on non-equilibrium statistical theory incorporating a consideration of the influence of microstructure, e.g. grain boundaries and hydrogen embrittlement. A stochastic theory of corrosion has also been developed for the use with corrosion fatigue test data.

PREFACE

The work presented in this thesis is based on the results obtained by the research carried out in the Structural Integrity Research Institute University of Sheffield (SIRIUS), Department of Mechanical Engineering at the University of Sheffield between November 1994 and August 1997.

The content of this thesis is original except where particular references are specified. No part of this thesis has been submitted to any other university for a degree.

H. HU

August 1997

ACKNOWLEDGEMENTS

I wish to thank the Head of the Department of Mechanical Engineering, and British Steel Plc Swinden Technology Centre (STC) for the use of laboratory facilities.

I am most grateful to my supervisor **Dr. R. AKID** for his invaluable guidance, help and the continuous encouragement throughout the time of this project.

I am also thankful to Dr. W. Rudd and his fellow colleagues at STC for their help in completing the test schedule. Thanks are also due to Dr. Wei Zhang and Mr. C. J. Donohoe for their sincere advice and help.

I am especially indebted to the British Council and the Chinese Government for the award of a scholarship.

I would like to express my gratitude to all technical staff in particular Mr. J. Smith, Mr. J. V. Goodliffe and Mr R. J. Cummins for laboratory work, Mr. J. Clark and Mr. K. A. Rotchell who manufactured specimens, Ms. Dawn Bussy at the Sorby Centre for her help with the scanning electron microscope and Mr. Graham Johnson at UNISCAN Instruments for help with the surface roughness examination, Mr. D. L. Hallford for his photographic skills, Mr. Brian Keeling at Department of Engineering Materials for his help with the Vanox Image System.

Last but not least, I am grateful to my parents and other family members for their patience and my husband for his support and care throughout my stay in Sheffield.

Contents

NOMENCLATURE

The symbols most frequently used in the text are listed below. Those which are rarely used are defined in their context.

A, A' = transportation fatigue crack growth or corrosion coefficient

a = surface crack length

a_k = critical surface crack length

$a_{p/c}$ = pit/crack transition length

a_{th} = material threshold

$\frac{da}{dN}$ = surface fatigue crack growth rate

$(\frac{da}{dN})_{CF}$ = corrosion fatigue crack growth rate

B = thickness of compact tension specimen

b = Burgers vector

C = crack length within compact tension specimen

$\frac{dC}{dN}$ = fatigue crack growth rate within compact tension specimen

C_H = concentration value of hydrogen

c = half surface crack length

$\frac{dc}{dN}$ = growth rate of a half surface crack

c_0 = initial half surface crack length

c_k = critical half surface crack length

D = a parameter which is related to the strength of grain boundary

$D(x)$ = dislocation density function of a crack

d = average grain size

d_{th} = distance to the second major microstructural barrier affecting surface fatigue crack growth

E = Young's modulus

E_D = energy required for producing a dislocation of unit length

F_1 = geometry factor of a crack

f = frequency

$f(c, N), f(t)$ = fluctuation growth (or corrosion) rate

G_{IC} = crack extension force

G_{IC}^{H} = crack extension force under hydrogen effect

H_v = Vickers hardness number

$K(c, N), K(X)$ = transportation growth (or corrosion) rate

K_{IC} = fracture toughness

K_{ISCC} = threshold stress intensity for stress corrosion cracking

K_0 = stress intensity factor free of hydrogen effect

K_A = contribution of hydrogen ahead of a crack to the stress intensity factor

K_S = contribution of hydrogen at the side of a crack to the stress intensity factor

ΔK = stress intensity factor range

ΔK_{eff} = effective stress intensity factor range

ΔK_{th} = threshold stress intensity factor range

k = Boltzmann constant

L = average length of slip plane

M = number of grains through which a crack has passed

N = number of applied loading cycles

N_f = fatigue lifetime

N_0 = average number of mobile dislocation sources per unit volume

n = number of dislocations associated with crack opening displacement

P = applied load

$P(X_0, X; t)$ = probability density function of pit diameter

Q = fluctuation corrosion coefficient

R = stress ratio

r_0 = size of plastic zone

S = stress range

T = kinetic energy of a crack

$t_{p/c}$ = pit/crack transition time

U_T = potential energy of a crack

U' = activation energy of diffusion

U_g = influence of grain boundaries on energy of a crack

V = value of potential

V_0 = reference potential

W = net width of compact tension specimens

W_{IIA} = energy of dislocations ahead of the crack tip

W_{IIS} = energy of dislocations at the side of the crack flank

$X(t)$ = pit diameter

$\overline{X}$ = average pit diameter

X_{Lm}, X_{Pm} = (linear or parabolic) pit diameter with maximum probability density function

$\dot{X}(t)$, $\dot{X}_L$, $\dot{X}_P$ = (linear or parabolic) corrosion rate of material at time t

X_0 = initial diameter of corrosion pit

Y = geometry factor

Z = inclusion size

α = a parameter which is related to the distance between the initiation site of a crack and the first grain boundary

β = cyclic hardening exponent

$\beta(X)$ = fluctuation coefficient of corrosion

η = total relative deviation of $N_0, G'_{IC}, L, \sigma_0$

μ = shear modulus of metal

ν = Poisson's ratio

$\rho^A(x)$ = dislocation density function ahead of a crack

$\rho^S(x)$ = dislocation density function at the side of a crack

$\Delta\sigma$ = cyclic stress range

σ_0 = cyclic strength coefficient

σ_{ys} = yield stress

ζ = total deviation of A

Subscripts

A = location ahead of the crack tip

L = longitudinal direction (Ch. 3) or linear (Ch. 8)

T = transverse direction

V = vertical direction

m = maximum

P = parabolic

S = at the side of the crack

Chapter 1

Introduction

The increasing number of premature and often catastrophic failures of engineering structures has stimulated the re-evaluation of concepts used in the design and selection of materials. Environmental interactions which were generally ignored have received increasing attention in the past 30 years. Scientists and engineers have devoted extensive investigative time to the complex and often confusing details of environmental system interactions. Corrosion fatigue which represents one small branch of the interaction of materials with the environment, describes the behaviour of the material subjected to the combined action of cyclic loading and a corrosive environment. The complexity of this problem becomes apparent when one realises that corrosion fatigue is in fact influenced by a variety of mechanical, chemical and microstructural parameters which interact.

Corrosion fatigue is considered to be one of the most important factors in determining the life of static offshore structures such as platforms for oil and gas production: the fatigue properties of the offshore structural steels are adversely affected by the presence of aqueous, chloride-containing environments and they become susceptible to enhanced fatigue crack initiation and corrosion fatigue crack growth. Predominantly, as a result of wave action, an offshore installation will be subjected to about 10^8 stress cycles over a 20-year life, typically at an average frequency of 0.167 Hz (approximately one wave every six seconds) and this frequency

has been adopted as a standard in testing. This cyclic loading can lead to fatigue failures. Wave action has most effect on the parts of the structure between, and just below, the tide marks. Superimposed onto this cyclic loading is the effect of corrosion, which in open seawater is again greatest in and around the tidal area where there is very high oxygen availability. Hence, the possibility of fatigue or corrosion fatigue failure represents a major constraint in the design of offshore structures.

Offshore structures are subjected to cathodic protection in order to prevent their general corrosion. But the relationship between corrosion fatigue and cathodic protection is not completely understood, there is evidence both for acceleration and for reduction of corrosion fatigue crack growth rates by cathodic protection [1]. Maintenance of offshore structures and their long term integrity requires the ability to understand the effect of cathodic protection on their mechanical performance.

The steels currently used for the construction of offshore structures are low alloy steels, such as BS4360: 50D steel, and similar alloys. However, future designs may require lower topside and overall weights, for example in the use of tubulars having tensile strengths of the order of 800 and 1100 MPa [2]. The higher yield strength associated with these steels is also likely to increase the materials susceptibility to environmental damage. The RQT (roller quenched and tempered) series of plate products represent a step forward in the development of materials, specifically for offshore use and in other critical situations, where higher strength with good weldability is required. Since RQT501 may have the potential to replace BS4360: 50D steel and similar alloys, in the next generation of offshore platforms, a detailed investigation of the performance of this steel is required under specific experimental conditions, in particular that of its resistance to fatigue crack growth.

Measures used to avoid hydrogen embrittlement involve either removal of any diffused hydrogen or prevention of hydrogen adsorption on the metal surface. Inhibitors and additives that reduce the corrosion rate or increase the rate of hydrogen gas evolution can be helpful. Additives of Mo and V have been known to be beneficial to hydrogen embrittlement (stress corrosion cracking) in H_2S environments [3]. The reason for this is that higher tempering temperatures can be employed either to provide steels with a lower distribution density of hydrogen or to promote the formation of alloy carbides which act as hydrogen trap sites or a combination of both mechanisms.

Based on these findings, two different grades of RQT501 (with and without Mo and V additions) have been used in this project to evaluate the effect of such elements on hydrogen trapping during corrosion fatigue.

The microstructure of the material has a substantial influence on short fatigue crack growth behaviour. It is microstructural features such as texture and the distribution of effective barriers (grain boundaries, interfaces of different phases) to crack growth which brings about the anomalous or intermittent growth pattern of short cracks. The control of these barriers in terms of their size, strength and distribution has a profound effect on the fatigue resistance of materials.

Many attempts have been made to model fatigue crack growth behaviour. Of such models most are only applicable to some specific stage of the crack propagation process. The complex nature of short fatigue crack growth behaviour, and the relatively large scatter in experimental data require the use of statistical modelling methods. Of the existing theories, a recently developed method, i.e., the non-equilibrium statistical theory has been modified to take into consideration the microstructural features of a material thereby allowing a rationalisation of the experimental data.

In addition, since corrosion is time-dependant phenomenon, corrosion fatigue tests employing lower frequencies exhibit greater degradation than do tests at high frequencies where the overall exposure time at a given stress is greater [4, 5]. The corrosion process also has a statistical nature, hence a stochastic theory may be useful to describe the corrosion growth process.

Corrosion fatigue studies concerning marine structural steels are of prime importance for the life prediction and reliability assessment of offshore structures. This project explores the initiation and growth behaviour of fatigue cracks in RQT501 steel, a recently developed material for offshore use. In particular it has been the aim of the project to understand the possible influence of microstructure, corrosive environment and hydrogen embrittlement on the fatigue behaviour.

The main structure of this thesis is composed of ten chapters.

- Chapter 2 presents a brief literature review on air fatigue, corrosion fatigue mechanisms and existing fatigue crack growth models.

- The metallographic examination including grain size, inclusion size and shape and hardness measurement of the RQT501 steel used for the fatigue experiments is introduced in Chapter 3.
- The experimental work and corresponding results based on the study of short fatigue crack growth behaviour under tensile loading are given in Chapter 4.
- Details of long fatigue crack test results are given in Chapter 5.
- Comparisons are made between long and short fatigue crack growth behaviour and between the steels with and without the addition of Mo and V in Chapter 6.
- A fatigue crack growth model, modified to incorporate the influence of microstructure on fatigue crack growth is presented in Chapter 7.
- Chapter 8 presents a stochastic theory for corrosion process which is applied to a corrosion fatigue model.
- In Chapter 9 a model concerning the effect of hydrogen embrittlement on crack growth is described.
- The conclusions drawn from the present work and some future work suggestions are outlined in Chapter 10.

Chapter 2

Literature Review

2.1 Introduction

The cyclic deformation and fatigue characteristics of materials have been studied extensively for over a century [6]. However, debate continues amongst researchers concerning the various models and mechanisms which describe the fatigue failure process. To facilitate a better understanding of the subject, the process has been broadly classified into three main categories, namely:

(a) pre-crack deformation,

(b) fatigue crack nucleation and

(c) fatigue crack propagation.

The trend in recent evaluations has been to define a concept involving 'crack growth rates' rather than to specify the 'total life to failure'. This new direction has stemmed from the change to a 'fail safe' criterion rather than the use of a 'safe life' criterion which means designing for a finite service life during which significant fatigue damage will not occur. The fail safe criterion generally assumes that either cracks are present in the material before service or that cracks are initiated very early in the service history. These realistic assumptions suggest that crack growth controls fatigue behaviour. Therefore, crack initiation and crack growth measurement, which are also often made to provide data for application to structures in service to assess the risk of

failure or to predict the remnant life of structure known to contain cracks, represent important parts of the material property studies. Efforts are now underway to include a wide range of corrosion fatigue data in major design codes. Such data will provide a basis for predictive criteria for the safe utilisation of materials in a variety of environments.

2.2 Pre-crack Deformation

This step serves as the primary building block for the initiation and growth of cracks arising during the fatigue process. A number of research investigations [7-9] have shown that pre-crack deformation is accompanied by large amounts of irreversible plastic deformation that generate high local dislocation densities on slip planes. Modifications to the microstructure depend on the initial state and the test conditions and the resistance to deformation of a material may increase, decrease or remain unchanged. Cyclic hardening or softening is manifested externally as slip bands that are "persistent". It is these bands that eventually serve as initiation sites through the formation of intrusions and extrusions.

2.3 Fatigue Crack Initiation

2.3.1 Fatigue Crack Initiation in Air

Over the years, research in the general area concerning the fatigue behaviour of metals has led to several hypotheses for fatigue crack initiation [10-22]. Most investigators generally agree that initiation occurs at the surface although sub-surface nucleation has also been reported [10]. Fatigue cracks generally initiate

- where a surface roughness exists due to a stress concentration [13],
- from persistent slip bands in which minute extrusions and intrusions may form [17],
- within large grains [18] or at relatively weak grain boundaries [19],
- from non-metallic inclusions or oxides [20, 21, 22], due to
    - (1) cracking of the matrix close to the inclusion,
    - (2) decohesion or debonding at the inclusion/matrix interface,

(3) cracking of the inclusion itself,

- at second phase particles due to incompatible deformation with the matrix [21],
- at relatively soft regions such as the precipitate free zones adjacent to grain boundaries [17].

Other studies [20] of high strength carbon steels have shown that oxide inclusions were more damaging than other inclusions such as sulphides. Crack initiation was found to be dependant upon the size and shape of the inclusions.

A number of models for fatigue crack initiation have been proposed and can be generally classified into:

(1) single slip system models (Figure 2.1) [15, 23],

(2) alternating parallel slip system models (Figure 2.2) [16] and

(3) two intersecting slip line models (Figure 2.3) [11].

These crack initiation models, in which slip behaviour is characteristic of a given material and microstructure, are all attractive for ductile materials primarily because they are extremely general in their description of the nucleation process. None of the above models require deformation along specific slip systems nor is the deformation associated with specific conditions to be operable. Consequently, these models are preferred to other models which require specific conditions to be operable. The models based on repeated slip cannot satisfactorily explain the fatigue crack nucleation phenomenon in brittle materials. Typically these materials include: dispersion strengthened composites, high yield strength steels or materials containing brittle second phase particles. Thus, from the multitude of proposed models, it is clear that they cannot serve as a generalised interpretation for the crack nucleation phenomena observed in a wide range of materials. This situation is further complicated by the addition of an aggressive environment which adds difficulty to the development of a universal model.

2.3.2 Aqueous Environmental Effect on Fatigue Initiation

Contact with an aggressive environment probably has a similar effect on fatigue life as the machining of a sharp notch into the surface in that a pit, which acts as a stress concentration site, assists in the formation of a crack. It may be surmised that at its

basic level the corrosive environment simply facilitates the formation of geometric discontinuities on the surface of metal specimens. These discontinuities then give rise to fatigue cracks during cyclic loading.

Several mechanisms have been proposed in an attempt to provide a meaningful explanation of the role played by the environment on fatigue crack initiation. These mechanisms include but are not necessarily limited to:

(1) formation of corrosion pits and stress concentration at the base of the pit [24, 25],

(2) surface film rupture and preferential electrochemical attack at the ruptured sites [26],

(3) strain enhanced dissolution of slip steps [27-31] and

(4) lowering of surface energy due to adsorption of a specific species for the environment (hydrogen embrittlement) [32].

Surface inclusions are favourable sites for pitting initiation. Sulphides are inclusions which are particularly detrimental because they suffer chemical attack even from mildly aggressive environments. Furthermore, in plain-carbon and low-alloyed steels, sulphide inclusions act as cathodes of local cells and cause the surrounding metal to be anodically dissolved. Mixed sulphide-oxide inclusions have been found to be the most vulnerable sites for pit nucleation in both stainless, and carbon steels [33].

All the mechanisms that have been proposed involve a synergistic contribution of mechanical and chemical parameters. While some of the mechanisms require a dominance of the mechanical aspects, other mechanisms are influenced by the chemical aspects of the phenomenon.

2.4 Fatigue Crack Propagation

2.4.1 Three Stages of Fatigue Crack Propagation

It has been well established that fatigue crack propagation rate (da/dN) in metals generally varies with the stress intensity factor range $\Delta K = (K_{max} - K_{min})$ (Figure 2.4). In most metals, crack growth rates vary over a wide range, typically between 10^{-8} and 10^{-2} mm/cycle and may be divided into three distinct stages.

- At low crack growth rates typically below 10^{-6} mm/cycle, little is known about the mechanisms of crack growth, although growth rates are strongly sensitive to microstructure, load ratio $R = K_{min}/K_{max}$, stress history and environment. This region of growth is termed Regime I. The threshold stress intensity factor range below which no cracking occurs is termed ΔK_{th}.
- At crack growth rates between 10^{-6} and 10^{-3} mm/cycle, cracking proceeds by a transgranular ductile striation mechanism and there is little influence of microstructure and load ratio on propagation rates. This region is denoted Stage II or the Paris regime [34] region where da dN is related to ΔK by

$$da/dN = m_1 \Delta K^{m_2} \tag{1.1}$$

where m_1 and m_2 are scaling constants.

In cases where oxides or corrosion products build up or where surfaces are very rough the Paris law does not appear to be followed and ΔK is often replaced by ΔK_{eff}. The effective stress intensity is defined as [35]:

$$\Delta K_{eff} = K_{max} - K_{cl}$$

where K_{cl} is the stress intensity factor at which the two fracture surfaces first contact each other during the unloading portion of the cycle. Such contact prevents further crack closure and thereby lowers the cyclic stress intensity.

- At growth rates above 10^{-3} mm/cycle, instability is approached before final failure and the crack growth rate is much faster than that predicted by the Paris equation. This region is often termed Stage III of the fatigue process. Crack growth in this stage is influenced by microstructure, mean stress, and component thickness, but is not significantly affected by the test environment. The fracture mode in this region varies from cleavage to intergranular fibrous fracture [36, 37].

2.4.2 Concept of Short Fatigue Crack

Observation that short and long cracks behave differently were first made for fatigue crack growth during 1975-1980s [38-45]. Recent theories describing short cracks have

found increasing interest among researchers [46-64]. Three types of small cracks have been defined [13, 46, 50]:

(1) microstructurally short cracks (MSC): this type would include those that are of a size of the order of the microstructural features such as grain size or inclusion size. Plastic deformation near the crack tip is very much influenced by material microstructure and the grain boundaries will block or retard crack growth. The assumption of a macroscopic continuum in fracture mechanics is violated because of microstructural inhomogeneity.

(2) physically short cracks (PSC): In this type the length of the crack would be comparable to the plastic zone size. The crack closure is not fully developed because of the short crack wake.

(3) chemically short cracks: the third type would include those that are larger than the microstructural dimensions and the plastic zone size. But the crack-tip chemical environment controls the crack growth rate and is often different from the bulk environment. Short cracks may have a different crack-tip environment from long cracks, so that the propagation rate will be different.

A similar size characterisation can be made for short stress corrosion cracks; however, the length of chemically short stress corrosion cracks and corrosion fatigue (CF) cracks may differ because of the added effect of convection from mechanical pumping action on the crack tip chemistry during cyclic loading [43].

In all three cases short fatigue cracks were found to propagate at rates considerably higher than those of long cracks for what were thought to be similar crack driving forces described by ΔK [47-48]. Crack growth behaviour is characterised by alternating periods of acceleration, and deceleration but eventually becoming equal to long crack propagation rates at higher stress intensity ranges [49]. Ritchie and Lankford [45] recommended the use of an equivalent elastic-plastic field parameter to normalise the driving force between short and long fatigue cracks.

Crack initiation and the short crack growth stages are often inseparable because it is difficult to measure the behaviour of cracks of less than 10 μm in length and because the transition between initiation and growth may be continuous and not so distinct. Therefore, information on the behaviour of short cracks is more readily available than details of initiation.

Short crack growth behaviour may differ from long crack growth behaviour because of chemical gradients within the crack and also because cracks are short relative to microstructural features, plastic zone size and stress intensity factor fields. It has been pointed out that short cracks initially grow at a fast rate but then slow down and halt temporarily or arrest depending upon the applied stress level, as they approach a barrier to their growth (for example a grain or phase boundary) [52]. Over the past twenty years, studies of short crack growth using techniques such as optical, acoustic or electron microscopy have show that material microstructure plays a major role in short crack growth [13, 42, 52-54]. For the safe design of engineering components and structures, it seems appropriate that some microstructural aspects should be incorporated while analysing the short crack growth behaviour.

A significant level of understanding is necessary regarding differences between short and long cracks in terms of environmental effects. Several studies have been initiated in this direction [55-58]. There is evidence that short stress corrosion cracks can (1) propagate more slowly [65] or (2) propagate more rapidly [58, 66] than long cracks. Both cases have been demonstrated for (1) intergranular stress corrosion cracking of type 304 stainless steel [65], and (2) aqueous hydrogen-induced crack growth of high strength steels [66]. Crack size, shape, and geometry have also been shown to influence such large increases in the growth rates of short cracks [59, 66]. Thus, generalised relationships cannot be developed for the different interactions between metal and/or environments until a full physical understanding of the phenomena is established.

2.4.3 Fatigue Limit

The determination of the fatigue limit has played a significant role in the design of engineering components. Recent studies involving the observation of cracks whose size corresponds to that of the microstructural dimensions of the material have further enhanced the understanding of the fatigue limit phenomenon. As a result of work conducted over the last decade a new definition of fatigue limit has emerged. This limit is now seen not as a limit below which cracks fail to grow but one associated with the inability of very small surface defects or cracks to propagate beyond microstructural

barriers that are inherent within the material. For tests conducted in air, the fatigue limit stress range is related to the microstructural characteristics of the material through such factors as: grain size, texture and phase distributions which result from chemical composition, mechanical working and heat treatment processes. When tests are conducted under identical loading conditions but within an aggressive environment the fatigue limit stress shows a serious reduction and in many instances an elimination of this limit may occur.

2.4.4 Models of Fatigue Crack Propagation

A model for fatigue crack propagation should ideally take into account the influence of all the parameters that affect the propagation of a fatigue crack in a given material under given conditions. Unfortunately, such a comprehensive model has not yet been developed, primarily because of the large number of parameters involved. These parameters may be divided into two classes: the first includes "intrinsic" parameters which characterise the material itself (Young's modulus: E, shear modulus: μ, yield strength: σ_{ys}, ultimate tensile strength: σ_u, strain-hardening exponent: β, plane strain fracture toughness: K_{IC}, threshold stress intensity: ΔK_{th}), the second being the "extrinsic" parameters such as temperature, frequency, environment, specimen geometry, maximum stress intensity factor: K_{max}, minimum stress intensity factor: K_{min}, stress intensity factor range: ΔK, load ratio: R, etc. Careful and systematic experimental studies of the dependence of fatigue crack propagation on these numerous parameters require a great effort, the success of which in developing an ideal model is without guarantee. Scientists and engineers must critically design and carry out some specific experiments and then compare the experimental data with the models. The models may vary from purely empirical to very fundamental.

No attempt has been made to summarise the enormous literature which exists on correlation between da/dN and ΔK because many others have done this, e.g. Ref. [67]. However, it is now generally recognised that the driving force for short crack propagation is not properly characterised in terms of conventional linear-elastic or elastic-plastic fracture mechanics.

One recent, very broad review which will serve as an introduction to fatigue crack growth was published in 1986 [68]. Most of fatigue crack growth theories require a physical criterion that determines the extent to which the fatigue crack can advance. Table 2.1 [60-63, 69-85] only lists several theories proposed to explain the propagation of fatigue cracks and the relationships developed for crack growth. The theories proposed for crack growth are generally categorised into three major parts:

(1) phenomenological models, developed essentially on an empirical basis [33, 84], of which crack opening displacement (COD) models are representative;

(2) dislocation-based models [85], which give a specific process for crack advance in term of a micromechanism; and

(3) models for short fatigue crack [60-63].

- *Paris equation and COD models*

It must be stressed that the Paris equation (equation (1.1)) was proposed on a purely empirical basis. Therefore the primary use of this equation and of its derived version is to provide a data correlation scheme and a means to conveniently represent fatigue crack propagation data for engineering calculations. The values of the parameters m_1 and m_2 are experimentally determined, and predictions cannot be made if the mechanical properties of the material are changed or the extrinsic parameters (R, temperature, frequency) vary. These equations should be viewed as simply proposing a form for the fatigue crack propagation curves and not as prediction tools. In as much as the intrinsic parameters that they do identify are monotonic tensile and fracture properties they implicitly assume that fatigue crack propagation behaviour is controlled by these processes. It is not clear that this is the case. With these restrictions, such equations can be useful to the design engineer for the computation of structural resistance to fatigue crack propagation. They do not, however, provide guidance to the materials engineer for the development of alloy composition and thermomechanical treatment which would enhance fatigue crack propagation resistance.

Another group of theories were based on a shear sliding or COD criterion [76-81, 85]. Several variations of this concept have been presented by investigators by incorporating some of the material parameters into the crack growth rate equations. The COD theories have not been accepted universally because the crack propagation

rates are only a small fraction of the COD and clearly further modifications are necessary to derive any quantitative relationships that can compare favourably with the observed experimental crack growth rates.

- *Dislocation models*

Dislocation-based models address the problem along guidelines which are physically sound and based on fundamental mechanisms. In these approaches, however, the crack advance mechanism is highly idealised and assumptions (necessary to obtain solutions) are often over simplified Furthermore, Weertman's theory [75, 76, 85] and indeed any theory based on crack blunting and COD approaches generally lead to a fixed value of the exponent m_2 in the Paris equation, a conclusion which is clearly in conflict with the experimental values of m_2 varying generally in the range of 2 to 6 depending on material and testing conditions. Theoretical models based on crystal dislocation theory, such as that proposed by Yokobori et al. [82, 83], have the advantage of predicting a theoretical value of exponent m_2 which will change from one material to another, depending on the basic properties of dislocation motion in the material.

- *Short crack models*

Recently two models have been established which describe the discontinuous growth of a crack propagating through a polycrystalline material [60-63]. These models consider the propagation of a crack subject to growth rate perturbations arising from barriers inherent within the microstructure, e.g. grain or phase boundaries. The model derived by Hobson and Brown considers growth in essentially two regimes, that is, up to and then beyond the major microstructural barrier [60]. A similar development to that of the Brown-Hobson model is the theoretical model of Navarro and de los Rios which is based on a theory of continuously distributed dislocations [61-63].

Most short crack growth models are based on experiment and are semi-quantitative and therefore require further validation before becoming fully accepted.

All the proposed theories of crack propagation have shown a limited degree of success in terms of the different regions of the crack growth curve. The significant differences observed in the crack growth rates between short cracks and long cracks clearly indicate that several of the experimental/material/environmental variables may

have to be incorporated in the various equations before they can be generalised for a specific portion of the crack growth curve.

2.5 Corrosion Fatigue

The typical phenomena for corrosion products, the dissolution of the crack surface, and the interaction and coalescence of numberless cracks are well known. These phenomena have been studied by many researchers; however, the physical background of corrosion fatigue has not been discussed.

An Englishman Haigh, well known for his other fatigue work, in 1917 first mentioned corrosion fatigue and his studies were concerned with the qualitative aspects of material degradation [86], while in 1929 an American, McAdam [87] carried out many corrosion fatigue tests which are still referenced today by some authors, showing clearly how the fatigue limit was affected by increasing the time of immersion within an environment prior to air fatigue cycling.

Components or structures which had not been considered to be critically affected by fatigue up to recent times, suddenly exhibited fatigue problems, for example oil rigs in the North Sea. As a consequence, large research initiatives started, some results of which were reported in two large meetings in Paris in 1980 [88] and in Delft in 1987 [89], a veritable collection of information on corrosion fatigue of steels.

Many important problems of corrosion fatigue have yet to be resolved, for example why only a few minutes in a corrosive medium can have a detrimental effect, which however hardly increases even after several days.

2.5.1 Three Types of Behaviour

The observation of fatigue crack growth in-air coupled with observed effects of environments led to the classification of the process of corrosion fatigue crack growth onto three types of behaviour (Figure 2.5).

(1) True corrosion fatigue: the combined action of cyclic loading and corrosion, enhances crack growth under all conditions of loading except when the component is loaded to very high ΔK so that the system

undergoes very rapid rates of crack growth. In this rapid growth stage, the cause of crack growth is mechanical and is so rapid that it overshadows any effect of the chemical processes related to corrosion [90, 91].

(2) Stress corrosion fatigue: exhibits little or no environmental effects at low values of ΔK where the crack growth rates are very low. These low levels represent tests at stress intensities below the threshold stress intensity for stress corrosion cracking (SCC). This threshold stress intensity represents the minimum value of stress intensity necessary to cause crack growth K_{ISCC}. Environmental contribution to cyclic crack growth therefore only occurs at the high ΔK values where sustained crack growth can occur [90, 92].

(3) The third type of behaviour is a combination of the (1) and (2) types. Because of this combination, the behaviour can be generally adapted to describe fatigue in many metal-environment systems.

2.5.2 Rate Controlling Processes in Environment Assisted Fatigue Crack Growth

The mechanism of corrosion fatigue crack growth involves the interactive kinetics of the numerous process. The major processes that take place during corrosion fatigue crack growth are illustrated schematically in Figure 2.6 [93]. It can be summarised that there are several different steps, any of which can determine the crack growth kinetics [94].

(1) The supply of reactants and removal of products from the crack tip region.

(2) Reaction at the crack tip surface.

(3) Diffusion of atoms ahead of the crack tip.

(4) Partitioning of ions at the various microstructural sites.

(5) Rupture of protective films during cyclic straining.

(6) Production of freshly fractured surfaces by fatigue.

(7) Build up of corrosion products which influence crack closure and the effective stress intensity.

The above processes can act independently or synergistically and the importance of each process is different for each metal/environment system.

2.5.3 Corrosion Fatigue Models

The proposed models for predicting the corrosion fatigue long crack growth behaviour of metals are depicted in Table 2.2 [94] and can be categorised into [95]:

(1) Process superposition,

(2) Process competition,

(3) Process interaction.

Each of these models has been shown to correlate with specific experiments on steels and aluminium alloys, but no single model will explain all the available results in steels and aluminium alloys and little correlation has been developed for other alloy systems.

- *Process superposition model*

The superposition model assumes that the rate of crack growth in any environment can be predicted by summing the crack growth rates for pure mechanical fatigue and the rate for stress corrosion cracking processes. This model initially proposed that the processes occur simultaneously, but without interaction. More recently, the model incorporated possible interaction by the inclusion of a corrosion fatigue term. The general form for the rate of crack growth in any aggressive environment is therefore the sum of three components [91]:

$$(\frac{da}{dN})_e = (\frac{da}{dN})_{AIR} + (\frac{da}{dN})_{SCC} + (\frac{da}{dN})_{CF}$$

The first component $(da/dN)_{AIR}$, represents the influence of purely mechanical fatigue and is independent of frequency. The contribution of sustained load crack growth $(da/dN)_{SCC}$ term is applicable at test levels above K_{ISCC}, while the corrosion fatigue term, $(da/dN)_{CF}$ involves a cycle-dependent contribution which requires synergistic interaction of mechanical fatigue and stress corrosion cracking. The model is based on a stepwise procedure involving numerical or graphical analysis of data.

The superposition model is derived from empirical equations and has now been refined to the stage of semi-quantitative prediction of crack growth rates. However, because of the empirical nature of the models a reasonable correlation with experiment must exist even if the model has no physical basis. Any attempt to establish a totally quantitative model must incorporate the microfracture and microstructural events and distinguish the role of the aggressive environment without empirical determination of constants and equation forms.

- *Process competition model*

The process competition model is based on the assumption that fatigue crack growth rate involves competition among various processes. A typical schematic of the model is shown in Figure 2.7. For a given stress ratio, the relative roles of the competitive processes are frequency dependent. At low frequencies, true corrosion fatigue is unlikely, while stress corrosion processes will dominate. Stress ratio R can also determine which process is important for a given test frequency. If R is near zero or negative, stress corrosion is minimised and true corrosion fatigue processes will dominate.

Fatigue studies on a high strength aluminium alloy [96] and steel [97] using hydrogen gas showed that the process competition model overestimated the crack growth rates. The predicted growth rates are much higher than those observed in regions below K_{ISCC}. This is the major disadvantage of this model. The high predicted contribution due to stress corrosion cracking and predicted crack growth rates which are not representative of a true corrosion fatigue process, if the system is susceptible to stress corrosion.

- *Process interaction model* [95]

The process interaction model was developed to allow interactions to occur, particularly in alloy systems which exhibit a high degree of susceptibility to stress corrosion cracking [98]. Due to interactions one process may be inhibited or enhanced by the action of the other. A superposition equation which allowed for these interactions was developed where the fatigue and stress corrosion cracking components were added by:

$$(\frac{da}{dN})_e = m_1(\Delta K_{eff})^{m_2} + \int_0^{1/f} A\nu K_{eff}\alpha dt$$

Where ΔK_{eff} is the effective stress intensity factor which is adjusted to account for blunting and crack branching. The term ν accounts for the influence of load cycle on stress corrosion rate, f is the frequency and m_1, m_2, A and α are constants which are experimentally determined. As in the previous models, this model has been shown to correlate with data for steel and aluminium alloys in air and salt water [98]. Further experiments need to be performed to explain the effects of waveform and to establish the role of inhibiting reactions before the model can semi-quantitatively predict corrosion fatigue crack growth rates.

All the models proposed for corrosion fatigue are semi-quantitative and at worst, strictly empirical. The susceptibility of steel and aluminium alloys to stress corrosion cracking and corrosion fatigue has resulted in the large number of experiments with these material systems. One of the major assumptions made by all the crack propagation models is that the mechanical contribution to fracture of the fatigue process in the aggressive environment is the same as that measured in air. However, recent experimental investigations have shown that environment can influence the deformation and fracture behaviour of a material [92]. Though preliminary results show that the crack growth rates correlate with either of the three models, further work must be performed to include the influence of environment on the fatigue behaviour thus enhancing the validity of any of these crack propagation models.

The modelling of short fatigue crack growth in a corrosive environment has been made based upon the empirical model developed by Brown and Hobson for air fatigue tests, which incorporates a term representing the corrosion process of metal dissolution, namely [57]

$$(\frac{da}{dN})_{CF} = (\frac{da}{dN})_{AIR} + (\frac{da}{dN})_{DISS}$$

2.5.4 Corrosion Fatigue Mechanisms

Corrosion fatigue is in fact influenced by a variety of mechanical, chemical and microstructural parameters which interact, as shown in more recent reviews [95, 99].

Several different mechanisms have been proposed to explain corrosion fatigue behaviour of metals. These mechanisms include [95]:

(1) preferential electrochemical attack of plastically deformed metal [99],

(2) rupture of protective surface films,

(3) electrochemical damage to protective surface films,

(4) surface energy reduction due to adsorption of aggressive chemical species (especially atomic hydrogen (Figure 2.8)) and

(5) crack closure due to the wedging action of corrosion products.

2.5.5 Cathodic Protection

Cathodic protection is widely used to prevent general corrosion of non-stainless, carbon and C-Mn steels. It is also less frequently used to prevent general corrosion of other alloys and to prevent certain forms of localised corrosion. Properly designed, installed and maintained cathodic protection systems when applied to appropriate structures and components exposed to suitable environmental conditions, achieve these objectives very effectively. However, application of cathodic protection can also have detrimental side effects on the integrity of structures and components. Research has shown that even though protection reduces crack growth resulting from stress-assisted dissolution, the hydrogen evolved, via the cathodic reaction, may accelerate crack growth rates [100-101]. However due to the complex nature of corrosion fatigue, the crack growth can vary significantly, depending on the material, environment, specimen geometry and other factors. A detailed investigation is therefore usually required for a specific material under specific experimental conditions.

Cathodic protection essentially utilises the electro-chemistry of the corrosion reaction to prevent removal of metal ions from the surface. The principle is to eliminate the anodic sites on a structure, that is to make the whole structure a cathode. This can be achieved by applying an impressed current between an external anode and the steel which opposes the current resulting from the metal dissolution processes, providing electrons, and hence supporting reactions:

$$O_2 + 2H_2O + 4e^- \rightarrow 4OH^-$$

or

$$H^+ + e^- \rightarrow H$$

$$2H \rightarrow H_2$$

on the metal to be protected. The "thermodynamic" basis for a conventional cathodic protection system is to shift the metal potential from the active to the immune region where unreacted metal is the most stable product. This is associated with the lowest corrosion risk and is an essential requirement in environment where steel does not exhibit a region of passivity (e.g. seawater).

The hydrogen is generated by electrochemical reactions along the crack surfaces. The driving force for the reactions is the electrochemical potential difference between the bare surface at the crack tip, and the adjacent filmed surfaces along the crack flank. The rate of the reaction, and hence the rate of hydrogen production, depends on the local "chemical environment" at the crack tip region (i.e. electrochemical potential, and species concentration) and the nature of the reaction processes. The local environment is expected to be different from the bulk, and is determined by the electrochemical mass transport processes and the reactions at the crack tip and along the crack flank.

These results do not mean that the crack-tip potential is always the same irrespective of the potentials applied to the outer surfaces. Landles et al. [102] measured the potential drop along real cracks and the crack-tip potentials, for a high yield strength steel (HY80) immersed in seawater. They demonstrated that potential gradients were insignificant and the applied potentials almost reached the crack tips, when the applied potential was not too far from the free-corrosion potential, such as at -0.6 and -0.8 V_{SCE}. In addition, they reported the changes in pH in simulated cracks in seawater, reaching about pH 6 at -0.6 V_{SCE} applied potential and about pH 9 at -0.8 V_{SCE}.

Numerous reports have been published throughout the literature showing the influence of cathodic polarisation on fatigue crack growth. Such studies involve both smooth and pre-cracked specimens. A number of interesting conclusions may be drawn from these studies. The approach, which uses smooth specimens to generate curves of cyclic stress range against the number of cycles to failure ($S \sim N_f$ curve), indicates that cathodic protection in seawater restores the corrosion fatigue properties of low and intermediate strength steels to at least, and possibly to better than, the fatigue properties in air. Conversely the second approach, which uses pre-cracked specimens

and fracture mechanics techniques to generate curves of crack growth rate against cyclic stress intensity range (ΔK), indicates that cathodic protection in seawater results in a further acceleration of the corrosion fatigue crack growth rate of low and intermediate strength steels, especially at high R ratios and low frequencies. This conflict is as yet not fully resolved but it has been suggested that the eliminating of pitting, a non-triaxial stress state and highly oxygenated crack tip condition for short cracks offset the effects of hydrogen on polarised smooth specimen [103]. It is also apparent, although seldom discussed, that amongst such data there appears to be a notable increase in the threshold stress intensity for specimens tested under cathodic polarisation (CP). Results from both smooth and pre-cracked specimens raise the question as to the importance of initial defect development under applied CP. In summary it was suggested that the primary benefits of CP occur when the crack is less than 40 ~ 50 μm in length and that as crack lengths increase growth rates become comparable with those found for freely corroding conditions [103].

The effect of cathodic protection on the fatigue and corrosion fatigue properties of low and intermediate strength steels, and on the fatigue and corrosion fatigue performance of offshore structures, is still not fully understood and remains a very active research area [104, 105].

2.5.6 Hydrogen Embrittlement

Enhancement of crack growth in high-strength steels by either dissolved hydrogen or external hydrogen, and by hydrogenous environments, is a well-known material problem, and is commonly termed "hydrogen embrittlement". This problem has direct bearing on structural integrity, durability and reliability, and is of broad technological importance. To develop methods for alleviating this problem, both the fundamental processes that lead to hydrogen entry and diffusion and the subsequent chemical and physical changes in the steel that lead to embrittlement must be understood. These methods may involve controlling or altering the environment, or modifying the composition or microstructure of the steel.

It is well established that high strength, low alloy, quenched and tempered steels (i.e. those with yield strengths in the range 900 ~ 1700 MN m^{-2}) are potentially

susceptible to hydrogen embrittlement. The susceptibility increases with strength level. Typically, however, at the higher strength levels, these steels exhibit slow crack growth (which is usually intergranular with respect to the prior austenite grain boundaries) when simultaneously exposed to aqueous environments (particularly if they contain chlorides) and static tensile stresses. The cracking is due to the small amount of hydrogen generated by the cathodic, hydrogen evolution reaction that is not evolved as molecular hydrogen gas but instead enters the steel as atomic hydrogen. Attempts to protect such steels cathodically would therefore be quite disastrous. The amount of hydrogen evolved and entering the steel would be increased and components and structures would suffer severe embrittlement and cracking.

Recent observations have shown that most types of hydrogen-induced fracture modes are at least microscopically ductile even though macroscopically brittle behaviour is observed. As a result, it has been proposed that hydrogen enhanced localised plasticity, which is directly associated with the hydrogen-induced fracture, is the controlling factor in hydrogen-induced cracking of iron and steels [106, 107].

In hydrogen charging studies, contradictory experimental results, either softening or hardening, have been observed depending on the charging conditions (hydrogen fugacity, temperature, strain rate, purity of iron, and other significant experimental factors) [108]. Lewandowski and Thompson [109] have shown in blunt notch samples of 1080 steel that hydrogen-induced "cleavage" produces a microscopically more ductile surface compared to non-hydrogenated samples. There is also the very strong evidence in Fe-3 wt% Si [110] that enhanced localised plasticity did not assist the cracking process but retarded it.

It has also been pointed out that the extent to which fatigue crack growth is enhanced by hydrogen tends to increase with increasing hardness [33]. In the hardest material, the rate of cracking was accelerated by a factor of over 100. These results support evidence from tests conducted under static load that the susceptibility of gas cylinder steels to the effects of hydrogen is largely controlled by the hardness of the steel, chemical composition and microstructure appearing to exert less influence.

The increasingly adverse influence of cathodic potentials on fatigue crack growth rate may be explained on the basis of a hydrogen embrittlement mechanism. It can be speculated that the two competing processes in this situation are hydrogen

build-up or its availability at the crack tip and the effective crack tip strain rate in developing freshly created metal. Hydrogen entering the metal lattice at the crack tip via freshly created surfaces, builds up to a concentration sufficient to induce brittle cleavage fracture over a distance ahead of the crack tip, the extent of which is determined by the effective strain rate at the crack tip. Mobile dislocations can also carry hydrogen atoms to increase the apparent diffusivity. Once the hydrogen reaches the crack tip, it is partitioned among the various microstructural elements (grain boundaries, internal interfaces, dislocations, voids, microcracks and foreign atoms), where a large percentage of it is trapped. The trapping essentially binds a percentage of the mobile hydrogen to specific microstructural elements, thus making it unavailable for further embrittlement of the material. This results in the continuous need for additional hydrogen supply as the crack grows. Once the hydrogen is partitioned and trapped, embrittlement occurs, and this lowers the material's resistance to crack growth. When combined with the ongoing mechanical fatigue process, an enhancement in the crack growth rate results [111]. Both the lattice-dissolved and trapped hydrogen can influence various modes and stages of the internal crack and propagation processes.

At the free corrosion potential, the evidence also points to a dominant influence of hydrogen embrittlement, although in these circumstances dissolution at the crack tip may be thermodynamically possible. The observation of brittle fracture and the increase in fatigue crack growth rate produced by environmental changes are all consistent with such a view.

The inclusion/metal interface can act as either a site for microcrack and void initiation or a trap and sink for hydrogen. Consequently, it can either enhance or inhibit hydrogen damage. In quenched steel, the sulphide/metal boundaries are often decohered because MnS and other sulphides contract more on cooling than does the martensite. The resulting cavity between the inclusion and the matrix has often been considered to act as an irreversible trap for hydrogen.

Slip at the crack tip is considered to play an important role in fatigue crack growth. There are some other suggestions that dissolved hydrogen facilitates dislocation multiplication and motion, and decreases the flow stress [101]. These lead to a mechanism whereby hydrogen absorbed into steel activates the fatigue crack growth process, that is cyclic plastic-deformation.

The precise mechanism of hydrogen embrittlement is still not fully understood, although it has been suggested that atomic hydrogen enters the metal lattice and causes decohesion, hence lowering the loads necessary to cause fracture.

2.6 Statistical Theory of Fatigue

In general, large amounts of scatter in experimentally obtained fatigue data have been observed. This indicates that the reliability of such data must be evaluated before it is applied to the design of machines and structures. The fatigue life of plain specimens is controlled mainly by the initiation and propagation lives of a small surface crack. Therefore, to clarify the statistical behaviour of a small crack is important to understand the physical background of the reliability of fatigue damage. Several studies concerning the statistical behaviour of a small crack in air have been reported; however, such studies made in corrosive environments are rare. In corrosion fatigue, cracks are initiated from corrosion pits, then they propagate accompanied by the interaction and coalescence of other cracks. Accordingly, an investigation of the statistical characteristics of corrosion fatigue is crucial to the safe design of machines and structures operating in corrosive environments.

A century of experimental research into fatigue crack growth has demonstrated that fatigue cracks grow in an inherently stochastic manner. There are always large fluctuations, sometimes over an order of magnitude or more, in macroscopic observables such as the instantaneous crack velocity, da/dN, and the cycles to failure. Yet before the last decade there were very few attempts to analyse quantitatively the relationship between these fluctuations and the intrinsic variability of the various material characteristics, such as local grain size, yield stress, and crystal orientation, that control the mechanics of growth. The attention of fundamental theories was usually restricted to the law of average growth rate, and its dependence on stress level, grain size, environment, etc.

More recently, the statistical nature of fatigue has received a lot of attention [112-125] and significant effort has been made to match more sophisticated and flexible statistical models to experimental data. They include formulations in terms of diffusion equations [112, 113] and conservation equations for probability densities

[114]; Monte Carlo simulations [115, 116]; Markov chains [117-121]; birth processes [122]; point processes [123]; and stochastic differential equations [113, 117, 124]. However, the variety in mathematical formulation does not constitute the most important division between these various approaches. From a functional point of view, most of them may instead be considered to fall into two categories.

In the first, more numerous category, the models begin with the least generality necessary to reproduce the average and variance of engineering growth rate data (for example Refs. [112, 113, 117, 118, 123, 125]). In some cases, the sophistication has been gradually increased as the relevance of further details of the statistical data, such as the covariance of crack velocities measured at different lengths, has been recognised [113]. These models usually purport to have some ability to calculate the effects of changes in stress level, even to the case of spectral loading, but in a way that is based on simplistic growth rate laws. Such approaches are probably valid accounts of the statistics of cracks that grow according to linear elastic fracture mechanics. However, they are probably inaccurate and certainly physically unrealistic when applied to the propagation of short fatigue cracks. In many circumstances, short crack propagation constitutes a large proportion of the fatigue lifetime.

The second category of probabilistic models has attempted to address this shortcoming by building explicitly upon detailed knowledge of the micromechanics of short crack growth. For example, in certain popularly studied aluminium alloys, deterministic laws have been established that describe the dependence of growth rate on the immediate microstructural environment of the tips of surface fatigue cracks. The microstructure is itself stochastic, and it has been shown in Monte Carlo simulations [116] and by a kinetic model [114] that the fluctuations observed in growth rate data can be directly traced to fluctuations in the grains being traversed. These models have been and will continue to be extremely useful in connecting growth data with micromechanical theories.

In general these works are phenomenological and only in isolation study the statistical nature of one problem of fatigue, for example, the statistical nature of fatigue crack growth or fatigue life. References [126-129] have studied, in unison, the microscopic mechanism of fatigue and its macroscopic statistical nature on the basis of non-equilibrium statistical concepts and methods. But the effect of microstructure on

short crack growth behaviour has not been considered thoroughly. Therefore a new explanation is required. In this work, we try to prove that short fatigue crack propagation can be described theoretically in microscopic terms and with non-equilibrium statistical concepts and methods.

Chapter 3

Metallographic Examination of RQT501 Steel

3.1 Material

The material used for all the experiments was RQT501, a low carbon structural steel platen plate of 12.5 mm thickness without the addition of Mo and V and of 25 mm thickness with Mo and V additions product developed for marine applications. The material was tested in the 'as received' condition with no additional heat treatments of the plates. The chemical composition and mechanical properties of the steels are given in Table 3.1.1 and Table 3.1.2 respectively.

3.2 Grain Size

Figure 3.2.1 presents a schematic of the orientation and position of the microstructure studied. A metallographic examination was performed on a polished and etched cross-section. Photomicrographs representative of the microstructure of the tempered martensite observed are shown in Figure 3.2.2. As shown in Figure 3.2.2, there was little variation in grain size.

Quantitative analyses of the grain sizes and distributions based on measurements made using the computer based Replica Analysis System (Repan) are given in Figures 3.2.3-3.2.8. A schematic of these analyses has been shown in

Table 3.2.1. Based on these results it may be concluded that there is no appreciable effect of orientation on grain size. The average grain size of both steels was found to be 8.6 μm and 10.7 μm respectively.

3.3 Inclusion Types

From the scanning electron microscope (SEM) type JEOL-JSM-6400 it has been observed that for both steels the types of inclusions can be divided into three categories. Analyses of both steels show that oxide and sulphide inclusions are present. Oxide types are seen to consist of Al and Mg oxides (Figures 3.3.1-3.3.2) while sulphide inclusions are present as Mn, Fe and Ca sulphides (Figures 3.3.3-3.3.4). In both types of inclusions, i.e., oxides and sulphides, mixed elemental types can be seen (see Figures 3.3.5-3.3.6) with the dark part of the inclusion being the oxide, while the light part is representative of sulphide. This occurs possibly because Al_2O_3 particles act as nuclei for the precipitation of sulphides during solidification of the steel from the melt. In terms of inclusion content, there are no obvious differences between the two kinds of steel.

3.3.1 Inclusion Size

For both steels the quantitative characterisation of inclusions, as presented in Figures 3.3.7-3.3.12, was made using data from an Optomax v Image Analyser (VANOX). Details for both feature analysis and field analysis from both VANOX and Repan analyses are given in Tables 3.3.1-3.3.4. It can be seen from these figures that for both steels the average inclusion size is around 8 μm, and the area fraction of inclusion is less than 0.9 %.

- **Steel A: 12.5 mm thick (no Mo/V)**

Along the rolling direction (L direction) only one section shows that the inclusion size (Z) is larger than along an other direction (face 1: $Z_L > Z_T$). However on the other section the opposite result (face 2: $Z_L < Z_V$) is found.

- **Steel B: 25 mm thick (with Mo + V)**

Along the rolling direction the inclusion size is slightly larger than it is along other directions (face 1: $Z_L > Z_T$, face 2: $Z_L > Z_V$).

In these experiments, the results of one section of Steel B are little different from other specimens. However microscopical examination shows that there are large inclusions in the section.

In general, the inclusion size and the inclusion density are smaller for Steel A than those for Steel B.

3.3.2 Inclusion Shape

The shape of inclusions in all specimens is predominately round despite the fact that the material has been rolled (Figures 3.3.1-3.3.6). It is most common for sulphides to begin to precipitate at an early stage of solidification and therefore assume globular shapes. These inclusions are much harder to deform during hot rolling than the sulphides which are among the last species to solidify and so they freeze as chain like formations or thin precipitates in the primary grain boundaries and between dendrites. The later type of sulphide, however, is relatively soft. During hot rolling they re-orient parallel to the major direction of rolling and further elongate to form thin sheets of MnS in parallel arrays. Hence, there are some elongated inclusions (Figures 3.3.13-3.3.14).

3.4 Measurement of Hardness

Hardness implies resistance to deformation; i.e., a measure of material resistance to permanent or plastic deformation.

The type of test used to determine hardness is Vickers hardness test, in which a 136° diamond pyramid is forced into the material being tested. The relationship between total test force and the area of indentation provides the measure of hardness.

3.4.1 Vickers Hardness Test

A diamond indenter, in the form of a pyramid with a square base and an angle of 136° between opposite faces, is forced into the LV section of the steel under a load of P = 500 g which is maintained for 20 seconds. The two diagonals d_1 and d_2 of the indentation left in the surface of the material after removal of the load are measured and their arithmetic mean d calculated. The area of the sloping surface of the indentation is calculated, the indentation being considered as a pyramid with a square base of diagonal d and vertex angle of 136° .

The Vickers hardness number is the quotient obtained by dividing the load P, expressed in kilograms force, by the sloping area of the indentation expressed in square millimetres.

$$H_v = \frac{\text{Applied Load (Kg)}}{\text{Contact area of indenter (mm}^2\text{)}}$$

$$= \frac{2P\sin\theta/2}{d^2} \times 1000$$

$$= 1854.37\frac{P}{d^2}$$

Where H_v: Vickers hardness number (kg/mm^2), P: Applied Load (g), θ: Angle between opposite faces (136°), d: Diagonal of indentation.

3.4.2 Results of Hardness Test

Five rows of indentations along the thickness (vertical direction) equally spaced were made. In each row the distance between two nearest pyramids is 1 mm. The distributions of Vickers hardness numbers are given in Figure 3.4.1 and Figure 3.4.2. The profiles of hardness across plate thickness for both steels show that Vickers hardness number tends to lower value in the centre than that on both sides of the sample. Average Vickers hardness numbers on the LV section are 202 HV500 for 12.5 mm thick Steel A (no Mo/V) and 216 HV500 for 25 mm thick Steel B (with Mo + V). From hardness conversion table for ferrous metals, this gives an equivalent tensile strength of 682 MPa (Steel A) and 737 MPa (Steel B) respectively which

approximate with the results of the tensile tests. Figure 3.4.3 and Figure 3.4.4 give the distributions of tensile strengths along the thickness for both kinds of steel.

The diameter of the centre region of the smooth hour-glass shaped specimen, used for short fatigue crack growth test, is about 6 mm. Average Vickers hardness numbers within this region are 198 HV500 for Steel A (no Mo/V) and 194 HV500 for Steel B (with Mo + V), which give equivalent tensile strengths of 680 MPa (Steel A) and 664 MPa (Steel B). As shown in Figure 3.4.2, the variation of the hardness across the centre part is larger in Steel B than that in Steel A.

3.5 Summary Remarks

Based on the metallography examination, the following conclusions have been made.

(1) The average grain size (d) for Steel A and Steel B is around 9 μm and 11 μm respectively.

(2) The mean inclusion size for both steels is about 8 μm. The area fraction of inclusion within the steels is less than 0.9 %.

(3) Average Vickers hardness number for 12.5 mm thick Steel A (no Mo/V) and 25 mm thick Steel B (with Mo + V) on the LV section is 202 HV500 and 216 HV500 respectively.

(4) Average Vickers hardness numbers within the centre region of the hour-glass specimens are 198 HV500 for Steel A (no Mo/V) and 194 HV500 for Steel B.

(5) The variation in the distribution of hardness is smaller for Steel A than for Steel B.

Chapter 4

Uniaxial Tensile Short Fatigue Crack Tests

4.1 Introduction

Offshore structures normally experience long-term low frequency wave loading, hence fatigue studies for materials employed on these structures have in the past been conducted extensively within natural and artificial seawater at low cyclic frequencies.

To date, much of the research work conducted has been concerned with fatigue crack growth using specimens with pre-existing defects, i.e. pre-cracked specimens. Undoubtedly this work has been invaluable particularly where a defect-tolerant approach is adopted. However it should be noted that for components which contain minimal surface defects the information provided from such studies is of limited value when, for example, predicting corrosion fatigue performance under applied cathodic polarisation.

In the present work, smooth shallow hour glass specimens of RQT501 steel have been used to evaluate the fatigue response ($S \sim N_f$ curve) and fatigue crack growth rate in air and in 3.5%NaCl solution or artificial seawater under freely corroding conditions and under applied cathodic polarisation (-950 mV vs. SCE). Long fatigue crack growth tests have also been conducted for this steel to enable a comparison of short and long fatigue crack growth which will be detailed in the next chapter.

4.2 Specimen and Experimental Procedures

Hour-glass shaped test specimens were machined from the centre part of the steel plate. The axis of the specimen is parallel to the rolling direction (RD) of the plate (Figure 4.1). The gauge area was carefully polished with a succession of finer grade emery papers after which polishing was completed using diamond pastes down to 1 μm grade. In order to reveal the effect of microstructure samples were etched in a 2% Nital solution for about 50 seconds for tests in air.

Cyclic fatigue loading was applied to specimens using a Mayes (± 100 kN) servo-hydraulic and servo-electric
fatigue testing machine. The standard test conditions were as follows:

- load control;
- applied stress ratio, R = minimum stress/maximum stress = 0.1;
- frequency, f = 5 ~ 10 Hz in air and 0.2 Hz in 3.5%NaCl solution under freely corroding conditions and cathodic polarisation;
- sinusoidal waveform.

5 ~ 10 Hz is used in air because fatigue life is relatively insensitive to frequency. Above 10 Hz it is recognised that the dynamic calibration of a fatigue machine can be susceptible to errors. 0.2 Hz is a favourable frequency for testing offshore materials in seawater as it lies close to that of seawave frequency (0.167 Hz) and provides a slight increase in the rate at which fatigue data are required.

To enable a comparison between the effect of 3.5%NaCl solution and that of artificial seawater, extra specimens were tested in artificial seawater. Fatigue crack growth data were obtained by taking acetate replicas from the surface of the centre region at certain intervals during the tests.

As a corrosive environment, 3.5%NaCl solution or artificial seawater kept at room temperature was used. The solution was continuously circulated between the corrosion vessel containing the specimen and the tank at a rate of about 800 cm^3/min by means of a pump. The solution was renewed for each test.

When tests were carried out under applied cathodic polarisation at the potential of -950 mV/SCE, a three electrode cell and a potentiostat (Figure 4.2) were used to control the potential of the specimen. The cell includes the fatigue specimen commonly

called the working electrode (WE), a reference electrode - a saturated calomel electrode (SCE) in contact with the solution via a salt bridge and an auxiliary electrode (AE) made of graphite to supply the current from the potentiostat. VoltaMaster 1, a powerful application software developed under Windows 3.1 was used to ensure complete control of the PGP201 potentiostat and efficient current ~ time data processing, which was used for the last three tests (SCA1CP, SCA5CP, and SCBS2).

The observations of fatigue damage on the specimen surface and measurements of crack length were made via plastic replicas using an optical microscope. The crack length, a, is the length along the circumferential direction on the specimen surface. The value of stress level, $\Delta\sigma$, is the nominal stress range at the minimum cross-section.

4.3 Analysis and Results

4.3.1 $S \sim N_f$ Curve

Figure 4.3 shows the $S \sim N_f$ curve in different environments corresponding to the data given in Tables 4.1-4.2 for both steels. The results of fatigue life data in laboratory air and in 3.5%NaCl solution under open circuit potential (OCP) and under applied cathodic polarisation (CP) (-950 mV/SCE) are drawn with broken lines, chain lines and solid lines respectively. The fatigue life to failure, N_f in 3.5%NaCl solution is smaller than that in air and the difference in N_f between 3.5%NaCl solution and air increases with decreasing stress range. The relationship between the stress range and fatigue lifetime was obtained through a regression analysis of the data giving the following equations:

$$\Delta\sigma^{n_1} N_f = n_2$$

where n_1 and n_2 are constants which are giving in Table 4.3. The results show that cathodic polarisation in 3.5%NaCl solution restores the fatigue endurance of the smooth specimens to values near those obtained in laboratory air. This means that cathodic polarisation is effective for the smooth specimens.

Figure 4.4 illustrates two different types of typical behaviour of the steel under fatigue loading conditions - "plastic accommodation" and progressive deformation [130]. As shown in Figure 4.4a, the plastic accommodation has the tendency to

stabilise, even for small loading amplitudes, there was often a slight increment of deformation with time, specimens were broken as fatigue cracking dominated failure. Figure 4.4b illustrates the shape of the progressive deformation curve for Steel B tested in 3.5%NaCl solution (OCP) at stress level of 527 MPa. Progressive deformation without accommodation occurs if there is decrease in cross-section due to necking. This different behaviour can be related to the high stress induced failure. A time-dependent deformation appears as soon as the stress reaches a sufficient value. At a higher stress level, the failure mode of the RQT501 steel was characterised by conventional tensile necking failure. Although fatigue cracking damage has sometimes also developed simultaneously, the necking instability emerged as the dominant mechanism of failure.

Therefore, the failure modes observed can be categorised into two regimes. These are:

(a) Fatigue cracking dominated failure (high-cycle fatigue) (curve II in Figure 4.3),

(b) Necking dominated failure (low-cycle fatigue) (curve I in Figure 4.3).

Fatigue cracking dominated failures arose due to the growth of surface cracks through the specimen, with no evidence of any unstably necking damage. Under high stress level testing conditions, the necking component dominates, and there is no fatigue cracking damage present. During testing of Sample SCSA2, necking damage was found within the material in addition to surface fatigue cracking damage. Fatigue cracking and necking damage initially developed independently and the likelihood of true interaction depended on the balance between them. Eventually the necking damage resulted in accelerated fatigue crack growth and a reduction in endurance. Therefore, it might be an extra reason why the fatigue strength under applied cathodic polarisation was smaller than that in air due to the frequency changing from 10 to 0.2 Hz in addition to the change of environment. In the present work, the fatigue dominated crack growth behaviour are mainly investigated.

- **Steel A (no Mo/V)**

The $S \sim N_f$ curves for Steel A in air and in 3.5%NaCl solution under applied cathodic polarisation are quite flat. Hence, it is not clear to see the transition point

from high-cycle fatigue failure to low-cycle necking failure. The fatigue limit in air is only about 30 MPa below the tensile strength and fatigue cracking dominated failures could be only found when the stress levels are within 10 MPa of the fatigue limit (516 MPa). If the stress level increases more, necking dominated failure occurs.

In 3.5%NaCl solution (OCP), the regimes of which corrosion fatigue cracking dominated (curve II) and necking dominated failure (curve I) are distinctive. As shown by curve II, the reduction in the cycles to failure, relative to air data, produced by testing smooth specimens in 3.5%NaCl solution is the result of corrosion, and particularly of pitting, accelerating initiation of corrosion fatigue cracks and possibly also propagation of very short cracks. Hence, the fatigue endurance (240 MPa) at 10^7 cycles in 3.5%NaCl solution is far below that in air. In regime I, due to the formation of cavities within grain boundaries is the main mechanism for necking failure, the corrosive 3.5%NaCl solution accelerates the process and therefore causes a reduction in the cycles to failure, relative to that in air.

Cathodic polarisation in 3.5%NaCl solution restored the fatigue properties mostly to the level observed in air firstly by eliminating the accelerated crack initiation and secondly by hindering the propagation of short cracks, since these processes have a predominant effect on the number of cycles to failure.

- **Steel B (with Mo + V)**

For Steel B, at the stress levels of 516 MPa and 495 MPa, compared with the fatigue life in air, the fatigue life in 3.5%NaCl solution (OCP) is reduced by approximately 87% and 93%, however, restored by about 25% and 27% respectively when cathodic polarisation is applied. Test in air, at the stress level of 475 MPa, was terminated at 2.2×10^6 cycles due to no-failure and the lack of any observable cracks found from the replicas thereby suggesting that the fatigue limit is around 480 MPa in air. In 3.5%NaCl solution, value of N_f was 151913 cycles for the stress level of 396 MPa. Under applied cathodic polarisation in 3.5%NaCl solution the fatigue lifetime is more than twice the value of that under freely corroding conditions.

It is deduced from the regression line that the fatigue endurance at 10^7 cycles is near 160 MPa in 3.5%NaCl solution which is considerably lower than 480 MPa in air and 390 MPa under applied cathodic polarisation.

An additional test, SCB1, was conducted for Steel B in 3.5%NaCl solution (OCP) under two different stress levels - 360 MPa for the first 35000 cycles and 495 MPa for the remaining 79237 cycles. Its lifetime (114237 cycles) is above that 62563 cycles under stress level of 495 MPa.

4.3.2 Crack Initiation

- *In air*

The cracks observed from the replicas taken were measured using an image analysis system. Observations made from replicas showed that in air many major cracks for Steel B originated from large non-metallic inclusion sites with an average size about 25 μm (arrowed in Figure 4.5). However, for Steel A, all the three in-air fatigue cracks were found to initiate from quite small sizes which were around that of the average grain size (9 μm). Figure 4.6 shows initiation and growth behaviour for two typical air fatigue cracks - Crack 1 and Crack 2. In one test of Steel B (with Mo + V) the phenomenon of the coalescence of two cracks that originated from inclusions was found as shown in Figure 4.7.

- *In 3.5%NaCl solution (OCP)*

The results of corrosion fatigue tests show that corrosion pits were generated during the early stages of cycling, then grew gradually with cycling. Figure 4.8 shows that some pits formed a crack and from Figure 4.9 it can be seen that a crack was initiated from a corrosion pit after the growth of the pit. The transition pit diameter from which a crack grows, $a_{p/c}$, and the time for the transition, $t_{p/c}$, seem to be dependent on the applied stress level as shown in Figure 4.10 and Tables 4.5-4.6. When the stress level increases, the transition pit diameter increases while the transition time decreases. A corrosion pit initiated under stress range above 471 MPa seems to be rather different in its properties from that generated under 396 MPa. That is, for the case of stress range over 471 MPa, comparatively small corrosion pits were generated with a high density. For the cases of 396 MPa, however, corrosion tended to general corrosion and a small number of corrosion pits whose diameters were relatively large were generated.

The above experimental results concerning the behaviour of a corrosion pit may be expected if one considers that although the generation of a corrosion pit does not necessarily need stress cycling, repetitions of relatively high stress under which a slip band is generated definitely contribute to the generation of a corrosion pit, because a corrosion pit is easily generated when a slip band exists. Hence at high stress levels the mechanical driving force dominates pit and crack growth. As for the behaviour of a corrosion pit under a low stress range where slip bands have a low density, the mechanical driving force is reduced and testing periods increase such that time-dependent corrosion reactions are of increasing importance. On the other hand, the pit growth and crack initiation behaviours are affected by stress cycling. The growth rate of a pit increases with an increase in stress level.

As shown in Figure 4.11, for the test of SCB1, due to the lower stress (360 MPa) during the first 35000 cycles, the crack initiated relatively later from a pit than that of SCB6 which was conducted at a stress level of 495 MPa, the same condition for the last 79237 cycles of SCB1.

- *In 3.5%NaCl solution under applied cathodic polarisation (-950 mV SCE)*

When cathodic polarisation was applied, i.e. under conditions of hydrogen evolution reaction, damage of the surface was observed, especially on the very edge of the surface near the polishing scratches and surface defects such as inclusions, some of which developed into cracks (Figures 4.12-4.14). In this case, such behaviour can be characterised as a sharp, local decrease in strength and embrittlement of the steel. The reason for such changes may be considered as local hydrogen embrittlement of the steel, under combined action of mechanical stresses and generated hydrogen playing a role of strong surface-active component.

Apparently, geometrical misfits and/or other structural imperfections such as scratches which might be present do not cause a critical local concentration of hydrogen in the absence of externally applied stresses. However, in the presence of an applied load, they can induce cleavage crack nucleation in hydrogen-charged iron. This probably occurs since in polycrystalline materials each grain deforms differently depending upon its crystal orientation and size with respect to the tensile axis.

Dislocations pile up at the grain boundaries during straining and localised shear stresses and strains result, causing cracks to nucleate and grow.

4.3.3 Crack Propagation

The propagation curves under applied cathodic polarisation in 3.5%NaCl solution are shown in the Figures 4.15a-4.15b for comparison with those in air and in 3.5%NaCl solution (OCP). The ratio of propagation life of a crack at its later growth stage (e.g. above 200 μm) to the total fatigue life is larger in 3.5%NaCl solution than that in air and that in 3.5%NaCl solution under applied cathodic polarisation as shown in Figures 4.16a-4.16b. The main reason for the decreasing growth rate in 3.5%NaCl solution may be due to the wedge action caused by the corrosion products. The application of cathodic polarisation delays the crack initiation but accelerates the growth rate when the crack length reaches a certain value, for example, about 100 μm at the stress level of 516 MPa.

The fatigue crack growth rates, da/dN, were estimated by using a secant method

$$\left(\frac{da}{dN}\right)_{i+\frac{1}{2}} = \frac{a_{i+1} - a_i}{N_{i+1} - N_i}$$

where a_i and a_{i+1} are two consecutive half surface crack lengths at N_i and N_{i+1} number of cycles respectively. Since the fatigue crack growth rate represents the growth of a crack at the mid point of two consecutive crack lengths, the corresponding average crack length at this point is $\frac{a_{i+1} + a_i}{2}$. Examples of experimental fatigue crack growth rates versus crack lengths under different environments are presented in Figures 4.17a-4.17b. It can be seen from these figures that fatigue cracking follows a similar trend, i.e., an initial rapid growth after which a deceleration and minimum growth rate occurs at a certain crack length. The growth rate of a crack is usually larger in 3.5%NaCl solution (OCP) than in air due to the corrosive dissolution. In 3.5%NaCl solution under applied cathodic polarisation, the growth rate of a crack is obviously higher than that both in 3.5%NaCl solution and in air when the crack length is around 100 μm ~ 1000 μm.

4.3.4 Etching Effect and Corrosion Fatigue in Artificial Seawater

From the $S \sim N_f$ curve (Figure 4.3) it can be seen that in air and in 3.5%NaCl solution (OCP) etched specimens show a small decrease in fatigue lifetime compared with unetched specimens. Figure 4.18 presents an example of the crack growth behaviour for the etched specimen tested in 3.5%NaCl solution and compared with the unetched specimen. It is thought that etching may slightly increase the probability of initiation of cracks.

Even though there was no obvious difference in fatigue lifetime between tests in artificial seawater and 3.5%NaCl solution (OCP), the number of pits on the surface of specimens tested in artificial seawater was less than that in 3.5%NaCl solution due perhaps to some precipitation of calcium carbonate ($CaCO_3$) or magnesium hydroxide ($Mg(OH)_2$) from chemical reactions which were observed forming on the surface therefore impeding the production and growth of the pits and delaying the onset of cracking. However, at a later stage of the failure, after the cracks had overcome the resistance of the film, it accelerated very quickly as shown in Figures 4.19a-4.19b.

Cathodic polarisation seemed to increase the concentration of Ca^{2+} and Mg^{2+} ions close to the surface due to the potential gradient caused by the polarisation. Hence precipitation of more soluble compounds were actually observed under applied cathodic polarisation. The restoration of fatigue lifetime to a level which was even greater than that in the air test at the same stress level means that some real differences in the fatigue resistance between 3.5%NaCl solution and that in artificial seawater have been observed.

4.3.5 Electrochemical Monitoring Results

Current measurements were recorded with the aid of a PC controlled potentiostat for the last three tests (SCA1CP, SCA5CP and SCBS2). Figure 4.20 shows the current density of cathodic polarisation as a function of the number of stress cycles during fatigue tests. The current density, initially about -8 mA/cm^2, increases with the number of cycles, and reaches a value between -6 mA/cm^2 and -3 mA/cm^2. Since these values

are much lower compared with the open circuit potential test, the specimens are considered to have been cathodically protected.

In artificial seawater one test (SCBS2) was conducted to monitor the open circuit potential change (vs. SCE) with number of cycles (as shown Figure 4.21) or the change of current density with cycles by keeping the potential to remain at the open circuit potential value (Figure 4.22). It is noted that the open circuit potential started at about -590 mV and gradually dropped to around -650 ~ -700 mV having an increasing cathodic tendency. While the current density increased to 80 mA/cm^2 (at 13000 cycles or 18 hours) at first, it then however dropped to 1 mA/cm^2. Sometimes it could be seen that the open circuit potential or the current density changed with the applied loading within one cycle and that the range of change was about 1 mV for the open circuit potential and 30 $\mu A/cm^2$ for the current density as shown in Figure 4.23. This suggests that a mechanical factor plays a role during the corrosion process through its effect on the rate of creation of bare metal surface at the localised regions of slip activity.

4.4 Summary Remarks

Short fatigue crack growth for an offshore structural steel, RQT501, has been investigated by conducting fatigue tests in different environments. The generation and growth behaviour of cracks from smooth hour-glass specimens was investigated through successive observation of plastic replicas. The resulting test data have shown that:

(1) The presence of 3.5%NaCl solution enhances fatigue crack initiation and propagation in the RQT501 steel. $S \sim N_f$ data indicate that cathodic polarisation of -950 mV vs. SCE partially restores the corrosion fatigue properties to those observed in air. The fatigue limit in air was found to be around 516 MPa for Steel A (no Mo/V) and 480 MPa for Steel B (with Mo + V) at $R = 0.1$ ($f = 5 \sim 10$ Hz) and the endurance line, estimated at $N_f = 10^7$ cycles, is at a stress range of around 240 MPa for Steel A (no Mo/V) and 160 MPa for Steel B (with Mo + V) in 3.5%NaCl solution under freely corroding conditions and at 480 MPa for Steel A (no Mo/V) and 390 MPa for Steel B (with Mo + V) under applied cathodic polarisation (-950 mV vs.

SCE) with (f = 0.2 Hz) for R = 0.1 uniaxial tensile loading. The fatigue life to failure, N_f in 3.5%NaCl solution is less than that in air and the difference in N_f between 3.5%NaCl solution and air increases with decreasing stress range.

(2) Fatigue cracks initiate mostly at defects such as inclusions due to strain incompatibility between the inclusion and the matrix in air, corrosion pits in 3.5%NaCl solution or artificial seawater under freely corroding conditions and surface defects and polishing microscratches under applied cathodic polarisation. The results show that corrosion pits are generated during the early stages of cycling, then grow gradually with cycling. Corrosion pit growth and crack initiation behaviour are dependent on the cyclic stress range. The growth rate of a pit increases with increase in stress range. In the presence of local stress raisers such as scratches, cleavage crack nucleation is substantially enhanced by hydrogen.

(3) The growth rate of a crack is usually larger in 3.5%NaCl solution than in air. The ratio of the propagation life of a crack at its later growth stage to the total fatigue life is larger in 3.5%NaCl solution than that in air and in 3.5%NaCl solution under applied cathodic polarisation. Fatigue crack growth rates in 3.5%NaCl solution and in air exhibit accelerations and decelerations which may be associated with effects of the microstructure, i.e. microstructural barriers. The application of cathodic polarisation delays the crack initiation, however accelerates its growth when the crack length reaches a certain value.

(4) Etching causes a small decrease in fatigue lifetime compared with tests using unetched specimens. Apart from pitting, film rupture is another mechanism affecting corrosion fatigue crack growth behaviour in artificial seawater.

Chapter 5

Long Fatigue Crack Growth Measurement Tests

5.1 Introduction

Offshore structures are designed for a finite lifespan (e.g. to withstand about 30 years of wave action). New materials, such as new grades of steel, have to be tested for their resistance to adverse conditions in order to provide data for use when developing reliability criteria. This is done by subjecting specimens of the material to known levels of cyclic stress in a corrosive environment. It is currently accepted that incipient cracks exist within large and complex metal structures due to weld defects and other manufacturing and lubrication defects. Thus, in this work, the "worst case" example has been studied; i.e. a "pre-cracked" specimen has been used for testing, and the results of long fatigue crack growth studies are presented in this chapter.

Long fatigue crack growth tests of two RQT501 steels (i.e. with and without the addition of Mo and V) were conducted both in air and in 3.5%NaCl solution under a constant amplitude loading system with a stress ratio of 0.1. Cathodic polarisation to -950 mV/SCE was also applied for some corrosion fatigue tests. Fatigue crack lengths were measured using a Direct Current Potential Drop (DCPD) technique and monitored via a chart recorder.

5.2 Test Procedures

5.2.1 Specimen Preparation

For measurements of the long fatigue crack growth rate, the two compositional grades were machined into compact tension (CT) specimens in which the notch was aligned perpendicular to the rolling direction. The dimensions of the CT test pieces are given in Figure 5.1.

The optical visibility of the crack tip at the surface of the specimen was improved by polishing each side of the specimen, across the expected plane of fatigue crack growth, using 320 grit abrasive paper.

5.2.2 Pre-cracking of Compact Tension Specimens

In order to create a sharp crack tip, prior to fatigue testing, specimens were pre-cracked as recommended by ASTM standard E399-81 [131]. An Amsler-Sercal high frequency (100 Hz) machine at the British Steel Plc Swinden Technology Centre was used. A maximum load near the estimated threshold regime (below 10^{-8} m/cycle, ΔK = 15 MPa$\cdot\sqrt{\text{m}}$) and lower than the maximum load for fatigue crack growth rate measurement was employed. The initial effective crack length, that is the length from the loading axis to the crack tip, measured on the front and back surfaces of the specimens was approximately 15 mm.

5.2.3 Two Lead DCPD Technique

The Direct Current, Potential Drop technique has been used with success for the detection of slow fatigue crack growth rates [132]. Briefly, this technique entails passing a constant current through a cracked, loaded test-piece, whilst simultaneously measuring the potential difference across the crack. As the crack extends, the uncracked cross-sectional area of the test-piece decreases, its electrical resistance increases, and the potential difference between two points on either side of the crack rises. By monitoring this potential increase and comparing it with a reference potential

(V_0), the crack length to test-piece width ratio (C/W) may be determined. In this project a two lead DCPD technique was adopted. The position of input current leads and output voltage are shown in Figure 5.2. Details of the DCPD calibration are given as follows.

- **Two lead DCPD method**

a) Attach the current lead terminals by stud welding to the top faces of the specimen as shown in Figure 5.2.

b) Spot weld the pure iron potential leads to the specimen as shown in Figure 5.2. This positioning ensures optimum sensitivity whilst providing an average crack length measurement.

c) Connect the current leads to the current lead terminals in any polarity and the potential leads directly to a chart recorder.

d) Turn on the DCPD power supply and adjust the polarity of the potential until a positive indication was recorded on the chart recorder and allow the power supply at least 20 minutes to warm up.

e) Adjust the current output of the DCPD power supply such that it gives an output of exactly 1 mm full scale deflection on a chart recorder. The resulting plot of change in potential (V) can then be expressed conveniently as V/V_0 (V_0 = 0.5) where the starting V/V_0 = 1.0.

- **DCPD Calibration**

The following procedure was adopted to calibrate the CT specimens, that is, to provide a relationship between crack length and V/V_0, where V is the value of potential and V_0 is the reference potential.

A) Scribe a series of straight lines at right angles across the plane of crack growth on both sides of the test specimen using a sharp hardened steel implement. For the current specimen 16 lines which were spaced at approximately 2 mm intervals from the root of the pre-crack to the back face.

B) Set up the DCPD monitoring equipment using a two lead technique.

C) Apply fatigue loading to the specimen whilst monitoring the crack length both on the chart recorder and by optical means on both faces of the specimen. After

significant crack growth has occurred, reduce the loads applied to the specimen such that a beach mark on the fracture face of the specimen is created. The surface lengths of the crack were recorded and marked on the chart recorder in this case estimated to 0.1 of a surface division.

D) When the test is finished and the specimen is broken, measure all crack lengths indicated by the beach marks on the fracture face of the specimen using a travelling microscope.

The average surface crack lengths are plotted against the associated l'/l'_0 as indicated in Figure 5.3. Using the in-house software 'Techni-Curve v 1.28', a polynomial fit of the data was derived. The highest degree of correlation between c'/W and l'/l'_0 was achieved from a 4th order polynomial, as given below.

Steel A (no Mo/V) - 12.5 mm thick:

$$\frac{c'}{W} = 0.3700045\left(\frac{l'}{l'_0}\right)^4 - 2.138943\left(\frac{l'}{l'_0}\right)^3 + 3.981608\left(\frac{l'}{l'_0}\right)^2 - 1.844886\left(\frac{l'}{l'_0}\right) - 0.06955685,$$

Steel B (with Mo + V) - 25 mm thick:

$$\frac{c'}{W} = 0.05416426\left(\frac{l'}{l'_0}\right)^4 - 0.2742297\left(\frac{l'}{l'_0}\right)^3 + 0.06113375\left(\frac{l'}{l'_0}\right)^2 + 1.560786\left(\frac{l'}{l'_0}\right) - 1.096641,$$

5.2.4 Fatigue Testing

Tests were carried out using a 25 kN Dartec fatigue machine under constant load control with a stress ratio: $R = 0.1$. All tests were conducted at room temperature with a sinusoidal waveform and frequency of 10 Hz in air and 0.2 Hz in 3.5%NaCl solution respectively. For tests in solution, a cell with a capacity of approximately 4 l was mounted around the notch and pre-crack. Fatigue crack growth was monitored using the two lead DCPD technique.

During corrosion fatigue tests, all areas of the DCPD leads which were immersed in sea water were isolated using a coating of epoxy resin to eliminate any galvanic effects between the leads and the specimen.

- *Calculation of stress intensity factor range*

For the CT specimen the stress intensity factor range ΔK was calculated based on the following equation:

$$\Delta K = \frac{\Delta P}{B\sqrt{W}} f(\theta)$$

where P is the applied load, B is the thickness of compact tension specimens and

$$\theta = \frac{C}{W}$$

where C is the crack length within compact tension specimen.

$$f(\theta) = \frac{(2+\theta)(0.886+4.64\theta-13.32\theta^2+14.72\theta^3-5.6\theta^4)}{(1-\theta)^{3/2}}$$

This expression is valid for $C/W \geq 0.2$ [131, 133-134].

- *Fractography*

Scanning electron microscopy (SEM) was employed in the examination of fracture surfaces in order to provide an overall picture of the fracture process and surface roughness.

It was found that corrosion products formed after testing in 3.5%NaCl solution interfered with fractographic examination. Loose corrosion products were therefore removed from the surfaces by ultrasonic cleaning in acetone.

5.3 Results

(a) *Fatigue crack growth rate data*

Six fatigue tests were conducted at room temperature for both kinds of steel respectively, of which two were conducted in air, two in 3.5%NaCl solution under open circuit potential (OCP) and the other two under cathodic polarisation with an applied potential of -950 mV/SCE.

The experimental results of fatigue crack growth rate, dC/dN, versus nominal stress intensity factor range, ΔK, are shown in Figures 5.4-5.9 and have been compared with data from the experiments conducted by Marston [135] for the same steels. There is no significant difference between those which were carried out in similar

environments particularly for Steel B. However for Steel A, the data sets do not show as good a correlation, probably because the geometry of both specimens is different.

It can be seen from Figure 5.10 that the fatigue crack growth rates in air increase with an increase in ΔK, and each could be described by the multiple "Paris" equations. When tested at OCP in 3.5%NaCl solution, fatigue crack growth rate similarly increased with an increase in ΔK. With the application of a cathodic potential, evidence of a "Plateau" in fatigue crack growth can be seen, implying that stress corrosion cracking/hydrogen embrittlement has augmented the fatigue mechanisms. Comparing the fatigue data in air and in 3.5%NaCl solution it is clear that at high ΔK, the fatigue crack growth rate in 3.5%NaCl solution is faster than that in air, but at low ΔK they appear to be similar.

(b) *Fractography*

Detailed examinations were carried out where ΔK values of 20, 25, 30 and 40 $MPa\cdot\sqrt{m}$ were encountered along the centre line of the fracture surfaces of specimens tested in air and 3.5%NaCl solution.

Figures 5.11-5.13 show the fracture surfaces at $\Delta K = 20\ MPa\cdot\sqrt{m}$ for various environmental conditions. In general, there was no significant difference in the appearance of the fracture surface between in-air specimens (Figure 5.11) and freely corroded specimens (Figure 5.12) where transgranular propagation occurs predominantly except that corrosion sites exist for the later (Figure 5.14). However, as shown in Figure 5.13, the fatigue fracture surface morphology of specimens tested in 3.5%NaCl solution under applied cathodic polarisation having brittle, hydrogen-induced fracture modes (intergranular and transgranular propagation), is obviously different from that in air and in 3.5%NaCl (OCP).

At high ΔK levels "crack branches" were present on the fracture surfaces in all testing environments. These were perpendicular to the fracture surface and highly elongated in the direction of fatigue crack propagation (Figure 5.15).

Roughness of the fatigue fracture surface has shown that cathodic polarisation caused more asperities than those in air and in 3.5%NaCl (OCP). Detailed examination for Steel A (no Mo/V) (Figures 5.16-5.18) verifies this result.

5.4 Discussion

- *Effect of cathodic protection on fatigue crack growth*

The present fatigue test data for RQT501 steel, at an applied cathodic potential of -950 mV/SCE (Figure 5.10), shows that within the ΔK range applied, fatigue crack growth rates are higher than those obtained without CP application for Steel A. For Steel B, the presence of a plateau in the fatigue crack growth rate curve, typical of stress-corrosion fatigue possibly arising from hydrogen embrittlement is clearly evident, however the ΔK range over which this occurs is small compared to that observed for Steel A. The plateau seen in the $dC/dN \sim \Delta K$ curve has been interpreted by Austen [136] as stress corrosion fatigue. Cracking by this mechanism occurred due to intergranular stress corrosion cracking which initiated during the part of the fatigue cycle which exceeded K_{ISCC}. Before and after the plateau region cracking was by 'stress corrosion fatigue' and the mechanism was transgranular growth.

Regression equations for the data under different environments for both steels are given in Table 5.1. Data on fatigue crack growth rates at three levels of ΔK (20, 30 and 40 MPa$\cdot\sqrt{m}$) in various environments are given in Table 5.2. The presence of the corrosive solution increases fatigue crack growth rates by a factor of up to 4 and 3 over those in air for Steel A and Steel B respectively. Cathodic polarisation is more serious, producing fatigue crack growth rates of up to 6 and 5 times those found in air for Steel A and Steel B respectively.

- *Effect of crack closure on fatigue crack growth rate*

Crack closure is a well known phenomenon having important effects on the growth rate of fatigue cracks under certain circumstances. This effect has been used to explain the influence of a corrosive environment on fatigue crack growth.

Fatigue crack growth in this work was measured using a DCPD method and monitored via a chart recorder. A comparison of load and DCPD during a load cycle shows clearly that the greatest drop in DCPD output potential was coincident with the minimum load in the cycle. Furthermore the size of the fall in DCPD first increased and then decreased with an increase in crack length and the related ΔK. Such a result is consistent with a fall in output potential during a load cycle due to contact between

previously separated crack surfaces, i.e. crack closure. Hence the concept of the effective stress intensity factor range ($\Delta K_{eff} = K_{max} - K_{cl}$) (Figure 5.19) was applied to account for crack closure effects. The relationship between the crack opening ratio ($\Delta K_{eff}/\Delta K$) and ΔK in the tests obtained in the tests is plotted in Figures 5.20-5.21.

Although the voltage induced by the movement of the specimen is probably an additional influence to the cyclic fluctuation, however it is quite difficult to see the phenomenon from all the tests conducted in air for both steels.

The fatigue crack growth rate dC/dN as a function of ΔK_{eff} can be compared with that associated with the nominal ΔK in Figure 5.22. It can be seen that fatigue crack growth is much faster when using ΔK_{eff}.

- *Relationship between hydrogen embrittlement and closure effect*

The trend in crack closure shows that it only becomes significant when ΔK is around 20 ~ 40 MPa$\cdot\sqrt{m}$, and in this region, a plateau exists in the $dC/dN \sim \Delta K$ data sets of tests carried out under applied cathodic polarisation. At high ΔK values fatigue crack growth rates are higher and closure effects are minimal.

It was noticed by Irving et al [137] that the proportion of intergranular fracture is also heavily influenced by ΔK. The general shape of the curve showing the proportion of intergranular fracture versus ΔK was that of an inverted U showing a similar trend, with respect to closure, as found in the current studies. At ΔK values less than 3 ~ 4 MPa$\cdot\sqrt{m}$ there was negligible intergranular fracture; the proportion increased with increasing ΔK, reaching a peak for all the steels at ΔK values of 12 ~ 16 MPa$\cdot\sqrt{m}$. In the high purity steel, intergranular fracture then declines to low levels (<10% at ΔK > 25 MPa$\cdot\sqrt{m}$). This behaviour was repeated in the impure steel but the incidence then rose again at the largest ΔK values.

It is thought that under applied cathodic polarisation, crack closure is caused mainly by surface roughness which is dependent on the proportion of intergranular fracture. However, under freely corroding conditions, the crack closure is mainly the result of the presence of corrosion products.

The dependence of intergranular fracture or closure effect on crack velocity strongly suggests a formation mechanism whose operation is limited by diffusion of

active species from the crack tip into crack tip plastic zone. A likely candidate is hydrogen, which would be formed by the reaction of clean metal, formed at the crack tip on each load cycle, under applied cathodic polarisation. Once formed, the hydrogen could diffuse into the plastic zone, and cause local reduction of the cohesive strength of the grain boundaries. The critical areas would be the region of maximum hydrostatic stress, as tensile stresses normal to the crack plane would also be a maximum in this region. Operation of such a mechanism would be limited by the rate of supply of hydrogen. At high crack velocities there would be insufficient time for hydrogen to diffuse to the region of maximum triaxial stress, and intergranular fracture would decline. At low crack velocities, the rate of hydrogen production at the crack tip will be insufficient to promote grain boundary decohesion, and intergranular fracture will again be reduced.

5.5 Summary Remarks

Long fatigue crack growth of an offshore structural steel, RQT501, has been investigated by conducting fatigue tests in different environments. The resulting test data have shown that:

(1) Long fatigue crack growth is faster in 3.5%NaCl solution than for that in air, for both Steels A + B.

(2) Under applied cathodic polarisation, long fatigue crack growth is much faster when compared with freely corroding conditions with fatigue cracking exhibiting a typical plateau in fatigue crack growth rate as a function of ΔK, in a brittle, predominantly intergranular or transgranular propagation manner, suggesting that a hydrogen embrittlement mechanism may be operative.

Chapter 6

Comparison between Short and Long Fatigue Crack Test Results and the Effect of Mo and V Additions

6.1 Stress Intensity Factor Range

In order to enable a comparison of short and long fatigue and corrosion fatigue crack growth, the short fatigue crack data were used to calculate the stress intensity factor range ΔK using equation (6.1). Here the shape of a crack was represented by $c/a = 0.5$ as shown in Figure 6.1. Hence the stress intensity factor range ΔK at the deepest point B of a semi-elliptical crack front is [138, 139]

$$\Delta K = F_I \Delta\sigma\sqrt{\pi C} \qquad (6.1)$$

Where F_I is the geometry factor of the crack given in Table 6.1.

Short fatigue crack growth rate data in air and in 3.5%NaCl solution are presented as plots of dC/dN against ΔK in Figures 6.2. These results show fatigue crack growth rates were usually higher in 3.5%NaCl solution than in air and in 3.5%NaCl solution under applied cathodic polarisation. Figures 6.3-6.5 show that

short fatigue crack test results correlate well with long fatigue crack growth data at ΔK values above 10 MPa$\cdot\sqrt{m}$. In 3.5%NaCl solution (OCP) a short fatigue crack is rather accelerated as compared with that for a long fatigue crack for a given value of ΔK. Within the region of ΔK = 10 ~ 40 MPa$\cdot\sqrt{m}$, the fatigue crack growth rate in 3.5%NaCl solution under applied cathodic polarisation is higher than for both 3.5%NaCl solution (OCP) and air.

6.2 The Effect of Mo and V Additions on Long Fatigue Crack Growth of RQT501 Steels

Table 6.2 shows fatigue crack growth rate in 3.5%NaCl solution under CP application for both kinds of steel. The data are given as enhancement factors on the rates found under OCP conditions. The results from Steel A shows that, there is considerable enhancement of fatigue crack growth (for example, the rate of fatigue crack growth in Steel A at ΔK = 15 MPa$\cdot\sqrt{m}$ is nearly 3 times faster under CP application than under OCP conditions). This enhancement of fatigue crack growth is also shown for Steel B; in fact, Steel A shows greater susceptibility to the effects of cathodic polarisation than Steel B. For example, at ΔK above 25 MPa$\cdot\sqrt{m}$, Steel A under CP application shows that fatigue crack growth enhancement increases with the increasing ΔK, but Steel B shows opposite trend (Table 6.2), suggesting that some benefit, in terms of reduced corrosion fatigue crack growth under CP application, arises from the addition of Mo and V.

Figures 6.6-6.8 show a comparison of the long fatigue crack growth rate test results between both steel specimens in three different environments. In air the fatigue behaviour of both steels is very similar. However, it is noted that when ΔK at the onset of the Paris region, the fatigue crack growth rates of Steel B tend to lower values than those of Steel A as shown in Figure 6.9, Meanwhile prior to specimen failure, the fatigue crack growth rates of Steel B are higher than those of Steel A. The transition point (32 MPa$\cdot\sqrt{m}$) of the phenomenon is deduced from the regression line as shown in Figure 6.9.

For tests in 3.5%NaCl solution under freely corroding conditions, a similar trend occurred and transition point is found to be 43 MPa·$\sqrt{m}$ (Figure 6.10). The range in which those values of dC/dN of Steel B higher than Steel A becomes smaller compared with test results in air. Moreover, under applied cathodic polarisation, the fatigue crack growth rate of Steel B is no more higher than that of Steel A as shown in Figure 6.11. This suggests that the addition of Mo and V improves the fatigue crack growth resistance in 3.5%NaCl solution especially when cathodically polarised.

In the present experiments the crack closure phenomenon was observed to be most marked for Steel A under applied cathodic polarisation (Figure 6.12), though the $\Delta K_{eff}/\Delta K$ was always about 0.9 or greater under freely corroding conditions (Figure 6.13), however for Steel B, the difference in $\Delta K_{eff}/\Delta K$ between tests with and without cathodic polarisation is not as significant.

The mechanism suggested for this improved resistance is one in which the addition of V and Mo changes the diffusion coefficient of hydrogen through the steel. This is based upon the following suggestions:

1) The diffusion coefficient of hydrogen is low and the solubility of hydrogen is high in the V and Mo 'modified' steel compared with the 'unmodified' steel. This has been proved by hydrogen permeation test results in Ref. [135].
2) The composition, morphology and distribution of fine precipitates are different between the V and Mo modified and the unmodified steel. The difference in solubility and diffusion coefficient of hydrogen between both steels can be explained by the difference in effective hydrogen trapping induced by precipitates within the microstructure.

6.3 Comparison of Short Fatigue Crack Growth Behaviour between Steel A and Steel B

In air, within the regime of the necking dominated failure, the $S \sim N_f$ curve of Steel A (no Mo/V) is a little lower than that of Steel B (with Mo + V) as shown in Figure 6.14. This is reasonable when considering that the yield stresses of both steels are related to their low-cycle fatigue behaviour, i.e., the yield stress of Steel A (508 MPa) is smaller than that of Steel B (515 MPa). However, when fatigue cracking dominated failure

occurs, Steel A shows better fatigue endurance behaviour than that of Steel B. This is also understandable when considering that fatigue cracks in Steel B initiate from relative large inclusions or defects having an average size of 25 μm, while for Steel A this value is only around 9 μm which is approximately the average grain size for the steel. Therefore, it is little more difficult for the initiation of a fatigue crack in Steel A than that in Steel B. Moveover, the larger inhomogeneity in the distribution of the hardness for Steel B, compared with that of Steel A as found in Chapter 3, may be the another reason why a crack is likely to show non-propagating behaviour in Steel A while, on the contrary, it is difficult to find non-propagating cracks for Steel B. Meanwhile, it reflects that the initiation and growth of short fatigue cracks contribute to a large part of the fatigue lifetime.

In a corrosive environment. pitting is the main mechanism for crack initiation for both steels, and the trend of the $S \sim N_f$ curve for Steel A (no Mo/V) is similar to that of Steel B (with Mo + V) as shown in Figure 6.15. However, it was observed that the diameter of a pit at the pit/crack transition point for Steel A was smaller than that for Steel B, under same stress levels. Additionally, more cycles were needed for the transition process for Steel A than that of Steel B (Figure 6.16). This may be correlated to the differences in their chemical compositions and microstructures such as grain size, inclusion size and density.

When cathodic polarisation was applied, the possibility of pitting was reduced, and the trends of the $S \sim N_f$ curves for both steels are quite similar to that in air, i.e. the curve for Steel A is very flat, and for Steel B the line is shifted towards the line in air as shown in Figure 6.17. However, the extrapolation value of fatigue endurance at 10^7 cycles for Steel A is about 93% of the fatigue limit in air, while the value for Steel B is approximately 81%, showing different efficiency in the improvement of fatigue resistance under the cathodic polarisation. This behaviour may be attributed to the addition of Mo and V which can act as a trap and sink for hydrogen. Because the increase of concentration of hydrogen adsorbed onto the steel surface of Steel B appeared to favour the initiation and propagation of the surface fatigue crack.

Comparisons between both steels of the experimental crack lengths versus the corresponding number of cycles or the ratio of number of cycles to fatigue life and

fatigue crack growth rates versus crack lengths under different stress levels in different environments are presented in Figures 6.18-6.25.

In air, it is quite obvious that there are two major decelerations of fatigue short fatigue crack growth rates for Steel A, however, one deceleration for Steel B as shown in Figure 6.19. The first major deceleration for Steel A occurs when the crack length is around 10 μm, which is referred to the material threshold [140], a_{th}, where the crack seems to be blocked by the first grain boundary. The second one (d_{th}) is at about 40 μm, and represents the distance between the initial site of the crack and the second grain boundary. It means that the second grain is a large one, of 30 μm, which is above the average value of grain size (9 μm). It is reasonable if it is assumed that for a fine-grained material, an initial crack grows easily from a small grain into a large grain due to the initial crack growth rate depends mainly on the distance to the nearest microstructural barrier which limits the extent of plasticity ahead of the crack.

For Steel B, the material threshold condition increased to the second major barrier, which is around 80 μm, owing to the initiation of a crack from a large inclusion. When compared with Steel A, the effect of microstructure on fatigue crack growth rates of Steel B is smaller and fatigue resistance is reduced by bringing the two barriers closer together.

In 3.5%NaCl solution (OCP), the pit arising from environment effect, growing across several grains, permits a fatigue crack to grow across from one barrier to the other.

Based upon the previous discussion, it was concluded that the smooth specimens of Steel B (with Mo + V) have lower fatigue and corrosion fatigue crack growth resistance than Steel A (no Mo/V).

6.4 Summary Remarks

Based upon the above analysis, the following summary may be drawn:

(1) Short fatigue crack growth rate data in air and in 3.5%NaCl solution are presented as plots of dC/dN against ΔK. These results show fatigue crack growth rates were usually higher in 3.5%NaCl solution than in air. Short fatigue crack test results correlate well with long fatigue crack growth data

at ΔK values above 10 MPa$\cdot\sqrt{m}$. In 3.5%NaCl solution the growth rate of a short fatigue crack is accelerated when compared to that of a long fatigue crack. Within the region, ΔK = 10 ~ 40 MPa$\cdot\sqrt{m}$, the fatigue crack growth rate in 3.5%NaCl solution under applied cathodic polarisation is higher than that in both 3.5%NaCl solution (OCP) and air.

(2) Based upon fatigue crack growth rates, at a polarisation potential of -950 mV/SCE, in the region 20 < ΔK < 40 MPa$\cdot\sqrt{m}$ it appears that the addition of Mo and V improves the corrosion fatigue resistance of RQT501 steel. This improved resistance is attributed to the ability of Mo and V to trap hydrogen within the microstructure preventing a critical accumulation at the crack tip.

(3) For smooth specimens, in the case of fatigue cracking dominated failure and at the same stress level, Steel A (no Mo/V) shows longer fatigue and corrosion fatigue lifetime and better fatigue and corrosion fatigue resistance than that of Steel B maybe due to the differences in their chemical compositions and microstructures such as grain size, inclusion size and density. Additionally, the ability of Mo and V to trap hydrogen within the microstructure can cause localised hydrogen embrittlement which acts as an initiation site of a crack.

(4) The addition of Mo and V which can act as traps and sinks for hydrogen can either enhance or inhibit hydrogen damage.

Chapter 7

Modelling of Fatigue Crack Growth Behaviour Based on Non-equilibrium Statistical Theory

7.1 Introduction

During the last decade Professor Xing Xiusan [126-129] proposed a fatigue fracture theory based upon non-equilibrium statistical concepts and methods. This theory assumes that fatigue crack growth in metals is a non-equilibrium and irreversible process. The process obeys undeterministic statistical laws and therefore the fatigue crack growth equation should obey the following generalised Langevin equation:

$$\frac{dc}{dN} = K(c, N) + f(c, N) \tag{7.1}$$

where N denotes the number of applied loading cycles that a material is subject to; the dynamic variable c denotes the half surface crack length; $\frac{dc}{dN}$ denotes the growth rate of the half surface crack and $K(c, N)$ is the deterministic part of the growth rate of the half surface crack and is called the transportation growth rate of the half surface crack, which is determined by the average background structure, such as the grain size, and the applied cyclic stress; $f(c, N)$ is the stochastic aspect of the growth rate of the half surface crack, known as the fluctuation growth rate of the half surface crack, which is

determined by fluctuations such as a deviation in the average grain size or applied cyclic stress. This equation is based on the premise that the metallic microscopic structure may be regarded as an average background structure superimposed by stochastic fluctuation. However this work has focused mainly on characterising the long fatigue crack growth behaviour and as such no discussion currently seems to exist within the literature [126-129] concerning the short fatigue crack growth behaviour which is influenced more markedly by microstructural features such as grain boundaries.

In the present work, a fatigue crack growth model is developed based on non-equilibrium statistical theory incorporating a consideration of the influence of microstructure, e.g. grain boundaries.

7.2 Energy of a Crack

In Reference [128], the potential energy of a half surface crack, U, is composed of three parts:

$$U = U_1 + U_2 + U_3 \tag{7.2}$$

where U_1 is the surface energy and

$$U_1 = 2G_{IC}c \tag{7.2a}$$

Here , G_{IC} is the crack extension force. U_2 is the strain energy and

$$U_2 = -\frac{\pi(1-\nu^2)(\Delta\sigma)^2 c^2}{2E} \tag{7.2b}$$

Where $\Delta\sigma$ is the applied stress range; E is Young's modulus; ν is Poisson's ratio. U_3 is the dislocation energy and

$$U_3 = -\frac{nb(\Delta\sigma)c}{2} - \frac{(nb)^2 E}{8\pi(1-\nu^2)} \tag{7.2c}$$

In which b is Burgers vector; n is the number of dislocations associated with crack opening displacement.

However, when the uniform microstructure of the grain array is considered, it is assumed that the influence of grain boundaries on the half surface crack energy U_g is of the following nature

$$U_g = D\left|\sin(\frac{\pi c}{Md} + \alpha)\right| \tag{7.3}$$

Where d is the average grain size, D is a parameter which relates the strength of the grain boundaries and it is proposed here that D is related to the fatigue strength, M denotes the number of grains through which the half surface crack has passed, α is related to the distance between the original crack (with half length c_0) and the grain boundary r (Figure 7.1) and $\alpha = \frac{r}{d}\pi$. Here, for mathematical simplicity, the deflections of cracks at grain boundaries are neglected.

Therefore the total potential energy is given as

$$U_T = 2G_{IC}c - [\frac{\pi(1-\nu^2)(\Delta\sigma)^2 c^2}{2E}] - [\frac{nb(\Delta\sigma)c}{2}] - [\frac{(nb)^2 E}{8\pi(1-\nu^2)}] + D\left|\sin(\frac{\pi c}{Md} + \alpha)\right| \tag{7.4}$$

7.3 Transportation Growth Rate

According to the principle of energy conservation,

$$\frac{d(T + U_T)}{dN} = 0$$

Due to the nature of the propagation of fatigue cracks, that is, normally quasi-static; the kinetic energy, T, is insignificant. Substituting equation (7.4) into this equation, the equation for the transportation growth rate of a half surface crack under the action of a cyclic stress is obtained:

$$\begin{aligned} &2G_{IC}\frac{dc}{dN} - [\frac{\pi(1-\nu^2)(\Delta\sigma)^2 c}{E}\frac{dc}{dN}] - (\frac{nb\Delta\sigma}{2}\frac{dc}{dN}) - [\frac{(\Delta\sigma)c}{2}\frac{d(nb)}{dN}] \\ &-[\frac{nbE}{4\pi(1-\nu^2)}\frac{d(nb)}{dN}] + (\frac{\pi D}{Md})\left|\cos(\frac{\pi c}{Md} + \alpha)\right|\frac{dc}{dN} = 0 \end{aligned} \tag{7.5}$$

Where $\frac{dc}{dN}$ is the transportation growth rate $K(c, N)$ in equation (7.1). Here it is appropriate to denote $\frac{dc}{dN}$ as the transportation growth rate because all the macroscopic physical quantities in equations (7.4) are average values.

In obtaining the solution of this equation, the condition that the rate of change of cyclic stress per cycle

$$\frac{d(\Delta\sigma)}{dN} = 0$$

is used. It has been proven that the number of dislocations emitted respectively from two symmetric slip planes of the crack tip is equivalent to the same number of dislocations of opposite sign squeezed in the crack tip [128].

Then from equation (7.5), the transportation growth rate is obtained by:

$$\frac{dc}{dN} = \frac{[\frac{(\Delta\sigma)c}{2} + \frac{nbE}{4\pi(1-\nu^2)}]\frac{d(nb)}{dN}}{2G_{IC} - [\frac{(\Delta\sigma)^2\pi(1-\nu^2)c}{E}] - (\frac{nb\Delta\sigma}{2}) + (\frac{\pi D}{Md})\left|\cos(\frac{\pi c}{Md} + \alpha)\right|} \tag{7.6}$$

It is evident that at this stage the transportation growth rate for a fatigue crack is closely related to

$$\frac{d(nb)}{dN} > 0$$

i.e. to the number of dislocations emitted per cycle from the crack tip. If

$$\frac{d(nb)}{dN} = 0$$

then $\frac{dc}{dN} = 0$, and the crack has no transportation growth.

In order to find an expression for $\frac{dc}{dN}$ in equation (7.6), the following relations are used to calculate $\frac{d(nb)}{dN}$ [128].

$$nb = n_k b = \frac{2\pi\Delta\sigma(1+\nu)c}{E} \tag{7.7}$$

$$c = c_k = \frac{G_{IC}E}{\pi(1-\nu^2)(\Delta\sigma)^2} \tag{7.8}$$

$$\frac{d(nb)}{dN} = \frac{1}{N_0 L^2}(\frac{\Delta\sigma}{\sigma_0})^{\frac{1}{\beta}} \tag{7.9}$$

where N_0 is the average number of mobile dislocation sources per unit volume, L is the average length of slip plane, β is the cyclic hardening exponent and σ_0 is the cyclic strength coefficient.

Substituting equations (7.7)-(7.9) into equation (7.6), the half surface crack growth rate can be obtained by

$$\frac{dc}{dN} \approx \frac{(\Delta\sigma)^{\frac{1}{\beta}+1} c}{N_0 L^2 \sigma_0^{\frac{1}{\beta}} [2G_{IC} - \frac{2\pi(1-\nu^2)(\Delta\sigma)^2 c}{E} + \frac{\pi D}{Md}\left|\cos(\frac{\pi c}{Md} + \alpha)\right|]} \tag{7.10}$$

From equation (7.10) It can be seen that the process of fatigue crack propagation can be divided into three stages:

- Stage I (short) fatigue crack growth
- Stage II fatigue crack growth
- Stage III fatigue crack growth

7.3.1 Stage I (Short) Fatigue Crack Growth

For short fatigue cracks, the growth equation given in (7.10) can be rewritten as

$$\frac{dc}{dN} \approx \frac{(\Delta\sigma)^{\frac{1}{\beta}+1} c}{N_0 L^2 \sigma_0^{\frac{1}{\beta}} (2G_{IC} + \frac{\pi D}{Md}\left|\cos(\frac{\pi c}{Md} + \alpha)\right|)}$$

$$\approx \frac{Md(\Delta\sigma)^{\beta} c}{\pi D N_0 L^2 \sigma_0^{\frac{1}{\beta}}\left|\cos(\frac{\pi c}{Md} + \alpha)\right|}(1 - \frac{2G_{IC} Md}{\pi D\left|\cos(\frac{\pi c}{Md} + \alpha)\right|})$$

Figure 7.2 presents a schematic of fatigue crack growth behaviour within first ten grains described by equation (7.10) for Steel B (with Mo + V). Here $\Delta\sigma$ = 500 MPa, σ_0 = 600 MPa, $N_0 = 5\times10^6$ mm^{-3}, $L = 10$ μm, d = 10 μm, G_{IC} = 75 N/mm, $D = 480$ N, $\alpha = \pi/4$, $\beta = 0.1$, $\nu = 0.29$, $E = 2.06\times10^5$ MPa.

Equation (7.10) is also used to calculate the transportation growth rate of a half surface crack and a comparison of this equation with the experimental data is shown in Figures 7.3 and 7.4 (D = 516 N for Steel A (no Mo/V)) in air.

For most materials, the interaction of a short fatigue crack with a microstructural barrier causes the following behaviour:

(1) As a short crack approaches a microstructural barrier, (e.g. a grain boundary or a secondary phase), its growth rate will decelerate due to the effect of the barrier.

(2) The major retardation effects associated with microstructural barriers occurs within the first few grains. As crack length increases, microstructural effects decrease.

(3) As the applied stress is reduced the fatigue crack growth rate decreases proportionately.

7.3.2 Stage III Fatigue Crack Growth

For a long crack, the growth rate of the half surface crack is approximately equal to:

$$\frac{dc}{dN} \approx \frac{E(\Delta\sigma)^{\frac{1}{\beta}-1}}{2\pi(1-\nu^2)N_0L^2\sigma_0^{\frac{1}{\beta}}}\left[\frac{(\Delta K)^2}{Y^2K_{IC}^2-(\Delta K)^2}\right] \qquad (7.11)$$

where K_{IC}, the fracture toughness of the metal is given by:

$$K_{IC}^2 = \frac{G_{IC}E}{1-\nu^2}$$

$$\Delta K = Y\Delta\sigma(\pi c)^{\frac{1}{2}}$$

where ΔK is the stress intensity factor range and Y is a geometry factor. It is evident that equation (7.11) agrees with the Forman empirical formula [141] if only from the point of view of $\frac{dc}{dN} \propto (\Delta K)^2 \Big/ [Y^2K_{IC}^2-(\Delta K)^2]$.

7.3.3 Stage II Fatigue Crack Growth

When $YK_{IC} >> \Delta K$, equation (7.11) becomes

$$\frac{dc}{dN} \approx \frac{(\Delta\sigma)^{\beta}}{2\pi Y^2G_{IC}N_0L^2\sigma_0^{\frac{1}{\beta}}}(\Delta K)^2 \qquad (7.12)$$

giving the transportation growth rate of a half surface crack for a small growth rate. This shows that the transportation growth rate is proportional to the cyclic stress amplitude $\Delta\sigma$ and the half surface crack length c, and inversely proportional to the mobile dislocation sources density N_0, the crack extension force G_{IC}, the length of slip

plane L, and the cyclic strength coefficient σ_0. It can be seen that equation (7.12) agrees with the Paris empirical formula if only from the point of view of $\frac{dc}{dN} \propto (\Delta K)^2$.

For simplicity, equation (7.12) is written as

$$\frac{dc}{dN} = K(c,N) = Ac = m_1(\Delta K)^2$$

where A, the transportation growth coefficient is given as:

$$A = \frac{(\Delta\sigma)^{\frac{1}{\beta}+1}}{2G_{IC}N_0L^2\sigma_0^{\frac{1}{\beta}}} = \frac{\pi(\Delta\sigma)^2}{Y^2}m_1 \qquad (7.13)$$

7.4 Fluctuation Growth Rate

Assuming the transportation growth rate originates from the average structure, all the physical quantities for calculating the transportation growth rate previously described are considered as average values. In reality the mobile dislocation source density N_0, the crack extension force G_{IC}, the length of slip plane L, the grain size d, the value of D and the cyclic strength coefficient σ_0 are all structurally sensitive, and therefore will fluctuate about some average value because of inhomogeneous fluctuation within the microscopic structure of the metal. Therefore these values should be revised, i.e., from $N_0, G_{IC}, L, D, d, \sigma_0$ to $N_0+\Delta N_0, G_{IC}+\Delta G_{IC}, L+\Delta L, D+\Delta D, d+\Delta d, \sigma_0+\Delta\sigma_0$. Here the prefix Δ represents the deviation of each quantity, originating from the inhomogeneous fluctuation of the microscopic structure. Thus, corresponding to the transportation growth rate (7.10), the total growth rate of the half surface crack is

$$\frac{dc}{dN} \approx \frac{(\Delta\sigma)^{\frac{1}{\beta}+1}c}{(N_0+\Delta N_0)(L+\Delta L)^2(\sigma_0+\Delta\sigma_0)^{\frac{1}{\beta}}\{2(G_{IC}+\Delta G_{IC}) - \frac{2\pi(1-\nu^2)(\Delta\sigma)^2c}{E} + \frac{\pi(D+\Delta D)}{M(d+\Delta d)}\left|\cos(\frac{\pi c}{M(d+\Delta d)}+\alpha)\right|\}} \qquad (7.14)$$

$$\approx \frac{(\Delta\sigma)^{\frac{1}{\beta}+1}c}{2G'_{IC}N_0L^2\sigma_0^{\frac{1}{\beta}}}[1+(\frac{\Delta N_0}{N_0}+\frac{\Delta G'_{IC}}{G'_{IC}}+\frac{2\Delta L}{L}+\frac{\Delta\sigma_0}{\beta\sigma_0})]$$

$$= A'c[1+(\frac{\Delta N_0}{N_0}+\frac{\Delta G'_{IC}}{G'_{IC}}+\frac{2\Delta L}{L}+\frac{\Delta\sigma_0}{\beta\sigma_0})]$$

where

$$G'_{IC} = G_{IC} - [\frac{2\pi(1-\nu^2)(\Delta\sigma)^2c}{E}] + (\frac{\pi D}{Md})\left|\cos(\frac{\pi c}{Md}+\alpha)\right|$$

$$A' = \frac{(\Delta\sigma)^{\frac{1}{\beta}+1}}{2G'_{IC}N_0L^2\sigma_0^{\frac{1}{\beta}}}$$

$$\Delta G'_{IC} = \Delta G_{IC} + [\frac{\pi(D+\Delta D)}{2M(d+\Delta d)}]\left|\cos(\frac{\pi c}{M(d+\Delta d)}+\alpha)\right| - (\frac{\pi D}{Md})\left|\cos(\frac{\pi c}{Md}+\alpha)\right|$$

From the last formula of equation (7.10), it is considered that the relative deviations $\frac{\Delta N_0}{N_0}$, $\frac{\Delta G'_{IC}}{G'_{IC}}$, $\frac{\Delta L}{L}$, $\frac{\Delta\sigma_0}{\sigma_0}$ are much less than 1, and the higher order terms of the relative deviations may be neglected. ΔL is related to the spacing between the barriers and the crack.

Now let the total relative deviations be

$$\eta = \frac{\Delta N_0}{N_0} + \frac{\Delta G'_{IC}}{G'_{IC}} + \frac{2\Delta L}{L} + \frac{\Delta\sigma_0}{\beta\sigma_0} \tag{7.15}$$

Thus

$$\frac{dc}{dN} \approx A'c(1+\eta) \tag{7.16}$$

Where $A'c$ is the average growth rate and $\eta A'c$ is the fluctuation growth rate. Equation (7.16) can then be written as

$$\frac{dc}{dN} = A'Fc \tag{7.17}$$

Where $F = 1+\eta$. For short fatigue crack growth, when the stress level is not very high, F in equation (7.17) will not be a constant and can change greatly as the fatigue crack growth rate or stress decreases. This is due mainly to the interaction of short fatigue cracks with the material microstructure and, among all microstructural factors, the blocking effect of microstructural barriers is the most obvious effect.

For RQT501 steel, based upon equation (7.17), the fatigue crack growth behaviour follows the trend shown in Figures 7.5 and 7.6 (where η takes 3, 0 and -0.8 respectively). Where for steel A, based on the analysis in Section 6.3 that short fatigue crack initiation behaviour is associated with that growing across large grains, the first or second grain sizes where crack initiated are adopted from test results for each specimen instead of the average grain size used for the calculation in Figure 7.3.

Figure 7.7 shows, based on the present work, a prediction of the short fatigue crack growth rates for the experimental data of Hobson [59, 60, 142] where $\sigma_0 = 683$ MPa, $N_0 = 5\times10^6$ mm^{-3}, $L = 0.097$ mm, $d = 0.097$ mm, $G_{IC} = 60$ N/mm, $D = 220$ N, $\alpha = \pi/4$, $\beta = 0.1$, $\nu = 0.29$, $E = 2.06\times10^5$ MPa.

7.5 Fatigue Lifetime

By integrating equation (7.17), the relationships of $c \sim N$ and $S \sim N_f$ can be obtained quantitatively as equations (7.18) and (7.19). Here, the term $\frac{1}{Md}\left|\cos(\frac{\pi c}{Md}+\alpha)\right|$ is approximately replaced by $\frac{1}{c}$.

$$N = \frac{N_0 L^2 \sigma_0^{\frac{1}{\beta}}(1+\eta)}{(\Delta\sigma)^{\frac{1}{\beta}+1}}[2G_{IC}\ln\frac{c}{c_0} - \frac{2\pi(1-\nu^2)(c-c_0)(\Delta\sigma)^2}{E} + \pi D(\frac{1}{c_0}-\frac{1}{c})] \quad (7.18)$$

$$N_f = \frac{N_0 L^2 \sigma_0^{\frac{1}{\beta}}(1+\eta)}{(\Delta\sigma)^{\frac{1}{\beta}+1}}[2G_{IC}\ln\frac{c_k}{c_0} - \frac{2\pi(1-\nu^2)(c_k-c_0)(\Delta\sigma)^2}{E} + \pi D(\frac{1}{c_0}-\frac{1}{c_k})] \quad (7.19)$$

Where c_k is the critical length of the specimen. It can be seen from equation (7.19) that the growth of short fatigue cracks contributes to a large proportion of the fatigue lifetime because N_f is determined mainly by the term which includes the factor D. Table 7.1 and Figures 7.8-7.10 present the results of fatigue lifetime and the $a \sim N$ curve calculated from equations (7.18) and (7.19) for RQT501 steel in air.

From equation (7.18), it is seen that the number of cycles needed for a crack growing from an half length c_1 to c_2 can be easily determined by

$$N_{21} = \frac{N_0 L^2 \sigma_0^{\frac{1}{\beta}}(1+\eta)}{(\Delta\sigma)^{\frac{1}{\beta}+1}}[2G_{IC}\ln\frac{c_2}{c_1} - \frac{2\pi(1-\nu^2)(c_2-c_1)(\Delta\sigma)^2}{E} + \pi D(\frac{1}{c_1}-\frac{1}{c_2})] \quad (7.20)$$

or

$$N_{21} = \frac{1}{(\Delta\sigma)^{\frac{1}{\beta}+1}}[A_1\ln\frac{c_2}{c_1} - A_2(c_2-c_1)(\Delta\sigma)^2 + A_3(\frac{1}{c_1}-\frac{1}{c_2})] \quad (7.21)$$

where

$$A_1 = 2N_0L^2\sigma_0^{\frac{1}{\beta}}(1+\eta)G_{IC},\ A_2 = \frac{2\pi N_0L^2\sigma_0^{\frac{1}{\beta}}(1+\eta)(1-\nu^2)}{E},\ A_3 = \pi N_0L^2\sigma_0^{\frac{1}{\beta}}(1+\eta)D$$

For example, for Steel B, the number of cycles necessary for a crack growing from 15 mm to 40 mm under $\Delta\sigma$ = 400 MPa, is predicted to be approximately 17900 cycles.

7.6 Summary

A model has been developed which describes the fatigue crack growth process developed upon a modification of the non-equilibrium statistical theory of fatigue fracture. Compared with other fatigue theories, the main characteristics of this theory are

(1) an emphasis on the close relationship between fatigue crack growth and the microstructure of the material.

(2) a dislocation model describing fatigue crack growth is employed in the present study to simulate fatigue crack growth behaviour and to predict the fatigue crack growth rates throughout the fatigue lifetime.

It is accepted of course, that the process of fatigue fracture is very complicated, and influenced by many factors. In this respect this new theoretical explanation, still has many aspects which need refining.

Chapter 8

Stochastic Theory of Corrosion

8.1 Introduction

Many studies have investigated crack initiation and growth behaviour during the corrosion fatigue process; however, only a few studies have examined pit initiation and growth behaviour [14, 55, 143-146].

Corrosion has an important effect on the mechanical and physical properties of metals and alloys. The process of corrosion may be described using statistical functions, and in this respect, the statistical nature of corrosion has received increased attention [147] although in general, these studies are phenomenological. From the statistical point of view, the main purpose of this chapter is to correlate the microscopic mechanism of corrosion with its macroscopic statistical nature, and to establish a theory of corrosion on the basis of non-equilibrium statistical concepts and methods, in order to make it possible for the important macroscopic quantities to be derived theoretically and expressed in terms of more basic physical quantities. This chapter will also provide a discussion on the physical basis of the statistical fluctuation of corrosion and the fluctuation corrosion coefficient and obtain an analytical distribution function and a formula for the average diameter of the corrosion pit which agrees with experimental observation.

Why does the corrosion law have a statistical nature? What is its physical basis? In order to answer these questions, it is evident that it is important to study the

microscopic structure of materials. It is well known, owing to the inhomogeneity of defects, chemical composition and phase varieties in real materials, that its microscopic structure is always inhomogeneous. This structural inhomogeneity leads to fluctuations of the corrosion rate and therefore a statistical corrosion law. In principle the fluctuation of corrosion rate can be obtained from calculating the effect of all the different contributions giving rise to material inhomogeneity. Such an approach is in reality impossible due to the individual characteristics giving rise to such material inhomogeneity. For convenience therefore the microscopic structure of a material is regarded as an average background structure superimposed by inhomogeneous fluctuations due to a variety of inherent defects. The physical basis of the statistical fluctuation of corrosion arises from two main contributions: the first is the fluctuation of the environment and the second the microscopic structural background of the material. Both may be regarded as dynamic fluctuations, hence, the process of corrosion can be discussed in terms of a stochastic process.

It is well known that corrosion pits initiate and grow in the early stages of the corrosion fatigue process. Corrosion cracks start to grow from these corrosion pits and cause the final failure of the specimen. In clarifying the damage evolution during the corrosion fatigue process, it is important to investigate the initiation and growth behaviour of the corrosion pits.

In the present study, tensile fatigue tests of a RQT501 steel were carried out in 3.5%NaCl solution. The generation and growth behaviour of corrosion pits from which cracks initiated has been investigated through successive observation due to the plastic replication method, in order to clarify the effect of stress range on the initiation and growth behaviour of the corrosion pits.

8.2 Stochastic Corrosion Equations

The stochastic equation which may be used to describe the process of corrosion is given in equation (8.1). Where t is the time for corrosion, $X(t)$ the diameter of corrosion pit formed and $\dot{X}(t) = {}^{dX}/_{dt}$ the corrosion rate of the material at time t. Because fluctuations of the environment or of the microscopic structure lead to

stochastic fluctuations of the corrosion rate, the corrosion rate should obey the following generalised Langevin equation:

$$\dot{X}(t) = K(X) + \beta(X) f(t) \tag{8.1}$$

Where $K(X)$ is termed the transportation corrosion rate, $\beta(X)f(t)$ the fluctuation corrosion rate, $f(t)$ the fluctuation function, and $\beta(X)$ the fluctuation coefficient. It is obvious in reality that most of the processes of concern in engineering are not Markovian in a strict sense, however, a number of problems may be solved by assuming a Markovian nature in those processes [148]. Certainly speaking, a Markov approximation of the corrosion process is reasonable if the major concern is that of a change between two states, with sufficient duration of time apart, in comparison to the correlation time of the process. Hence for the convenience of calculation, it is assumed that the process of corrosion to be a Markov process, and the fluctuation function $f(t)$ to have a Gaussian distribution which satisfies

$$\begin{aligned} &< f(t) >= 0 \\ &< f(t) f(t') >= Q\delta(t - t') \end{aligned} \tag{8.2}$$

Where δ is the Dirac function, and Q is the fluctuation corrosion coefficient. Care must be taken here to appreciate that the fluctuation corrosion coefficient Q differs from the ordinary diffusion coefficient.

Equation (8.1) represents the dynamic variation which occurs with time. According to stochastic theory the equation of the probability density evolving with time, which is equivalent to equation (8.1), is the Fokker-Planck equation [149, 150]

$$\frac{\partial P(X_0, X; t)}{\partial t} = -\frac{\partial}{\partial X}[K(X)P(X_0, X; t)] + \frac{Q}{2}\frac{\partial}{\partial X}[\beta(X)\frac{\partial \beta(X)}{\partial X}P(X_0, X; t)] \tag{8.3}$$

Where $P(X_0, X; t)dX$ is the probability that the initial corrosion pit, of the diameter X, grows to a diameter between X and $X + dX$ at time t, often called the probability density function, which represents the probability distribution of the pit diameter at time t. The physical meaning of equation (8.3) is that the rate of change of the probability density function of the pit diameter ($\partial P(X_0, X; t)/\partial t$) is determined by the transportation corrosion, the first term of equation (8.3) containing $K(X)$), and the fluctuation corrosion, the term containing $Q(t)$ on the right side of equation (8.3), together.

Given the natural fluctuations of the environment and metallurgical structure it is appropriate to derive a relationship between $\beta(X)$ and $K(X)$ in equations (8.1) and (8.3) [151]:

$$K(X)=A\,\beta(X) \tag{8.4}$$

Here A is a constant which is independent of X.

8.3 Transportation Corrosion Function

Given that A, $\beta(X)$, and Q are known, $P(X_0, X; t)$ can be solved from equations (8.3) and (8.4). When A, $\beta(X)$, and Q are obtained from the microscopic mechanism, the statistical theory of corrosion will be set up on the basis of the microscopic structure.

The transportation corrosion rate of material can be assumed to obey either linear or parabolic corrosion kinetics [152]:

$$K_L(X) = A_L \tag{8.5a}$$

$$K_P(X) = \frac{A_P}{X} \tag{8.5b}$$

Where A_L is the linear rate constant which is a function of the metal, the composition of the environment, pressure, and temperature etc., and A_P is the parabolic rate constant which increases exponentially with temperature T, following the Arrhenius equation:

$$A_P = A_0 \exp(-\frac{U'}{kT}) \tag{8.6}$$

Where A_0 is a constant that is a function of the metal/environment system; U' is the activation energy for diffusion; and k is the Boltzmann constant.

8.4 Fluctuation Corrosion Coefficient

As mentioned above, $f(t)$, the fluctuation corrosion rate, of the generalised Langevin equation, is expressed by the equivalent fluctuation corrosion coefficient, Q, in the Fokker-Planck equation. If Q is given, $f(t)$ may be found. It is therefore necessary to adopt a method for determining Q. The method used to investigate directly the origin

of the fluctuation coefficient begins with the transportation coefficient $K(X, t)$ and on this basis Q can be found and represented by $K(X)$.

Given the assumption that transportation corrosion originates from the average structure, all the physical quantities for calculating the transportation corrosion rate given previously are regarded as average values. In reality A in equations (8.5a) and (8.5b) is environmentally and structurally sensitive, and must fluctuate about an average value because of the inhomogeneous nature of the environment and metallurgical structure.

Based on these assumptions let the total deviation, ς, about an average be:

$$\varsigma = \frac{\Delta A}{A}$$

Then equation (8.5a) becomes

$$\dot{X}_L(t) \approx A_L \pm \varsigma_L A_L \tag{8.7}$$

Where the term A_L is the average corrosion rate and $\varsigma_L A_L$ is the fluctuation corrosion rate. In order to find the fluctuation growth coefficient Q, the following method is used.

Integration of equation (8.7) gives

$$X_L = X_0 + A_L t \pm \varsigma_L A_L t = \overline{X}_L \pm \varsigma_L A_L t \tag{8.8}$$

Where $\overline{X}_L$ is the average pit diameter. From equation (8.8) the relative deviation of the pit diameter is obtained.

$$\frac{\sqrt{\Delta X}}{\overline{X}_L} \approx \frac{\sqrt{X_L^2 - \overline{X}_L^2}}{\overline{X}_L} = \sqrt{\varsigma_L(2 \pm \varsigma_L)} \approx \sqrt{2\varsigma_L} \tag{8.9}$$

Strictly speaking, the relative deviation of corrosion is obtained from equation (8.15) in the next section.

$$\frac{\sqrt{\Delta X}}{\overline{X}_L} = \frac{\sqrt{Q_L t}}{A_L t} \tag{8.10}$$

For times (t) less than the total corrosion life, the fluctuation corrosion coefficient for linear corrosion can be obtained as

$$Q_L = 2\varsigma_L A_L^2 t: \ (t < \tau) \tag{8.11a}$$

Where τ is the intrinsic life of corrosion, ζ_L relates to the fluctuation of A_L For parabolic kinetics corrosion a similar result for the fluctuation corrosion coefficient can be proved [128, 129].

$$Q_P = 2\zeta_P^2 A_P^2 t: (t < \tau) \tag{8.11b}$$

The probability density distribution function $P(X_0, X; t)$ for corrosion can be solved. From equations (8.4) and (8.5),

$$P_L(X_0, X; t)dX = \frac{1}{\sqrt{2\pi Q_L t}} \exp\{-\frac{[(X - X_0) - A_L t]^2}{2Q_L t}\}dX \tag{8.12a}$$

$$P_P(X_0, X; t)dX = \frac{X}{\sqrt{2\pi Q_P t}} \exp\{-\frac{[\frac{1}{2}(X^2 - X_0^2) - A_P t]^2}{2Q_P t}\}dX \tag{8.12b}$$

Here $P(X_0, X; t)$ should satisfy both the unification condition $\int_{X_0}^{\infty} P(X_0, X; t)dX = 1$ and the initial condition $P(X_0, X; t = 0) = \delta(X - X_0)$. If X_0 is neglected, the average pit diameter $\overline{X}$ and the most probable diameter X_{Lm} and X_{Pm} satisfy the following equations

$$\overline{X}_L = \int_{X_0}^{\infty} XP_L(X_0, X; t)dX = X_0 + A_L t \tag{8.13a}$$

$$\begin{aligned} \overline{X}_P &\approx [\int_0^{\infty} X^2 P_P(X_0, X; t)dX]^{1/2} \\ &= [\sqrt{\frac{2Q_P t}{\pi}} \exp(-\frac{A_P^2 t}{2Q_P}) + A_P t + A_P t \operatorname{erf}(\frac{A_P t}{\sqrt{2Q_P t}})]^{1/2} \end{aligned} \tag{8.13b}$$

$$\operatorname{erf}(X) = \frac{2}{\sqrt{\pi}} \int_0^X e^{-y^2} dy$$

$$X_{Lm} = X_0 + A_L t \tag{8.14a}$$

$$X_{Pm} = (\frac{X_0^2 + 2A_P t + \sqrt{(X_0^2 + 2A_P t)^2 + 8Q_P t}}{2})^{1/2} \approx (A_P t + \sqrt{A_P^2 t^2 + 2Q_P t})^{1/2} \tag{8.14b}$$

8.5 Discussion

That the average pit diameter increases with time can be easily understood from a corrosion experiment when A_L, A_P and Q_L, Q_P are regarded as constants during the corrosion process.

For linear corrosion it can be seen from equations (8.13a) and (8.14a) that

$$\frac{X_{Lm}}{X_L} = 1$$

$$\overline{X}_L = X_{Lm} \approx A_L t \propto t$$

The mean square deviation is given by

$$< \Delta X^2 >= Q_L t = 2\varsigma_L A_L^2 t^2 \tag{8.15}$$

For parabolic kinetics corrosion it can be seen from equations (8.13b) and (8.14b) that when $2Q_P t >> A_P^2 t^2$, fluctuation plays a main part,

$$\begin{cases} \overline{X}_P = (\dfrac{2Q_P t}{\pi})^{1/4} \exp(-\dfrac{A_P^2 t}{2Q_P}) \\ X_{Pm} = (2Q_P t)^{1/4} \\ \dfrac{X_{Pm}}{\overline{X}_P} = 1.33 \exp(-\dfrac{A_P^2 t}{2Q_P}) \end{cases}$$

For $X_{Pm}/\overline{X}_P$, the distribution is not invariant. Q_P is an adjustable physical quantity.

When $2Q_P t << A_P^2 t^2$, namely, corrosion depends to a large extent on the transportation term,

$$\begin{cases} \overline{X}_P \approx (2A_P t)^{1/2} \\ X_{Pm} \approx (2A_P t)^{1/2} \\ \dfrac{X_{Pm}}{\overline{X}_P} = 1 \end{cases}$$

If both terms are similar, i.e. $2Q_P t \approx A_P^2 t^2$, both terms play a part in determining $\overline{X}_P$, X_{Pm} In other words, the average value and the most probable value of the corrosion rate are composed of two parts. One is the fluctuation term (the term which

contains (Q_P), the other being the transportation term (the term which contains A_P). When $\frac{1}{2}X^2 >> A_P t$, the average value of X for parabolic kinetics can be given approximated by:

$$\bar{X}_P = \int_0^\infty X P_P(X_0, X; t) dX \approx \int_0^\infty \frac{X^2}{\sqrt{2\pi Q_P t}} \exp(-\frac{X^4}{8Q_P t}) dX = \frac{1}{\sqrt{2\pi}} \Gamma(\frac{3}{4})(2Q_P t)^{1/4} \qquad (8.16)$$

When $\frac{1}{2}X^2 << A_P t$, let $z = \frac{1}{2}X^2 - A_P t$, then

$$\bar{X}_P = \frac{1}{\sqrt{\pi Q_P t}} \int_{-A_P t}^\infty \sqrt{z + A_P t} \exp(-\frac{z^2}{2Q_P t}) dz$$

$$\approx \sqrt{\frac{A_P}{\pi Q_P}} \int_{-A_P t}^\infty (1 + \frac{z}{2A_P t}) \exp(-\frac{z^2}{2Q_P t}) dz \qquad (8.17)$$

$$= \sqrt{\frac{A_P t}{2}} [1 + \mathrm{erf}(\frac{A_P t}{\pi Q_P t})] + \frac{1}{2}\sqrt{\frac{Q_P}{\pi A_P}} \exp(-\frac{A_P^2 t}{2Q_P})$$

When t is large, $\exp(-\frac{A_P^2 t}{2Q_P}) \approx 0$, so from equations (8.16) and (8.17) $\bar{X}_P \propto t^{1/n}$, where n = 2 to 4. If X_0 is neglected, substituting $Q = 2\zeta_P^2 A_P^2 t$ into equations (8.13b) and (8.14b) then

$$\bar{X}_P = [\frac{2\zeta_P}{\sqrt{\pi}} \exp(-1/4\zeta_P^2) + 1 + \mathrm{erf}(\frac{1}{2\zeta_P})]^{1/2} (A_P t)^{1/2} \propto t^{1/2} \qquad (8.18)$$

$$X_{Pm} = (1 + \sqrt{1 + 4\zeta_P^2})^{1/2} (A_P t)^{1/2} \propto t^{1/2} \qquad (8.19)$$

The maximum value of the probability density function for the time t is

$$P_{Lm}(X_0, X_{Lm}; t) = \frac{1}{2A_L t\sqrt{\pi\zeta_L}} \qquad (8.20a)$$

$$P_{Pm}(X_0, X_{Pm}; t) \approx (\frac{\sqrt{1 + 4\zeta_P^2} + 1}{4\zeta_P^2 \pi A_P t})^{1/2} \exp[-\frac{(\sqrt{1 + 4\zeta_P^2} - 1)^2}{16\zeta_P^2}] \qquad (8.20b)$$

If $-\frac{1}{2} \le \zeta_P \le \frac{1}{2}$, equation (8.20b) can be rewritten approximately as

$$P_{Pm}(X_0, X_{Pm}; t) \approx (\frac{1}{2\zeta_P^2 \pi A_P t})^{1/2} \exp[-\frac{\zeta_P^2}{4}] \qquad (8.21)$$

From equations (8.20a) and (8.21) it can be seen that when $\zeta_P \to 0$, $P_m(X_0, X_m; t) \to \infty$ and uniform corrosion results. The probability of maximum pit

diameter $P_m(X_0, X_m; t)$ decreases with an increase of ς_P, which represents the localised corrosion.

8.6 Application of the Theory to Corrosion Fatigue Test Results

The observations of fatigue damage on the specimen surface and the measurements of the diameter of corrosion pits were made via plastic replicas using an optical microscope. The corrosion pit size, X, is the diameter along the circumferential direction on the specimen surface due to cracking at 90° to the applied loading direction.

In order to investigate the pit initiation and growth behaviour, successive observations of the specimen surface during the corrosion fatigue process were performed. As a representative value of the pit initiation time, the pit from which a crack initiates is considered. Figure 8.1 shows the variation in the pit diameter at the specimen surface under different levels of stress ($\Delta\sigma$). In this figure a parabolic relationship between the pit diameter and time appears to exist for the plots. For comparative purposes equation (8.19) is plotted as lines for different stress levels. Here $\zeta_P = 0.5$ is taken.

The value of A_P can be determined by approximating the experimental data with equation (8.19). It can be seen that the value of A_P increases with an increase in stress range. Furthermore, there is linear relationship between A_P and stress range as shown in Figure 8.2. Therefore, the following equation holds:

$$A_P = B_1\Delta\sigma - B_2 \tag{8.22}$$

B_1 and B_2 are constants having values of 1.18 (Steel A), 8.53 (Steel B) and 534 (Steel A), 3911 (Steel B) respectively. The value of A_P in the high loading test is larger than that in the low loading test. For this reason, the corrosive current generated during the corrosion fatigue process is increased by the application of stress, because the number of initiation sites for the corrosive reaction in the specimen, such as slip steps and slip lines, increases as a result of the application of stress range.

Under applied cyclic stress, the failure processes of the specimen in a corrosive environment are composed of two stages - pitting and cracking. When $a < a_{p/c}$, pitting

is the main mechanism and equation (8.19) describes the stress corrosion process and the pit growth rate is

$$\frac{da}{dN} = \frac{dX_{Pit}}{dN} = \frac{(1+\sqrt{1+4\varsigma_P^2})A_P}{2fX_P} \tag{8.23}$$

when $a > a_{p/c}$, corrosion fatigue cracking dominates the failure mechanism and the model in Chapter 7 may be applied to describe the process. The corrosion fatigue crack growth rate is

$$\frac{da}{dN} = \frac{da_{Crack}}{dN} \approx \frac{(1+\eta)(\Delta\sigma)^{\frac{1}{\beta}+1}a}{N_0 L^2 \sigma_0^{\frac{1}{\beta}}[2G_{IC} - \frac{\pi(1-\nu^2)(\Delta\sigma)^2 a}{E} + \frac{\pi D}{Md}\left|\cos(\frac{\pi a}{2Md}+\alpha)\right|]} \tag{8.24}$$

The pit/crack transition parameter, $a_{p/c}$, can be decided by the following equation

$$(\frac{dX_{Pit}}{dN})_{x_{Pit}=a_{p/c}} = (\frac{da_{Crack}}{dN})_{a_{Crack}=a_{p/c}} \tag{8.25}$$

The fatigue lifetime is achieved by

$$N_f = N_{p/c} + N_{p/c \to a_k} \tag{8.26}$$

where

$$N_{p/c} = \frac{fa_{p/c}^2}{(1+\sqrt{1+4\varsigma_P^2})A_P} \tag{8.27}$$

$$N_{p/c \to a_k} = \frac{(1+\eta)N_0 L^2 \sigma_0^{\frac{1}{\beta}}}{(\Delta\sigma)^{\frac{1}{\beta}+1}}[2G_{IC}\ln\frac{a_k}{a_{p/c}} - \frac{\pi(1-\nu^2)(a_k - a_{p/c})(\Delta\sigma)^2}{E} + 2\pi D(\frac{1}{a_{p/c}} - \frac{1}{a_k})] \tag{8.28}$$

when $a < a_{p/c}$, the $a \sim N$ relation is

$$N = \frac{fa^2}{(1+\sqrt{1+4\varsigma_P^2})A_P} \tag{8.29}$$

when $a > a_{p/c}$,

$$N = N_{p/c} + \frac{(1+\eta)N_0 L^2 \sigma_0^{\frac{1}{\beta}}}{(\Delta\sigma)^{\frac{1}{\beta}+1}}[2G_{IC}\ln\frac{a}{a_{p/c}} - \frac{\pi(1-\nu^2)(a - a_{p/c})(\Delta\sigma)^2}{E} + 2\pi D(\frac{1}{a_{p/c}} - \frac{1}{a})] \tag{8.30}$$

In the present model the influence of microstructure on the growth rate of a fatigue crack is determined by the parameter D, which is related to the value of the fatigue strength. When tests were conducted within an aggressive environment the fatigue endurance value showed a severe reduction. Figures 8.3-8.6 and Figure 7.8 present a comparison between the model and corrosion fatigue test results where D = 120 N.

8.7 Summary

It can be seen from equation (8.12) that that the probability density function, $P_1(X_0, X; t)$ is a normal distribution function about X and its shape changes continuously with an increase in the corrosion time t under the effects of transportation corrosion and fluctuation corrosion. The probability density distribution function for the pit diameter based on parabolic kinetics $P_1(X_0, X; t)$ is neither a normal distribution alone nor a pure log normal distribution. Furthermore it can be seen from equations (8.13a), (8.14a), (8.15), (8.18), (8.19) and (8.20) that the average pit diameter, the most probable pit diameter, the mean square deviation and the maximum value of probability density function change with corrosion time t and A, and are a function of the metal, the composition of the environment, applied stress range, and temperature.

In general for a given metal and corrosive environment, the longer the corrosion time t, the bigger will be the average pit diameter and the mean square deviation, and the smaller the maximum value of probability density function. When the corrosion time t is given, a large value of A, will produce a greater average pit diameter and the mean square deviation, and a small value of the maximum value of probability density function. Because A is a macroscopic measurable quantity, its effect on average pit diameter, mean square deviation and maximum value of probability density function can be measured directly, so that it provides us with an opportunity to correlate theory and experiment.

The fluctuations in environment and of metallurgical structure are the physical basis for the corrosion statistical fluctuation found in engineering materials. Based on this concept the stochastic corrosion growth is given. The distribution function and the

average pit diameter are obtained, and it has been shown that these results coincide with the experiments.

The initiation and growth behaviour of corrosion pits were also investigated using a RQT501 steel, and the following results were obtained.

(1) The pit growth rate is given by equation (8.19) and the corrosion coefficient A_p increases with an increase in stress range.

(2) In order to appreciate the behaviour of short cracks under corrosion fatigue conditions, it follows that the dominant features of damage mechanisms require to be incorporated into analytical models to describe curves such as $da/dN \sim N$ curve of Figures 8.3-8.4 and $a \sim N$ curve of Figures 8.5-8.6. This can be achieved by considering the separate regimes, namely

stress corrosion pitting and

corrosion fatigue cracking

The statistical distribution characteristics of pit diameter and corrosion rate have been proved by experiment, however, what the exact property of the distribution function is, what physical quantities it depends on and with what form of function it changes, all remain to be judged systematically by experiments. Therefore, some results obtained in this chapter can only be regarded as theoretical prediction.

Chapter 9

A Dislocation Model of the Effects of Hydrogen on Crack Growth

9.1 Dislocation Model

It is well known that the high stress around a crack tip is favourable for hydrogen uptake and causes an accumulation of hydrogen which may be effective in enhancing crack growth rates. This distribution of hydrogen will also give rise to the change of the stress intensity factor range ΔK. It is possible to use dislocations to simulate the plastic deformation in the vicinity of the crack due to that the presence of hydrogen should produce strain field [153]. There may be some difference between the hydrogen located ahead of the crack and those at the side of the crack. The former tends to increase ΔK and the latter to decrease it. A simple dislocation model (Figure 9.1) is assumed. The dislocations around the crack are produced by the distribution of hydrogen.

9.2 Calculation of Stress Intensity Factor

Now the dislocation model is used to calculate and compare the contributions to the stress intensity factor between the hydrogen ahead of the crack and that at the side of

the crack. Here the question of steady propagation is discussed and a quasi-static approximation method, namely consider some state after the crack develops, is adopted.

If $\rho^{\wedge}(x)$ and $\rho^{S}(x)$ are respectively the dislocation density function ahead of the crack and at the side of the crack see Figure 9.1, and $D(x)$ is the dislocation density function of the crack, for $|x| \le \frac{a}{2}$, then:

$$A\int_{-\frac{a}{2}}^{\frac{a}{2}} \frac{D(x')}{x-x'}dx' + \Delta\sigma - A\int_{-\frac{a}{2}}^{\frac{a}{2}} \frac{\rho^{S}(x')}{x'-x}dx' + A\left(\int_{-\infty}^{-\frac{a}{2}} + \int_{\frac{a}{2}}^{\infty}\right)\frac{\rho^{\wedge}(x')}{x'-x}dx' = 0 \qquad (9.1)$$

Where $A = \frac{\mu b}{2\pi(1-\nu)}$, $\Delta\sigma$ is the applied stress range, μ is the shear modulus, and ν is the Poisson's constant. Let

$$F_S(x) = -A\int_{-\frac{a}{2}}^{\frac{a}{2}} \frac{\rho^{S}(x')}{x'-x}dx' \qquad (9.2)$$

$$F_A(x) = -A\left(\int_{-\infty}^{-\frac{a}{2}} + \int_{\frac{a}{2}}^{\infty}\right)\frac{\rho^{\wedge}(x')}{x'-x}dx' \qquad (9.3)$$

$$F(x) = \Delta\sigma + F_S(x) + F_A(x) \qquad (9.4)$$

then equation (9.1) becomes

$$A\int_{-\frac{a}{2}}^{\frac{a}{2}} \frac{D(x')}{x-x'}dx' + F(x) = 0 \qquad (9.5)$$

The solution of equation (9.5) is

$$D(x) = \frac{1}{\pi^2 A}\int_{-\frac{a}{2}}^{\frac{a}{2}} \sqrt{\frac{a^2-4x'^2}{a^2-4x^2}}\,\frac{F(x')}{x-x'}dx' + \frac{2I}{\pi\sqrt{a^2-4x^2}} \qquad (9.6)$$

The second term on the right hand side of equation (9.6) is a homogeneous solution. Integrating equation (9.6) gives the constant, I, by the following equation

$$I = \int_{-\frac{a}{2}}^{\frac{a}{2}} D(x)dx \qquad (9.7)$$

Because $F(x)$ is symmetric to the axis y, thus the integration of equation (9.7) is zero, namely $I = 0$.

Let $x < a/2$ and set $s = \left|x - \frac{a}{2}\right| << \frac{a}{2}$, from equation (9.6) the expression of the dislocation density in the vicinity of the crack tip is approximately:

$$D(x) = \frac{K}{\pi^2 A\sqrt{a}}(-s)^{1/2} \tag{9.8}$$

Where

$$K = 2\sqrt{\frac{a}{2\pi}}\int_0^{\frac{a}{2}} \frac{2F(x')}{\sqrt{a^2 - 4x'^2}}dx' \tag{9.9}$$

That is, the stress intensity factor at the crack tip,

$$K_0 = \sqrt{\pi a}\Delta\sigma \tag{9.10}$$

$$K_S = 2\sqrt{\frac{a}{2\pi}}\int_0^{\frac{a}{2}} \frac{2F_S(x')}{\sqrt{a^2 - 4x'^2}}dx' \tag{9.11}$$

$$K_A = 2\sqrt{\frac{a}{2\pi}}\int_0^{\frac{a}{2}} \frac{2F_A(x')}{\sqrt{a^2 - 4x'^2}}dx' \tag{9.12}$$

Then

$$K = K_0 + K_S + K_A \tag{9.13}$$

where K_0 is the stress intensity factor free of hydrogen effect, K_A and K_S represent respectively the contribution of hydrogen ahead of the crack and at the side of the crack to the stress intensity factor.

- *Contribution of hydrogen ahead of the crack*

  The size of the plastic zone is given by [154]

$$r_0 = \frac{1}{6\pi}\left(\frac{K_{IC}}{\sigma_{ys}}\right)^2 \tag{9.14}$$

According to existing experimental information, it has been shown that the dislocation density $\rho^A(x)$ is proportional to the concentration value of hydrogen C_H [155]. Without loss of generality, it is always possible to postulate that

$$\rho^A(x) = \lambda C_H(x)$$

where λ is a dimensional constant.

The actual distribution is expected to be non-uniform and to be governed by the exact nature of the chemical reactions local to the crack tip region. The absorbed hydrogen resides in the subsurface layer of metal and is available for transport to the crack tip region by diffusion. The diffusion process is driven by the gradient of hydrogen's chemical potential which depends, in turn, upon the hydrogen's activity and the hydrostatic stress gradient. Because of the large hydrostatic stress at the crack tip, large concentrations of hydrogen can accumulate there.

Assume $\rho^{A}(r_0+\frac{a}{2})=0$, $\rho^{A}(\frac{a}{2})=\rho_m^{A}=\alpha C_{Hm}$, i.e. the hydrogen diffusion is induced by the stress gradient so that the dislocation density at the crack tip is relatively large. Here C_{Hm} is the hydrogen concentration near crack tip. The dislocation density outside the plastic deformation zone is zero. Assuming that $\rho^{A}(x)$ is a linear function of x, then:

$$\rho^{A}(x)=-\frac{\rho_m^{A}}{r_0}x+\frac{\rho_m^{A}}{r_0}(r_0+\frac{a}{2}),\ \frac{a}{2}<x<r_0+\frac{a}{2} \tag{9.15}$$

ρ_m^{A} is the concentration of hydrogen near the crack tip. From equation (9.3) and substituting equation (9.15) into it gives:

$$F_A(x)\approx\frac{1}{2}A\rho_m^{A}r_0\left(\frac{1}{r_0+\frac{a}{2}-x}+\frac{1}{r_0+\frac{a}{2}+x}\right) \tag{9.16}$$

where the following two approximate relations are used:

$$\left(\frac{x-r_0-\frac{a}{2}}{r_0}\right)\ln\left(\frac{r_0+\frac{a}{2}-x}{\frac{a}{2}-x}\right)\approx -1-\frac{1}{2}\frac{r_0}{r_0+\frac{a}{2}-x}$$

$$\left(\frac{x+r_0+\frac{a}{2}}{r_0}\right)\ln\left(\frac{\frac{a}{2}+x}{r_0+\frac{a}{2}+x}\right)\approx -1-\frac{1}{2}\frac{r_0}{r_0+\frac{a}{2}+x}$$

Substituting equation (9.16) into equation (9.12) gives:

$$K_A=\sqrt{\pi\frac{a}{2}}A\rho_m^{A}\sqrt{\frac{r_0}{r_0+a}} \tag{9.17}$$

- *Contribution of hydrogen at the side of the crack*

The dislocation density is expected to be largest along the crack flank regions adjacent to the crack tip and decrease as the distance from the crack tip increases.

Let $\rho^S(\frac{a}{2}) = \rho^S_m$, $\rho^S(0) = \rho^S_0$, ρ^S_m and ρ^S_0 are relative to the size of plastic zone r_0 and the hydrogen concentration. The $\rho^S(x)$ is also assumed as a linear function of x

$$\rho^S(x) = 2\frac{\rho^S_m - \rho^S_0}{a}x + \rho^S_0 \qquad (9.18)$$

From equation (9.2) and substituting equation (9.18) into it gives:

$$F_S(x) \approx -2A(\rho^S_m - \rho^S_0)[1 - \frac{4x^2}{a(a+2x)}] + 2A\rho^S_0\frac{2x}{a+2x} \qquad (9.19)$$

where an approximate relation:

$$\ln(\frac{a-2x}{a+2x}) \approx -\frac{4x}{a+2x}$$

is used. Substituting equation (9.19) into equation (9.11) gives:

$$K_S = 4(\frac{a}{2\pi})^{1/2} A[3(\frac{\pi}{2} - 1)\rho^S_0 - (\pi - 2)\rho^S_m] \qquad (9.20)$$

9.3 Discussion

Through above calculation, it can be seen that $K_A > 0$, therefore the hydrogen distribution ahead of the crack causes an increase in the stress intensity factor and results in embrittlement. From equation (9.17), it can be seen that:

$$K_A = \sqrt{\pi\frac{a}{2}}A\rho^A_m \qquad \text{for short crack} \qquad (9.21a)$$

$$K_A = A\rho^A_m\sqrt{\frac{\pi r_0}{2}} \qquad \text{for long crack} \qquad (9.21b)$$

At the short crack stage, K_A is more dependent on the crack length and hydrogen concentration near the crack tip. However for a long crack, K_A tends to be only relative to the hydrogen concentration. Hence this part of the hydrogen contribution is more obvious within certain crack length.

When $\frac{2\pi-4}{3\pi-6} < \frac{\rho_0^S}{\rho_m^S} < 1$, $K_S > 0$, the hydrogen along the side of the crack flank plays a similar role to that ahead of the crack tip. However when $0 \le \frac{\rho_0^S}{\rho_m^S} \le \frac{2\pi-4}{3\pi-6}$, $K_S \le 0$, the hydrogen distribution at the side of the crack decreases the stress intensity factor and is favourable to resist crack growth.

In order to compare K_S and K_A, take $\rho_m^S = \rho_m^A$, $\rho_0^S = 0$, and from equations (9.17) and (9.20), then

$$\frac{K_S}{K_A} = -\frac{4(\pi-2)}{\pi}(1+\frac{a}{r_0})^{1/2} \tag{9.22}$$

If take $\rho_m^S = \rho_0^S$, i.e., a uniform distribution of hydrogen, of magnitude $\rho_0^S = \frac{\rho_0^S}{\alpha}$, along all boundaries.

$$\frac{K_S}{K_A} = -\frac{2(\pi-2)}{\pi}(1+\frac{a}{r_0})^{1/2}\frac{\rho_0^S}{\rho_m^A} \tag{9.23}$$

Because $0 \le \frac{\rho_0^S}{\rho_m^S} \le 1$, hence from equations (9.22) and (9.23), then

$$-\frac{4(\pi-2)}{\pi}(1+\frac{a}{r_0})^{1/2} \le \frac{K_S}{K_A} \le \frac{2(\pi-2)}{\pi}(1+\frac{a}{r_0})^{1/2}$$

$$-1.45(1+\frac{a}{r_0})^{1/2} \le \frac{K_S}{K_A} \le 0.73(1+\frac{a}{r_0})^{1/2} \tag{9.24}$$

It can be seen that when $\frac{K_S}{K_A} > -1$, which is possible, the influence of the dislocations induced by hydrogen at the side of the crack tip partially offsets the influence of the crack dislocations, which is similar to that of blunting a crack, namely the toughness increases, otherwise it is embrittled.

9.4 Crack Extension Force

If both tips of the crack expand along the axis x, the change of the stress state in the vicinity of the crack tip induces diffusion of hydrogen so that the dislocation density changes and dislocations are redistributed. The following equations are the energy of

changes and dislocations are redistributed. The following equations are the energy of the dislocations ahead of the crack tip, W_{HD}, and at the side of the crack flank, W_{HS}, respectively.

$$W_{\mathrm{HA}} = -2E_{\mathrm{D}} \int_{\frac{a}{2}}^{\frac{a}{2}+r_0} \rho^{\mathrm{A}}(x')dx'$$

$$= -2E_{\mathrm{D}} \int_{\frac{a}{2}}^{\frac{a}{2}+r_0} [-\frac{\rho_{\mathrm{m}}^{\mathrm{A}}}{r_0}x' + \frac{\rho_{\mathrm{m}}^{\mathrm{A}}}{r_0}(r_0 + \frac{a}{2})]dx'$$

$$= -E_{\mathrm{D}}\rho_{\mathrm{m}}^{\mathrm{A}} r_0$$

$$W_{\mathrm{HS}} = \pm 2E_{\mathrm{D}} \int_0^{\frac{a}{2}} \rho^{\mathrm{S}}(x')dx'$$

$$= \pm 2E_{\mathrm{D}} \int_0^{\frac{a}{2}} (-2\frac{\rho_{\mathrm{m}}^{\mathrm{S}} - \rho_{0}^{\mathrm{S}}}{a}x' + \rho_0^{\mathrm{S}})dx'$$

$$= \pm E_{\mathrm{D}}(\rho_{\mathrm{m}}^{\mathrm{S}} + \rho_0^{\mathrm{S}})\frac{a}{2}$$

where E_{D} is the energy required for producing a dislocation of unit length, and here the interaction among dislocations is neglected. The increase of the dislocation density of both sides of the crack may retard or increase the propagation of the crack and change the critical crack extension force. As the change of the crack extension force $G_{\mathrm{IC}}^{\mathrm{H}}$ due to the existence of hydrogen may be defined as the energy required for producing dislocations when the crack expands unit area.

$$\Delta G_{\mathrm{IC}}^{\mathrm{H}} = \frac{dW}{da} = \pm\frac{E_{\mathrm{D}}(\rho_{\mathrm{m}}^{\mathrm{S}} + \rho_0^{\mathrm{S}})}{2} \tag{9.25}$$

The total crack extension force is

$$G_{\mathrm{IC}}^{\mathrm{H}} = G_{\mathrm{IC}} + \Delta G_{\mathrm{IC}}^{\mathrm{H}} \tag{9.26}$$

where G_{IC} is the crack extension force free of hydrogen.

9.5 Crack Growth Behaviour Effect by Hydrogen Embrittlement

Because the diffusion process is assumed to be rapid in the fatigue crack growth process, only the steady-state distribution of hydrogen (the quasi-equilibrium assumption) is of interest [156]. The quasi-equilibrium distribution results when the time constant for diffusion is small with respect to the observational time scale of the fatigue crack growth experiments (i.e. $1/f$), and this distribution is determined by solving a "steady-state" diffusion problem (i.e. all time derivatives are set to zero) subject to a particular value of the driving force for diffusion.

The model adopted in Chapter 7 will be modified by substituting nb with $nb + \rho^{A}(c)$, G_{IC} with G_{IC}^{H} and $\frac{d\rho(c)}{dN} = 0$ in equation (7.6). Then the fatigue crack growth rate, the relationship between the half surface crack length and the number of cycles, and the fatigue lifetime (equations 7.17-7.19) are rewritten as

$$\frac{dc}{dN} \approx \frac{(1+\eta)(\Delta\sigma)^{\frac{1}{\beta}+1} c}{N_0 L^2 \sigma_0^{\frac{1}{\beta}} [2G_{ic}^{H} - \frac{\rho^{A}(c)\Delta\sigma}{2} - \frac{2\pi(1-\nu^2)(\Delta\sigma)^2 c}{E} + \frac{\pi D}{Md}\left|\cos(\frac{\pi c}{Md} + \alpha)\right|]} \quad (9.26)$$

$$N = \frac{N_0 L^2 \sigma_0^{\frac{1}{\beta}} (1+\eta)}{(\Delta\sigma)^{\frac{1}{\beta}+1}} [(2G_{ic}^{H} - \frac{\rho^{A}(c)\Delta\sigma}{2}) \ln\frac{c}{c_0} - \frac{2\pi(1-\nu^2)(c-c_0)(\Delta\sigma)^2}{E} + \pi D)(\frac{1}{c_0} - \frac{1}{c})] \quad (9.27)$$

$$N_i = \frac{N_0 L^2 \sigma_0^{\frac{1}{\beta}} (1+\eta)}{(\Delta\sigma)^{\frac{1}{\beta}+1}} [(2G_{ic}^{H} - \frac{\rho^{A}(c)\Delta\sigma}{2}) \ln\frac{c_k}{c_0} - \frac{2\pi(1-\nu^2)(c_k-c_0)(\Delta\sigma)^2}{E} + \pi D)(\frac{1}{c_0} - \frac{1}{c_k})] \quad (9.28)$$

It can be seen from these results that fatigue crack growth rate increases but fatigue lifetime decreases with the hydrogen concentration around the crack tip which is related to the parameter $\rho^{A}(c)$ in the above equations. The equations (9.26)-(9.28) have also been used for the calculation of the $da/dN \sim N$, $a \sim N$ curves and fatigue lifetimes under cathodic polarisation as shown in Figures 9.2-9.4 and 7.8 and Table 7.1.

Here, because experimental data are not ample and $2G_{IC}^{H} - \frac{\rho^{A}(c)\Delta\sigma}{2}$ is adopted approximately as 20 N/mm.

9.6 Summary

It is proposed that the distribution of dislocations around the crack tip is affected by hydrogen adsorption due to the nature of the stress state at the crack tip being favourable for hydrogen uptake. Accordingly, a model for hydrogen embrittlement has been developed. The theoretical formulae for the fatigue crack growth rate and lifetime have been derived from the new proposed model. All the results are universal and agree with the experimental data.

Chapter 10

Conclusions and Future Work Plan

10.1 Conclusions

Based upon the experimental and theoretical work undertaken within this study the following conclusions may be drawn:

(1) *Metallography Examination*

- RQT501 steel exhibits a uniform tempered martensite microstructure having a uniform grain size and distribution of inclusions (oxide and sulphide).
- The average grain size of steels with and without the addition of Mo and V is 11 μm and 9 μm respectively.
- The inclusion size for both steels is around 8 μm. The area fraction of inclusions within the steel is less than 0.9%.
- Hardness profiles taken for each steel show a systematic variation of hardness from the outer edge to the centre section.

(2) *Fatigue Crack Growth Behaviour*

- Fatigue crack growth behaviour is characterised by initial crack development from inclusions in air, corrosion pits in 3.5%NaCl solution or artificial seawater

under freely corroding conditions and surface defects and polishing microscratches under applied cathodic polarisation (-950 mV/SCE).

- The influence of mechanical factor on the transition behaviour from a pit to a crack increases with the increase of the stress range when the stress is above the yield stress. However when the stress is below the yield stress, the mechanical effect seems to be different as the number of pits decreases while some large pits appears.

- The presence of 3.5%NaCl solution accelerates corrosion fatigue crack initiation and also accelerates propagation of both short and long corrosion fatigue cracks in RQT501 steel. Applied cathodic polarisation inhibits crack initiation and propagation of very short (with very low ΔK) cracks and therefore has a beneficial effect on the $S \sim N_f$ curves for the steel in 3.5%NaCl solution. However, cathodic polarisation accelerates propagation of longer fatigue cracks. Since the fatigue design of offshore installations is based on $S \sim N_f$ data the practical implications of these conclusions for long service and extended fatigue lives are considerable.

- Short fatigue crack test results correlate well with long fatigue crack growth data at ΔK values above 10 MPa$\cdot\sqrt{m}$ as well. Under applied cathodic polarisation, long fatigue crack growth is much faster when compared with freely corroding conditions. and fatigue cracking exhibits a typical plateau in fatigue crack growth rate as a function of ΔK, suggesting that a hydrogen embrittlement mechanism may be operative.

(3) *Effect of Mo and V Additions*

- At a polarisation potential of -950 mV/SCE, in the region $20 < \Delta K < 40$ MPa$\cdot\sqrt{m}$, it appears that the addition of Mo and V improves the corrosion fatigue resistance of RQT501 steel.

- For smooth specimens, in the case of fatigue cracking dominated failure and at same stress level, Steel A (no Mo/V) shows longer fatigue and corrosion fatigue lifetime and better fatigue and corrosion fatigue resistance than that of Steel B.

- The addition of Mo and V which can act as traps and sinks for hydrogen can either enhance or inhibit hydrogen damage. The ability of Mo and V to trap hydrogen within the microstructure can either cause localised hydrogen embrittlement which acts as an initiation site of a crack or prevent a critical accumulation at the crack tip by distributing the hydrogen within the microstructure.

(4) *Modelling of Fatigue Crack Growth Behaviour*

- Based upon non-equilibrium statistical theory a fatigue crack growth model has been developed to predict fatigue crack growth behaviour by $a \sim N$ curve, $da/dN \sim N$ curve and fatigue lifetime, with the consideration of the influence of microstructure for example grain boundaries and hydrogen embrittlement. Furthermore this analytical procedure has been adopted to construct a stochastic theory for corrosion behaviour which is incorporated into the corrosion fatigue model.

10.2 Recommendations for Future Work

It has been interesting for me to be involved in this field. It is also important to study the fatigue damage of machines and structures operating in corrosive environments, because such environments reduce fatigue strength far below the typical fatigue strength determined in air. The analysis of fatigue behaviour in corrosive environments is more complicated in comparison with that in air, because there are at least 30 mechanical, environmental, and metallurgical variables that contribute to interactions involved in corrosion fatigue processes. These indicate that to evaluate the corrosion fatigue damage and to improve materials behaviour it is still necessary to fully understand the interaction between various variables. Therefore much effort needs to be done both on the experimental and theoretical work. In this respect the following suggestions are made for future work.

(1) Due to the fact that fatigue is sensitive to many factors which may be different in each application area, extrapolating fatigue behaviour obtained by studying crack growth under constant amplitude loading conditions to in-service loading

is not easy as the latter has variable amplitude and frequency content. It is also possible that under realistic loading conditions, sequence effects can be significant, resulting in both fatigue crack acceleration and retardation which can neither be reproduced nor predicted by tests under constant amplitude loading. Therefore the future work will draw attention to the investigations of corrosion fatigue behaviour under different or special required load histories.

(2) The production rate of hydrogen depends on the electrochemical potential applied and pH value of the environment. The effect of Mo and V additions, necessary for hydrogen traps, on corrosion fatigue behaviour is still worthy of study. It would appear that some benefit is seen in lowering long corrosion fatigue crack growth rates. A study on steels having higher Mo/V contents would provide information on whether the Mo/V contents used in the steels in the current study are at an optimised value to give maximum corrosion fatigue resistance.

(3) The plastic replica method is available for the investigation of the fatigue behaviour in a corrosive environment, however, the gathering of plastic replicas removes corrosion products from the specimen surface and affects the distribution states of crack length. Therefore, there is currently a need to derive new non-destructive testing techniques for corrosion fatigue damage measurement. The scanning reference electrode technique offers the prospect of allowing in situ corrosion fatigue testing and evaluation of the localised damage for the smooth specimens.

(4) The analyses in the current work show that crack closure can exist due to the presence of the asperities resulting from corrosion products, or surface roughness, resulting in the change in the slopes of the fatigue crack growth curves.

Corrosion fatigue crack growth behaviour of RQT501 steels is sometimes characterised by multiple cracking. Information from the replicas shows that some fatigue cracks grew from separate pits and merged at a later stage, producing a single crack that accelerated the failure of the specimen.

Concerning the closure effect and crack coalescence, modifications to the present theoretical model will be considered.

References

1. Austen I. M. and Walker E. F. (1984), "Corrosion fatigue crack propagation in steels under simulated offshore conditions", in '*Fatigue 84 Proc. 2nd. Int. Conf. on Fatigue Threshold*' (Ed. Beevers C. J.), EMAS pub. Vol. 3, pp. 1457-1471.

2. Cole I. S., Brook R. and Howard I. C. (1990), "The environmental performance of higher strength steels for offshore applications", in '*Environment Assisted Fatigue*' (Ed. Scott P.) EGF 7, Mechanical Engineering Publications, London, pp. 353-366.

3. Shimomura Jun-ichi, Nakano Yoshifumi, Nakano Syozaburo and Ueda Syuzo (1991), "Improvement in resistance to disbonding of stainless steel - overlayed Cr-Mo steels", *ISIJ International*, Vol. 31, No. 4, pp. 379-386.

4. Akid R. and Wu X. J. (1994), "Frequency effects on the fatigue crack initiation and propagation in an offshore steel", in '*Proceedings (4th) International Offshore and Polar Engineering Conference*', Osaka, Japan, 10-15 April, 1994, Published by ISOPE, Colerado 80402-1107, USA, Vol. IV, pp. 142-147.

5. Wei R. P. and Chiou Song (1992), "Corrosion fatigue crack growth and electrochemical reactions for an X-70 linepipe steel in carbonate-bicarbonate solution", *Engineering Fracture Mechanics*, Vol. 41, No. 4, pp. 463-473.

6. Schutz W. (1996), "A history of fatigue", *Engineering Fracture Mechanics*, Vol. 54, No. 2, pp. 263-300.

7. Mughrabi H., Wang R., Differt K. and Essmann V. (1983), "Fatigue crack initiation by cyclic slip irreversible in high cycle fatigue", in '*Fatigue Mechanisms: Advances in Quantitative Measurement of Physical Damage*' (Eds. Lankford J., Davidson D. L. and Morris W. L.), ASTM publication, Baltimore, pp. 5-43.

8. Kocanda S. (1978), *Fatigue Failure of Metals*, Sijthoff & Noordhoff, The Netherlands.

9. Klesnil M. and Lukas P. (1980), *Fatigue of Metallic Materials*, Elsevier, Amsterdam.

10. Frith P. H. (1948), "Fatigue test on crank shaft steels: I - The effect of nitriding on the fatigue properties of a chromium-molybdenum steel; II - Test on nickel-chromium molybdenum and chromium-molybdenum-vanadium steels", *J. Iron Steel Inst.*, Vol. 159, Pt. 4, pp. 385-409.

11. Cottrell H. and Hull D. (1957), "Extrusion and intrusion by cyclic slip in copper", *Proc. Roy. Soc.*, Vol. A242, pp. 211-213.

12. Cheng Alex S. and Laird Campbell (1981), "Fatigue life behaviour of copper single crystals. Part II. - Model for crack nucleation in persistent slip bands", *Fatigue Engng Mater. Structures*, Vol. 4, No. 4, pp. 343-353.

13. Miller K. J. (1987), "The behaviour of short fatigue cracks and their initiation. Part II. - A general summary", *Fatigue Fract. Engng Mater. Struct.*, Vol. 10, No. 2, pp. 93-113.

14. Akid R. (1990), "The initiation and growth of short fatigue cracks in aqueous saline environment", in '*Environment Assisted Fatigue*' (Eds. Scott P. and Cottis R. A.), pp. 415-434.

15. Lin T. H. and Ito Y. M. (1969), "Mechanics of a fatigue crack nucleation mechanism", *J. Mech. Phys. Solids*, Vol. 17, No. 6, pp. 511-523.

16. Neumann P. (1969), "Coarse slip model of fatigue", *Acta Metall.*, Vol. 17, No. 9, pp. 1219-1225.

17. Pedersen K. (1986), "The effect of microstructure on fatigue crack initiation in Al-Mg-Si alloys", in '*Aluminium Alloys - Their Physical and Mechanical Properties*', Vol. II (Eds. Starke Jr E. A. and Sanders Jr T. H.), EMAS, pp. 921-936.

18. Radhakrishnan V. M. and Mutoh Y. (1986), "On fatigue crack growth in Stage 1", in '*The Behaviour of Short Fatigue Cracks*' (Eds. Miller K. J. and de los Rios E. R.), European Group on Fracture Publication, 1, pp. 87-99.

19. de los Rios E. R., Tang Z. and Miller K. J. (1984), "Short crack behaviour in a medium carbon steel", *Fatigue Engng Mater. Struct.*, Vol. 7, No. 2, pp. 97-108.

20. Shih T. Y. and Araki T. (1973), "The effect of non-metallic inclusions and microstructures on the fatigue crack initiation and propagation in high strength carbon steels", *Trans. ISIJ*, Vol. 13, pp. 11-19.

21. Morris W. L. (1978), "The effect of intermetallic composition and microstructure on fatigue crack initiation in Al 2219-T851", *Metall. Trans. A*, Vol. 9, No. 9, pp. 1345-1348.

22. Akid R., Wang Y. Z. and Fernando U. S. (1995), "The influence of loading mode and environment on fatigue crack growth in a high tensile strength steel", in '*Corrosion-deformation Interaction*' (Eds. Magin T. and Gras J. M.), International Conference on CDI' 92, Fontainebleau - France, 5-7 October, 1992, pp. 659-670.

23. Wood W. A. (1958), "Formation of fatigue cracks", *Phil. Mag.*, Vol. 3, pp. 692-699.

24. Wescott B. B. (1938), "Fatigue and corrosion fatigue of steels", *Mech. Engng*, Vol. 60, No. 11, pp. 813-822.

25. McAdam Jr D. J. and Geil G. W. (1941), "Pitting and its effect on the fatigue limit of steels corroded under various condition", *Proc. ASTM*, Vol. 41, pp. 696-732.

26. Chauhan P. K. and Gadiyar H. S. (1985), "An XPS study of the corrosion of Cu-10 Ni-alloy in unpolluted and polluted sea-water - the effect of $FeSO_4$ addition", *Corros. Sci.*, Vol. 25, No. 1, pp. 55-68.

27. Whitwham D. and Evans U. R. (1950), "Corrosion fatigue - the influence of disarrayed metal", *J. Iron and Steel Inst.*, Vol. 165, Pt. 1, pp. 72-79.

28. Hahn H. N. and Duquette D. J. (1979), "The effect of heat treatment on the fatigue and corrosion fatigue behaviour of CuNiCr Alloy", *Metallurgical Transactions A*, Vol. 10A, No. 10, pp. 1453-1460.

29. Hahn H. N. and Duquette D. J. (1978), "The effect of surface dissolution on fatigue deformation and crack nucleation in copper and copper 8% aluminium single crystals", *Acta Metall.*, Vol. 26, pp. 279-287.

30. Yan B. D., Farrington G. C. and Laird C. (1985), "The interaction of simultaneous cyclic strain and aqueous corrosive attack in the behaviour of persistent slip bands", *Acta Metall.* Vol. 33, No. 9, pp. 1953-1600.

31. Masuda H. and Duquette D. J. (1975), "The effect of surface dissolution on fatigue crack nucleation in polycrystalline copper", *Metallurgical Transactions A*, Vol. 6A, No. 1, pp. 87-94.

32. Stoltz R. E. and Pelloux R. M. (1972), "Mechanisms of corrosion fatigue crack propagation in Al-Zn-Mg alloys", *Metallurgical Transactions*, Vol. 3, No. 9, pp. 2433-2441.

33. Smialowski Michael (1985), "Initiation of hydrogen-induced cracking in iron and iron alloys", in '*Hydrogen Degradation of Ferrous Alloys*' (Eds. Orian Richard A., Hirth John P. and Smialowski Michael), Park Ridge, N. J. Noyes, pp. 561-578.

34. Paris P. C. and Erdogan F. (1963), "Critical analysis of crack propagation laws", *Journal of Basic Engineering, Transactions of ASME*, Series D, Vol. 85, pp. 528-539.

35. Sudarshan T. S. and Louthan Jr M. R. (1987), "Gaseous environment effect on fatigue behaviour of metals", *International Materials Reviews*, Vol. 32, No. 3, pp. 121-151.

36. Richards C. E. and Lindley T. C. (1972), "The influence of stress intensity and microstructure on fatigue crack propagation in ferritic materials", *Engng Fract. Mech.*, Vol. 4, pp. 951-978.

37. Ritchie R. O. and Knott J. F. (1973), "Mechanisms of fatigue crack growth in an alloy steel", *Acta Metall.*, Vol. 21, pp. 639-648.

38. Pearson S. (1975), "Initiation of fatigue cracks in commercial aluminium alloys and the subsequent propagation of very short cracks", *Engineering Fracture Mechanics*, Vol. 7, pp. 235-247.

39. Hudak S. J. (1981), "Small crack behaviour and the prediction of fatigue life", *J. Eng. Mater. Techno.*, Vol. 103, No. 1, pp. 26-35.

40. Schijve J. (1982), "The stress intensity factor of small cracks at notches", *Fatigue of Engineering Materials and Structures*, Vol. 5, No. 1, pp. 77-90.

41. Miller K. J. and Ibrahim M. F E. (1981), "Damage accumulation during initiation and short crack growth regimes", *Fatigue of Engineering Materials and Structures*, Vol. 4, No. 3, pp. 263-277.

42. Suresh S. and Ritchie R. O. (1984), "Propagation of short fatigue cracks", *Inter. Metal Rev.*, Vol. 29, No. 6, pp. 445-476.

43. Gangloff R. P. (1981), "The criticality of crack size in aqueous corrosion fatigue", Res. Mechanica Lett., Vol. 1, pp. 299-306.

44. Lankford J. (1985), "The influence of microstructure on the growth of small fatigue cracks", *Fatigue Fract. Eng. Mater. Struct.*, Vol. 8, No. 2, pp. 161-175.

45. Ritchie R. O. and Lankford J. (1986), "Small fatigue cracks - a statement of the problem and potential solutions", *Mater. Sci. Eng.*, Vol. 84, No. 1-2, pp. 11-16.

46. Ritchie R. O. (1984), "Near-threshold fatigue crack-propagation - A perspective on the role of crack closure", in '*Fatigue Crack Growth Threshold Concepts*', Ch. 29, pp. 227-261.

47. McCarver J. F. and Ritchie R. O. (1982), "Fatigue crack propagation threshold for long and short cracks in René 95 nickel-bass superalloy", *Mater. Sci. Eng.*, Vol. 55, pp. 63-67.

48. Taylor D. and Knott J. F. (1981), "Fatigue crack propagation behaviour of short cracks; the effect of microstructure", *Fatigue Engng Mater. Struct.*, Vol. 4, No. 2, pp. 147-155.

49. Liaw P. K. and Logsdon W. A. (1985), "Crack closure: an explanation for small fatigue crack growth behaviour", *Eng. Fract. Mech.*, Vol. 22, No. 1, pp. 115-121.

50. Tanaka Keisuke (1987), "Mechanism and mechanics of short fatigue crack propagation", *JSME International Journal*, Vol. 30, No. 259, pp. 1-13.

51. Gangloff R. P. and Wei R. P. (1986), "Small crack-environment interaction: The hydrogen embrittlement perspective", in '*Growth of Small Fatigue Cracks*' (Eds. Lankford J. and Ritchie R. O), Warrendale, Pa, Metallurgical Society of AIME, pp. 75-91.

52. Miller K. J. and de los Rios E. R. (Eds.) (1986), *The Behaviour of Short Fatigue Cracks*, EGF Publication 1. Mechanical Engineering Publications, London.

53. Ritchie R. O. and Lankford J. (Eds.) (1986), *Small Fatigue Cracks*, The Metallurgical Society Inc..

54. Miller K. J. (1991), "Metal fatigue - past, current and future", *Proc. Instn. Mech. Engrs.*, Vol. 205, pp. 1-14.

55. Akid R. and Wu X. J. (1994), "Environmental effects on short crack growth behaviour of Q2N steel", in '*Proceedings of Special Offshore Symposium China (SOSC)*', Beijing, China, 16-18 April, 1994, published by ISOPE, Colerado 80402-1107, USA, pp. 259-267.

56. Akid R. (1994), "Modelling environment-assisted short fatigue crack growth", in '*Advances in Fracture Resistance and Structural Integrity*' (Eds. Panasyuk V. and Taplin DMR et al), Published by Pergamon Press, pp. 261-269.

57. Akid R. and Miller K. J. (1991), "Short fatigue crack growth behaviour of a low carbon steel under corrosion fatigue conditions", *Fatigue Fract. Eng. Mater. Struct.*, Vol. 14, No. 6, pp. 637-649.

58. Morris W. L. (1980), "The non-continuum crack tip deformation behaviour of surface microcracks", *Metall. Trans.* A, 11, pp. 1117-1123.

59. Lukas P. and Kunz L. (1985), "The mechanism of fatigue crack propagation", *Ko Vove Materials*, Vol. 223, No. 6, pp. 701-714.

60. Hobson P. D., Brown M. W. and de los Rios E. R. (1986), "Two phases of short crack growth in a medium carbon steel", in '*The Behaviour of Short Fatigue Cracks*' (Eds. Miller K. J. and de los Rios E. R.), European Group on Fracture Publication, 1, pp. 441-459.

61. Navarro A. and de los Rios E. R. (1987), "A model for short fatigue crack propagation with an interpretation of the short-long crack transition", *Fatigue Fract. Engng Mater. Struct.*, Vol. 10, pp. 169-186.

62. Navarro A. and de los Rios E. R. (1988), "An alternative model of blocking of dislocations at grain boundaries", *Phil. Mag.* A, Vol. 57, pp. 37-42.

63. Navarro A. and de los Rios E. R. (1988), "A microstructurally-short fatigue crack growth equation", *Fatigue Fract. Engng Mater. Struct.*, Vol. 11, No. 5, pp. 169-186.

64. Jones R. H. and Simonen E. P. (1994), "Early stages in the development of stress corrosion cracks", *Materials Science and Engineering*, Vol. A176, pp. 211-218.

65. Eickemeyer J. (1987), "Effect of the initial crack depth on the kinetics of corrosion", *Corrosion*, Vol. 43, No. 11, pp. 693-698.

66. Gangloff R. P. (1985), "Crack size effects on the chemical driving force for aqueous corrosion fatigue", *Metall. Trans. A*, Vol. 16, No. 5, pp. 953-969.

67. Boyer H. P. (Ed.) (1986), *Atlas of Fatigue Curves*, Metals Park, OH, American Society for Metals.

68. Smith R. A. (Ed.) (1986), *Fatigue Crack Growth: Thirty Years of Progress*, Oxford, Pergamon Press.

69. Yokobori T. (1979), "A critical evaluation of mathematical equations for fatigue crack growth with special reference to ferrite grain size and monotonic yield strength dependence", in '*Fatigue Mechanisms*' (Ed. Fong J. T.), STP 675, Philadelphia, Pa, ASTM, pp. 683-701.

70. Liu H. W. (1961), "Crack propagation in thin metal sheet under repeated loading", *J. Basic Eng.*, Ser. D (Trans. ASEM), Vol. 83, pp. 23-34.

71. Paris P. C. (1964), "The fracture mechanics approach to failure", in '*Fatigue - An Interdisciplinary Approach, Proceedings of the 10th Sagamore Army Materials Research Conference*', Syracuse University Press, Syracuse, N. Y., pp. 107-132.

72. Raju K. N. (1972), "An energy balance criterion for crack growth under fatigue loading from considerations of energy of plastic deformation", *Int. J. Fract. Mech.*, Vol. 8, No. 1, pp. 1-14.

73. Cherepanov Genady P. and Halmanov Habil (1972), "On the theory of Fatigue Crack Growth", *Eng. Fract. Mech.*, Vol. 4, No. 2, pp. 219-230.

74. Rice J. R. (1966), "Mechanics of crack tip deformation and extension by fatigue", in '*Fatigue crack propagation*', ASTM STP, No. 415, Philadelphia, Pa: ASTM, pp. 247-309.

75. Weertman J. (1965), "Rate of growth of fatigue cracks calculated from the theory of infinitesimal dislocations distributed on a plane", in '*Proc. 1st Intern. Conf. on 'Fracture'*", Sendai, Japan, Vol. 1, pp. 153-160.

76. Weertman J. (1973), "Theory of fatigue crack growth based on a BCS crack theory with hardening", *Int. J. Fract. Mech.*, Vol. 9, No. 2, pp. 125-131.

77. Mura T. and Lin C. T. (1974), "Theory of fatigue crack growth for work hardening materials", *Int. J. Fract. Mech.*, Vol. 10, No. 2, pp. 284-287.

78. Schwalbe K. (1973), "Approximate calculation of fatigue crack growth", *Int. J. Fract. Mech.*, Vol. 9, No. 4, pp. 381-395.

79. Pook L. P. and Frost N. E. (1973), "A fatigue crack growth theory", *Int. J. Fract. Mech.*, Vol. 9, No. 1, pp. 53-61.

80. Tomkins B. (1968), "Fatigue crack propagation - an analysis", *Phil. Mag.*, Vol. 17, pp. 1041-1049.

81. Donahue R. J., Clark H. M., Atanmo P., Kumble R. and McEvily A. J. (1972), "Crack opening displacement and the rate of fatigue crack growth", *Int. J. Fract. Mech.*, Vol. 8, No. 2, pp. 209-219.

82. Yokobori T. and Ichikawa M. (1968), "Effect of elastic-plastic stress distribution near the crack tip on the nucleation theory of fatigue crack propagation", *Rep. Res. Inst. Strength Fract. Mater.*, Tôhoku Univ., Vol. 4, No. 2, pp. 45-53.

83. Yokobori T., Yokobori Jr A. T. and Kamei A. (1975), "Dislocation dynamics theory for fatigue crack growth", *Int. J. Fract. Mech.*, Vol. 11, No. 5, pp. 781-788.

84. Forman G., Keravey V. E. and Engle R. M. (1967), "Numerical analysis of crack propagation in cyclically loaded structures", *Transactions of ASME, Journal of ASME*, Journal of Basic Engineering, Vol. 89, pp. 459-469.

85. Weertman J. (1979), "Fatigue crack propagation theories", in '*Fatigue and Microstructure*', Metals Park, Ohio, American Society for Metals., pp. 279-306.

86. Haigh B. P. (1917), "Experiments on the fatigue of brasses", *J. Inst. Metals*, Vol. 18, pp. 55-86.

87. McAdam D. J. (1929), "Corrosion of metals under cyclic stress", *Proc. ASTM* 29, pp. 250-313.

88. Anon. (1980), "Steel in marine structures", *Int. ECSC Conf.*, 1980, Paris, Kommission der Euroräischen Gemeinschaften.

89. Noordhoek C. and de Back J. (Eds.) (1987), *Steel in Marine Structures*, Proceedings of the 3rd Int. ECSC Offshore Conf. on SIMS' 87, Delft, Amsterdam, Oxford, Elsevier.

90. Wei R. P. (1970), "Some aspect of environment-enhanced fatigue-crack growth", *Eng. Fract. Mech.*, Vol. 1, pp. 633-651.

91. Wei R. P. (1979), "On understanding environment-enhanced fatigue crack growth - A fundamental approach", in '*Fatigue Mechanisms*' (Ed. Fong J. T.), ASTM STP 675, pp. 816-831.

92. Wei R. P. and Landes J. D. (1969), "Correlation between sustained-load and fatigue crack growth in high strength steels", *Mater. Res. Stand., ASTM*, Vol. 9, No. 7, pp. 25-27.

93. Jaske C. E., Payer J. H. and Balint V. S. (1981), *Corrosion Fatigue of Metals in Marine Environments*, Columbus, Ohio, Battelle Press.

94. Hagn L. (1988), "Life prediction methods for aqueous environments", *Materials Science and Engineering*, Vol. A103, pp. 193-205.

95. Sudarshan S., Srivatsan T. S. and Harvey II D. P. (1990), "Fatigue process in metals - role of aqueous environments", *Eng. Fract. Mech.*, Vol. 36, No. 6, pp. 827-852.

96. Wei R. P. (1981), "Fatigue crack growth in aqueous and gaseous environments", in '*Environmental Degradation of Engineering Materials in Aggressive Environments*' (Eds. Louthan Jr M. R., Mcnitt R. P. and Sisson R. D.), Blackburg, Va, Virginia Polytechnic Institute Press, Ch. 94, pp. 73-81.

97. McIntyre P. (1983), "Hydrogen-steel interactions during cyclic loading", in '*Corrosion Fatigue*' (Eds. Parkins R. N. and Kolotyrkin Ya. M.), London, The Metals Society, Ch. 17, pp. 62-73.

98. Rhodes D., Musuva J. K. and Radon J. C. (1981), "The significance of stress corrosion cracking in corrosion fatigue crack growth studies", *Engng Fracture Mech.*, Vol. 15, No. 3-4, pp. 407-419.

99. Magin T. (1995), "Recent advances for corrosion-fatigue mechanisms", *ISIJ International*, Vol. 35, No. 3, pp. 223-233.

100. Yu J., Brook R., Cole I., Mcrabito D. and Demofonti G. (1996), "The effect of cathodic protection potential on corrosion fatigue crack growth rate of an offshore structural steel", *Fatigue Fract. Engng Mater. Struct.*, Vol. 19, No. 8, pp. 1019-1029.

101. Ouchi Hiroshi, Kobayashi Jun'ichi, Soya Isao and Okamoto Kentaro (1994), "Fatigue crack growth in a high-tensile strength steel in seawater and several other environments", *ISIJ International*, Vol. 34, No. 5, pp. 451-459.

102. Landles K., Congleton J. and Parkins R. N. (1984), "Potential measurements along actual and simulated cracks", in '*Embrittlement by the Localised Crack Environment*', The Metallurg val Society, Ch. 27, pp. 59-74.

103. Akid R. (1994), "The influence of cathodic overpotential on microstructural and physically-small crack growth", in '*Hydrogen Transport & Cracking Metals*' (Ed. Turnbull Alan), Proceedings of a Conference held at the National Physical Laboratory, UK., 13-14 April, 1994, pp. 50-61.

104. Anon. (1981), "Fatigue in off-shore structural steels: Implic. of the Dep. of Energy's Res. Programme", *Proc. Internat. Conf.*, London, 24-25 Feb., 1981, Published by Thomas Telford Ltd., London, (1981).

105. Jaske C. E., Payer J. H. and Balint V. S. (1981), *Corrosion Fatigue of Metals in Marine Environments*, Battelle Press, Columbus, Ohio.

106. Beachem C. D. (1972), "A new model for hydrogen-assisted cracking (hydrogen 'embrittlement')", *Metall. Trans.*, Vol. 3A, No. 2, pp. 437-451.

107. Hirth J. P. (1980), "Effects of hydrogen on the properties of iron and steel", *Metall. Trans.*, Vol. 11A, No 6, pp. 861-890.

108. Kimura H. and Matsui H. (1987), "Mechanism of hydrogen-induced softening and hardening in iron", *Scr. Metall.*, Vol. 21, No. 3, pp. 319-324.

109. Lewandowski J. J. and Thompson A. W. (1983), "Hydrogen effects on fracture in pearlitic 1080-steel", *Journal of Metals*, Vol. 35, No. 8, p. A 7.

110. Chen S. H., Katz Y. and Gerberich W. W. (1990), "On the directional dependency of microplasticity for [100] cleavage in Fe-3 wt-percent-Si single crystals", *Scr. Metall.*, Vol. 24, No. 6, pp. 1125-1130.

111. Thomas James P. and Wei R. P. (1992), "Corrosion fatigue crack growth of steels in aqueous solutions I: experimental results and modelling the effects of frequency and temperature", *Materials Science and Engineering*, Vol. A159, pp. 205-221.

112. Oh K. P. (1979), "A diffusion model for fatigue crack growth", *Proc. R. Soc. Lond.*, Vol. A367, pp. 47-58.

113. Sobczyk K. (1982), "On the Markovian models for fatigue accumulation", *J. Mech. Theor. Appl. Numeric Special*, pp. 147-160.

114. Cox B. N., Pardee W. J. and Morris W. L. (1987), "A statistical model of intermittent short fatigue crack growth", *Fatigue Fract. Engng Mater.* Struct., pp. 435-455.

115. Itagaki H. and Shinozuka M. (1972), "Application of the Monte Carlo technique to fatigue - failure analysis under random loading", in '*Probabilistic Aspects of Fatigue*', ASTM STP 511, pp. 168-184.

116. Morris W. L., James M. R. and Buck O. (1980), "Remaining fatigue lifetime prediction for retirement - for cause in aluminium alloys", in '*Proc. TMS Fall Meeting*', Pittsburgh, pp. 389-399.

117. Lin Y. K. and Yang J. N. (1983), "On statistical moments of fatigue crack propagation", *Engng Fract. Mech.*, Vol. 18, pp. 243-256.

118. Bogdanoff J. L. (1978), "A new cumulative damage model, Part 1", *J. Appl. Mech.*, Vol. 45, pp. 246-250.

119. Bogdanoff J. L. and Krieger W. (1978), "A new cumulative damage model, Part 2", *J. Appl. Mech.*, Vol. 45, pp. 251-257.

120. Bogdanoff J. L. (1978), "A new cumulative damage model, Part 3", *J. Appl. Mech.*, Vol. 45, pp. 733-739.

121. Bogdanoff J. L. and Kozin F. (1984), "Probabilistic models of fatigue crack growth - II", *Engng Fract. Mech.*, Vol. 20, pp. 255-270.

122. Ghonem H. and Provan J. W. (1980), "Micromechanics theory of fatigue crack initiation and propagation", *Engng Fract. Mech.*, Vol. 13, pp. 963-977.

123. Arone R. (1981), "A Statistical model for fatigue fracture under constant amplitude cyclic loading", *Engng Fract. Mech.*, Vol. 14, pp. 189-194.

124. Kozin F. and Bogdanoff J. L. (1981), "A critical analysis of some probabilistic models of fatigue crack growth", *Engng Fract. Mech.*, Vol. 14, pp. 59-89.

125. Virkler D. A., Hillberry B. M. and Goel P. K. (1979), "The statistical nature of fatigue crack propagation", *J. Engng Mater. Tech. Trans.*, ASME 101, pp. 148-153.

126. Xing X. S. (1986), "Nonequilibrium statistical theory of fatigue fracture I", *Scientia Sinica Series A*, Vol. A5, pp. 501-510 (in Chinese).

127. Xing X. S. (1986), "Nonequilibrium statistical theory of fatigue fracture II", *Scientia Sinica Series A*, Vol. A8, pp. 840-852 (in Chinese).

128. Xing X. S. (1987), "Nonequilibrium statistical theory of fatigue fracture", *Eng. Fract. Mech.*, Vol. 26, No. 3, pp. 393-419.

129. Xing X. S. (1989), "Nonequilibrium statistical foundation of fatigue fracture", *Eng. Fract. Mech.*, Vol. 32, No. 6, pp. 935-946.

130. Pellissier-Tanon A., Bernard J. L., Amzallag C. and Rabbe P. (1982), "Evaluation of the resistance of the 316 stainless steel against progressive deformation", in '*Low-Cycle Fatigue and Life Prediction*', ASTM STP 770 (Eds. Amzallag C., Leis B. N. and Rabbe P.), ASTM, 1982, pp. 69-80.

131. ASTM (1981), "Fatigue pre-cracking of K_{IC} fracture toughness specimens", *ASTM Standard E 399-81 Annex A*.

132. Jack A. R and Price A. T. (1970), "The initiation of fatigue cracks from notches in mild steel plates", *Int. J. Fracture Mech.*, Vol. 6, No. 4, pp. 401-409.

133. Srawley J. E. (1976), "Wide range stress intensity factor expressions for ASTM E399 standard fracture toughness specimens", *International Journal of Fracture Mechanics*, Vol. 12, June 1976, pp. 475-476.

134. Newman J. E. (1974), "Stress analysis of compact specimens including the effects of pin loading", in '*Fracture Analysis (8th Conference)*', ASTM STP 560, pp. 105-121.

135. Marston L. W. (1995), "The effect of hydrogen traps upon the corrosion fatigue performance of rolled, quenched and tempered (RQT) 501 structural steel", *MSc Thesis*, University of Sheffield, UK.

136. Austen I. M. (1983), "Quantitative understanding of corrosion fatigue crack growth", *BSC European Community Steel Commission Contract No 7210 KE 806 Report*, EUR 8560 EN.

137. Irving P. E. and Kurzfeld A. (1978), "Measurements of intergranular failure produced during fatigue crack growth in quenched and tempered steels", *Metal Science*, November 1978, pp. 495-502.

138. Murakami Y. and Aoki S. et al. (1987), *Stress Intensity Factors Handbook*, Vol. 2, Oxford, Pergamon, pp. 654-656.

139. Nisitani H. and Chen D. H. (1984), "Stress intensity factors for a semi-elliptic surface crack in a shaft under tension", *Trans. Japan Soc. Mech. Engrs.*, Vol. 50, No. 453, pp. 1077-1082.

140. Miller K. J. (1993), "Materials science perspective of metal fatigue resistance", *Materials Science and Technology*, Vol. 9, pp. 453-462.

141. Fuchs H. O. and Stephens R. L. (1980), *Metal Fatigue in Engineering*, John. Wiley, New York.

142. Hobson P. D. (1985), "The growth of short fatigue cracks in a medium carbon steel", *PhD thesis*, University of Sheffield.

143. Akid R. (1995), "Localised corrosion: a new evaluation approach", *Materials World*, Vol. 3, No. 11, pp. 522-525.

144. Ishihara Sotomi, Shiozawa Kazuaki, Miyao Kazyu and Inoue Masato (1992), "Effects of fluid flow rate and stress amplitude on the initiation and growth behaviour of corrosion pits on annealed carbon steel", *JSME International Journal*, Series I, Vol. 35, No. 3, pp. 367-373.

145. Szklarska - Smialowska Z. (1985), *Pitting Corrosion of Metals*, Published by National Association of Corrosion Engineers, Houston, Texas.

146. Akid R. (1997), "The role of stress-assisted localised corrosion in the development of short fatigue cracks", in '*Effect of the Enviroment on the*

Initiation of Crack Growth' (Eds. Van Der Sluys W. A., Piascik R. S. and Zawierucha R.), ASTM STP1298, pp. 3-17.

147. Shibata T. (1994), "Application of extreme-value statistics to corrosion", *Journal of Research of the National Institute of Standards and Technology*, Vol. 99, No. 4, pp. 327-336.

148. Kannan D. (1979), *An Introduction to Stochastic Processes*, North Holland, Amsterdam.

149. Kottalam J., Lindenberg K. and West B. J. (1986), "Statistical replacement for systems with delta-correlated functions", *J. Stat. Phys.*, Vol. 42, No. 5-6, pp. 979-1008.

150. Risken H. (1984), *The Fokker-Planck Equation*, Springer, Berlin.

151. Hu H. and Xing X. S. (1991), "Statistical Theory of Grain Growth", *Physica Status Solidi (b)*, Vol. 166, No. 2, pp K61-K67.

152. ASTM (1987), *Metal Handbook* (Ninth Edition) Vol. 13, *Corrosion.*

153. Ashby M. F. (1971), "The deformation of plastically non-homogeneous alloys", in '*Strengthening Methods in Crystals*' (Eds. Kelly A. and Nicholson R. B. N.), Applied Science Publishers LTD, London.

154. Meletis E. I., Lian K. and Huang W. J. (1992), "Vacancy-dislocation interactions and transgranular stress corrosion cracking", in '*Corrosion-deformation Interactions*' (Eds. Magnin T. and Gras J. M.), Fontainebleau - France, 5-7 October, 1992, pp. 69-81.

155. Ding H. Z. and Xing X. S. (1992), "Theory of hydrogen-assisted crack growth", *Journal of Materials Science*, Vol. 27, pp. 3203-3205.

156. Thomas James P. and Wei R. P. (1992), "Corrosion fatigue crack growth of steels in aqueous solutions II: modelling the effects of ΔK", *Materials Science and Engineering*, Vol. A159, pp. 223-229.

Figures

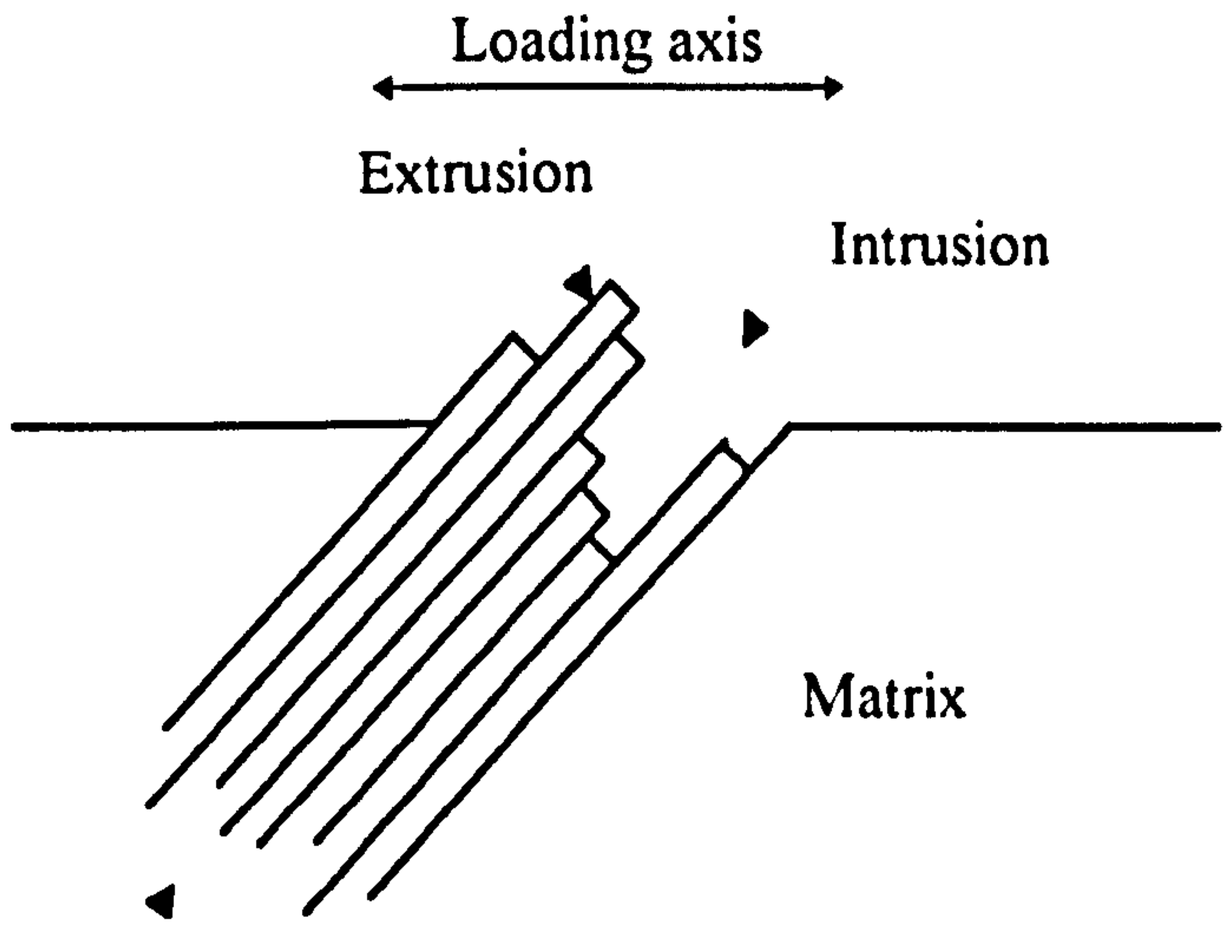

Figure 2.1 **Schematic of the single slip model of intrusion formation** (Ref. 23)

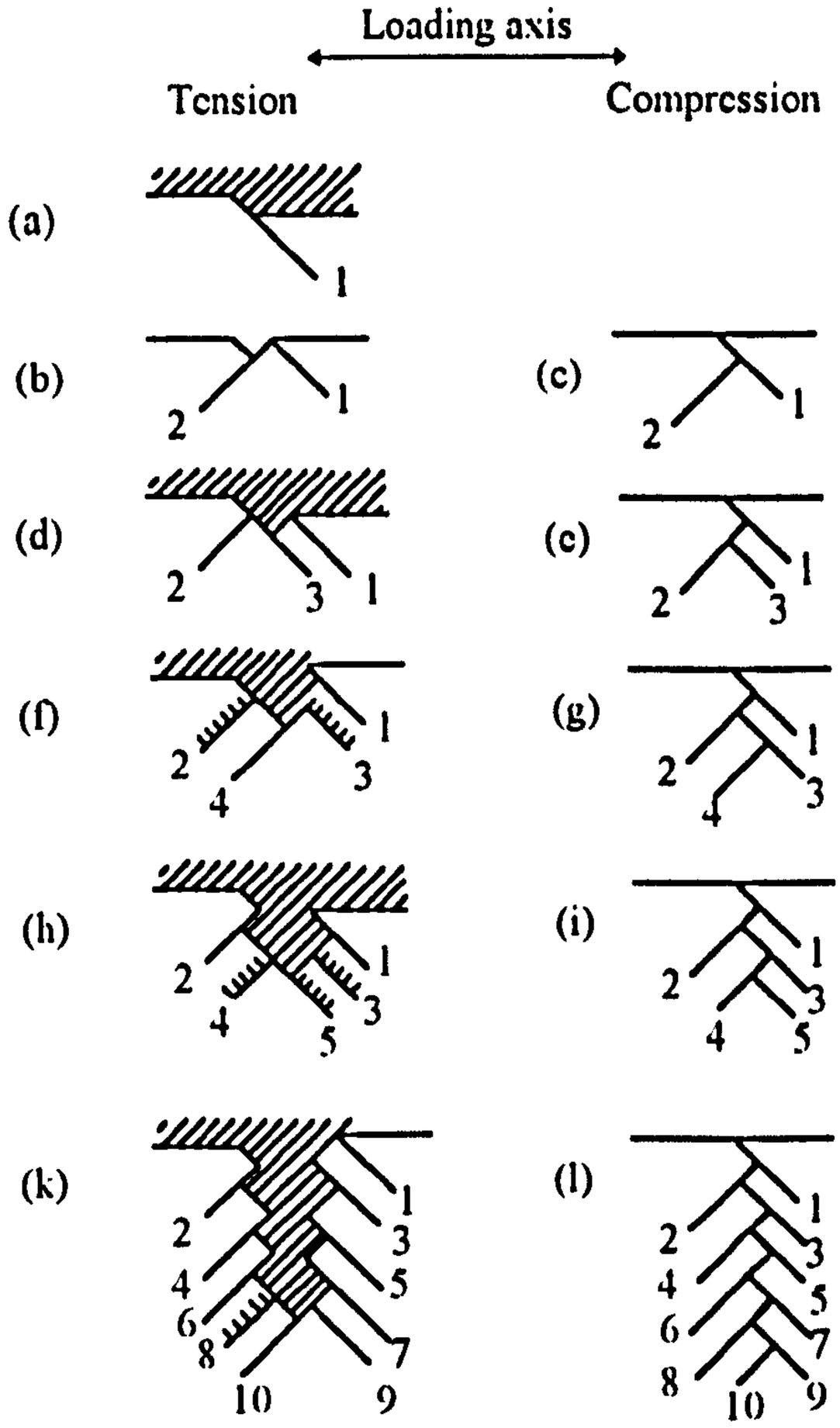

Figure 2.2 **Model for the formation of a crack by coarse slip.** The sequence of events is a, b, c, d, e, f, g, h, i, k, and l. In the figures of the right the applied stress is either zero or compressive. As the dislocations run out, a crack is created since motion along both planes occurs simultaneously (Ref. 16)

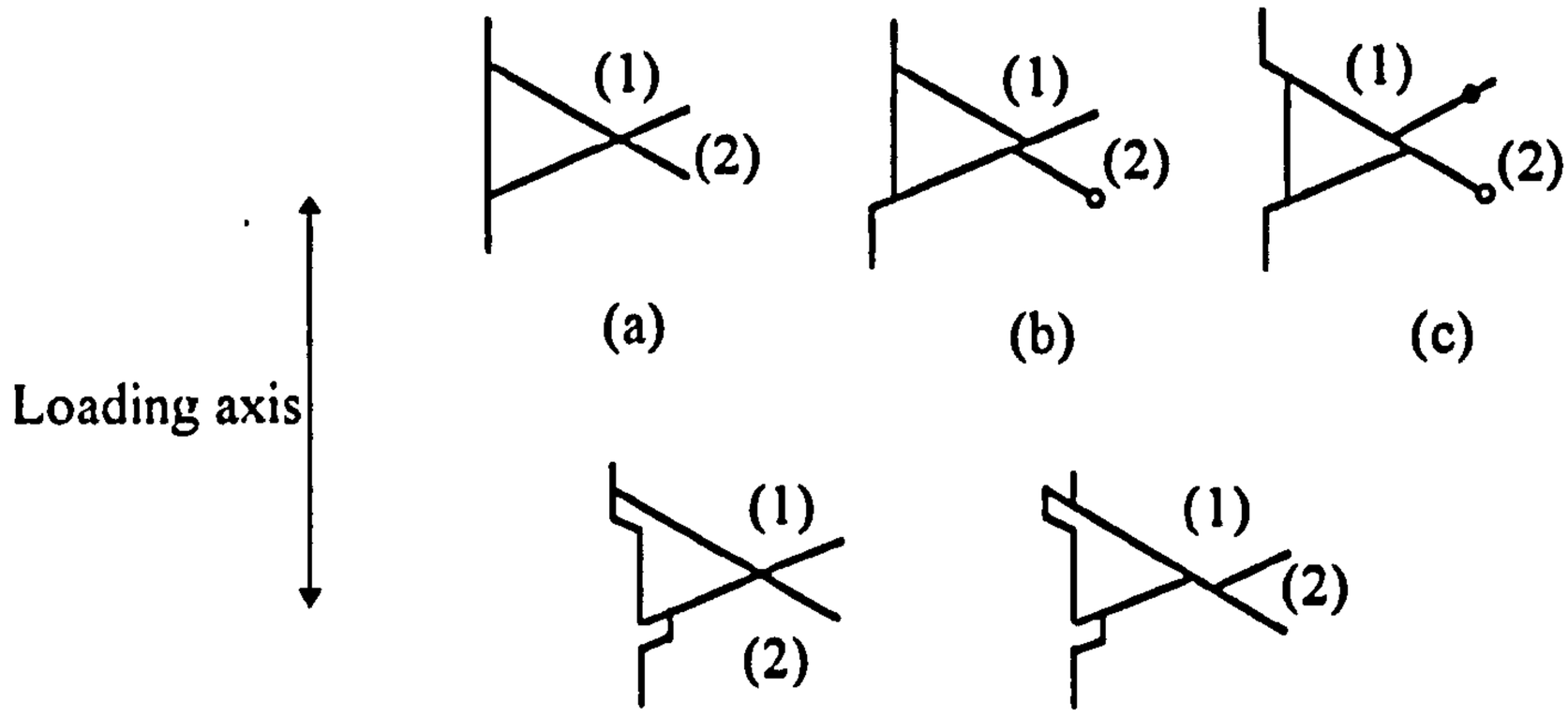

Figure 2.3 **Operation of two intersecting slip bands in a sequence resulting in the formation of intrusions and extrusions.** The forward cycle is represented by (b) and (c), and the reverse cycle by (d) and (e) (Ref. 11)

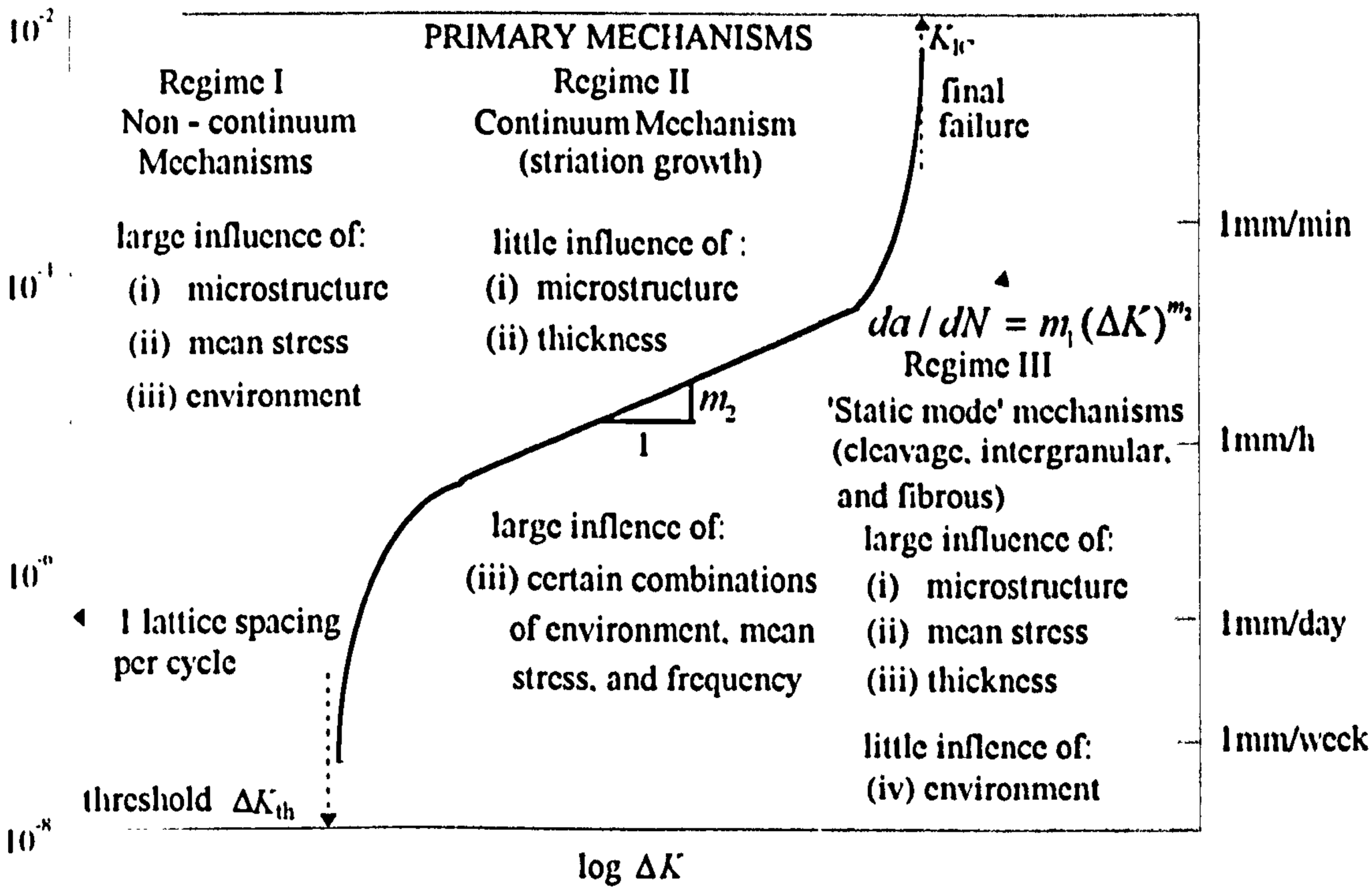

Figure 2.4 **Schematic variation of fatigue crack growth rate as function of stress intensity range** (Ref. 35)

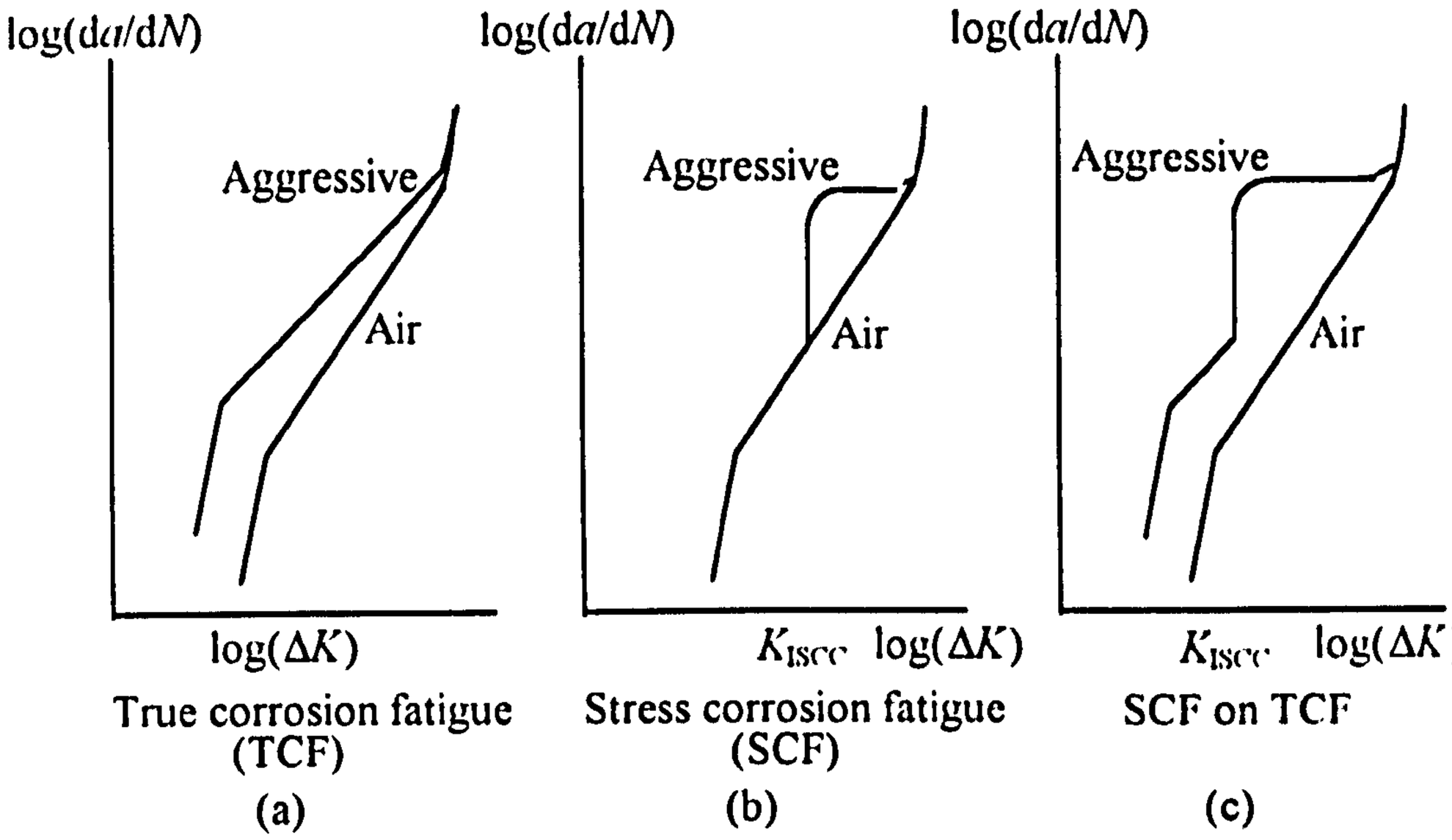

True corrosion fatigue (TCF) (a)

Stress corrosion fatigue (SCF) (b)

SCF on TCF (c)

Figure 2.5 **Illustration of the three types of corrosion fatigue behaviour** (Ref. 95)

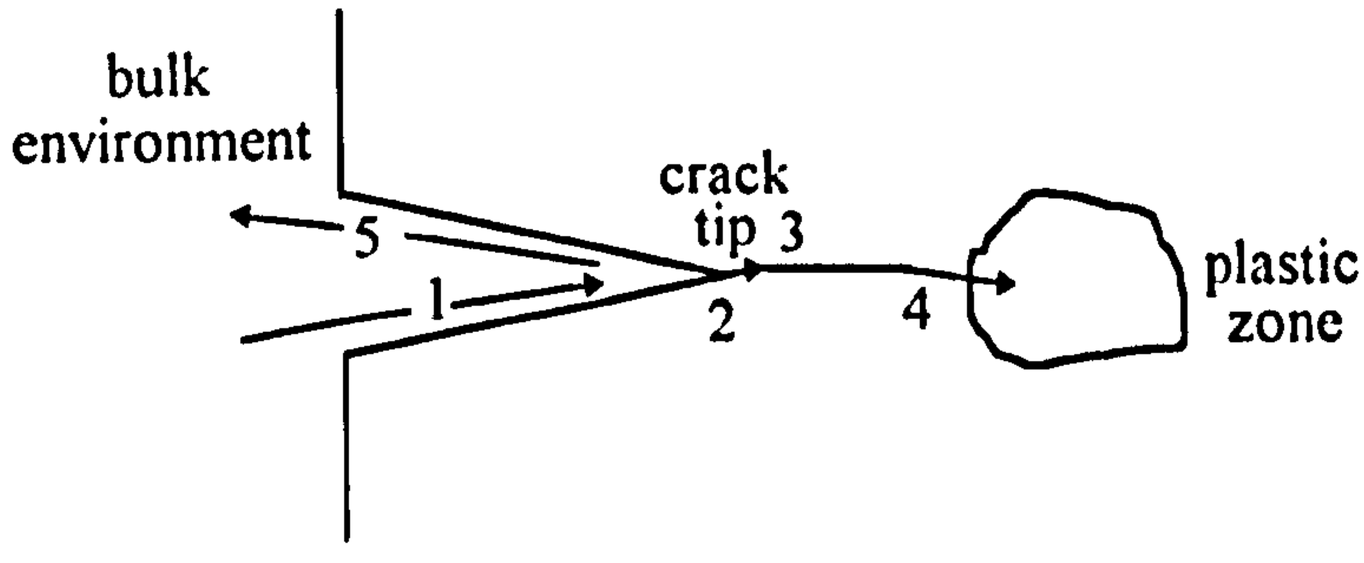

Figure 2.6 **Schematic of the processes occurring near the crack tip during corrosion fatigue.** 1. supply of reactants to crack tip; 2. chemical reaction with newly exposed metal; 3. adsorption of deleterious species; 4. diffusion of species to plastic zone; 5. removal of reacted products (Ref. 93)

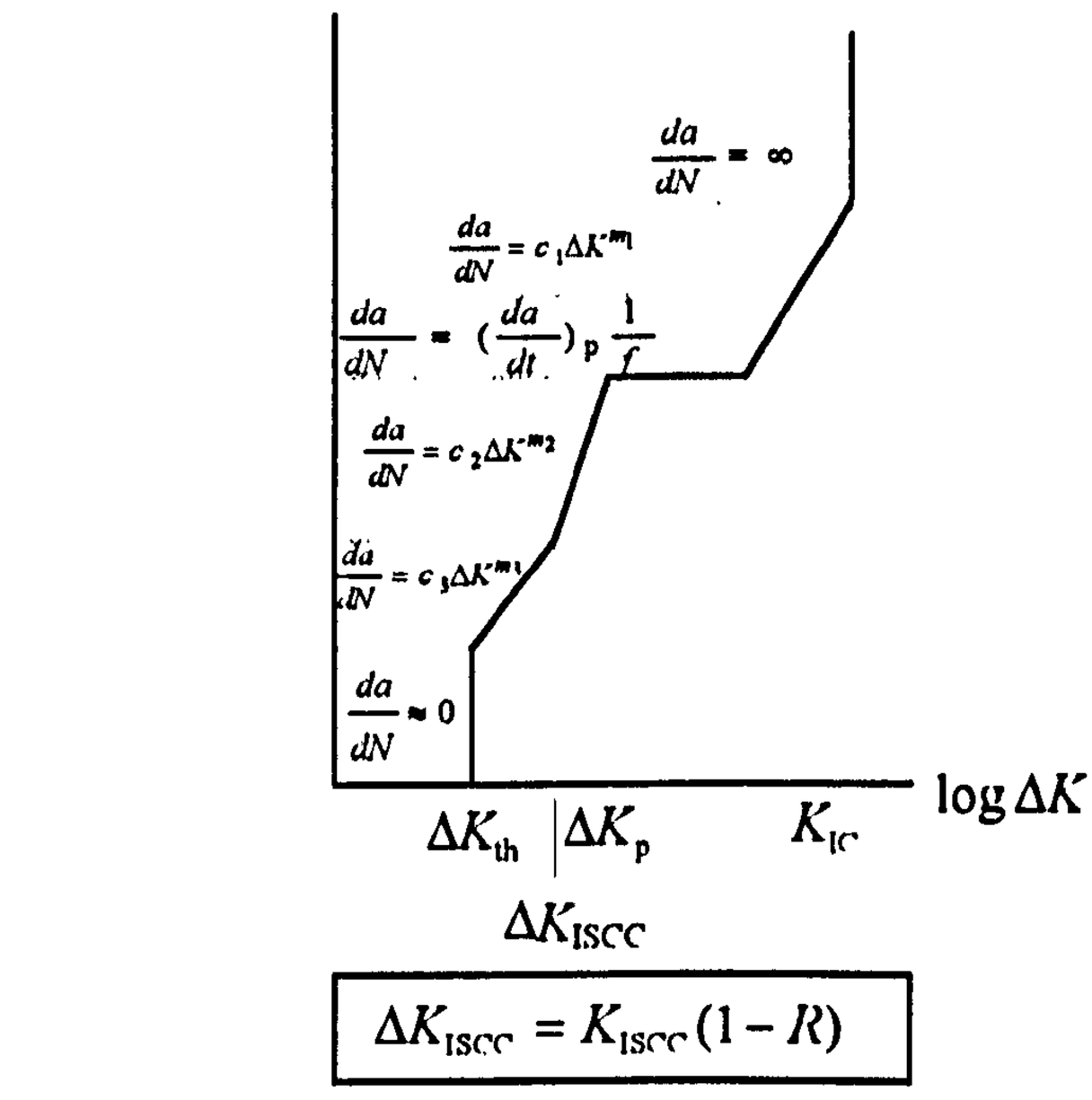

Figure 2.7 The process competition model of Austen and Walker (Ref. 95)

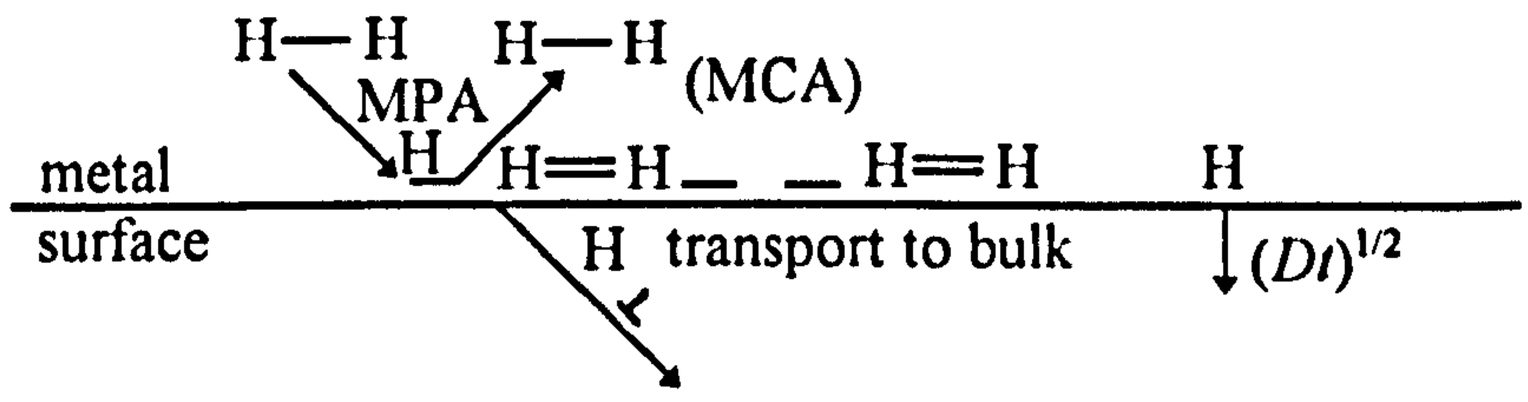

Figure 2.8 Schematic of adsorption of hydrogen gas on a clean metal surface (Ref. 35)

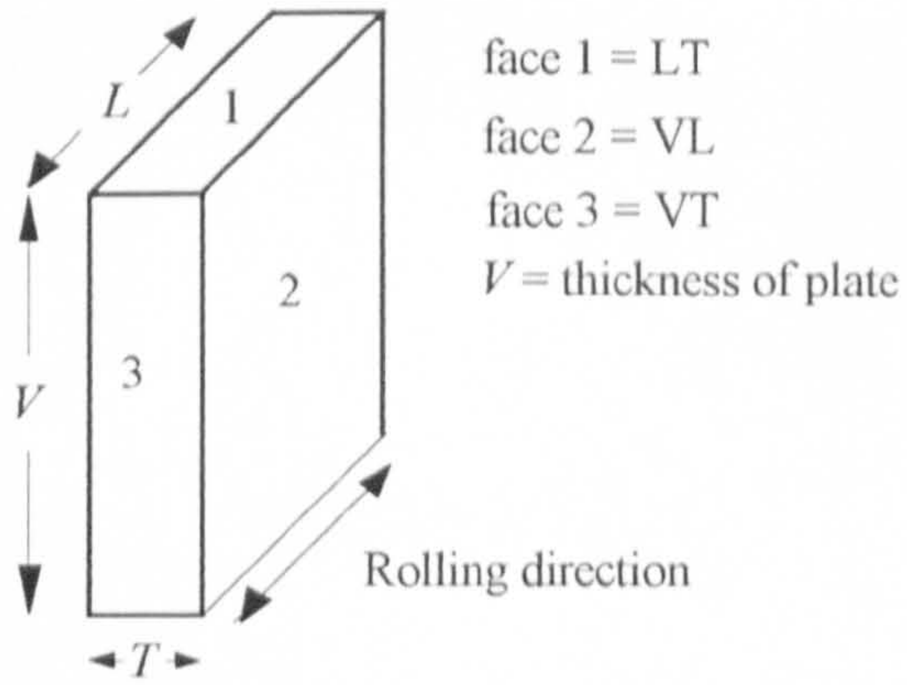

Figure 3.2.1 A schematic of the orientation and position of the microstructure studied

(3.2.2a) Steel A (no Mo/V)

(3.2.2b) Steel B (with Mo + V)

Figure 3.2.2 Micrographs of the microstructures showing tempered martensite for RQT501 steels with and without the addition of Mo + V

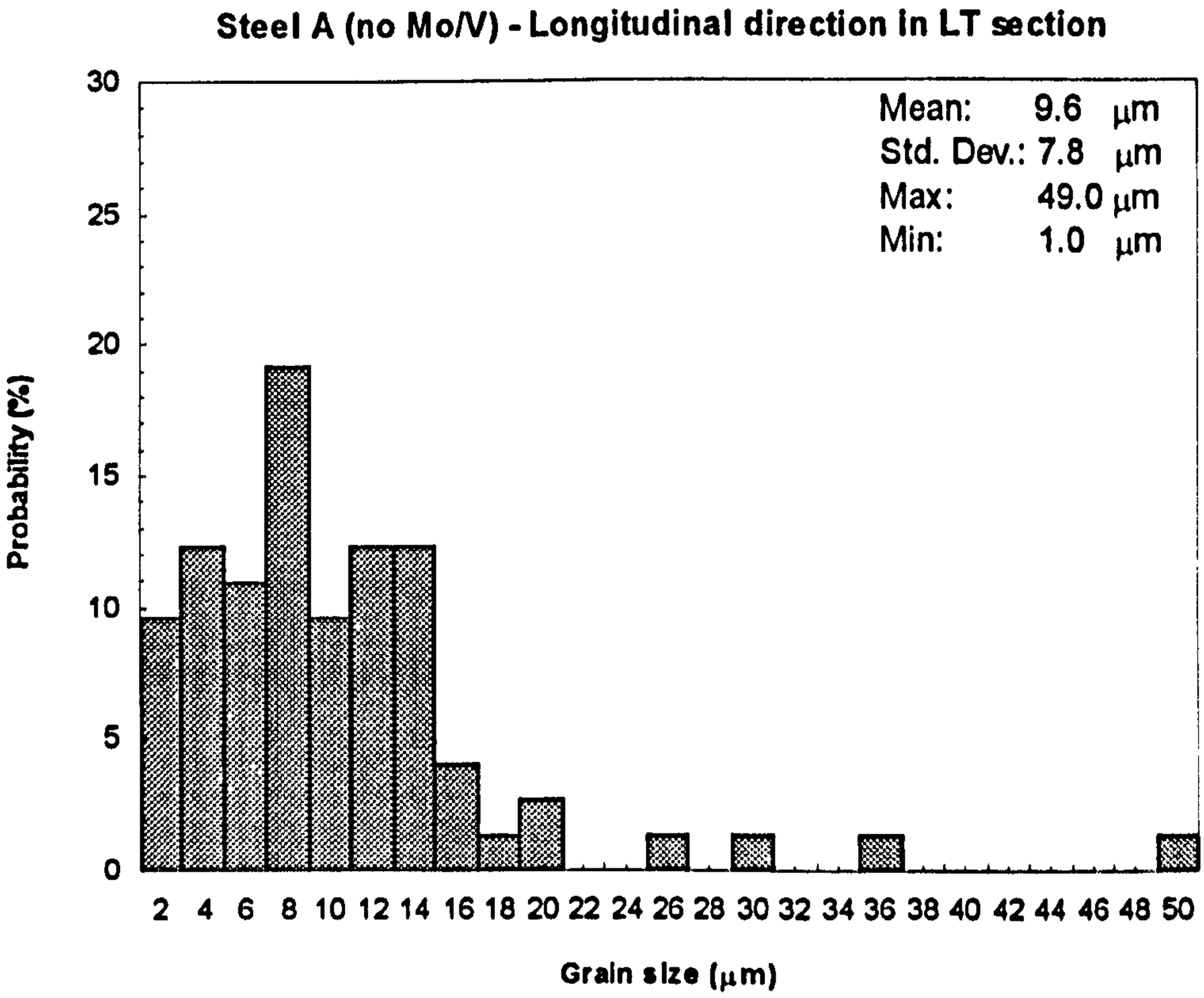

Figure 3.2.3 Grain size distribution in LT section of Steel A (no Mo/V)

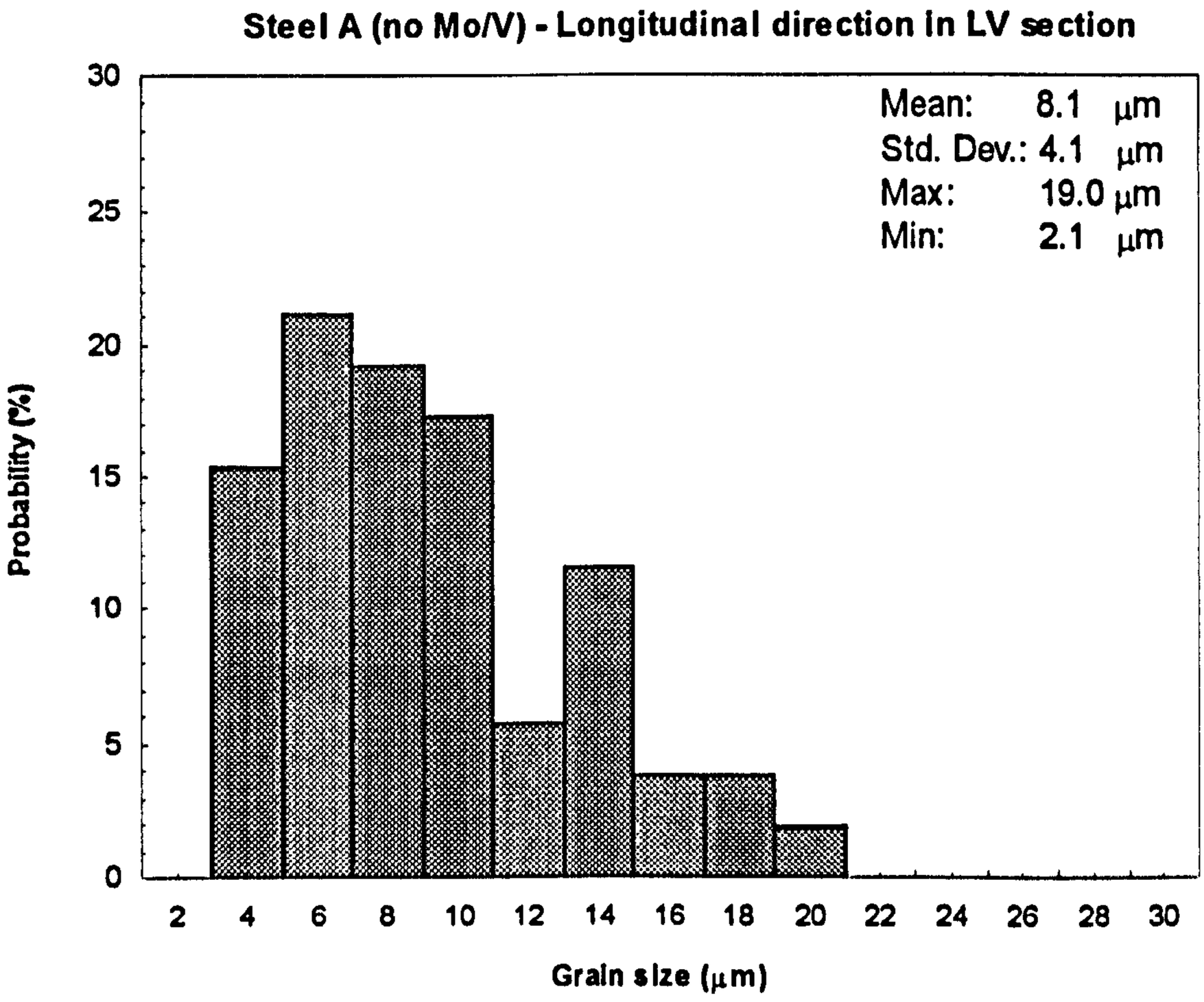

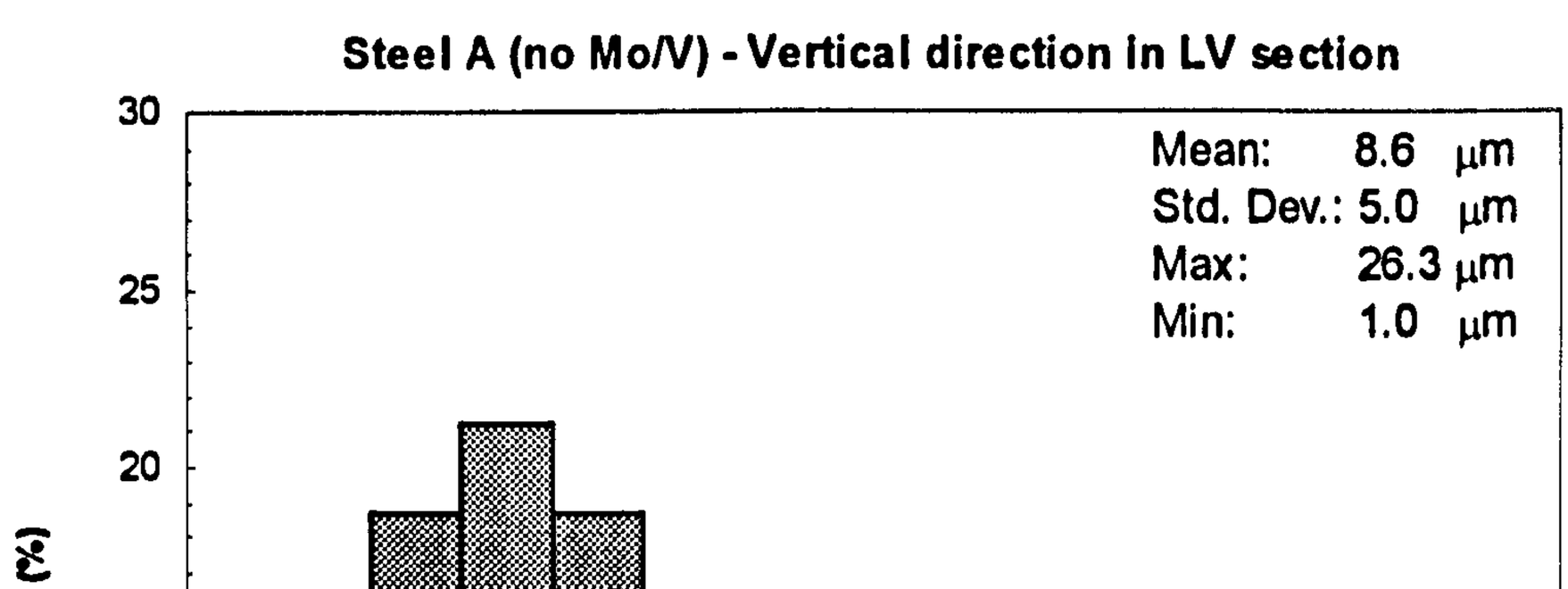

Figure 3.2.4 Grain size distribution in LV section of Steel A (no Mo/V)

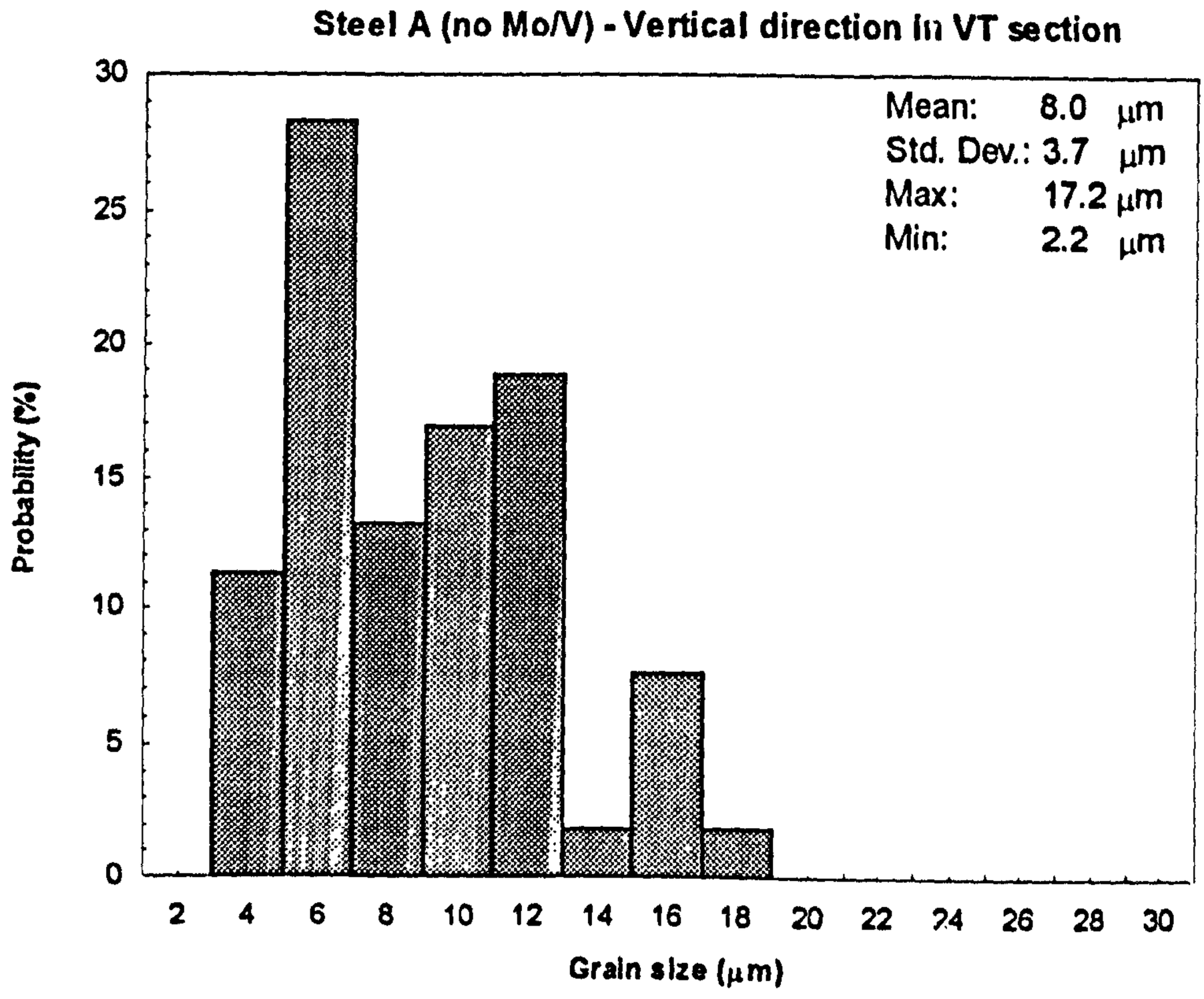

Figure 3.2.5 Grain size distribution in VT section of Steel A (no Mo/V)

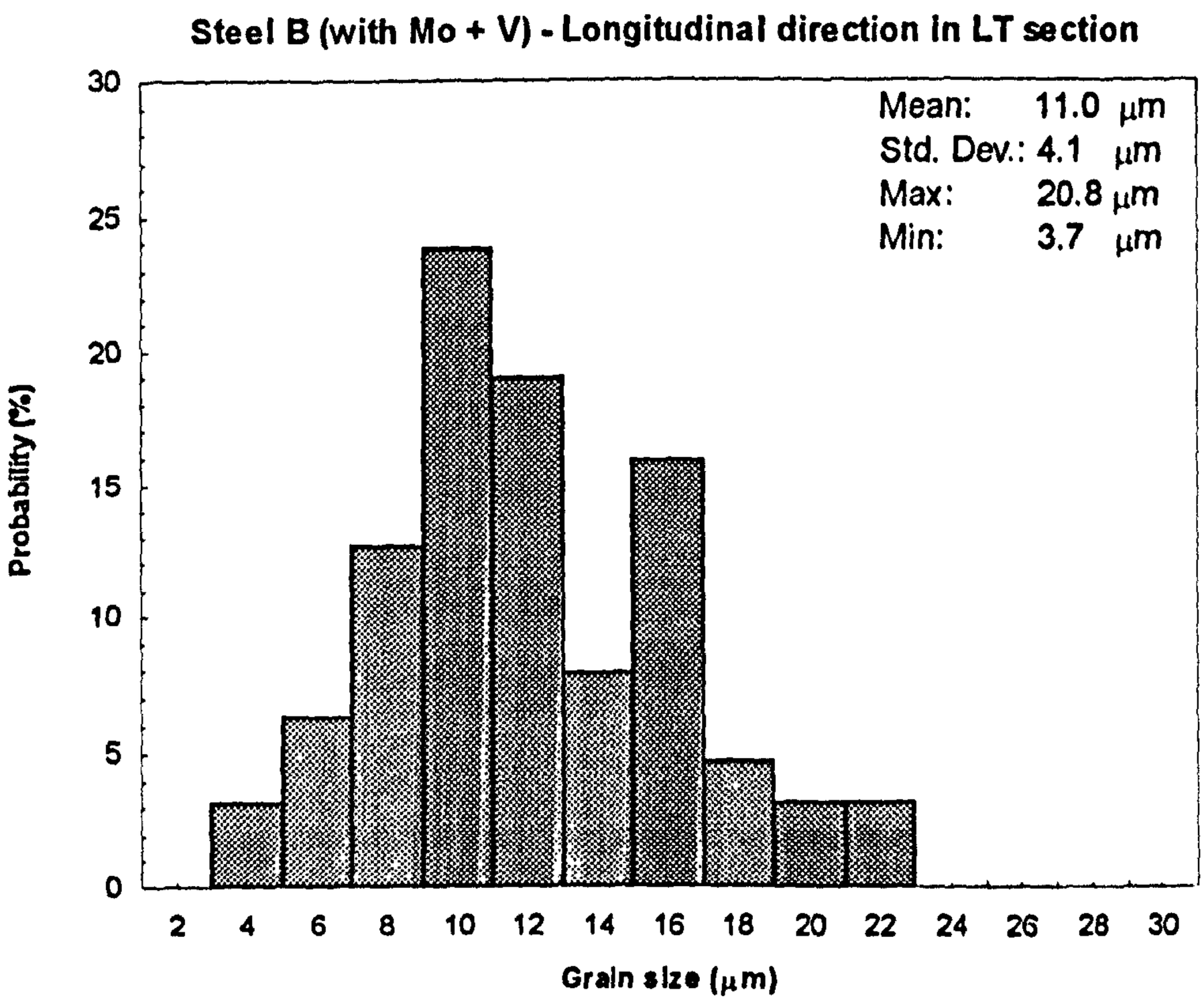

Figure 3.2.6 Grain size distribution in LT section of Steel B (with Mo + V)

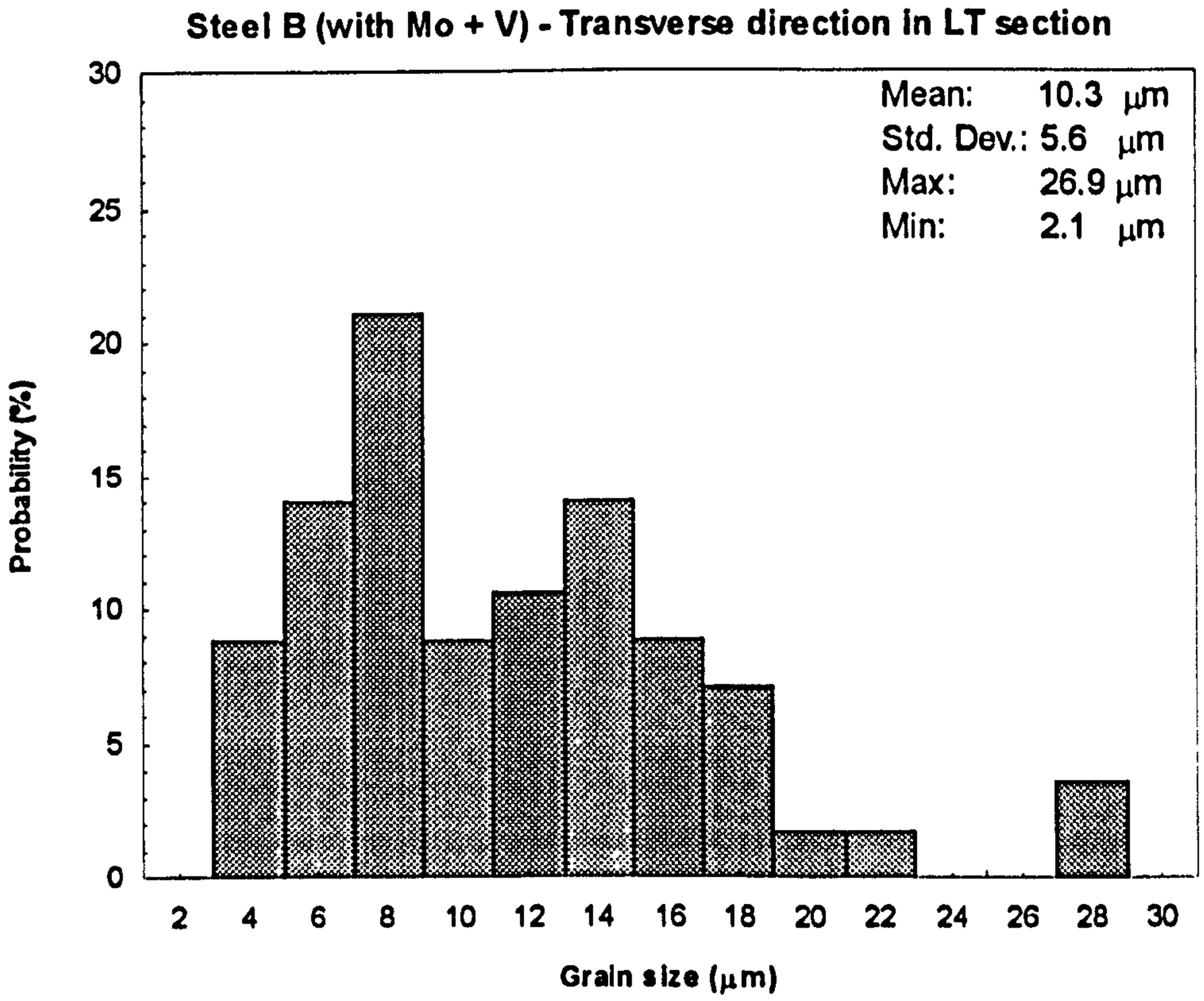

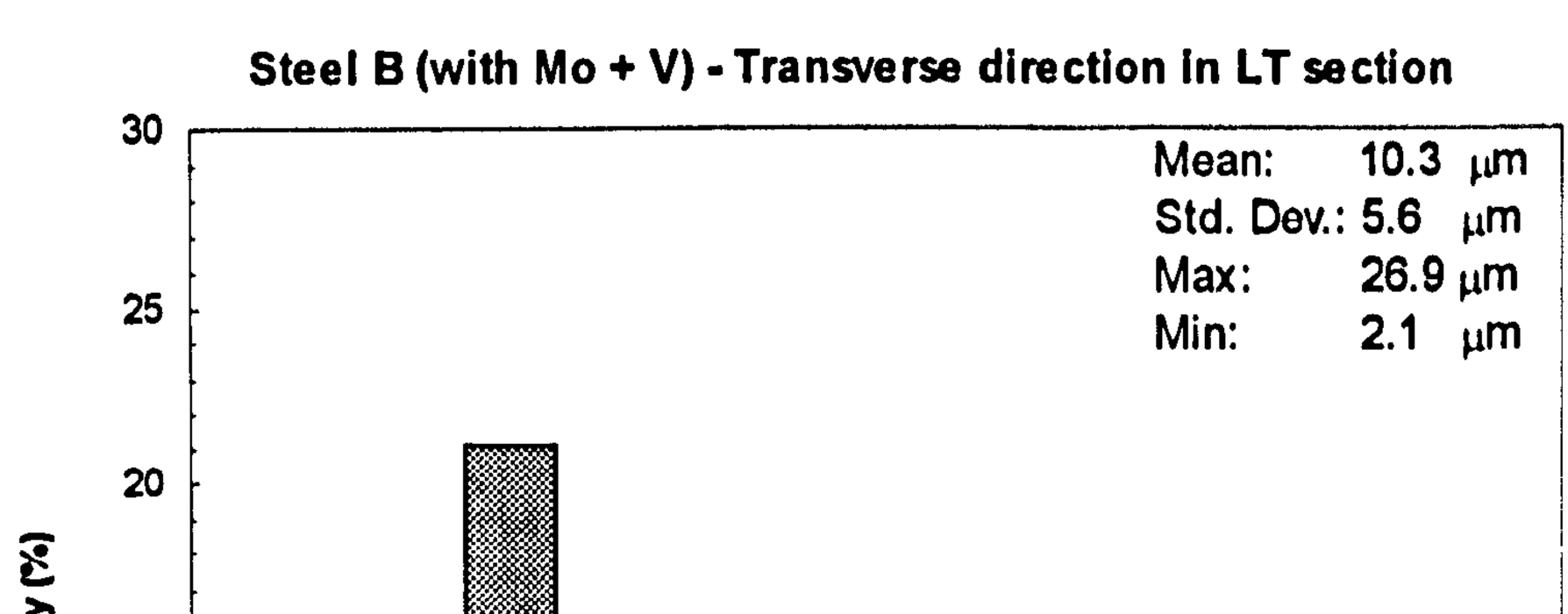

Figure 3.2.7 Grain size distribution in LV section of Steel B (with Mo + V)

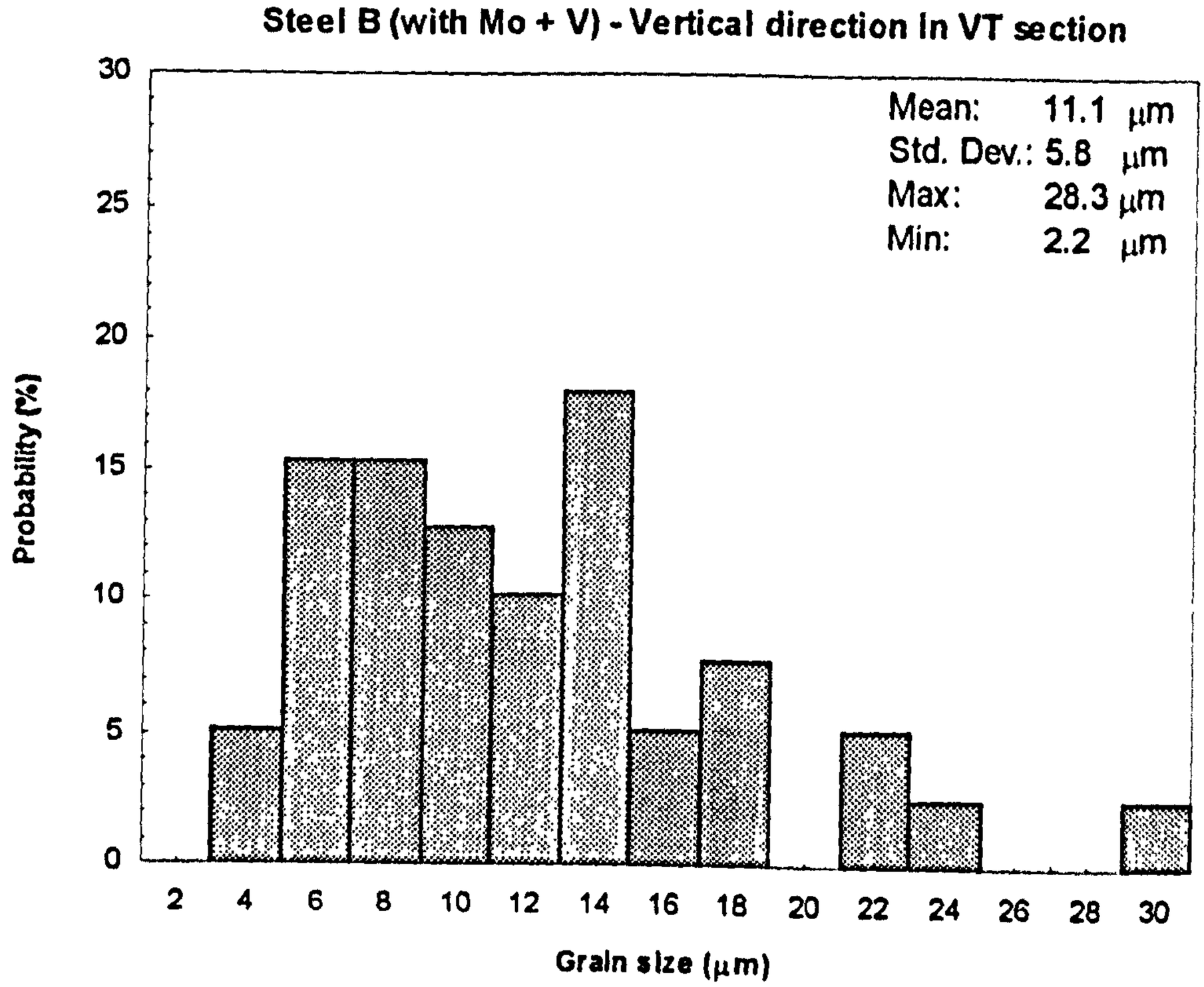

Figure 3.2.8 Grain size distribution in VT section of Steel B (with Mo + V)

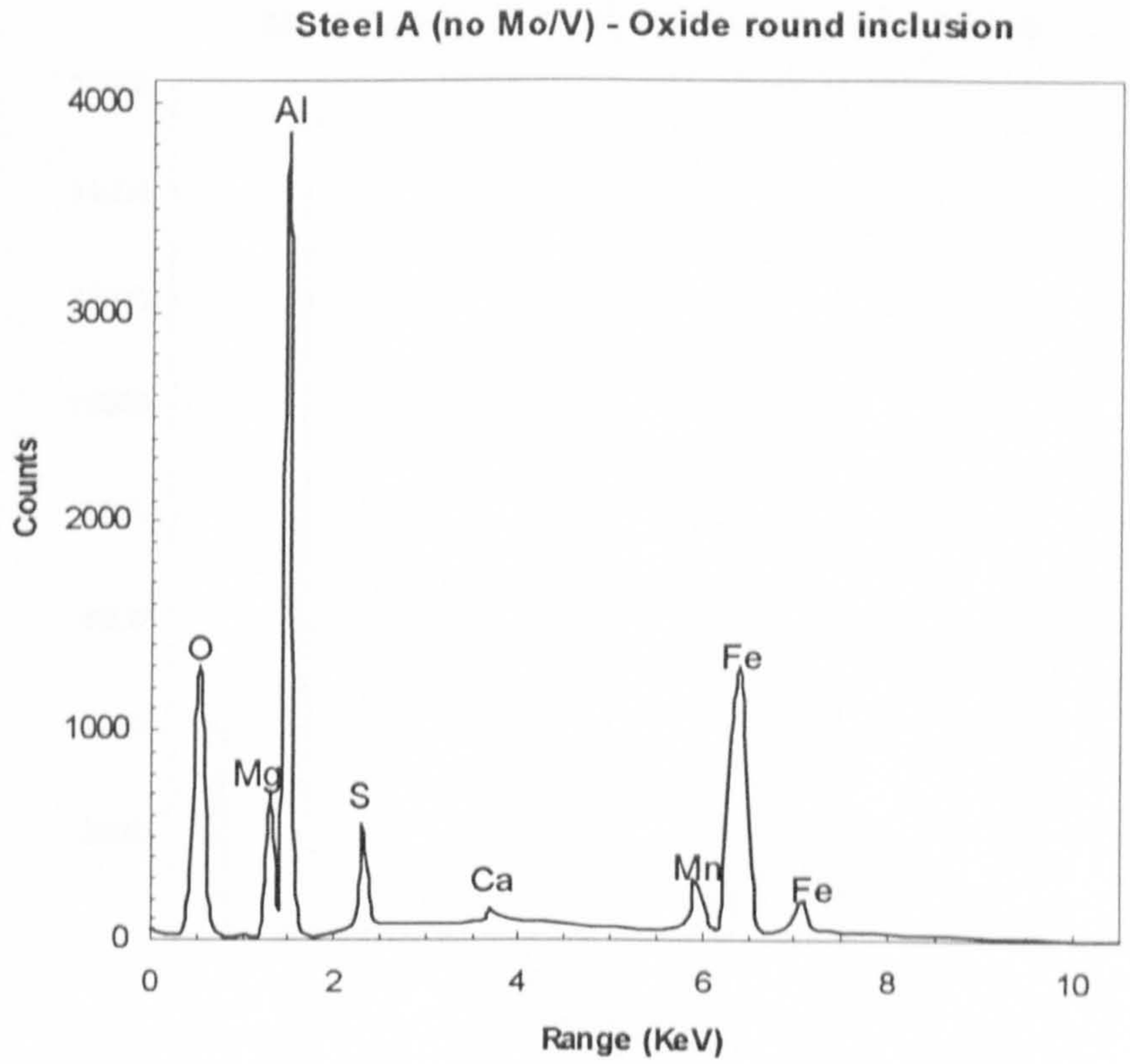

(3.3.1a)

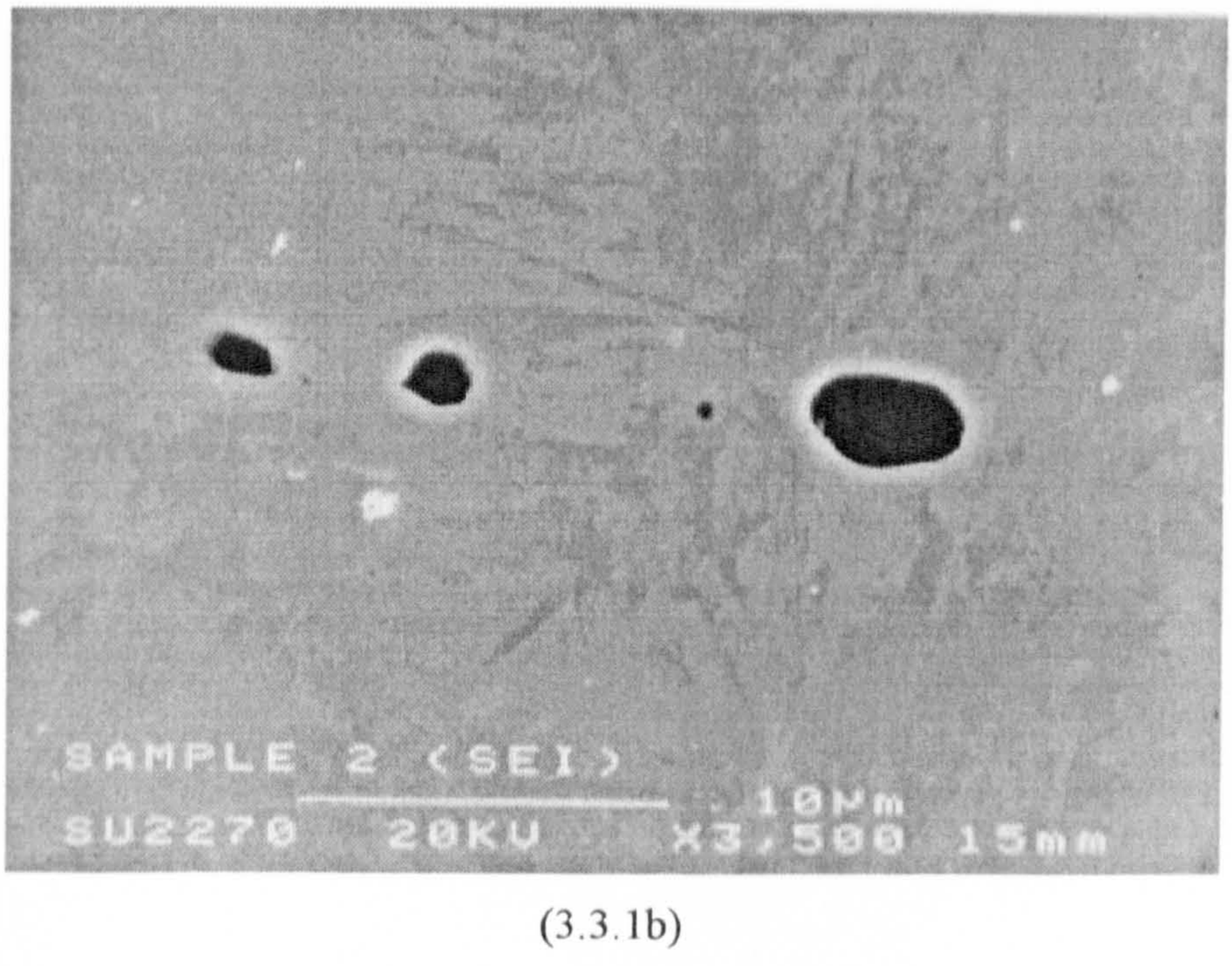

(3.3.1b)

Figure 3.3.1 Oxide round inclusion in LV section of Steel A (no Mo/V). (a) EDAC's analysis, (b) SEM micrograph

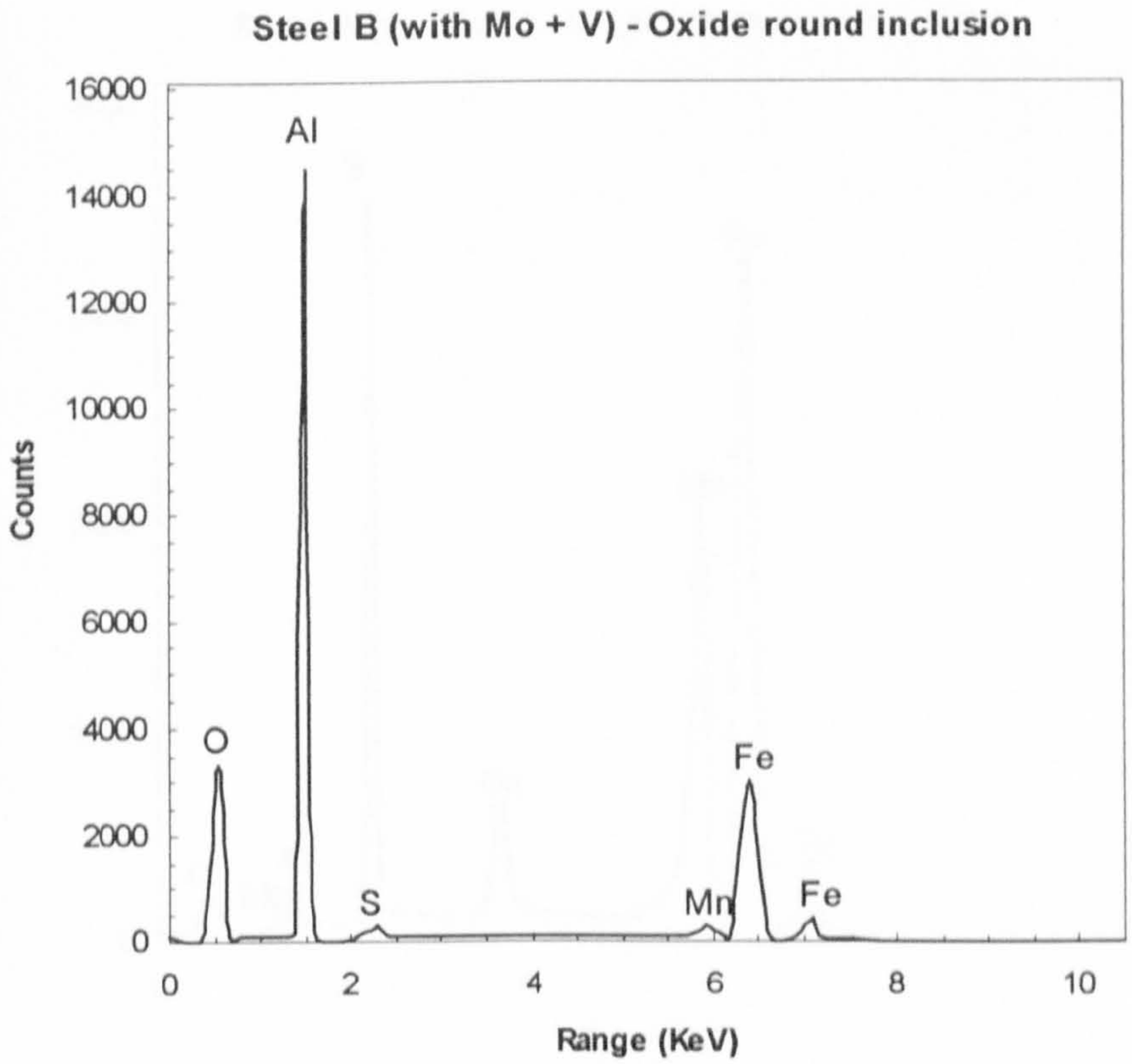

(3.3.2a)

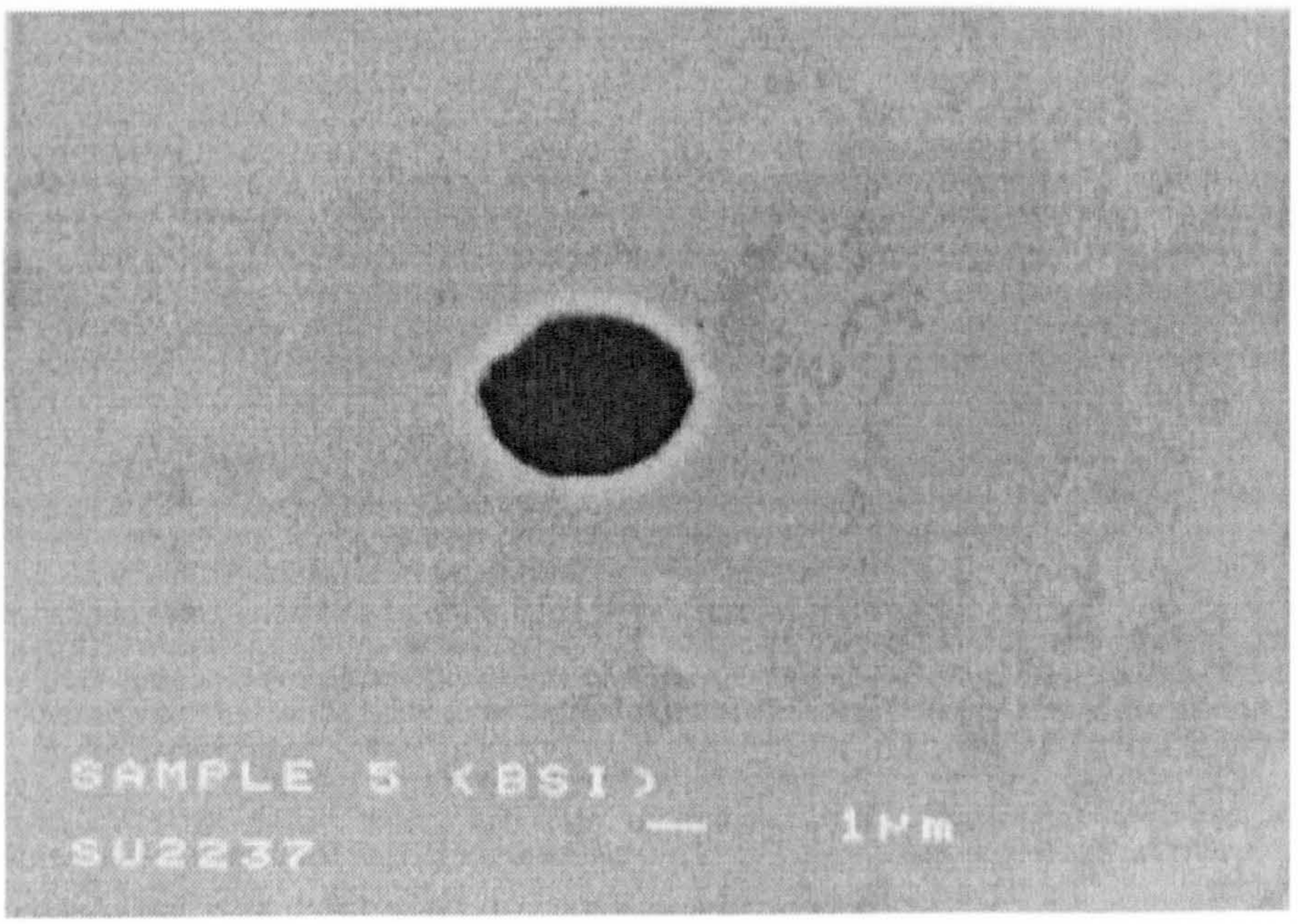

(3.3.2b)

Figure 3.3.2 Oxide round inclusion in LV section of Steel B (with Mo + V). (a) EDAC's analysis, (b) SEM micrograph

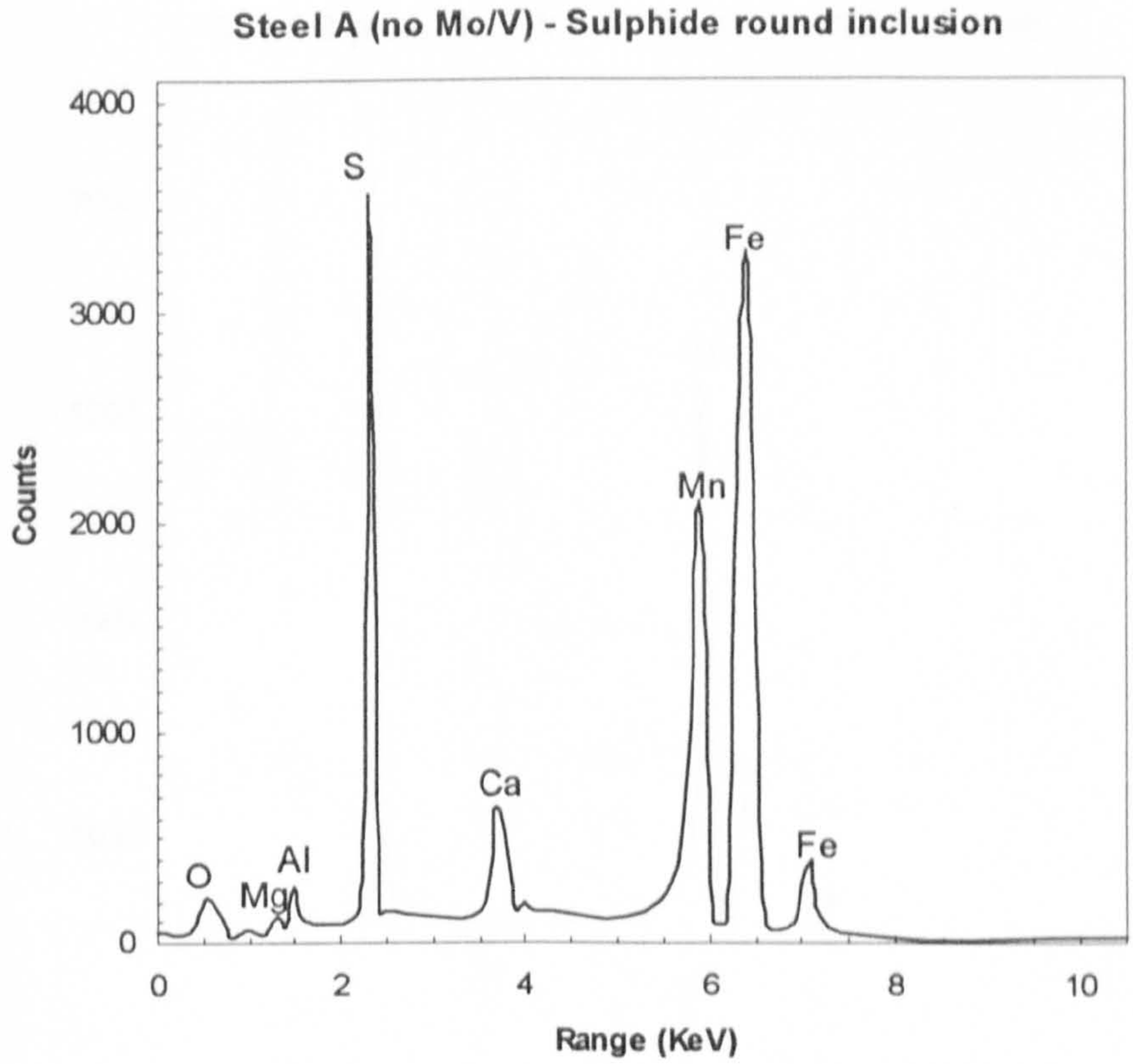

(3.3.3a)

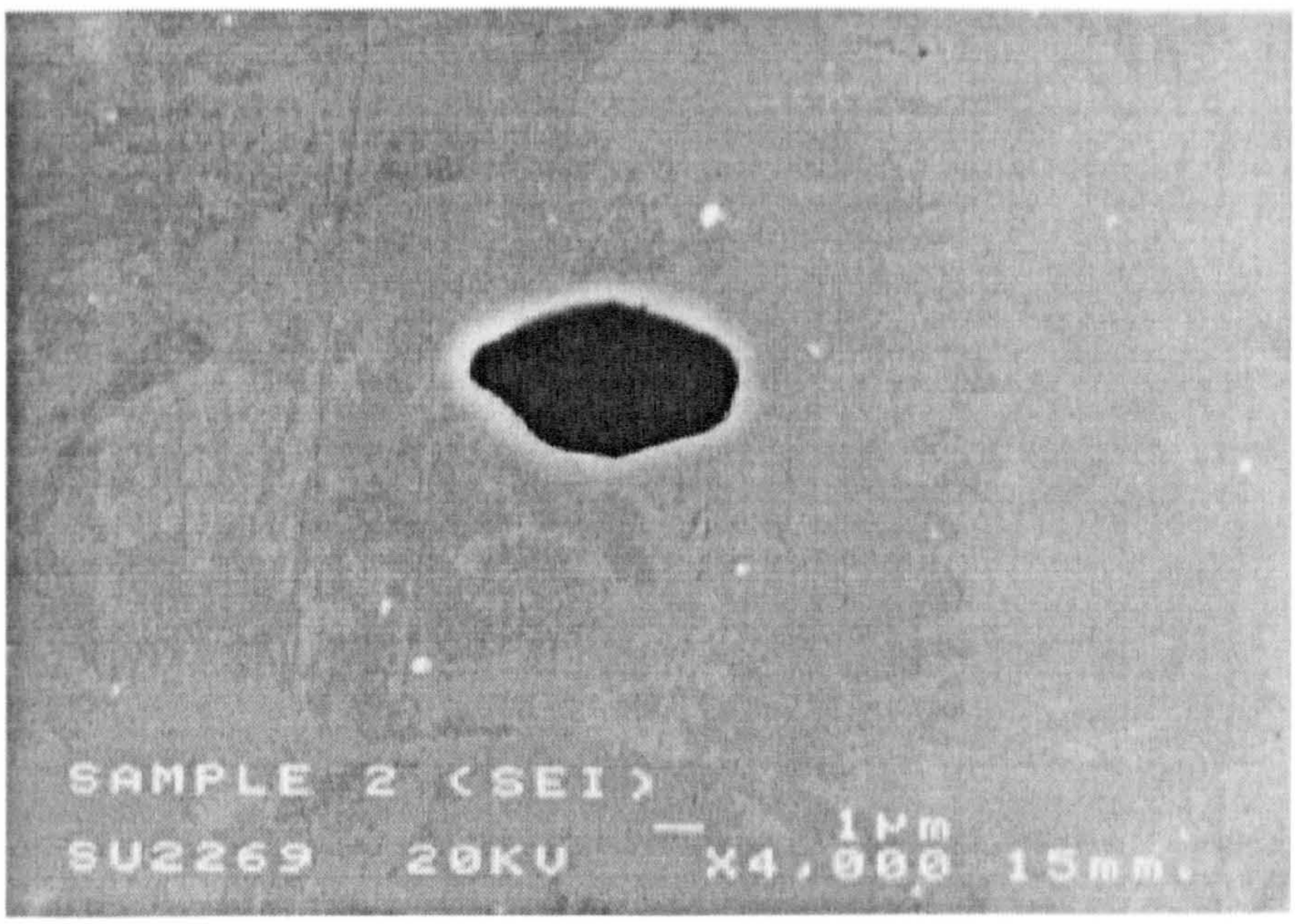

(3.3.3b)

Figure 3.3.3 Sulphide round inclusion in LV section of Steel A (no Mo/V). (a) EDAC's analysis, (b) SEM micrograph

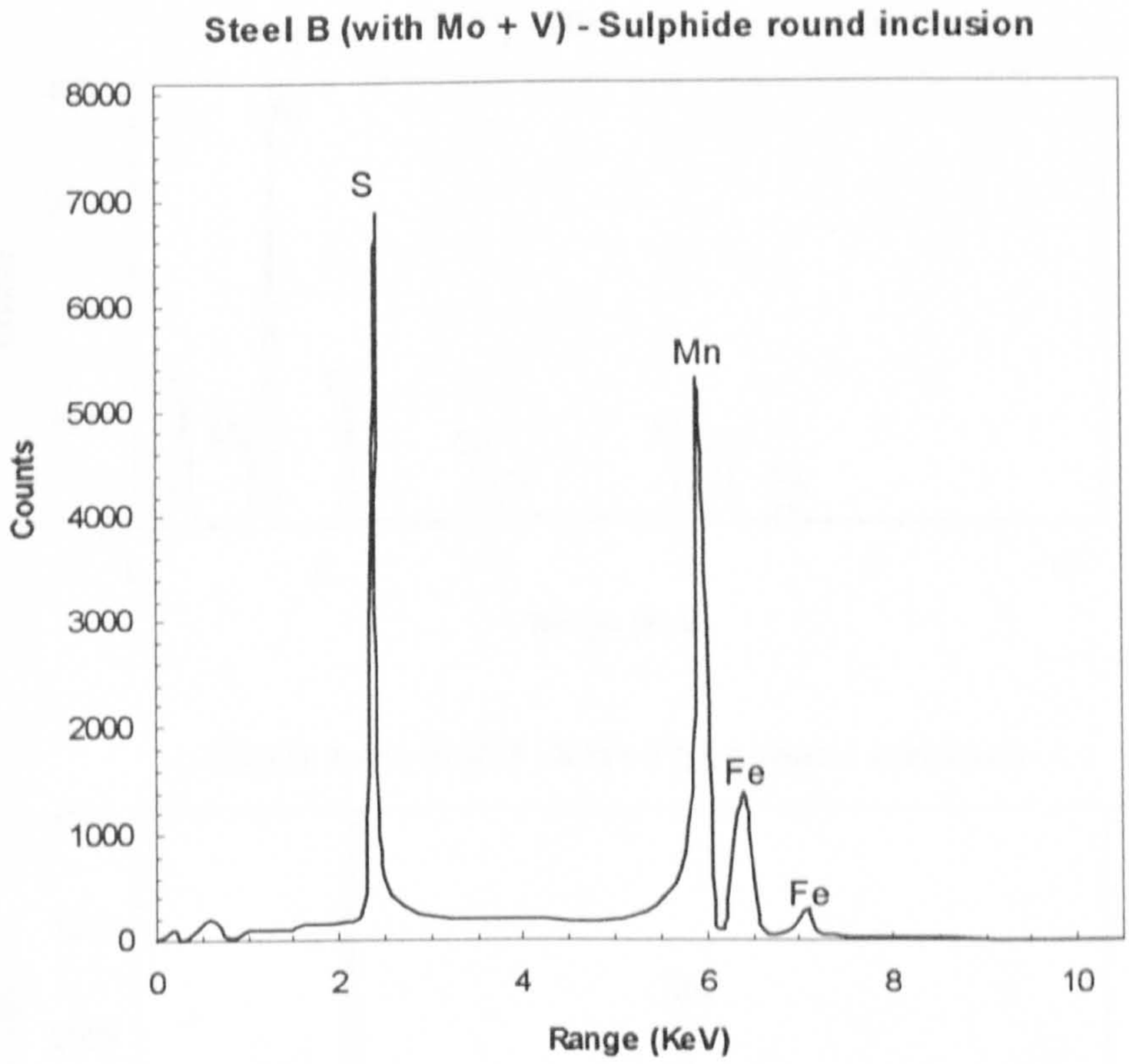

(3.3.4a)

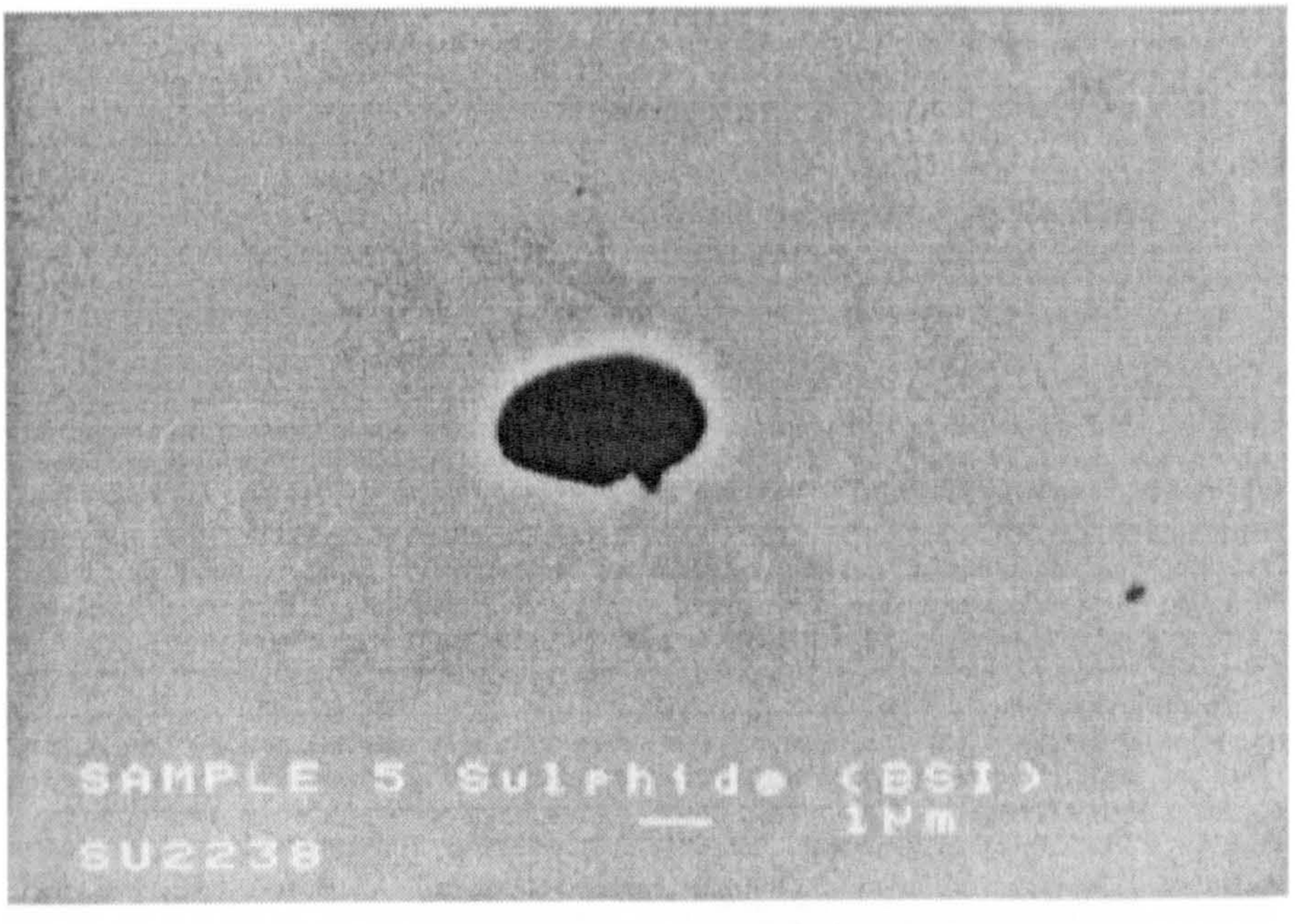

(3.3.4b)

Figure 3.3.4 Sulphide round inclusion in LV section of Steel B (with Mo + V). (a) EDAC's analysis, (b) SEM micrograph

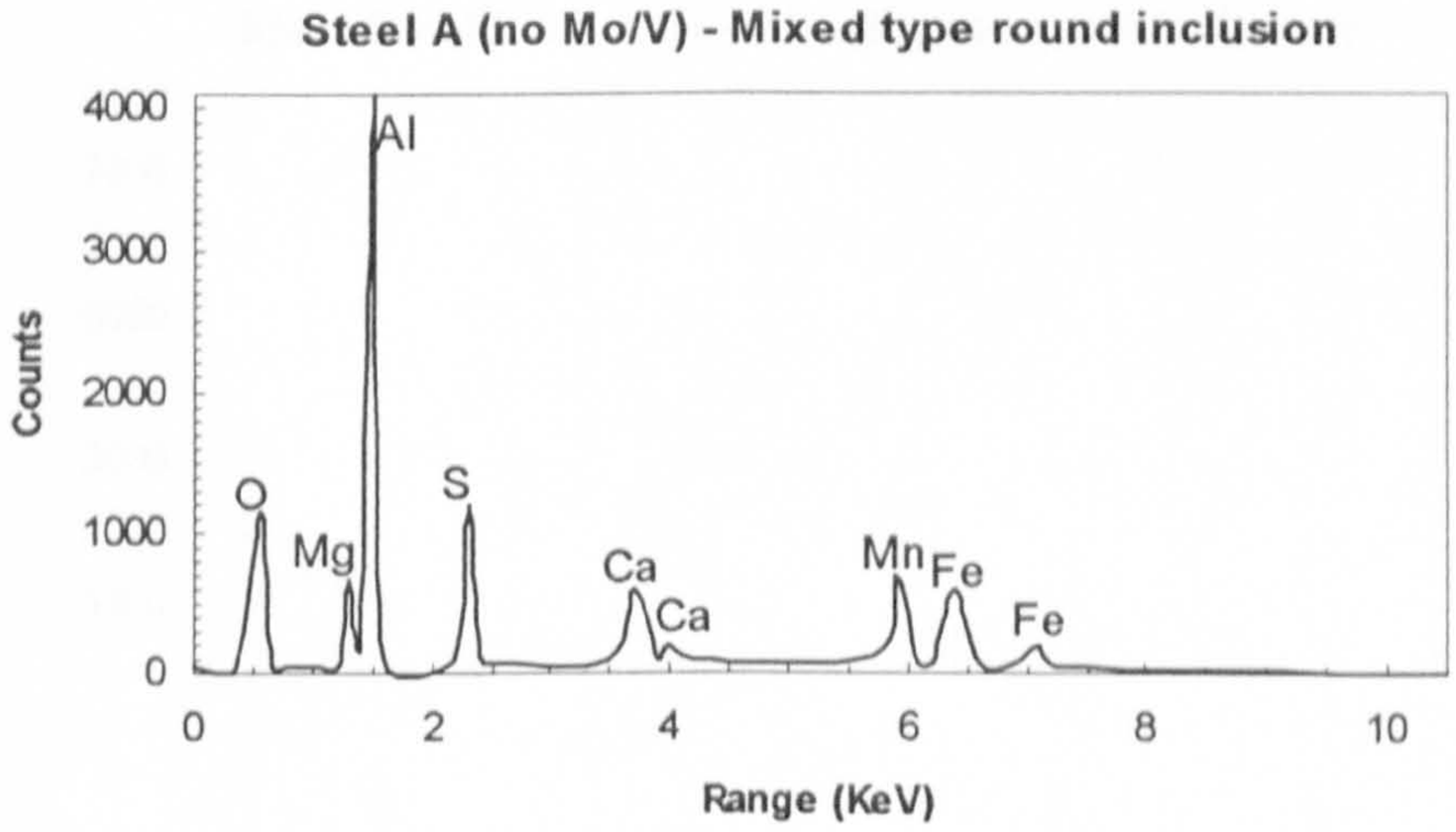

(3.3.5a)

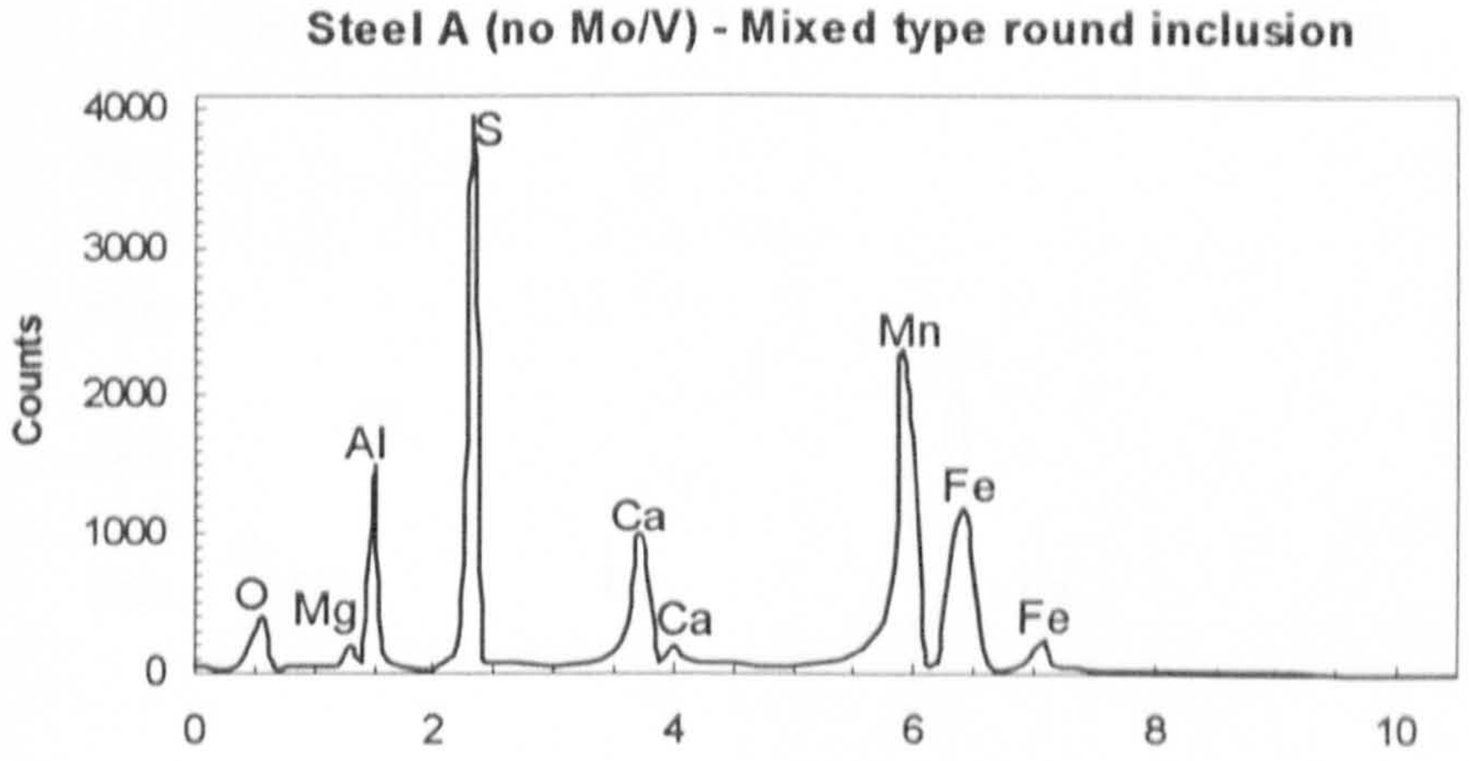

(3.3.5b)

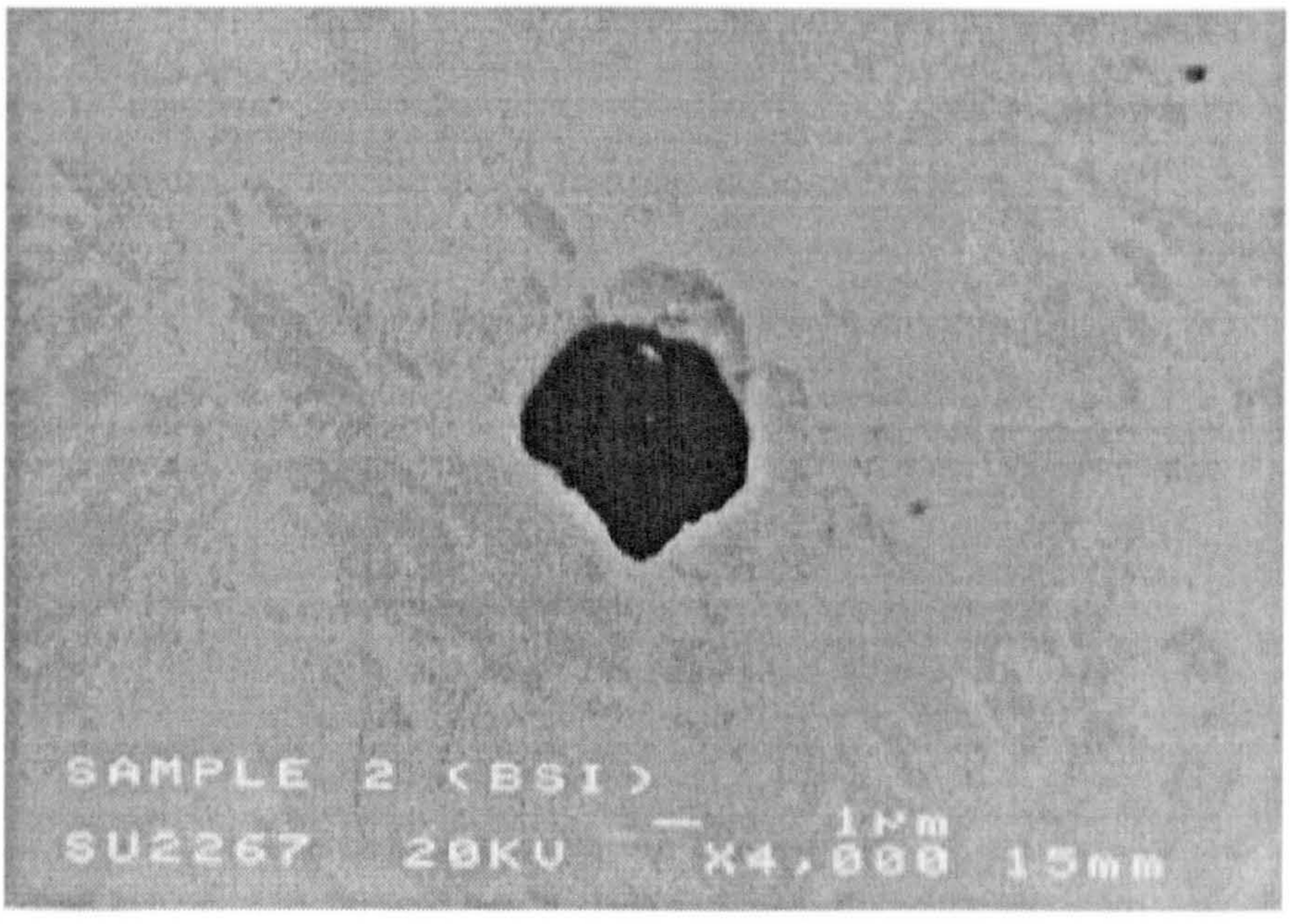

(3.3.5c)

Figure 3.3.5 Round inclusion of mixed type in LV section of Steel A (no Mo/V). (a) EDAC's analysis - Oxides, (b) EDAC's analysis - Sulphide, (c) SEM micrograph

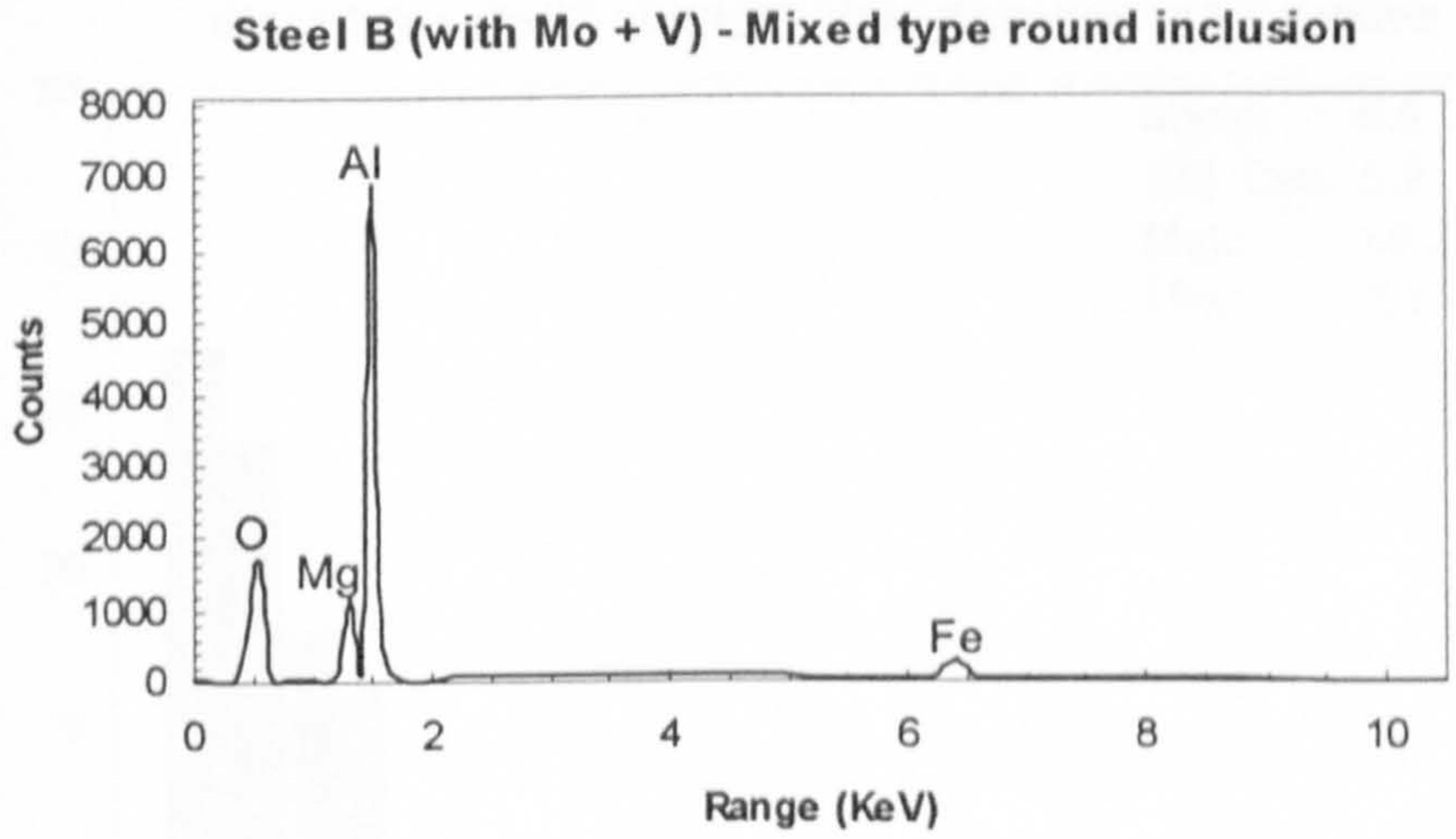

(3.3.6a)

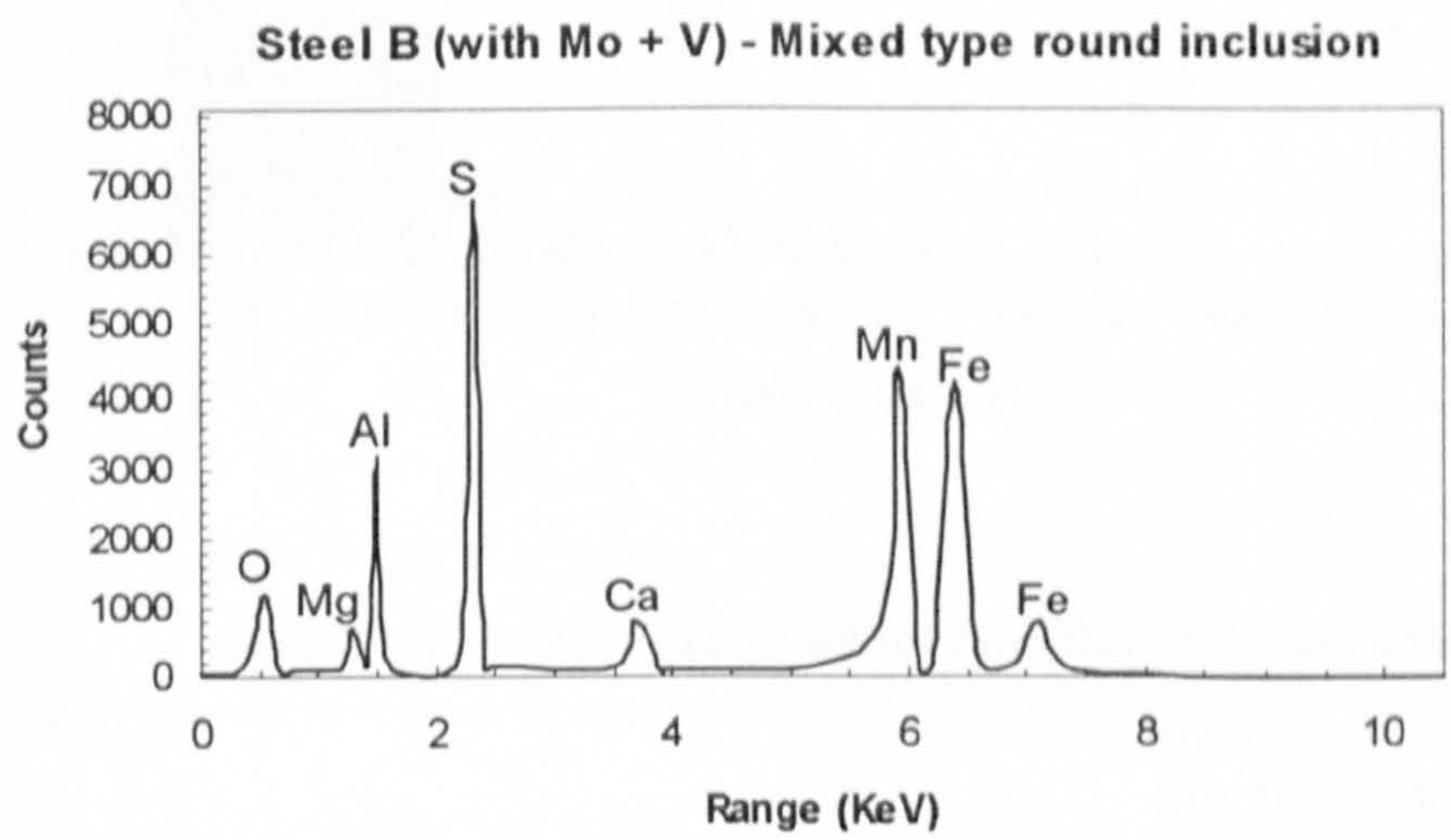

(3.3.6b)

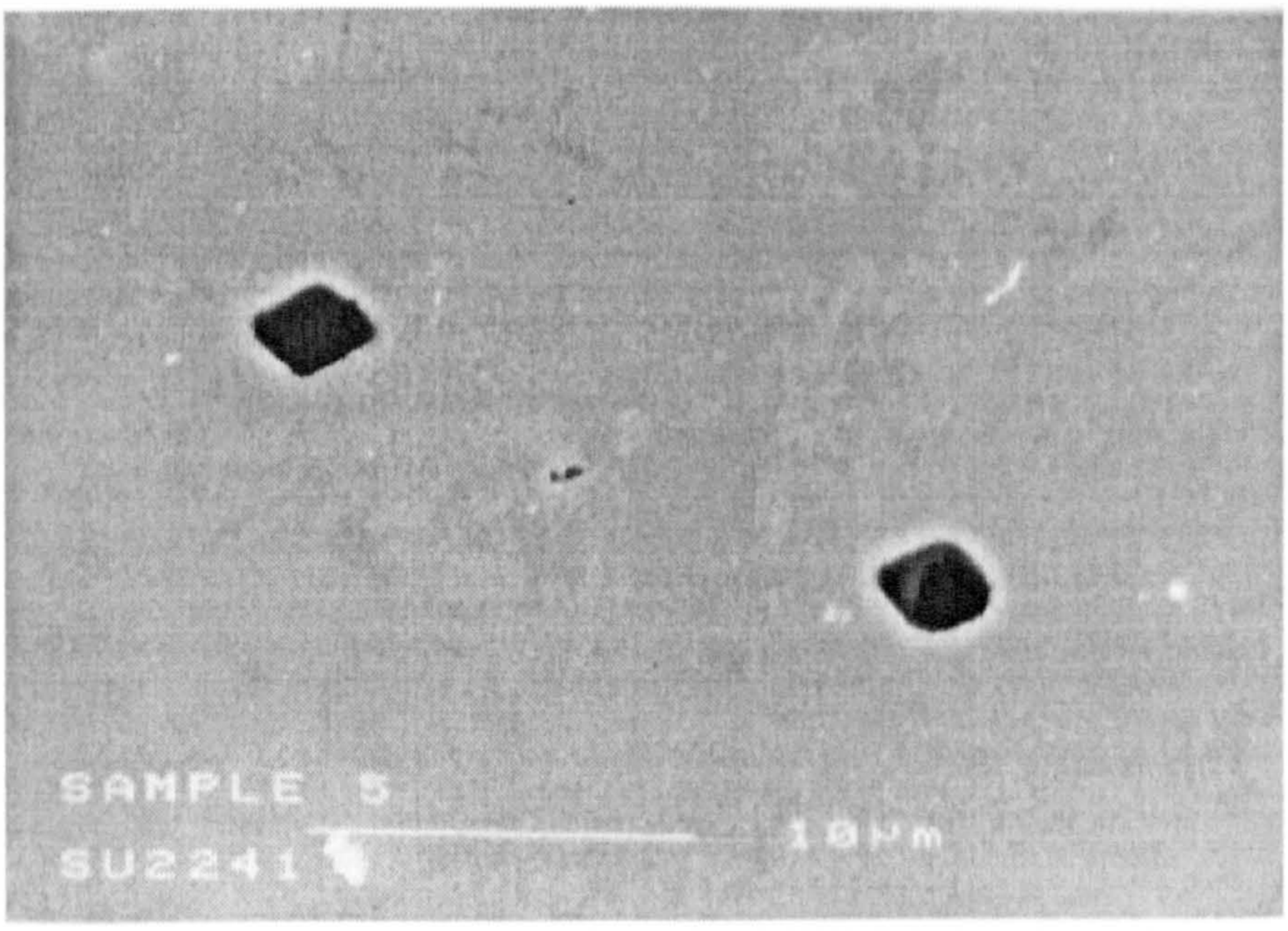

(3.3.6c)

Figure 3.3.6 Round inclusion of mixed type in LV section of Steel B (with Mo + V). (a) EDAC's analysis - Oxides, (b) EDAC's analysis - Sulphide, (c) SEM micrograph

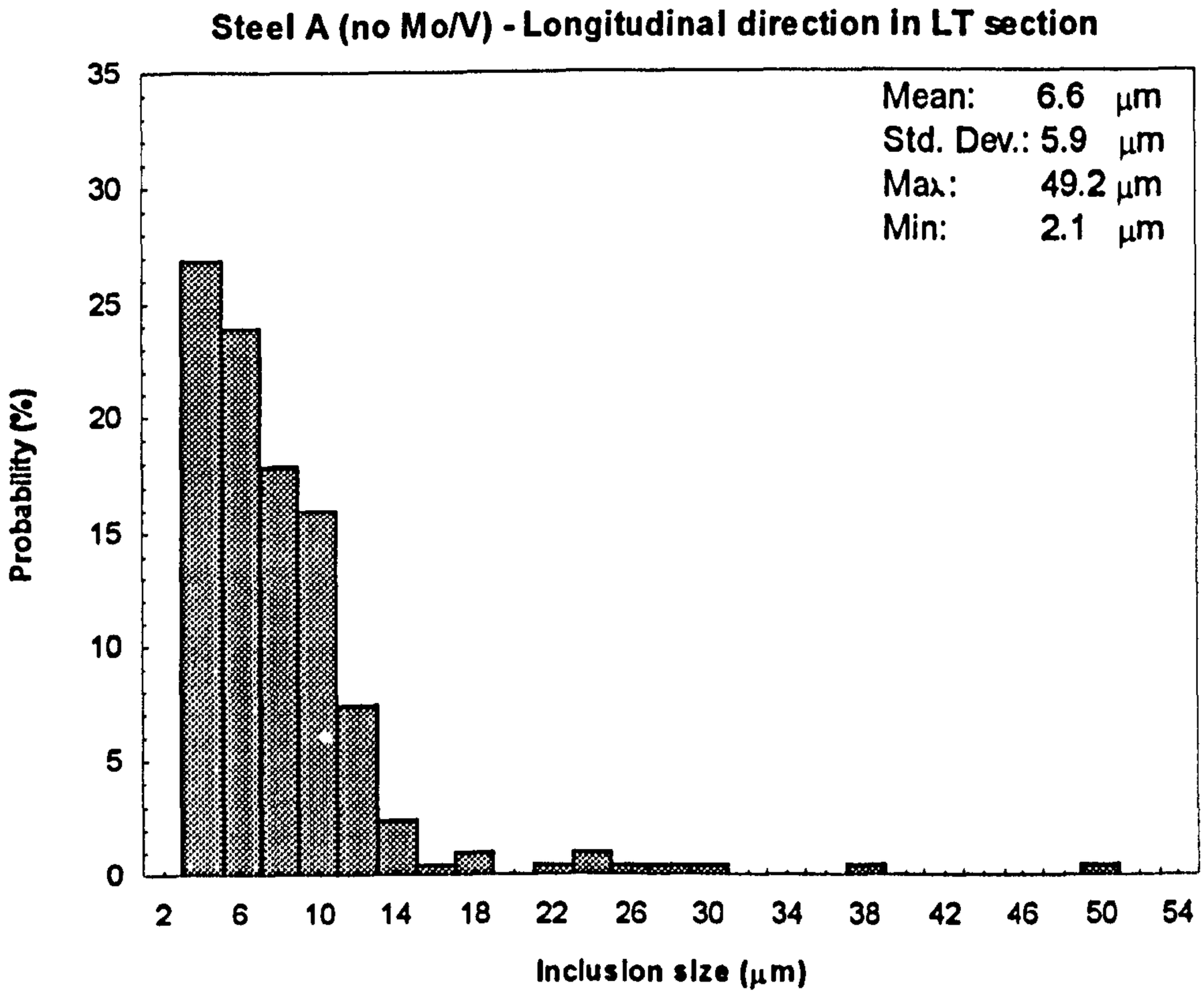

Steel A (no Mo/V) - Longitudinal direction in LT section
Mean: 6.6 µm
Std. Dev.: 5.9 µm
Max: 49.2 µm
Min: 2.1 µm
Probability (%)
0
5
10
15
20
25
30
35
2
6
10
14
18
22
26
30
34
38
42
46
50
54
Inclusion size (µm)

Figure 3.3.7 Inclusion size distribution in LT section of Steel A (no Mo/V)

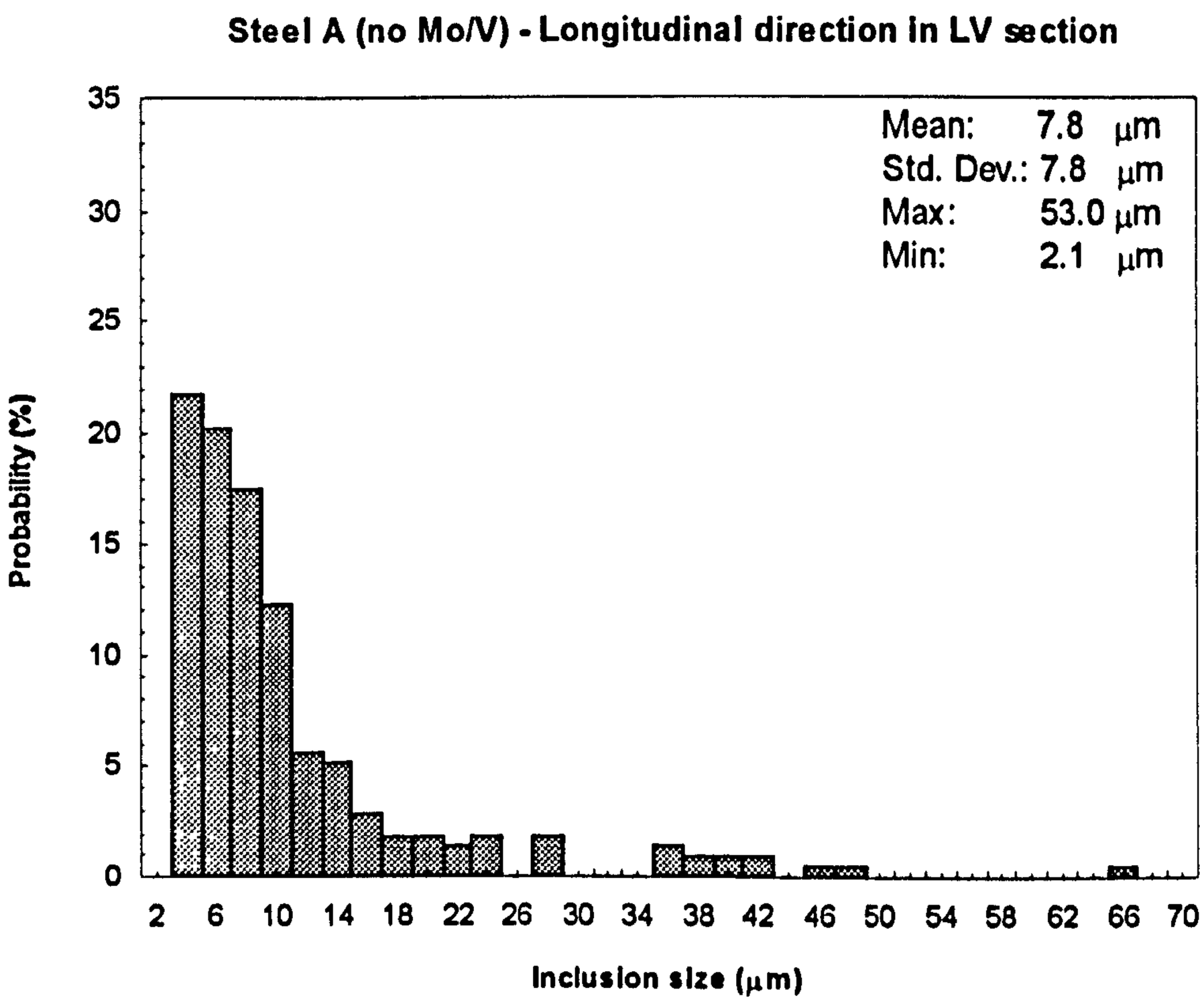

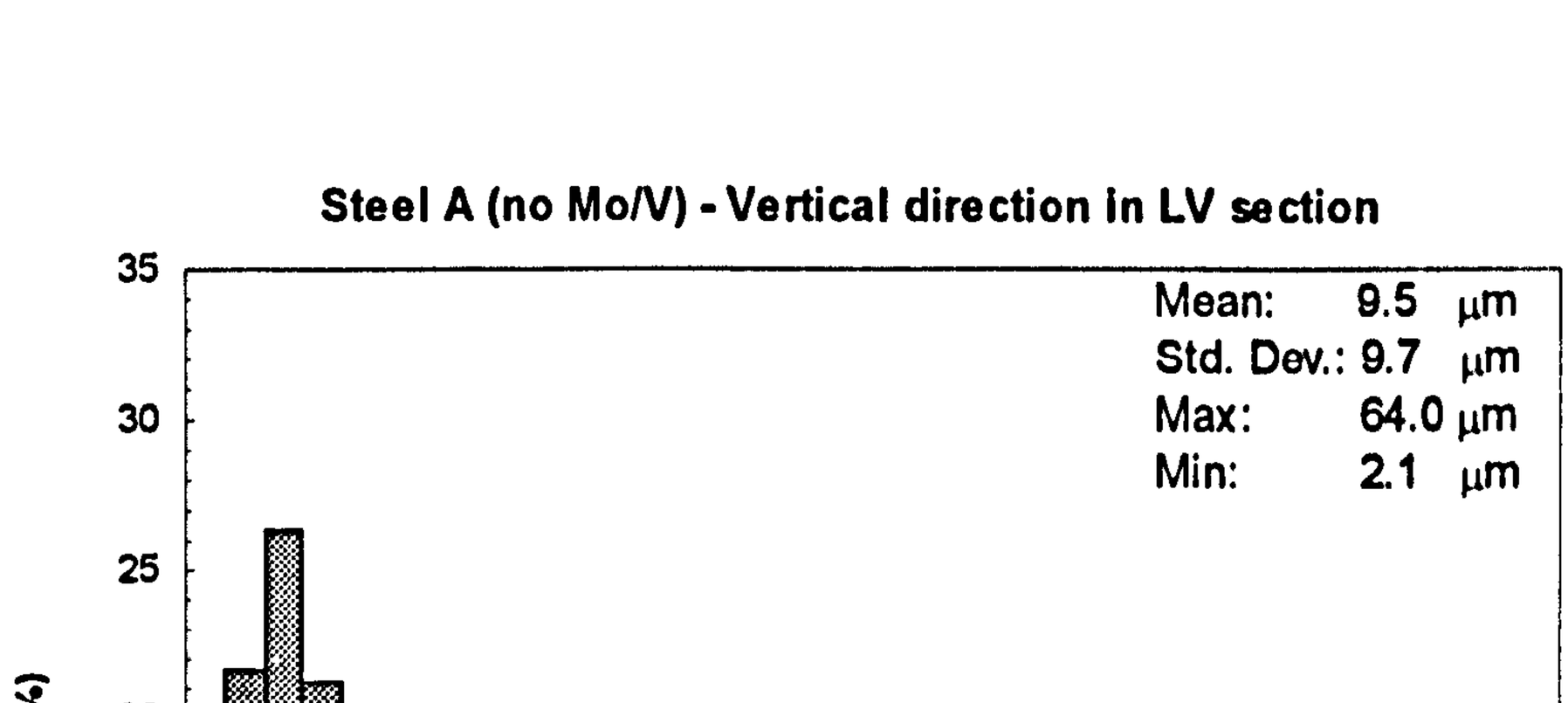

Figure 3.3.8 Inclusion size distribution in LV section of Steel A (no Mo/V)

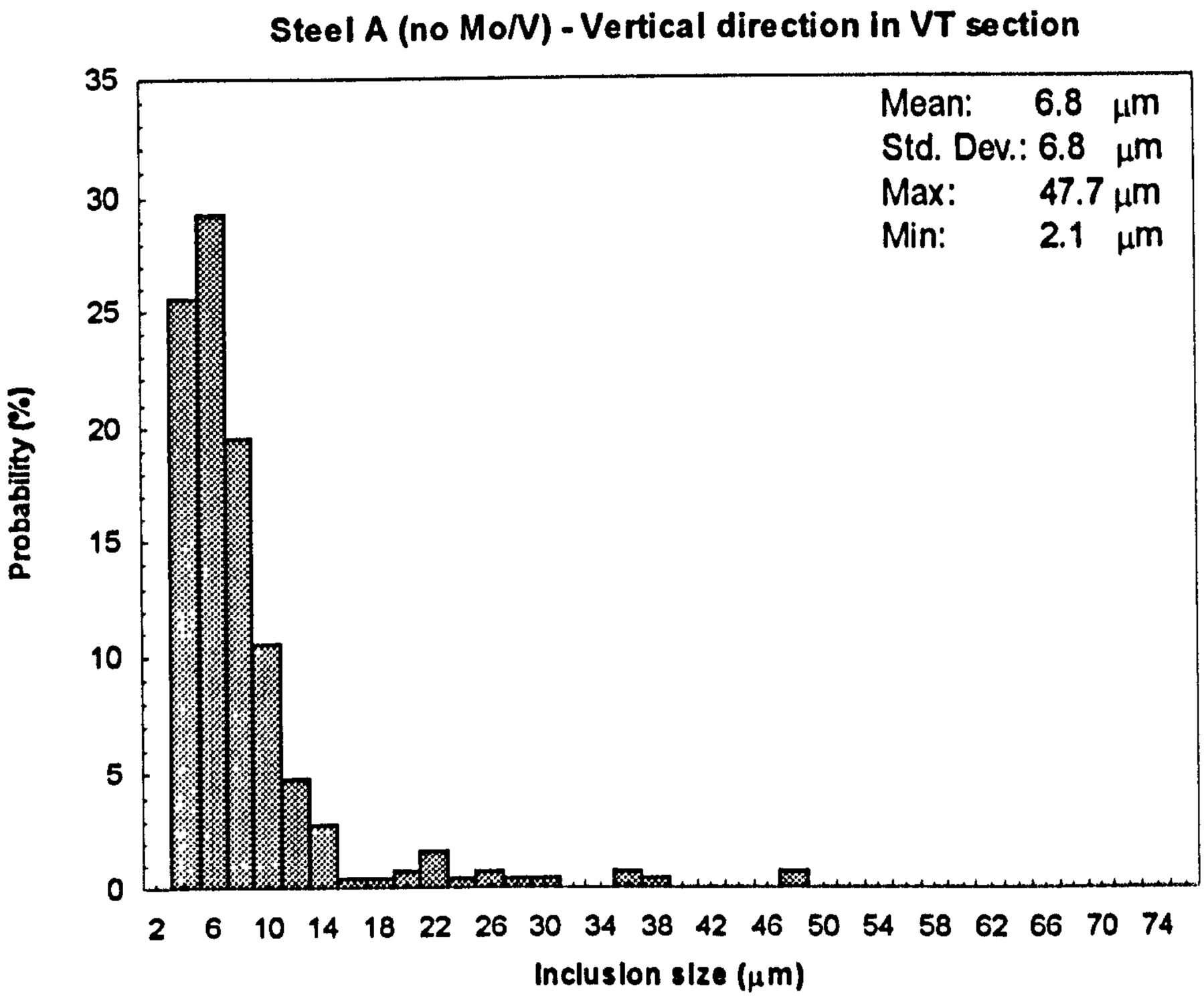

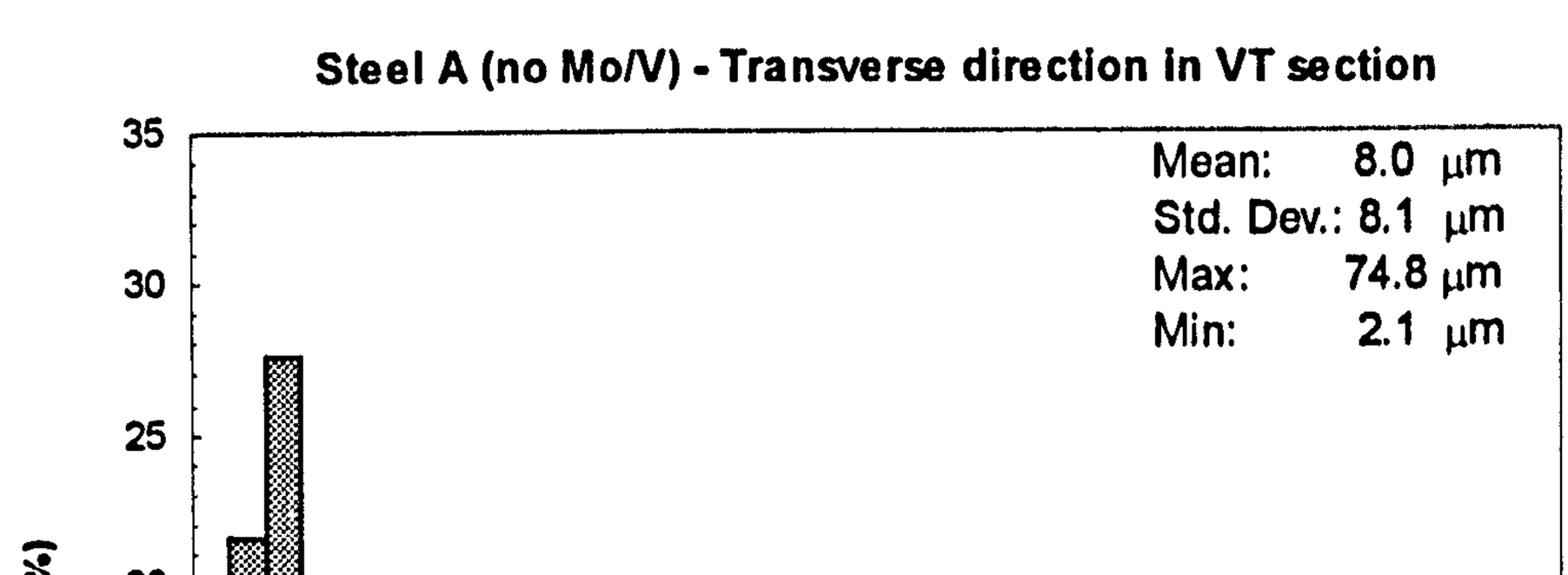

Figure 3.3.9 Inclusion size distribution in VT section of Steel A (no Mo/V)

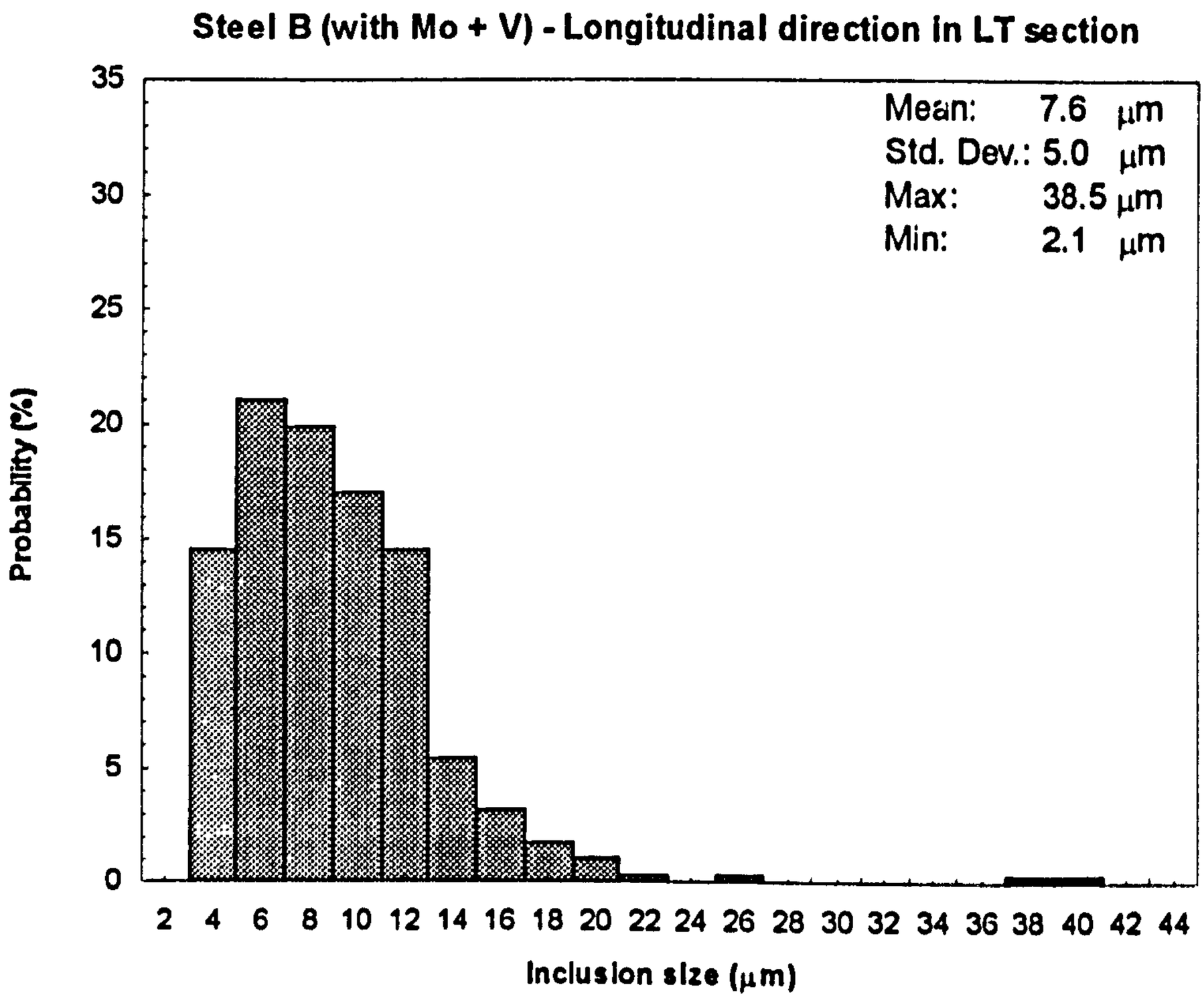

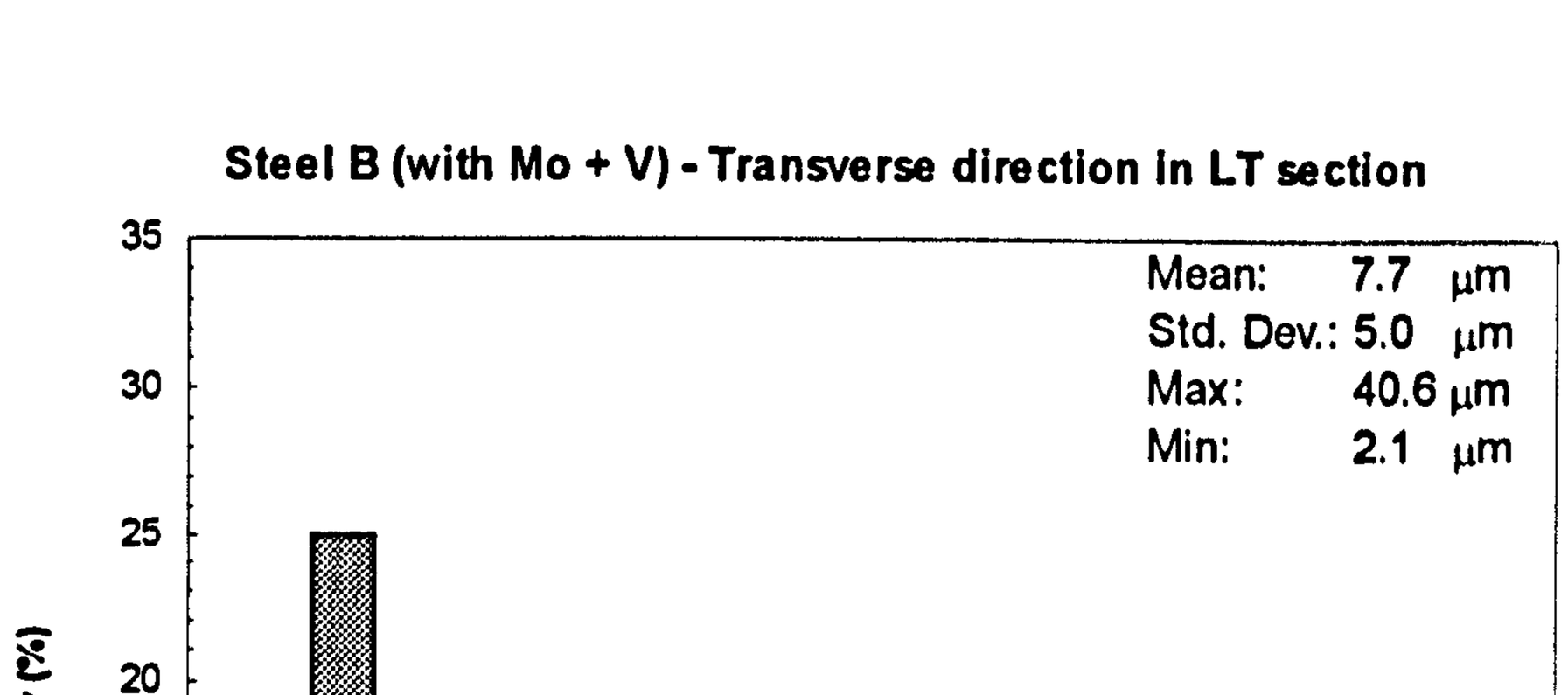

Figure 3.3.10 Inclusion size distribution in LT section of Steel B (with Mo + V)

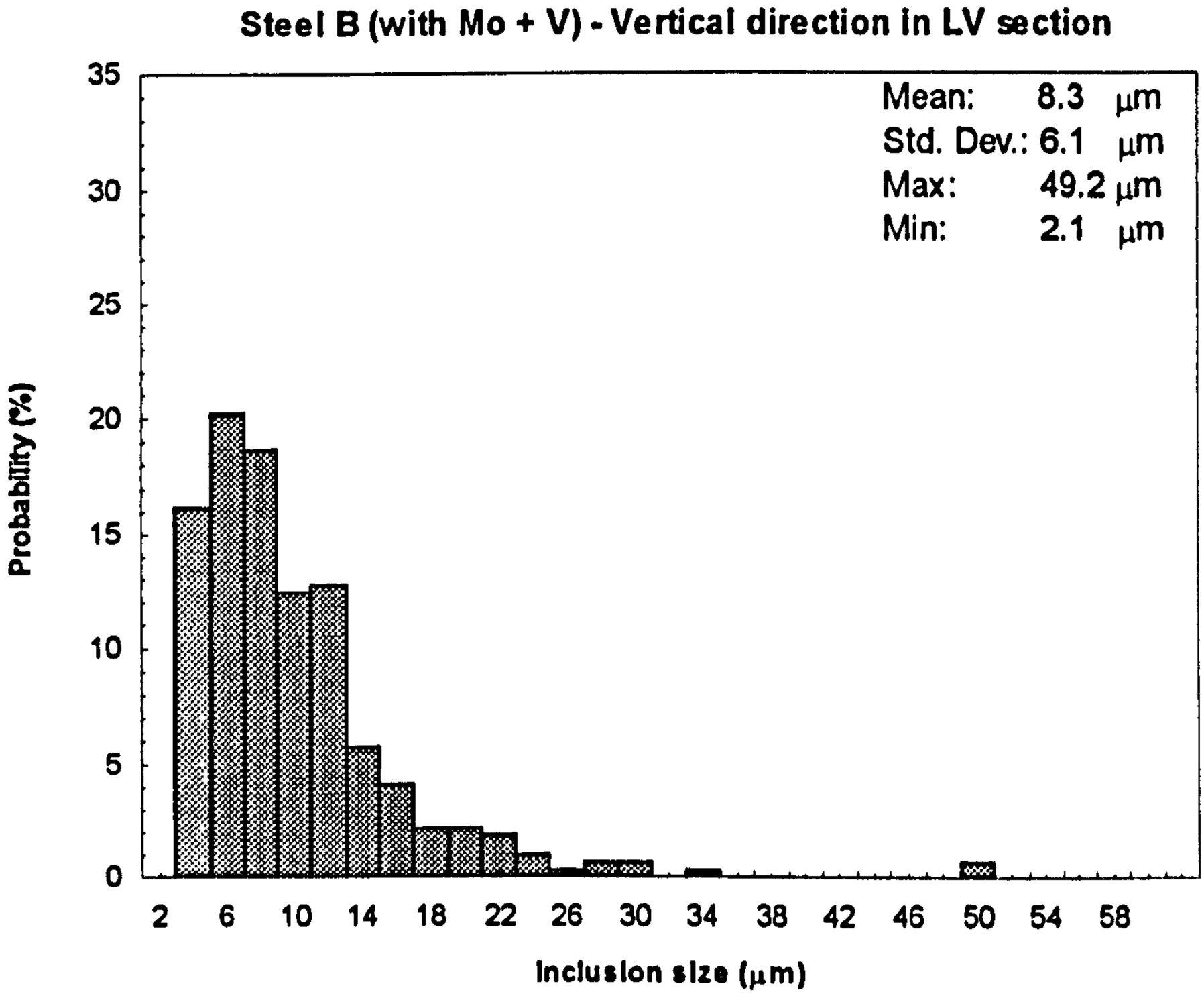

Figure 3.3.11 Inclusion size distribution in LV section of Steel B (with Mo + V)

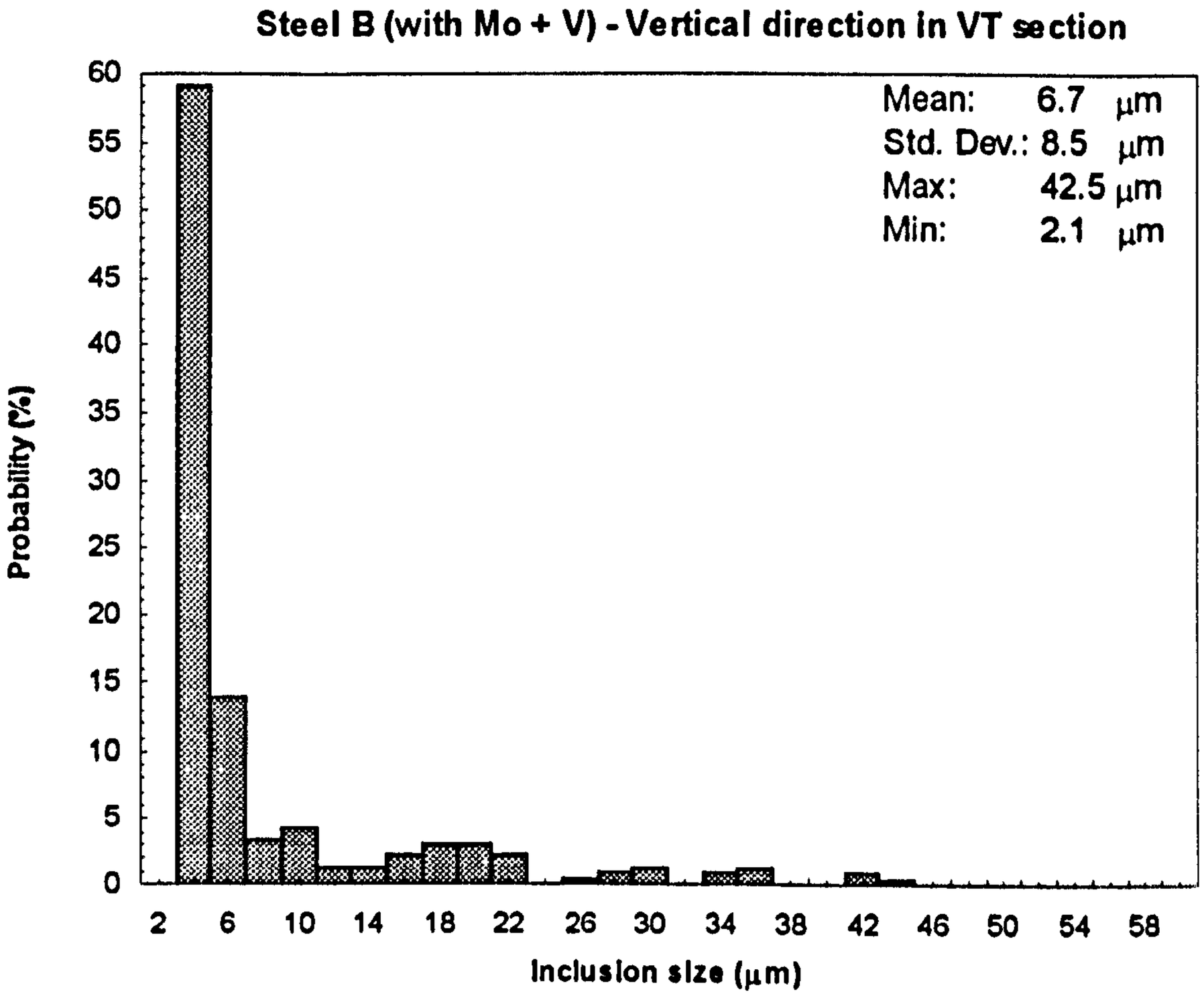

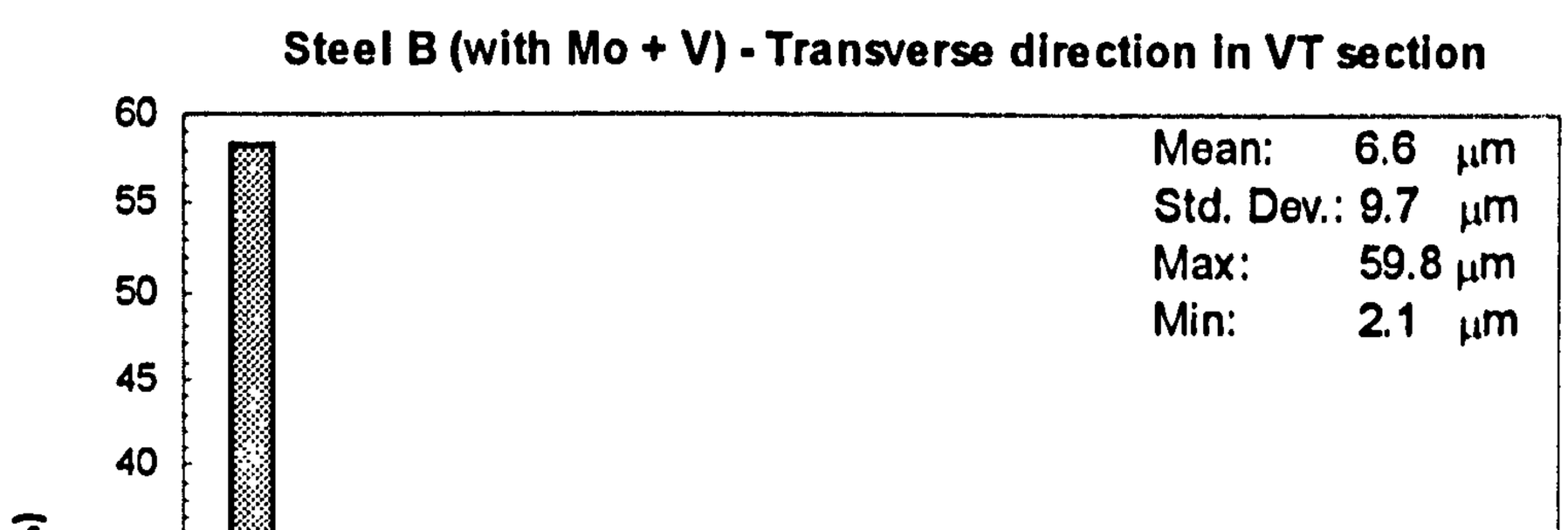

Figure 3.3.12 Inclusion size distribution in VT section of Steel B (with Mo + V)

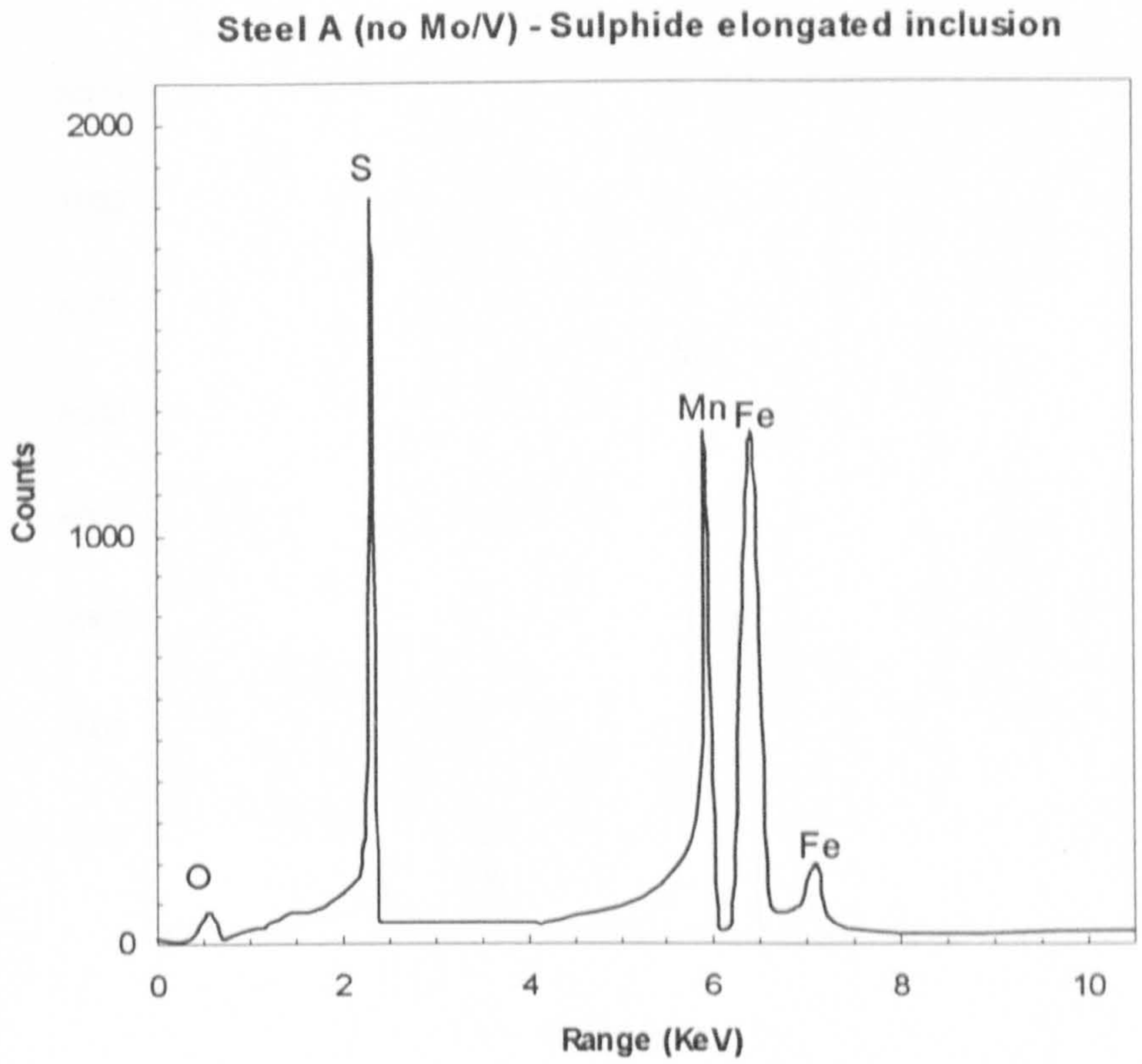

(3.3.13a)

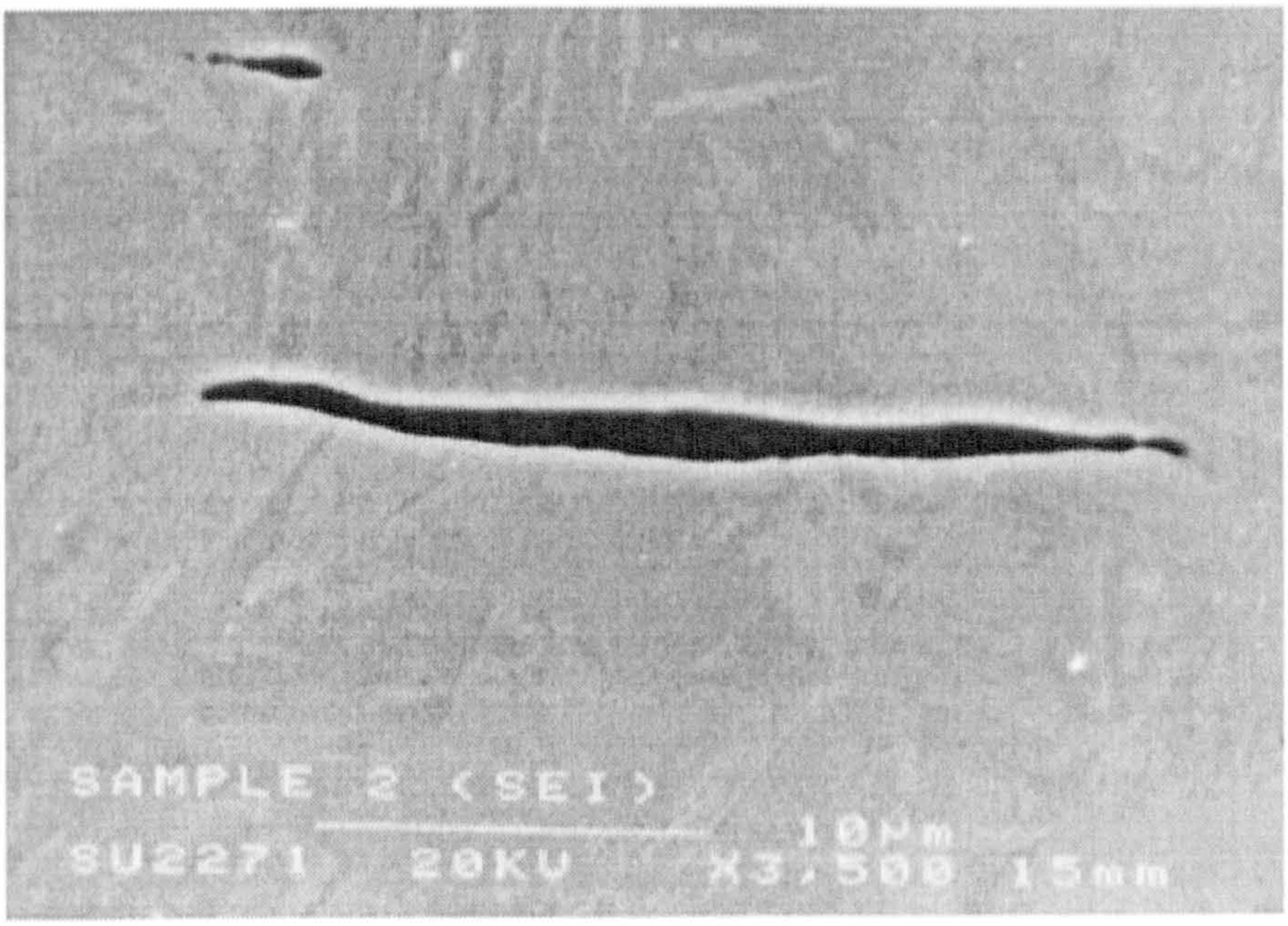

(3.3.13b)

Figure 3.3.13 Sulphide elongated inclusion in LV section of Steel A (no Mo/V).
(a) EDAC's analysis, (b) SEM micrograph

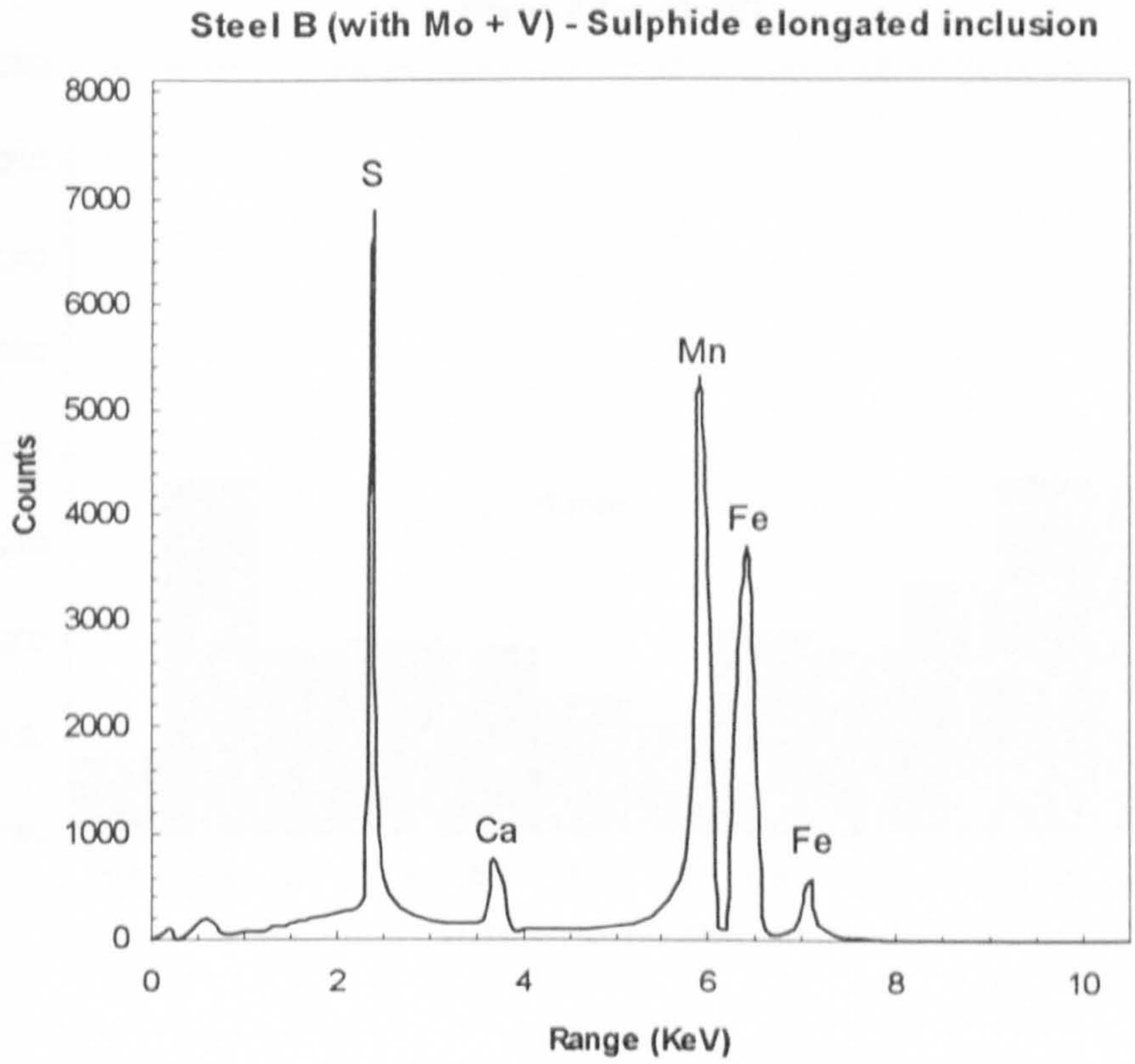

(3.3.14a)

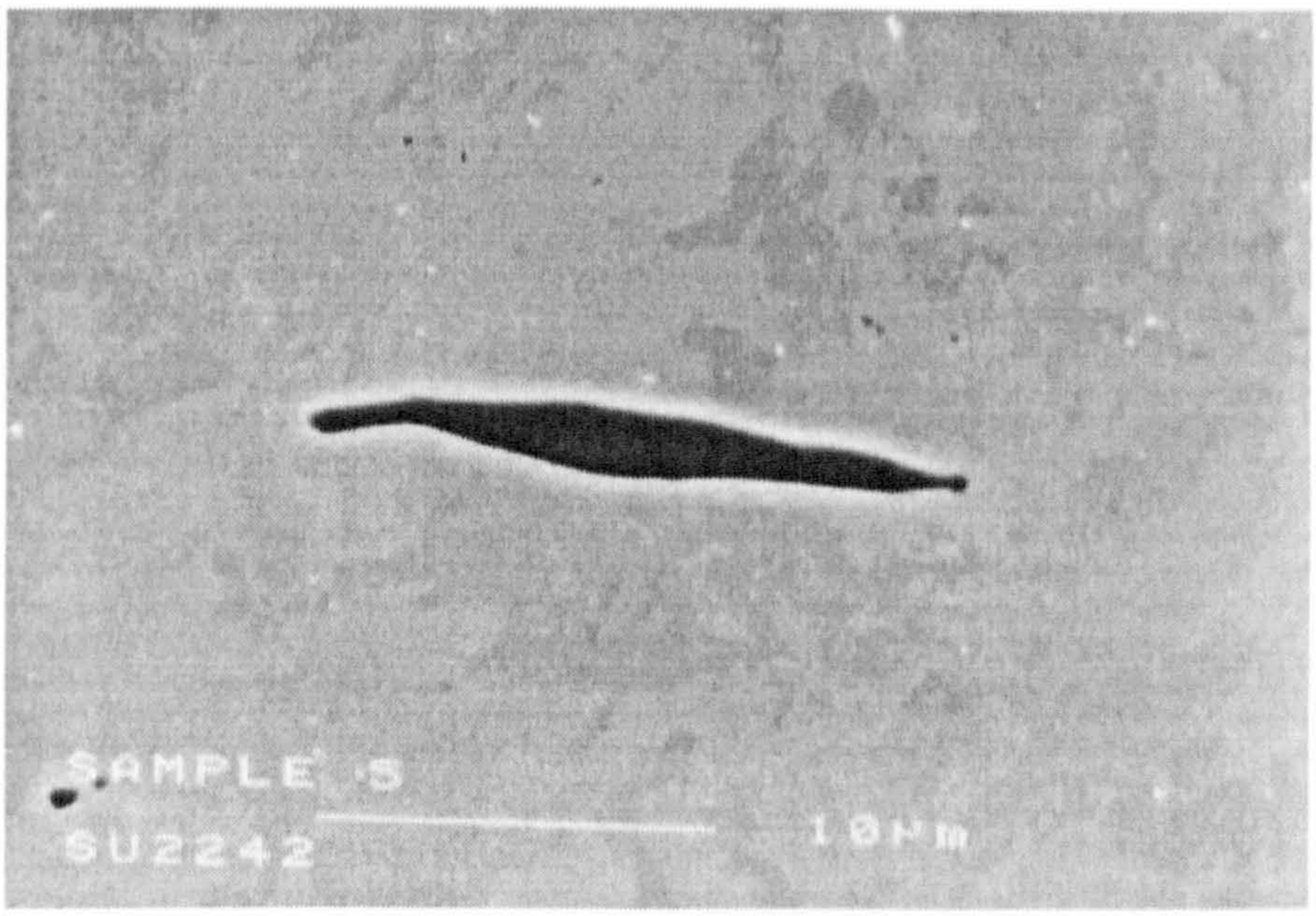

(3.3.14b)

Figure 3.3.14 Sulphide elongated inclusion in LV section of Steel B (with Mo + V). (a) EDAC's analysis, (b) SEM micrograph

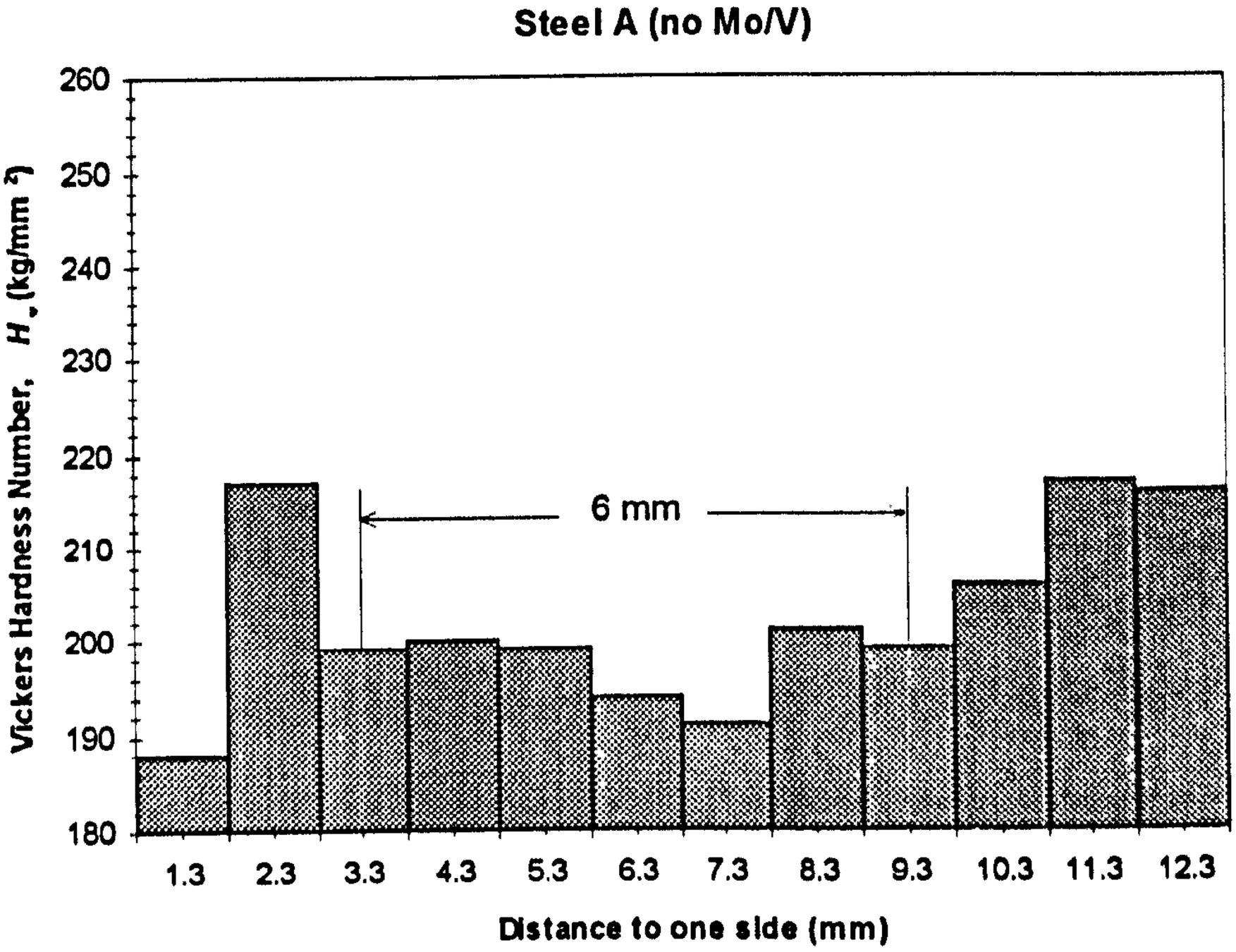

Figure 3.4.1 Distribution of Vickers Hardness Number along the thickness in Steel A (no Mo/V)

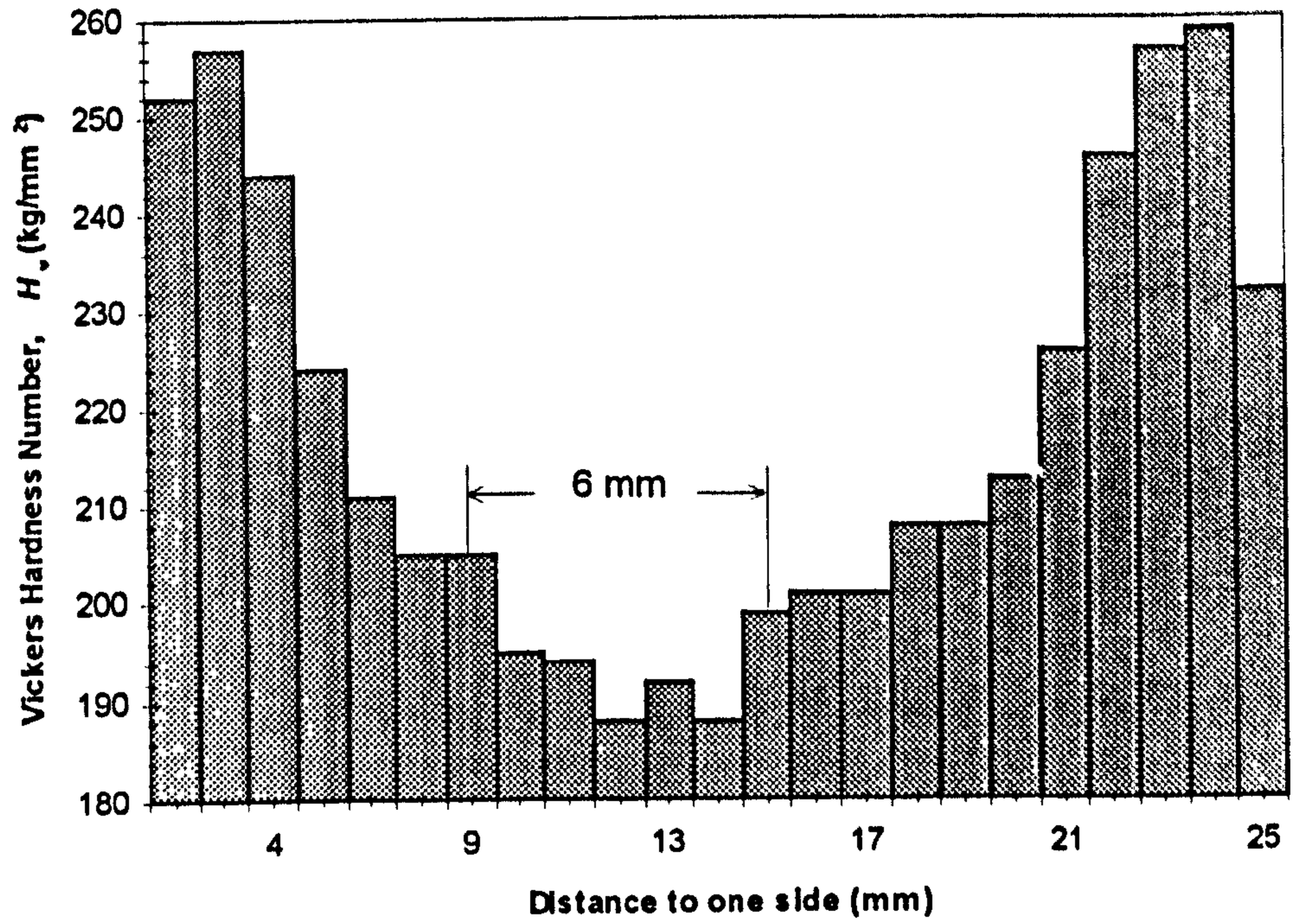

Figure 3.4.2 Distribution of Vickers Hardness Number along the thickness in Steel B (with Mo + V)

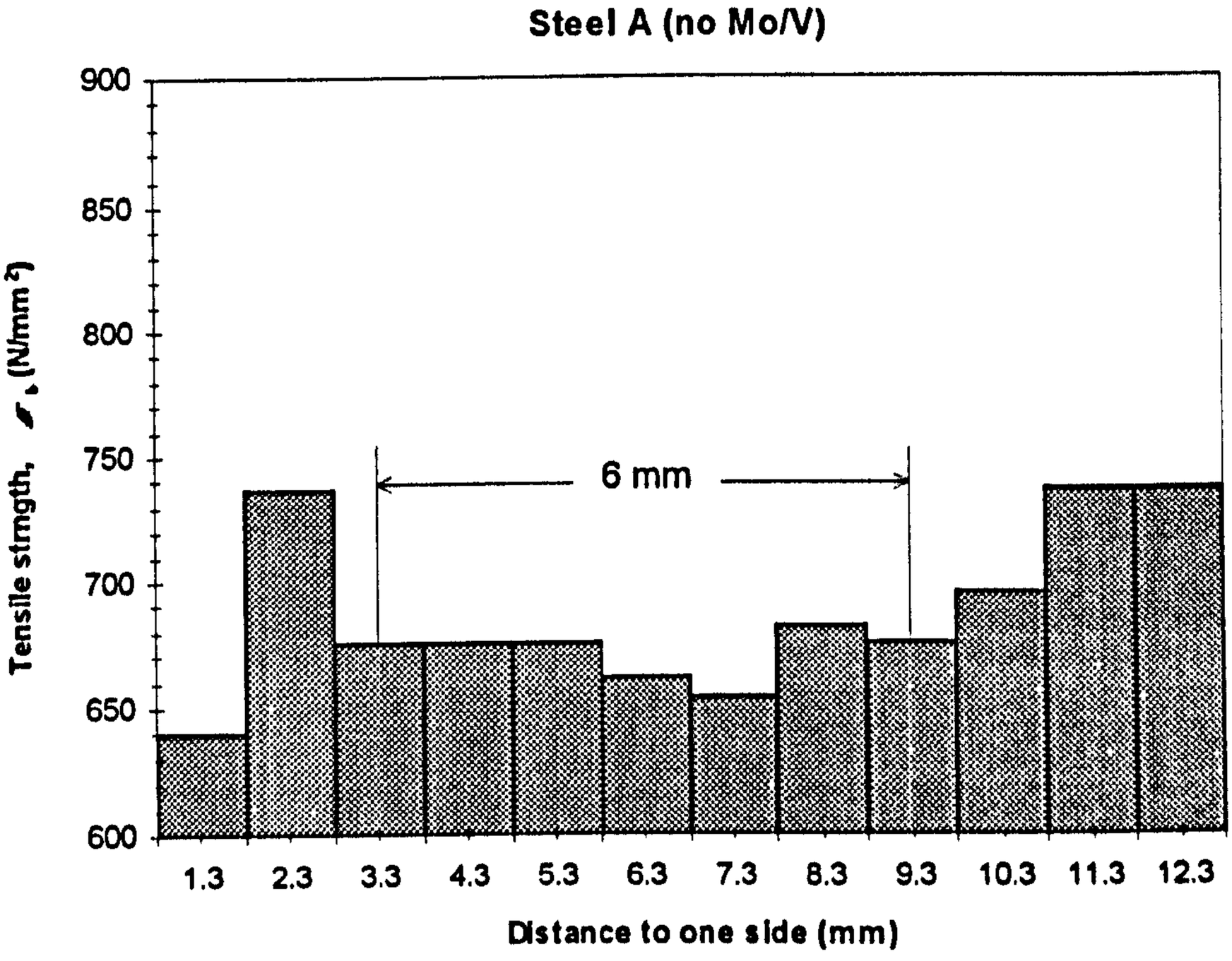

Figure 3.4.3 Distribution of tensile strength converted from the Vickers hardness number along the thickness in Steel A (no Mo/V)

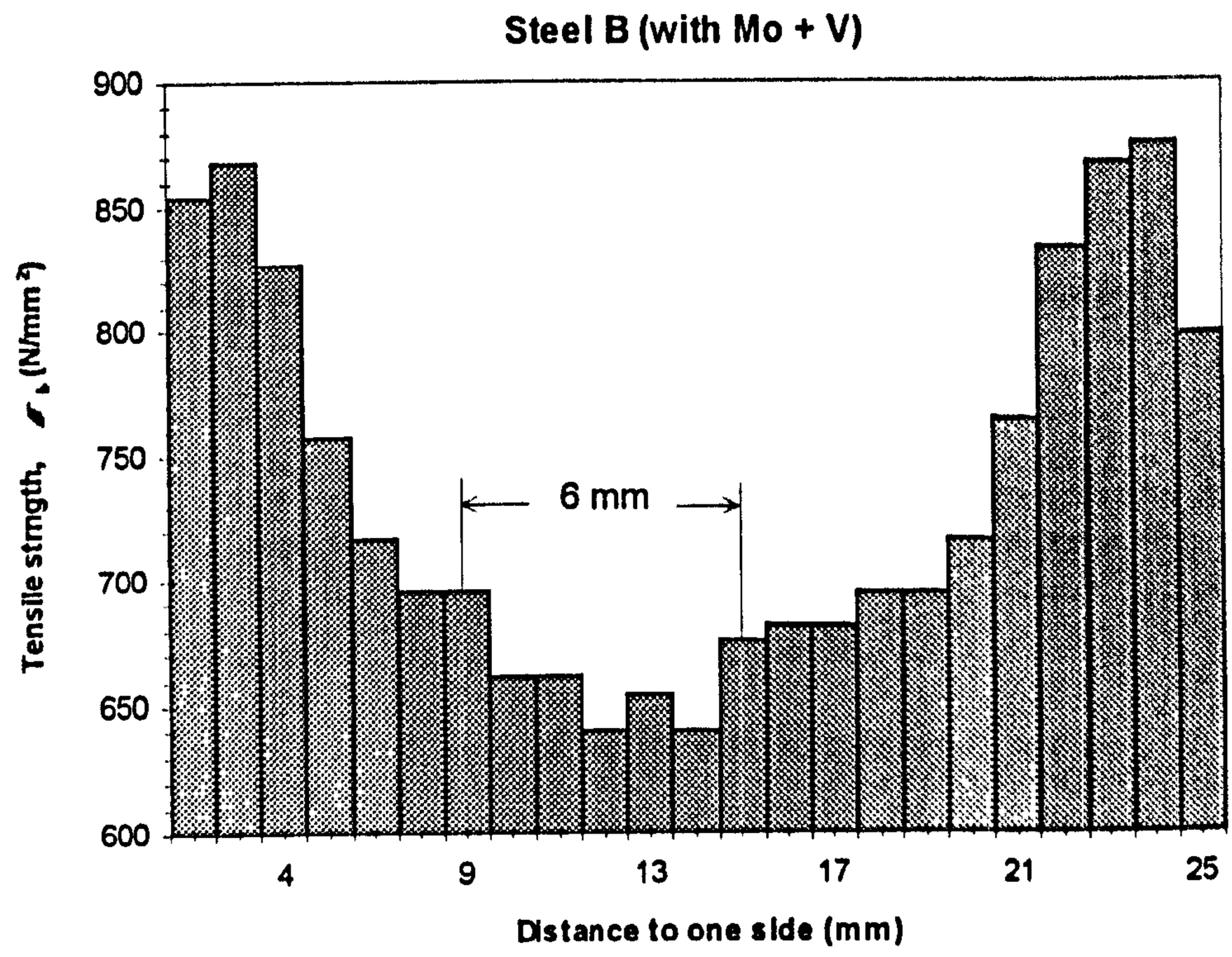

Figure 3.4.4 Distribution of tensile strength converted from the Vickers hardness number along the thickness in Steel B (with Mo + V)

All dimensions in mm

Tolerances +/- 0.2 unless stated

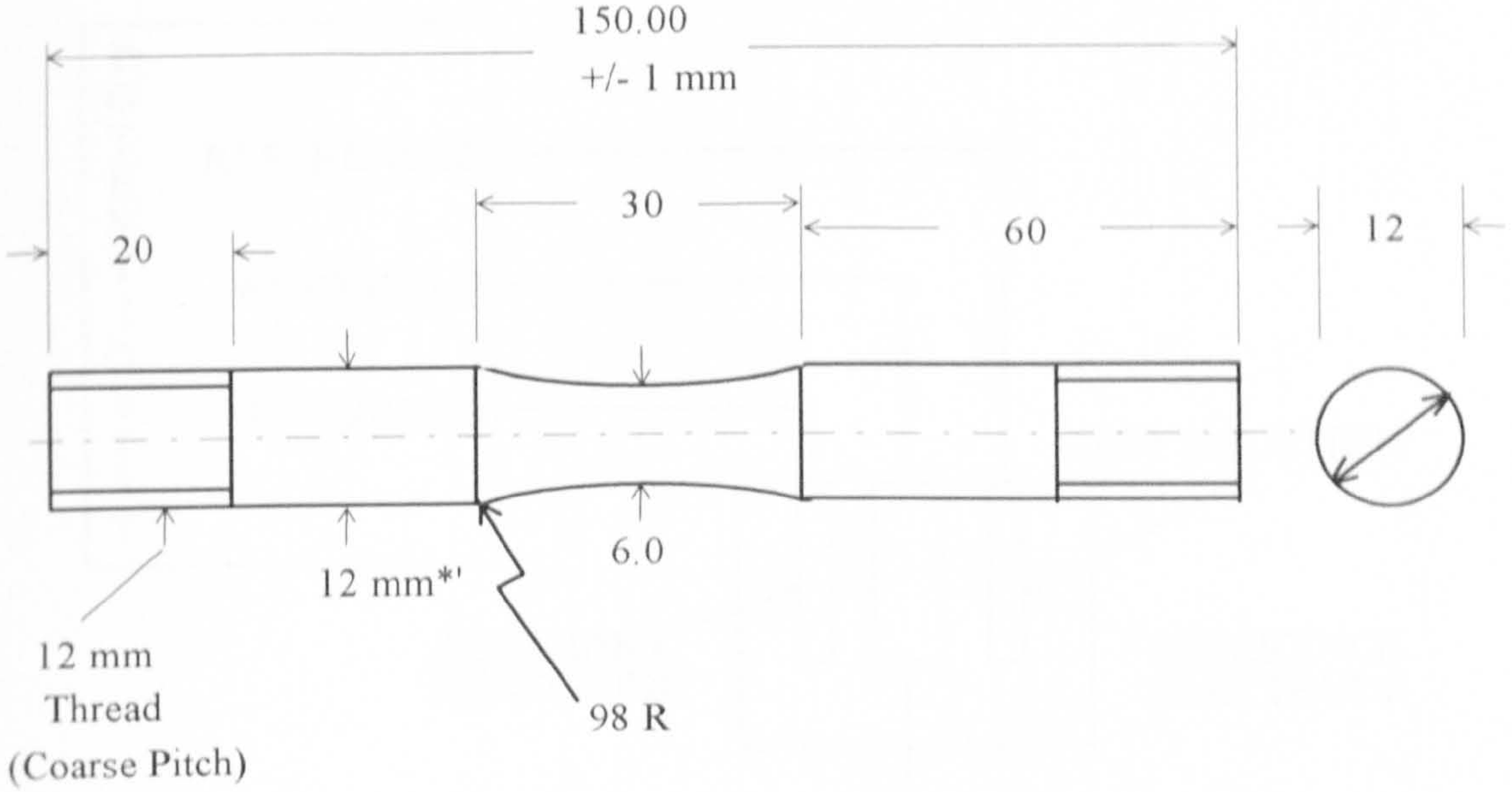

*' To suit corrosion cells

12 mm $^{-0.00}_{+0.08}$ mm

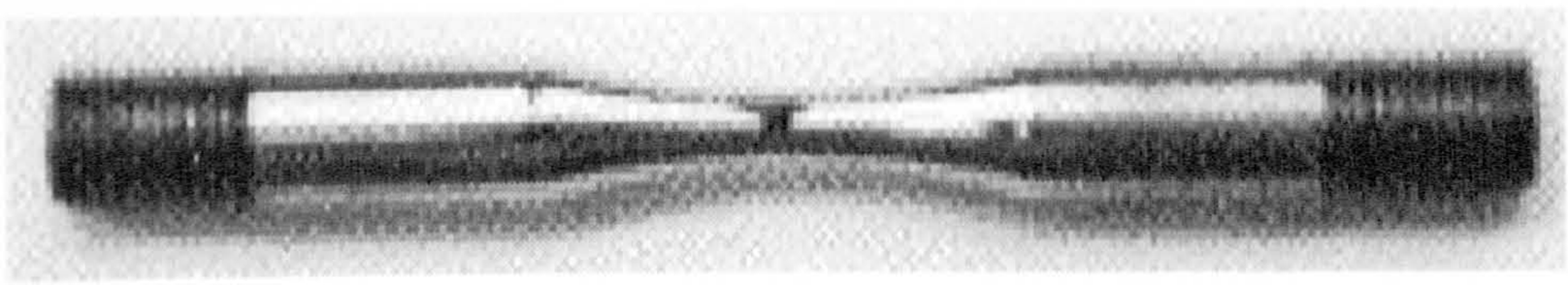

Figure 4.1 Hour-glass tensile fatigue test-pieces

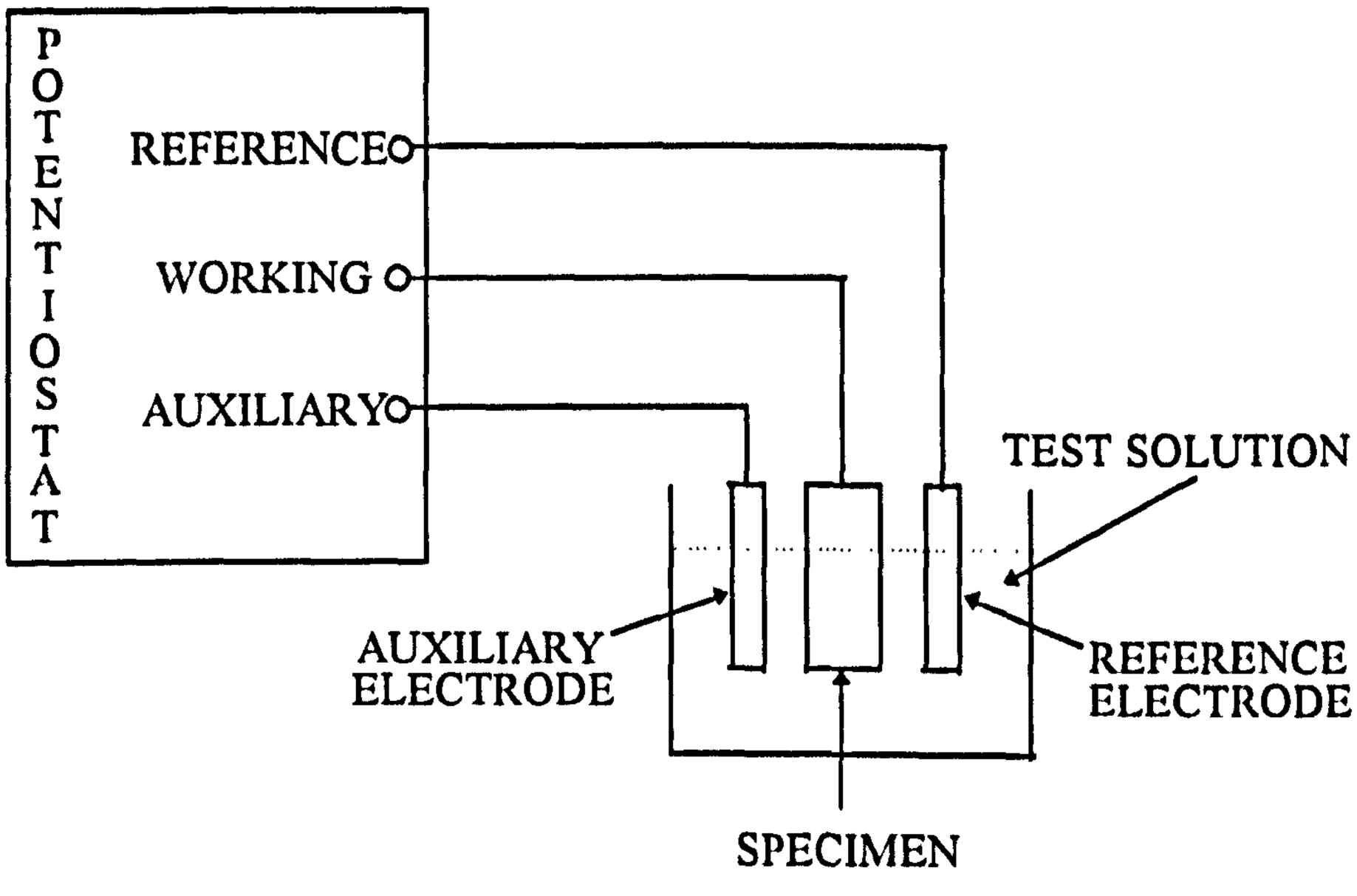

Figure 4.2 **Schematic of three electrode cell and potentiostat for cathodic polarisation application**

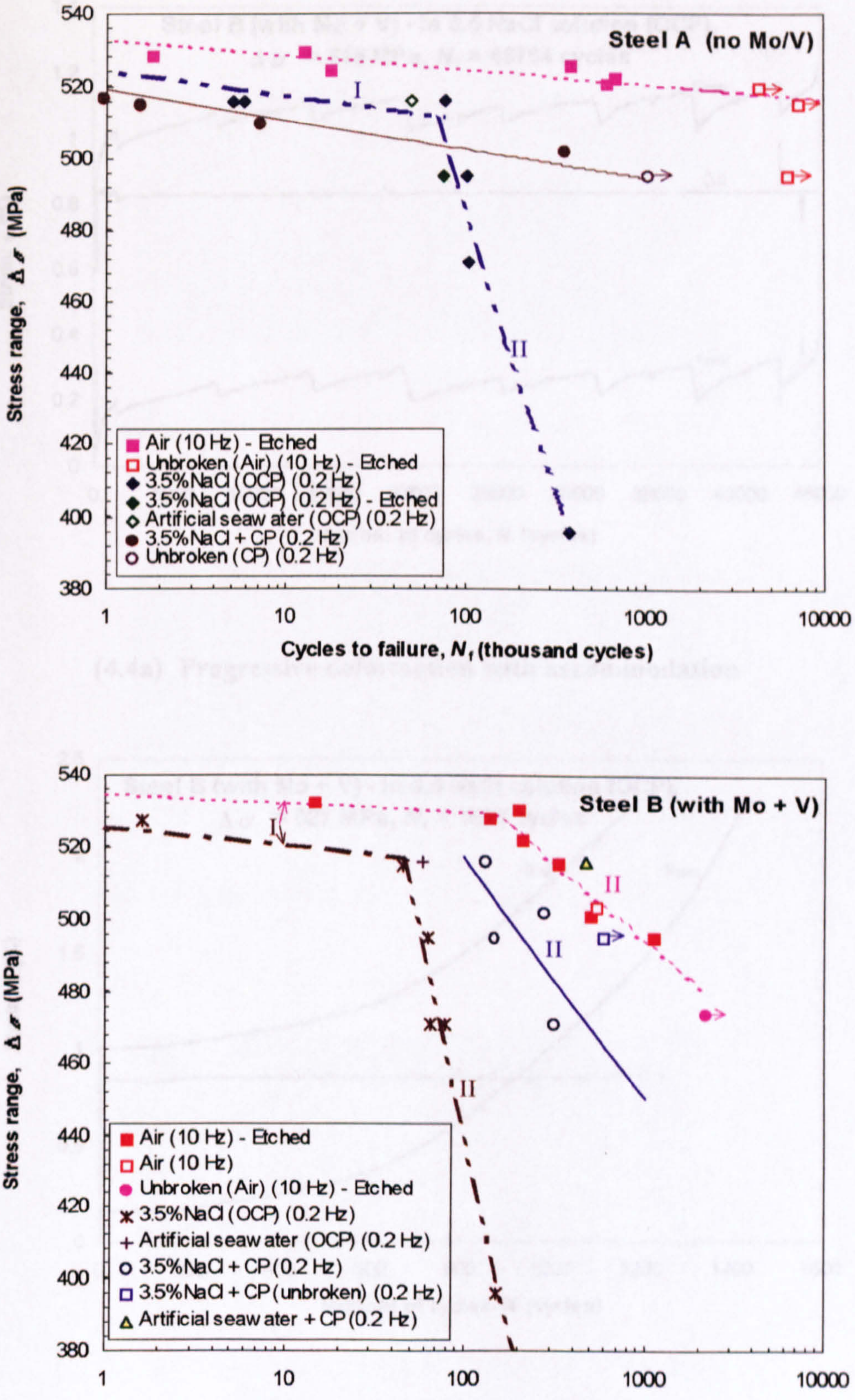

Figure 4.3 **The $S \sim N_f$ fatigue endurance curve for both steels in different environments** ($R = 0.1$)

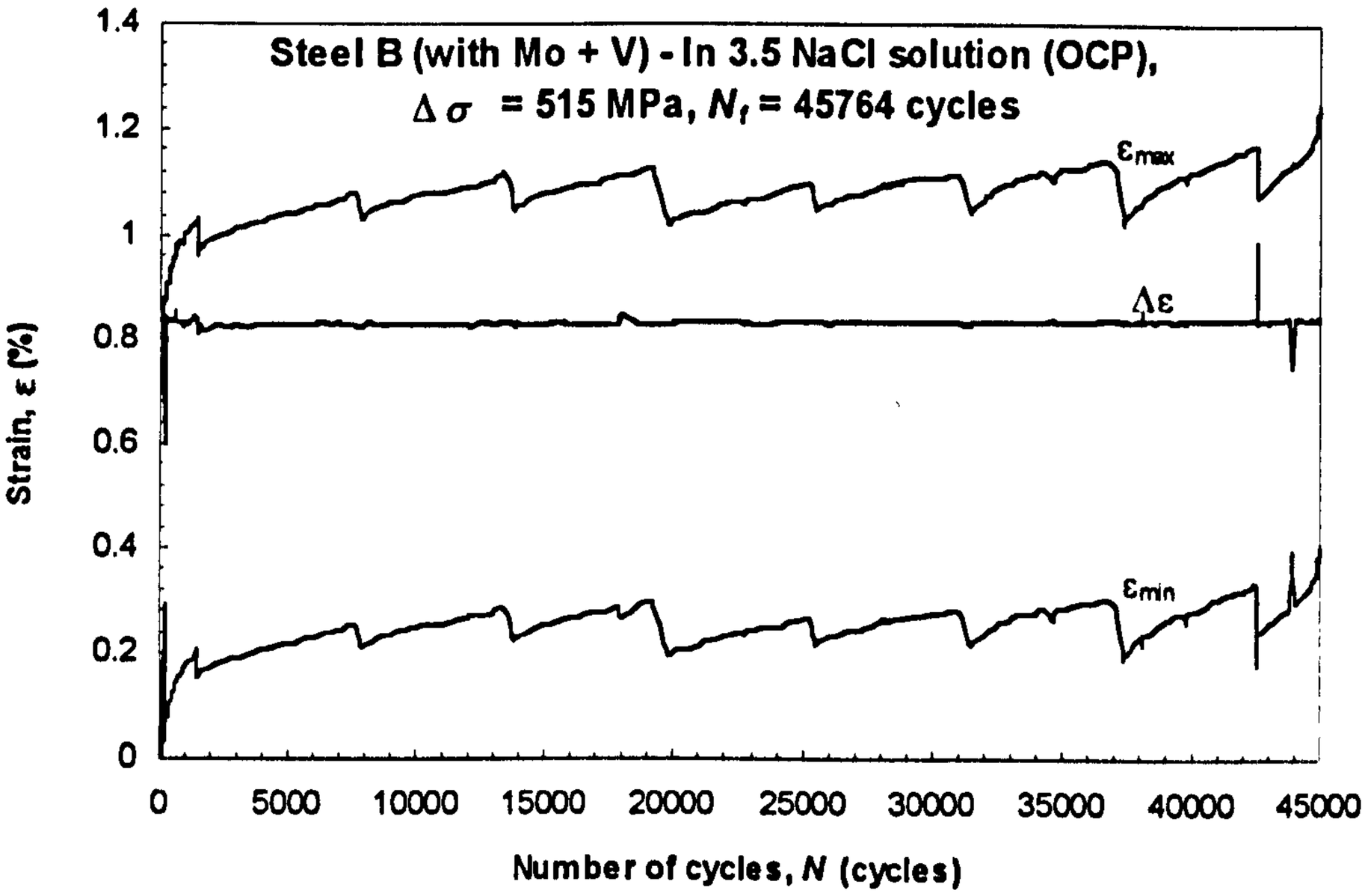

(4.4a) Progressive deformation with accommodation

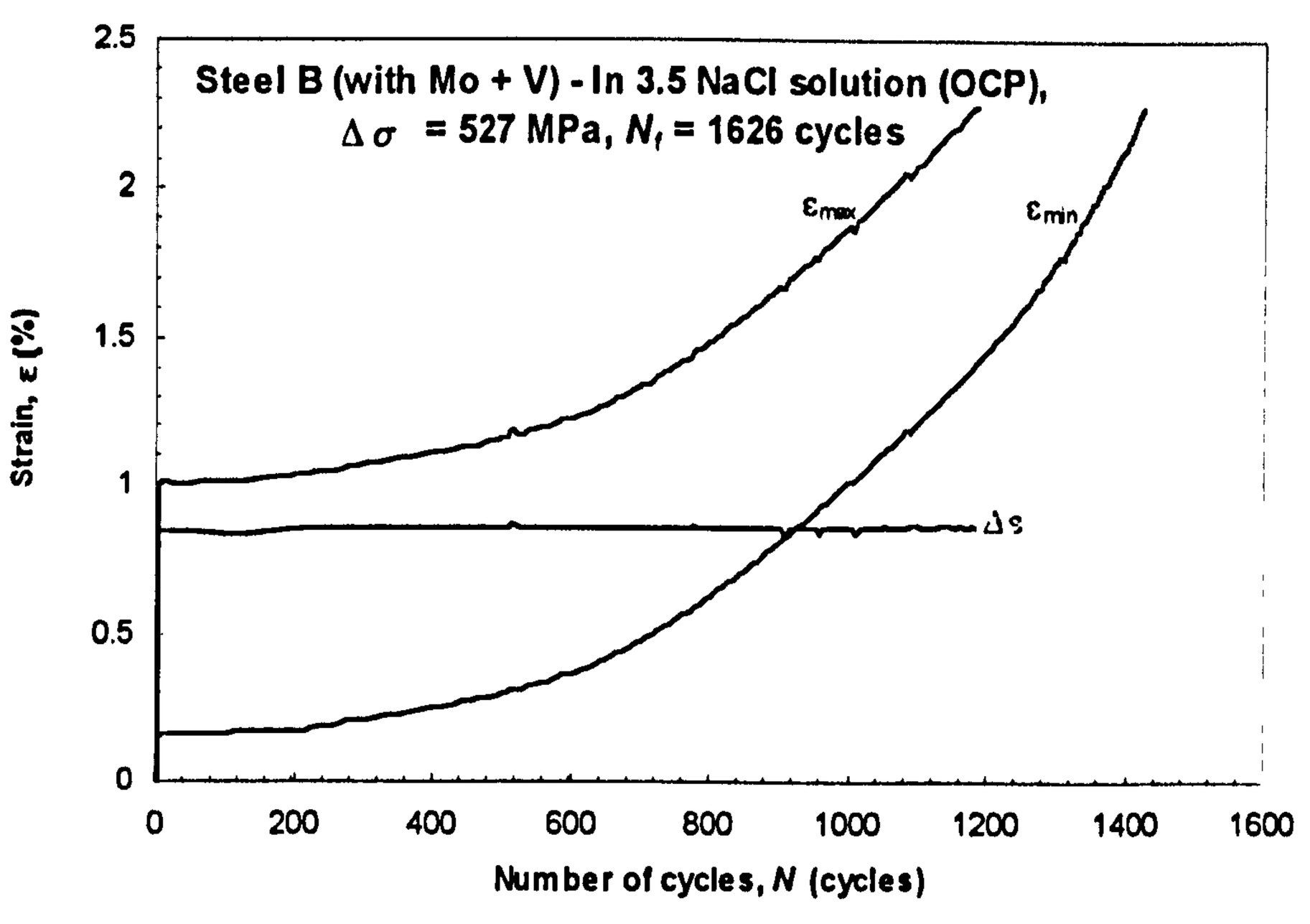

(4.4b) Progressive deformation without accommodation

Figure 4.4 **Different typical behaviour of the RQT501 steel under fatigue loading conditions**

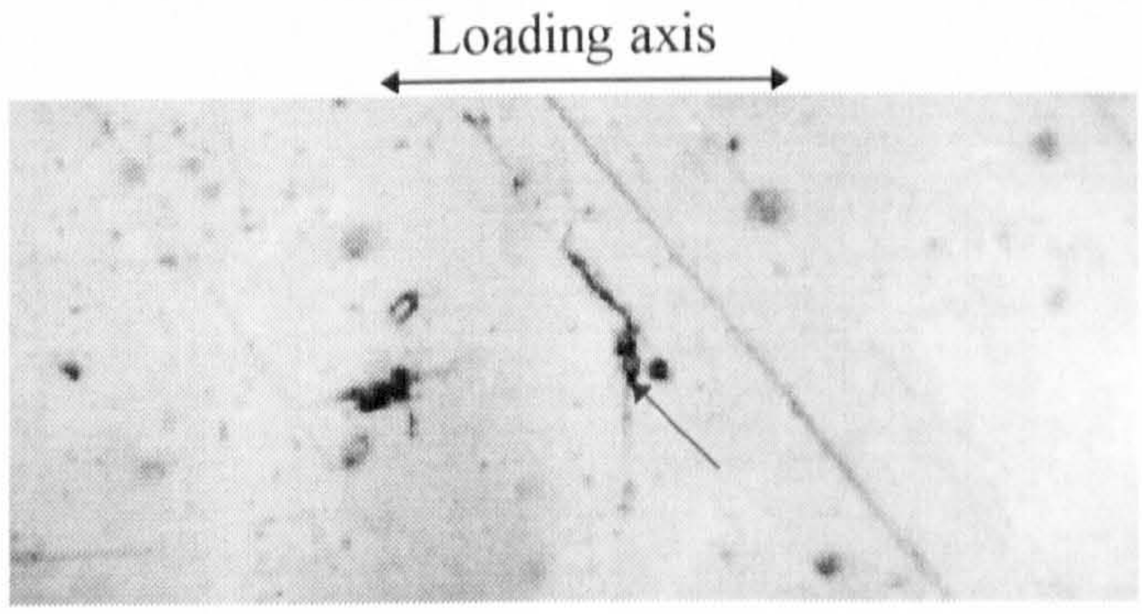

200 μm

(4.5a) Steel B (with Mo + V) - SB5, $\Delta\sigma$ = 522 MPa

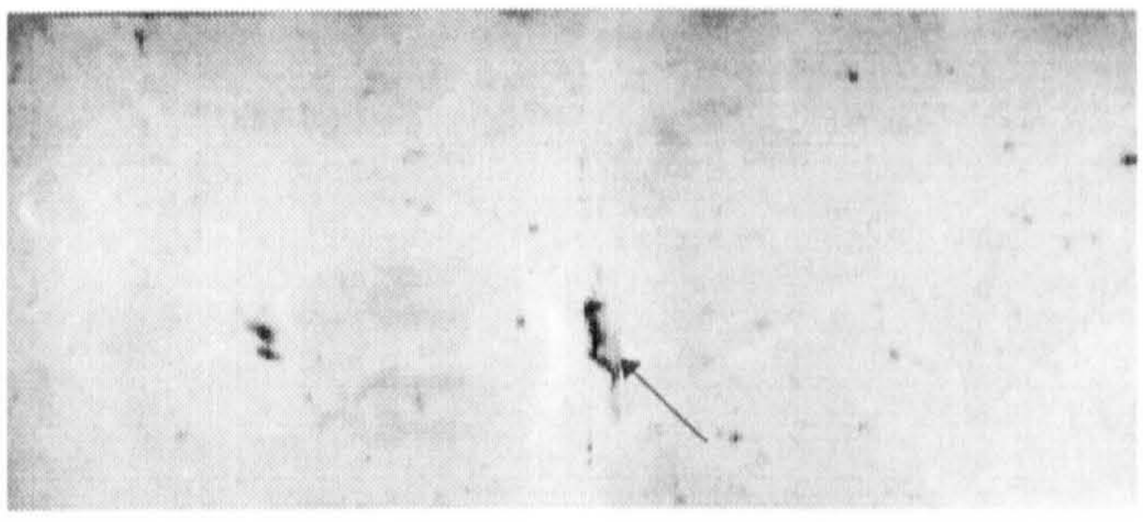

100 μm

(4.5b) Steel B (with Mo + V) - SB4, $\Delta\sigma$ = 530 MPa

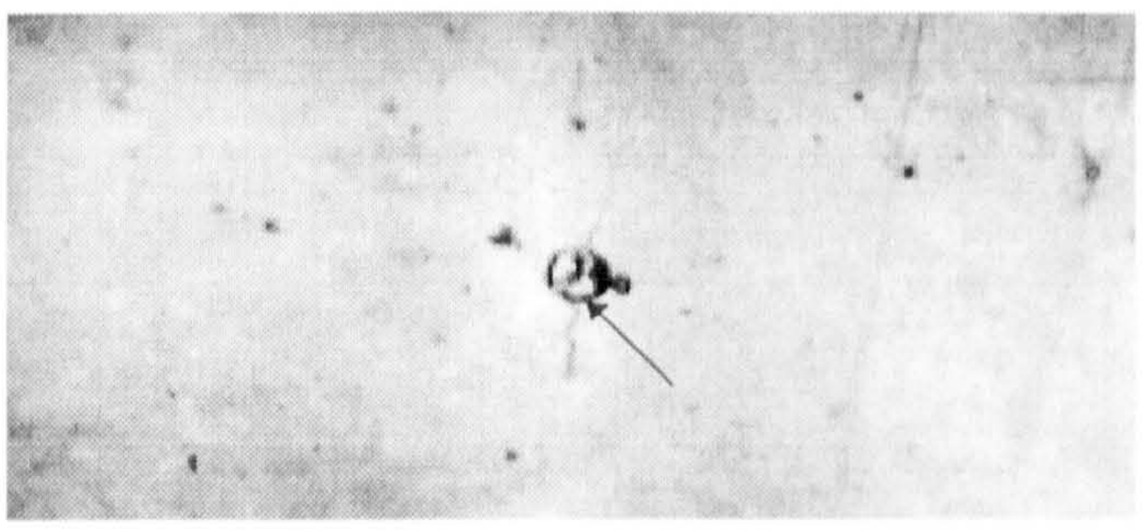

100 μm

(4.5c) Steel B (with Mo + V) - SB7, $\Delta\sigma$ = 502 MPa

Figure 4.5 Cracks initiated at inclusion sites for different in-air fatigue tests

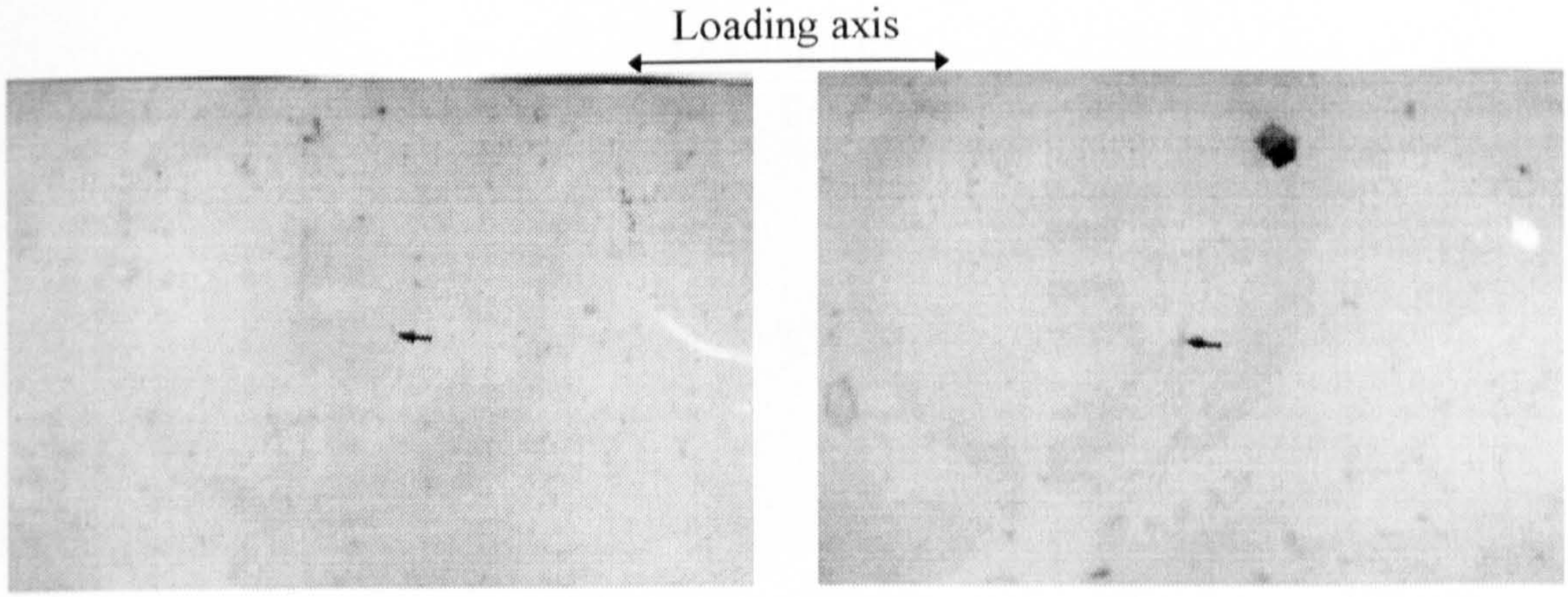

100 μm

(a) $\frac{N}{N_f} = 0.51$, $N = 1.7 \times 10^5$ cycles

100 μm

(b) $\frac{N}{N_f} = 0.56$, $N = 1.9 \times 10^5$ cycles

100 μm

(c) $\frac{N}{N_f} = 0.70$, $N = 2.4 \times 10^5$ cycles

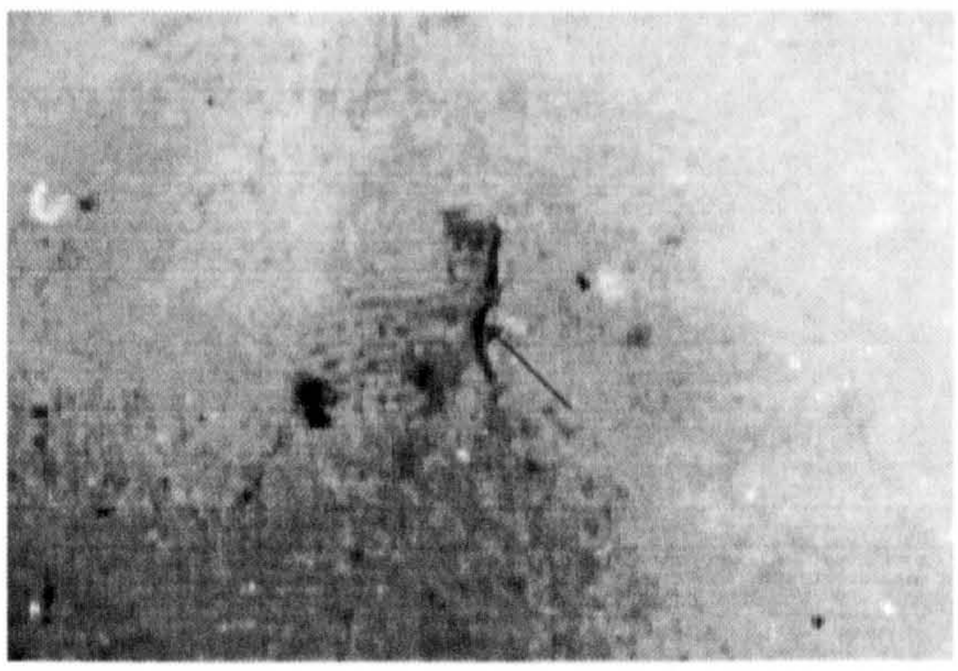

100 μm

(d) $\frac{N}{N_f} = 0.78$, $N = 2.6 \times 10^5$ cycles

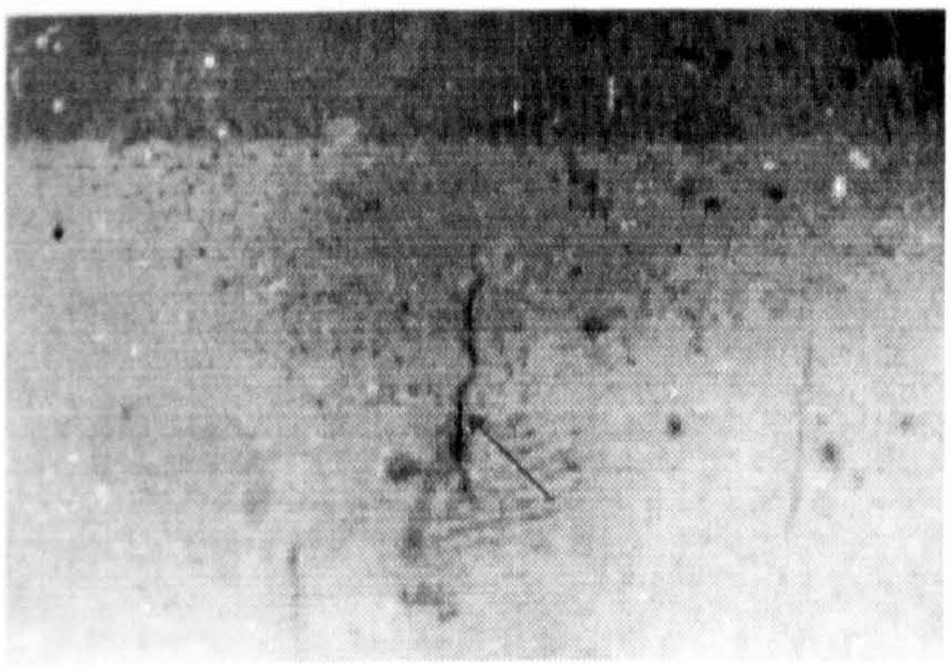

200 μm

(e) $\frac{N}{N_f} = 0.88$, $N = 3.0 \times 10^5$ cycles

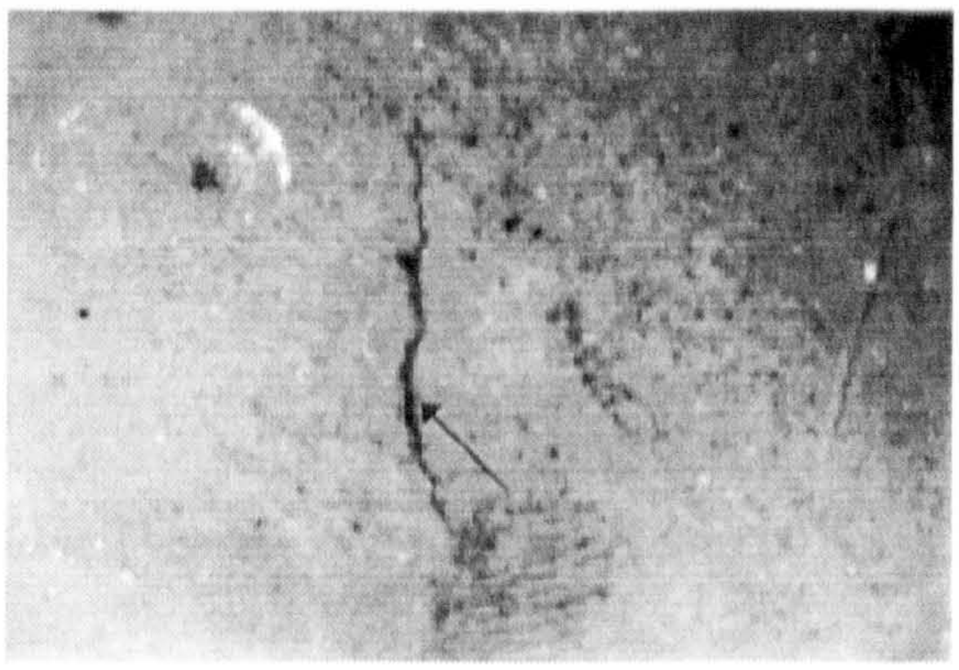

200 μm

(f) $\frac{N}{N_f} = 0.92$, $N = 3.1 \times 10^5$ cycles

(4.6a) Crack 1

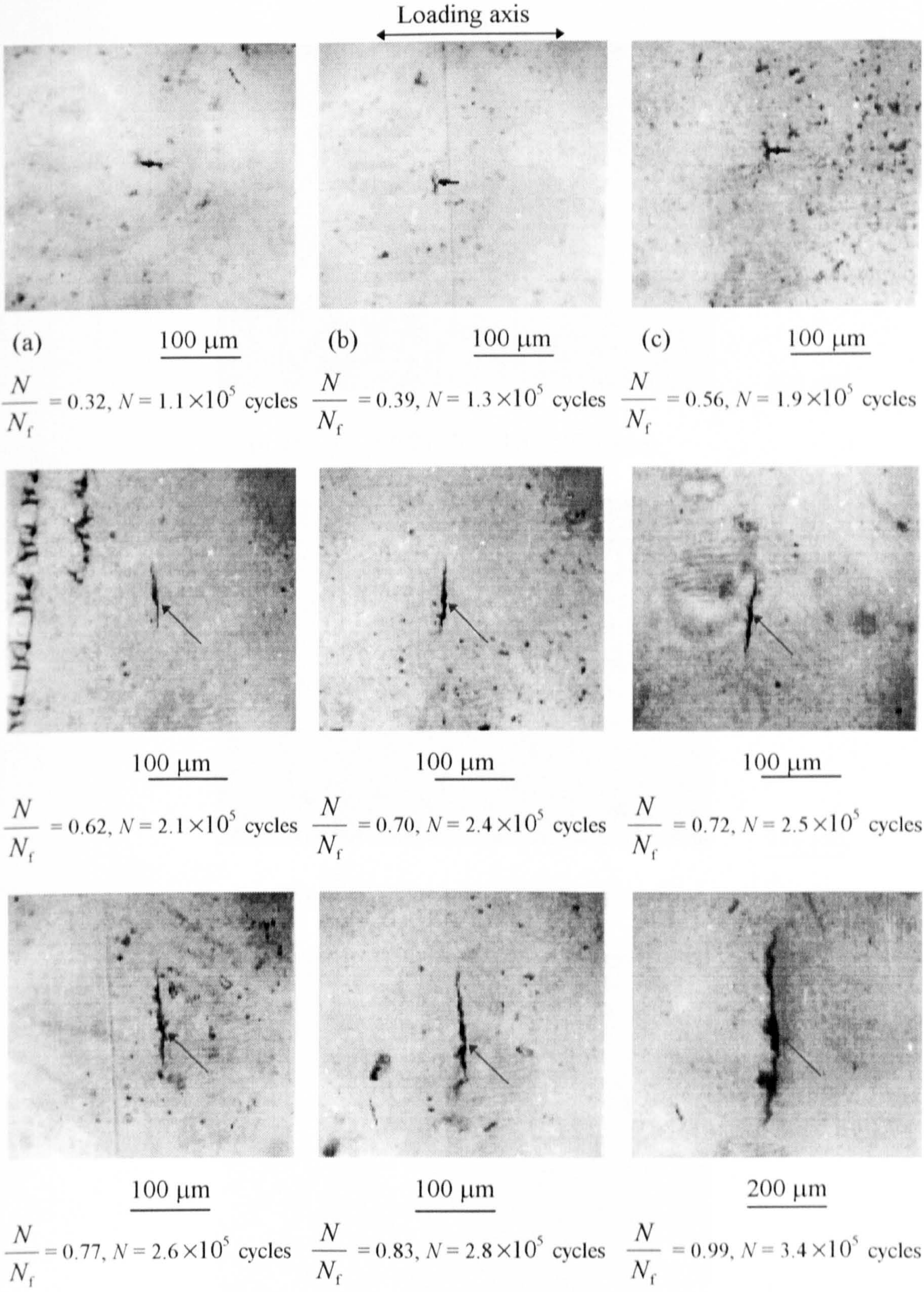

(4.6b) Crack 2

Figure 4.6 **Typical in-air fatigue crack initiation and growth behaviour** (SB6 - $\Delta\sigma$ = 573 MPa, N_f = 339240 cycles) - **Steel B** (with Mo + V)

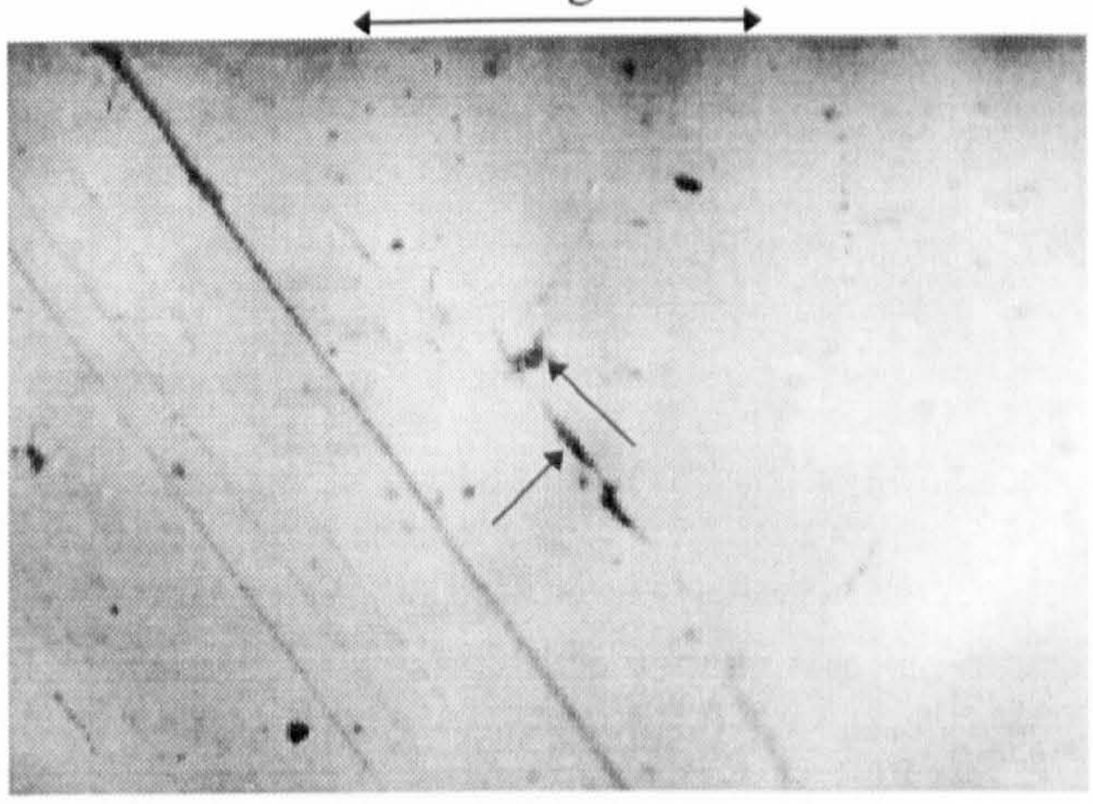

100 μm

(4.7a) $\frac{N}{N_f} = 0.21,\ N = 4.5 \times 10^4$ cycles

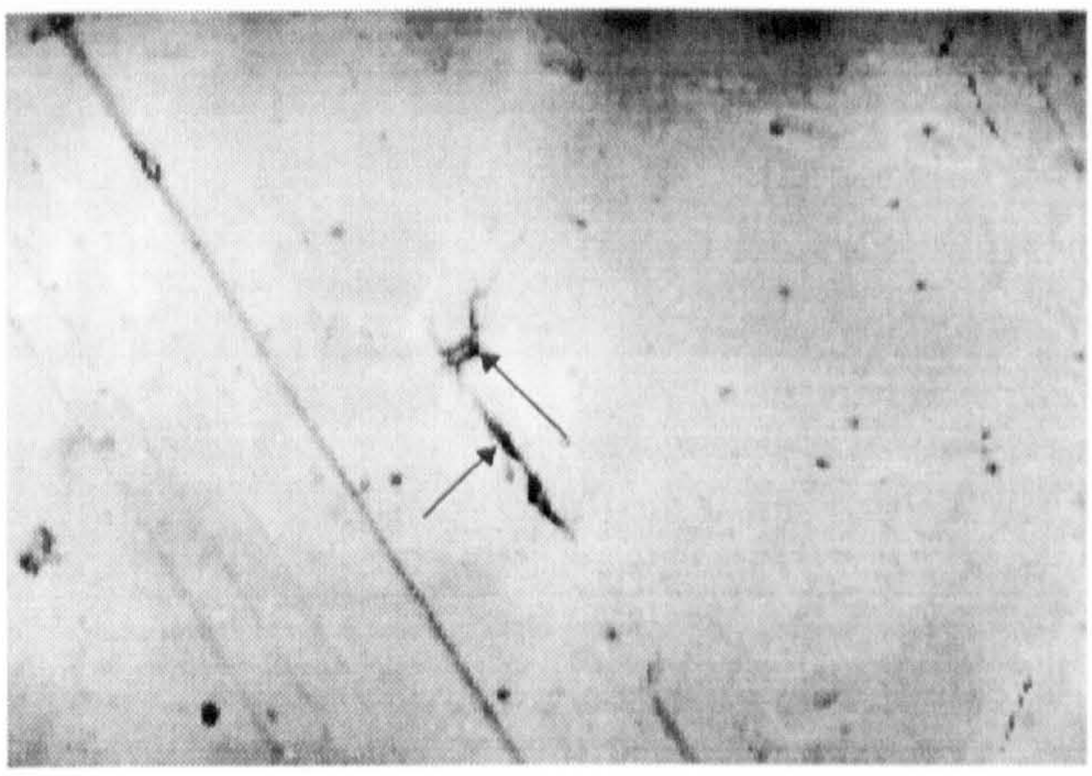

100 μm

(4.7b) $\frac{N}{N_f} = 0.49,\ N = 1.1 \times 10^5$ cycles

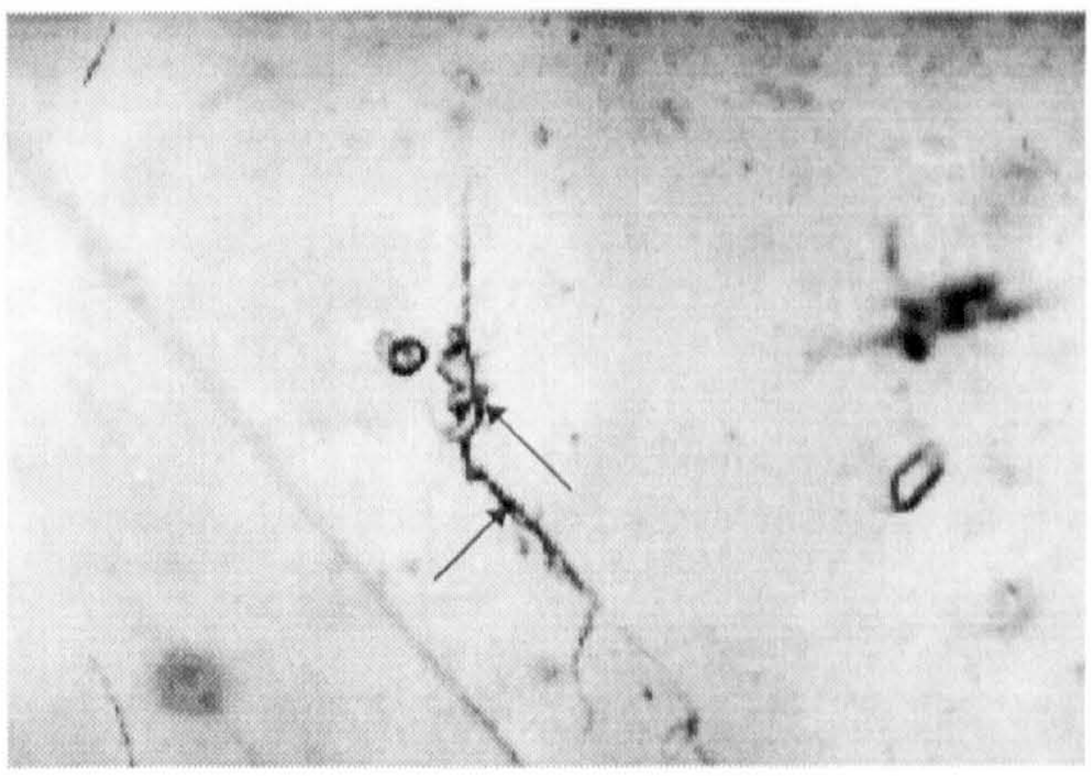

100 μm

(4.7c) $\frac{N}{N_f} = 0.70,\ N = 1.7 \times 10^5$ cycles

Figure 4.7 **Combination of two cracks which originate from inclusions in air** (SB5 - $\Delta\sigma = 522$ MPa, $N_f = 214190$ cycles) - **Steel B** (with Mo + V)

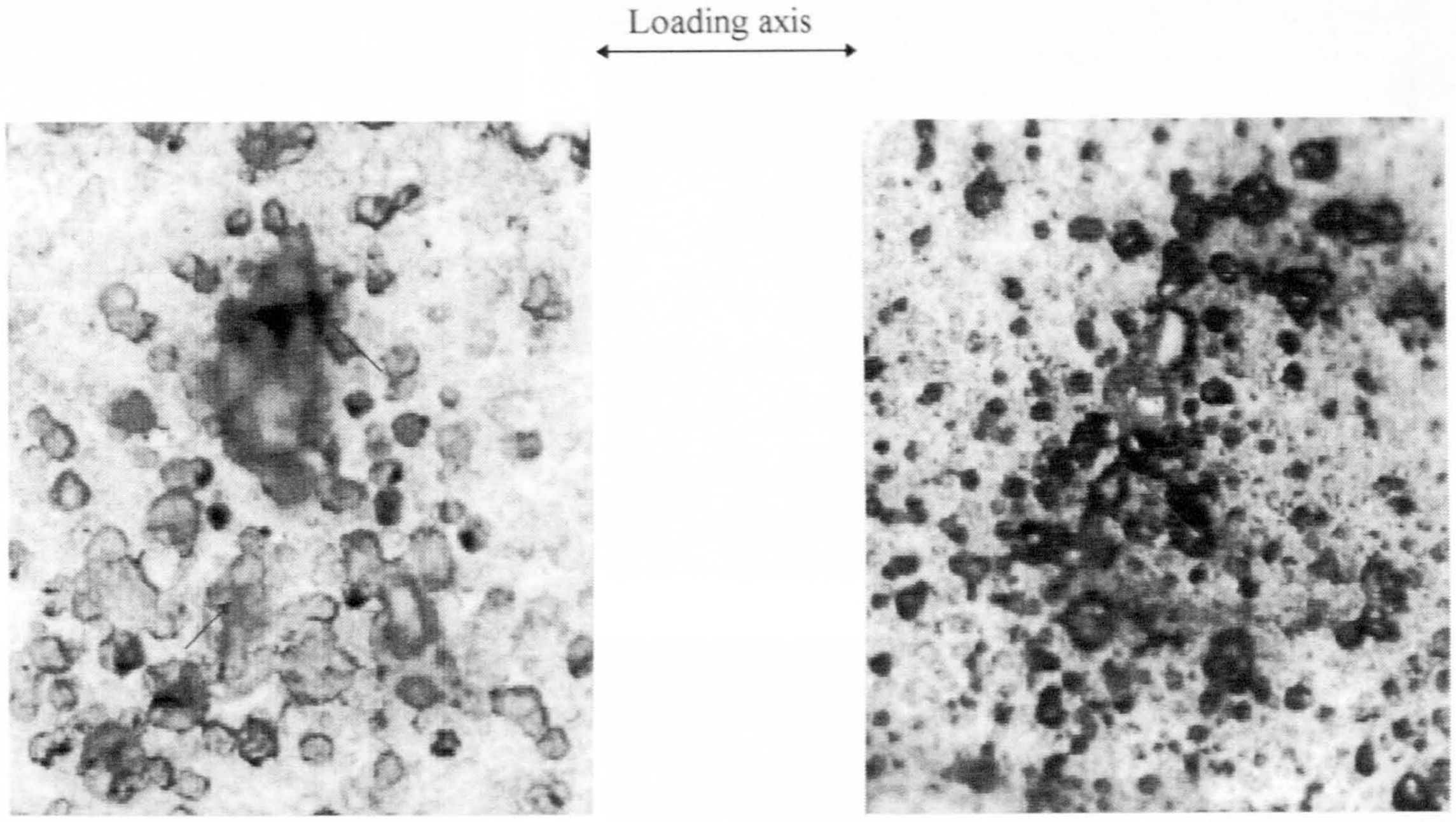

Figure 4.8 **Some pits form a crack in 3.5%NaCl solution** (OCP) (SCB5 - Crack 1, N_f = 65104 cycles, $\Delta\sigma$ = 471 MPa) **- Steel B** (with Mo + V)

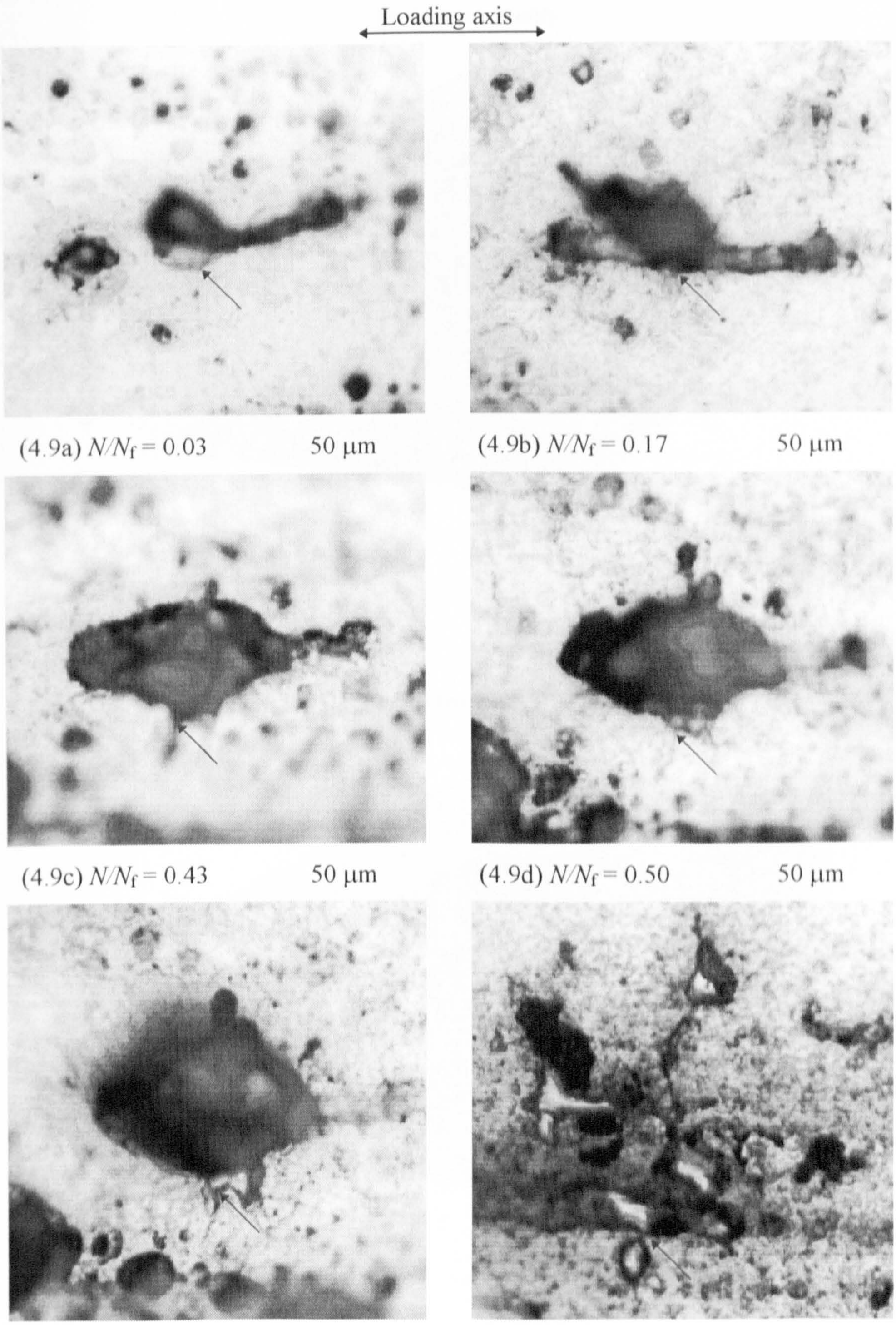

(4.9a) $N/N_f = 0.03$ 50 μm

(4.9b) $N/N_f = 0.17$ 50 μm

(4.9c) $N/N_f = 0.43$ 50 μm

(4.9d) $N/N_f = 0.50$ 50 μm

(4.9e) $N/N_f = 0.56$ 50 μm

(4.9f) $N/N_f = 0.98$ 200 μm

Figure 4.9 **A crack initiates from a pit in 3.5%NaCl solution** (OCP) (SCB2 - Crack 2, $N_f = 45764$ cycles, $\Delta\sigma = 516$ MPa) **- Steel B** (with Mo + V)

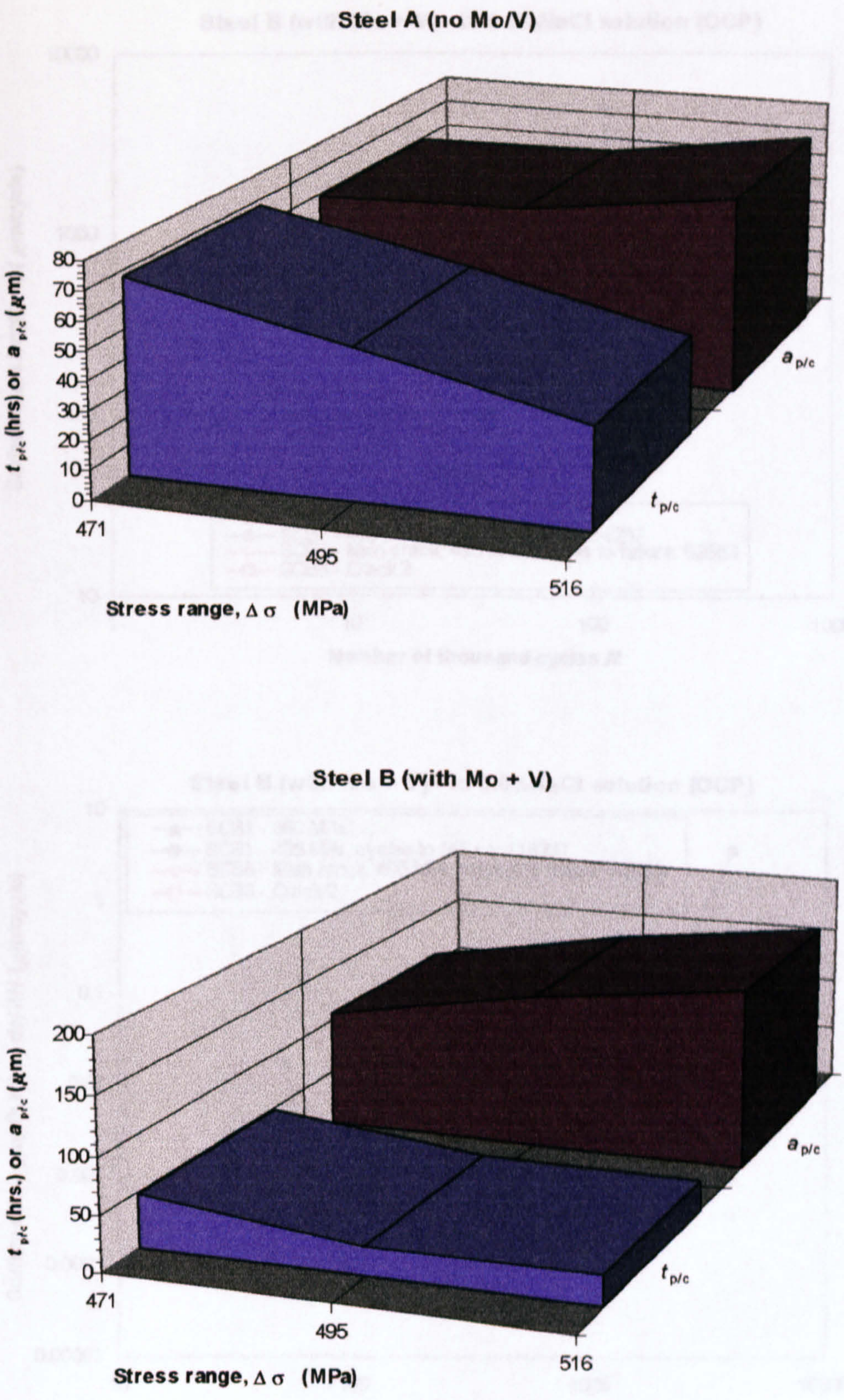

Figure 4.10 Pit/crack Transition behaviour under cyclic stress in 3.5%NaCl solution (OCP)

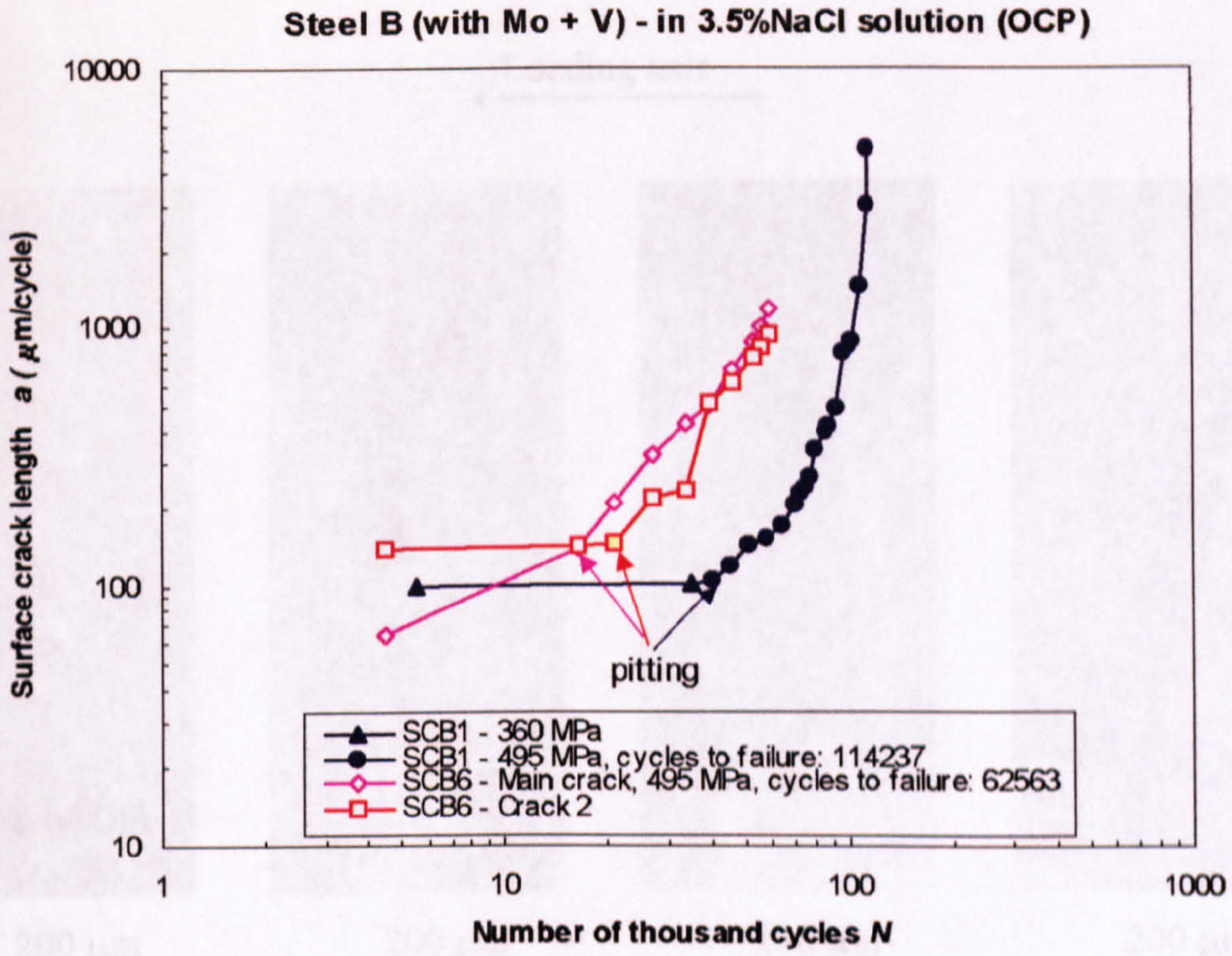

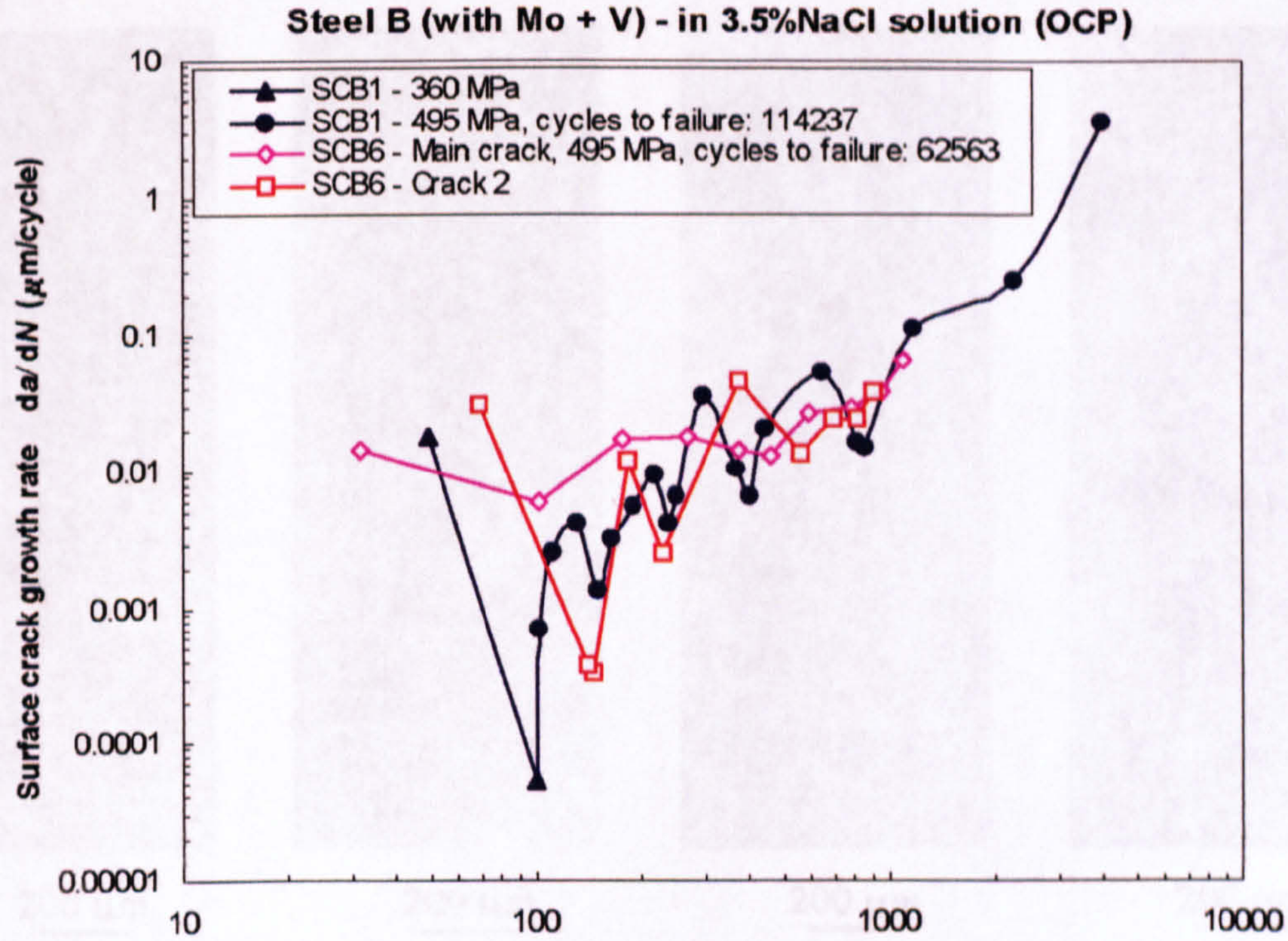

Figure 4.11 **Comparison of two tests under different loading conditions in 3.5%NaCl solution** (OCP) **- Steel B** (with Mo + V)

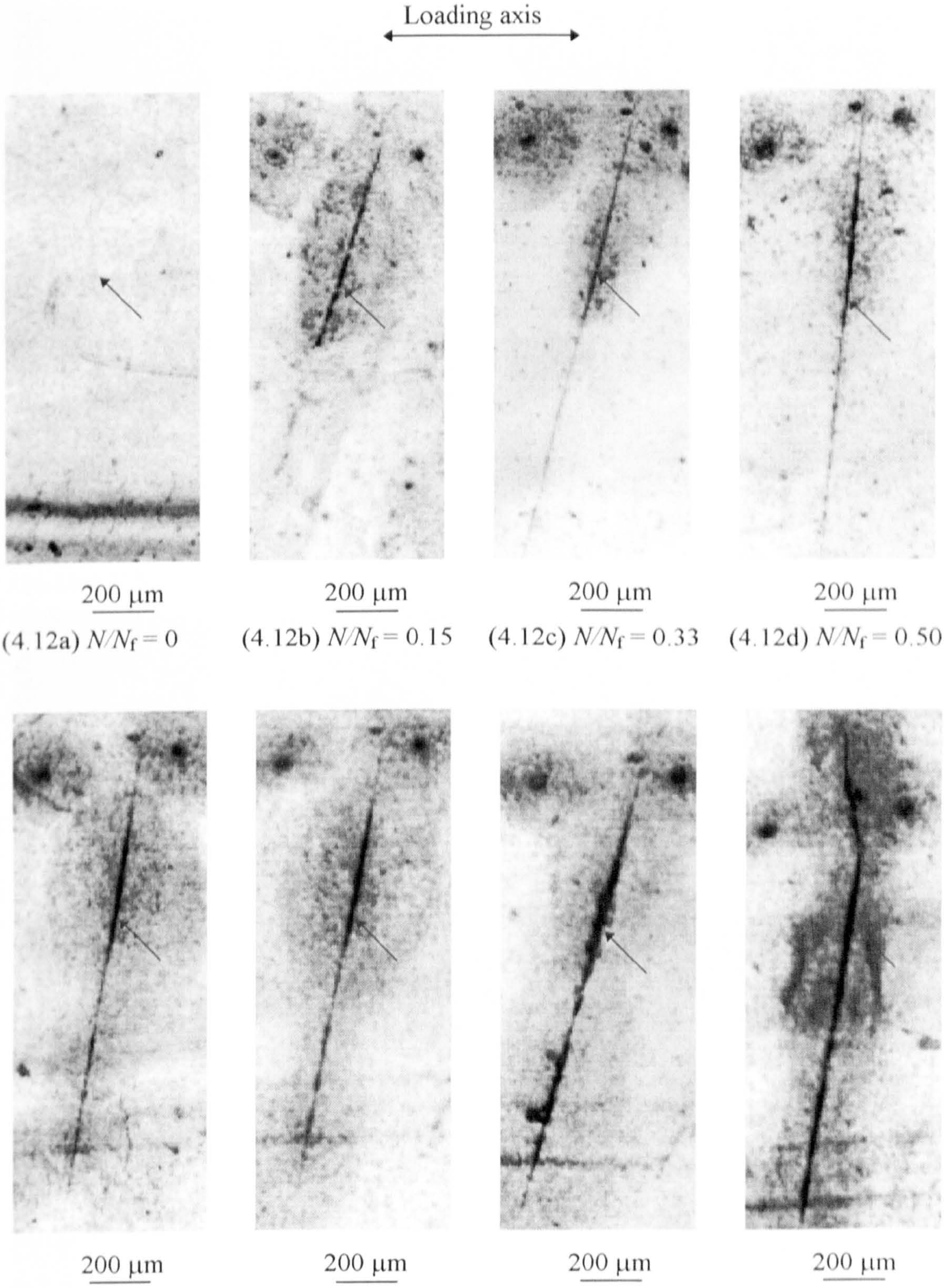

(4.12a) $N/N_f = 0$ (4.12b) $N/N_f = 0.15$ (4.12c) $N/N_f = 0.33$ (4.12d) $N/N_f = 0.50$

(4.12e) $N/N_f = 0.60$ (4.12f) $N/N_f = 0.75$ (4.12g) $N/N_f = 0.93$ (4.12h) $N/N_f = 0.99$

Figure. 4.12 A typical development of a scratch into a crack in 3.5%NaCl solution under CP (-950 mV/SCE) **application** (SCB10CP - Crack 3, $\Delta\sigma = 471$ MPa, $N_f = 314781$ cycles) **- Steel B** (with Mo + V)

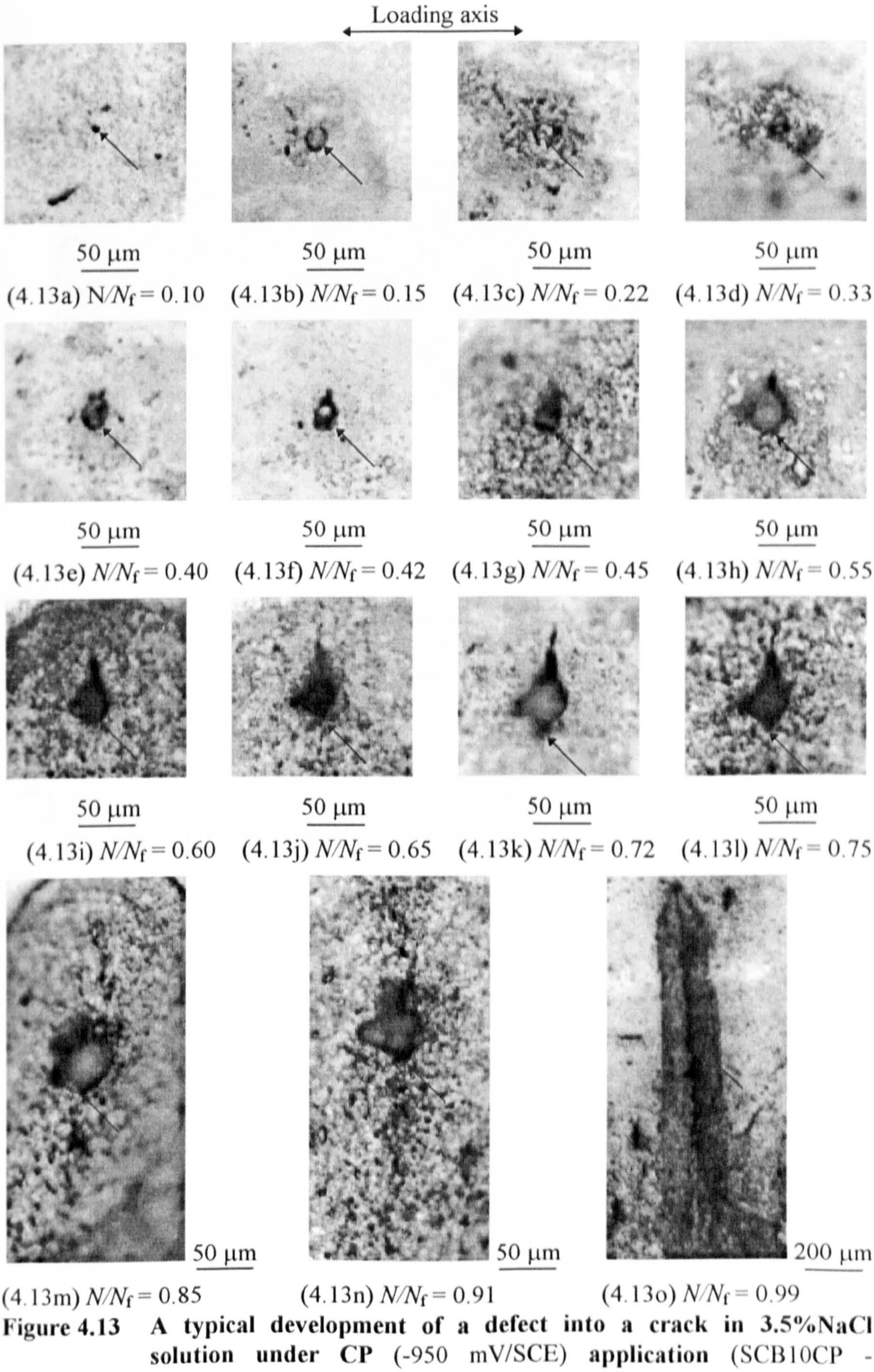

Figure 4.13 **A typical development of a defect into a crack in 3.5%NaCl solution under CP** (-950 mV/SCE) **application** (SCB10CP - Crack 2, $\Delta\sigma$ = 471 MPa, N_f = 314781 cycles) **- Steel B** (with Mo + V)

200 μm

(4.14a) SCB11CP - Crack 2

$N/N_f = 0.99$

$N_f = 282418$ cycles

$\Delta\sigma = 502$ MPa

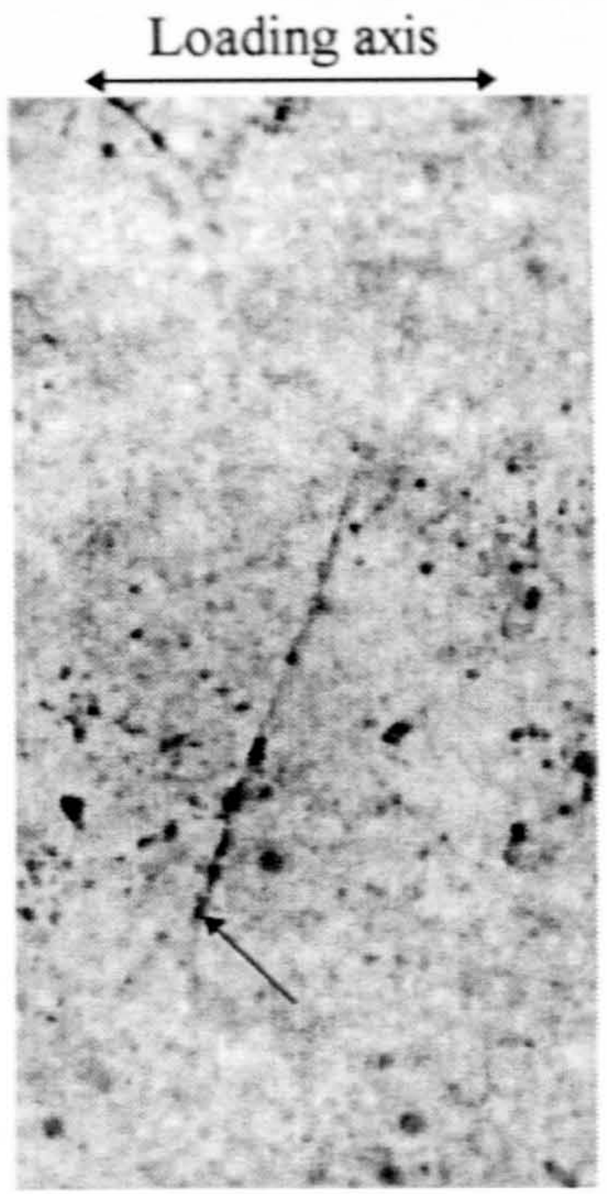

100 μm

(4.14b) SCB8CP

$N/N_f = 0.94$

$N_f = 131191$ cycles

$\Delta\sigma = 516$ MPa

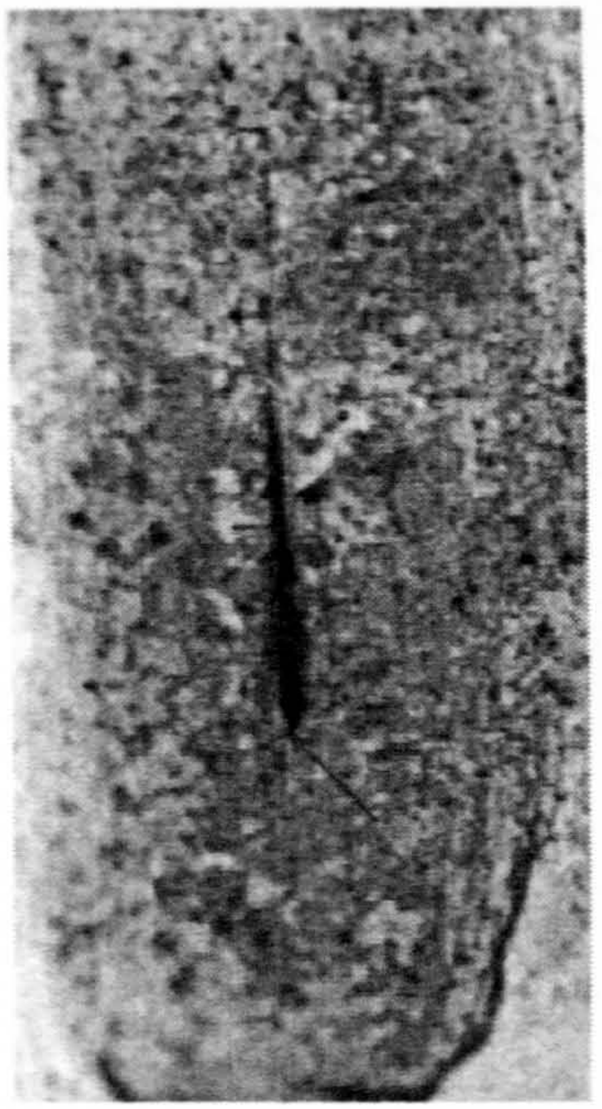

100 μm

(4.14c) SCB10CP - Crack 1

$N/N_f = 0.97$

$N_f = 314781$ cycles

$\Delta\sigma = 471$ MPa

Figure 4.14 Cracks initiate from the scratches for different tests in 3.5%NaCl solution under CP (-950 mV/SCE) **application - Steel B** (with Mo + V)

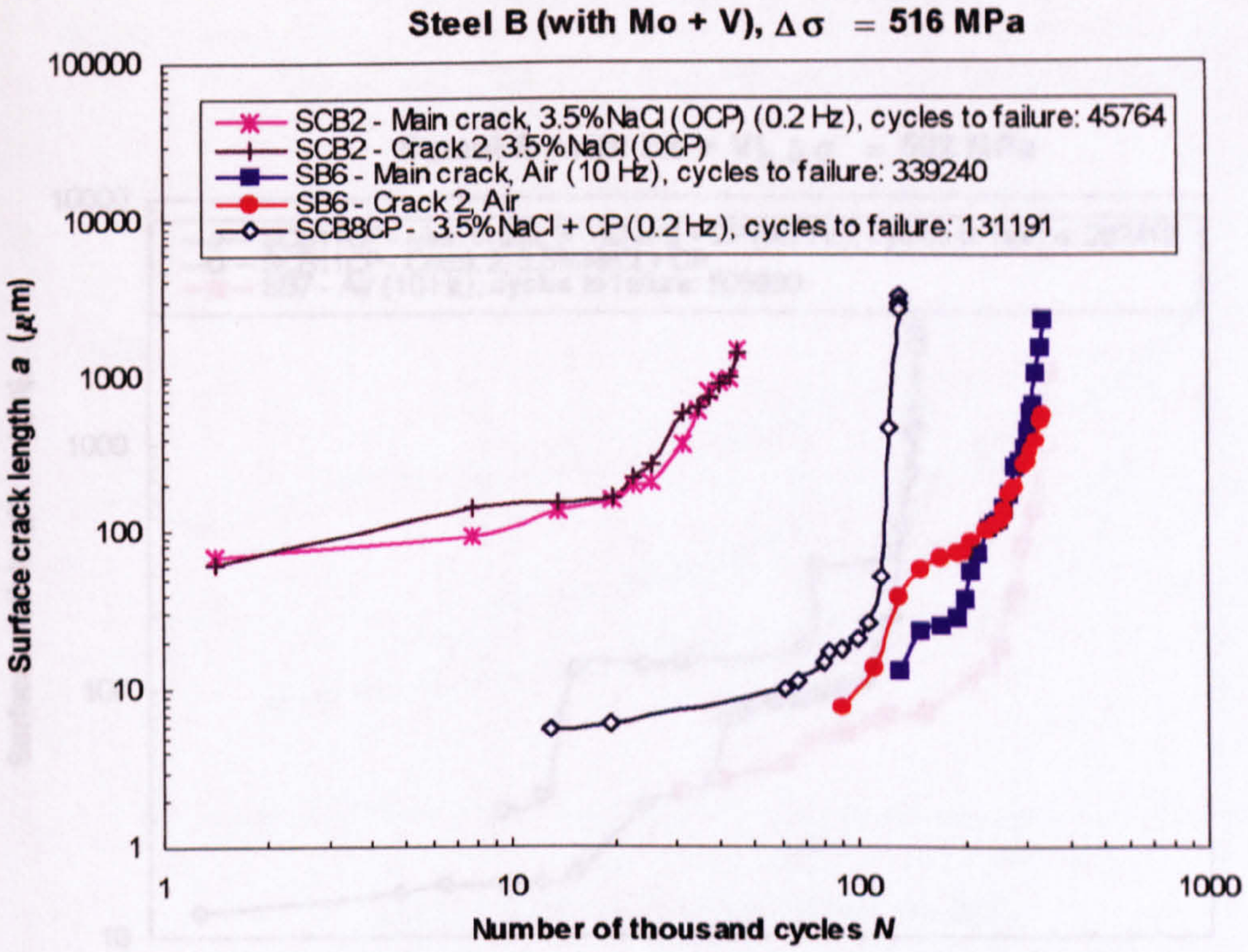

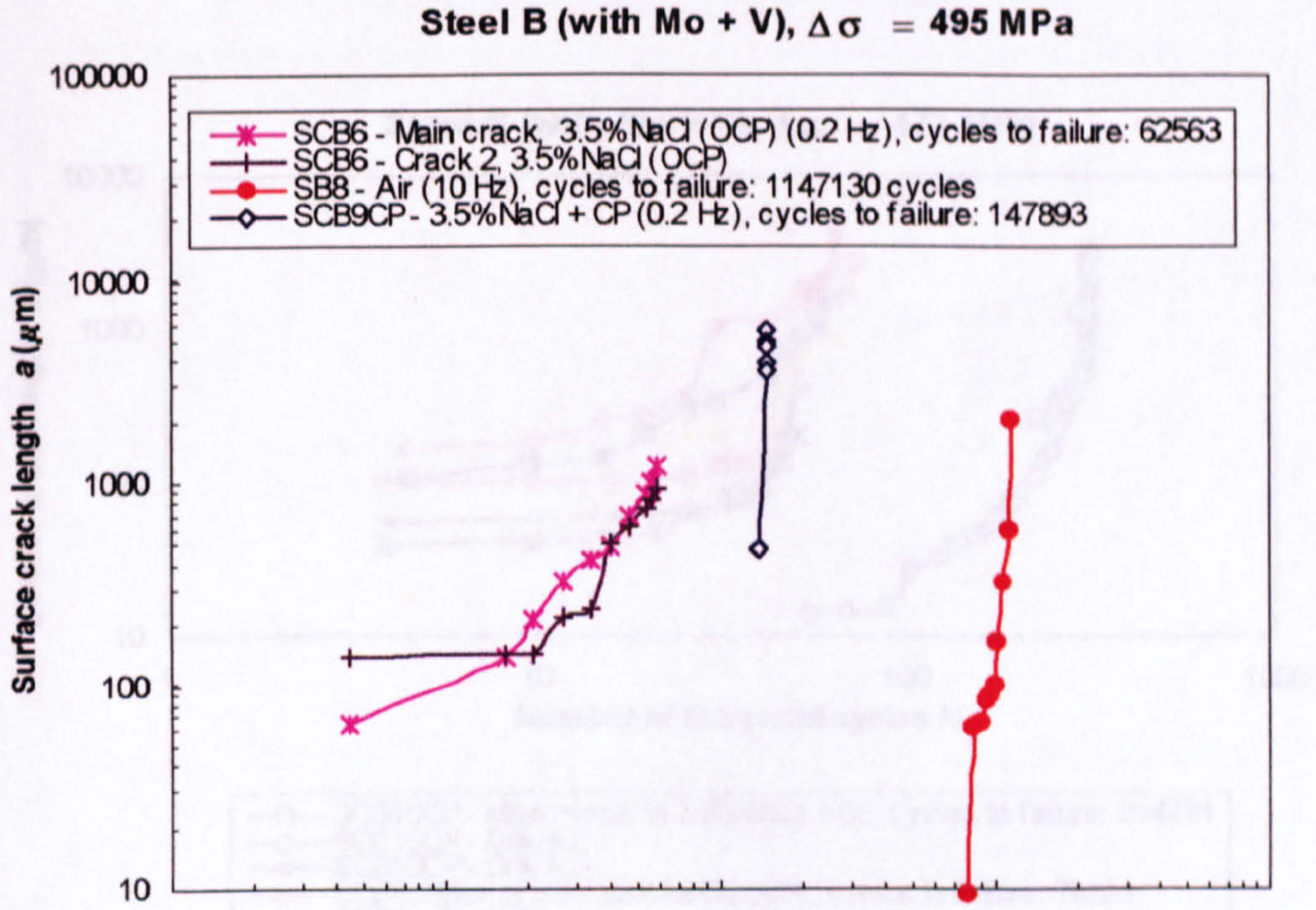

Figure 4.15a Short fatigue crack growth behaviour of Steel B (with Mo + V) **in different environments**

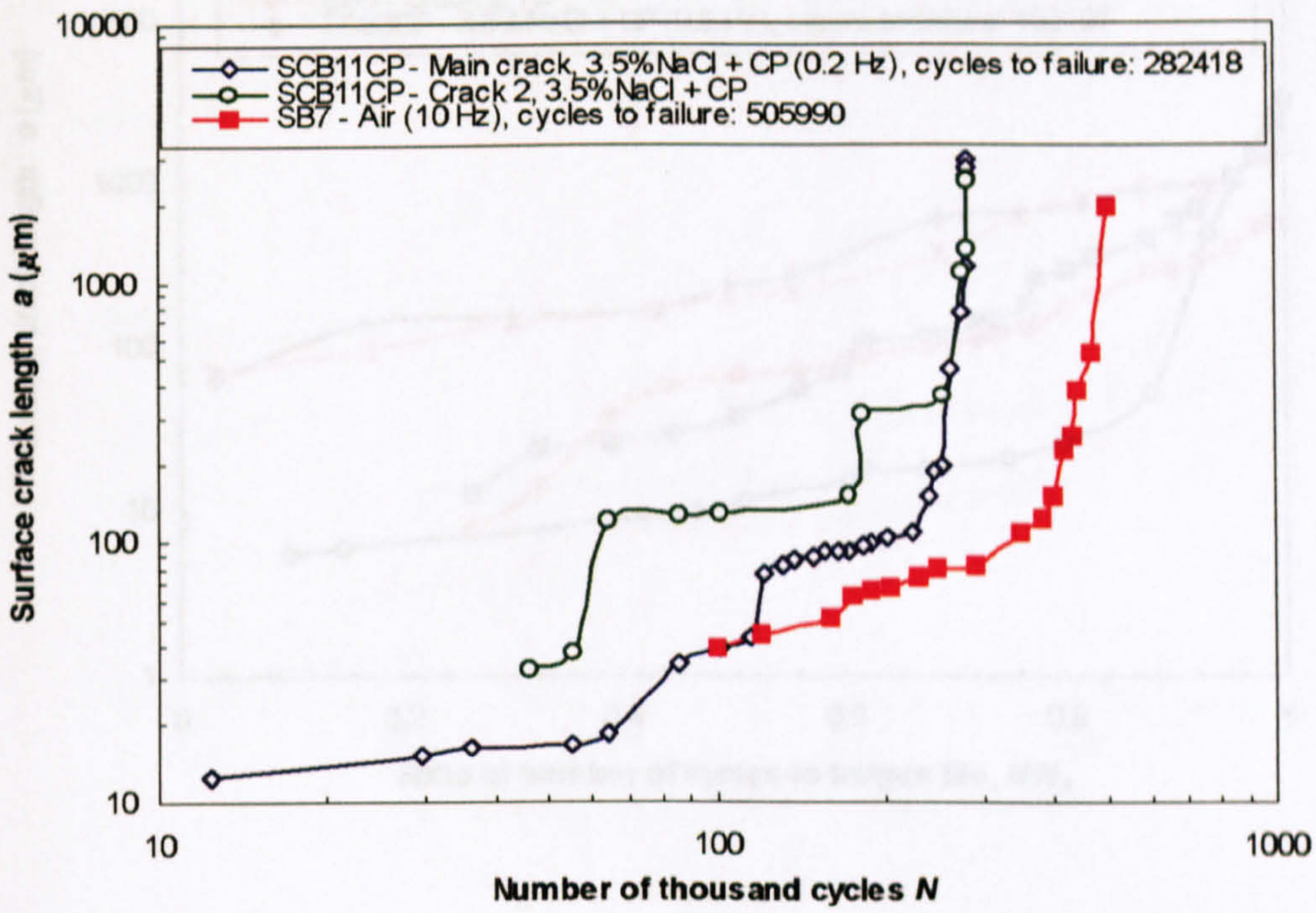

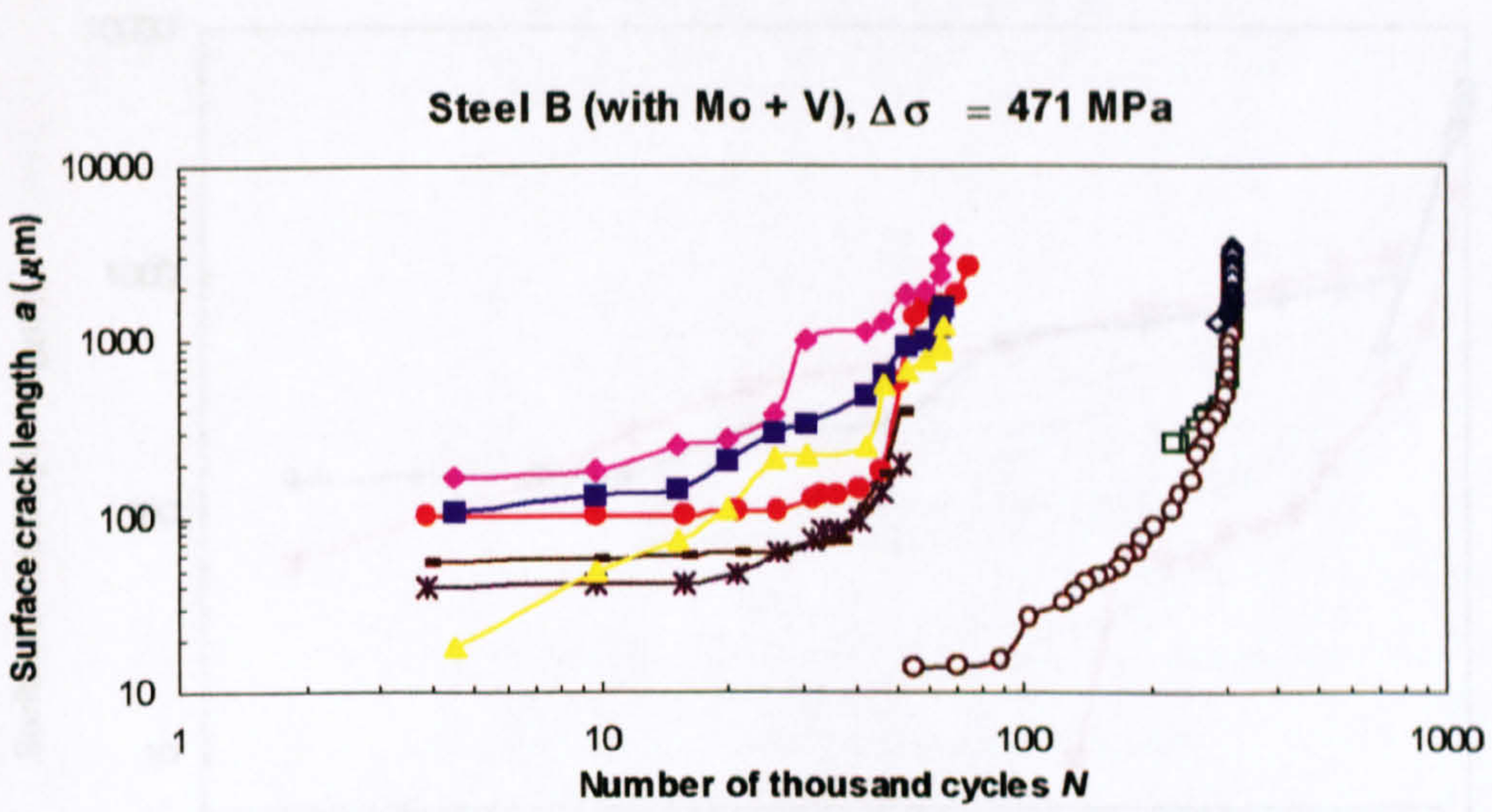

Figure 4.15b Short fatigue crack growth behaviour of Steel B (with Mo + V) **in different environments**

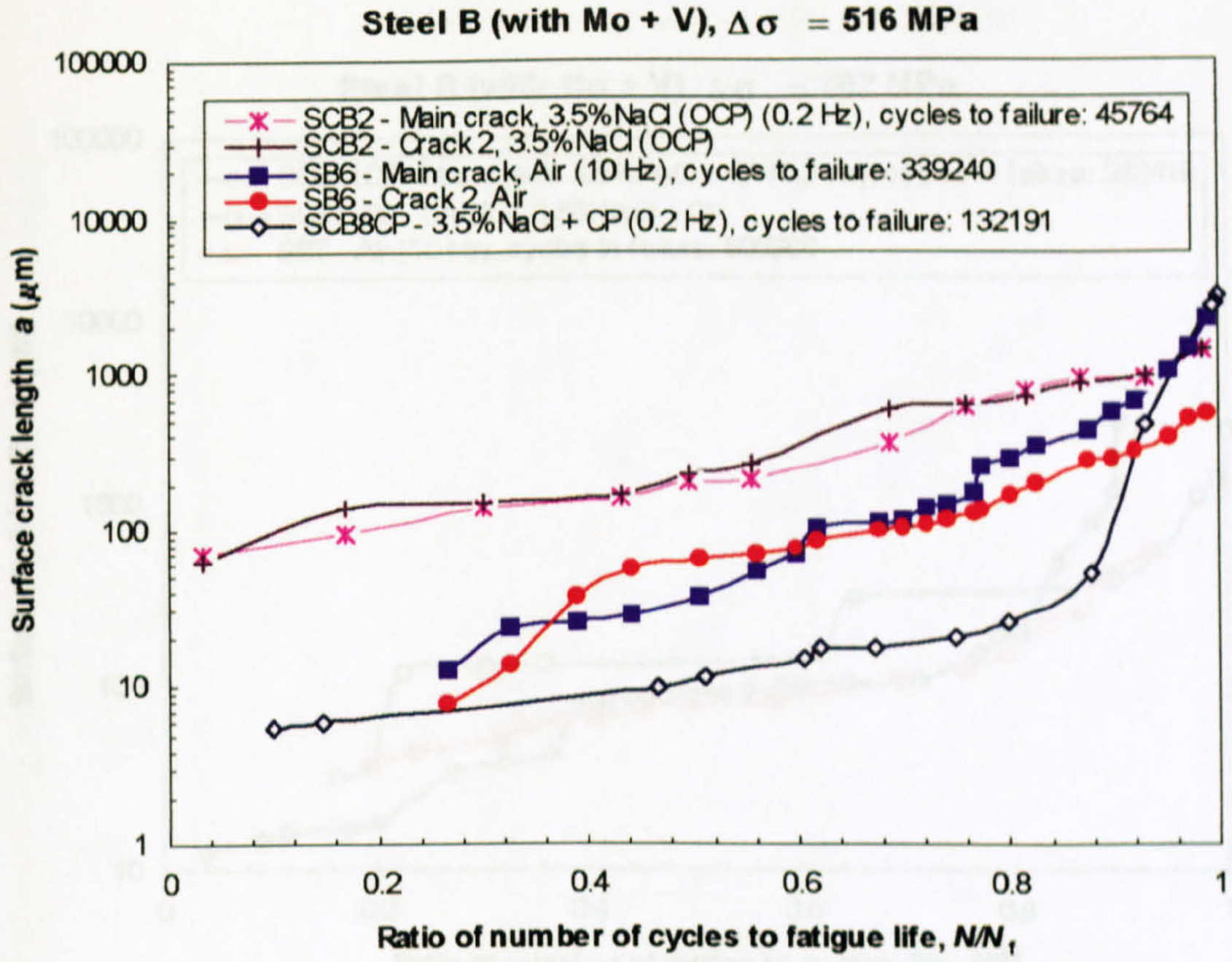

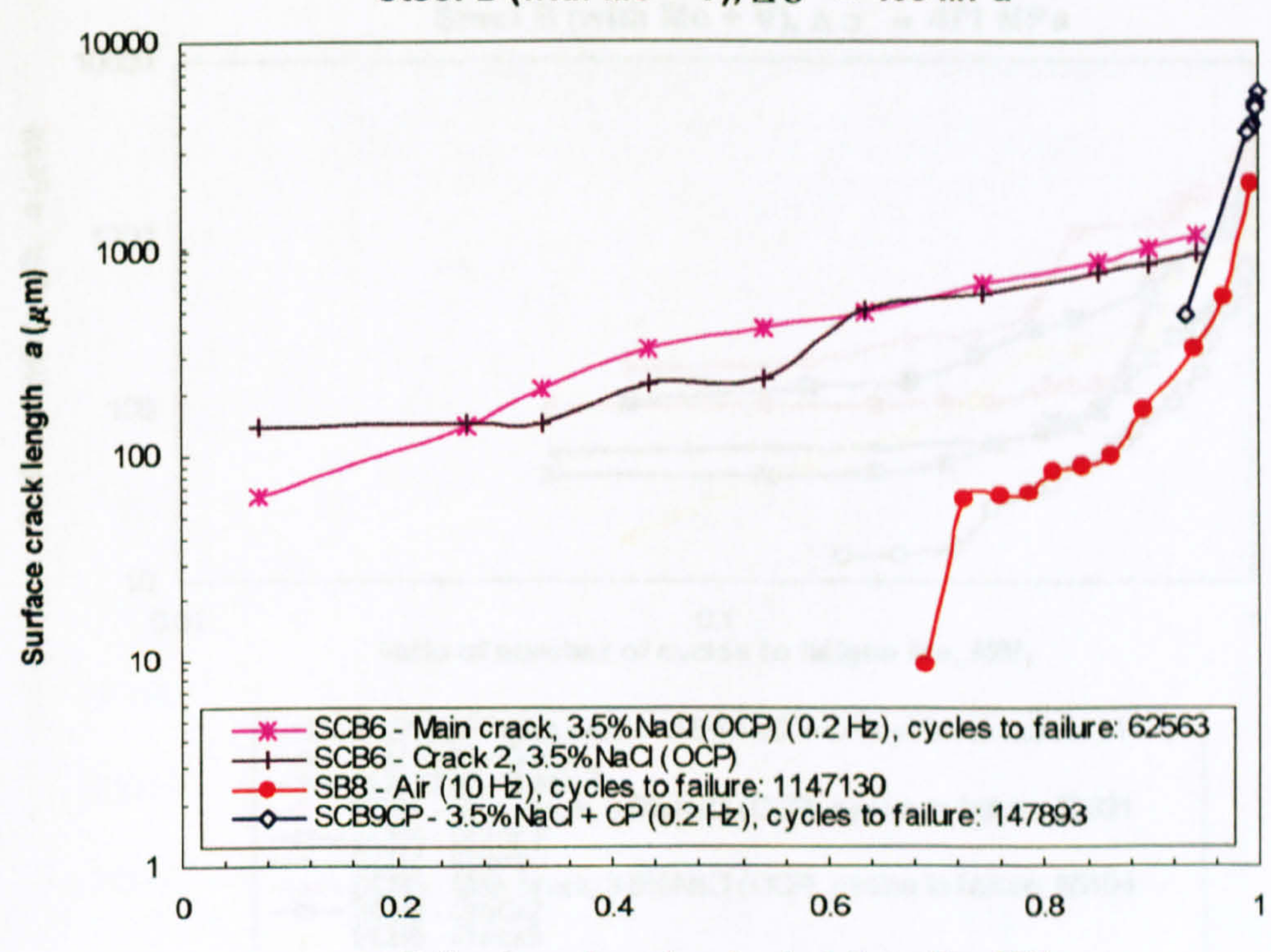

Figure 4.16a The surface crack length versus the ratio of propagation life to the total fatigue life for Steel B (with Mo + V)

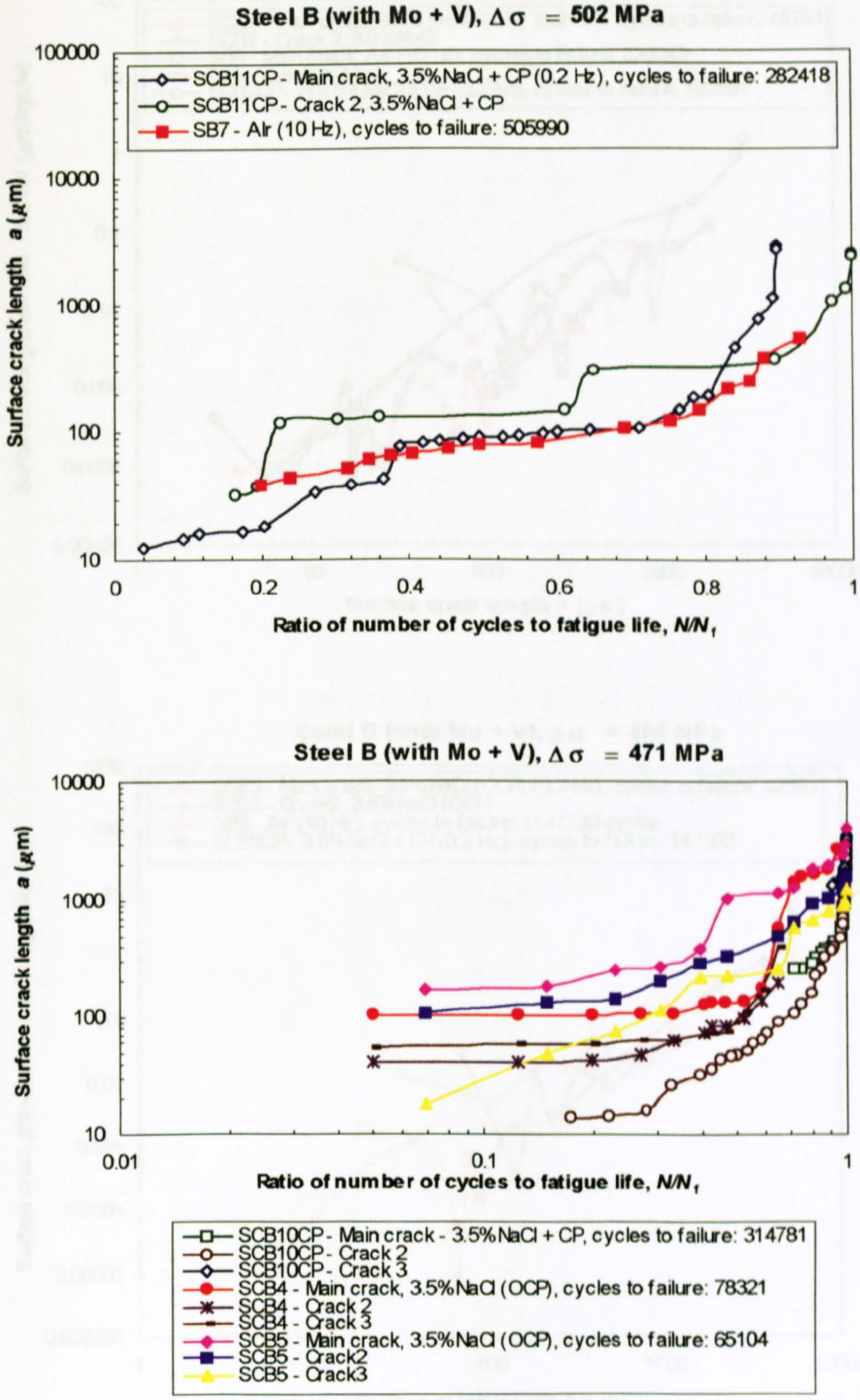

Figure 4.16b The surface crack length versus the ratio of propagation life to the total fatigue life for Steel B (with Mo + V)

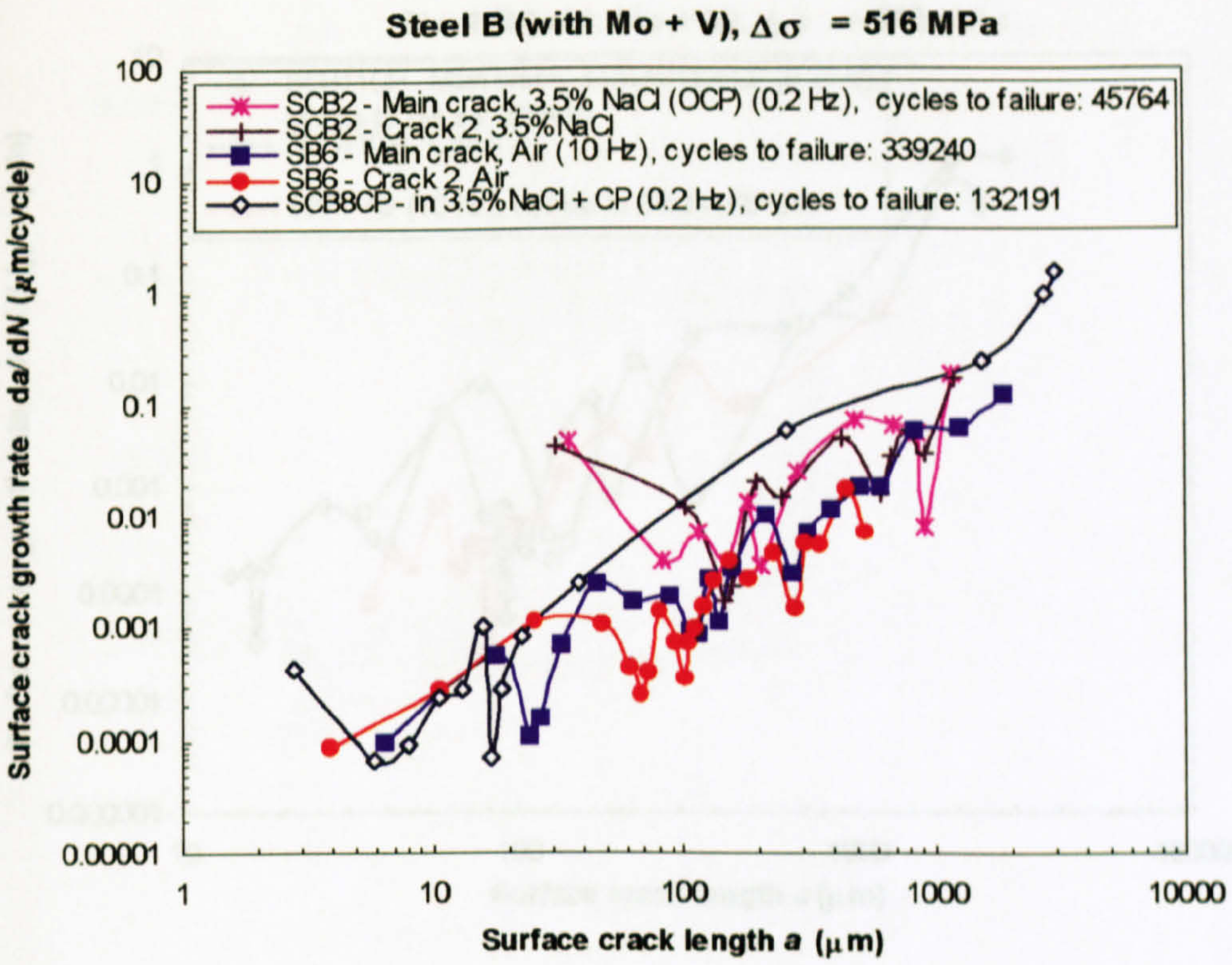

Figure 4.17a Surface fatigue crack growth rates versus crack lengths curve

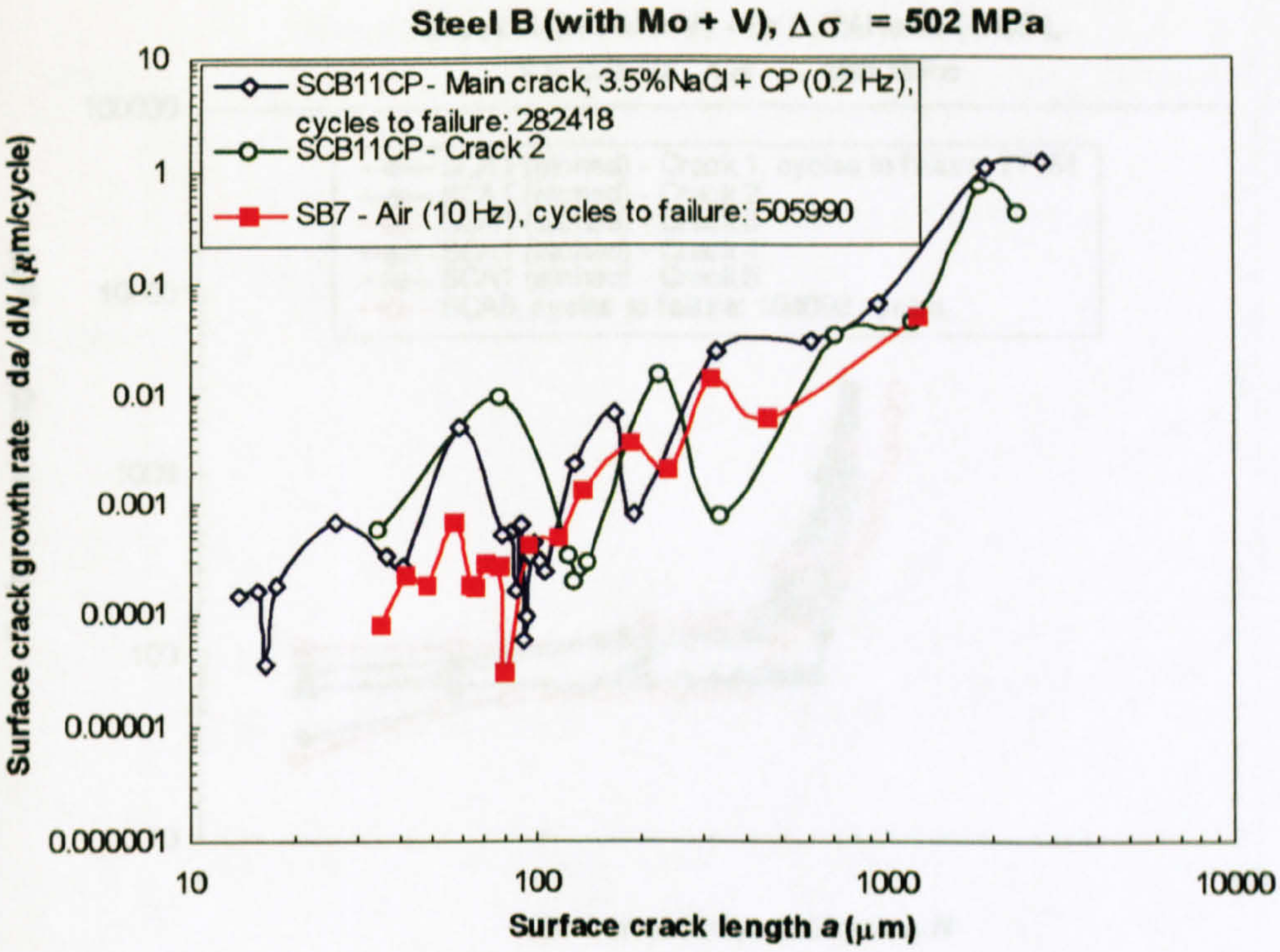

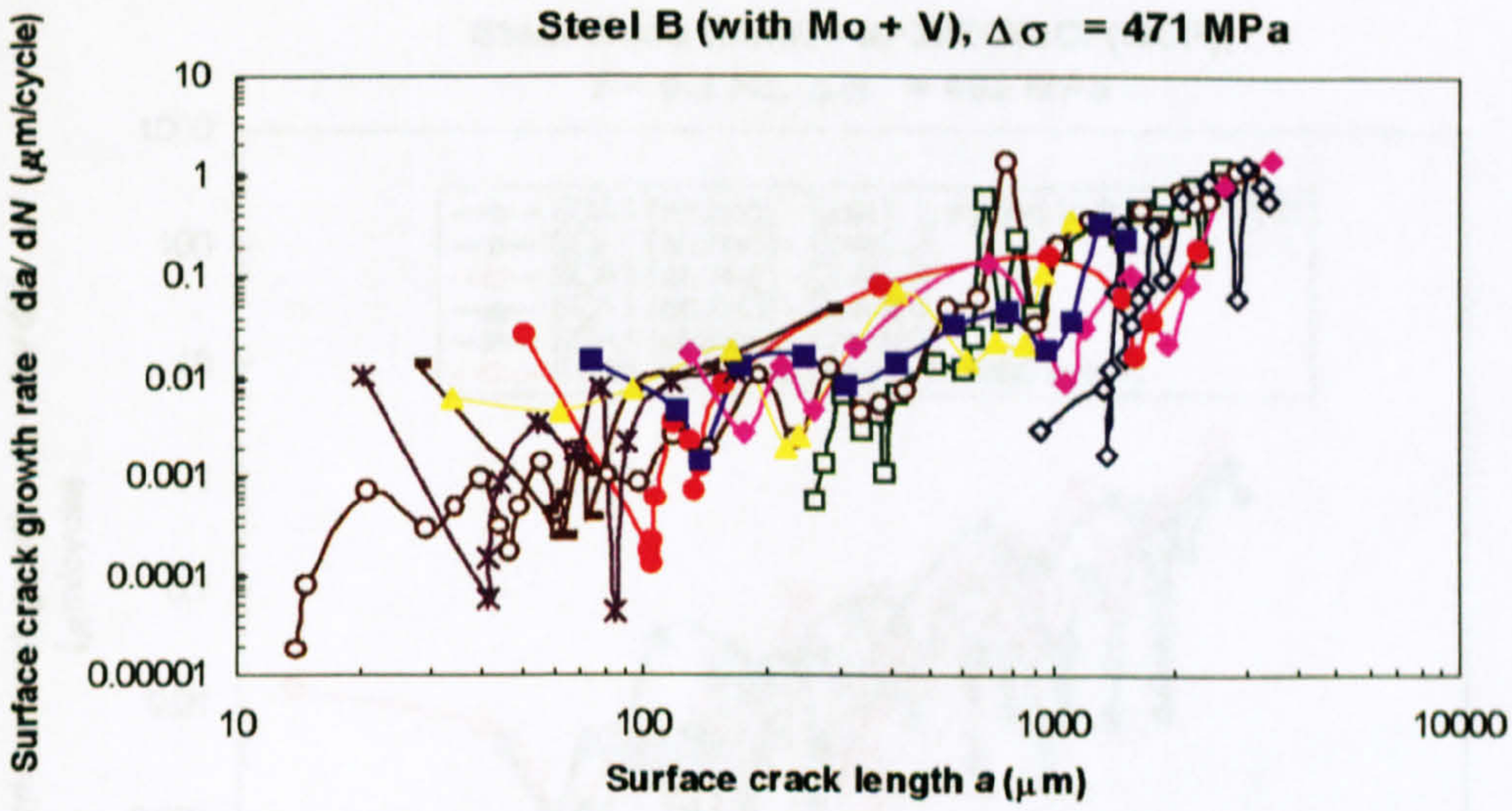

Figure 4.17b Surface fatigue crack growth rates versus crack lengths curve

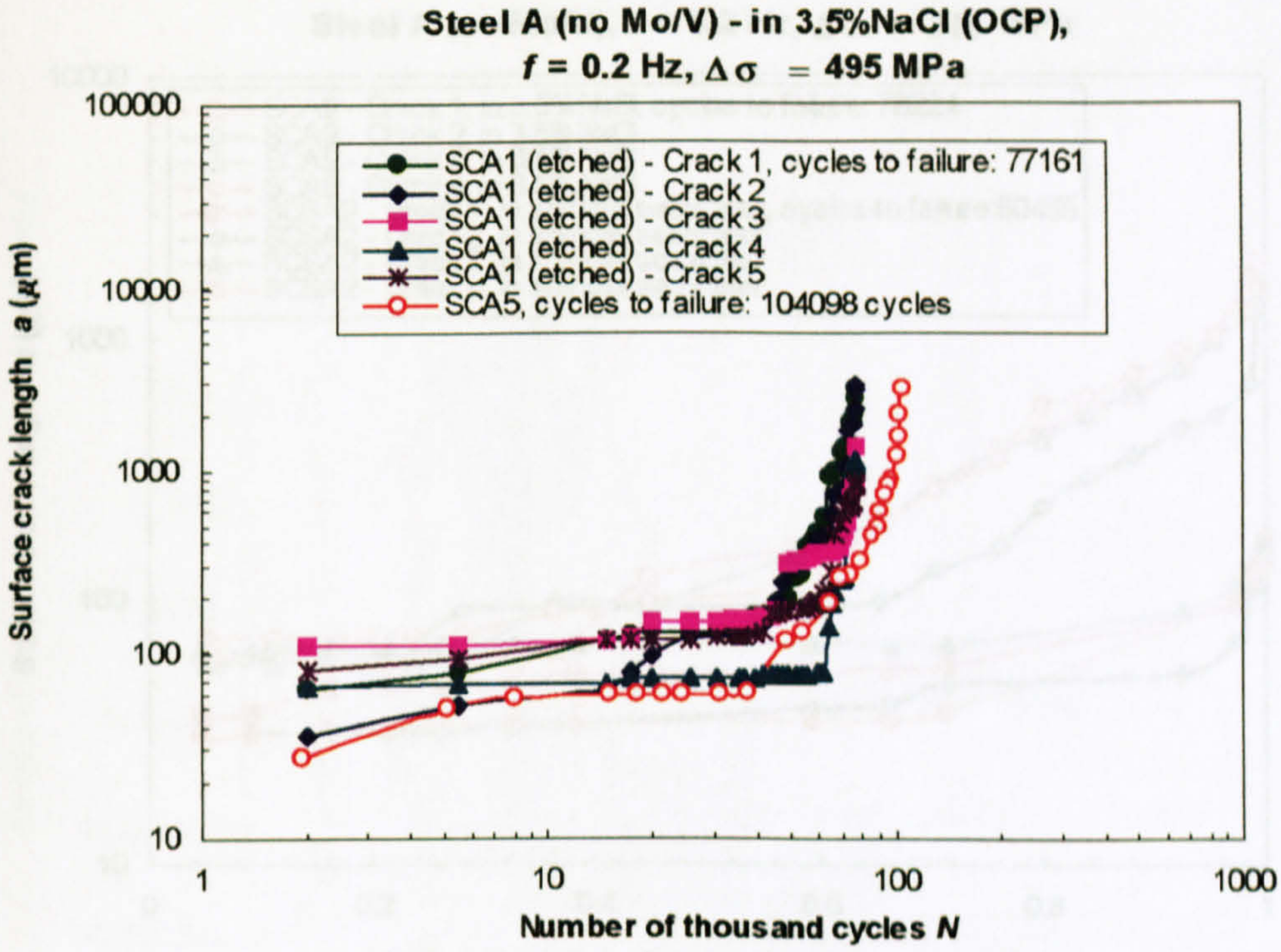

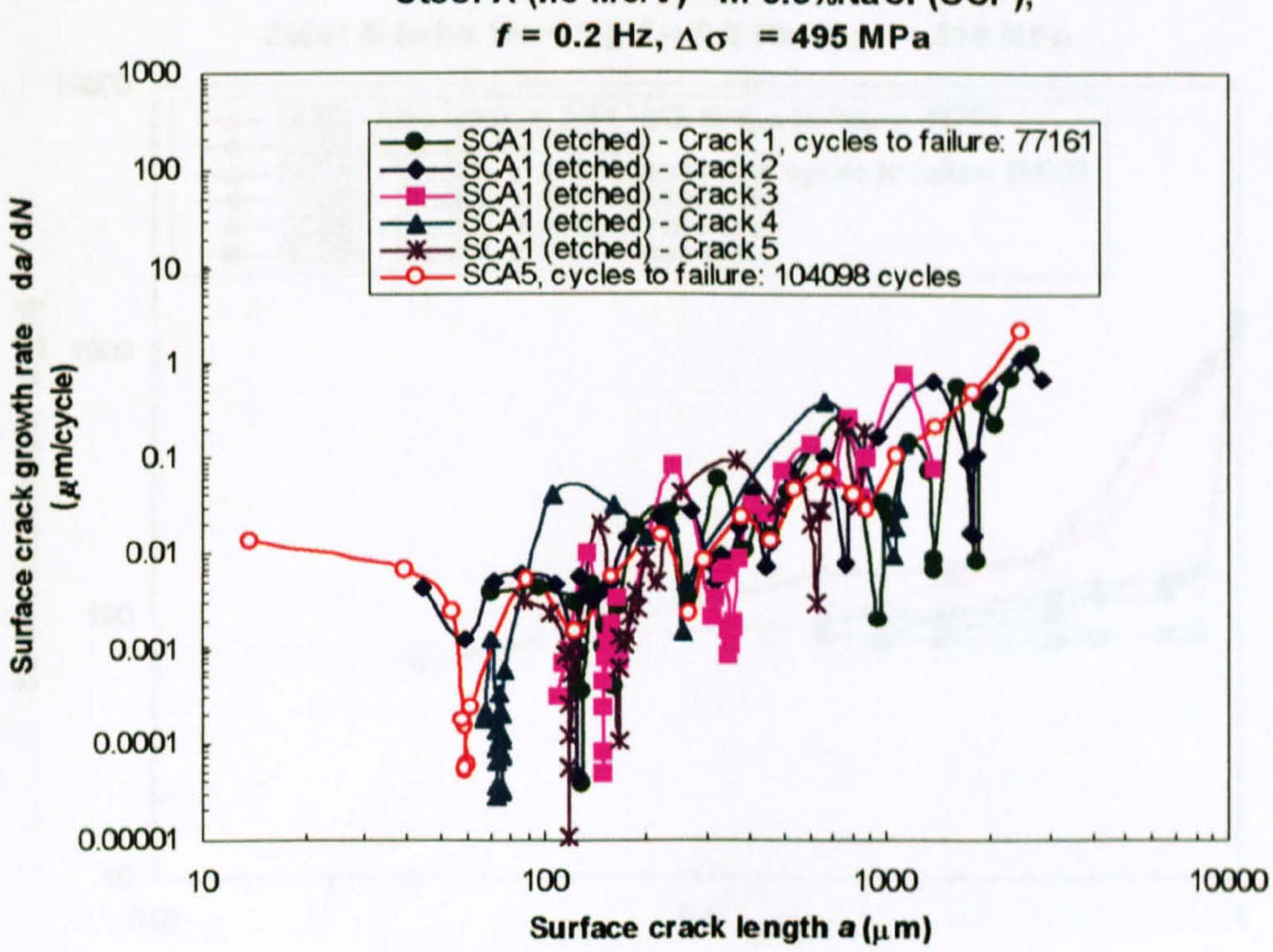

Figure 4.18 **Comparison of short fatigue crack growth behaviour between etched and unetched specimen - Steel A** (no Mo/V) **in 3.5%NaCl solution** (OCP)

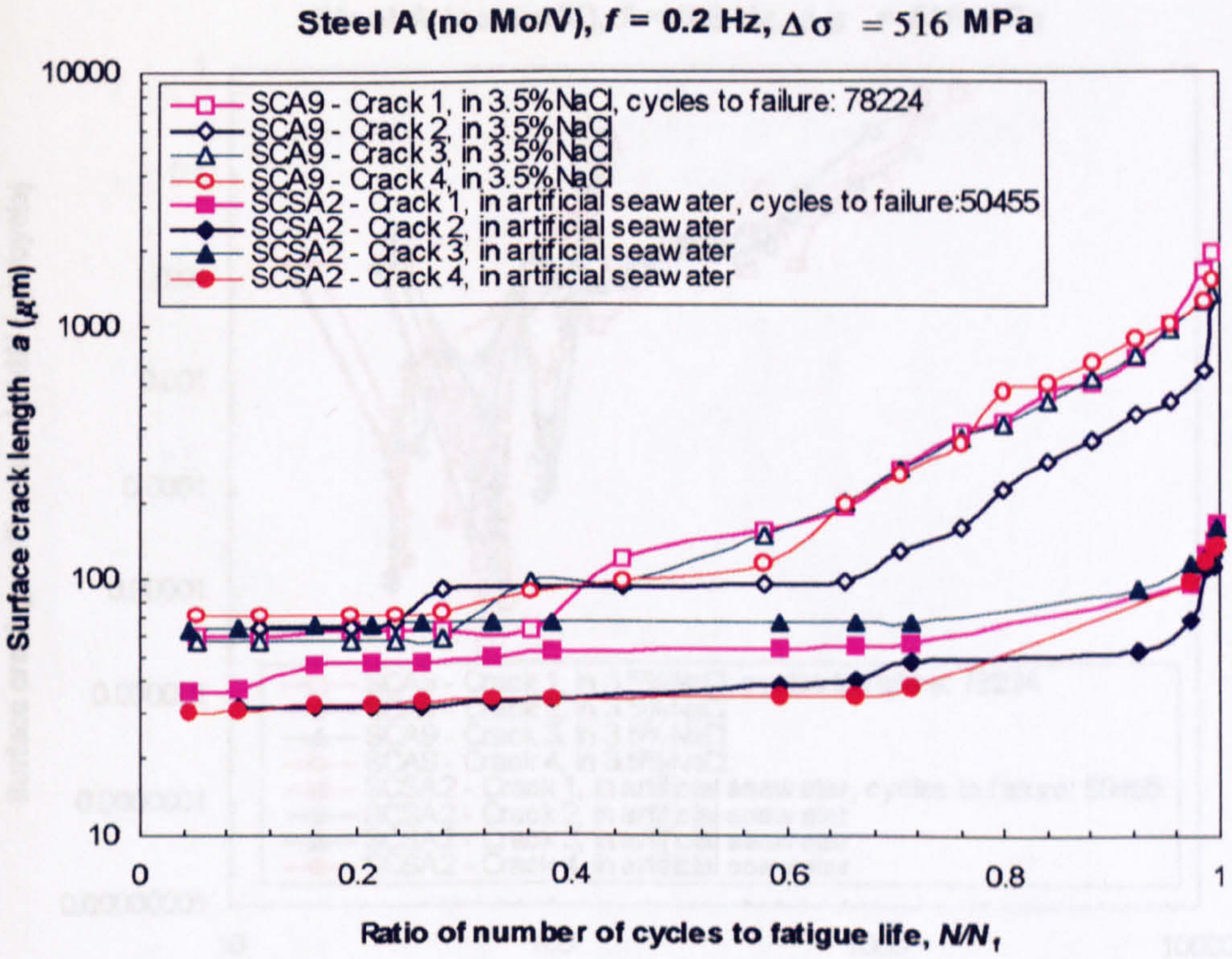

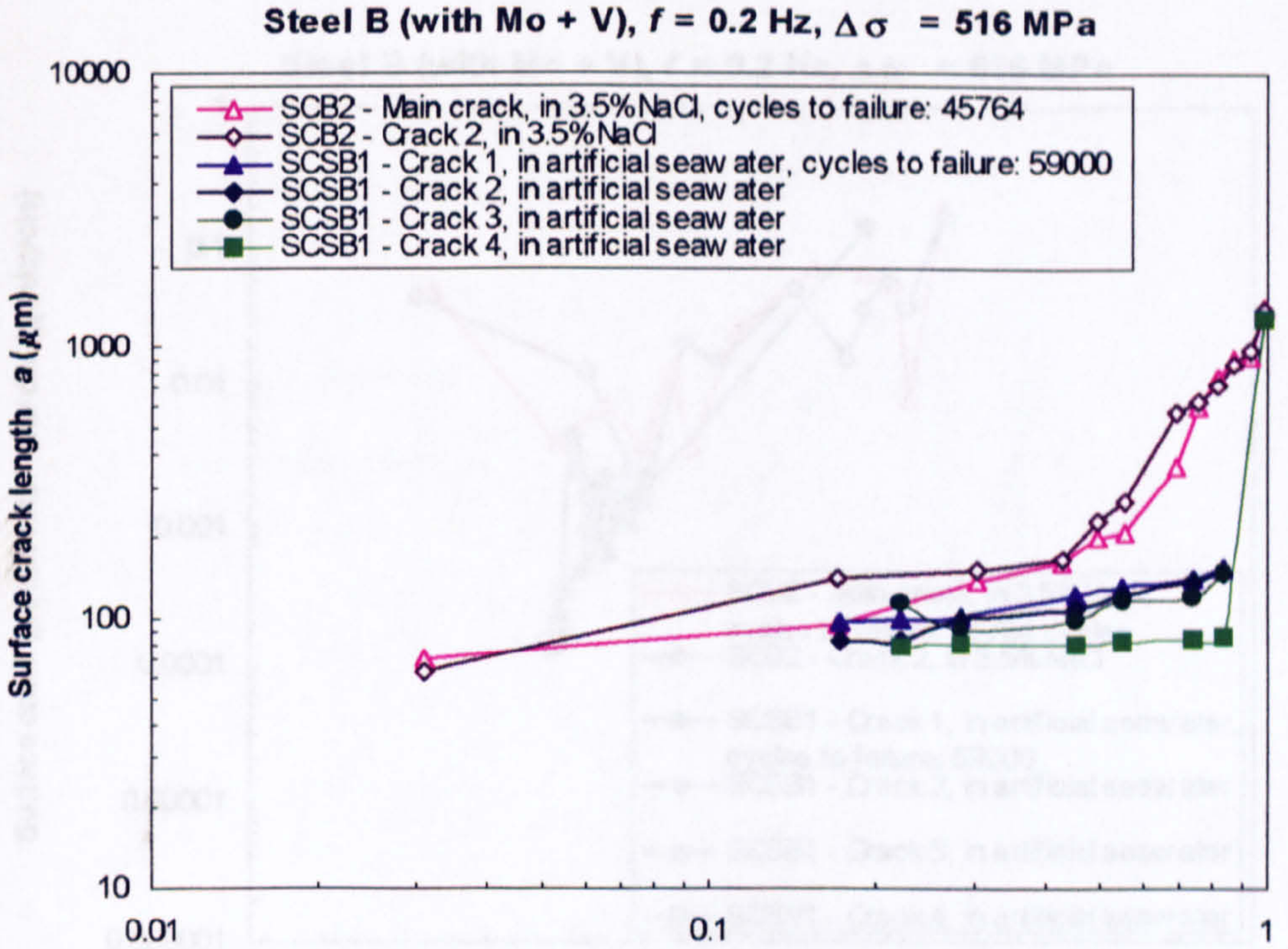

Figure 4.19a Comparison of short fatigue crack growth behaviour ($a \sim N/N_f$ curve) between tests in 3.5%NaCl solution and artificial seawater

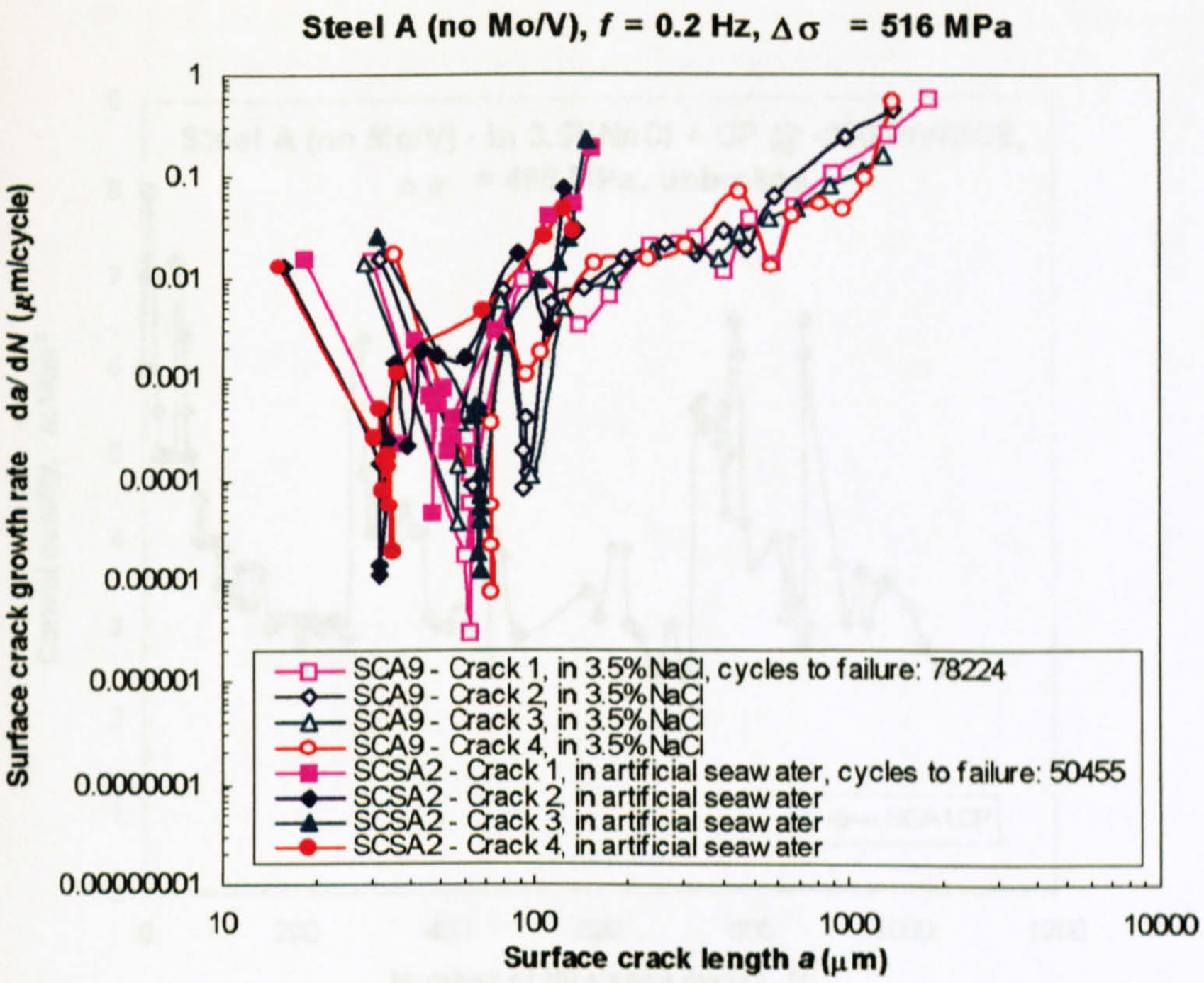

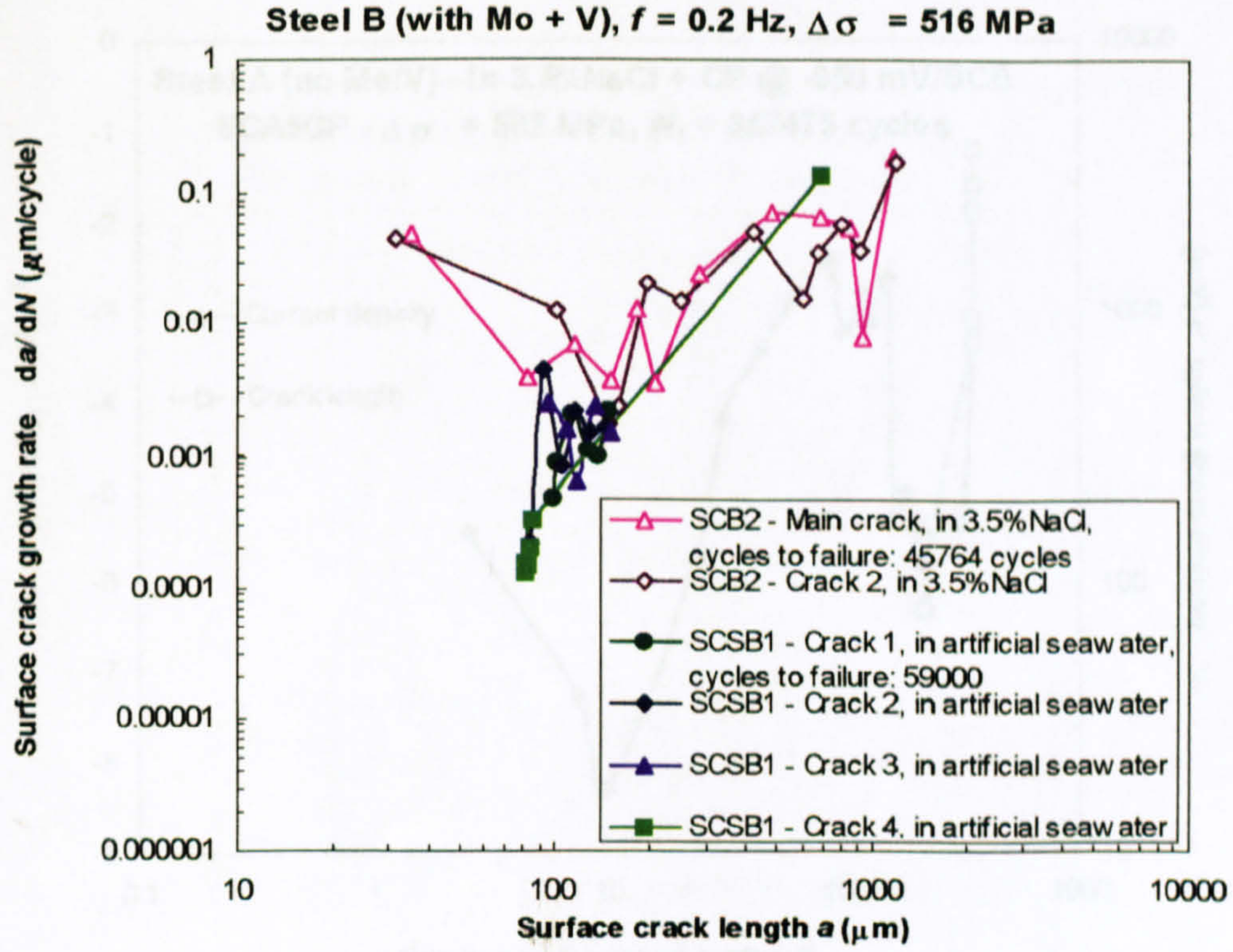

Figure 4.19b Comparison of short fatigue crack growth behaviour (da/dN ~ N curve) **between tests in 3.5%NaCl solution and artificial seawater**

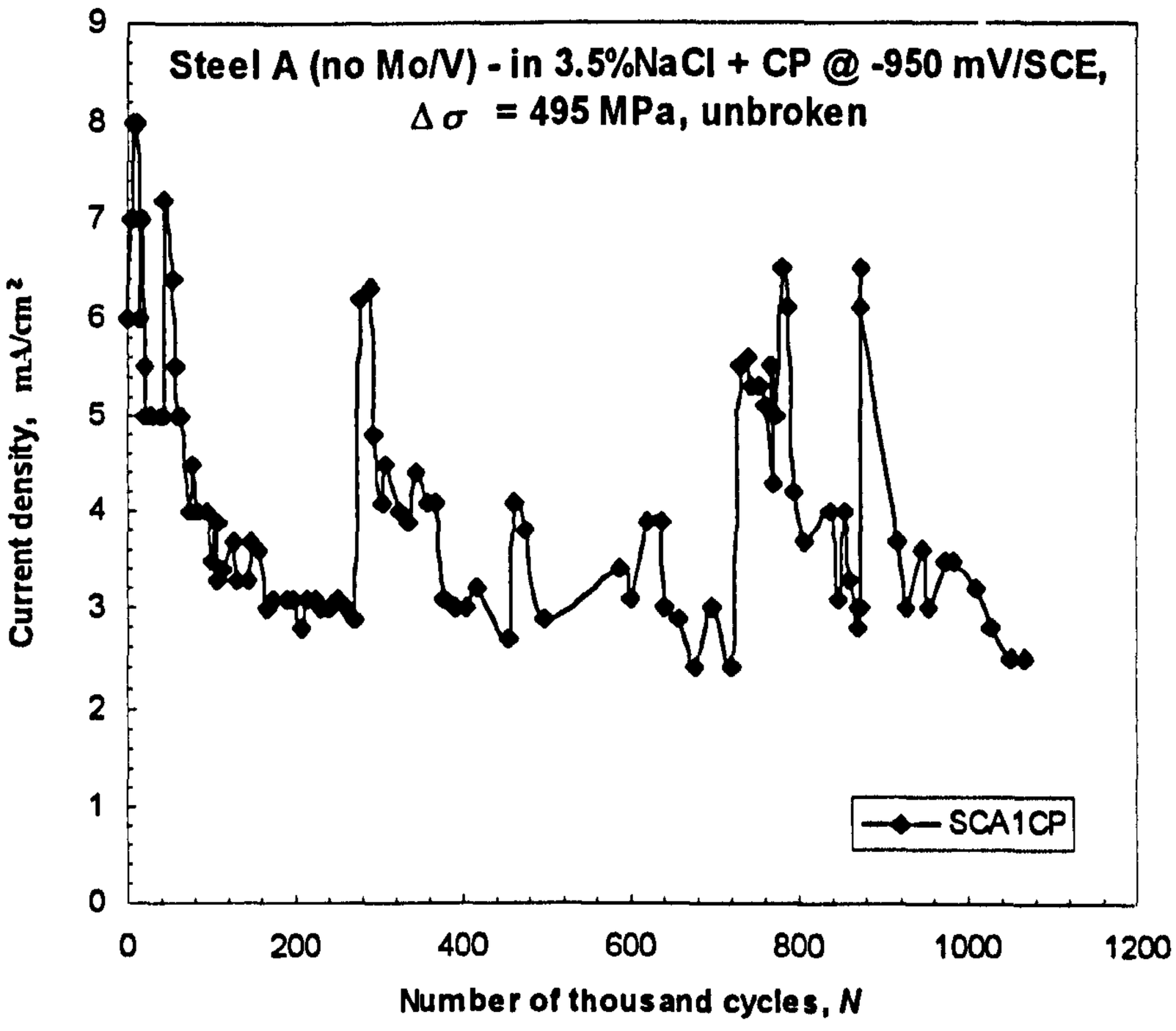

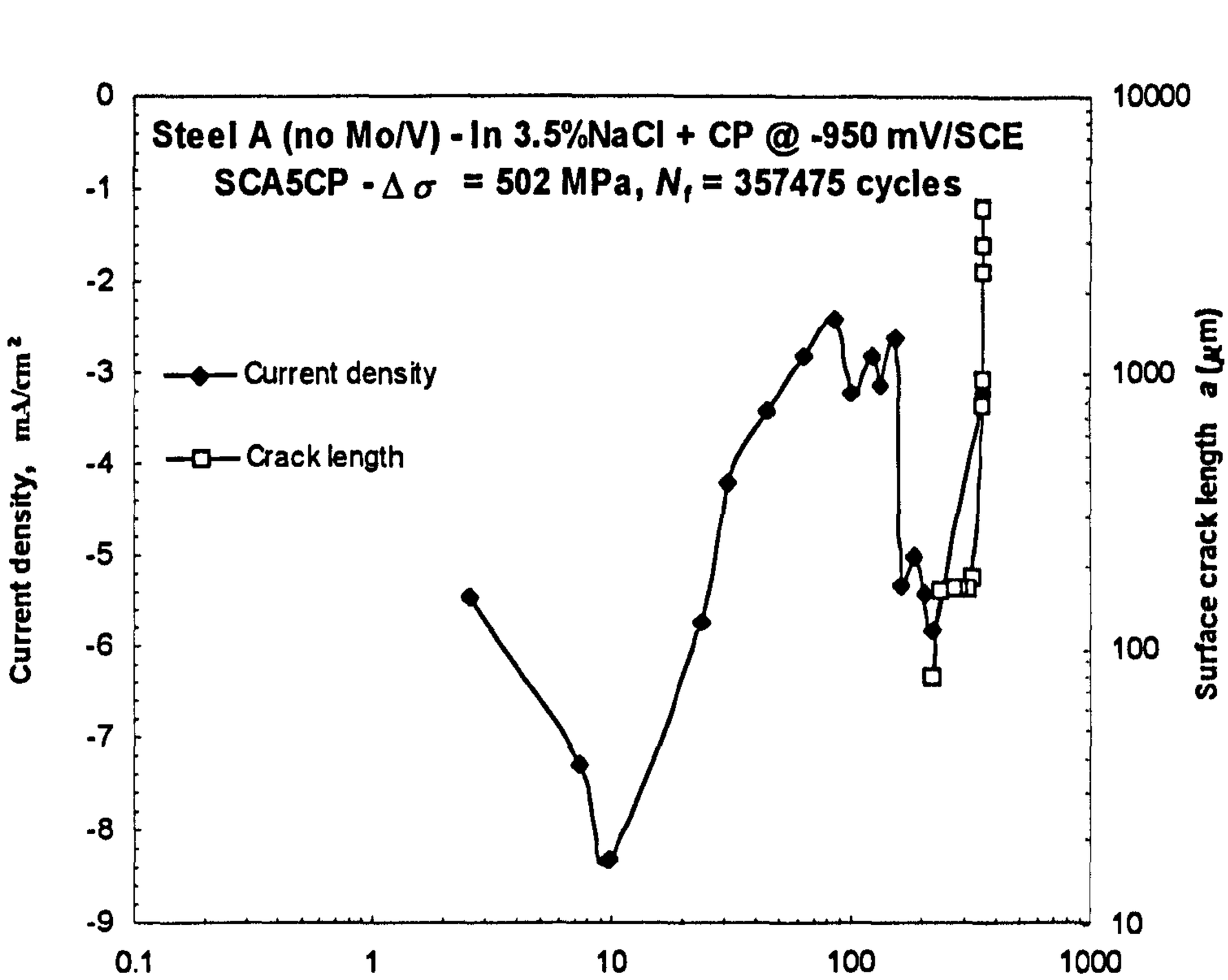

Figure 4.20 Recordings of current density in 3.5%NaCl solution under applied cathodic polarisation (-950 mV/SCE) - Steel A (no Mo/V)

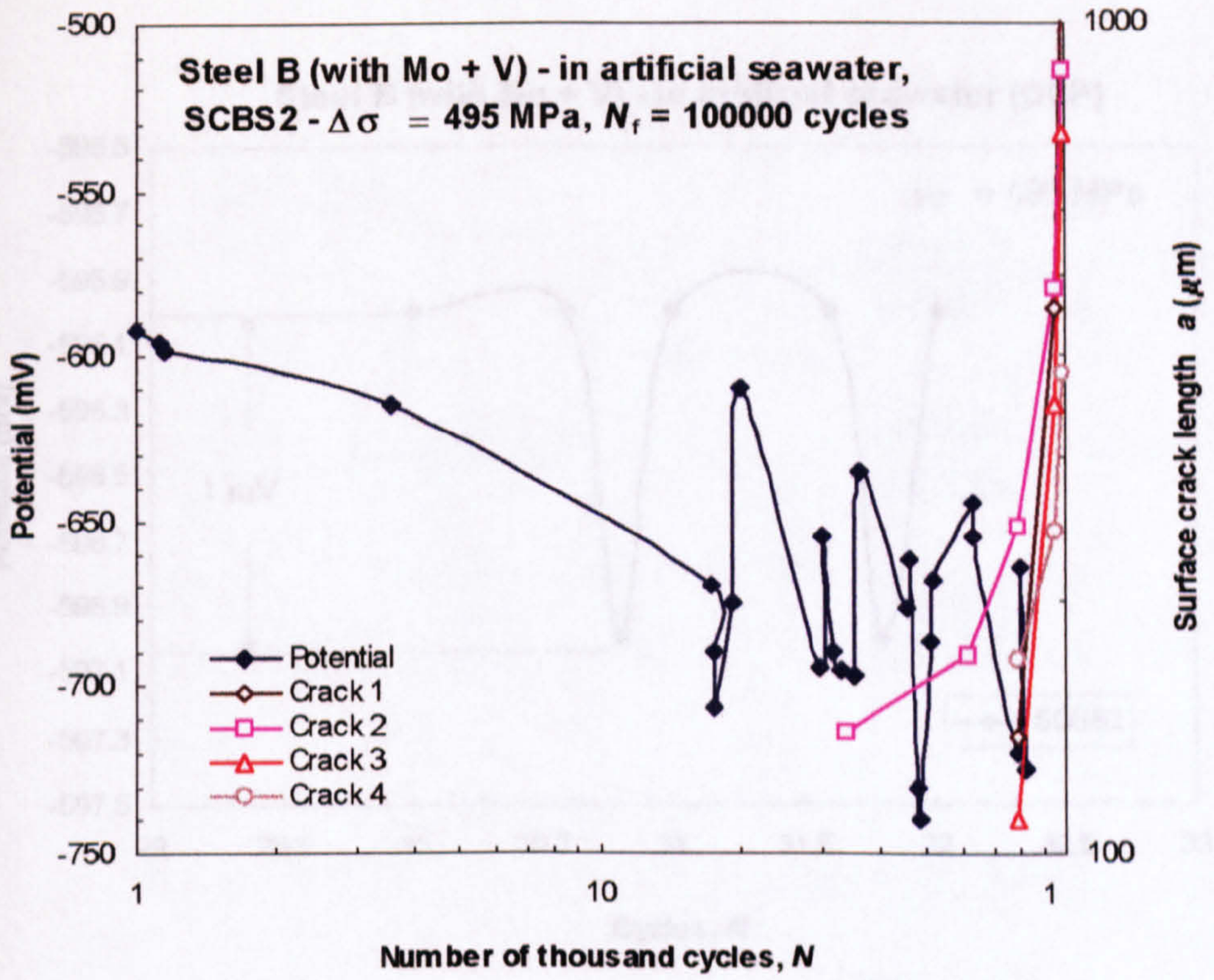

Figure 4.21 **Recording of potential of SCBS2 in 3.5%NaCl solution** (OCP) **- Steel A** (no Mo/V)

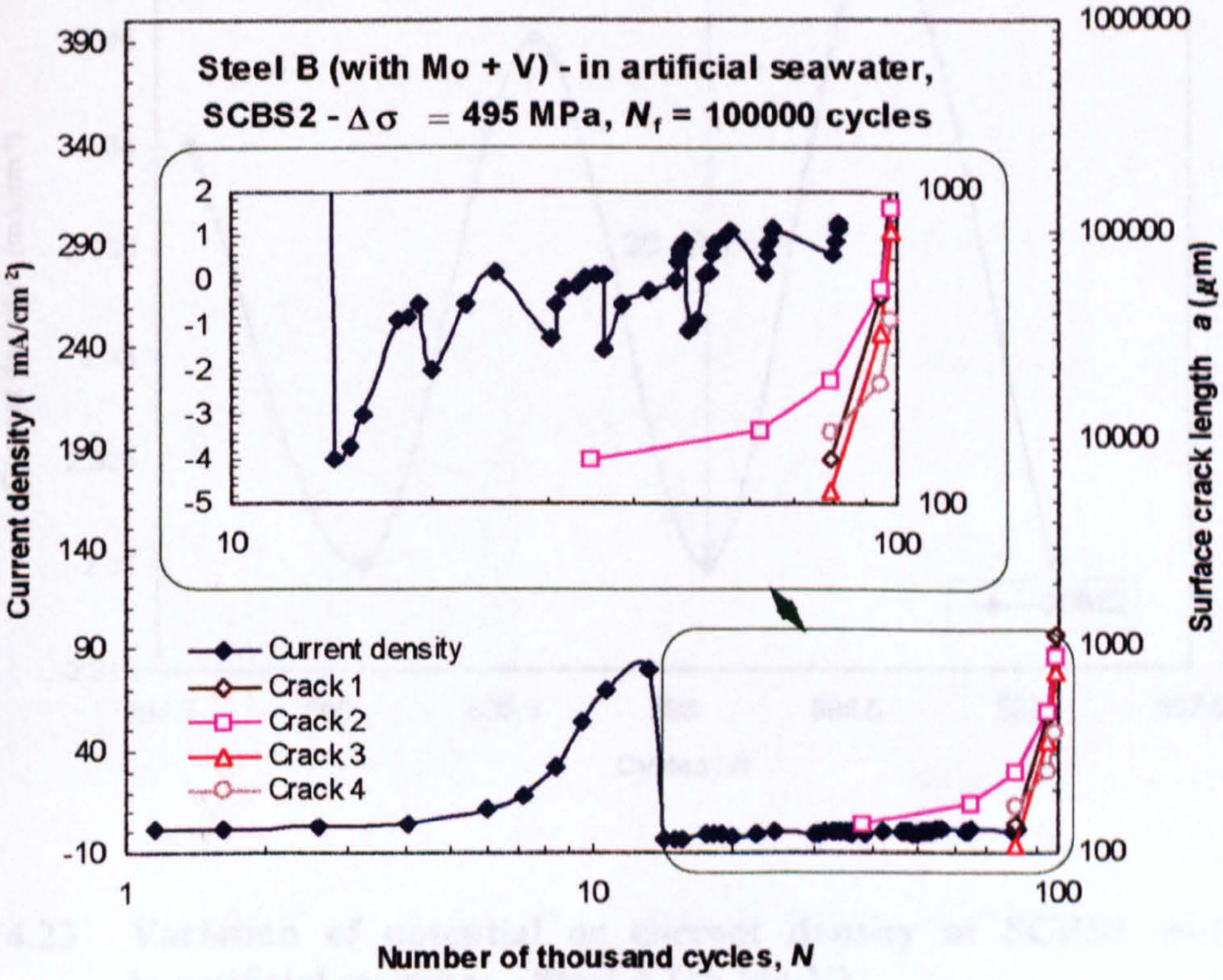

Figure 4.22 **Recording of current density of SCBS2 in artificial seawater - Steel A** (no Mo/V)

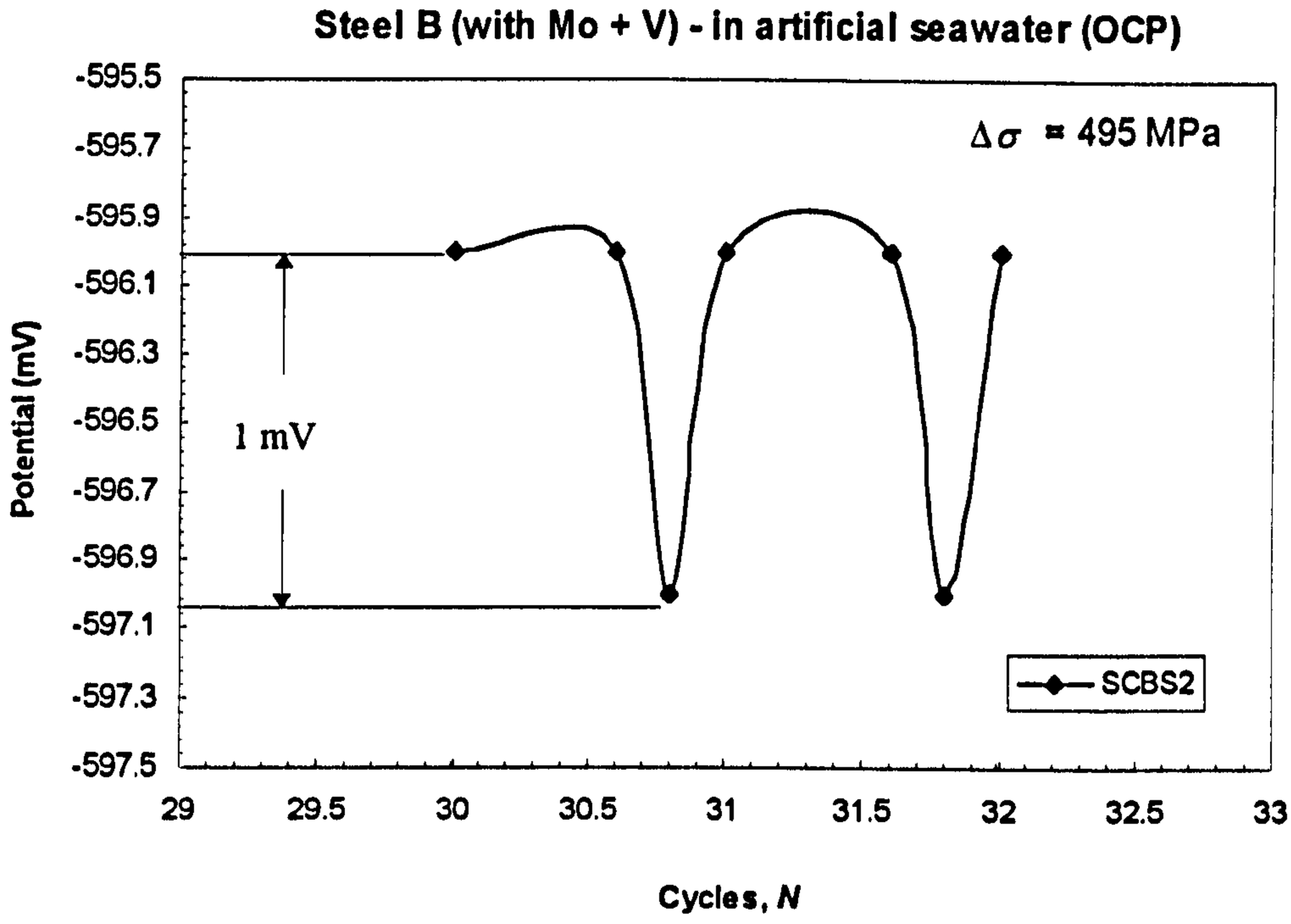

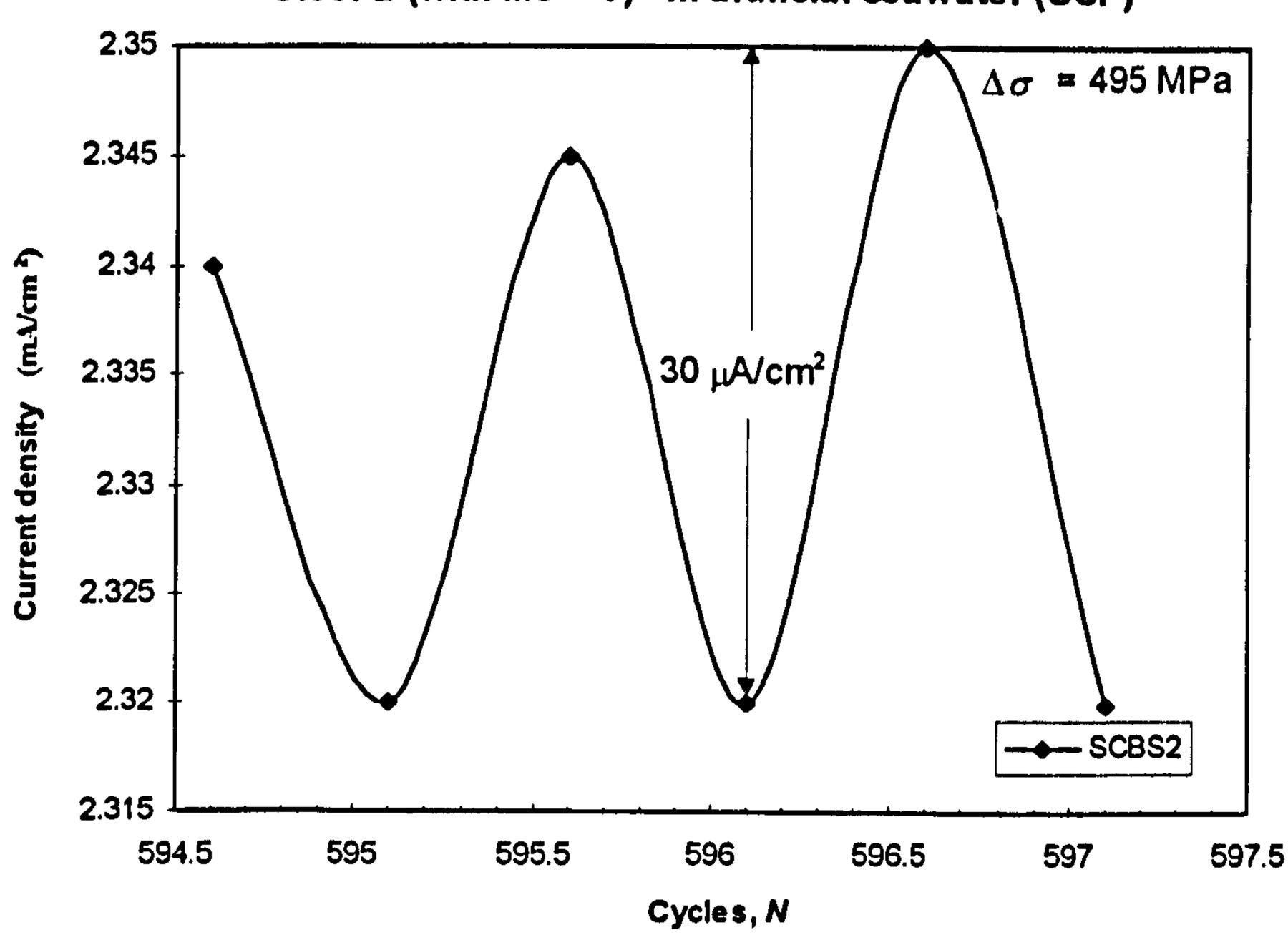

Figure 4.23 **Variation of potential or current density of SCBS2 with load in artificial seawater - Steel A** (no Mo/V)

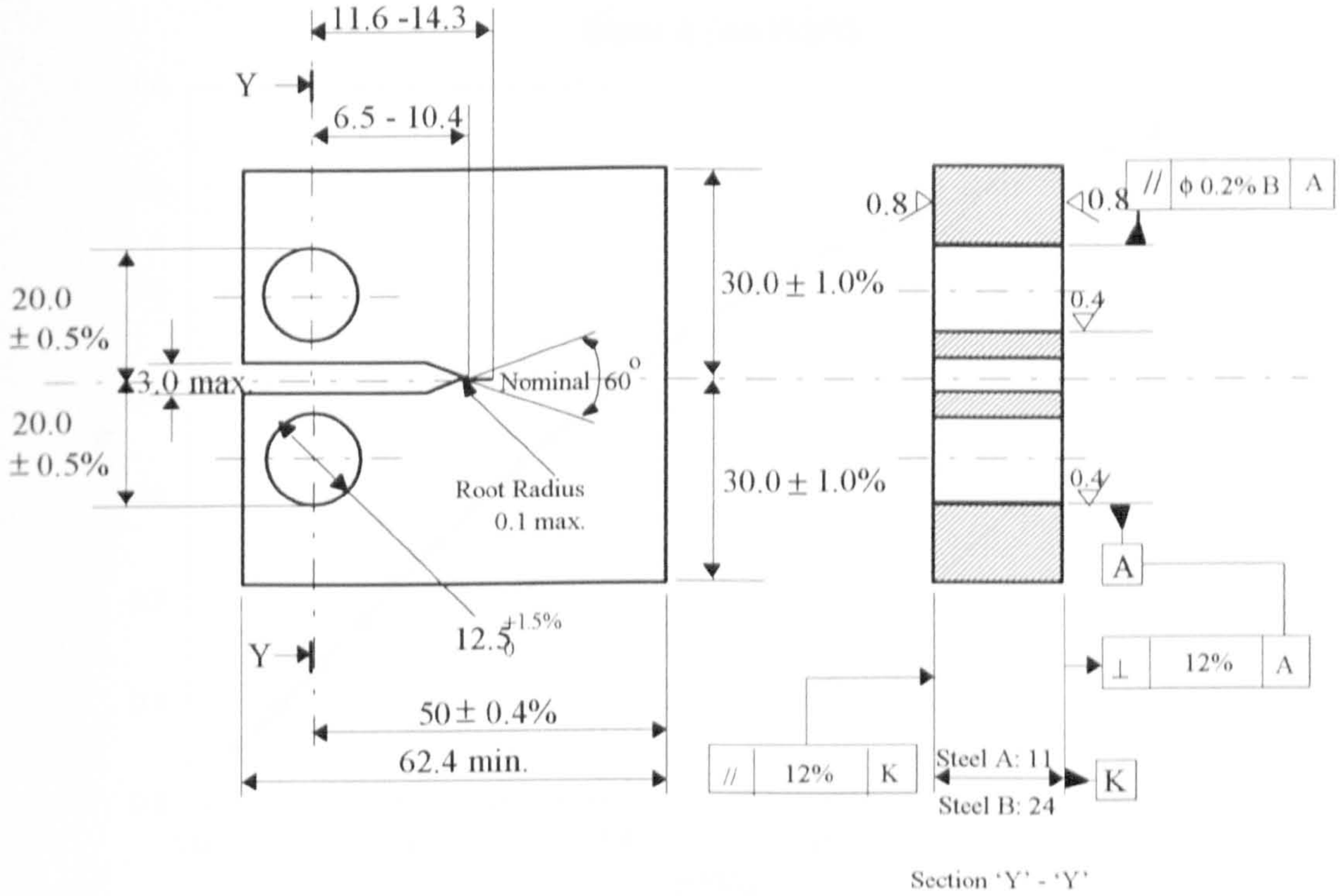

All dimensions are in millimetres

Figure 5.1 Proportional dimensions and tolerances for compact tension test pieces

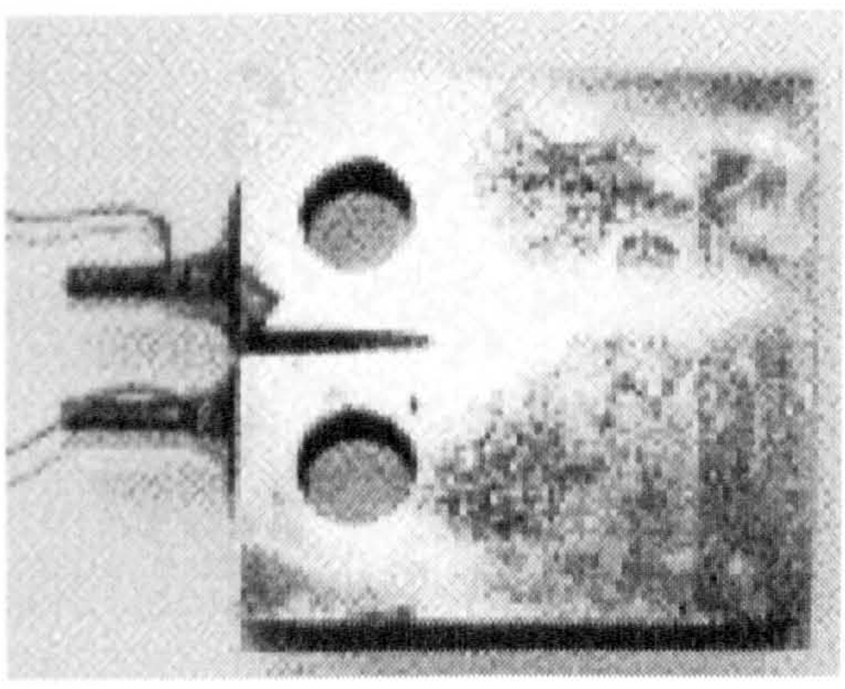

Figure 5.2 Schematic of a CT specimen showing 'normal' current lead positions (Input and Output) and active probes (V_{out})

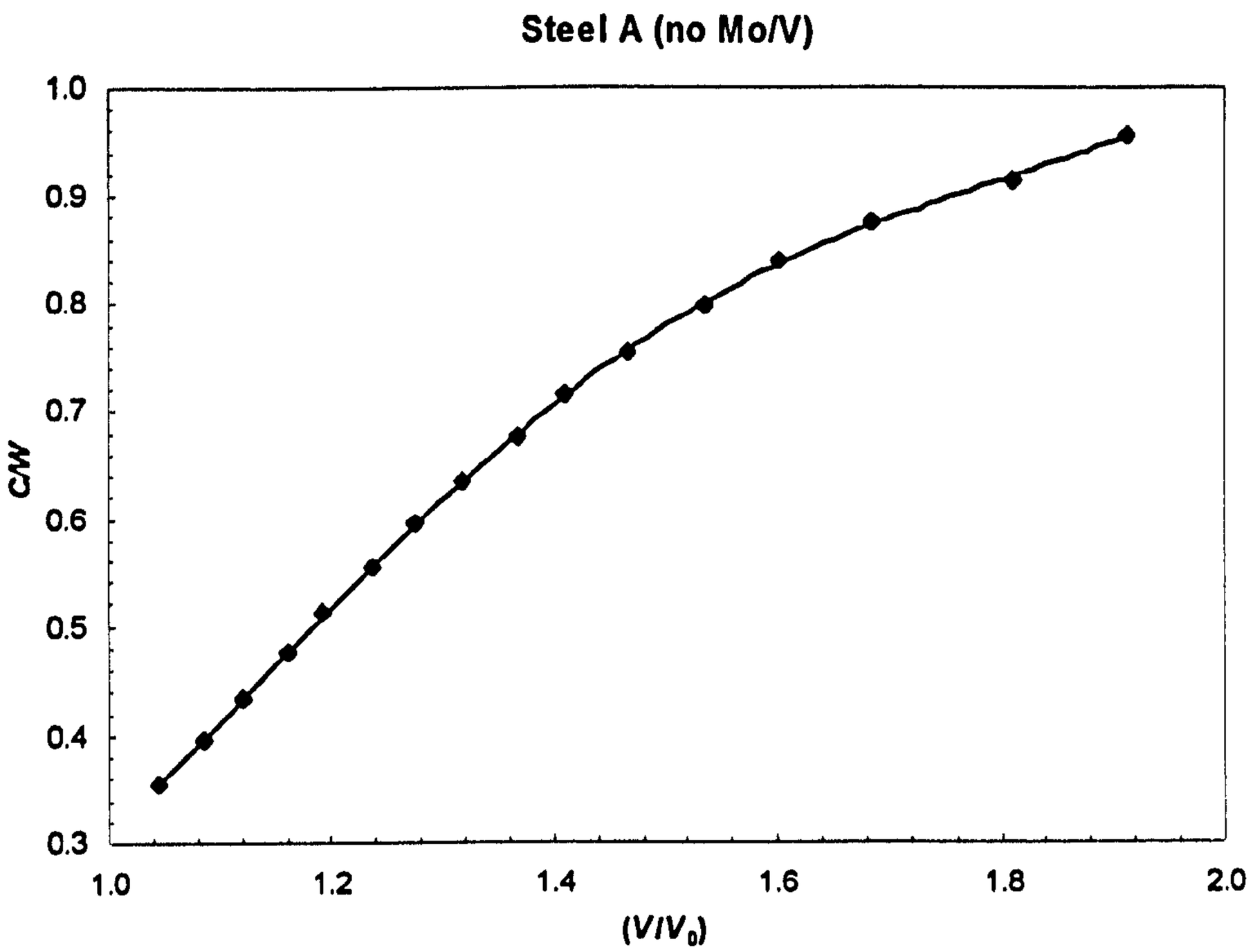

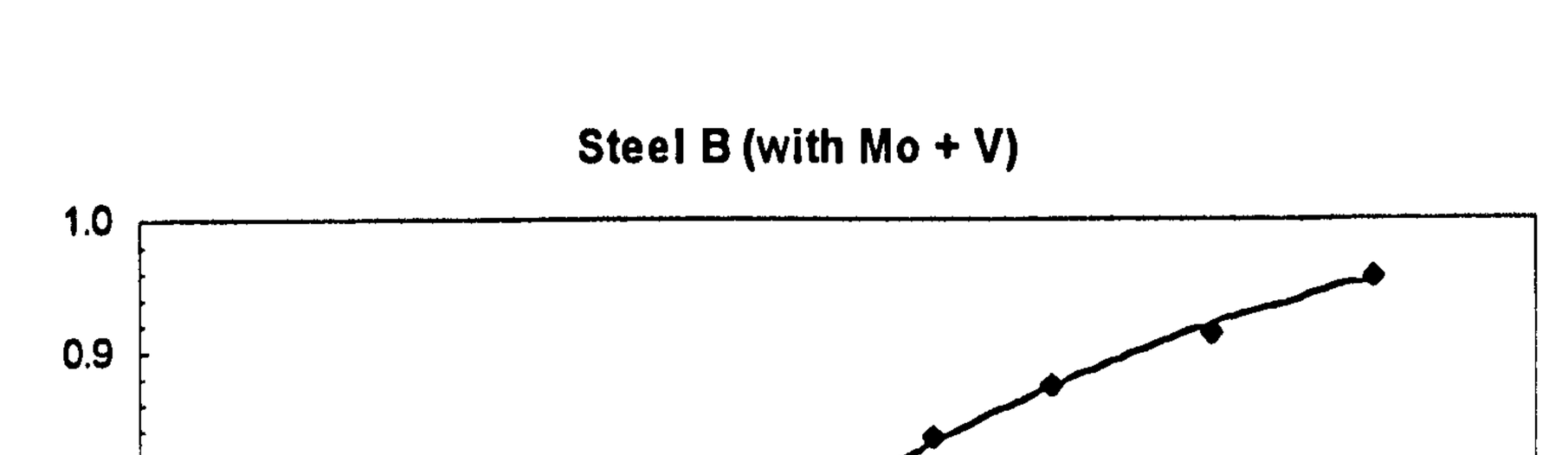

Figure 5. 3 Calibration of CT specimen

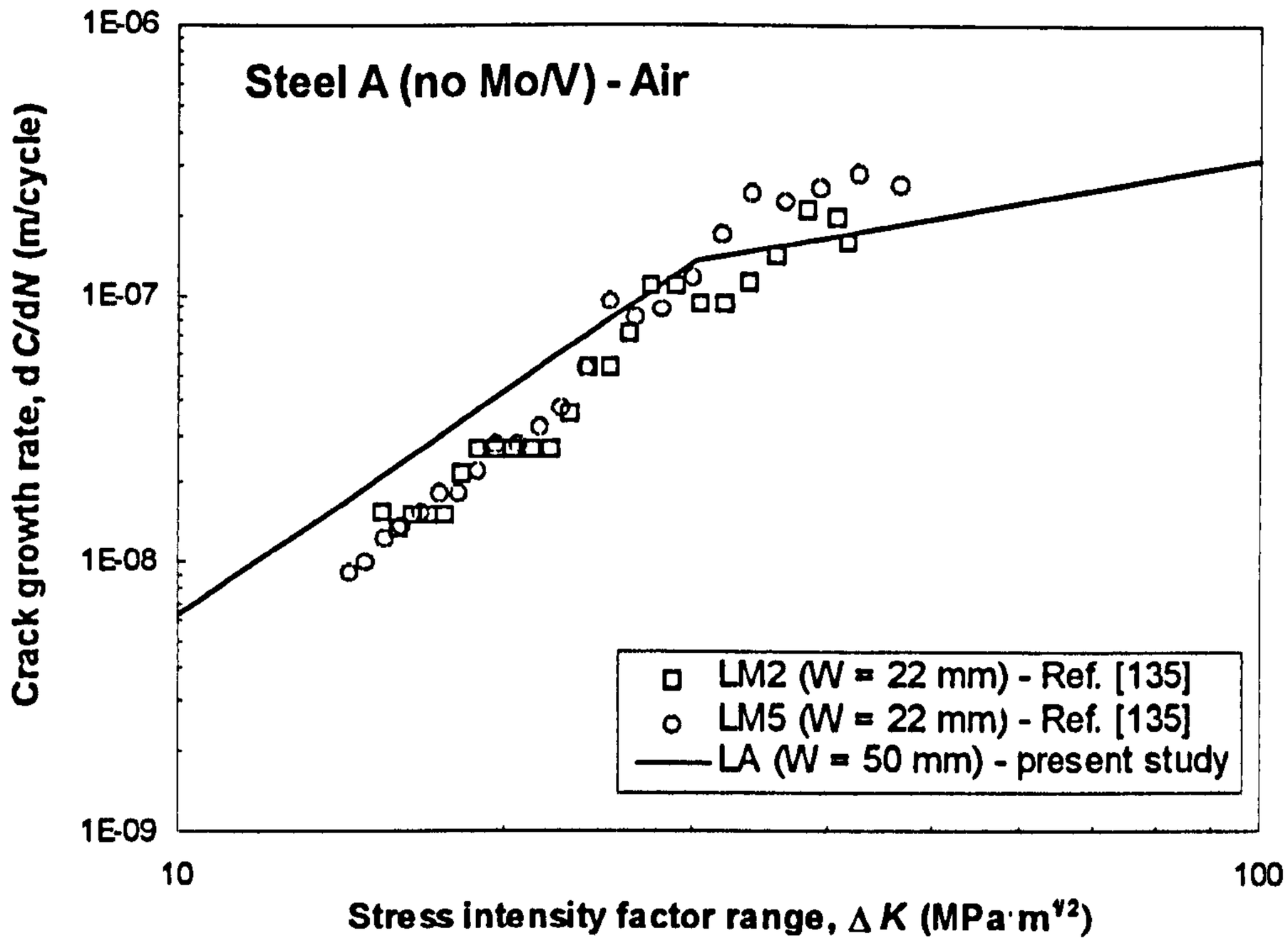

Figure 5.4 In-air long fatigue crack growth tests for Steel A (no Mo/V)

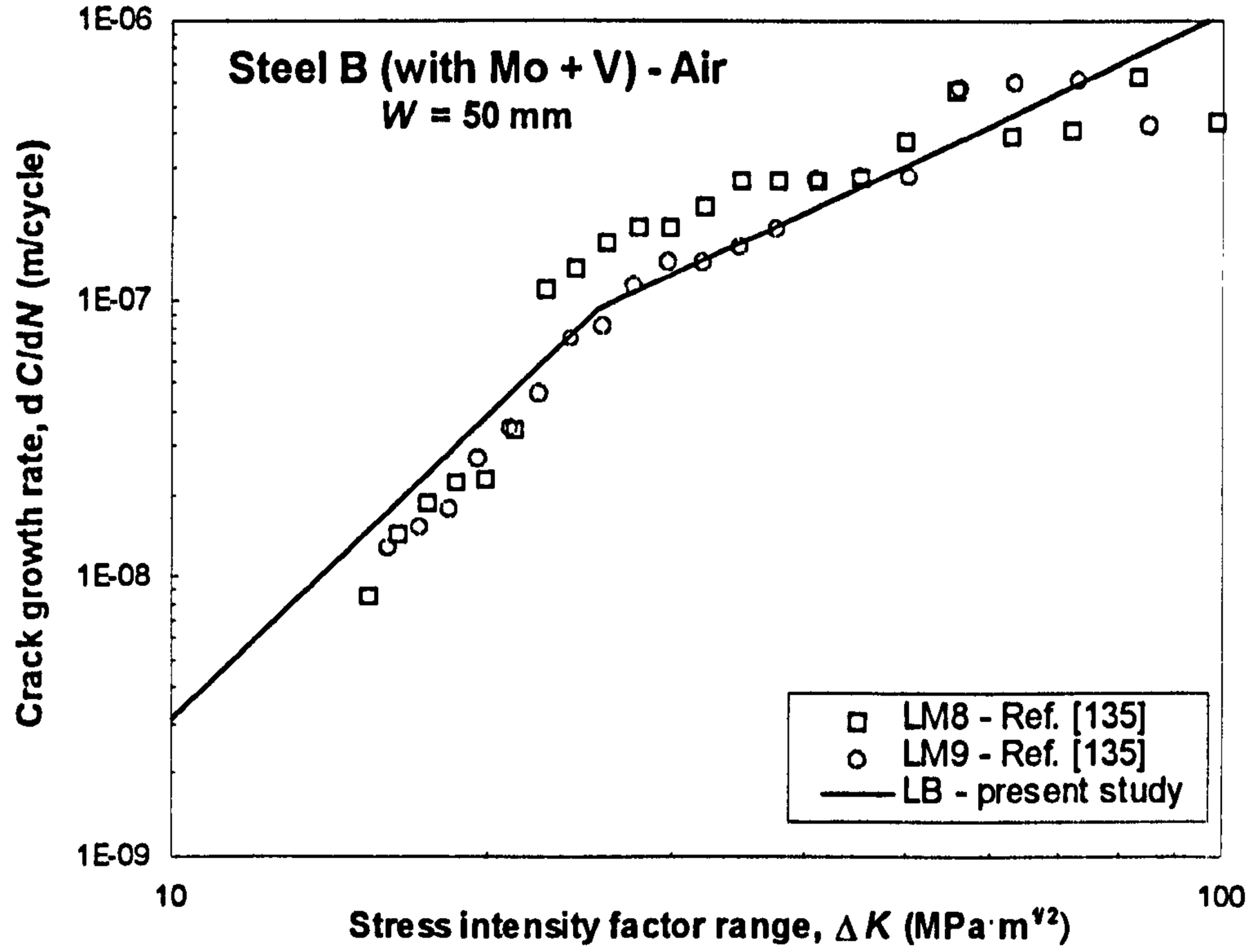

Figure 5.5 In-air long fatigue crack growth tests for Steel B (with Mo + V)

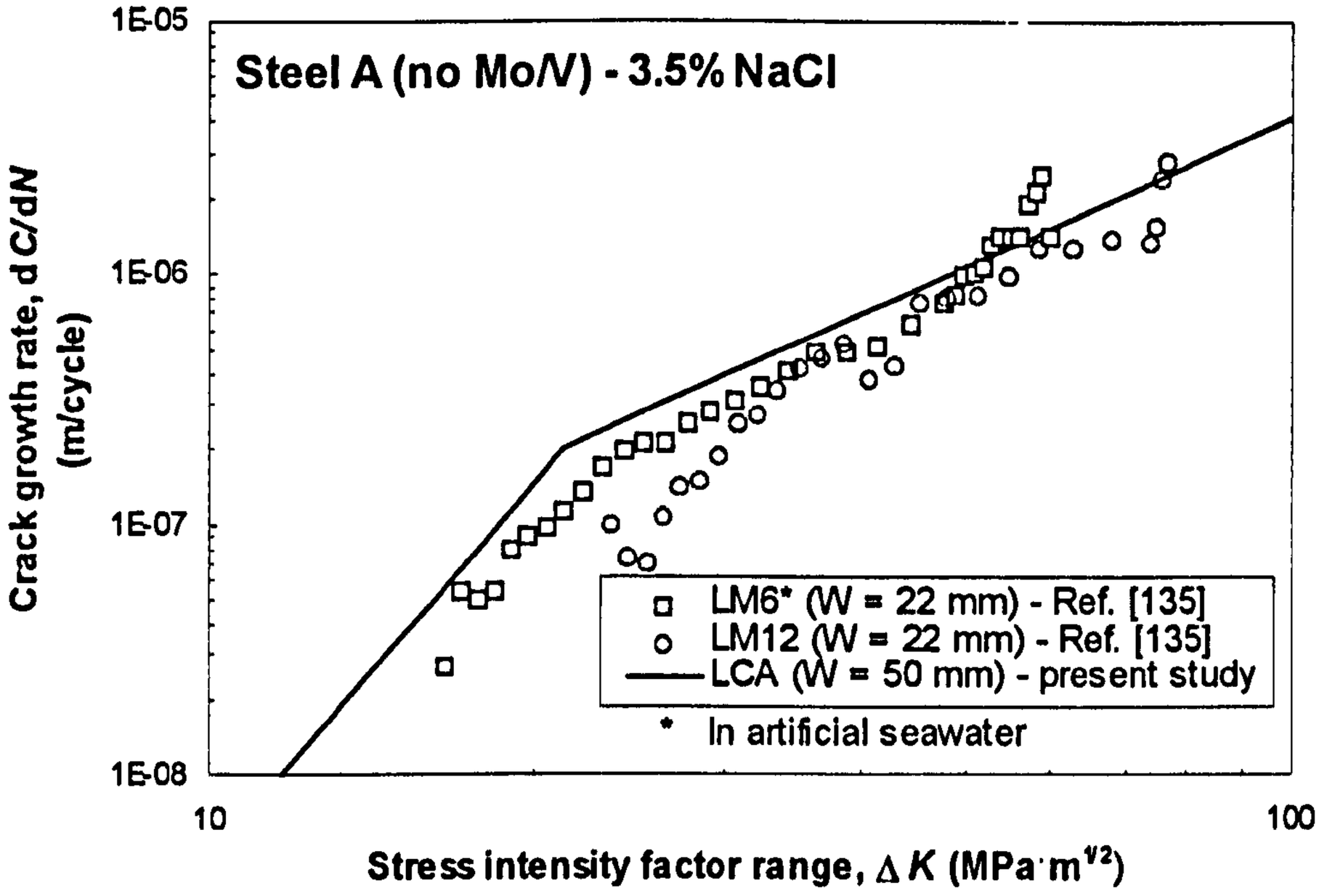

Figure 5.6 **Long fatigue crack growth tests for Steel A (no Mo/V) in 3.5%NaCl solution (OCP). Note: LM6 in artificial seawater**

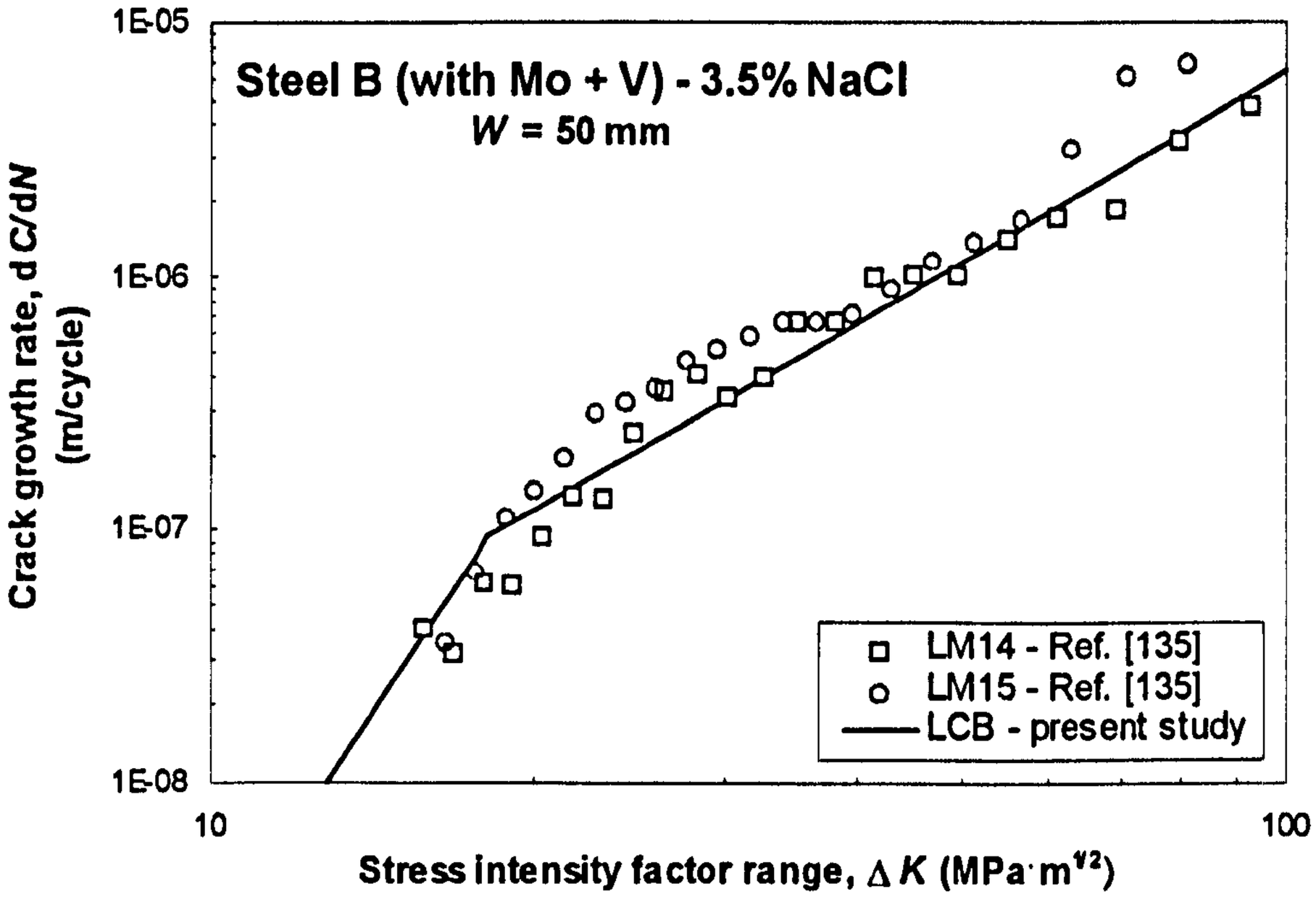

Figure 5.7 **Long fatigue crack growth tests for Steel B (with Mo + V) in 3.5%NaCl solution (OCP)**

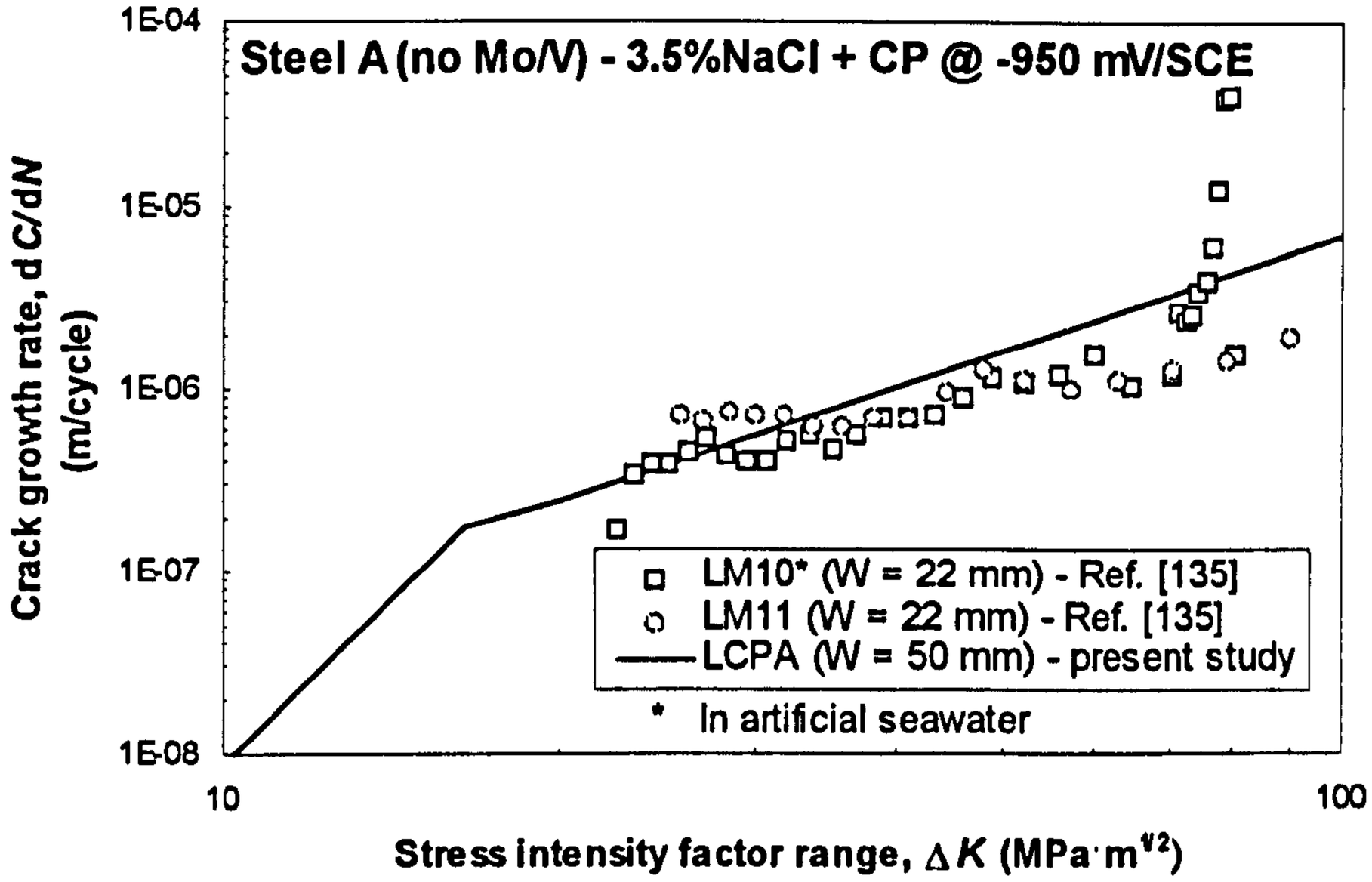

Figure 5.8 **Long fatigue crack growth tests for Steel A (no Mo/V) in 3.5%NaCl solution under CP** (-950 mV/SCE) **application. Note: LM10 in artificial seawater**

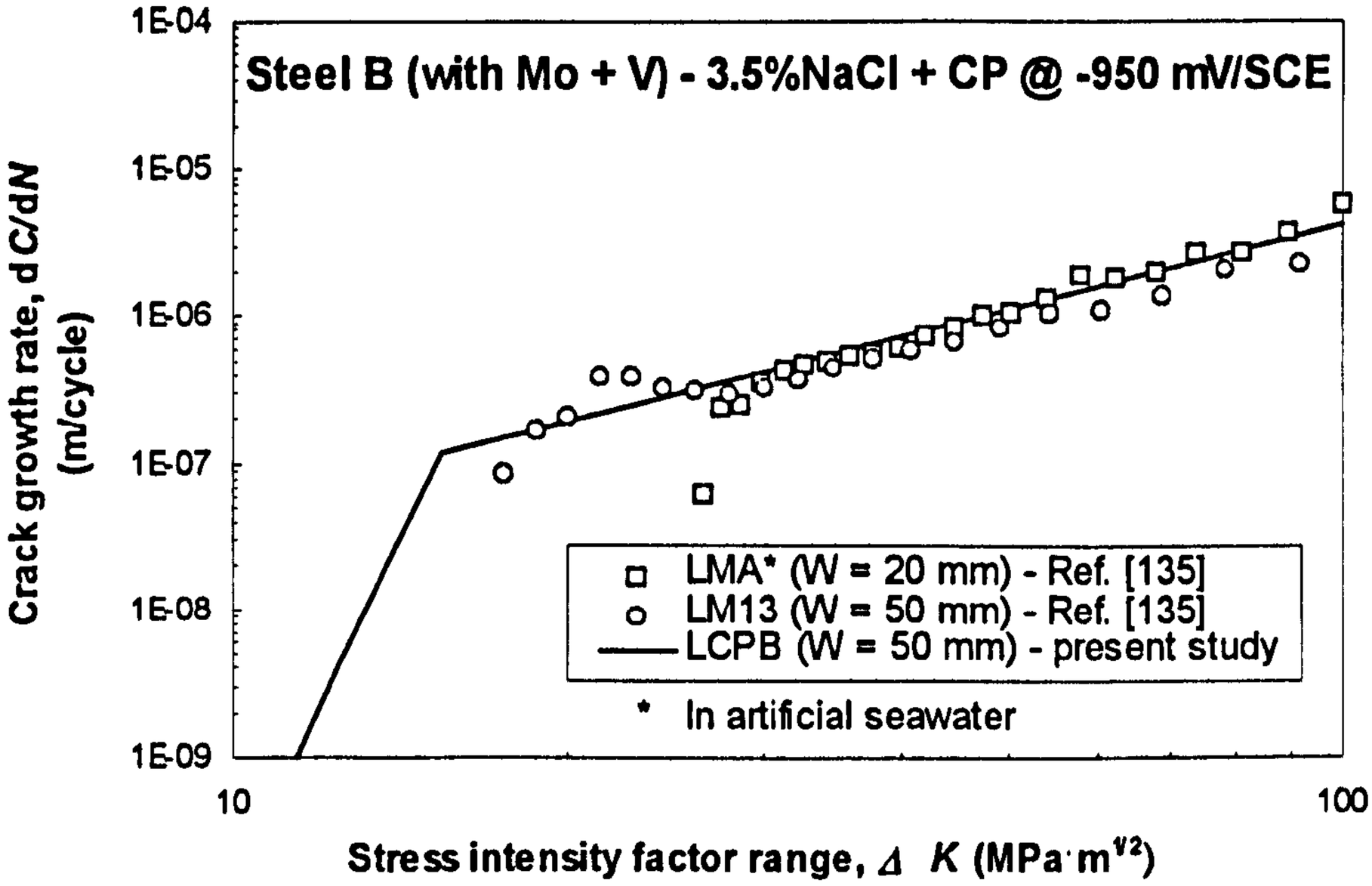

Figure 5.9 **Long fatigue crack growth tests for Steel B (with Mo + V) in 3.5%NaCl solution under CP** (-950 mV/SCE) **application. Note: LMA in artificial seawater**

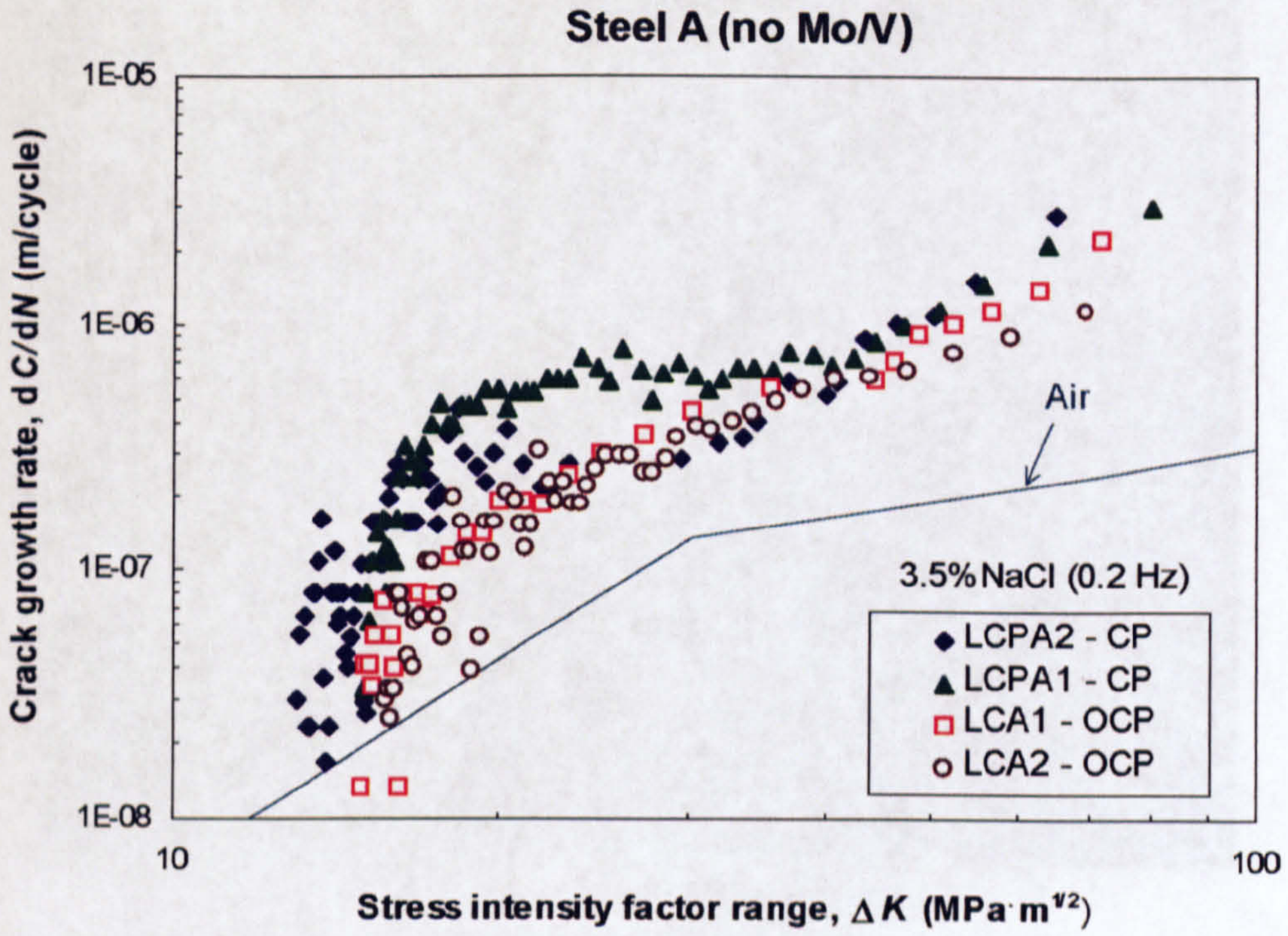

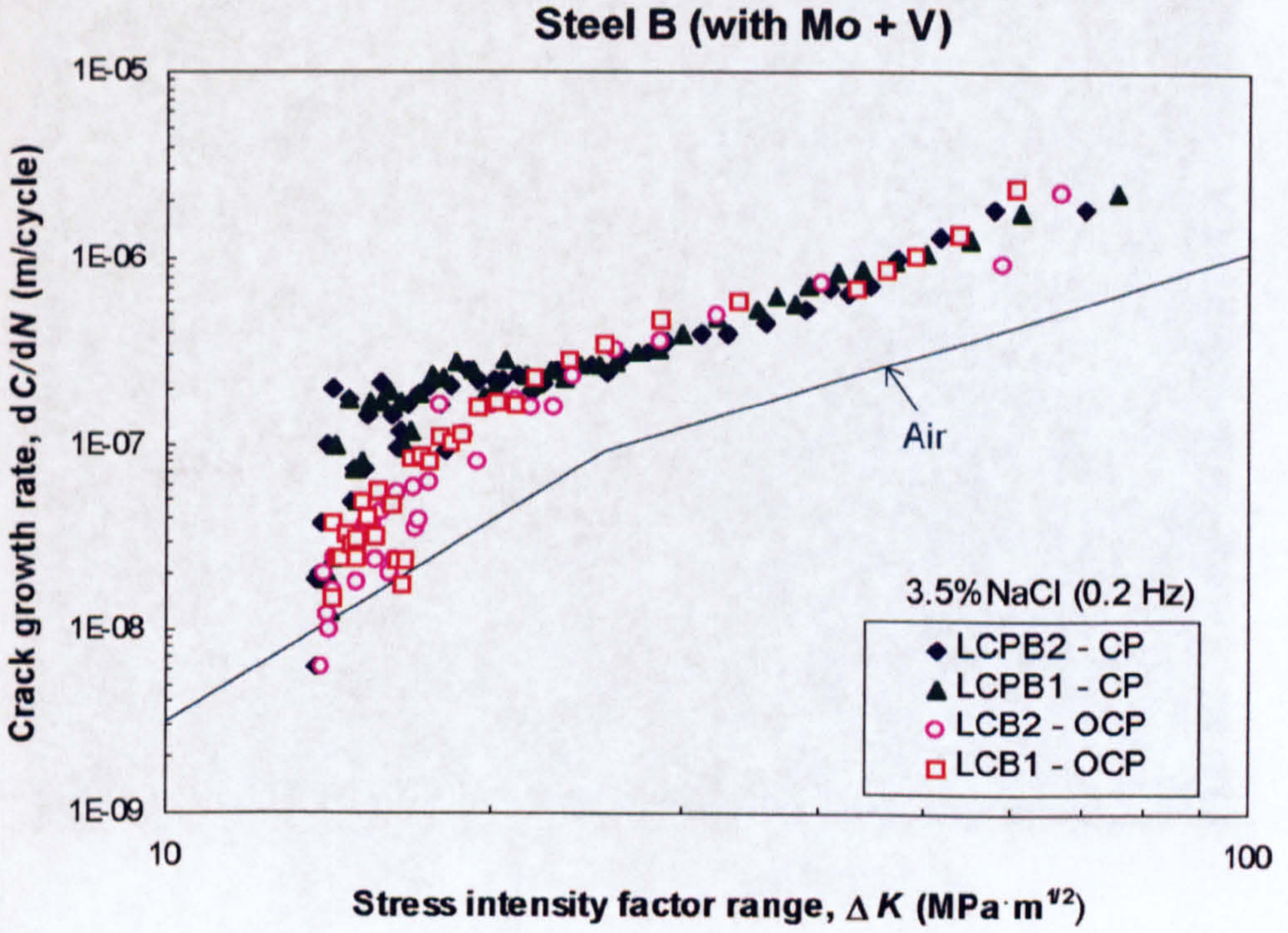

Figure 5.10 The effect of test environment on the fatigue crack growth rate

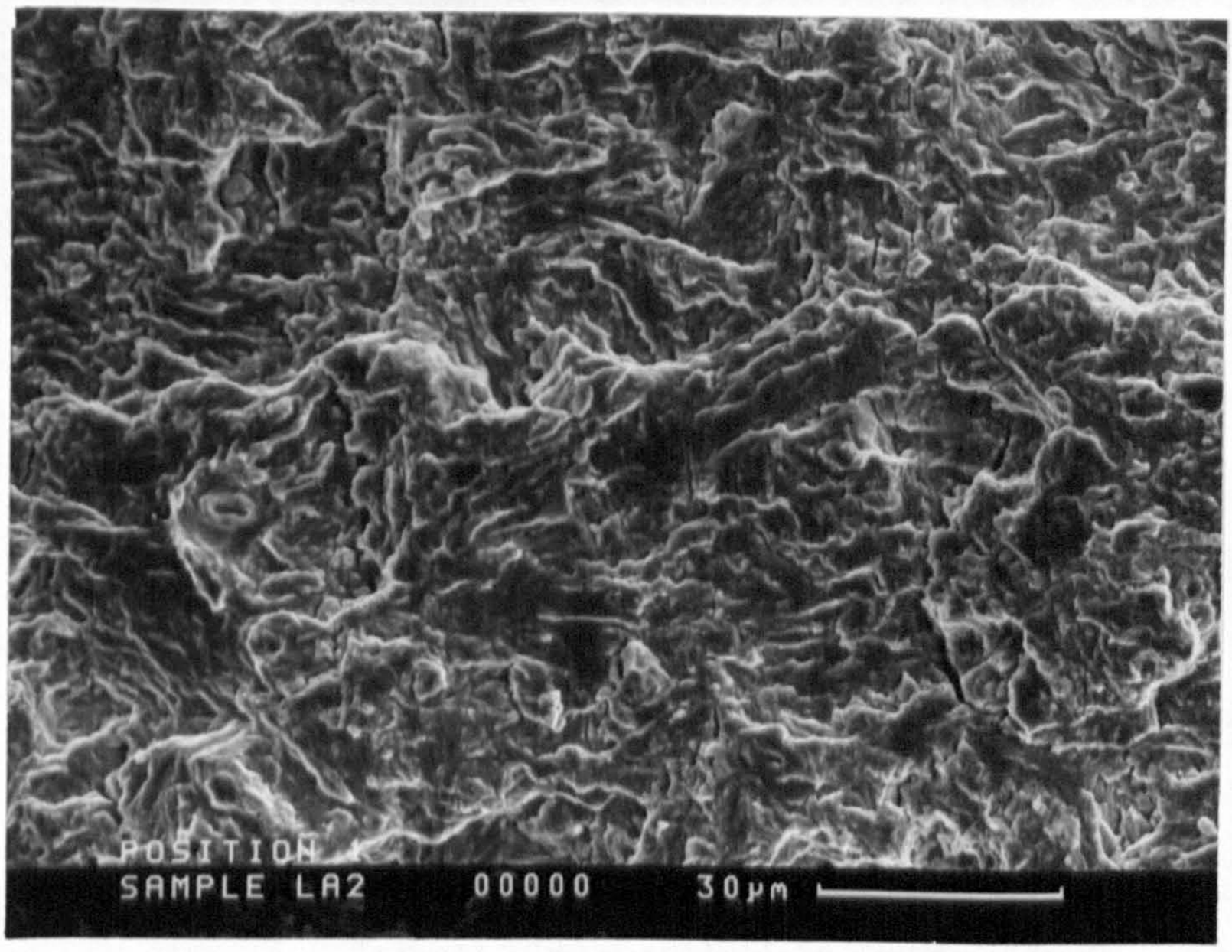

5.11(a) Steel A (no Mo/V)

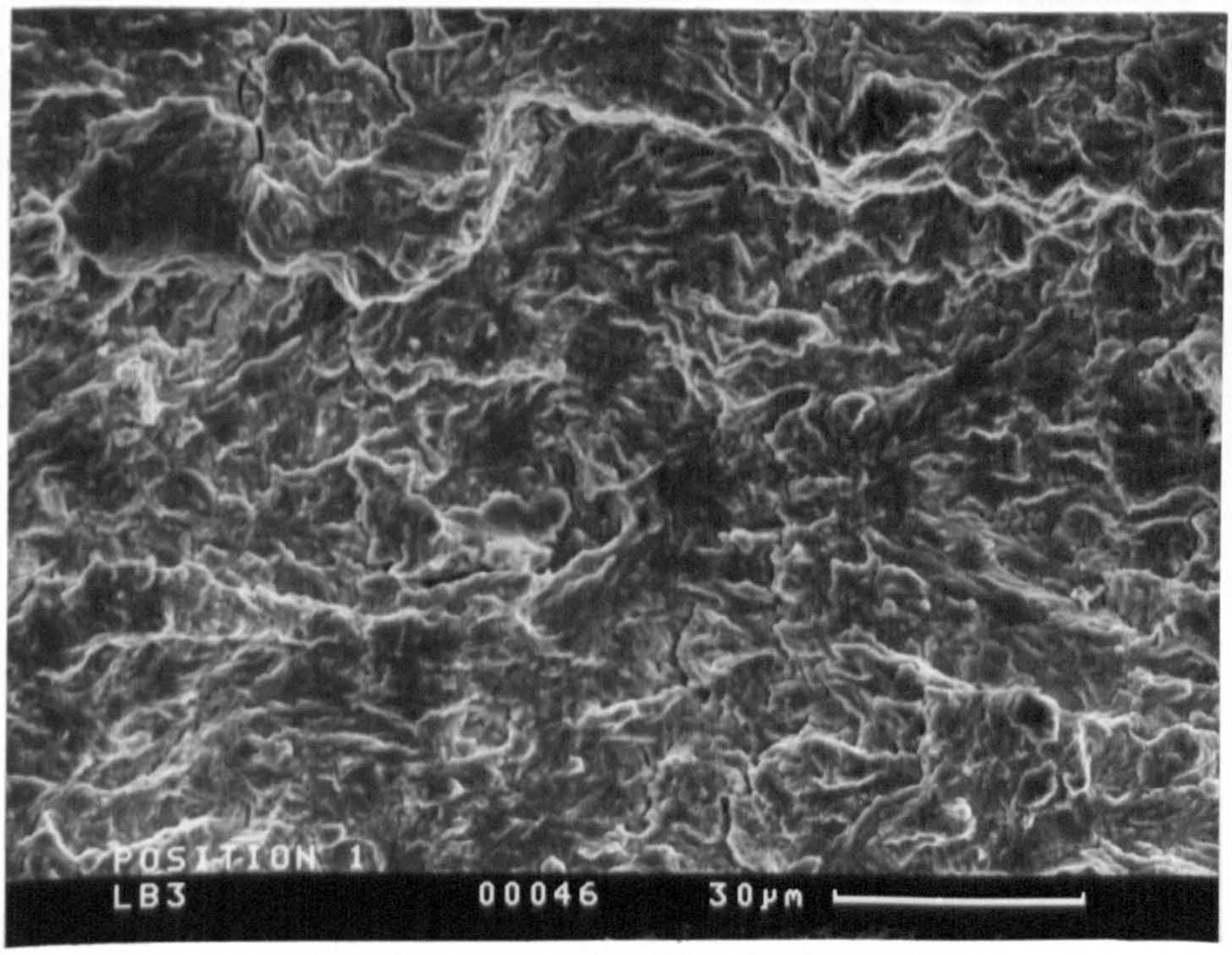

5.11(b) Steel B (with Mo + V)

Figure 5.11 Scanning electron micrographs of fatigue fractured CT specimens at $\Delta K \approx 20$ MPa$\cdot\sqrt{m}$ in air

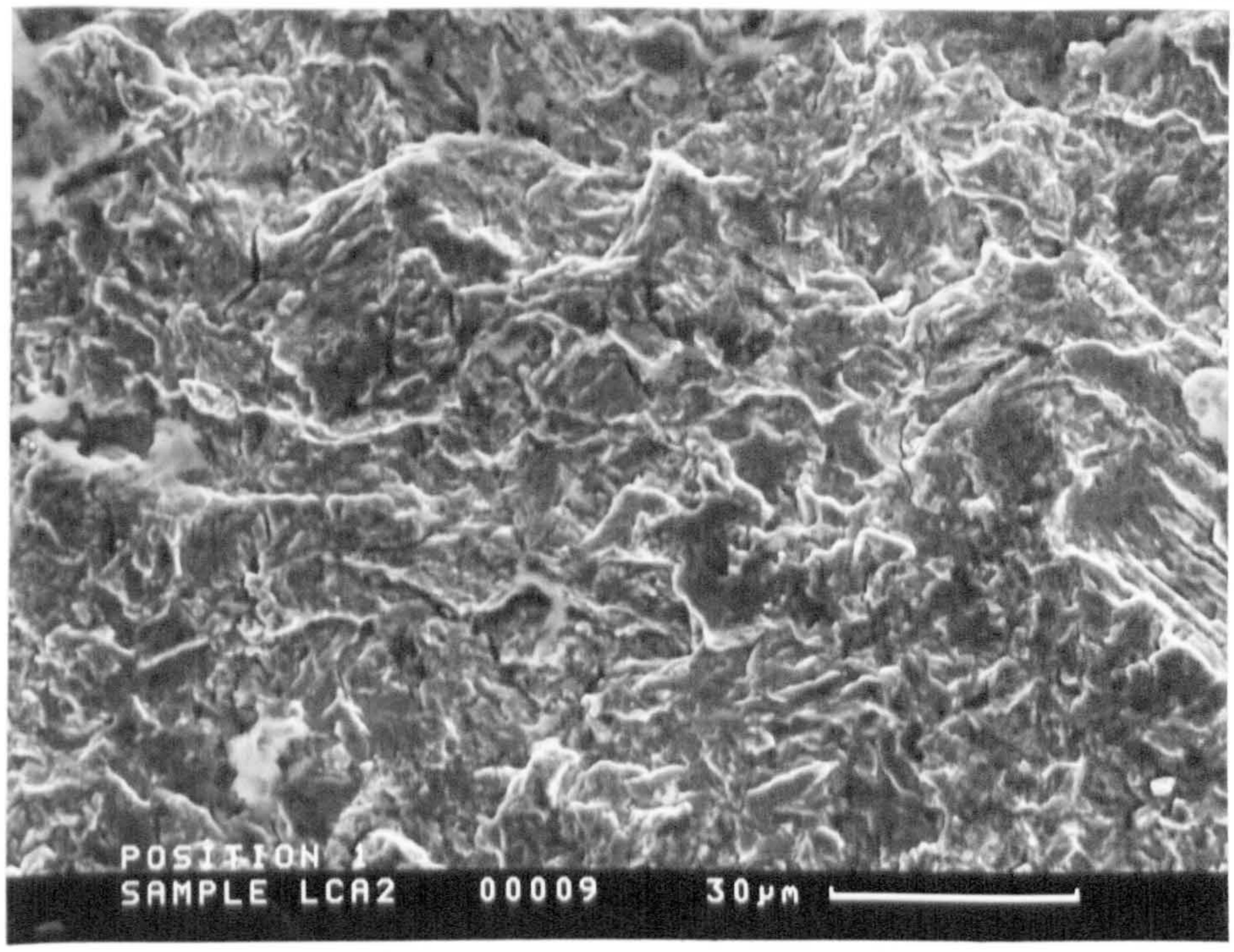

5.12(a) Steel A (no Mo/V)

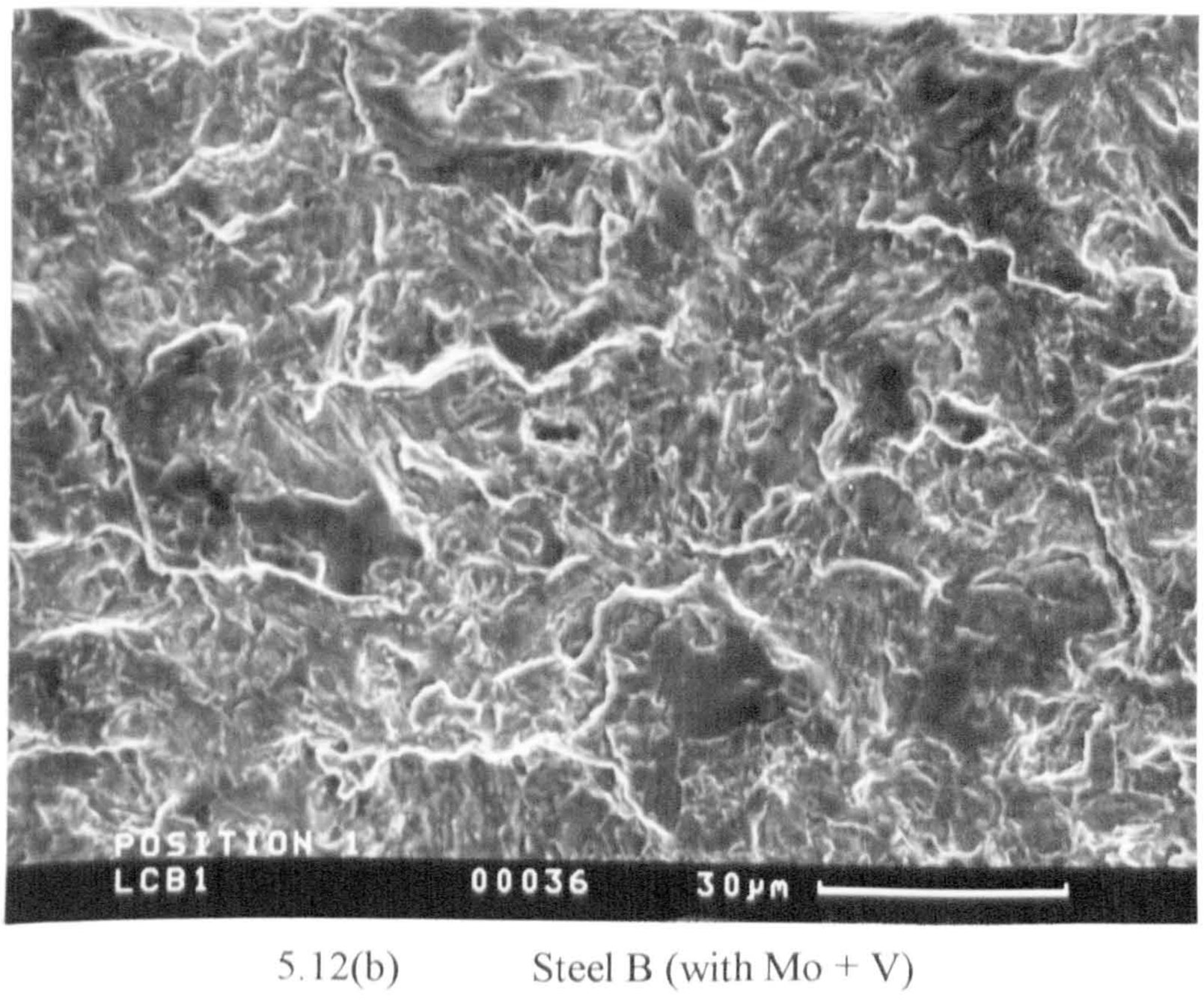

5.12(b) Steel B (with Mo + V)

Figure 5.12 Scanning electron micrographs of fatigue fractured CT specimens at $\Delta K \approx 20\ \mathrm{MPa}\cdot\sqrt{m}$ in 3.5%NaCl solution (OCP)

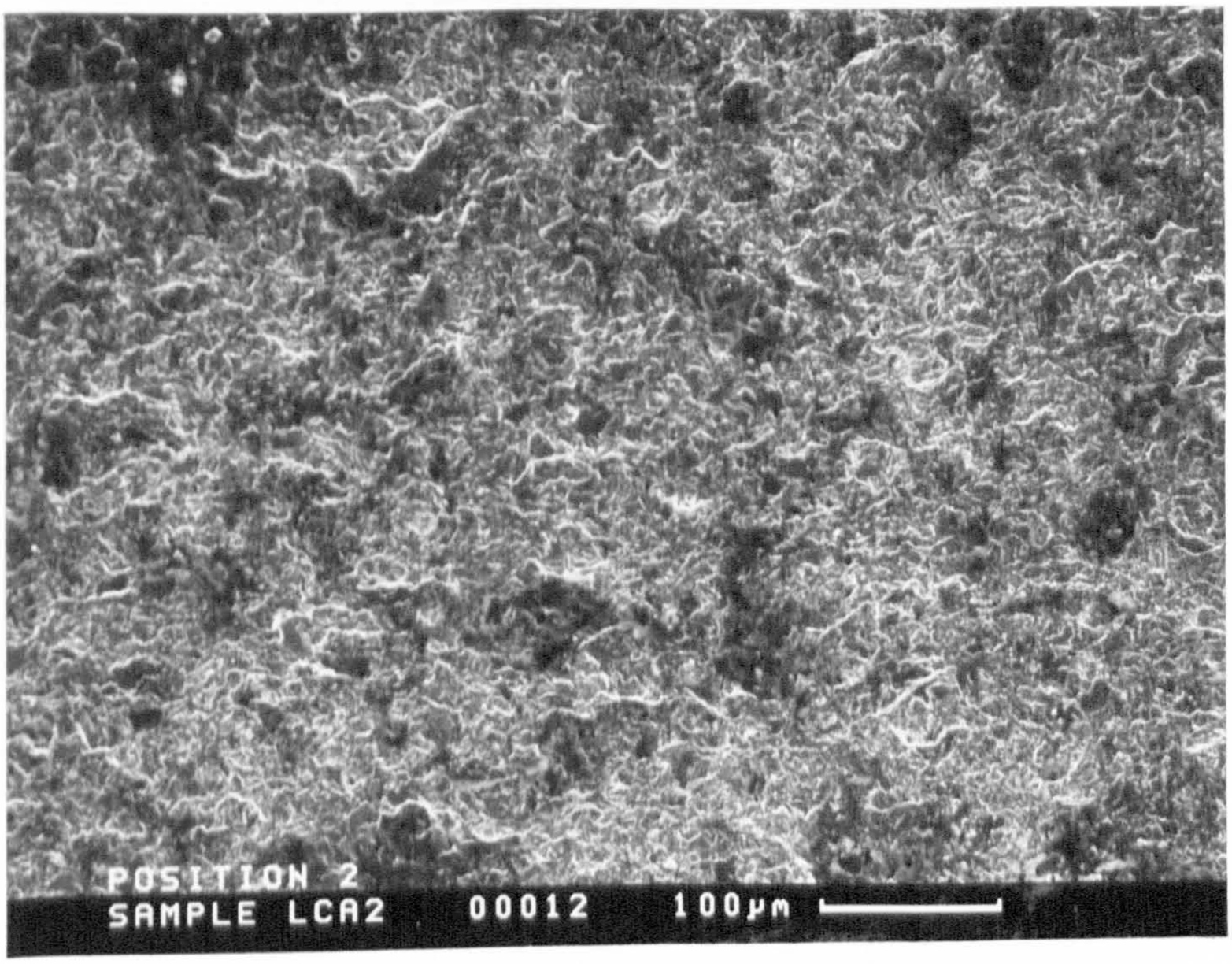

5.13(a) Steel A (no Mo/V)

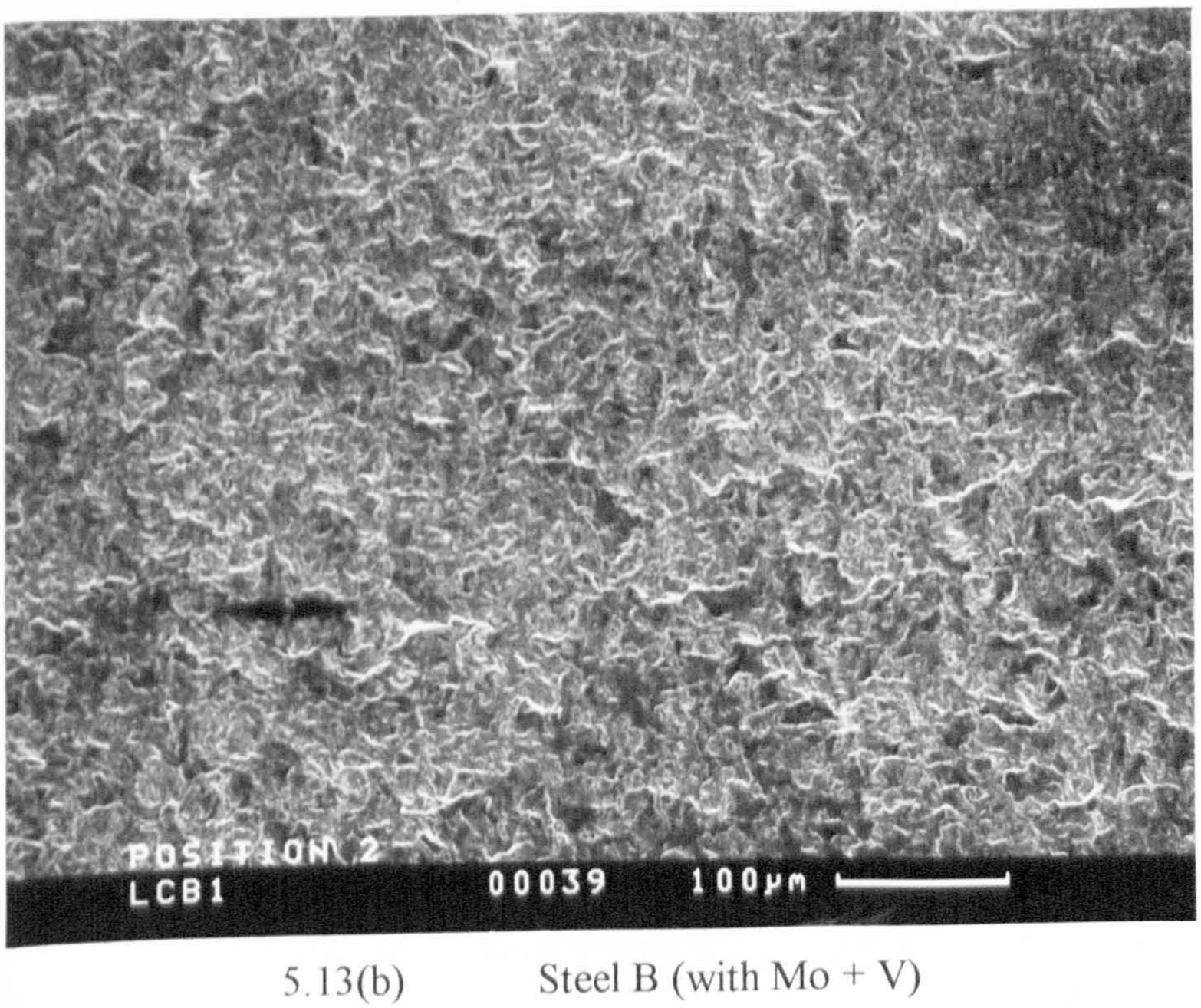

5.13(b) Steel B (with Mo + V)

Figure 5.13 Example of corrosion sites shown by SEM at $\Delta K \approx 25$ MPa$\cdot\sqrt{m}$ in 3.5%NaCl solution (OCP)

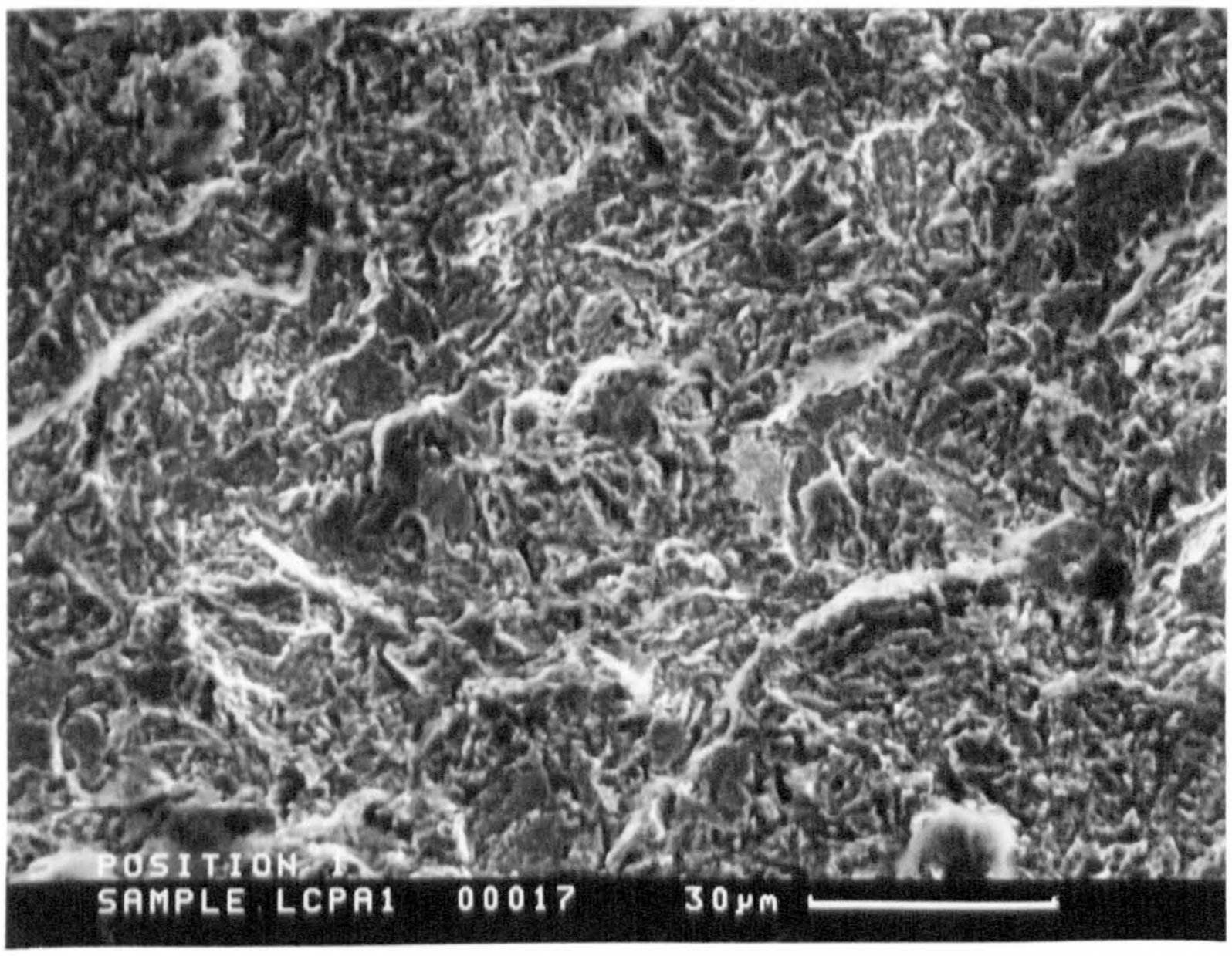

5.14(a) Steel A (no Mo/V)

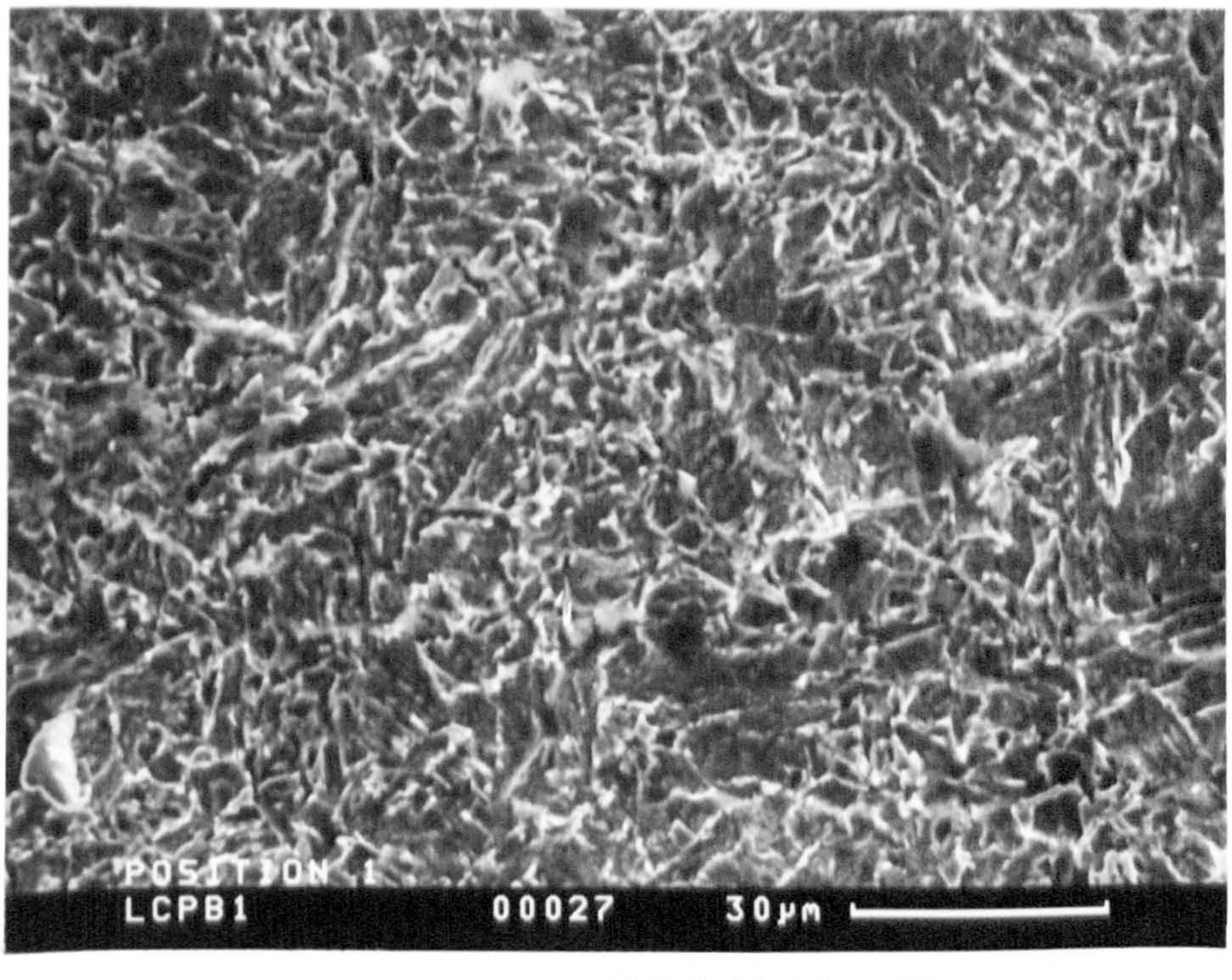

5.14(b) Steel B (with Mo + V)

Figure 5.14 Scanning electron micrographs of fatigue fractured CT specimens at $\Delta K \approx 20$ MPa$\cdot\sqrt{m}$ in 3.5%NaCl solution under applied cathodic polarisation (-950 mV/SCE)

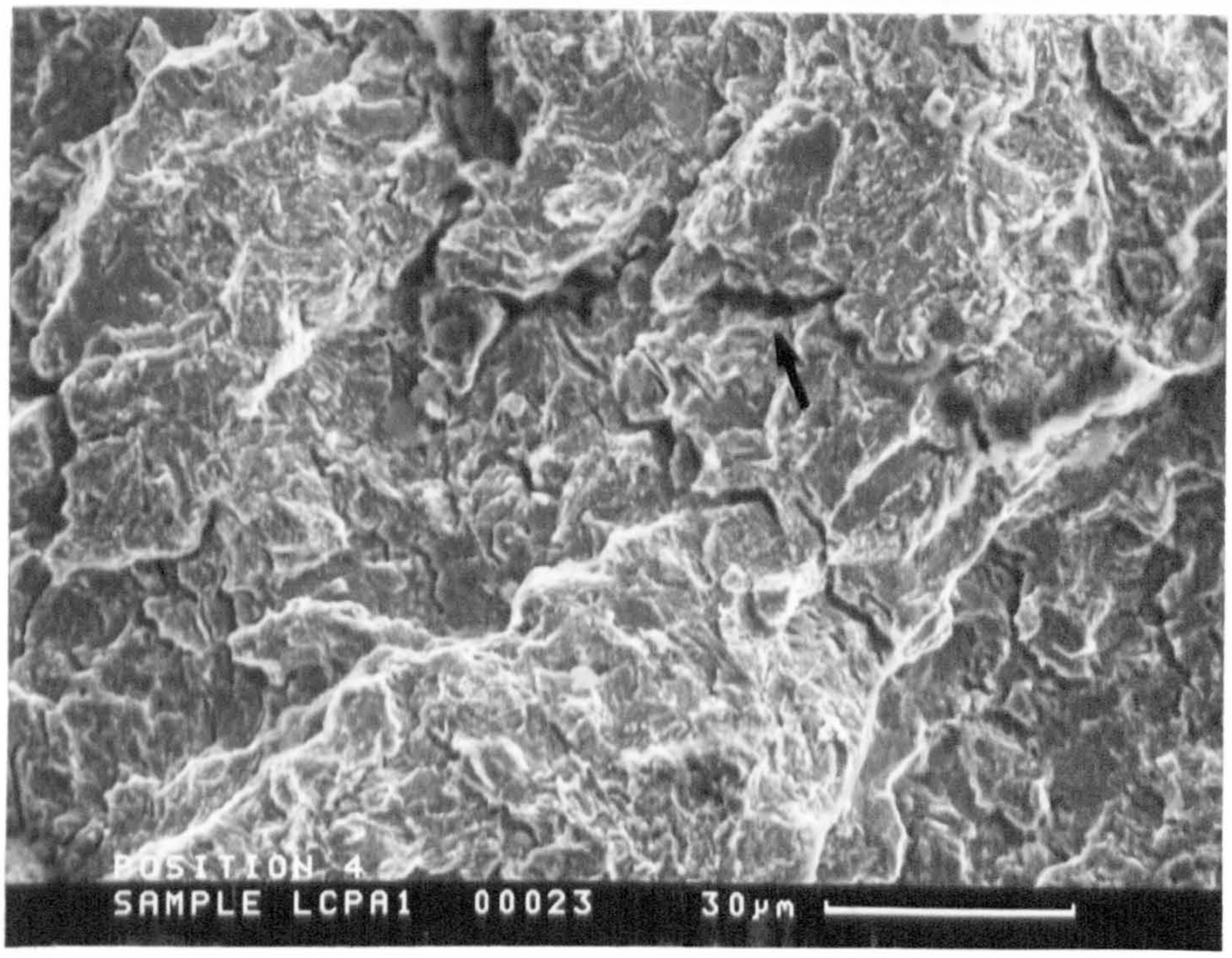

5.15(a) Steel A (no Mo/V) in 3.5%NaCl solution under CP application

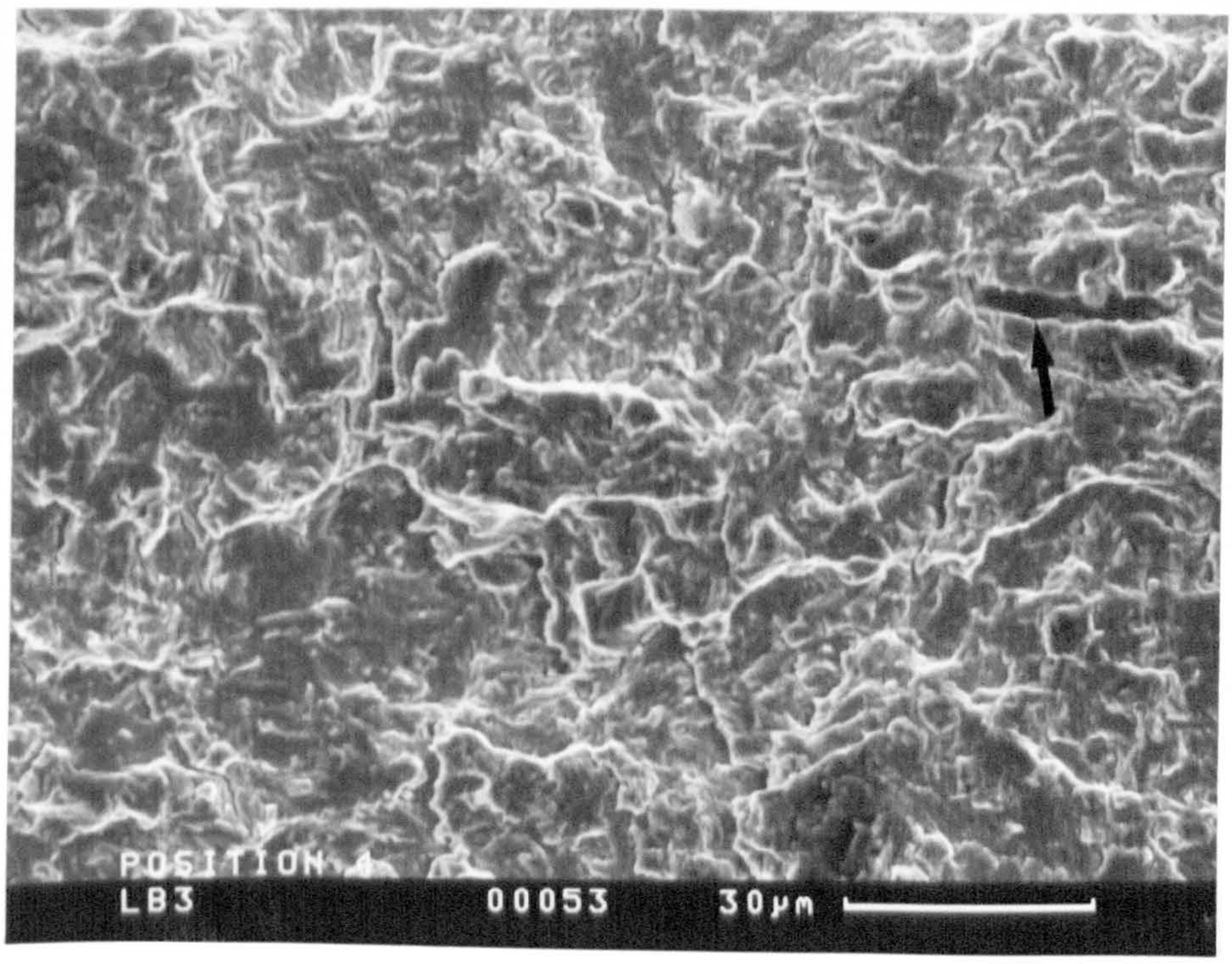

5.15(b) Steel B (with Mo + V) in air

Figure 5.15 Example of crack branches by SEM at $\Delta K \approx 40$ MPa$\cdot\sqrt{m}$

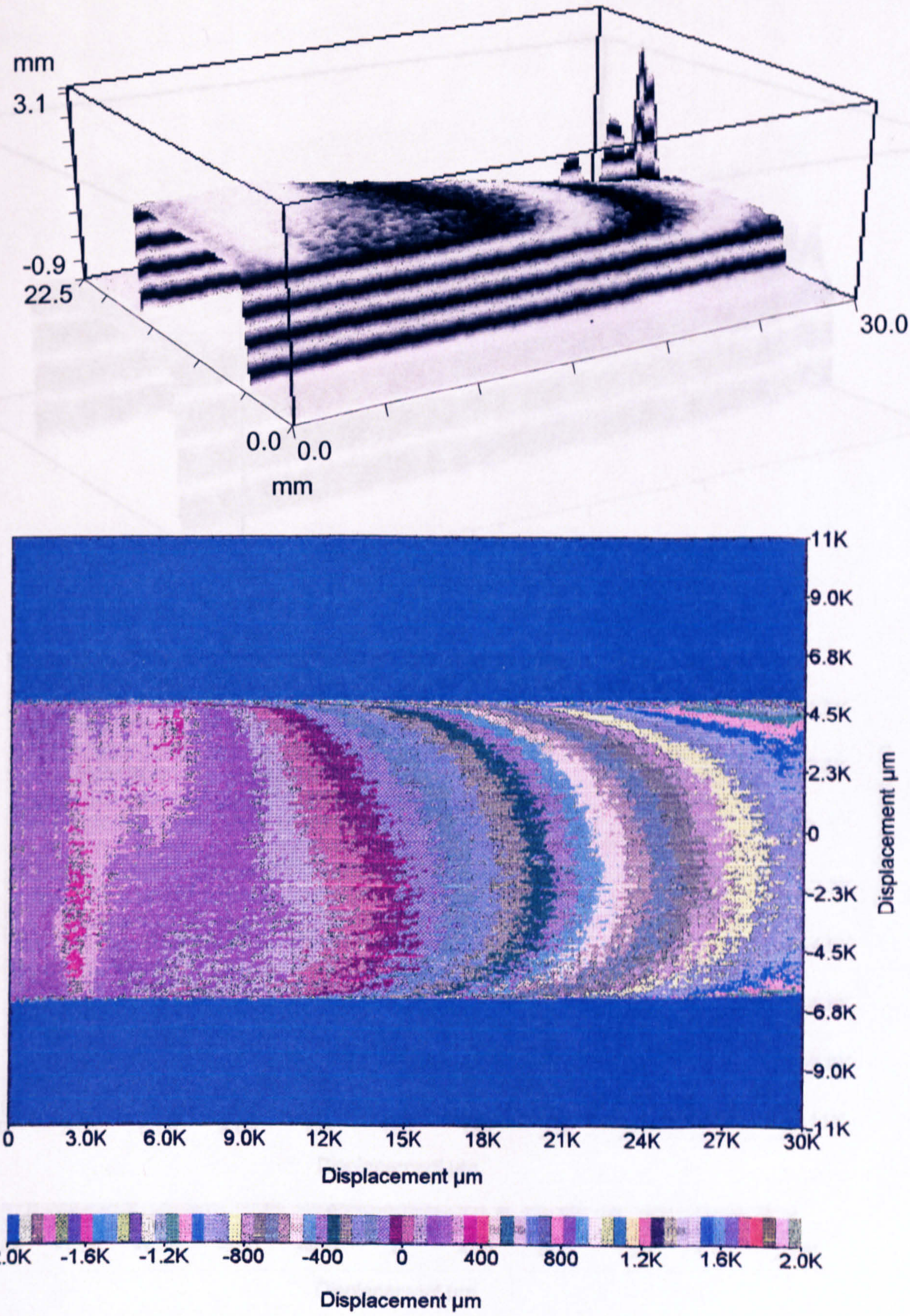

Figure 5.16 **Surface roughness outline of fatigue fractured specimen in air - Steel A** (no Mo/V)

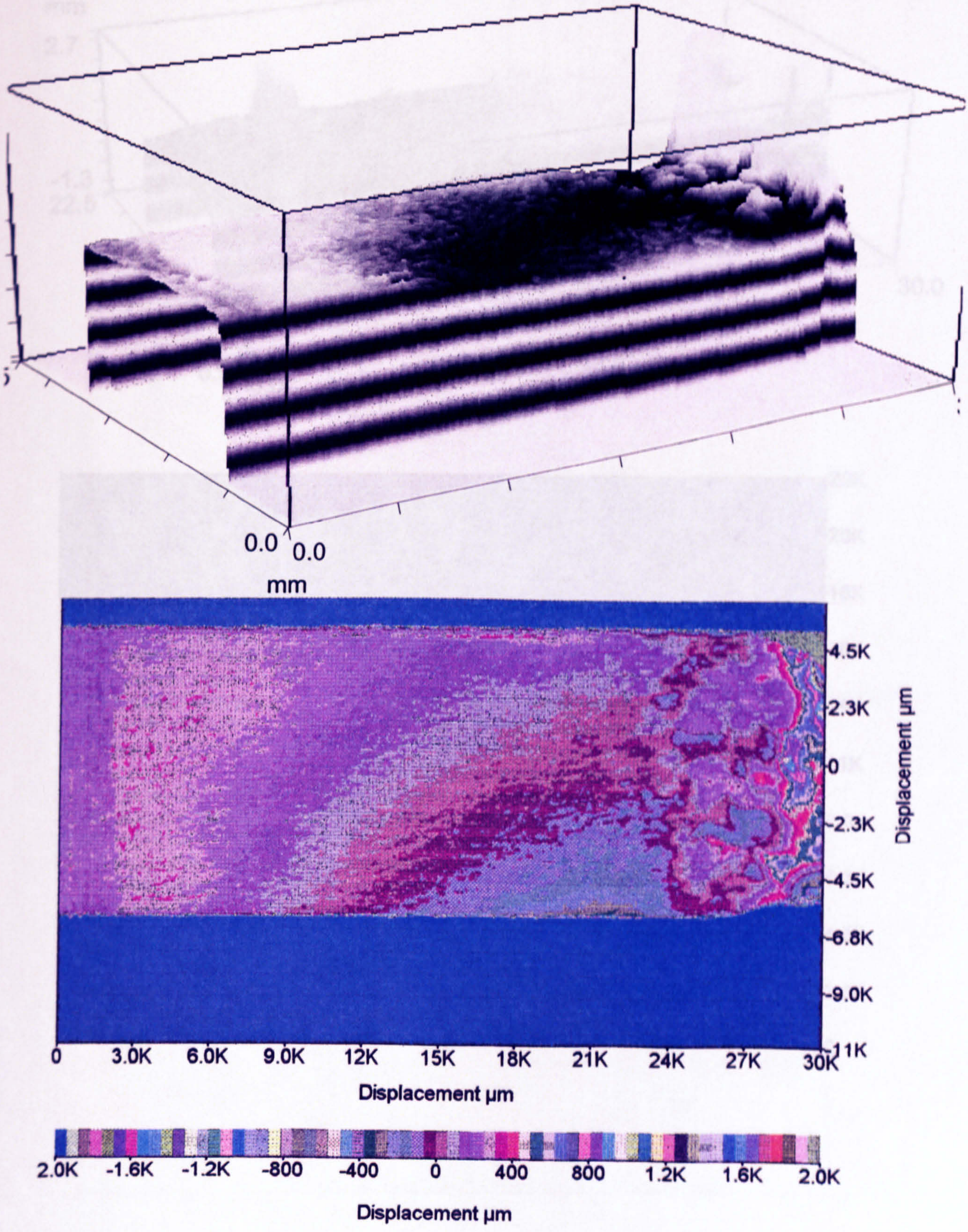

Figure 5.17 Surface roughness outline of fatigue fractured specimen in 3.5%NaCl solution (OCP) **- Steel A** (no Mo/V)

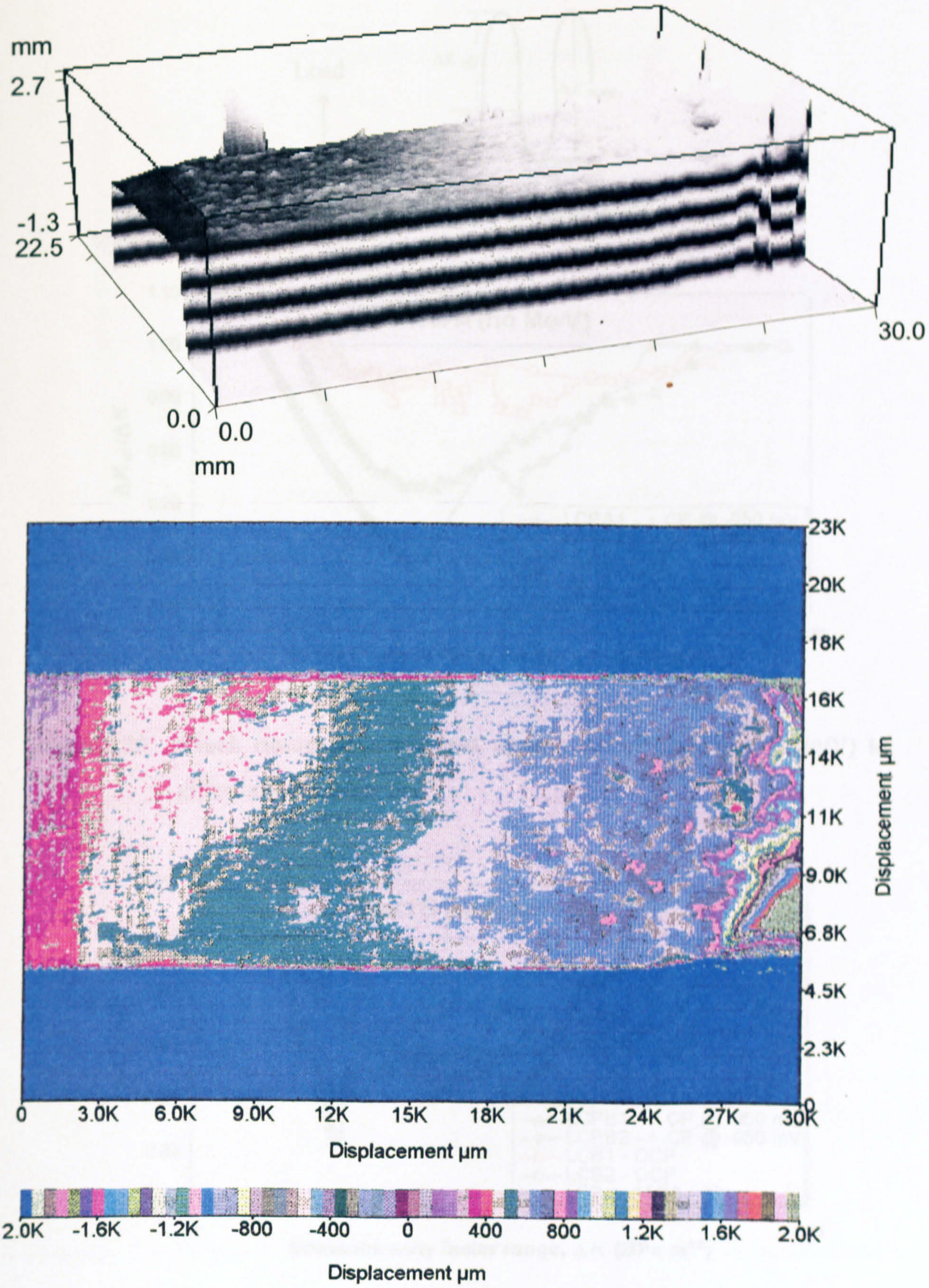

Figure 5.18 Surface roughness outline of fatigue fractured specimen in 3.5%NaCl solution under CP application - Steel A (no Mo/V)

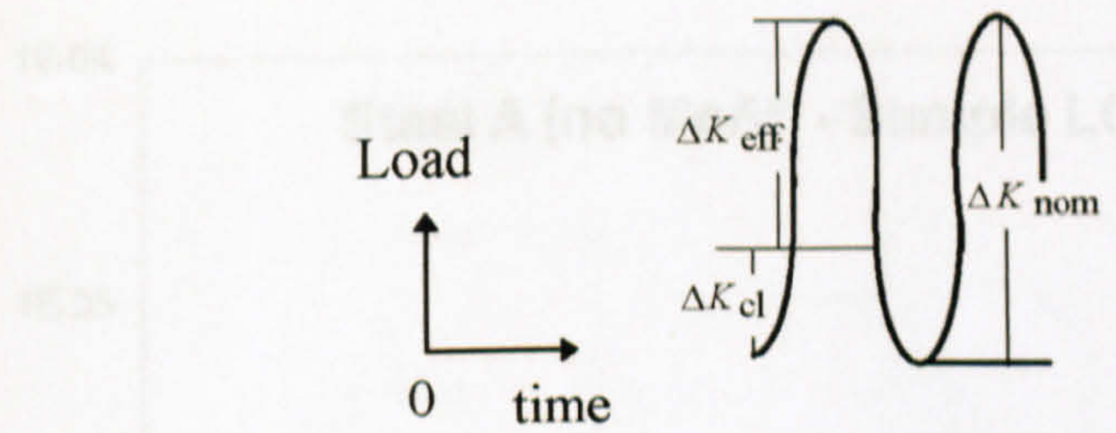

Figure 5.19 Schematic of effective stress intensity factor range

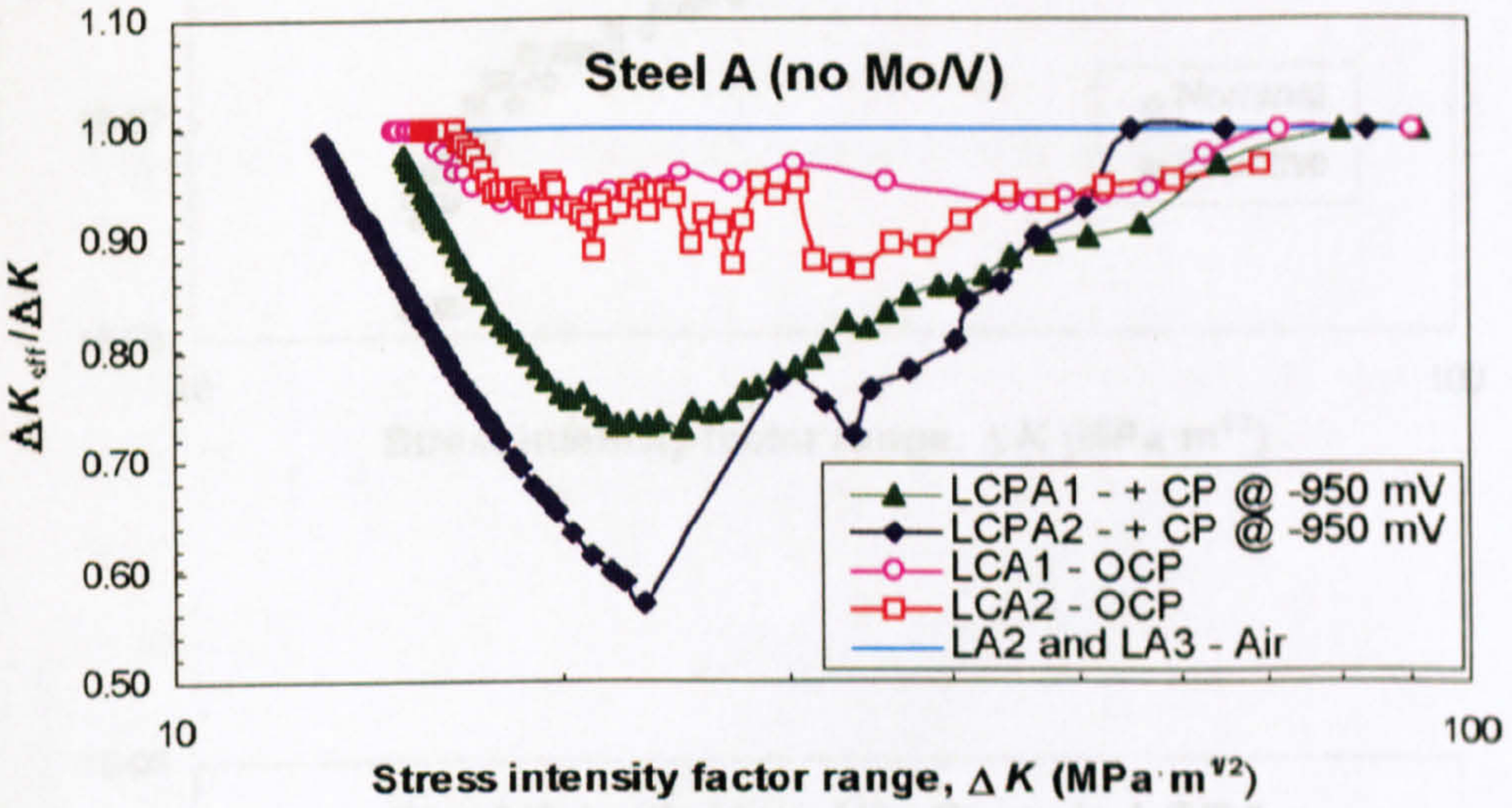

Figure 5.20 Crack closure affect plotted against ΔK of Steel A (no Mo/V) **in different environments**

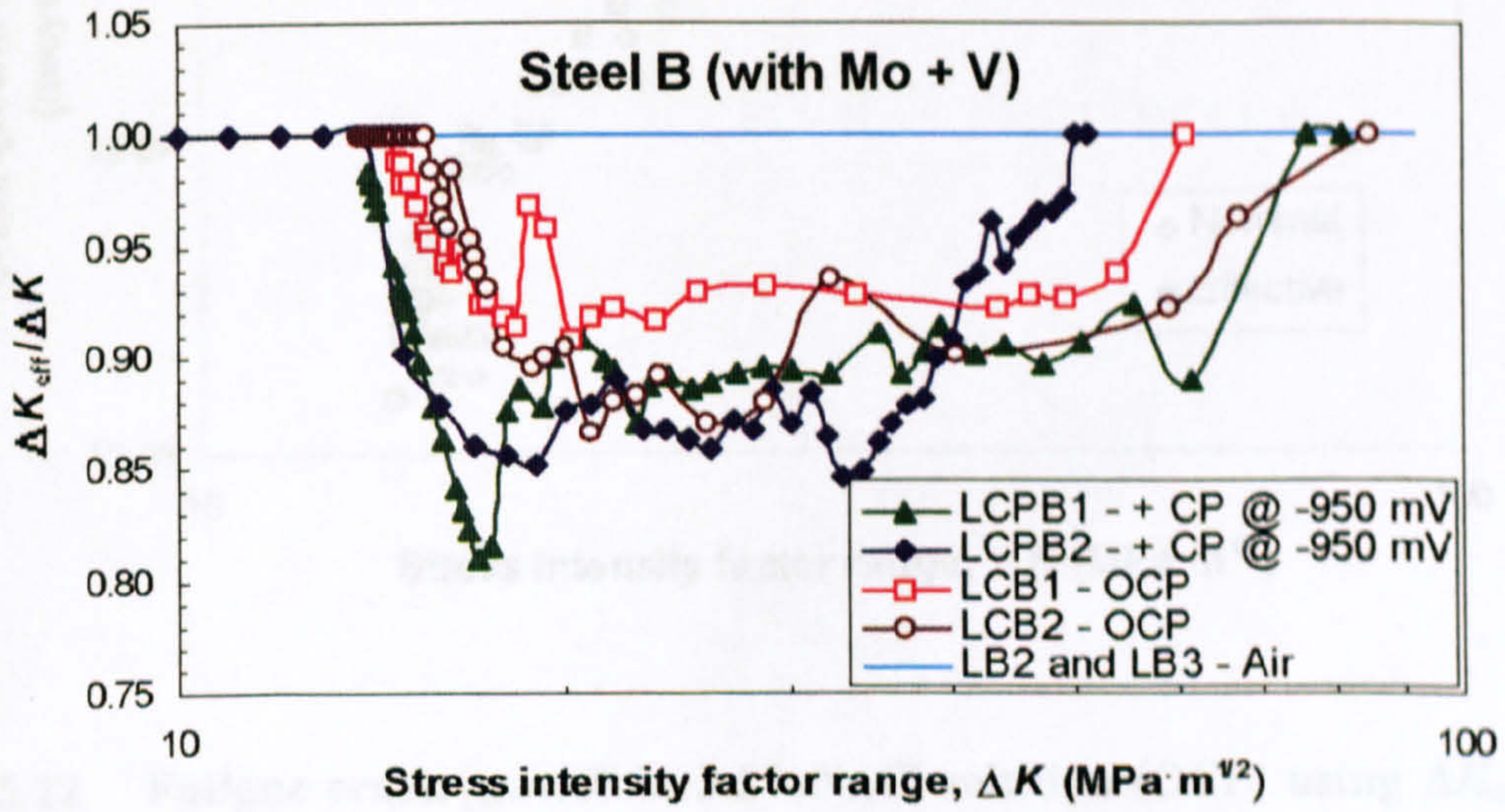

Figure 5.21 Crack closure affect plotted against ΔK of Steel B (with Mo + V) **in different environments**

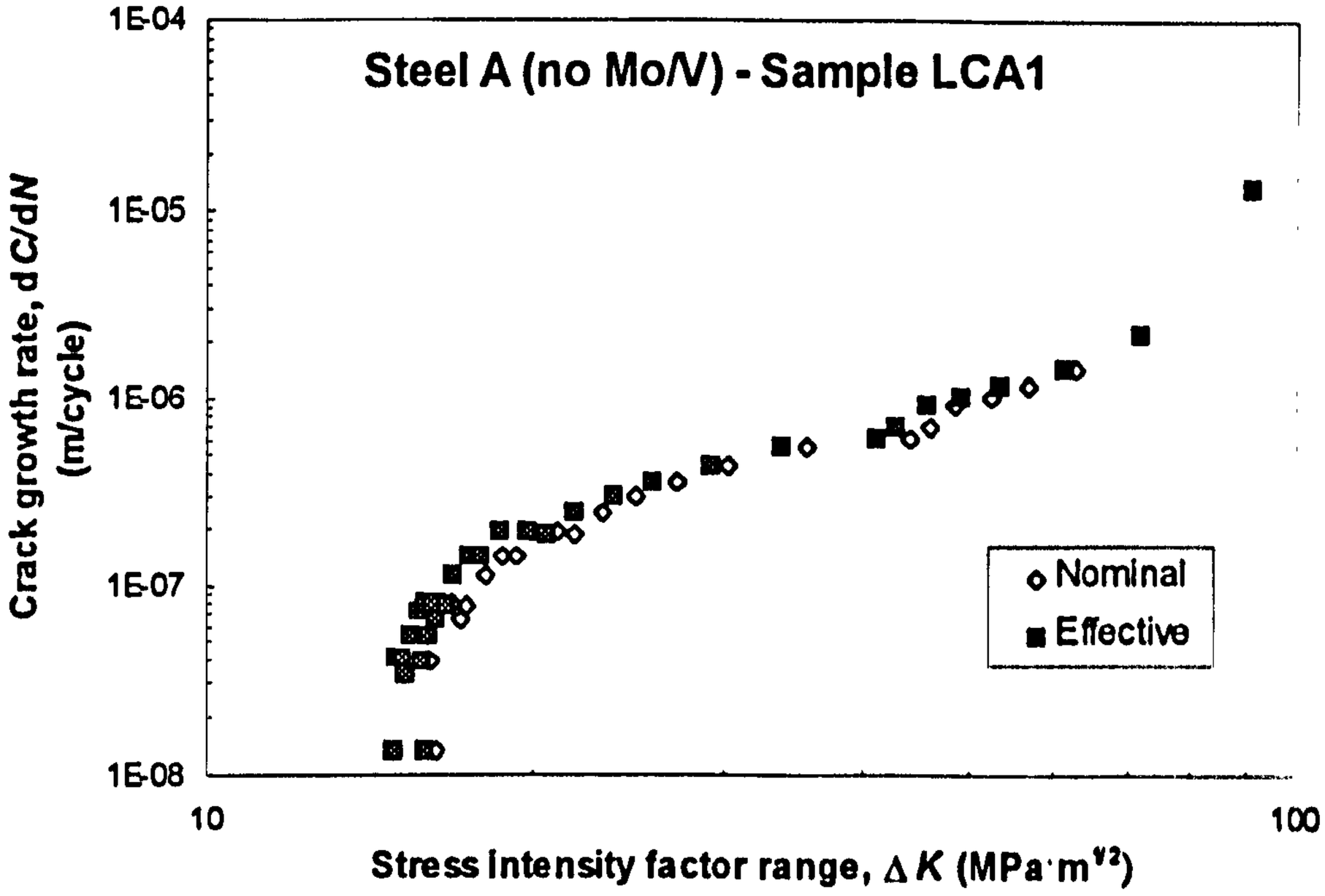

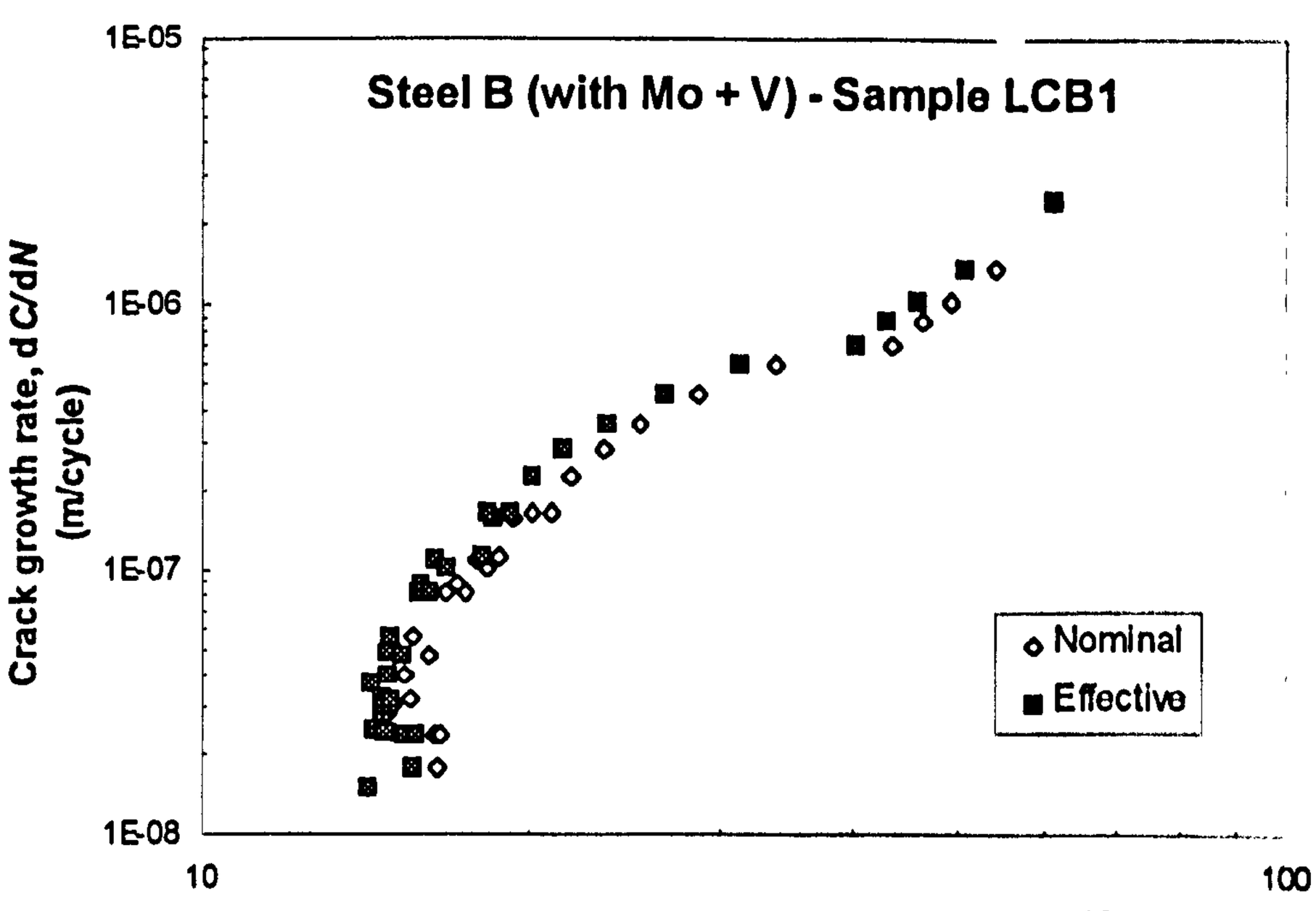

Figure 5.22 **Fatigue crack growth in 3.5%NaCl solution (OCP) using ΔK_{eff} and ΔK (nominal)**

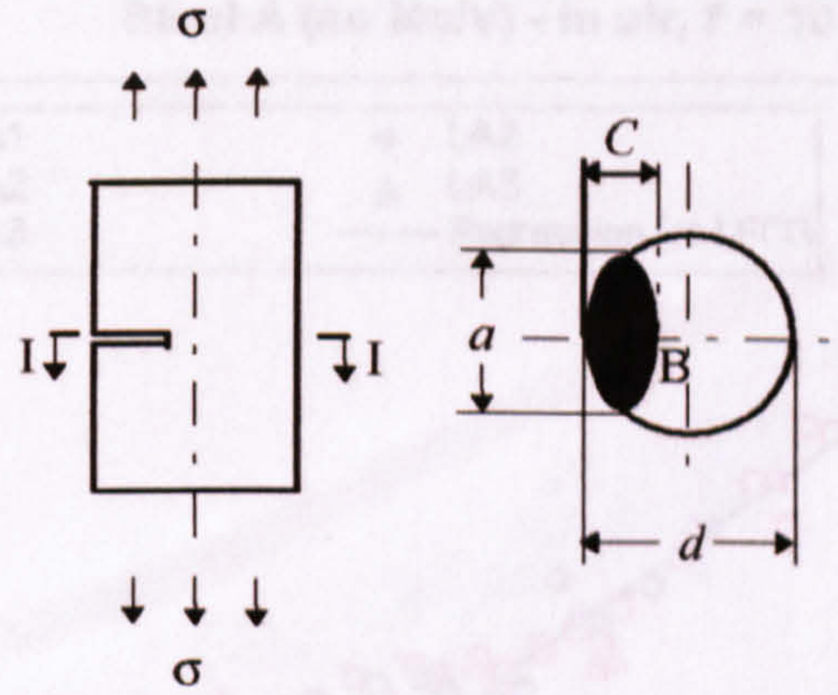

Figure 6.1 A semi-elliptical surface crack under tension

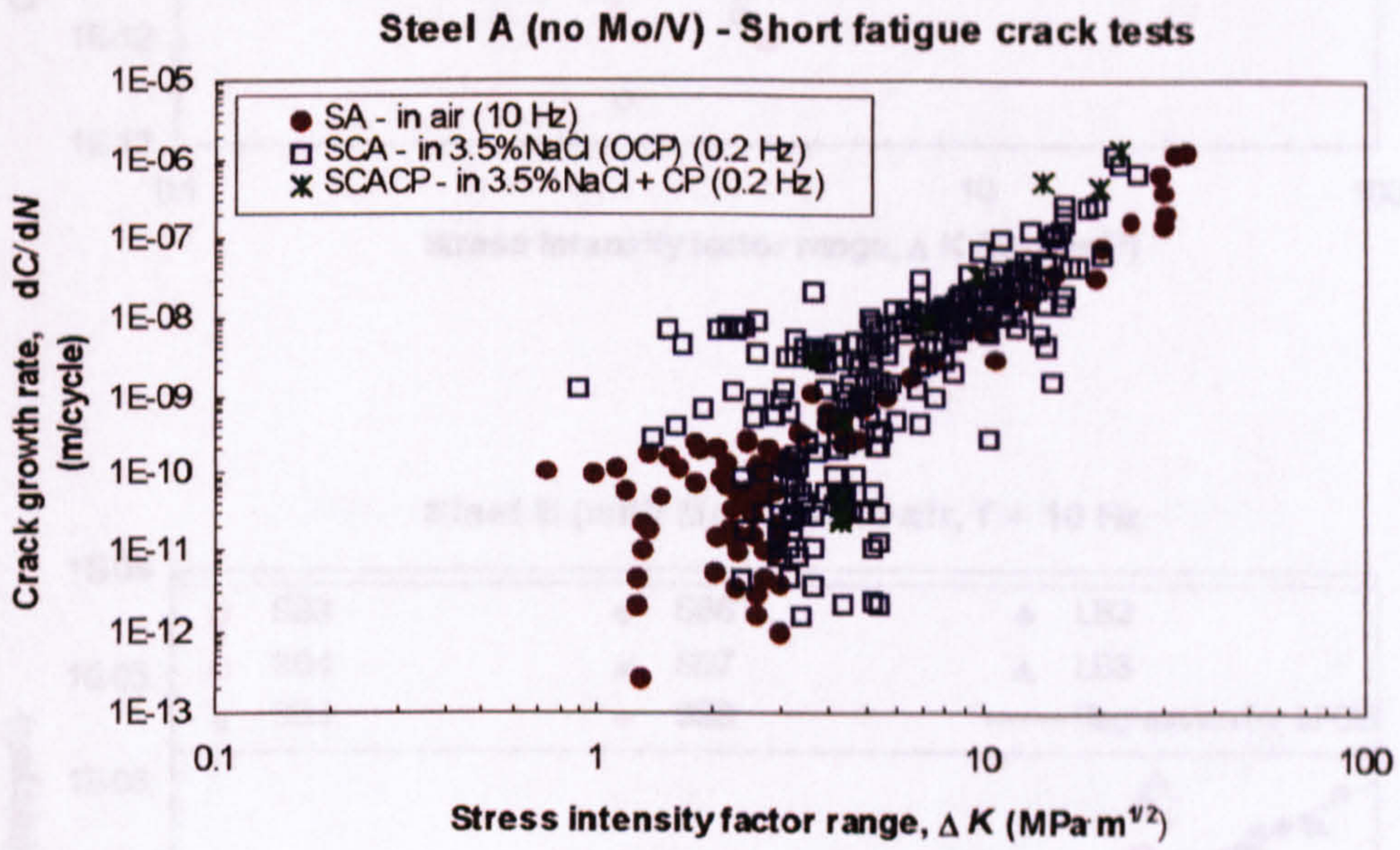

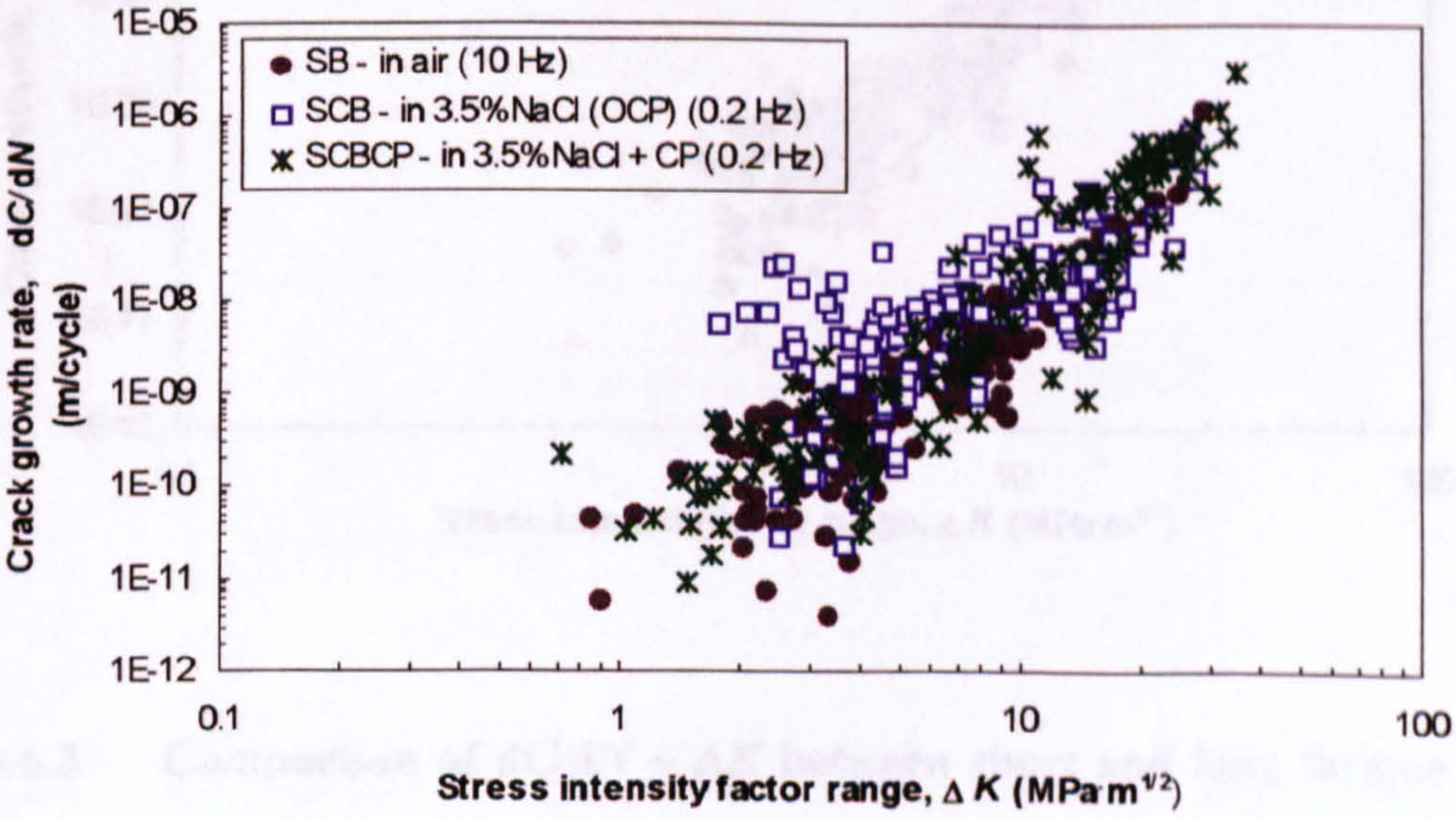

Figure 6.2 Short fatigue crack growth rate versus stress intensity factor range

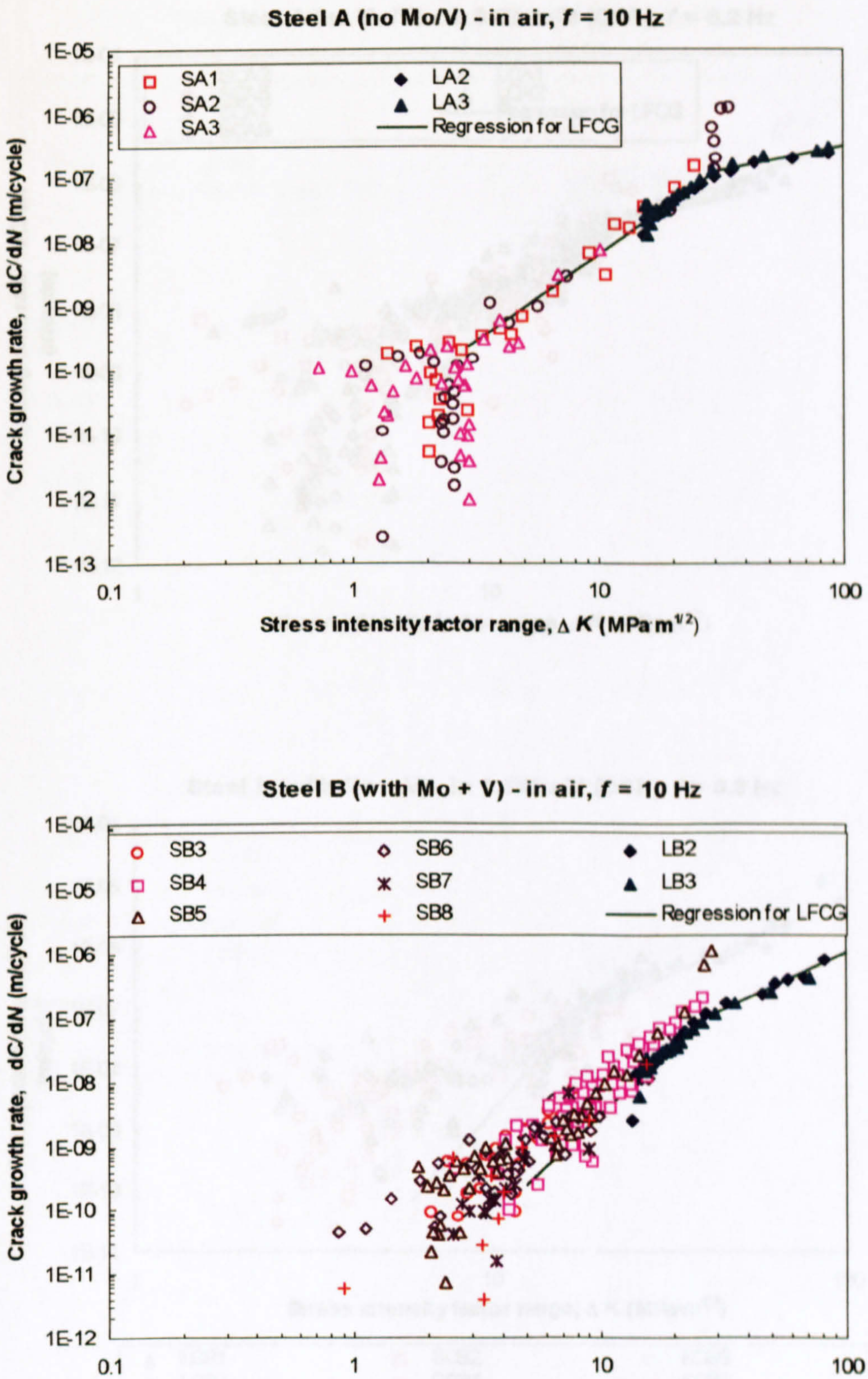

Figure 6.3 **Comparison of dC/dN ~ ΔK between short and long fatigue crack growth rate test results in air**

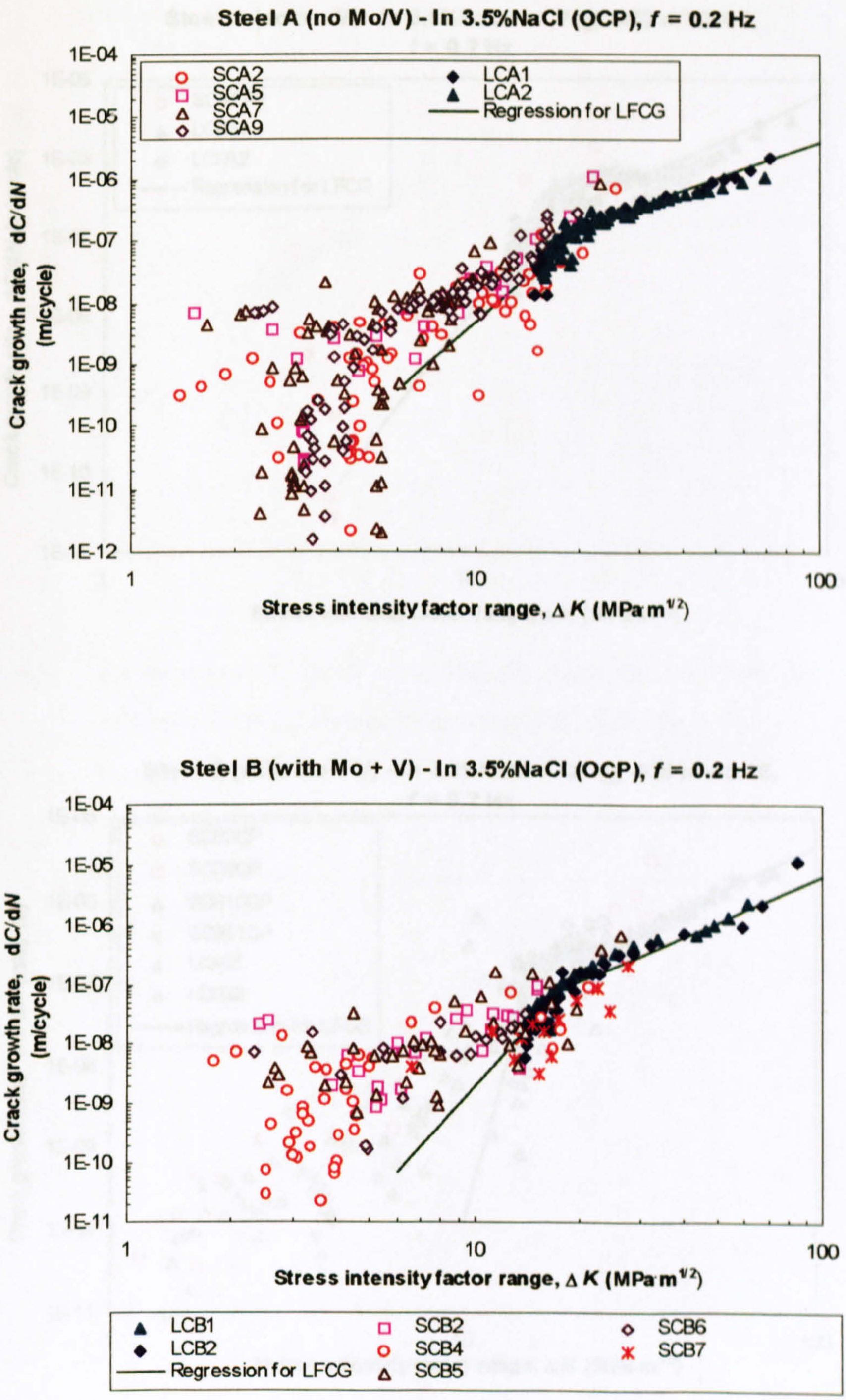

Figure 6.4 **Comparison of dC/dN ~ ΔK between short and long fatigue crack growth rate test results in 3.5%NaCl solution** (OCP)

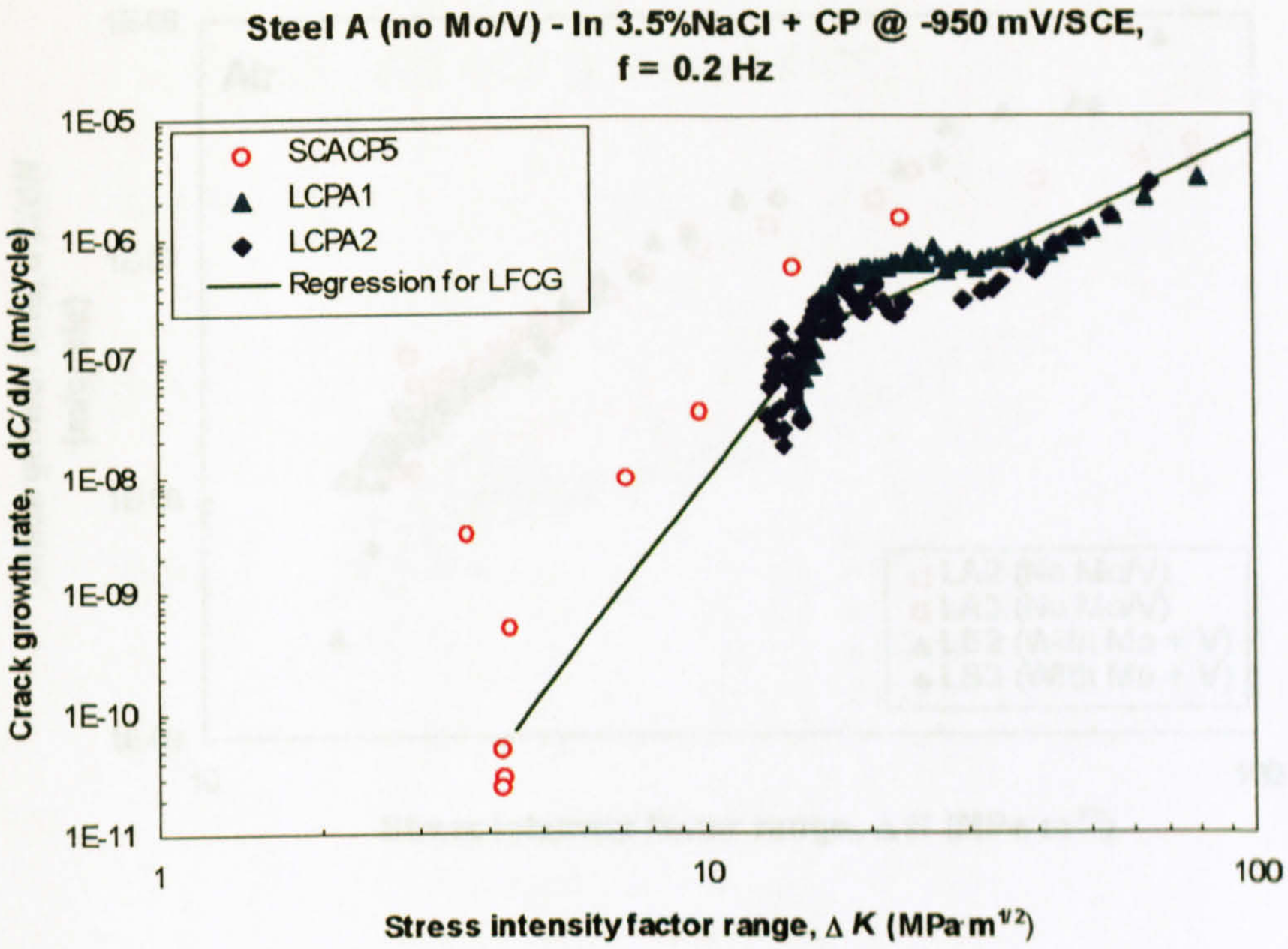

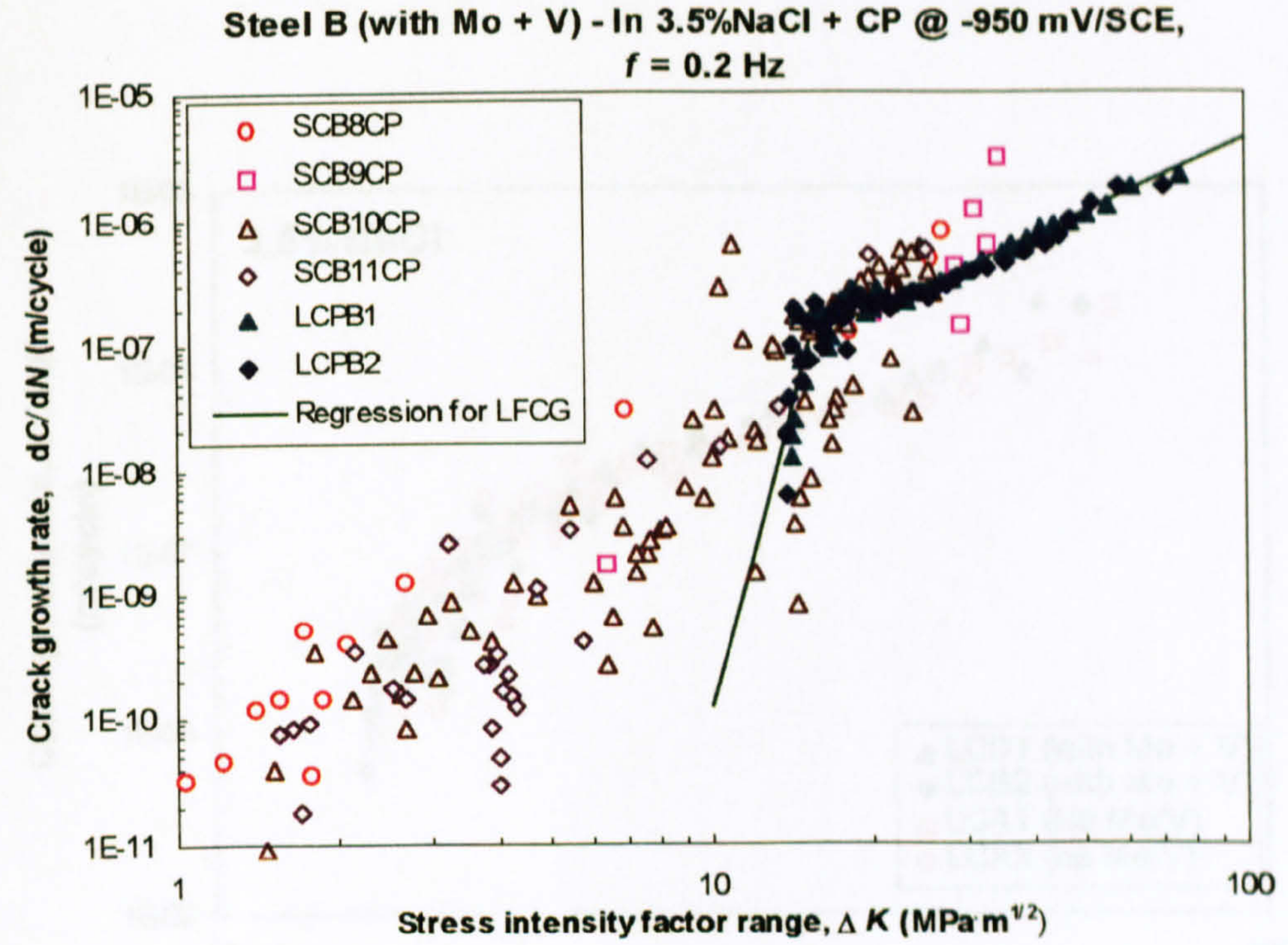

Figure 6.5 **Comparison of dC/dN ~ ΔK between short and long fatigue crack growth rate test results in 3.5%NaCl solution under CP application**

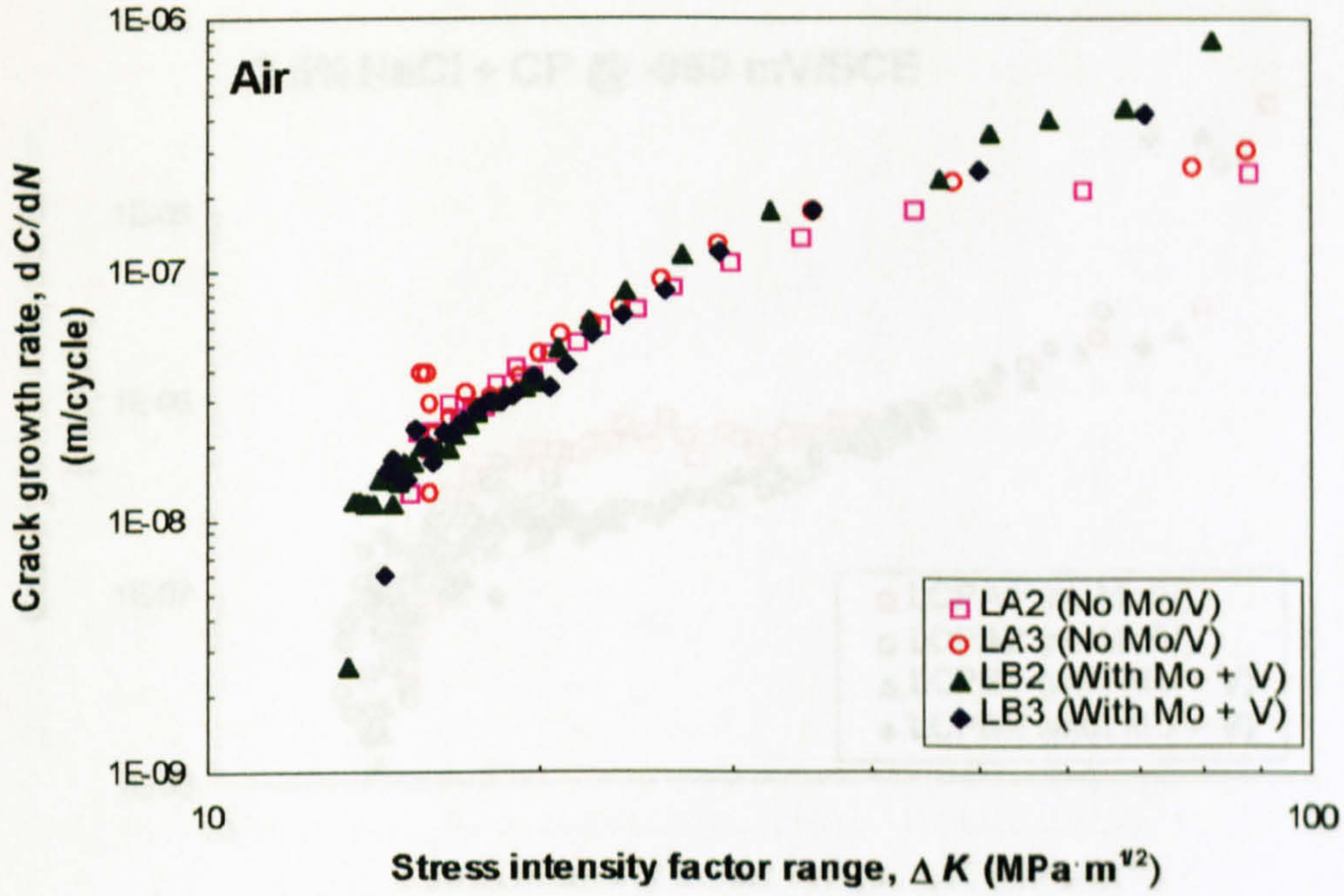

Figure 6.6 **Comparison of in-air long fatigue crack growth rate test results between Steel A** (no Mo/V) **and Steel B** (with Mo + V)

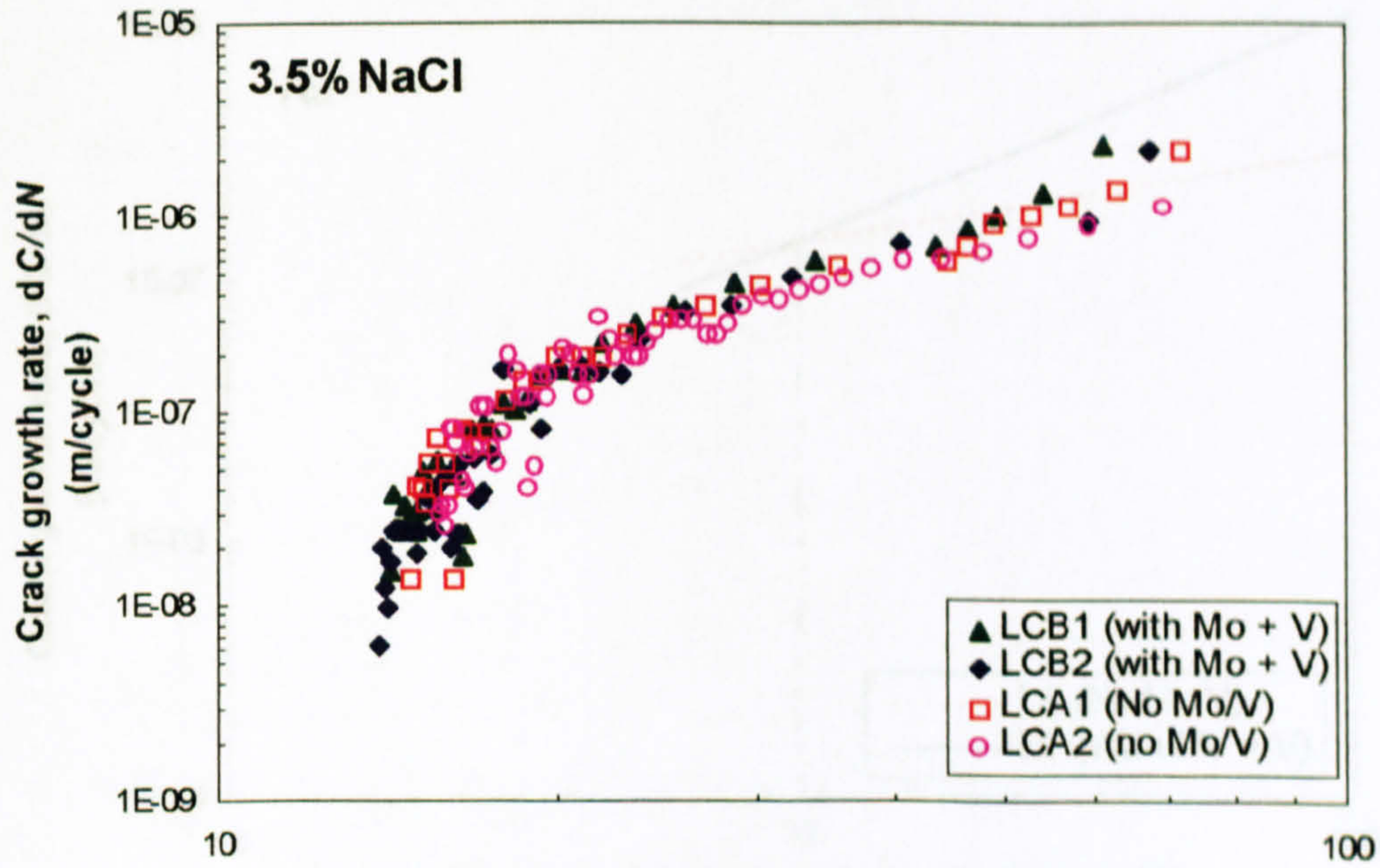

Figure 6.7 **Comparison of long fatigue crack growth rate test results in 3.5%NaCl solution** (OCP) **between Steel A and Steel B**

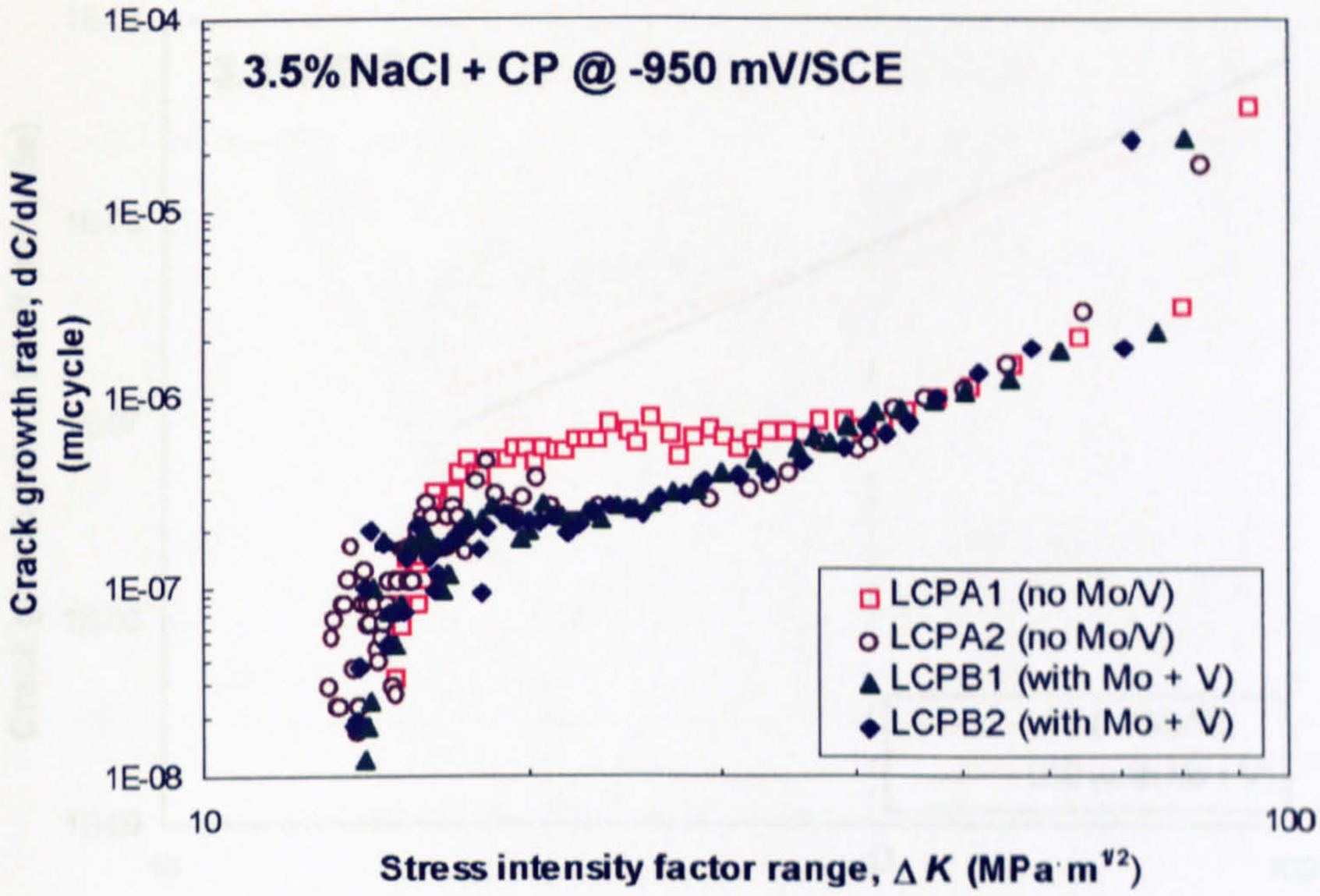

Figure 6.8 **Comparison of long fatigue crack growth rate test results in 3.5%NaCl solution under cathodic polarisation** (-950 mV/SCE) **between Steel A** (no Mo/V) **and Steel B** (with Mo + V)

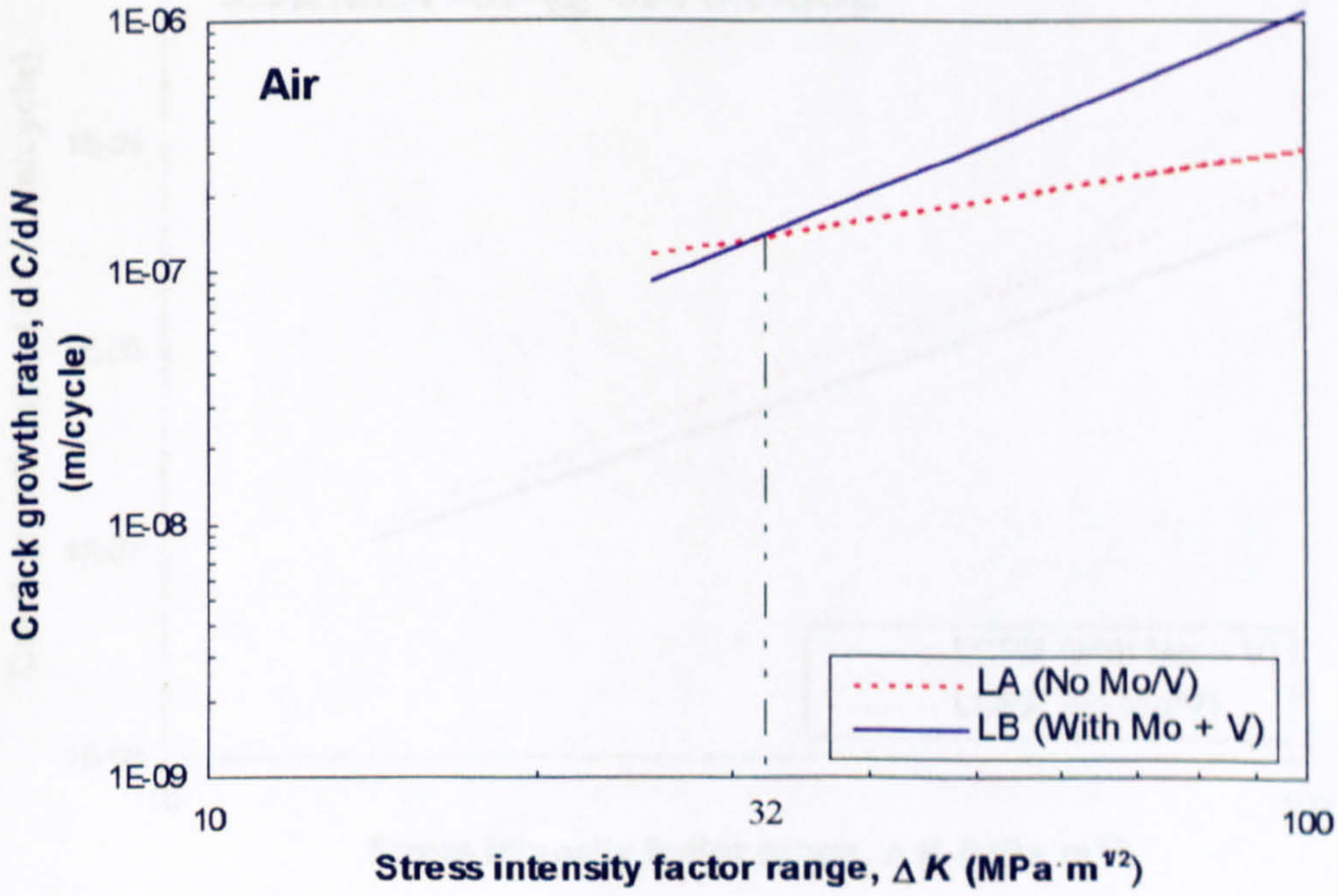

Figure 6.9 **The regression lines and transition point for both steels in air**

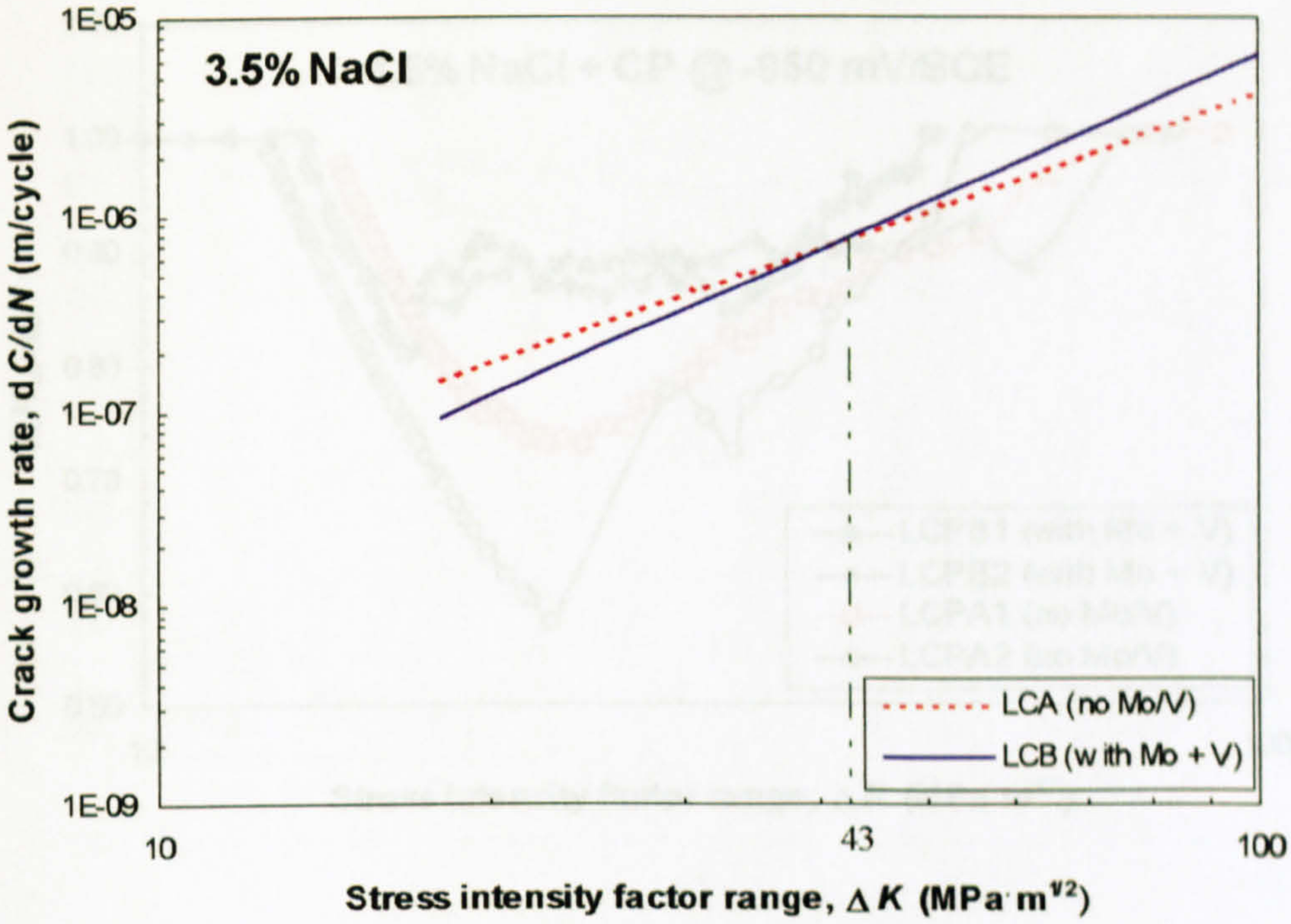

Figure 6.10 **The regression lines and transition point for both steels in 3.5%NaCl solution** (OCP)

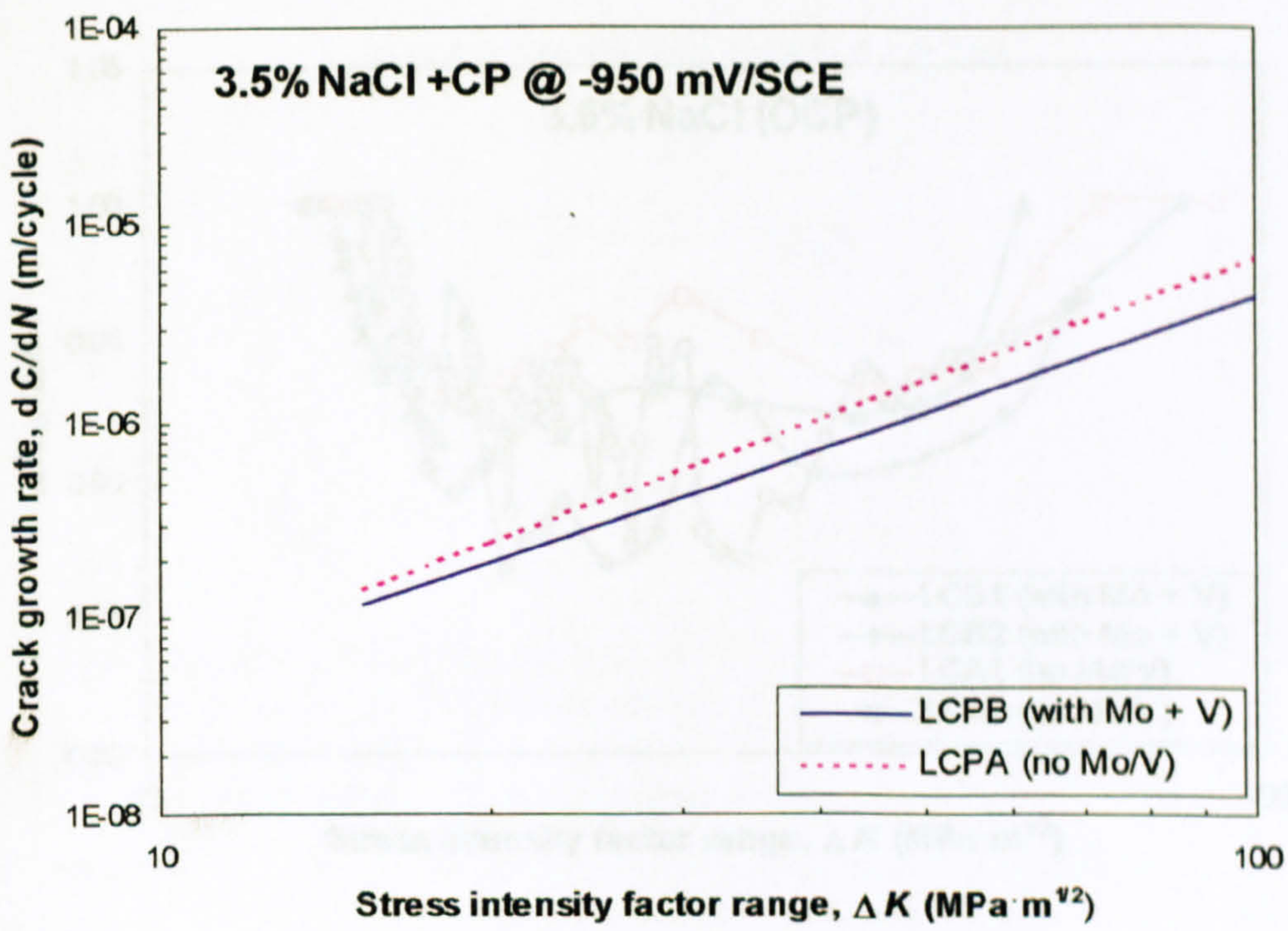

Figure 6.11 **The regression lines and transition point for both steels in 3.5%NaCl solution under CP** (-950 mV/SCE) **application**

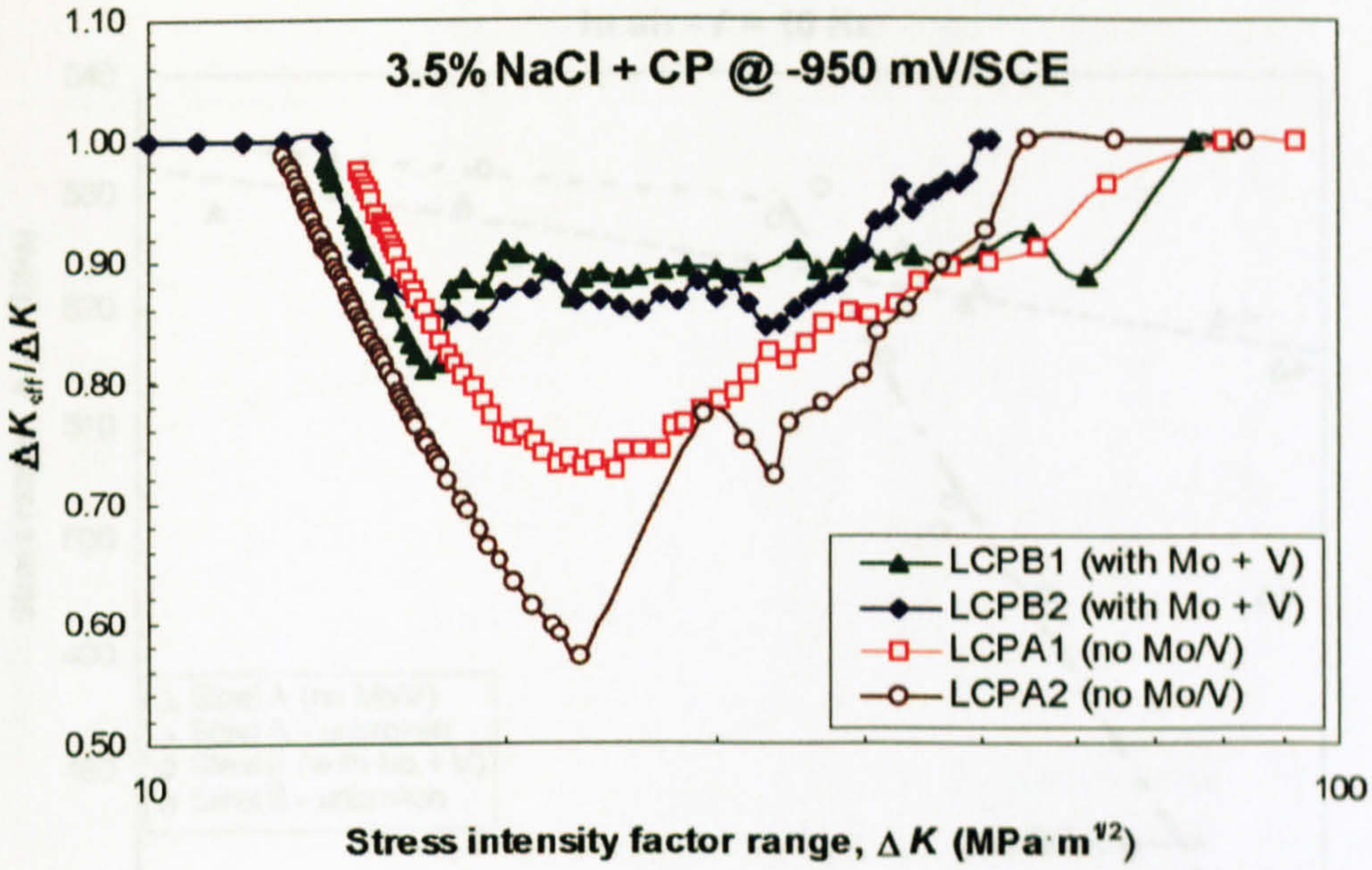

Figure 6.12 **Comparison of crack closure affect plotted against ΔK in 3.5%NaCl solution under CP** (-950 mV/SCE) **application between Steel A** (no Mo/V) **and Steel B** (with Mo + V)

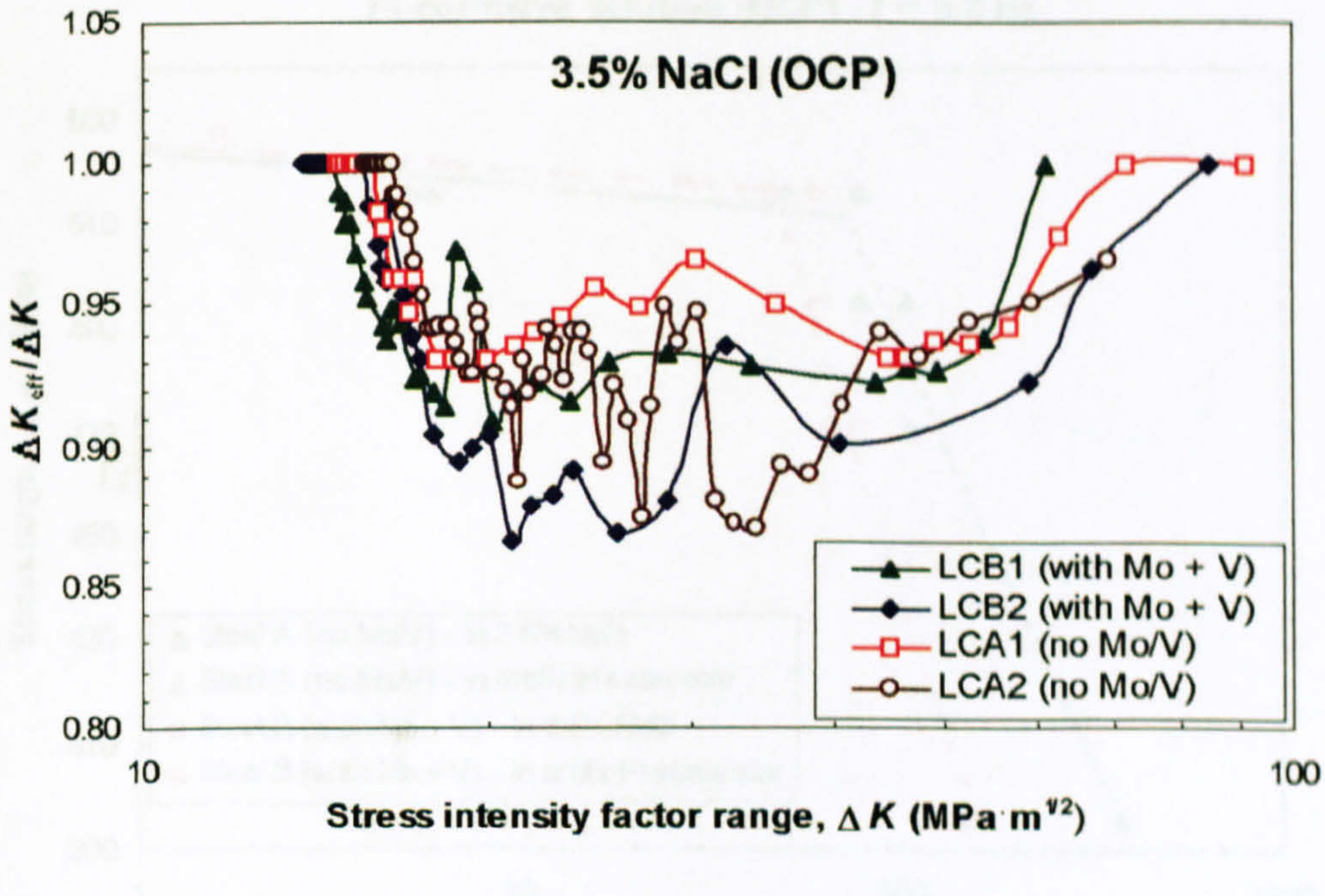

Figure 6.13 **Comparison of crack closure affect plotted against ΔK in 3.5%NaCl solution** (OCP) **between Steel A** (no Mo/V) **and Steel B** (with Mo + V)

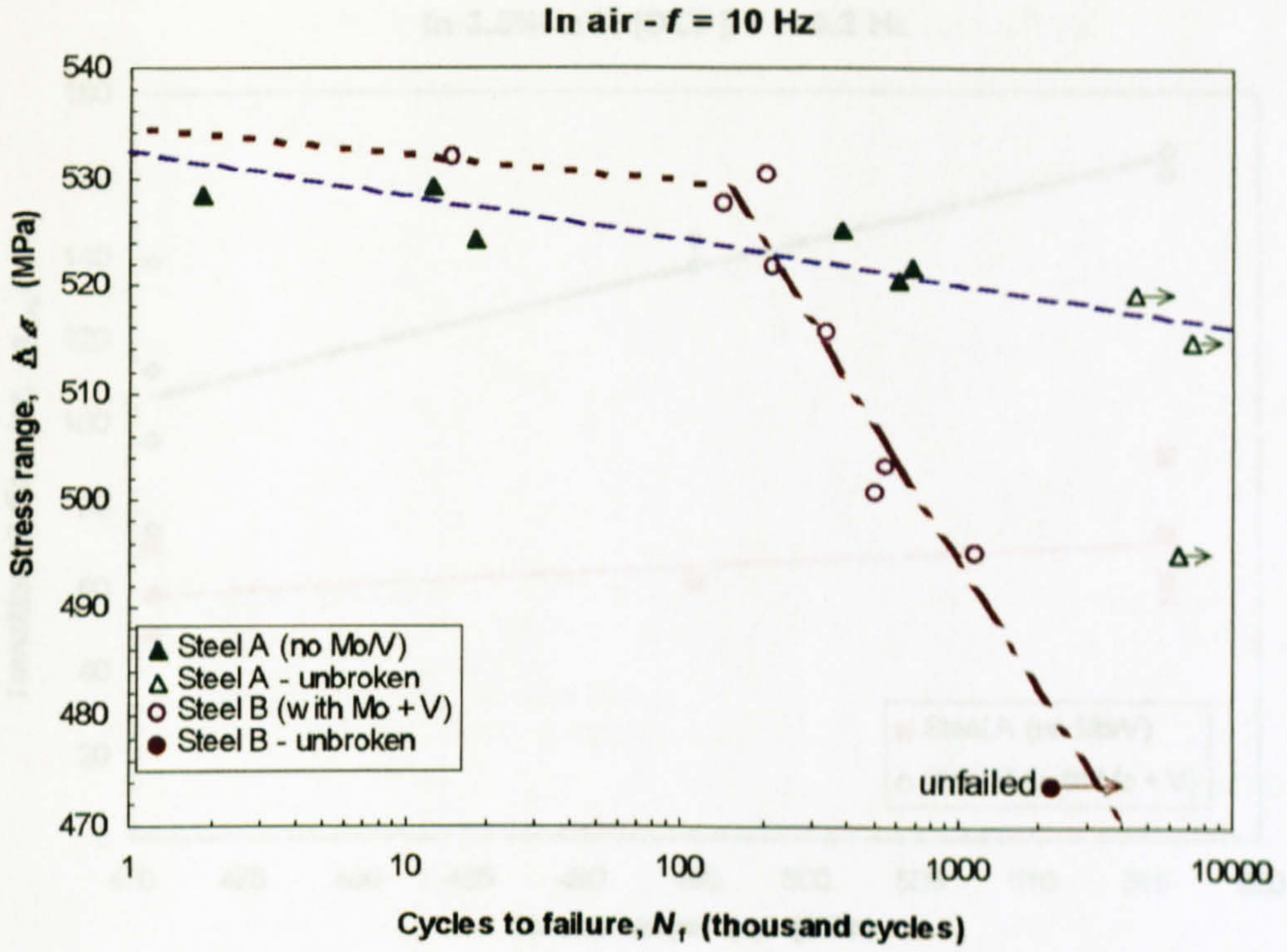

Figure 6.14 **Comparison of in-air $S \sim N_f$ curve between Steel A** (no Mo/V) **and Steel B** (with Mo + V)

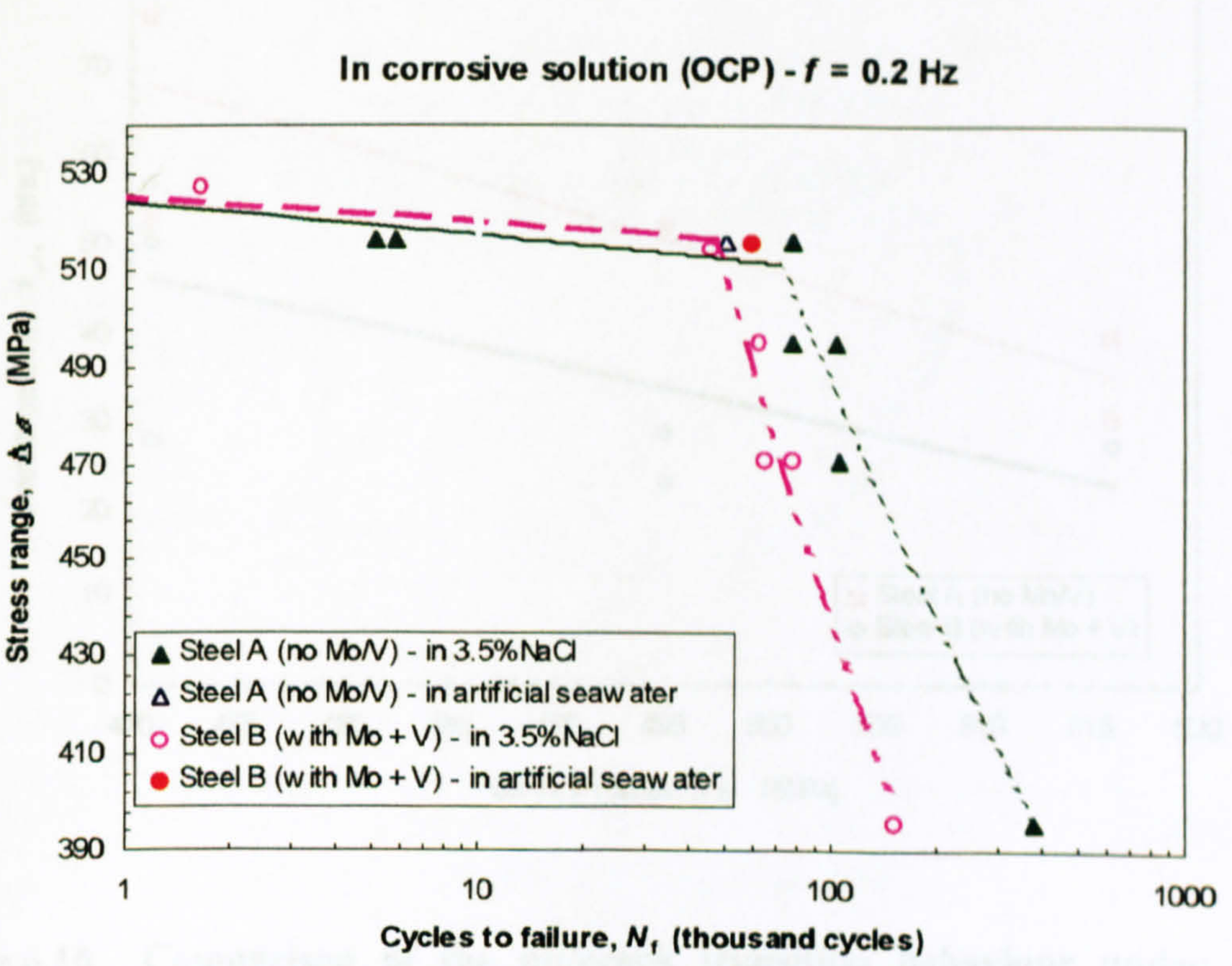

Figure 6.15 **Comparison of $S \sim N_f$ curve in 3.5%NaCl solution** (OCP) **between Steel A** (no Mo/V) **and Steel B** (with Mo + V)

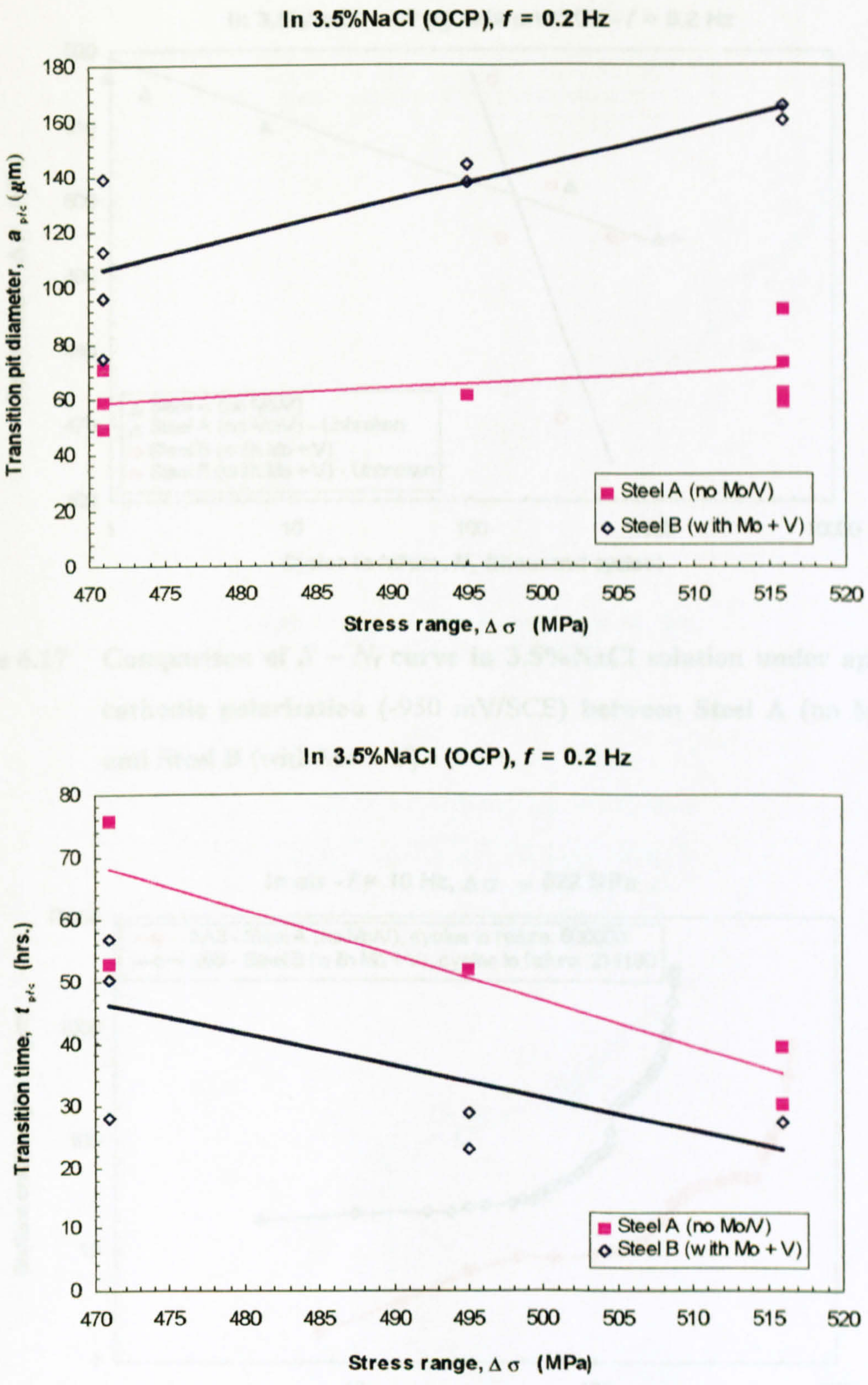

Figure 6.16 Comparison of the pit/crack transition behaviour under cyclic stress in 3.5%NaCl solution (OCP) between Steel A and Steel B

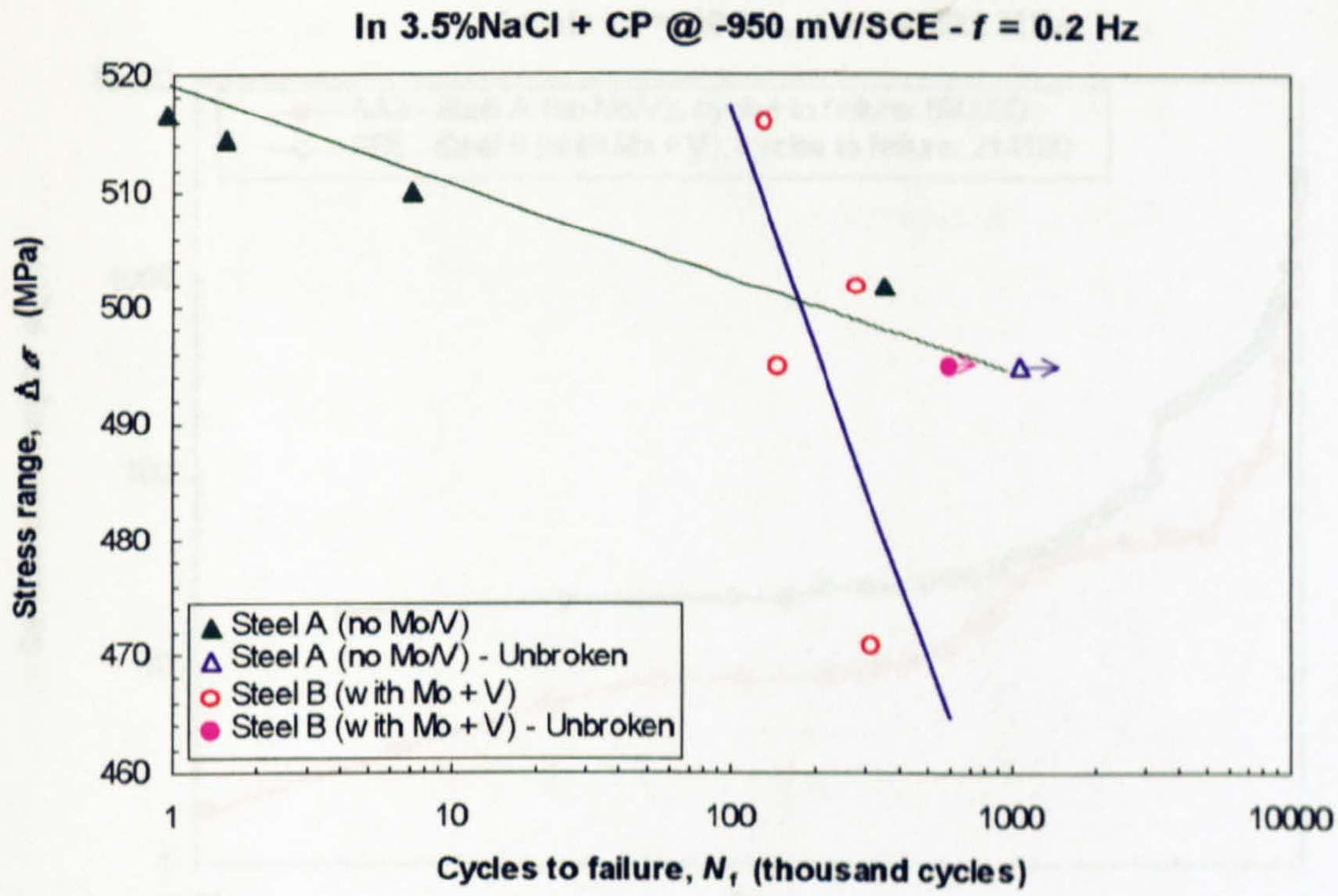

Figure 6.17 **Comparison of $S \sim N_f$ curve in 3.5%NaCl solution under applied cathodic polarisation** (-950 mV/SCE) **between Steel A** (no Mo/V) **and Steel B** (with Mo + V)

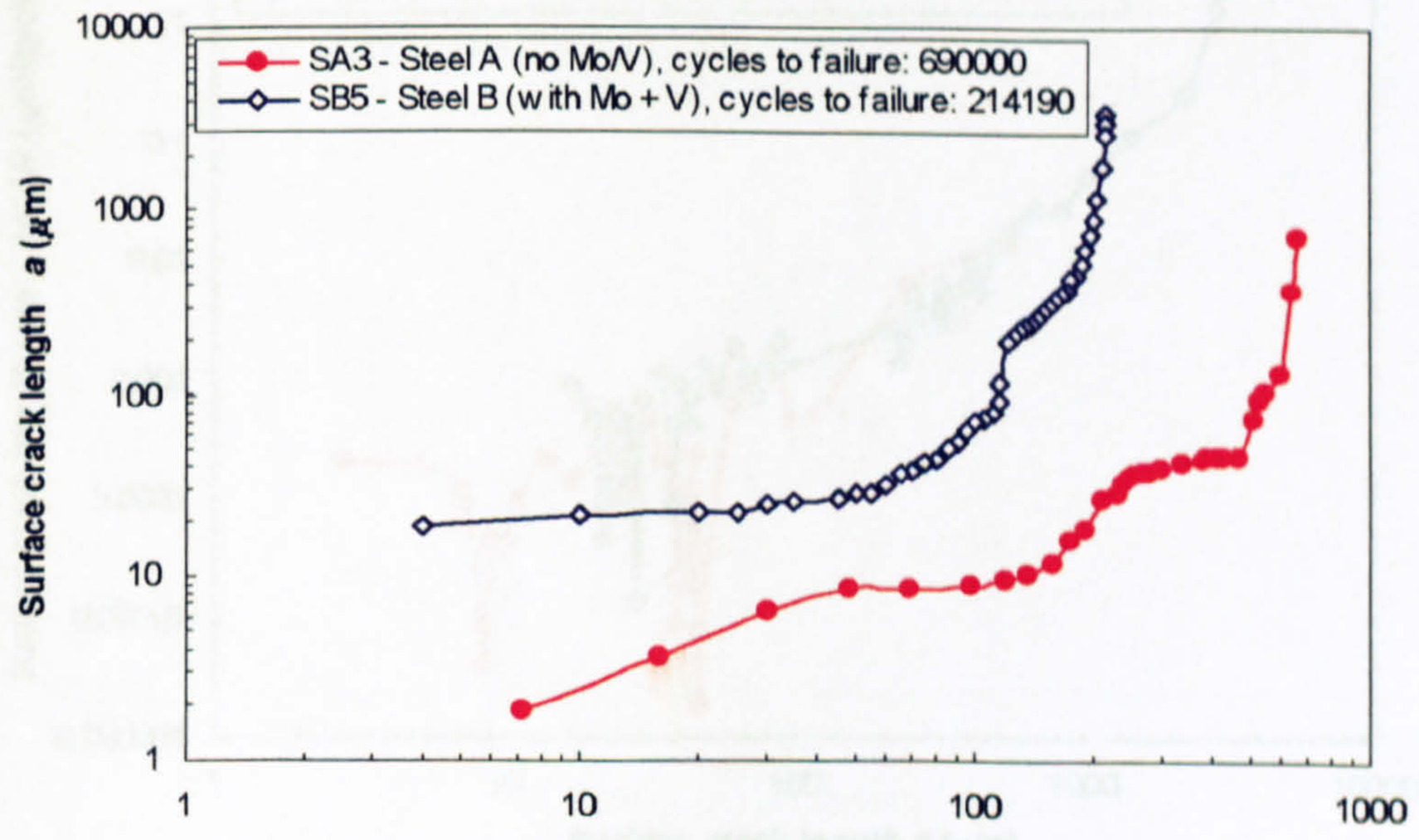

Figure 6.18 **Comparison of in-air $a \sim N$ curve between Steel A** (no Mo/V) **and Steel B** (with Mo + V)

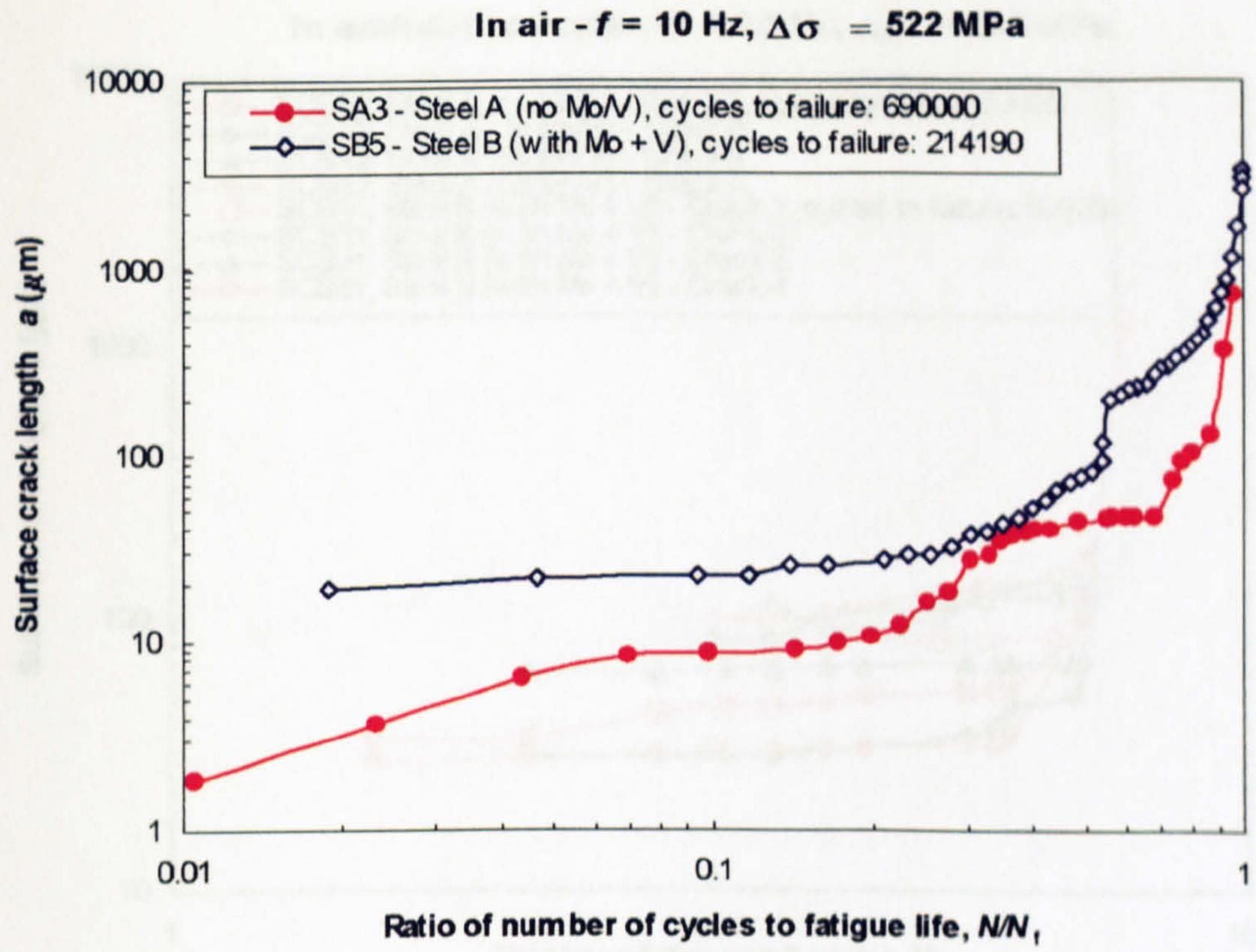

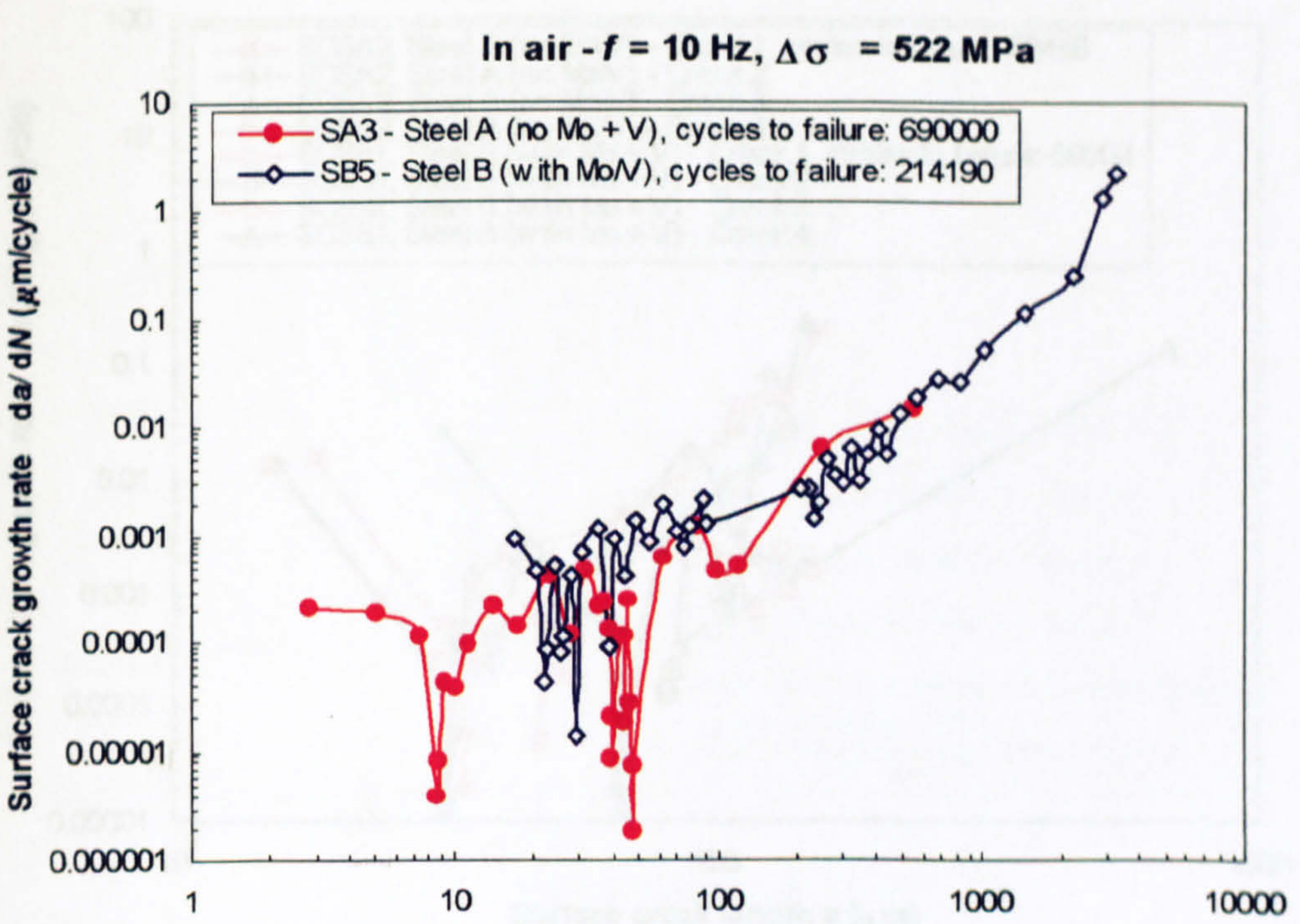

Figure 6.19 Comparison of fatigue crack growth behaviour at $\Delta\sigma$ = 522 MPa between Steel A (no Mo/V) **and Steel B** (with Mo + V)

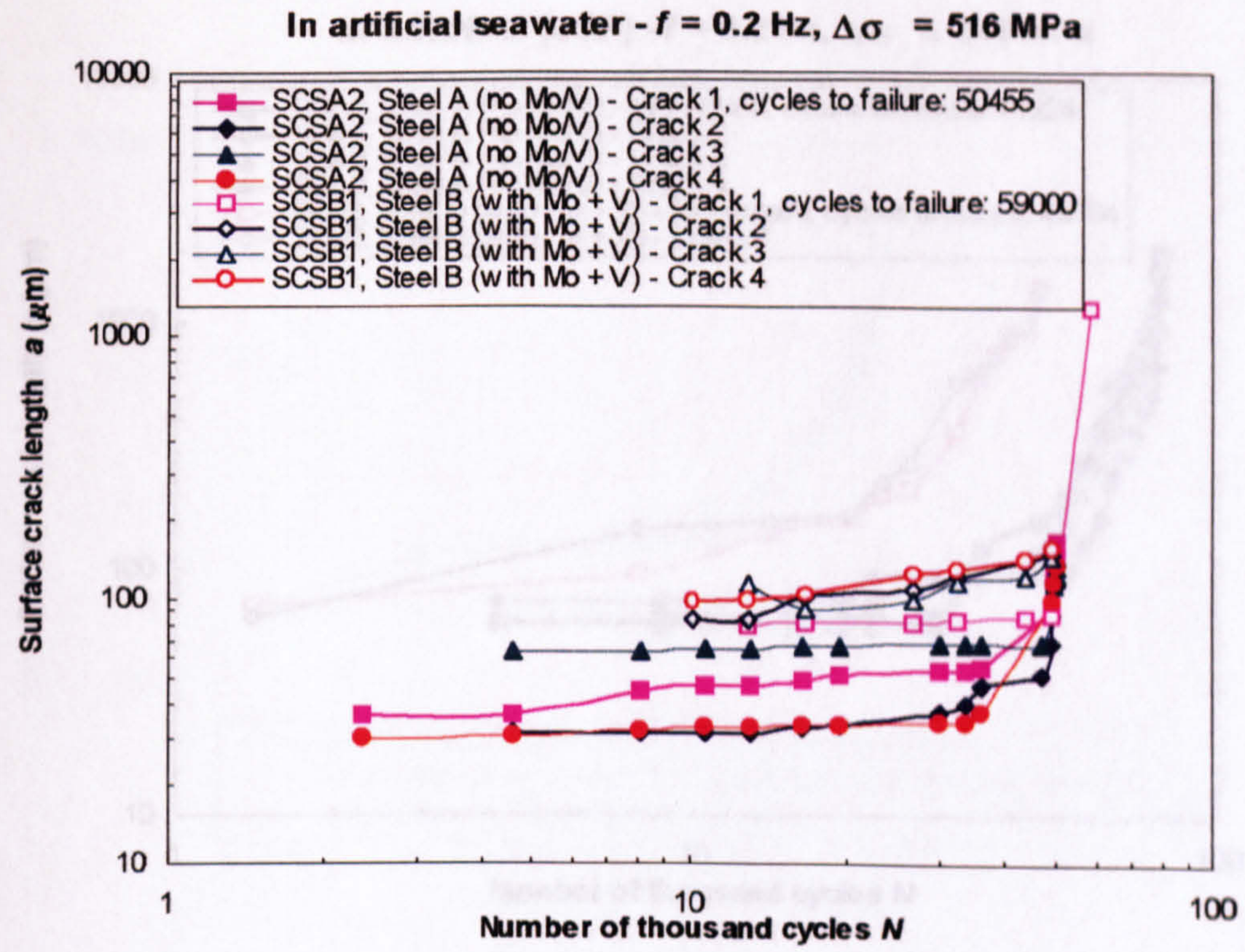

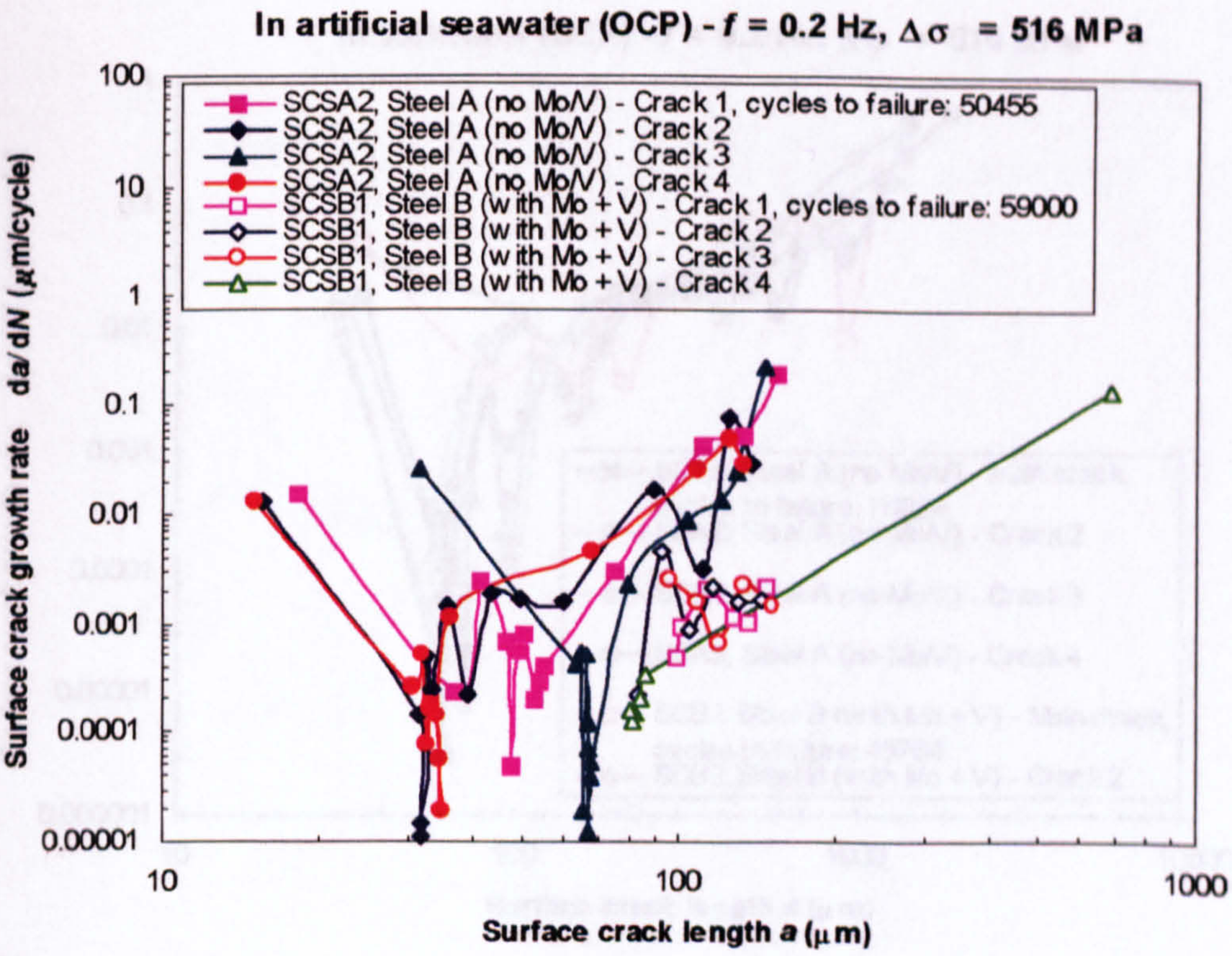

Figure 6.20 **Comparison of fatigue crack growth behaviour in artificial seawater** (OCP) **at** $\Delta\sigma$ **= 516 MPa between Steel A** (no Mo/V) **and Steel B** (with Mo + V)

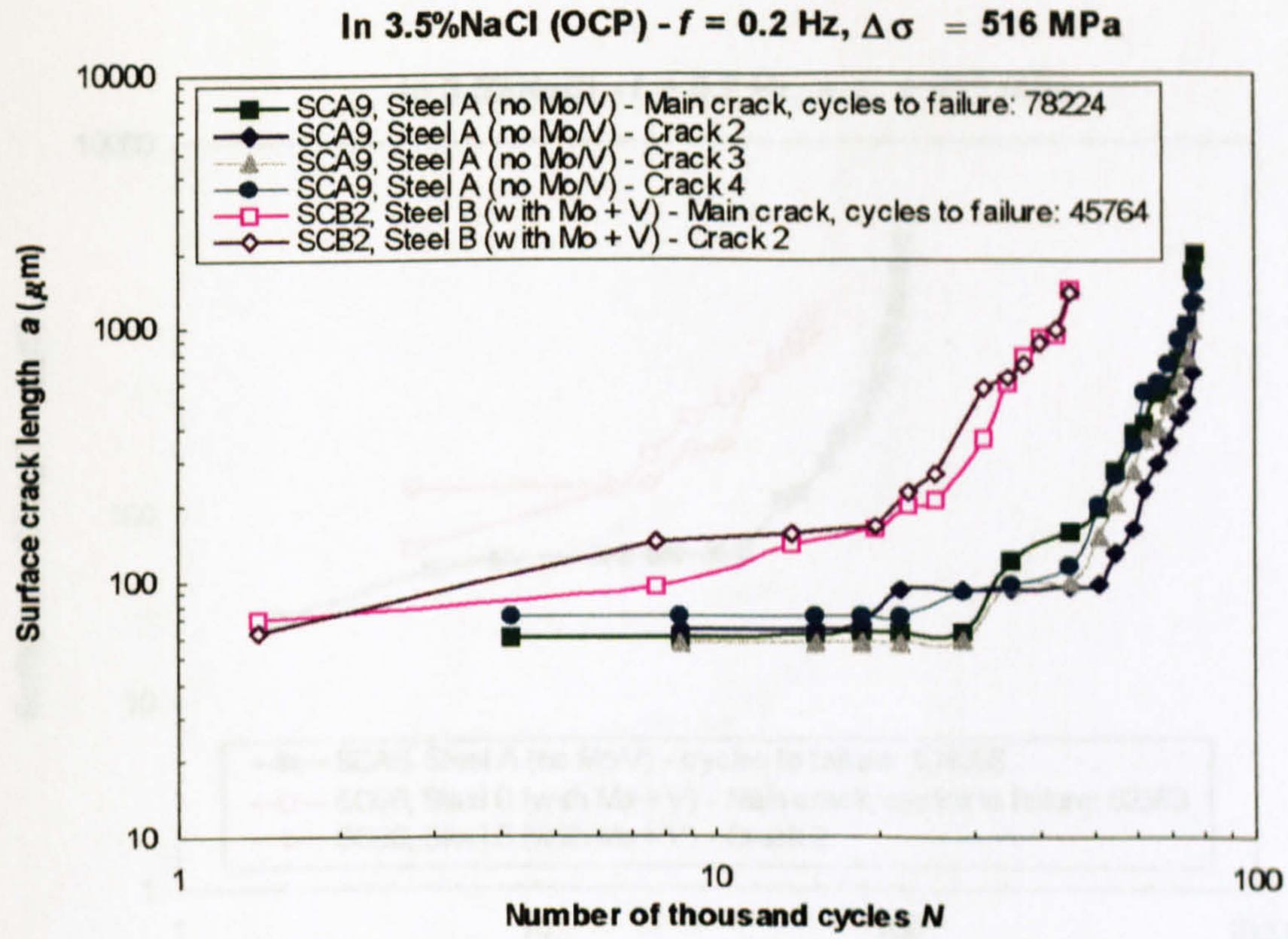

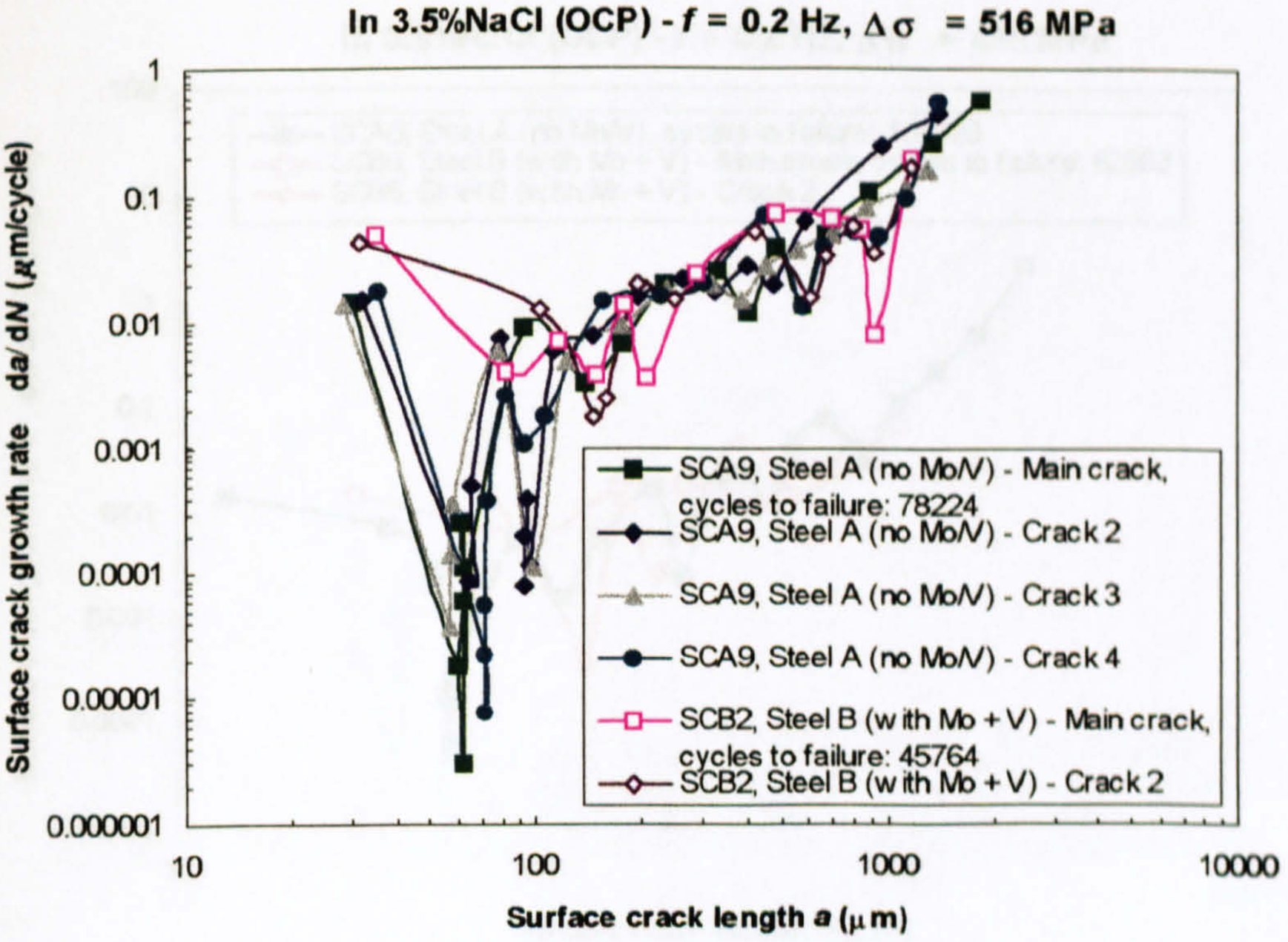

Figure 6.21 **Comparison of fatigue crack growth behaviour in 3.5%NaCl solution** (OCP) **at** $\Delta\sigma$ **= 516 MPa between Steel A** (no Mo/V) **and Steel B** (with Mo + V)

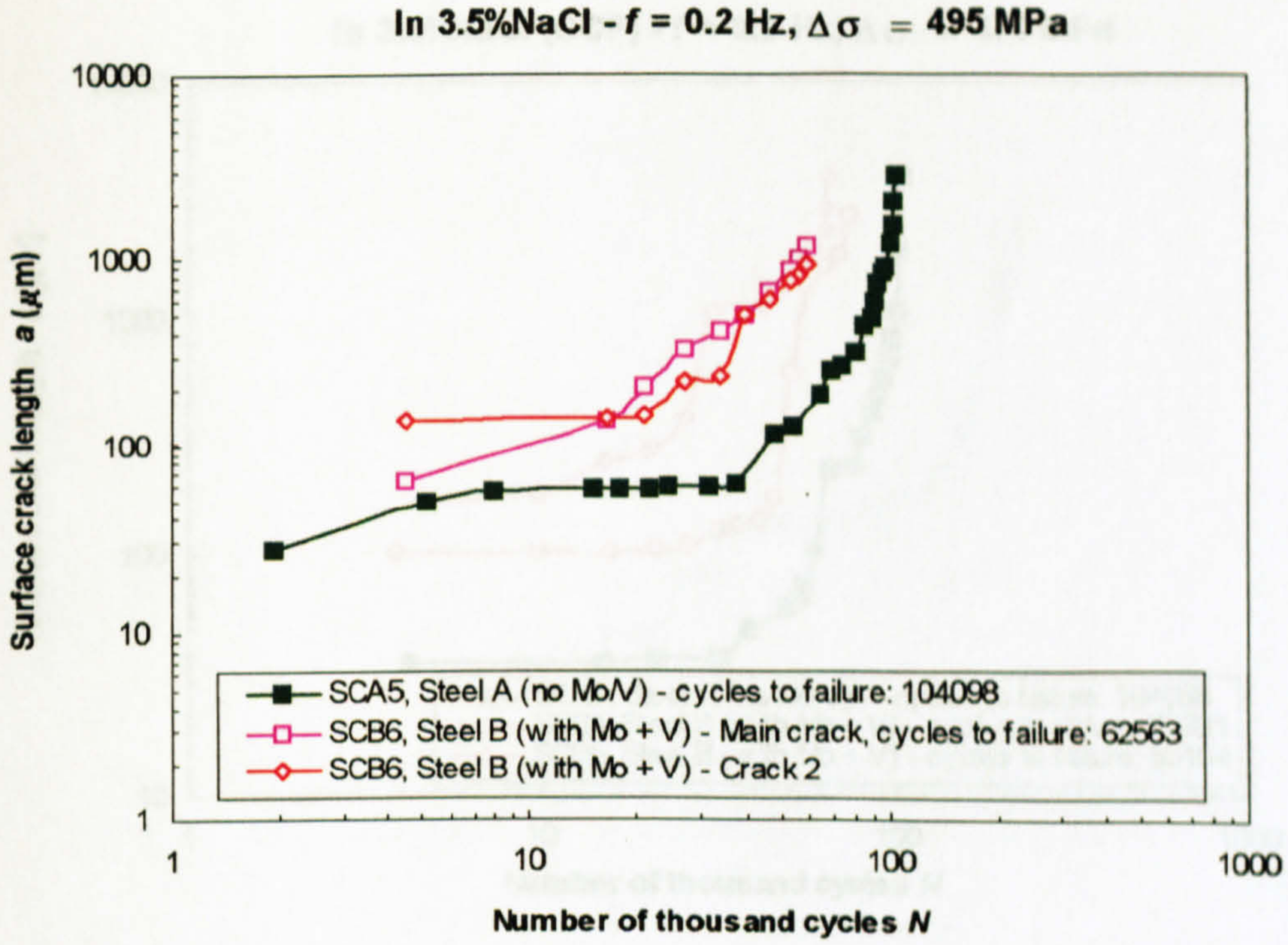

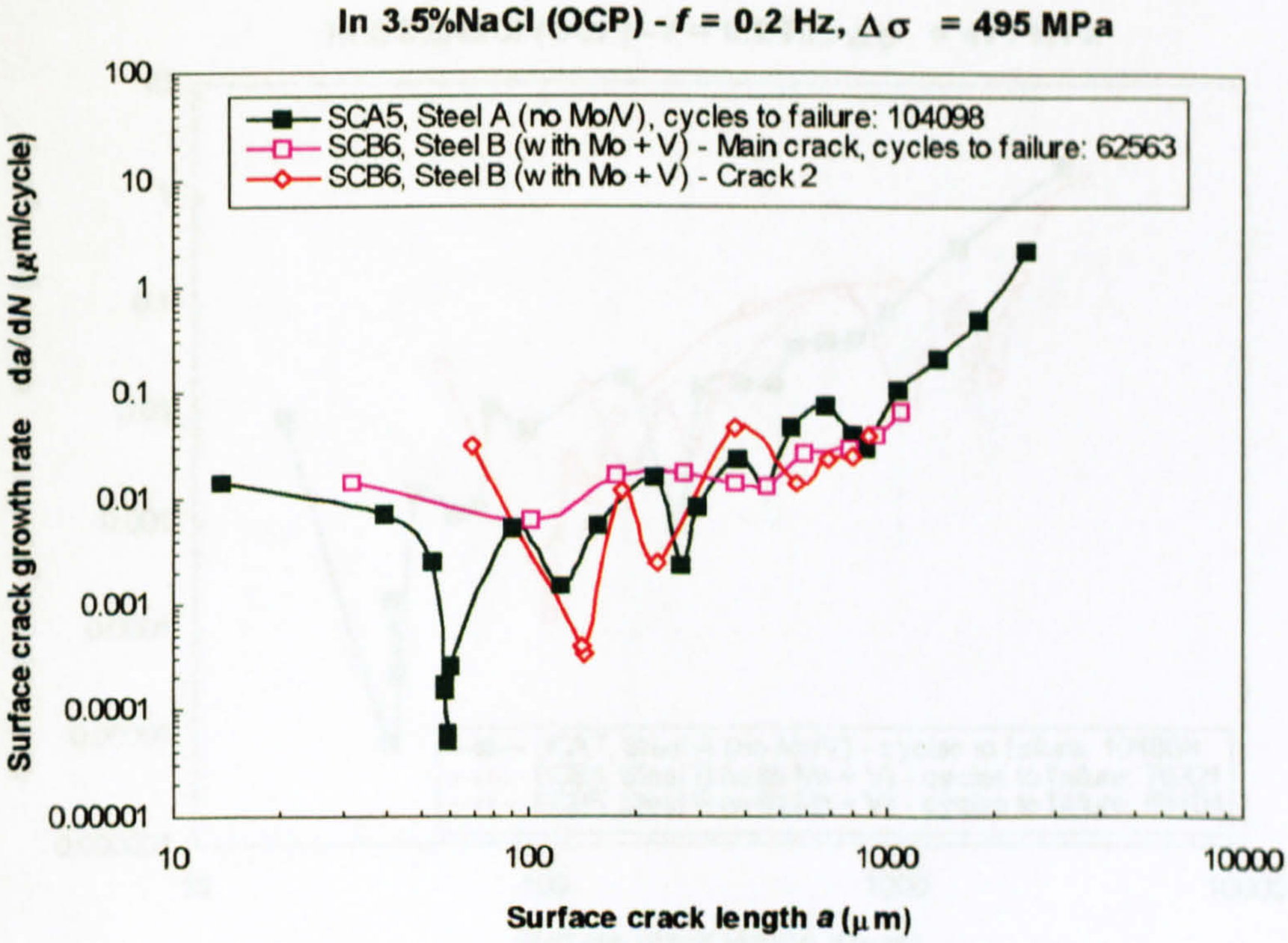

Figure 6.22 **Comparison of fatigue crack growth behaviour in 3.5%NaCl solution** (OCP) **at $\Delta\sigma$ = 495 MPa between Steel A** (no Mo/V) **and Steel B** (with Mo + V)

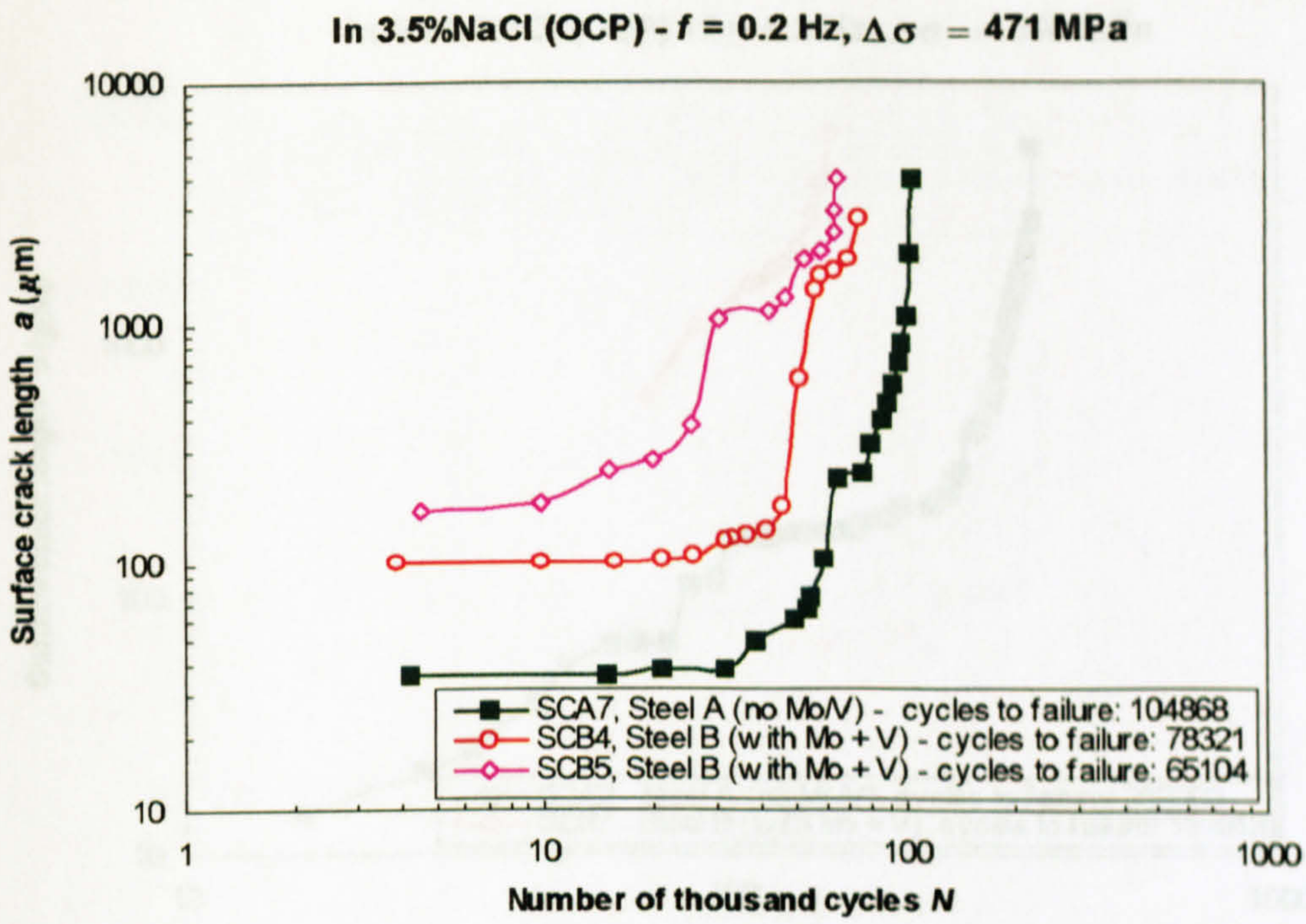

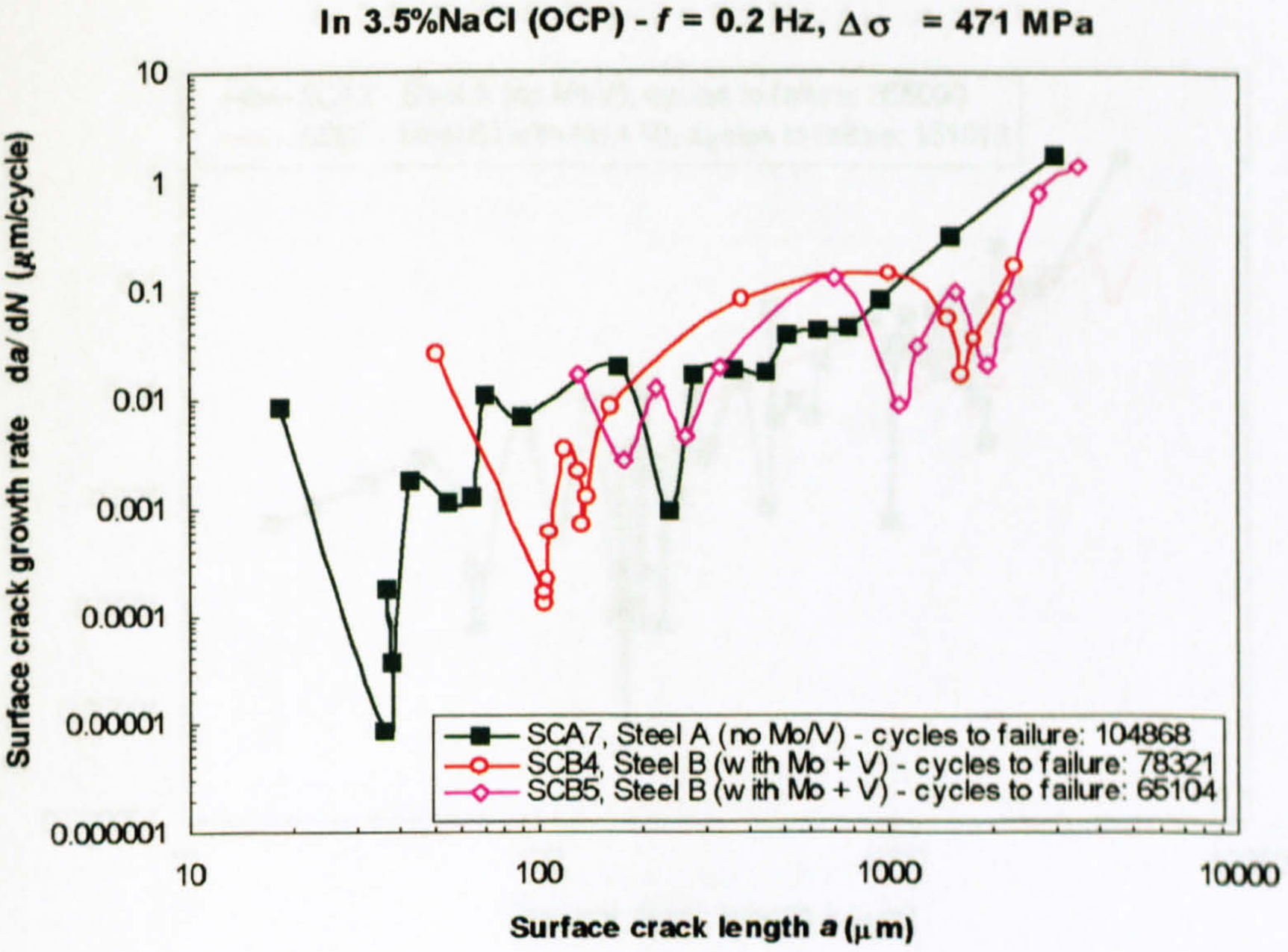

Figure 6.23 **Comparison of fatigue crack growth behaviour in 3.5%NaCl solution** (OCP) **at $\Delta\sigma$ = 471 MPa between Steel A** (no Mo/V) **and Steel B** (with Mo + V)

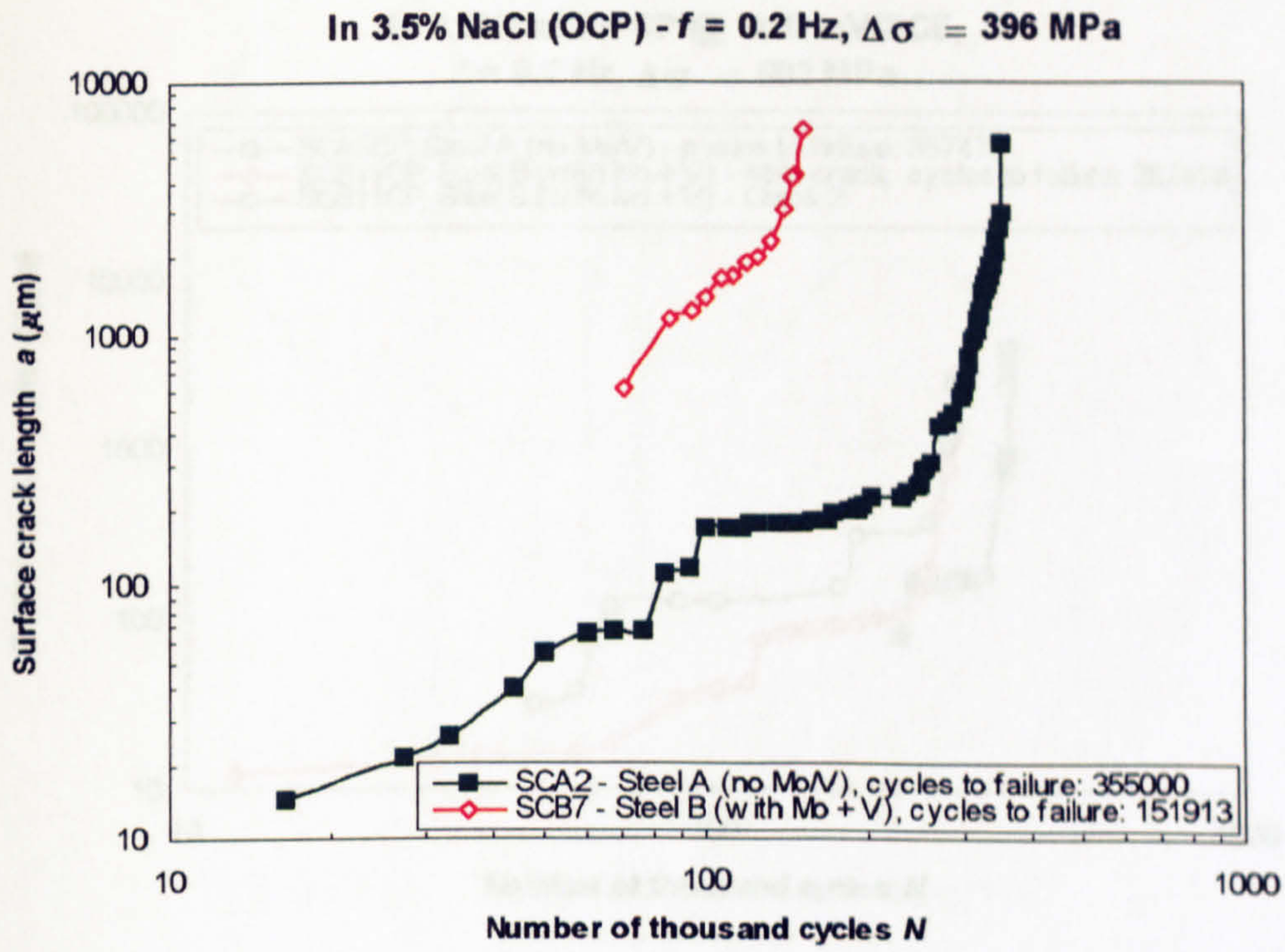

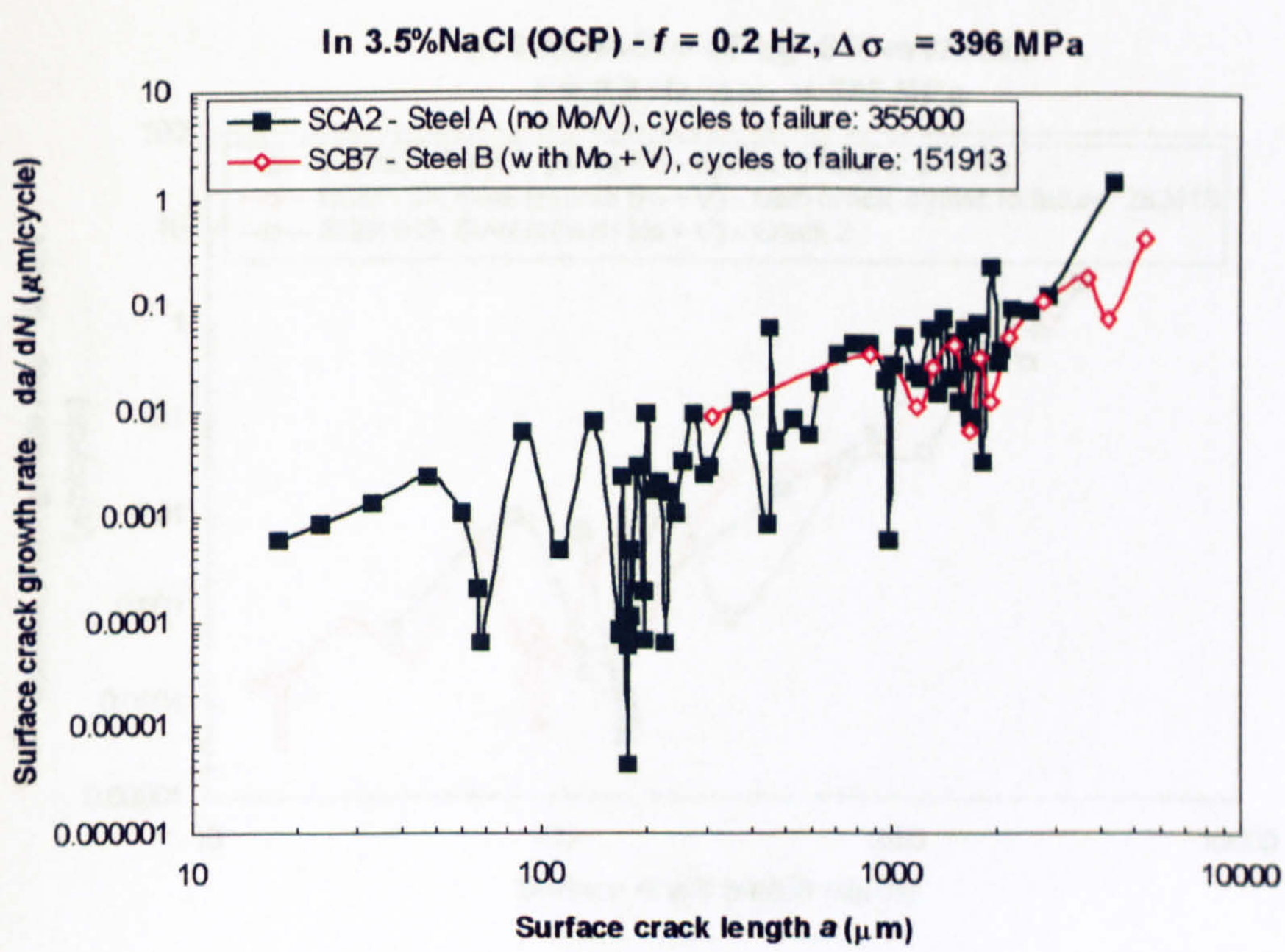

Figure 6.24 **Comparison of fatigue crack growth behaviour in 3.5%NaCl solution** (OCP) **at $\Delta\sigma$ = 396 MPa between Steel A** (no Mo/V) **and Steel B** (with Mo + V)

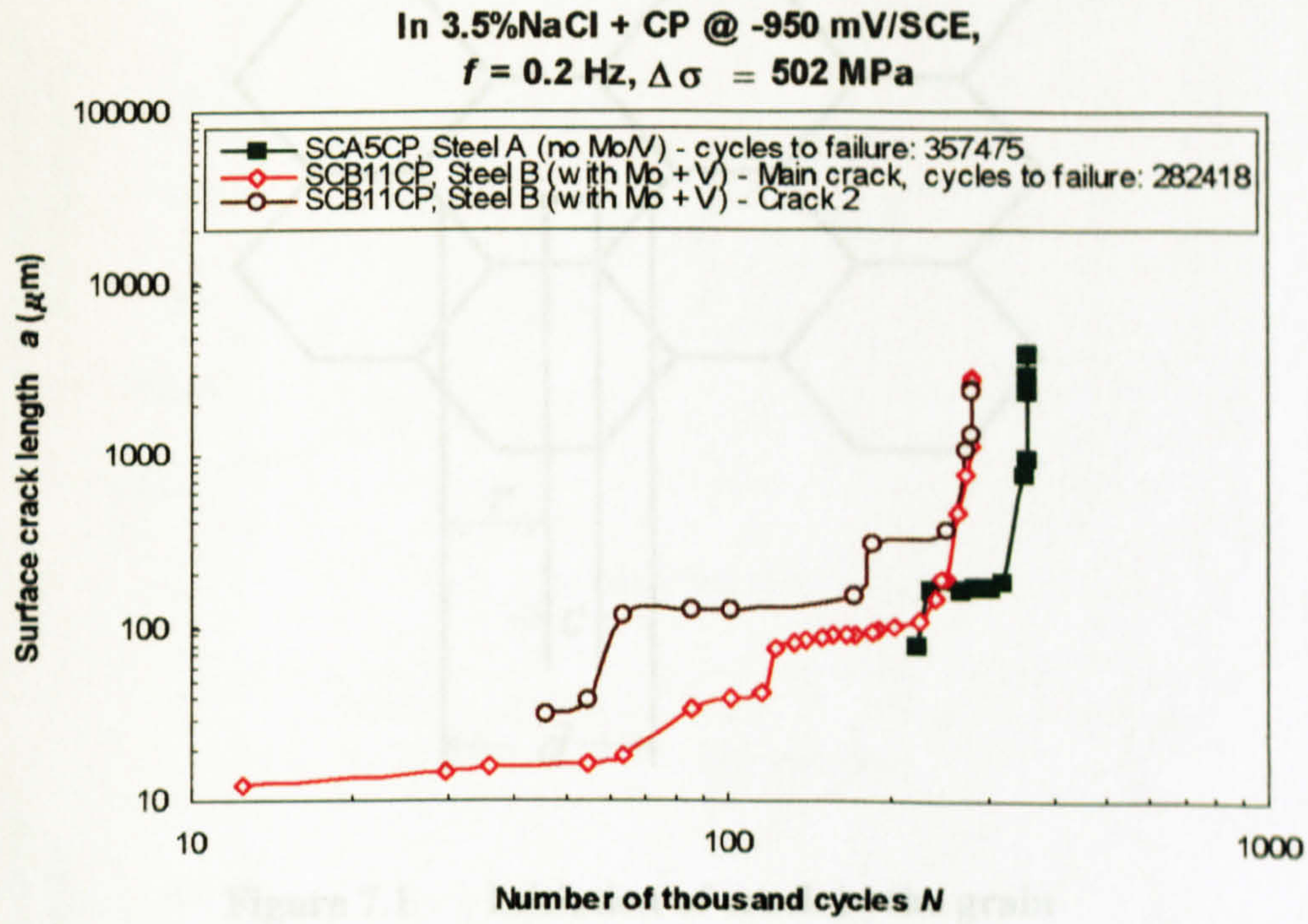

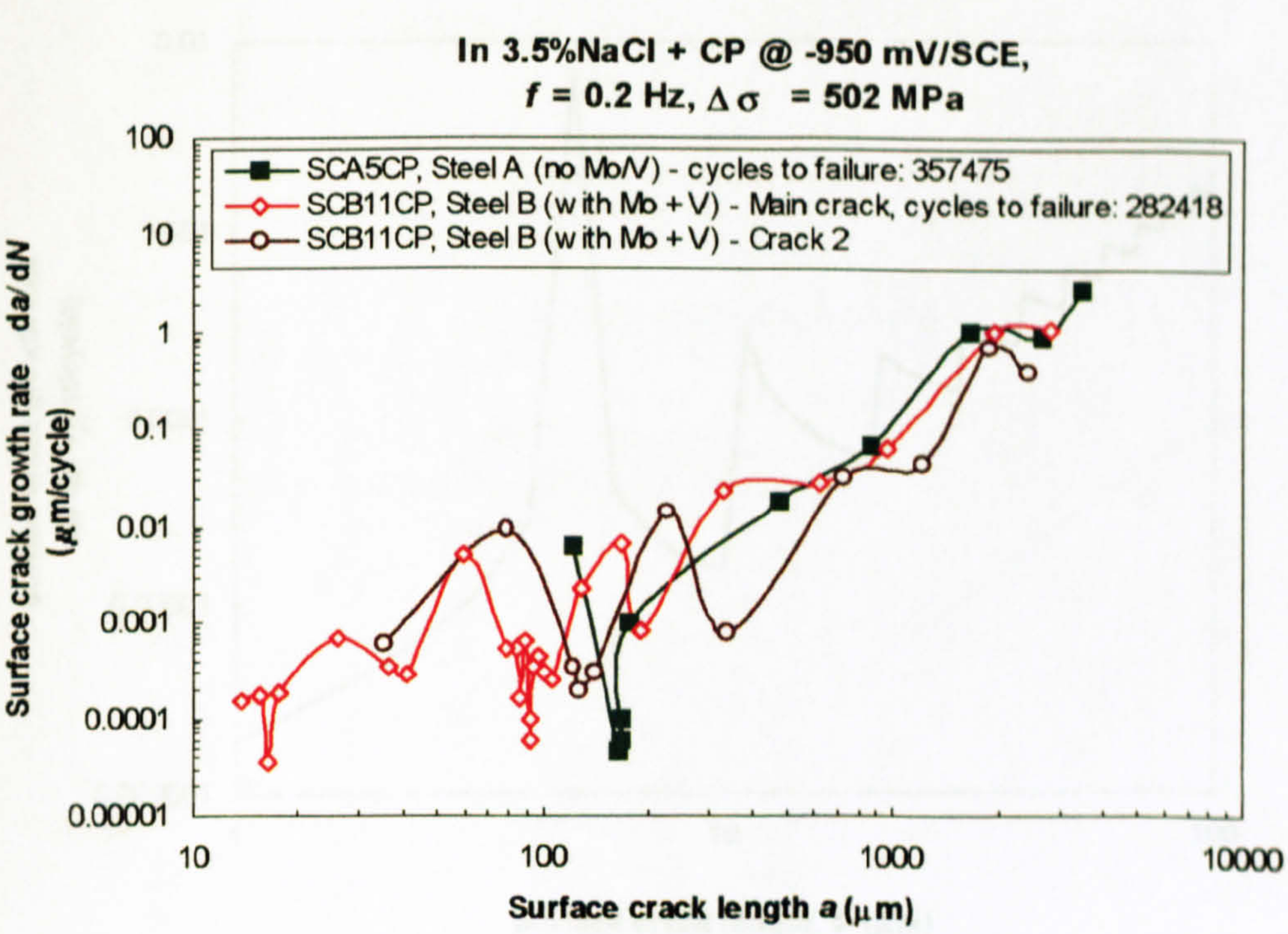

Figure 6.25 **Comparison of fatigue crack growth behaviour in 3.5%NaCl solution under CP** (-950 mV/SCE) **application at** $\Delta\sigma$ **= 502 MPa between Steel A** (no Mo/V) **and Steel B** (with Mo + V)

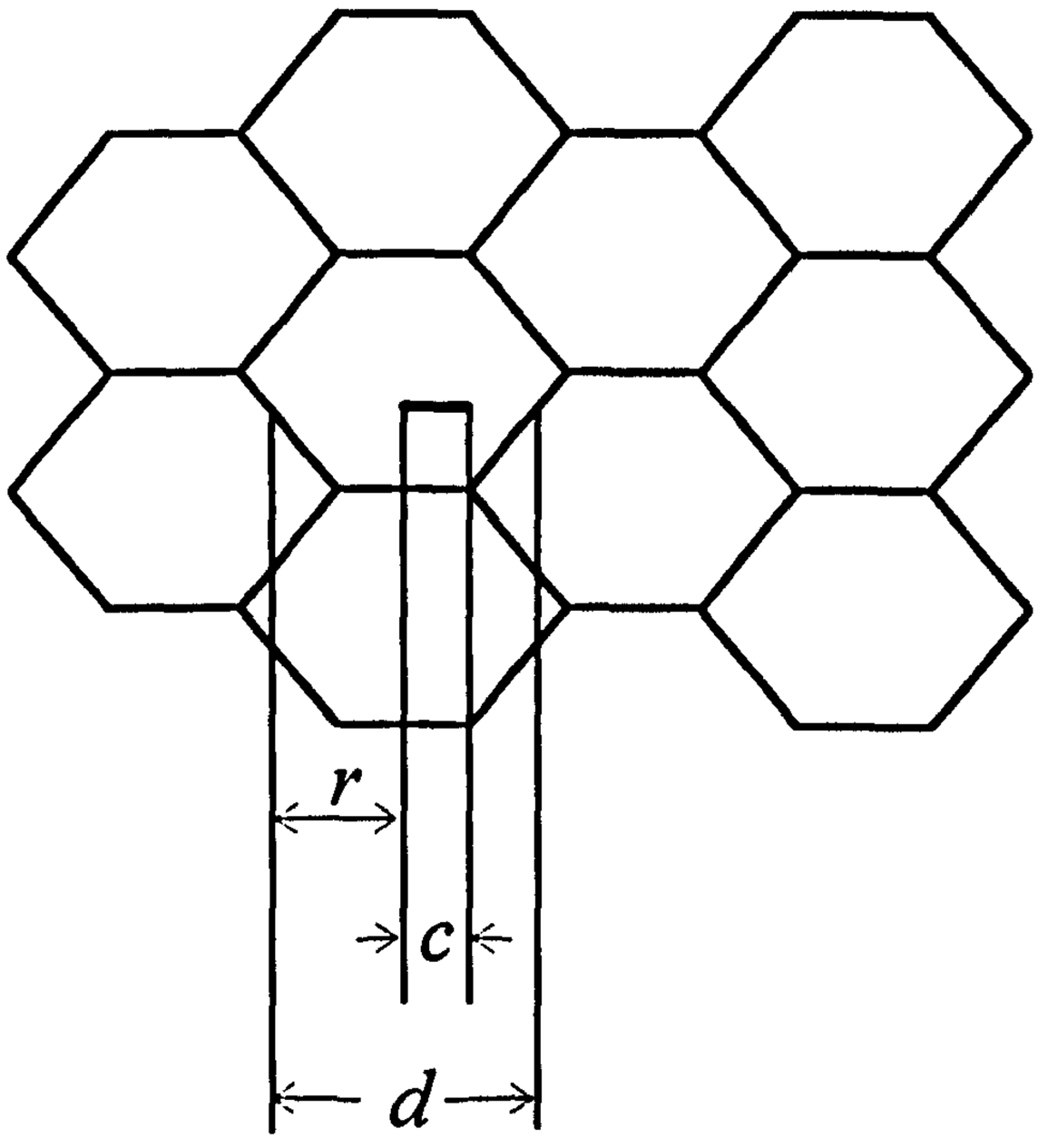

Figure 7.1 Initiation of crack in the grain

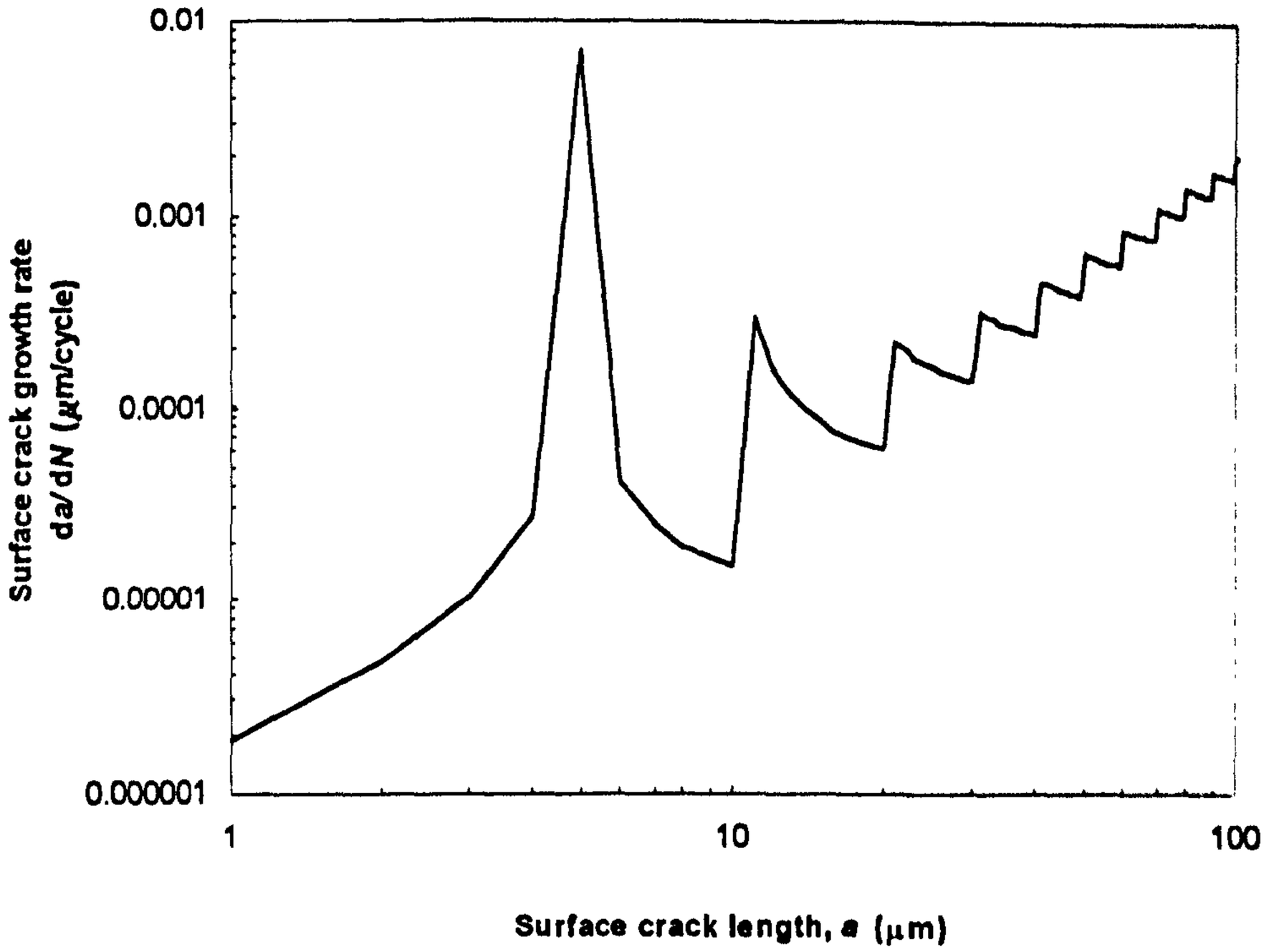

Figure 7.2 Crack growth rate within first 10 grains calculated from the model

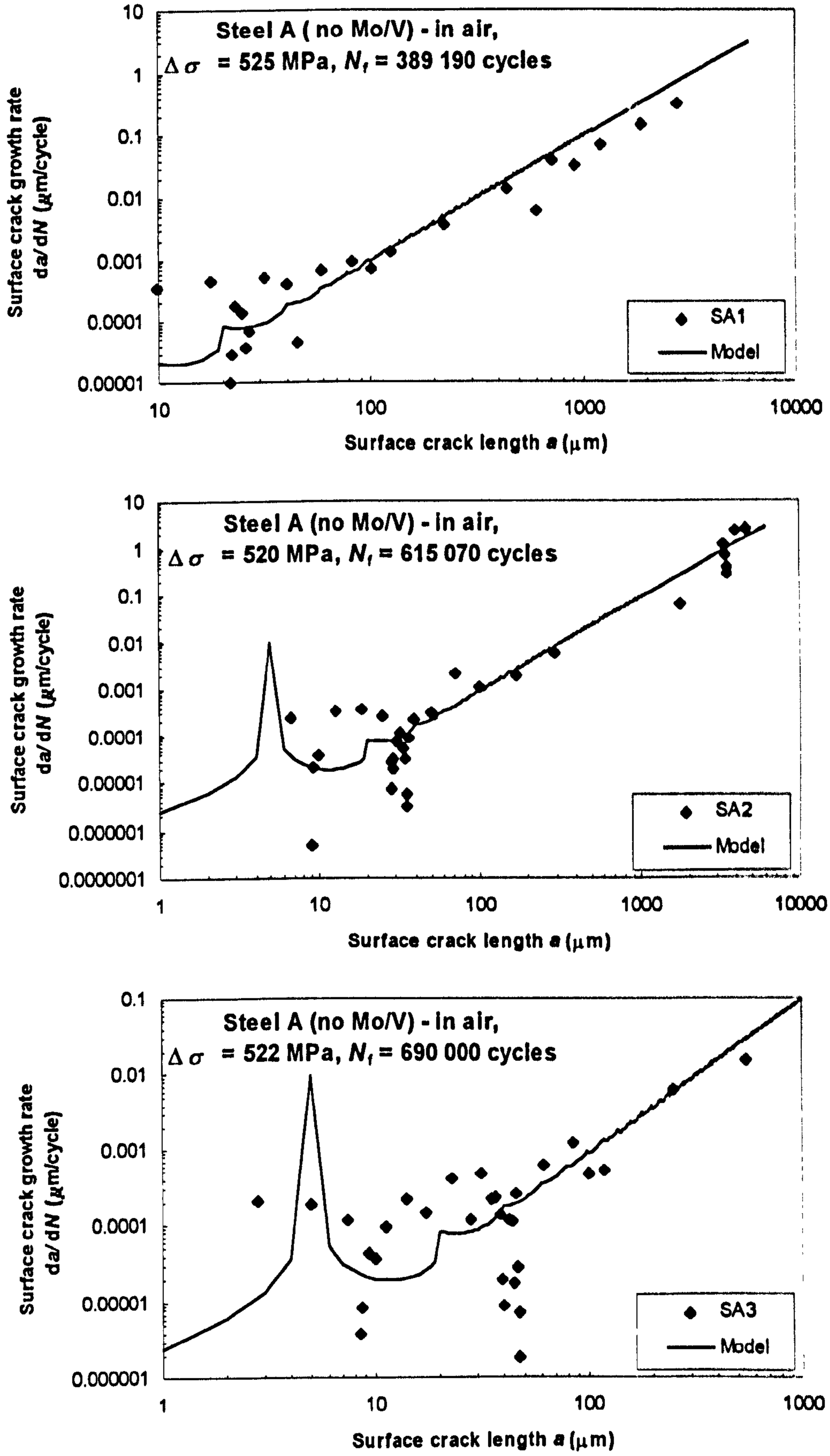

Figure 7.3 **In-air fatigue crack growth rate of Steel A (no Mo/V) calculated from the model**

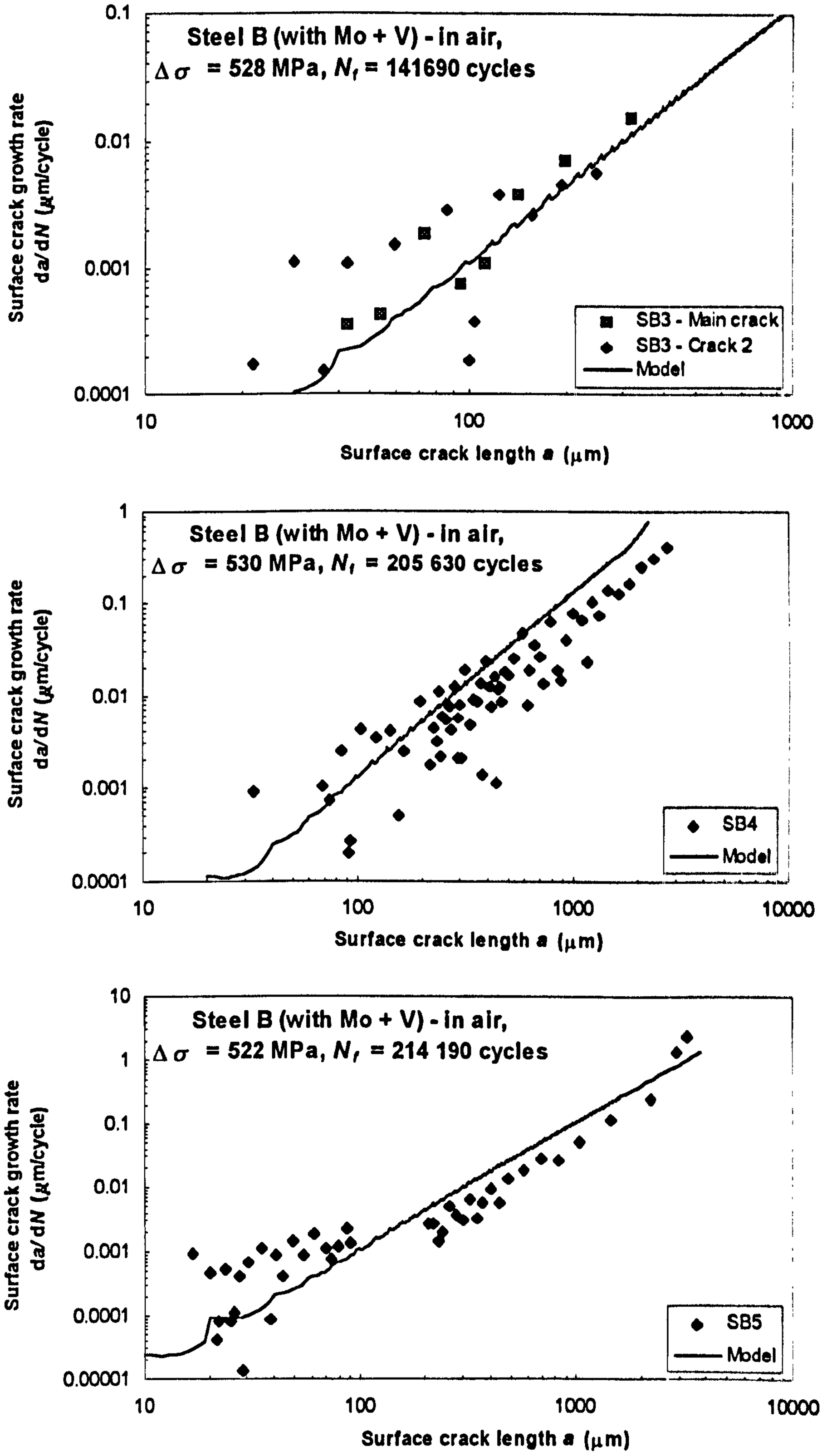

Figure 7.4 (a) **In-air fatigue crack growth rate of Steel B (with Mo + V) calculated from the model**

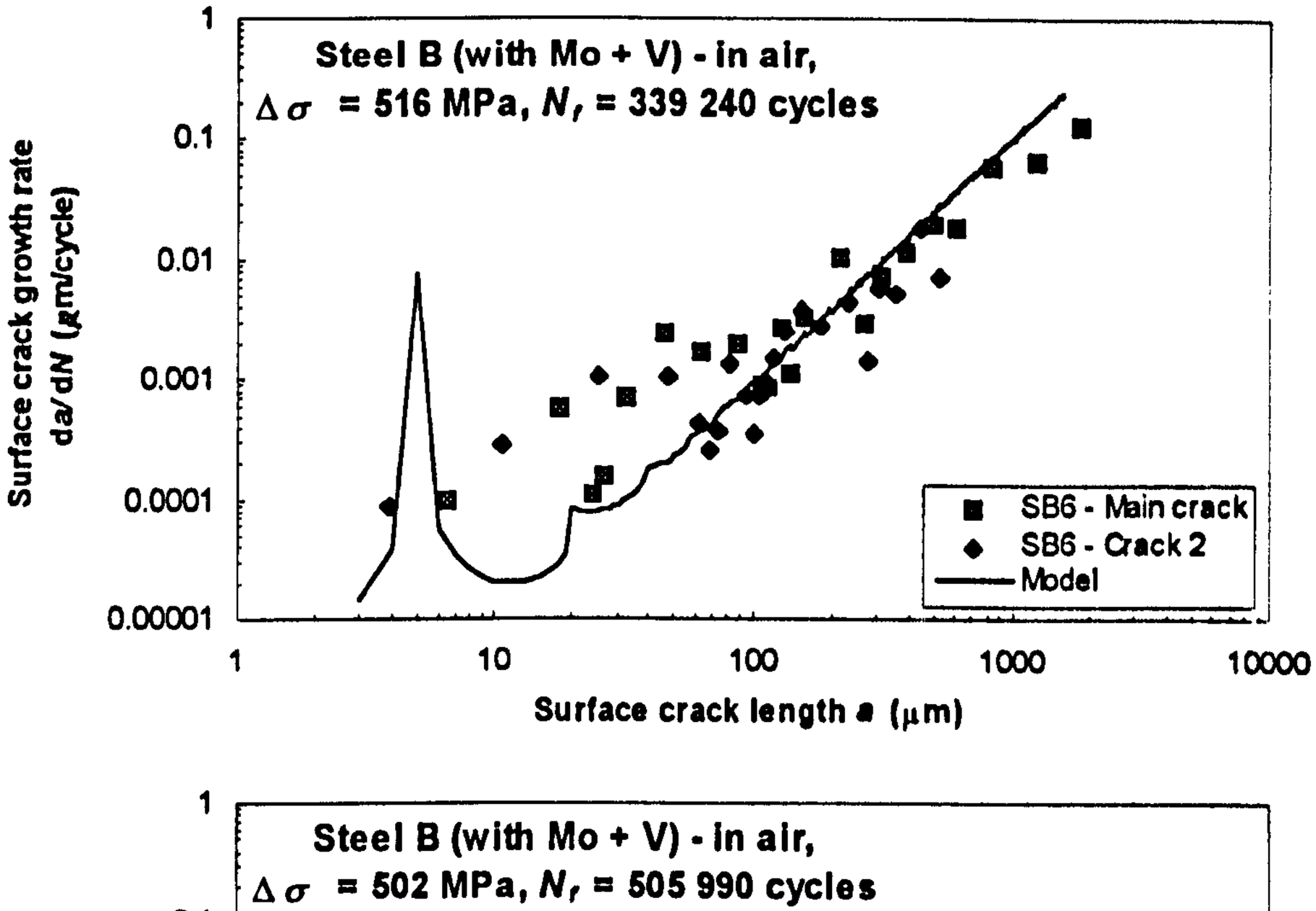

Figure 7.4 (b) **In-air fatigue crack growth rate of Steel B (with Mo + V) calculated from the model**

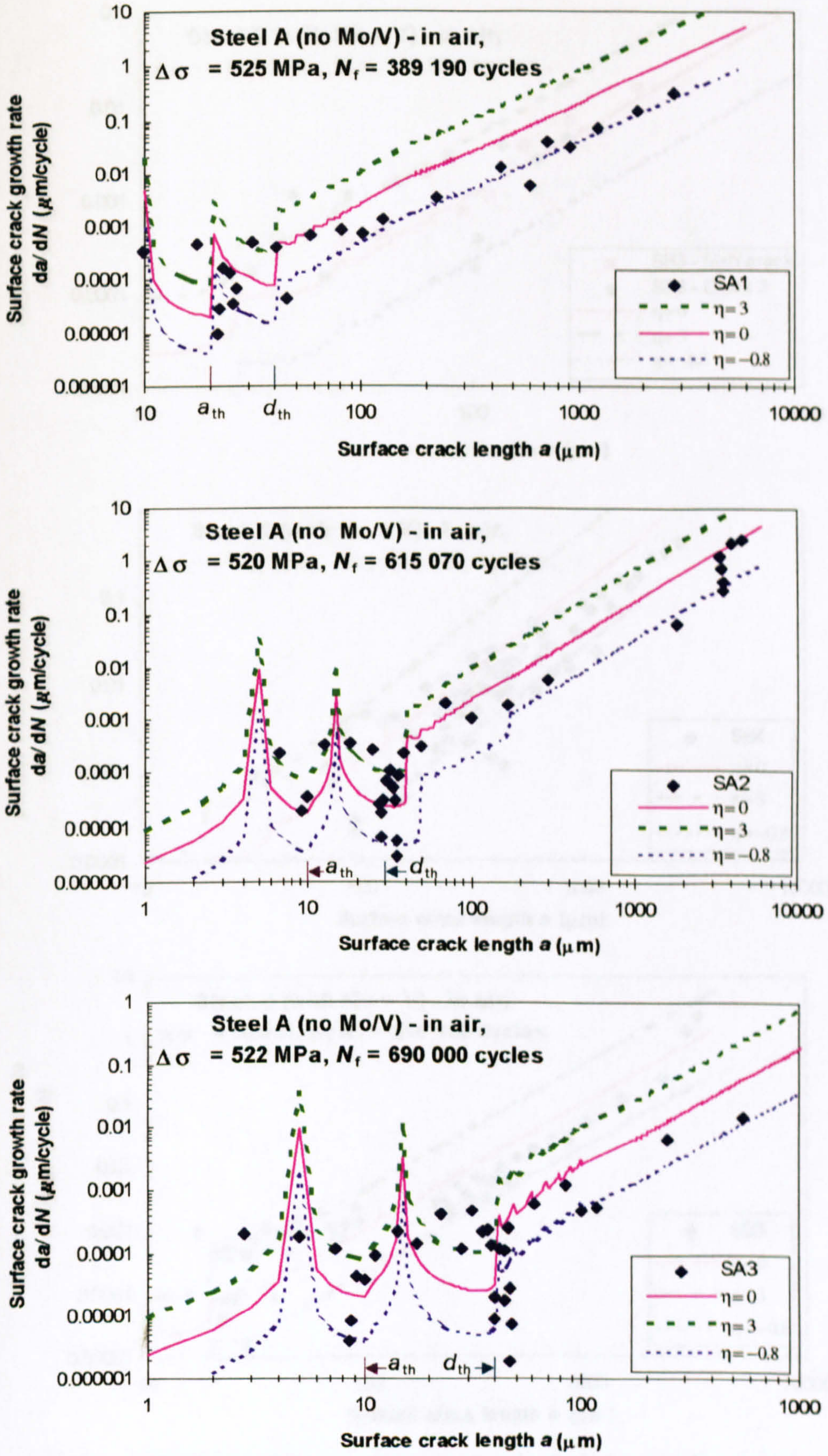

Figure 7.5 **Influence of fluctuation on in-air fatigue crack growth rate of Steel A** (no Mo/V)

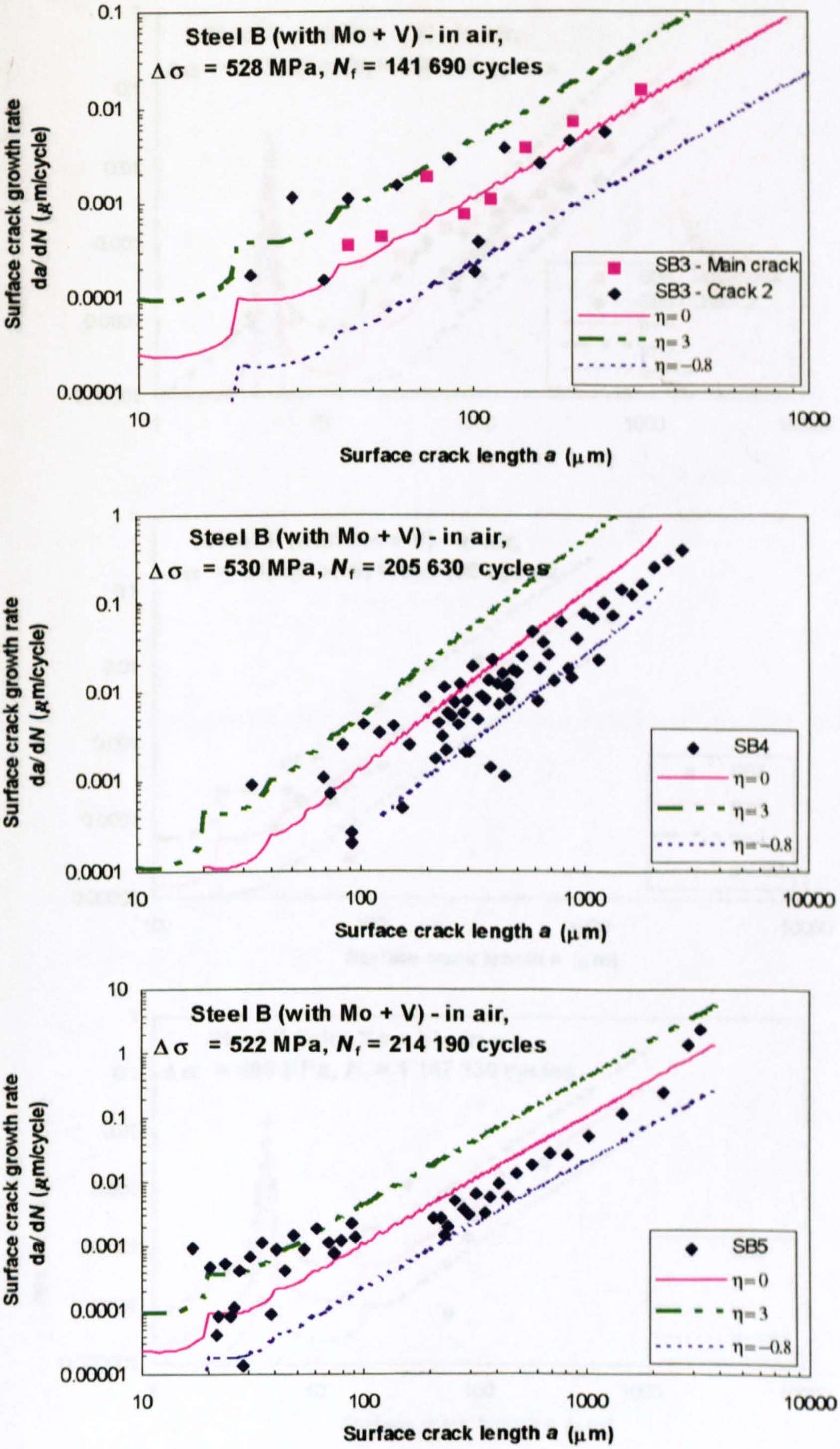

Figure 7.6(a) **Influence of fluctuation on in-air fatigue crack growth rate of Steel B** (with Mo + V)

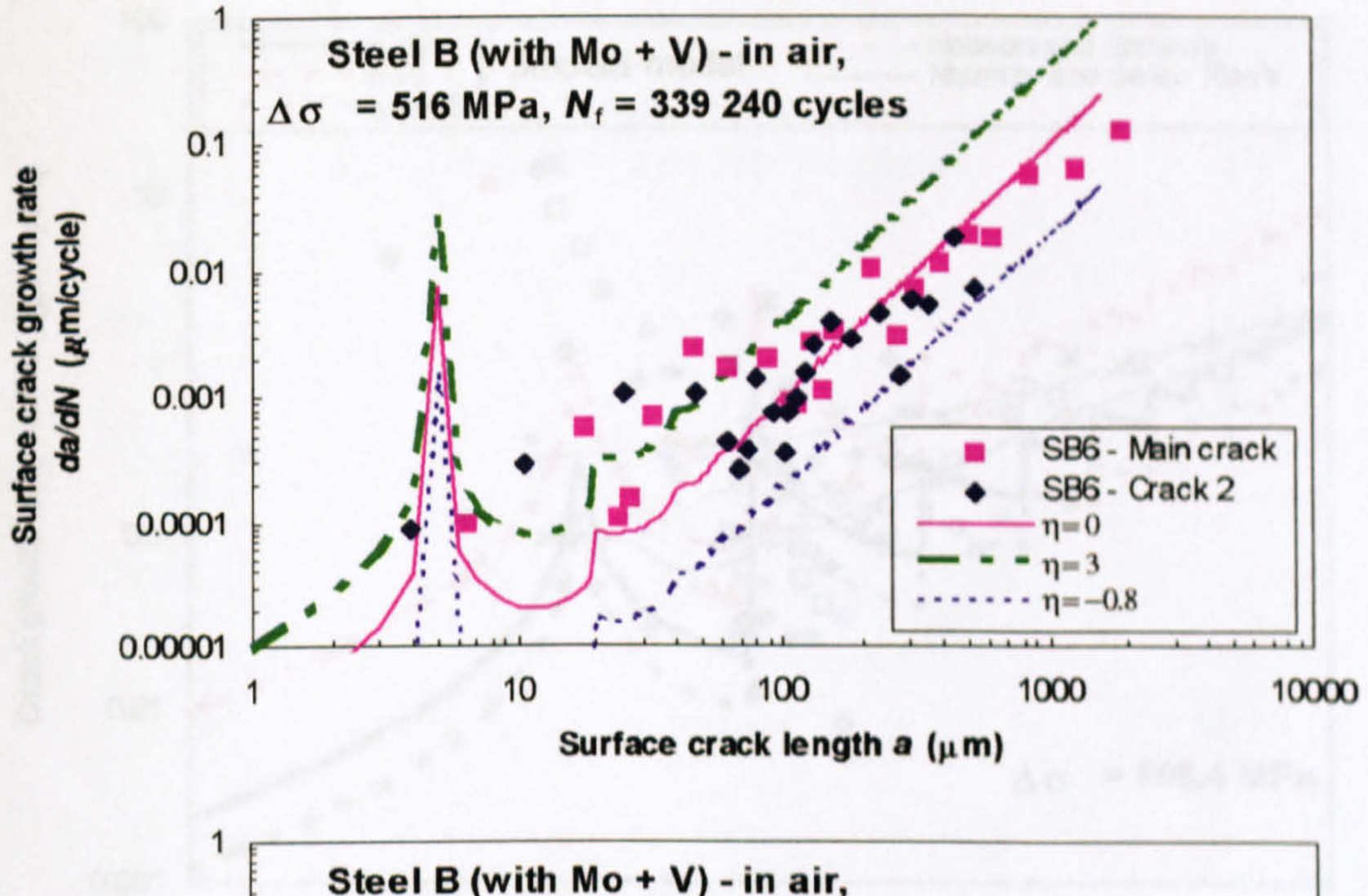

Figure 7.6(b) **Influence of fluctuation on in-air fatigue crack growth rate of Steel B** (with Mo + V)

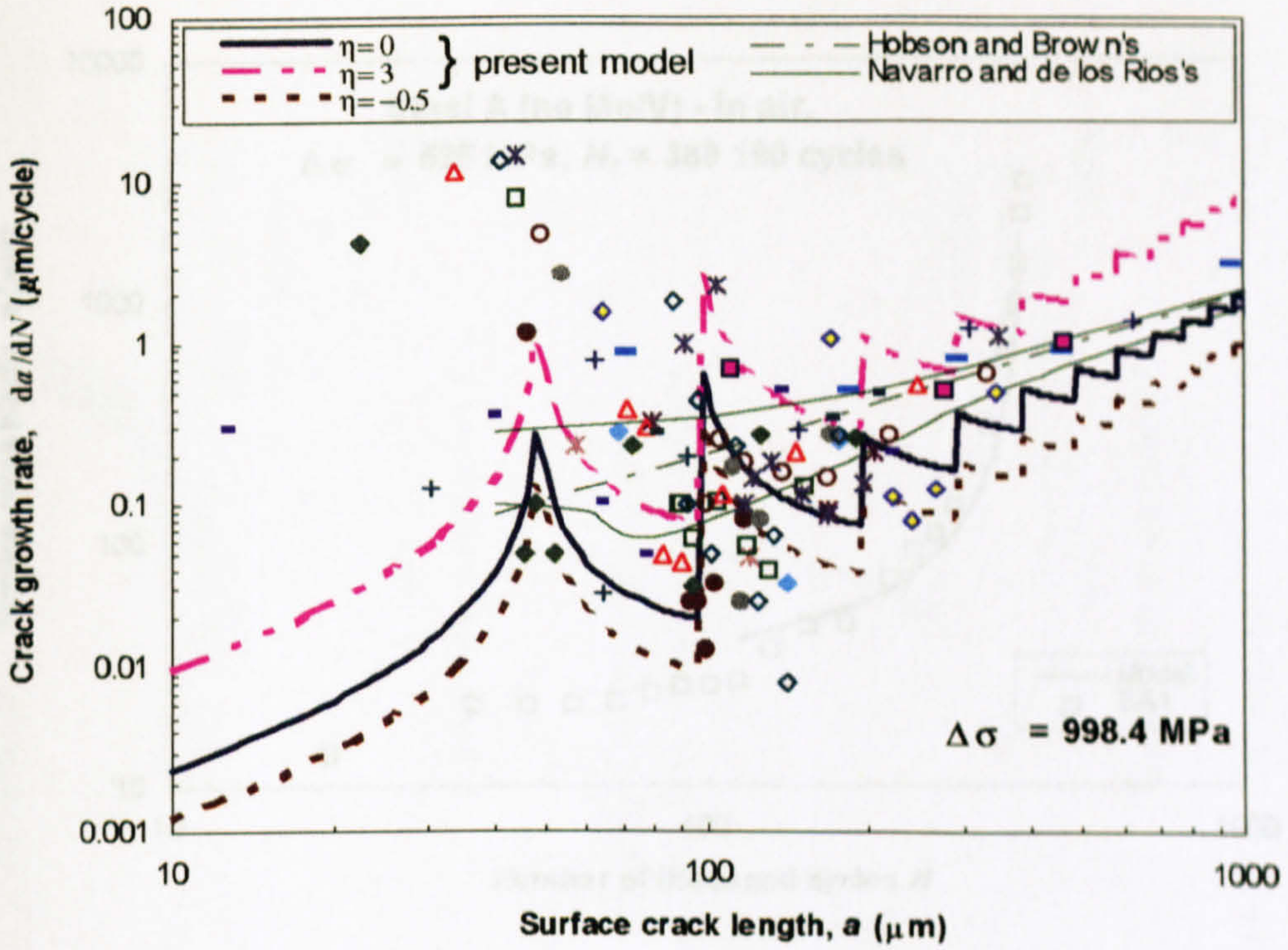

Figure 7.7 Calculation of fatigue crack growth rate based on Hobson's experiments [59, 60, 142]

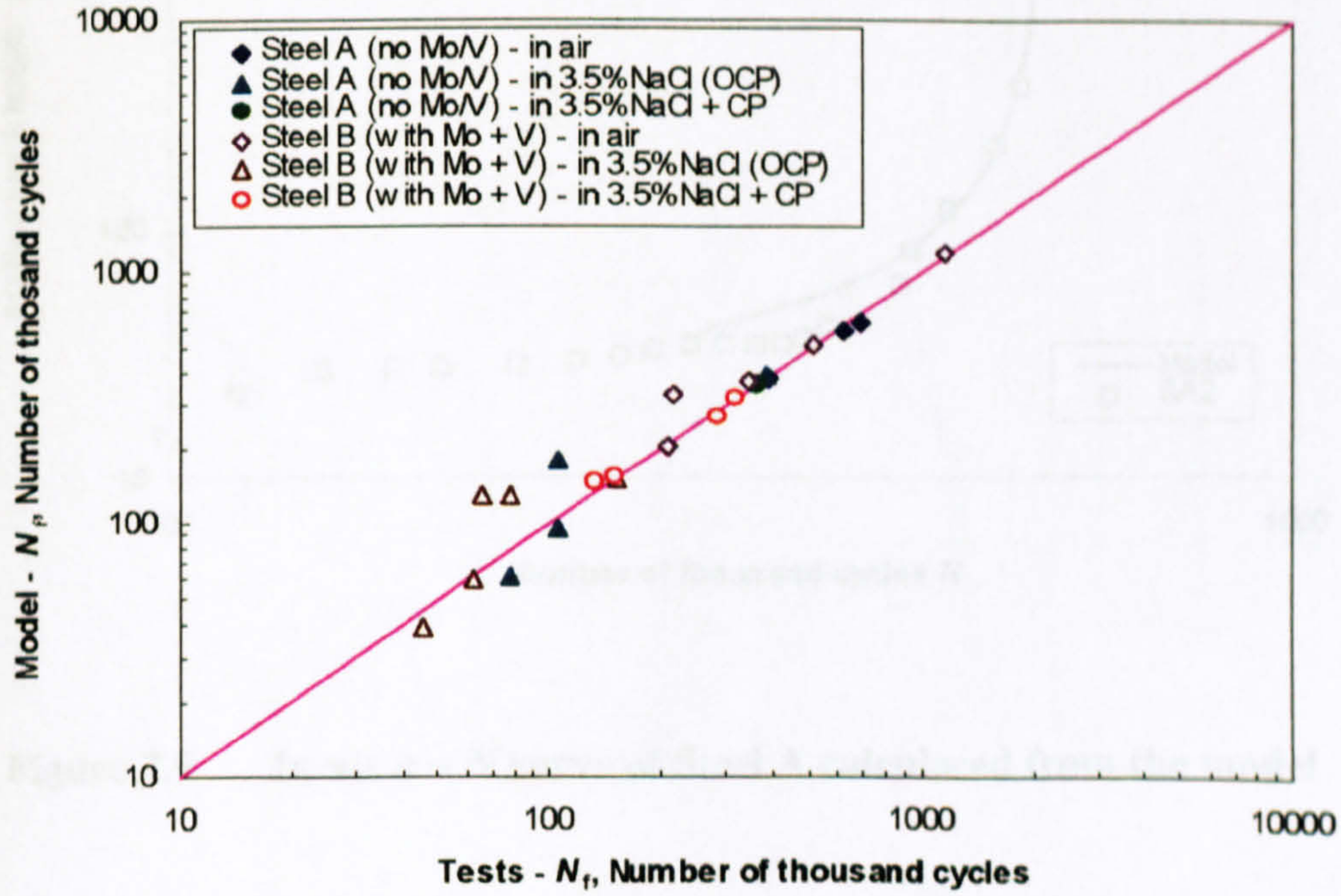

Figure 7.8 Calculation of the $S \sim N_f$ curve from the model

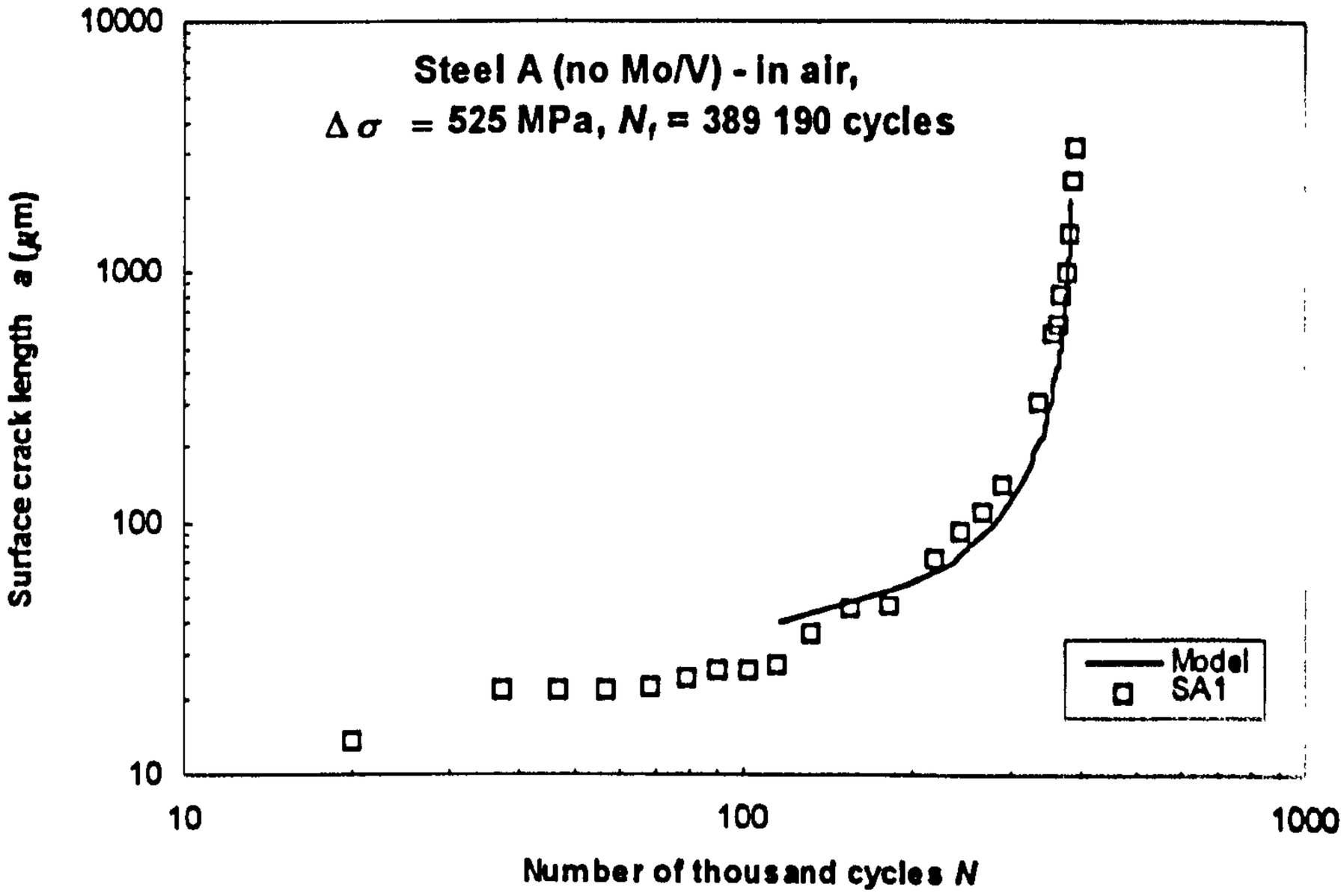

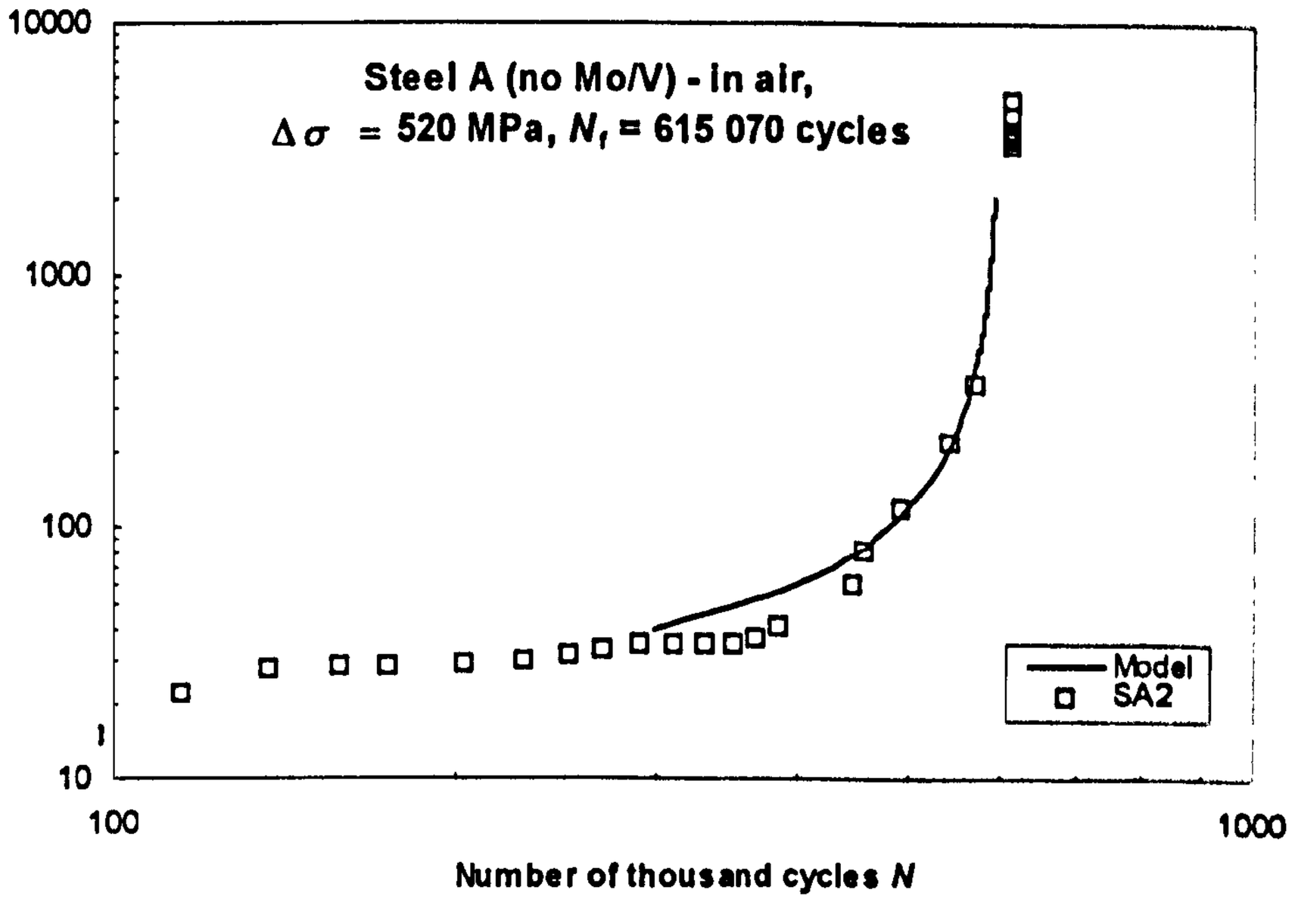

Figure 7.9 In-air $a \sim N$ curve of Steel A calculated from the model

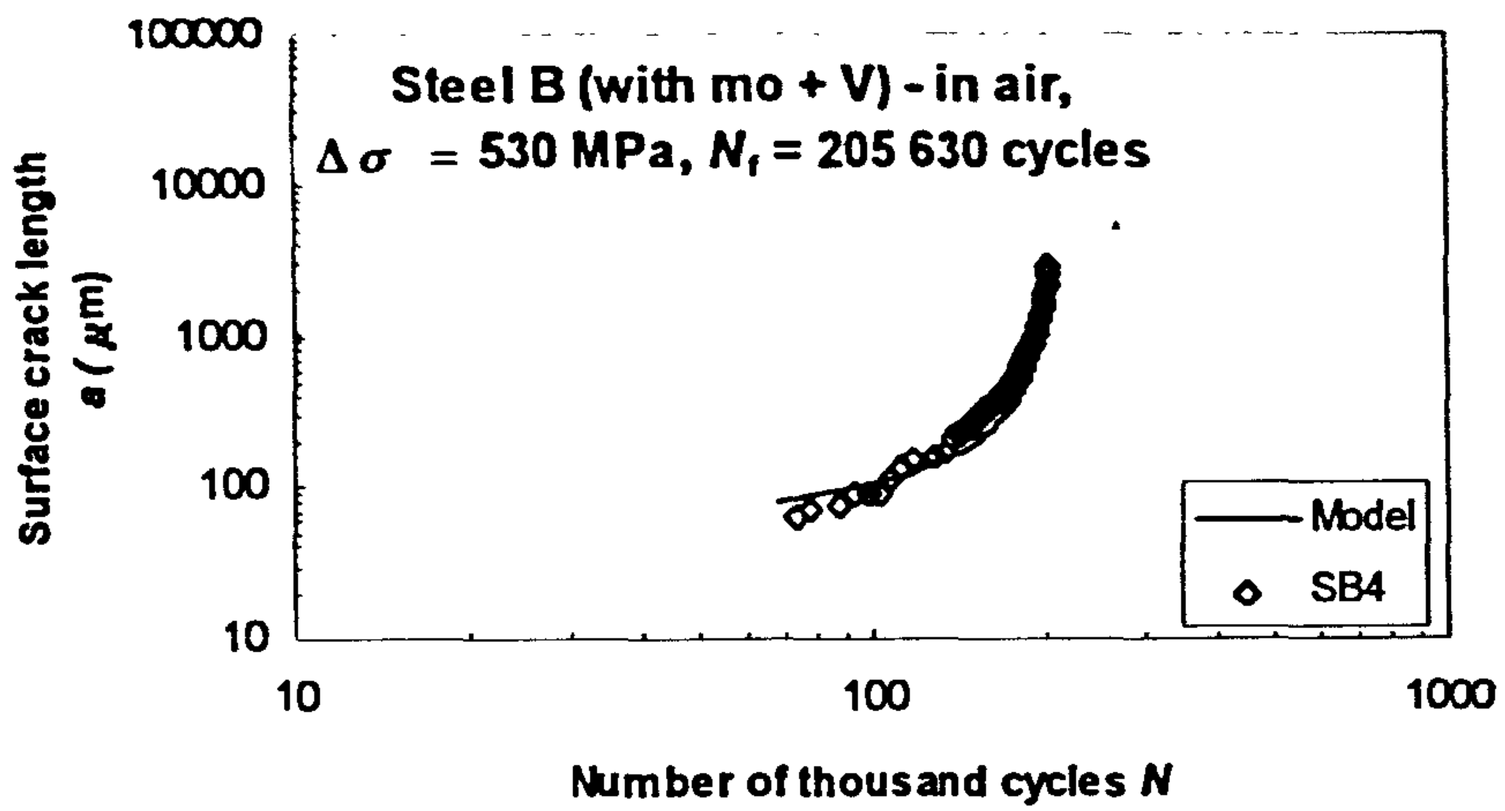

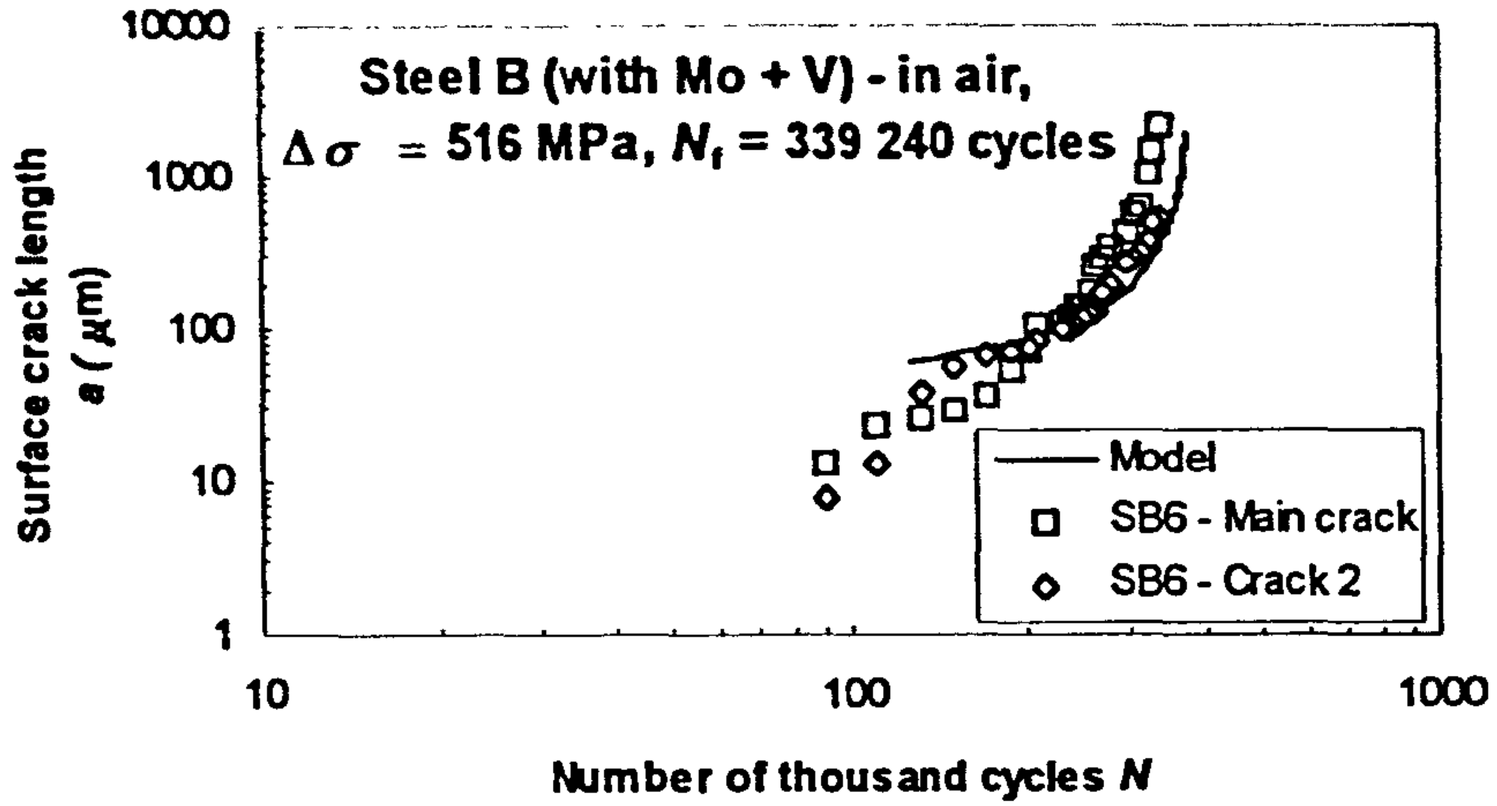

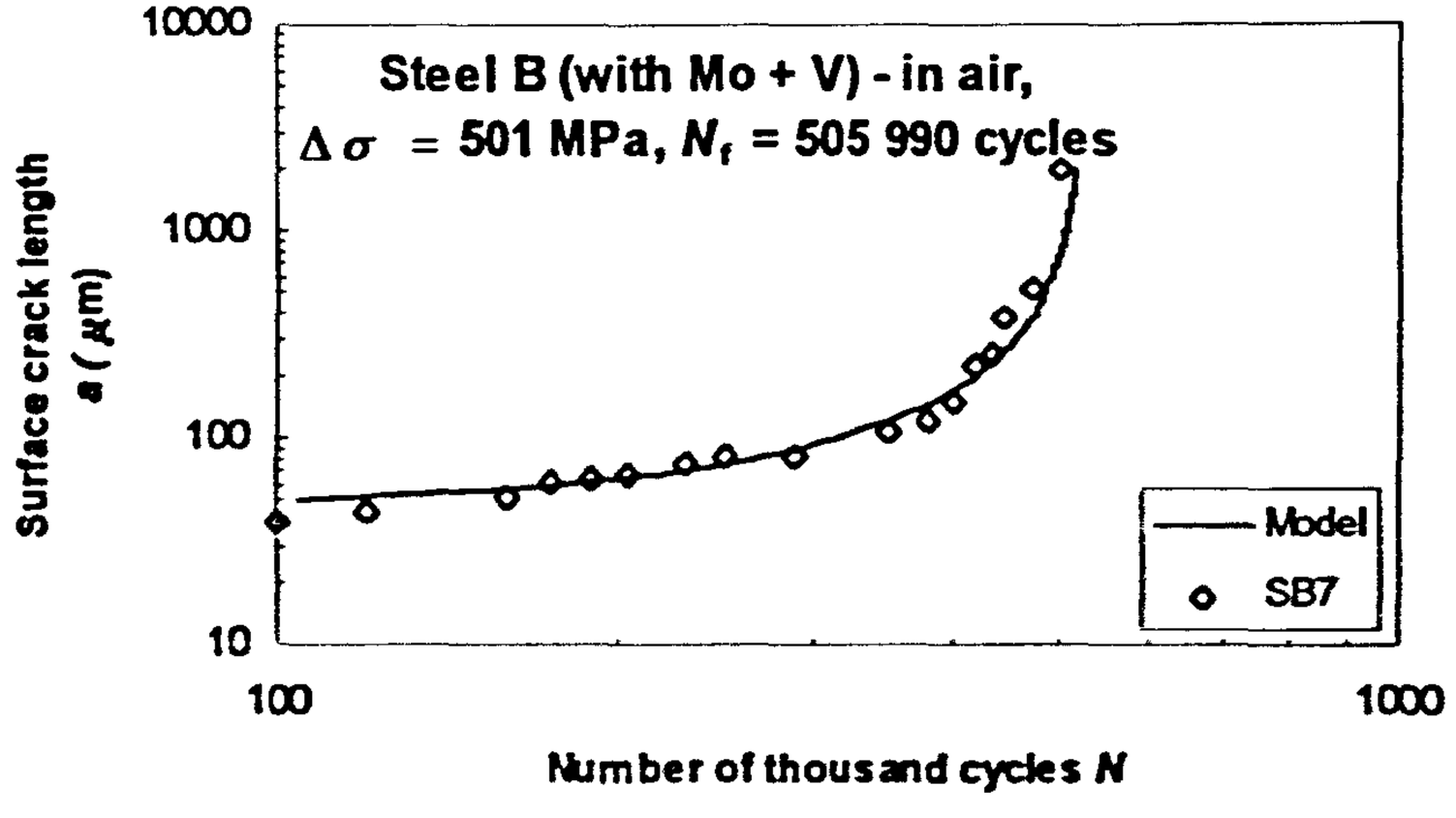

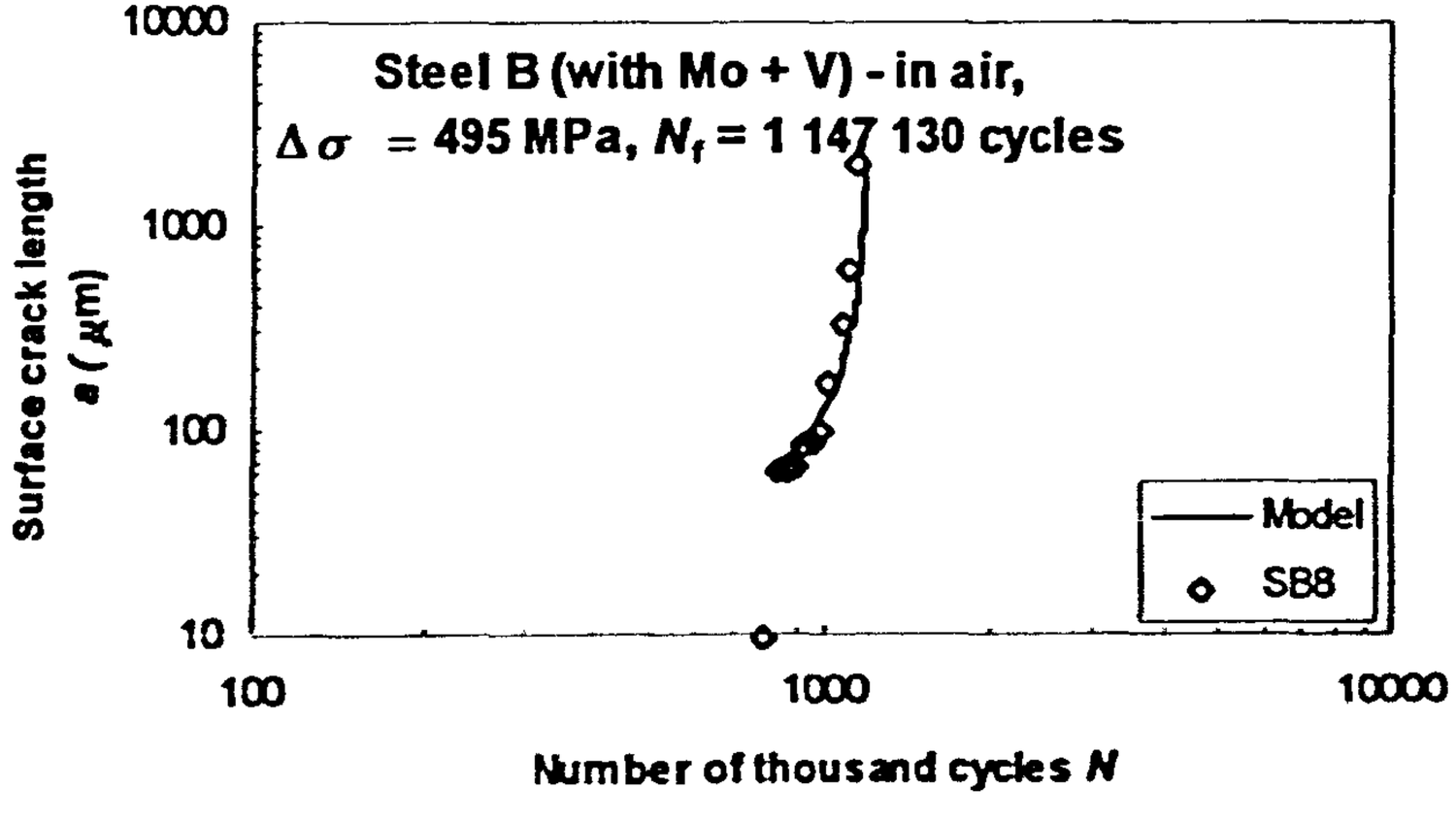

Figure 7.10 In air $a \sim N$ curve of Steel B calculated from the model

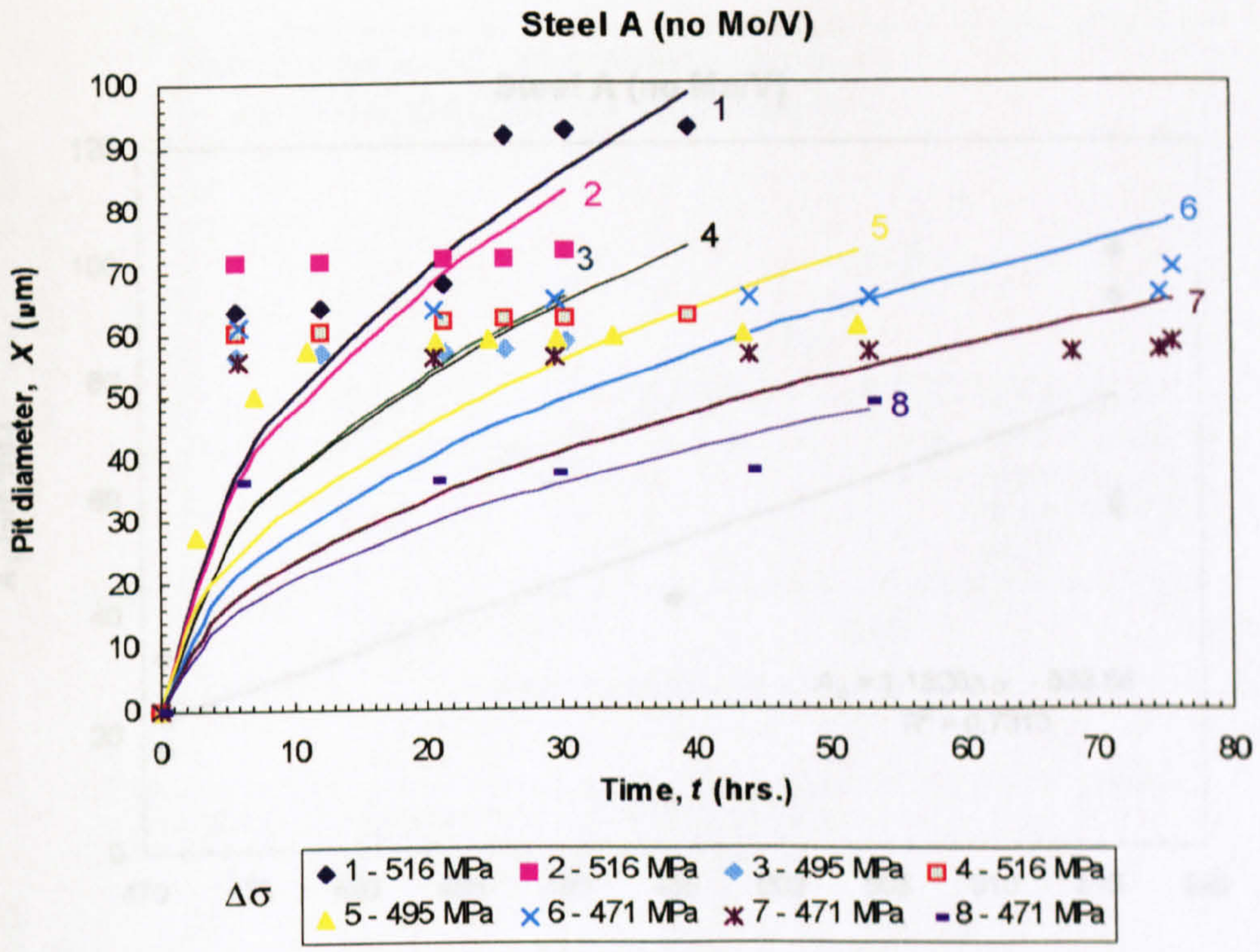

Figure 8.1 **The pit size distribution changes with the corrosion time for RQT501 steels in 3.5%NaCl solution** (OCP) (Solid lines represent a fit with equation (8.19) to the experimental data)

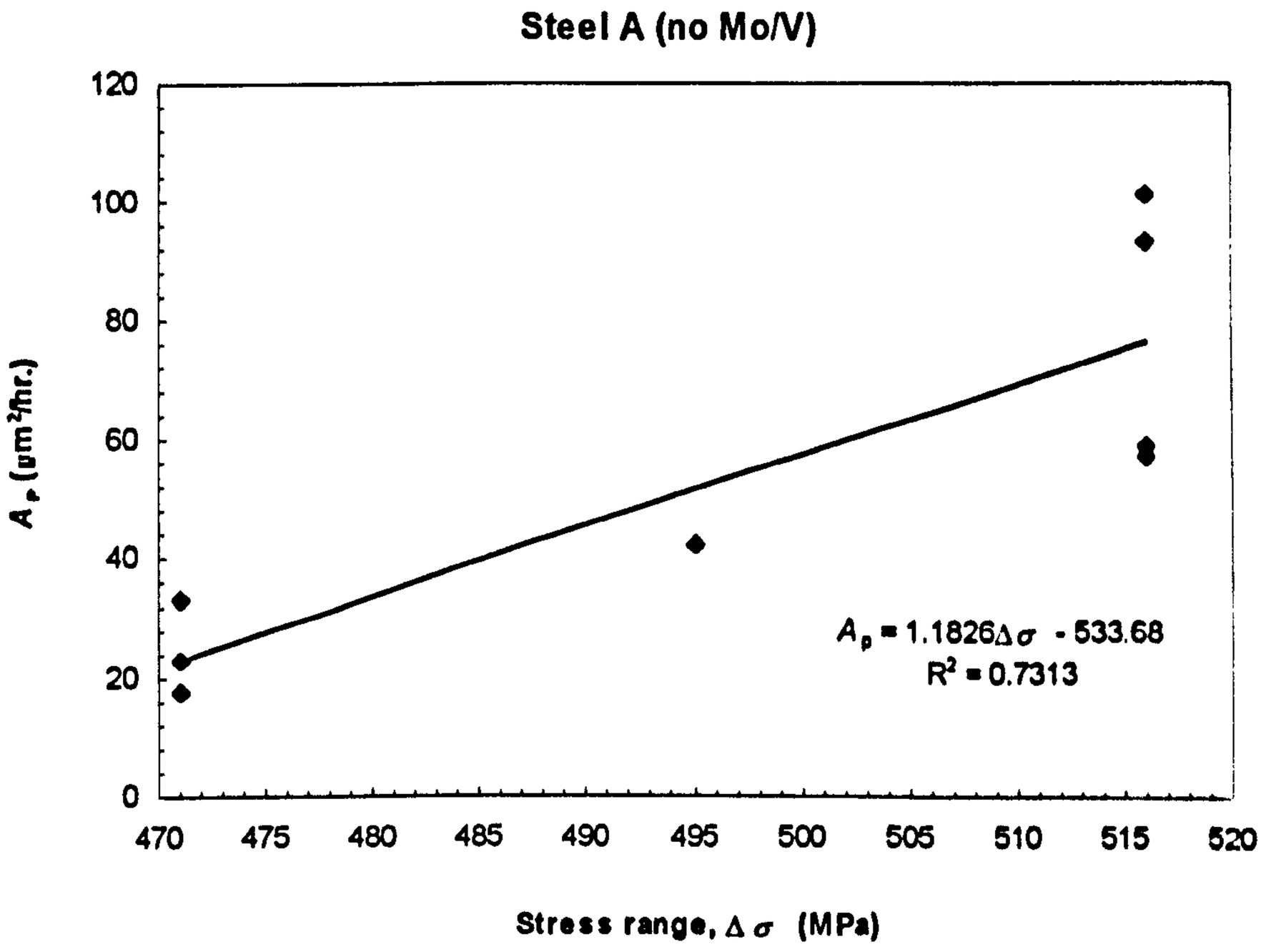

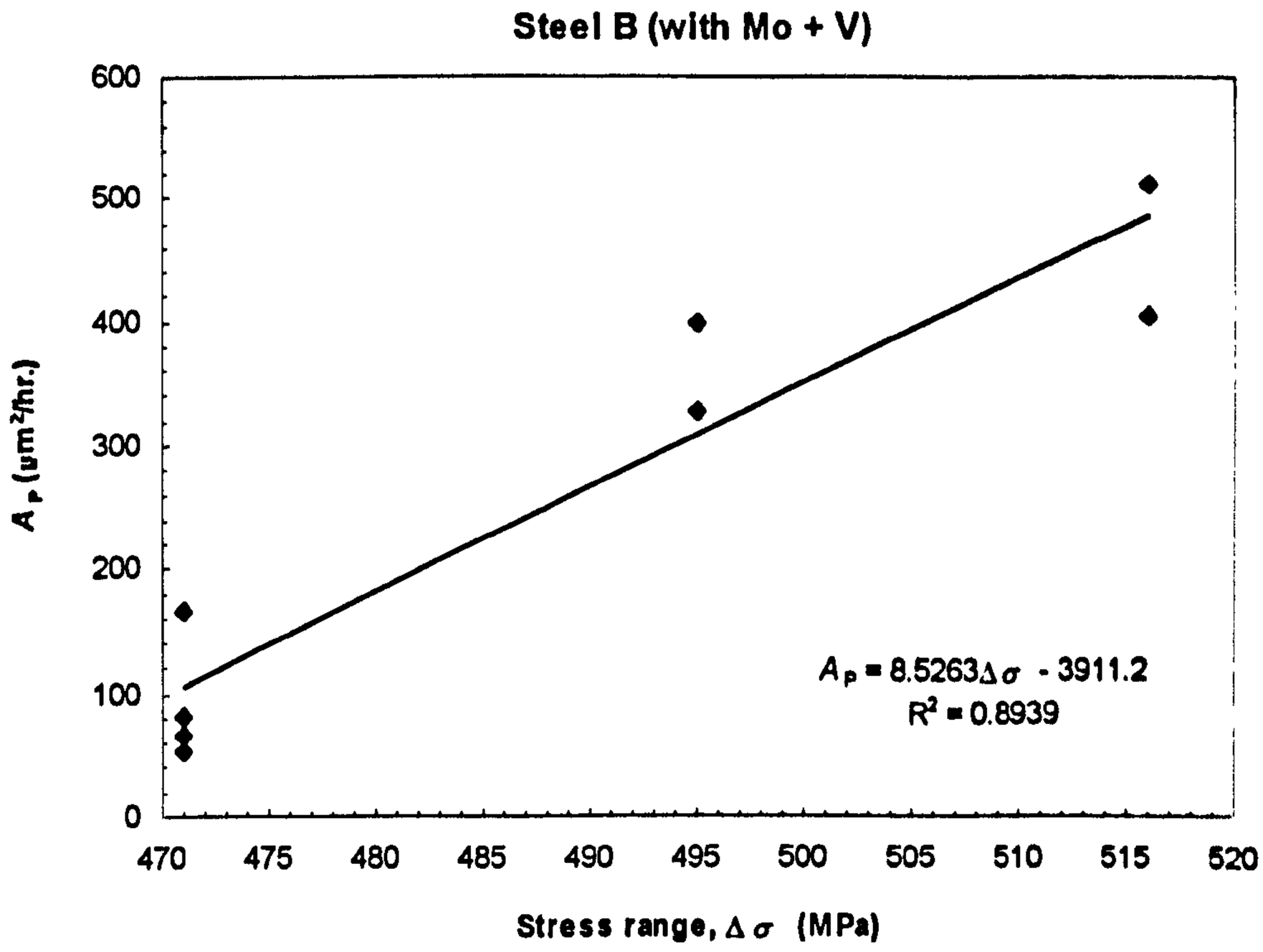

Figure 8.2 Relationship between A_P and $\Delta\sigma$

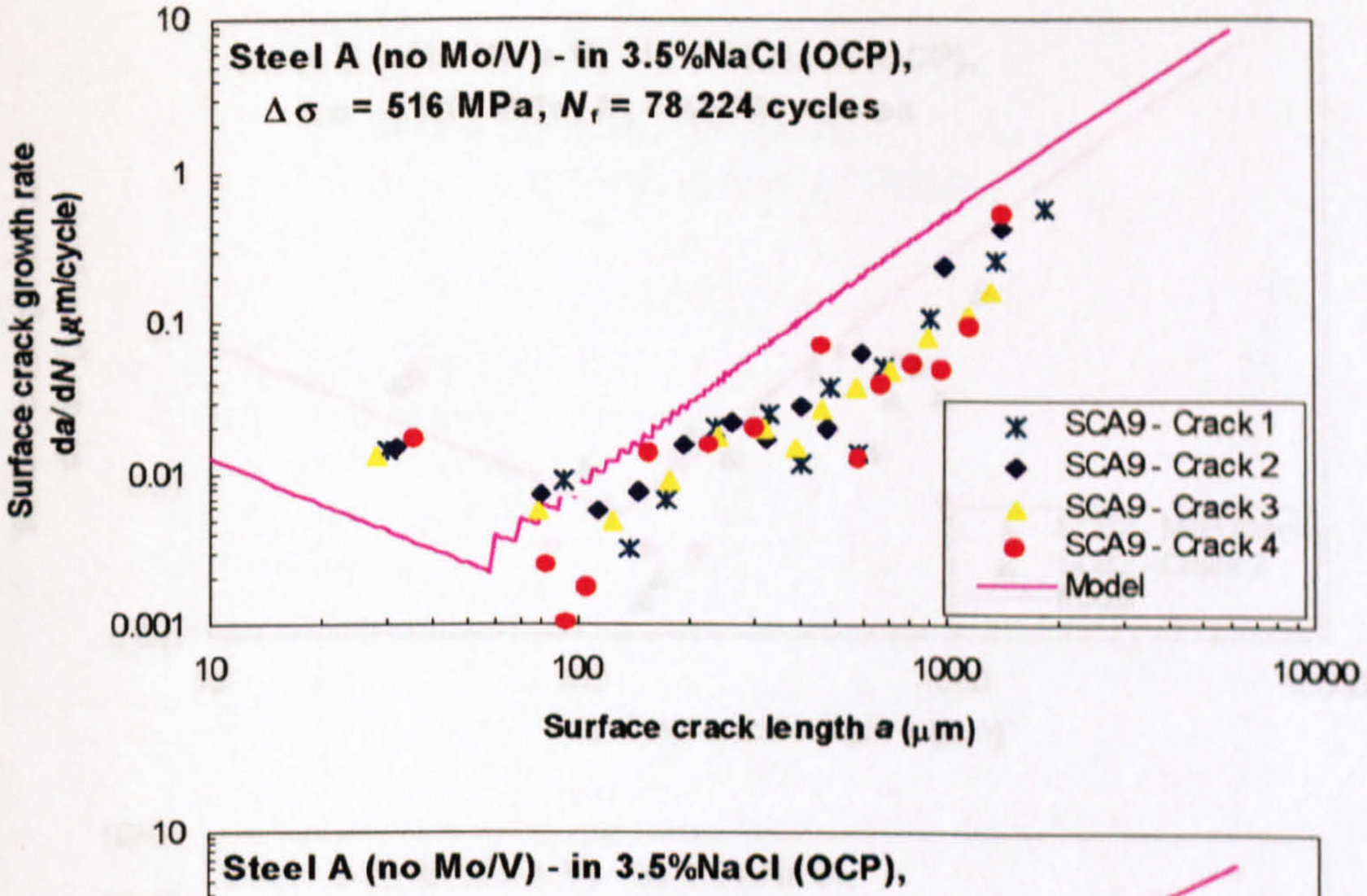

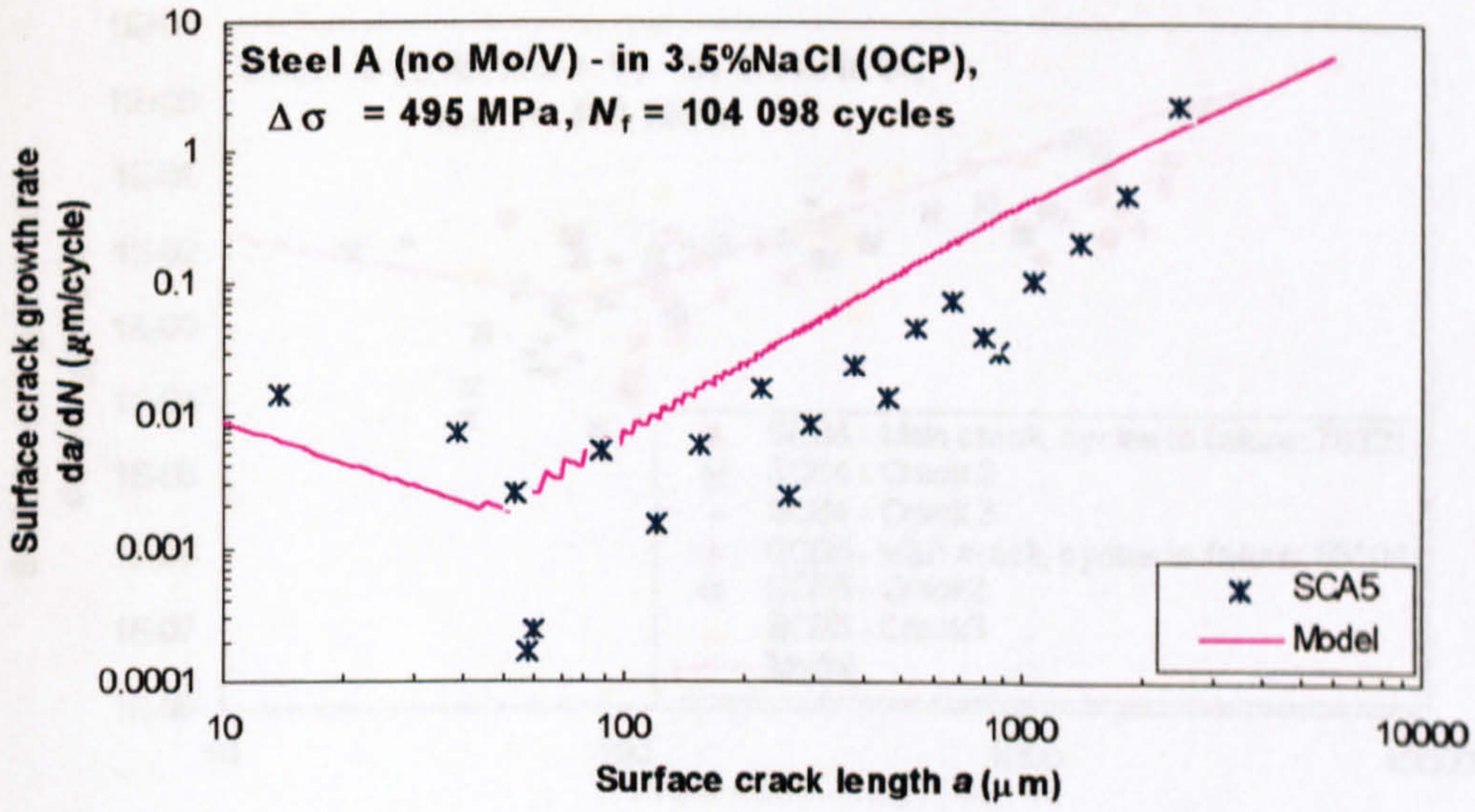

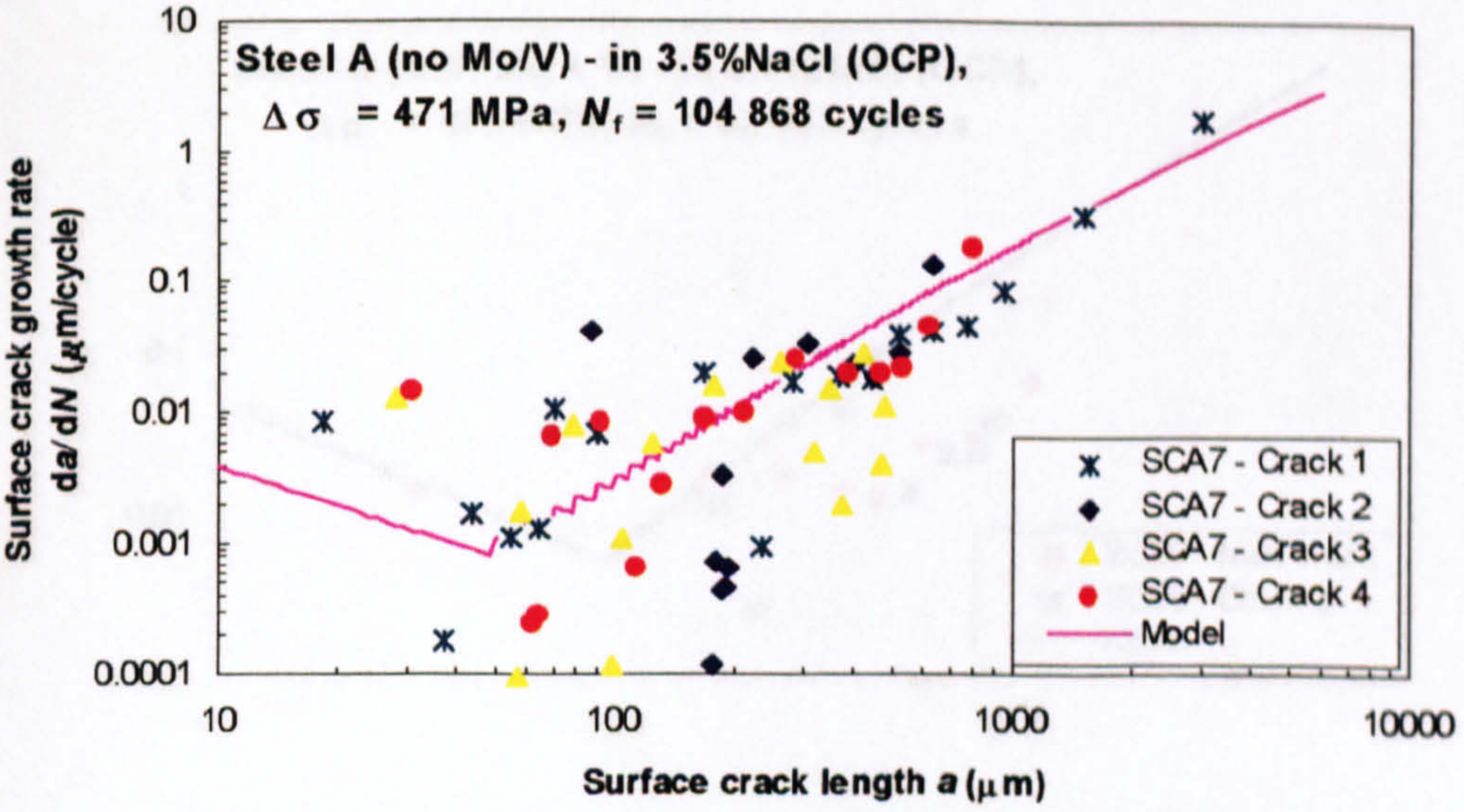

Figure 8.3 Corrosion fatigue crack growth rate of Steel A (no Mo/V) **in 3.5%NaCl solution** (OCP) **calculated from the model**

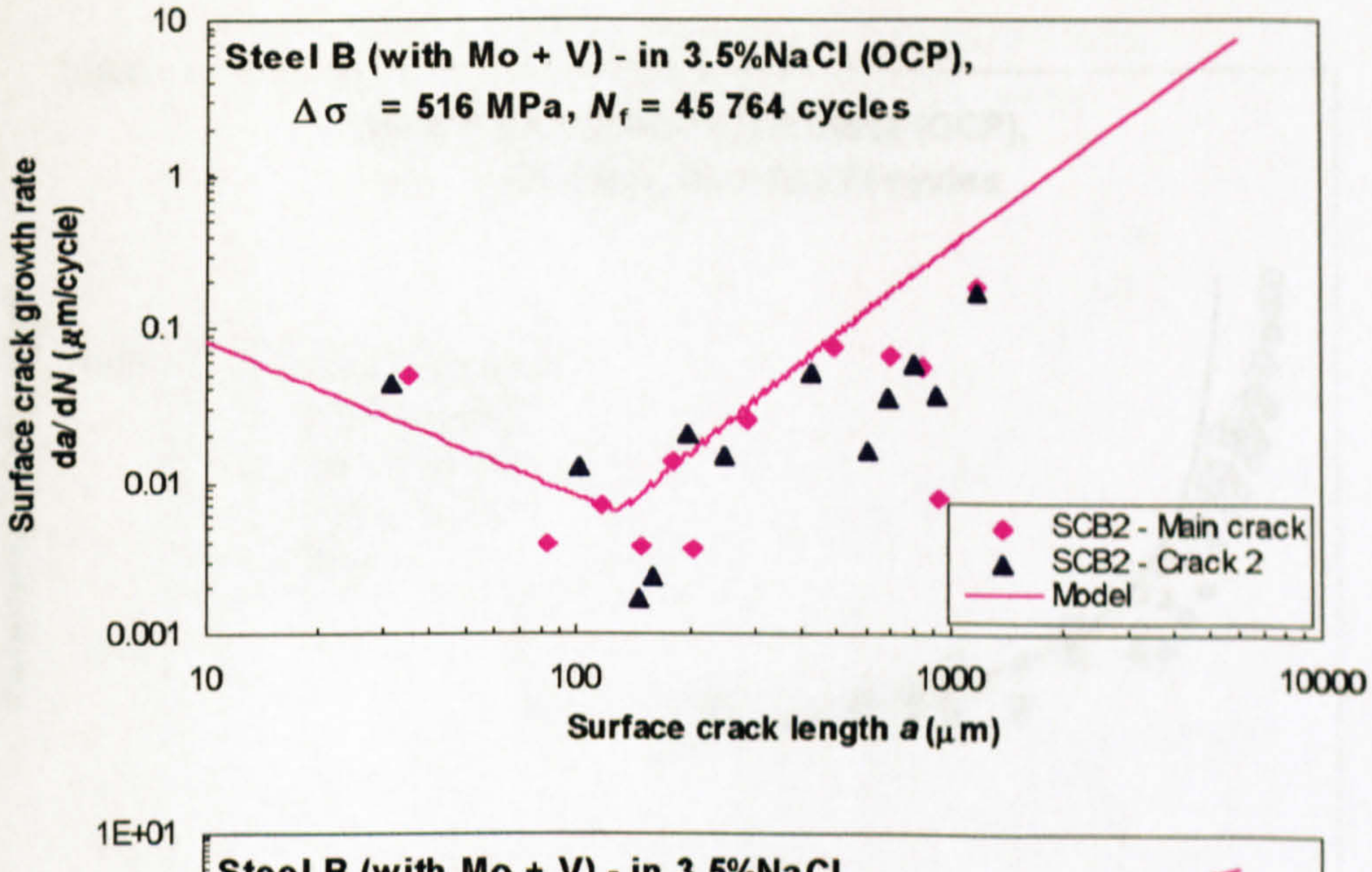

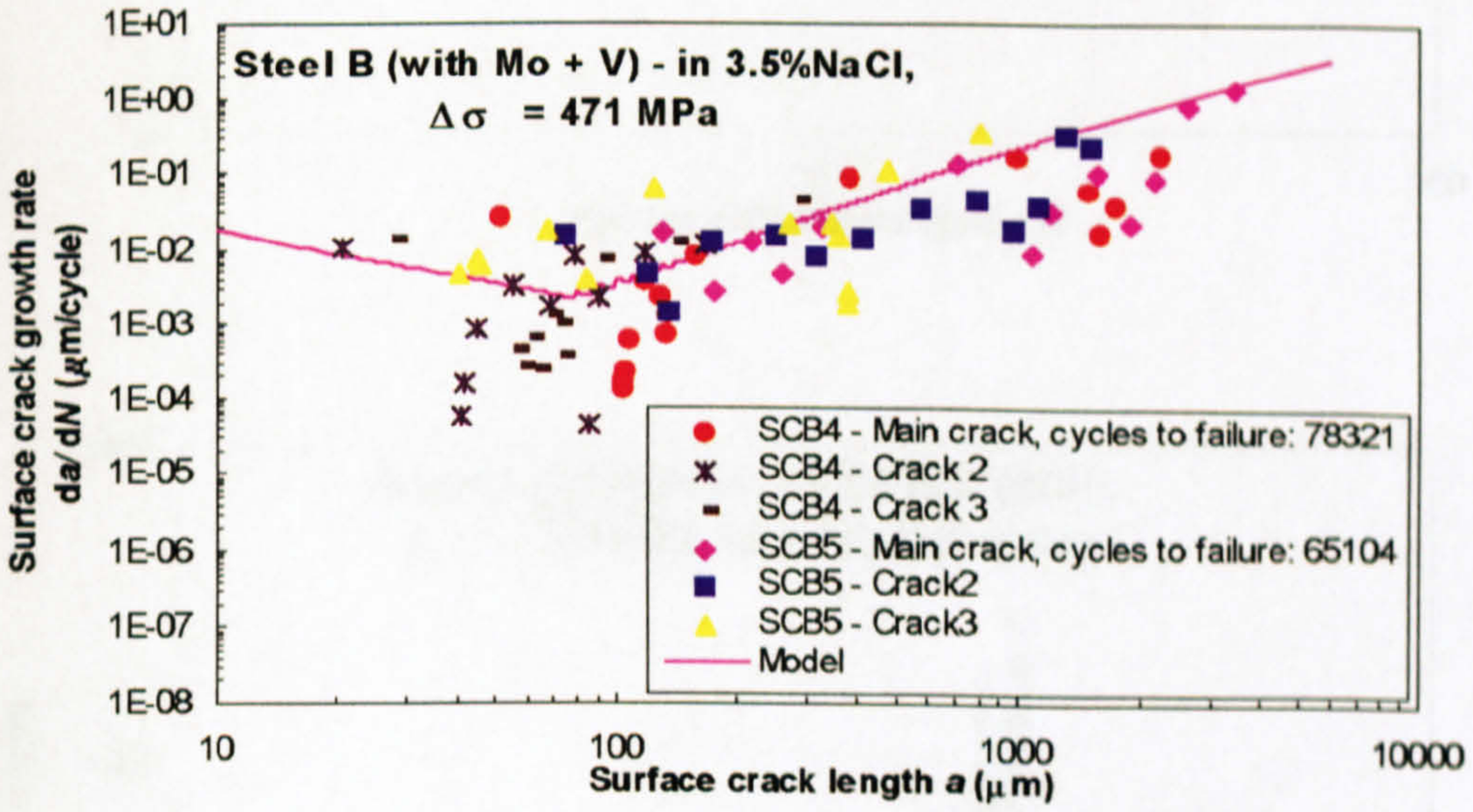

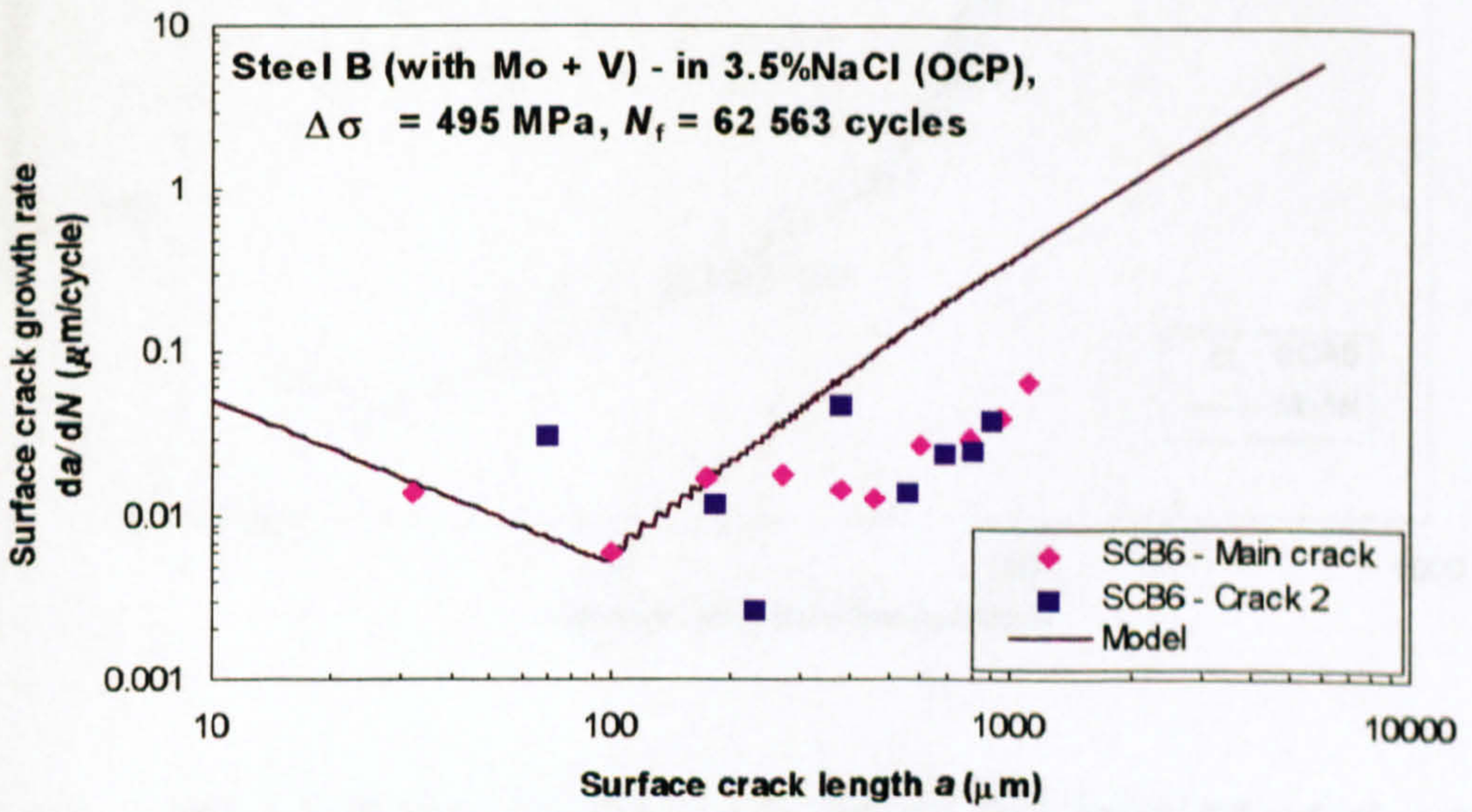

Figure 8.4 Corrosion fatigue crack growth rate of Steel B (with Mo + V) **in 3.5%NaCl solution** (OCP) **calculated from the model**

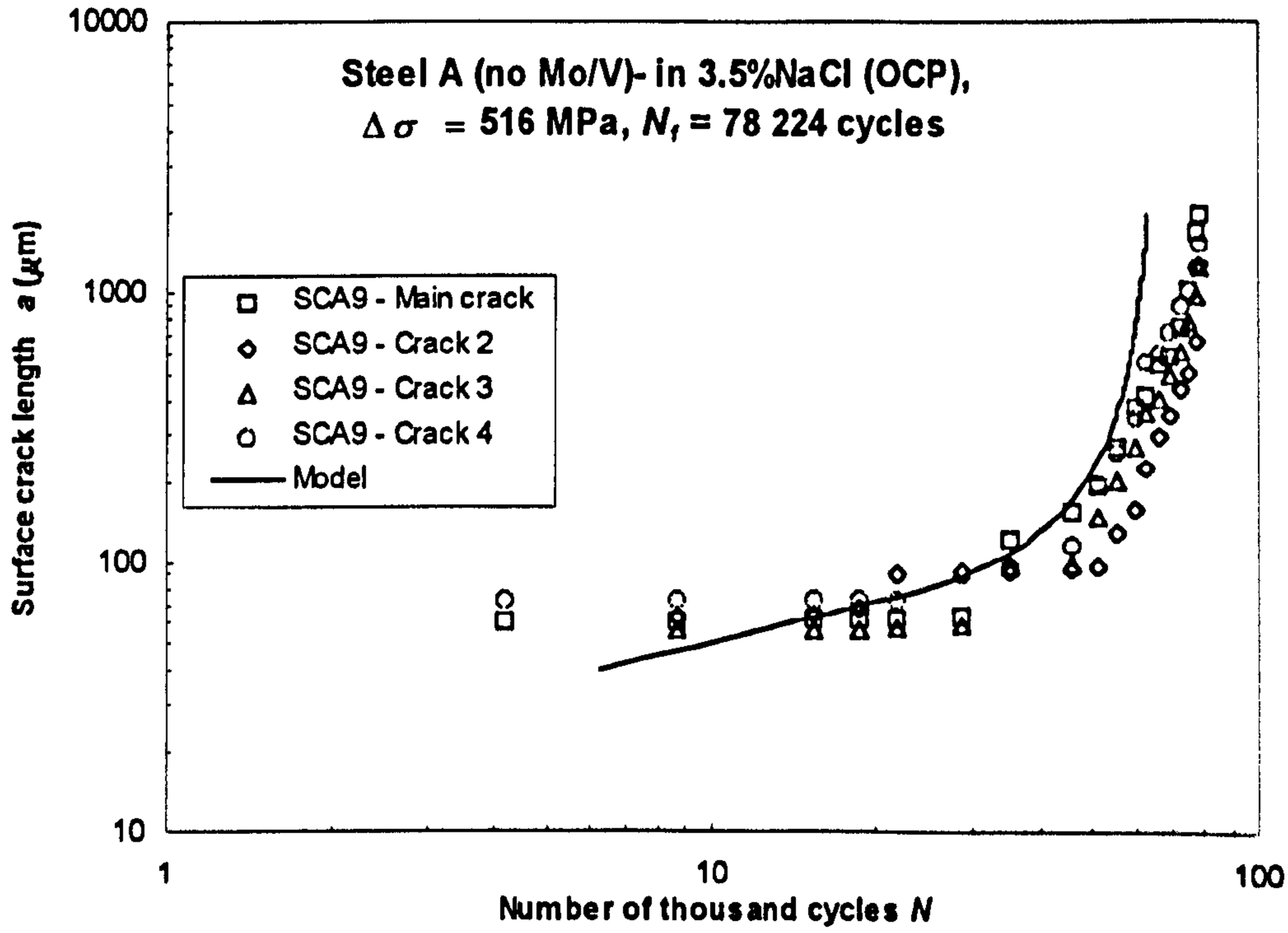

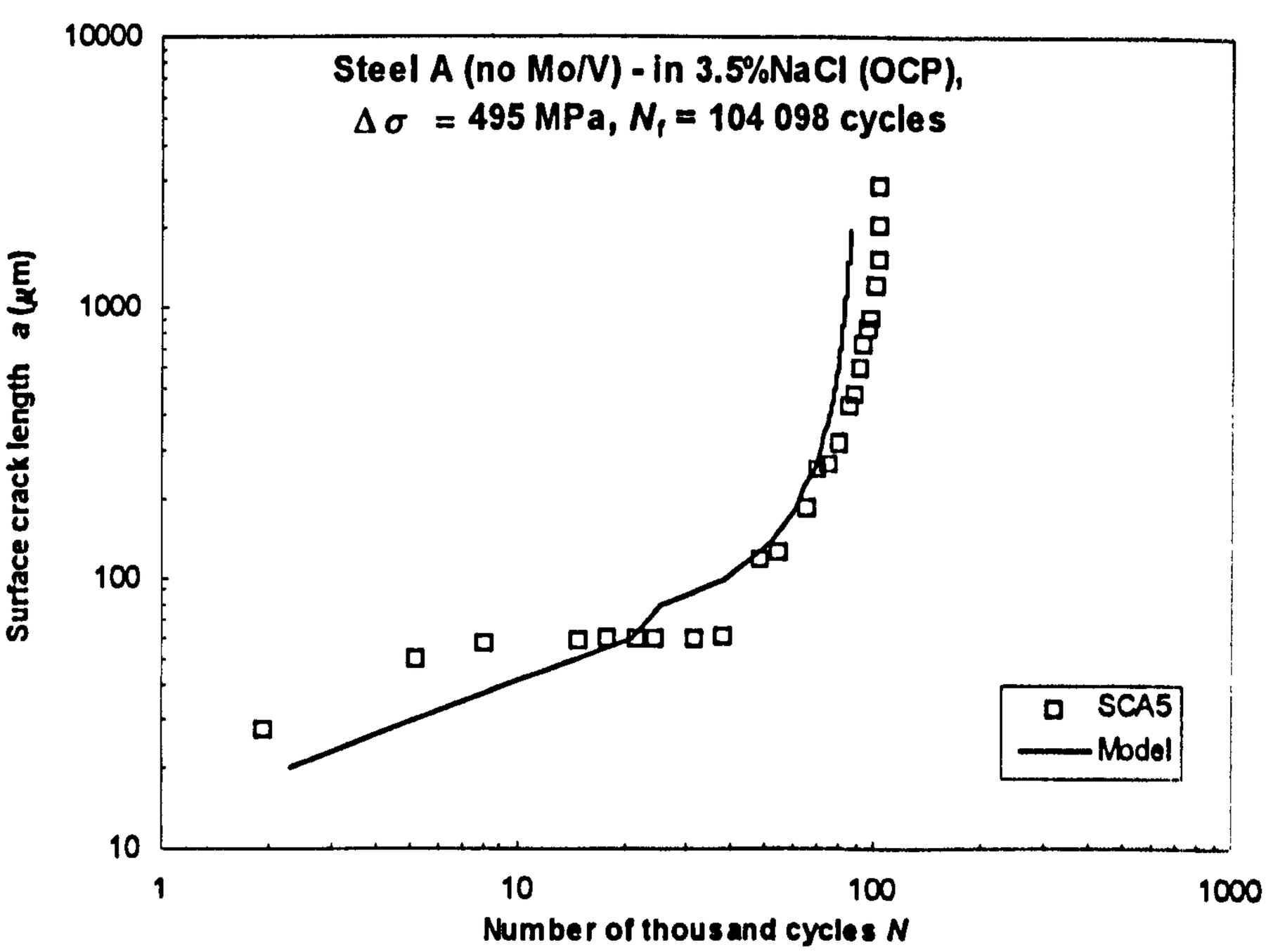

Figure 8.5 **The $a \sim N$ curve of Steel A** (no Mo/V) **in 3.5%NaCl solution (OCP) obtained from the model**

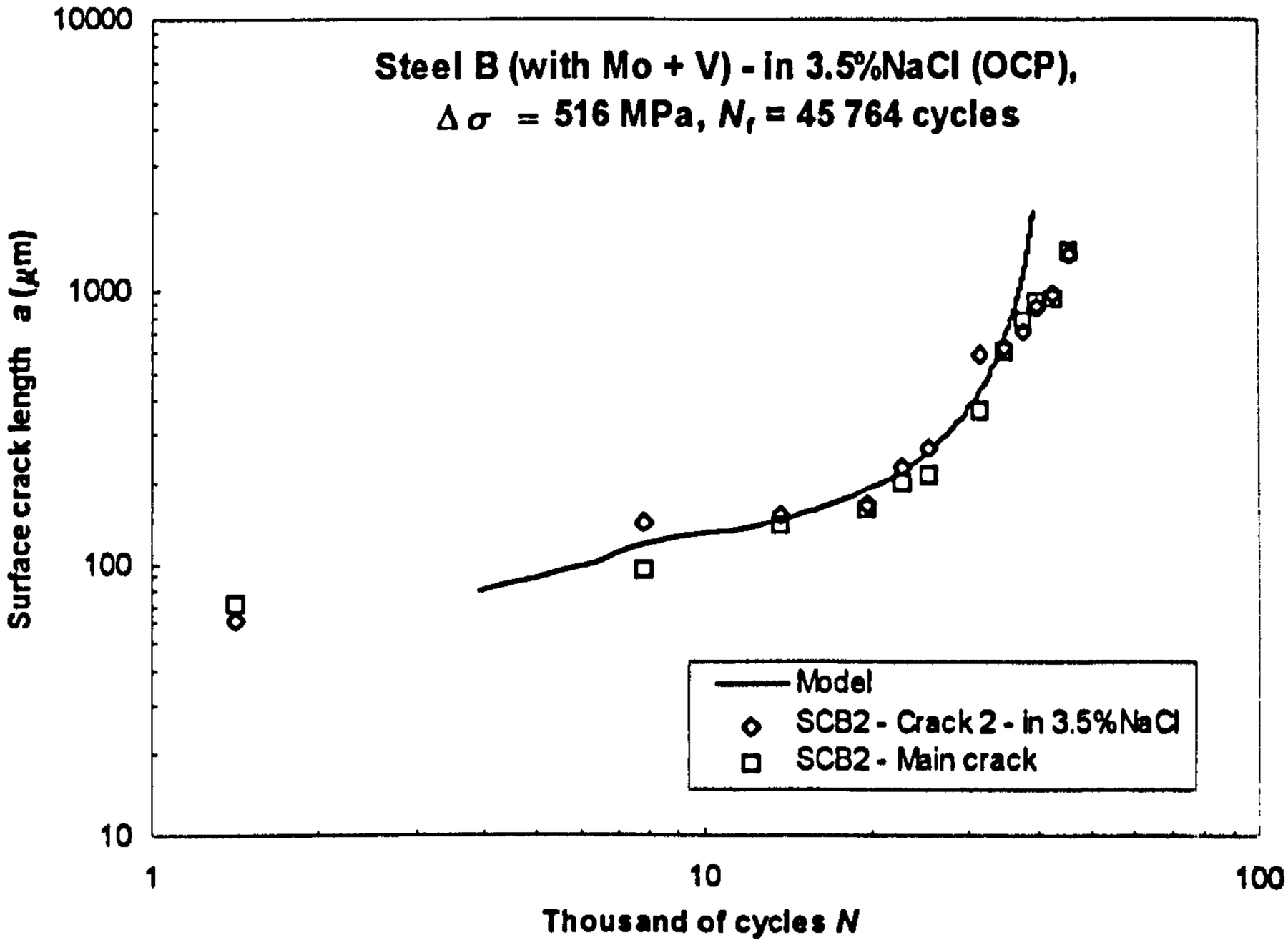

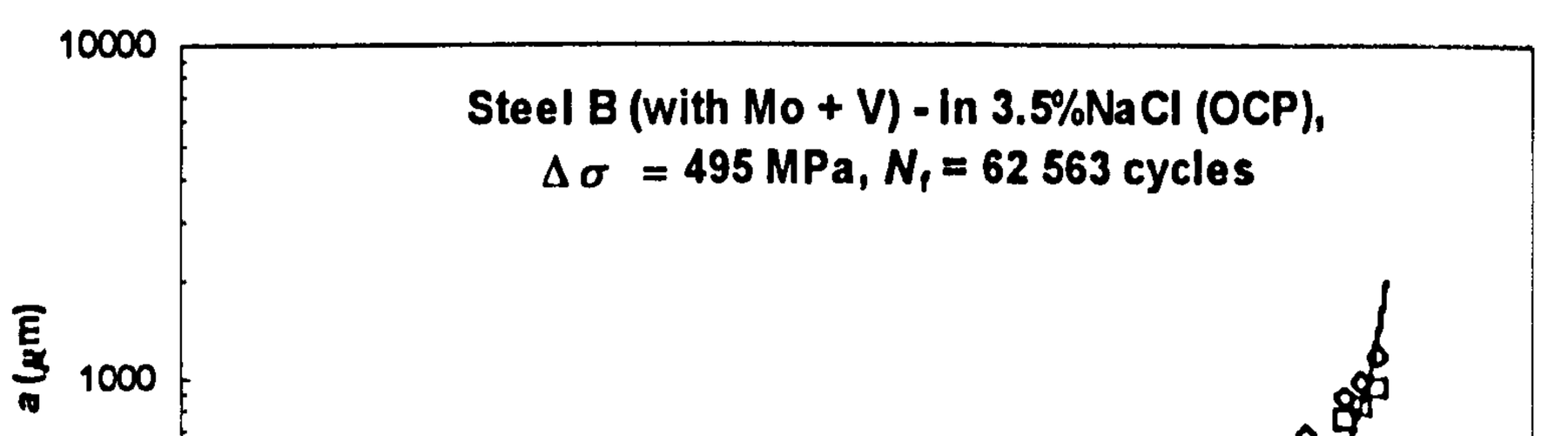

Figure 8.6 **The $a \sim N$ curve of Steel B (with Mo + V) in 3.5%NaCl solution (OCP) obtained from the model**

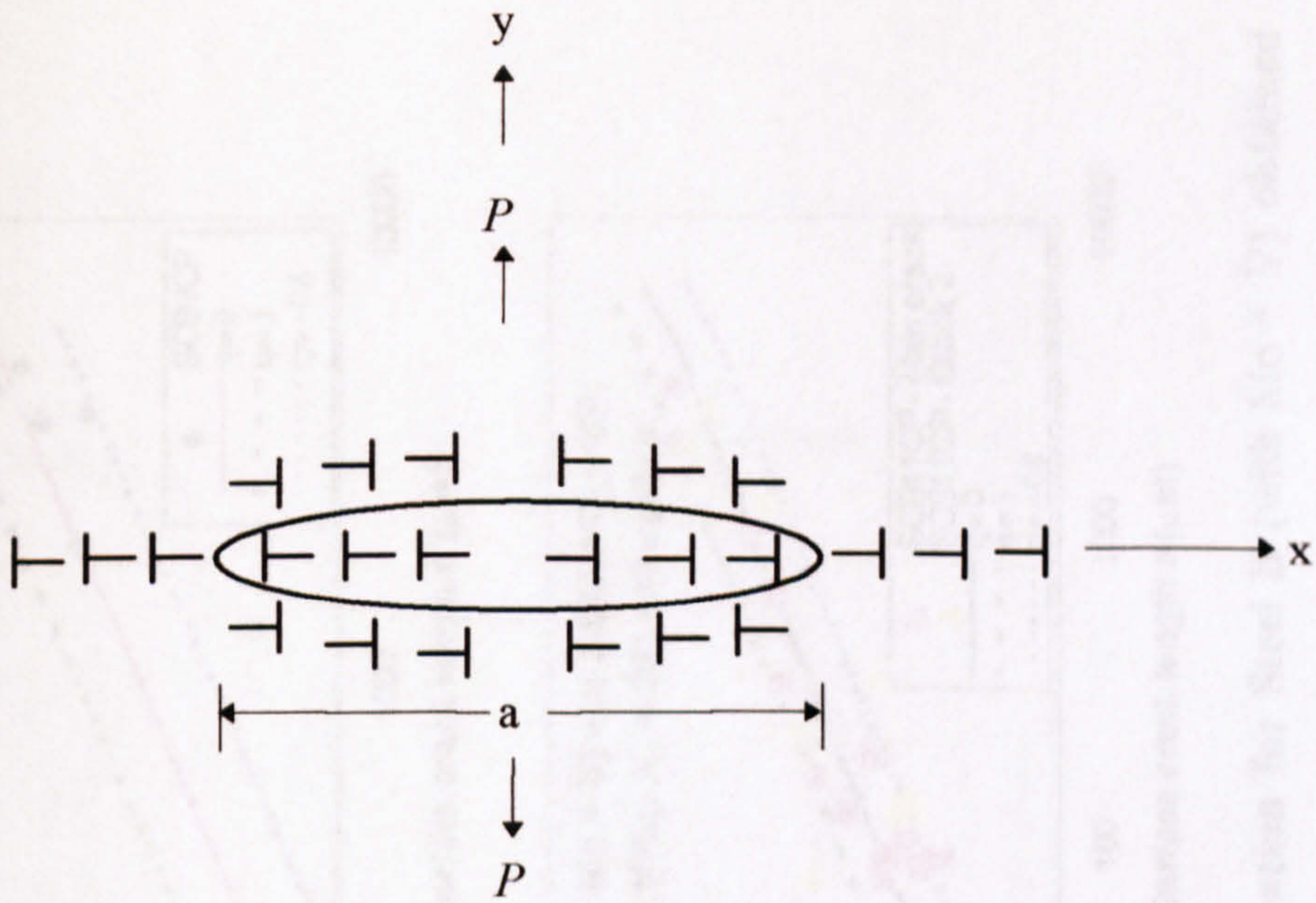

Figure 9.1 Dislocation model of hydrogen effect on the crack growth

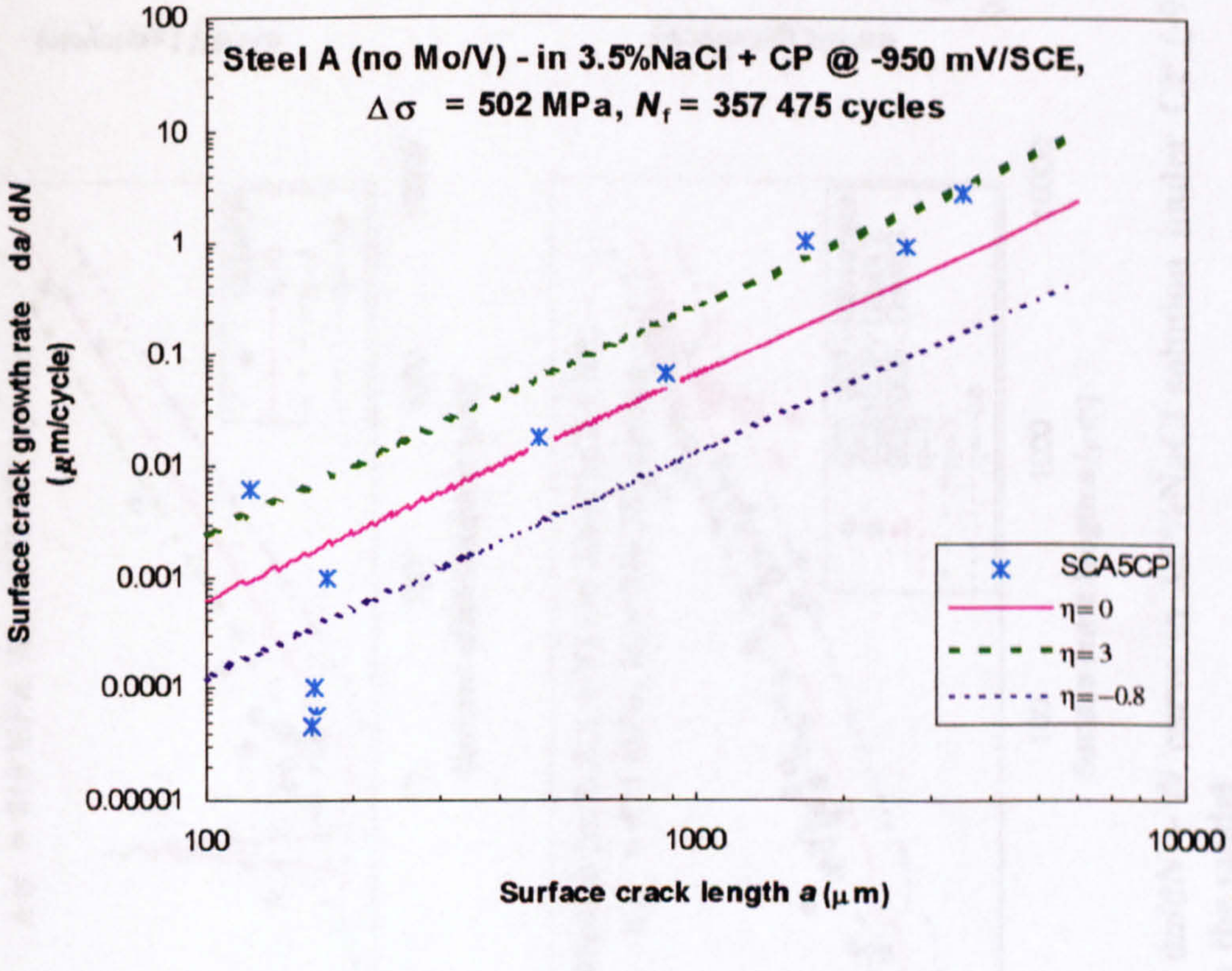

Figure 9.2 The d*a*/d*N* ~ *N* curve in 3.5%NaCl solution under CP (-950 mV/SCE) **application for Steel A** (no Mo/V) **obtained from the model**

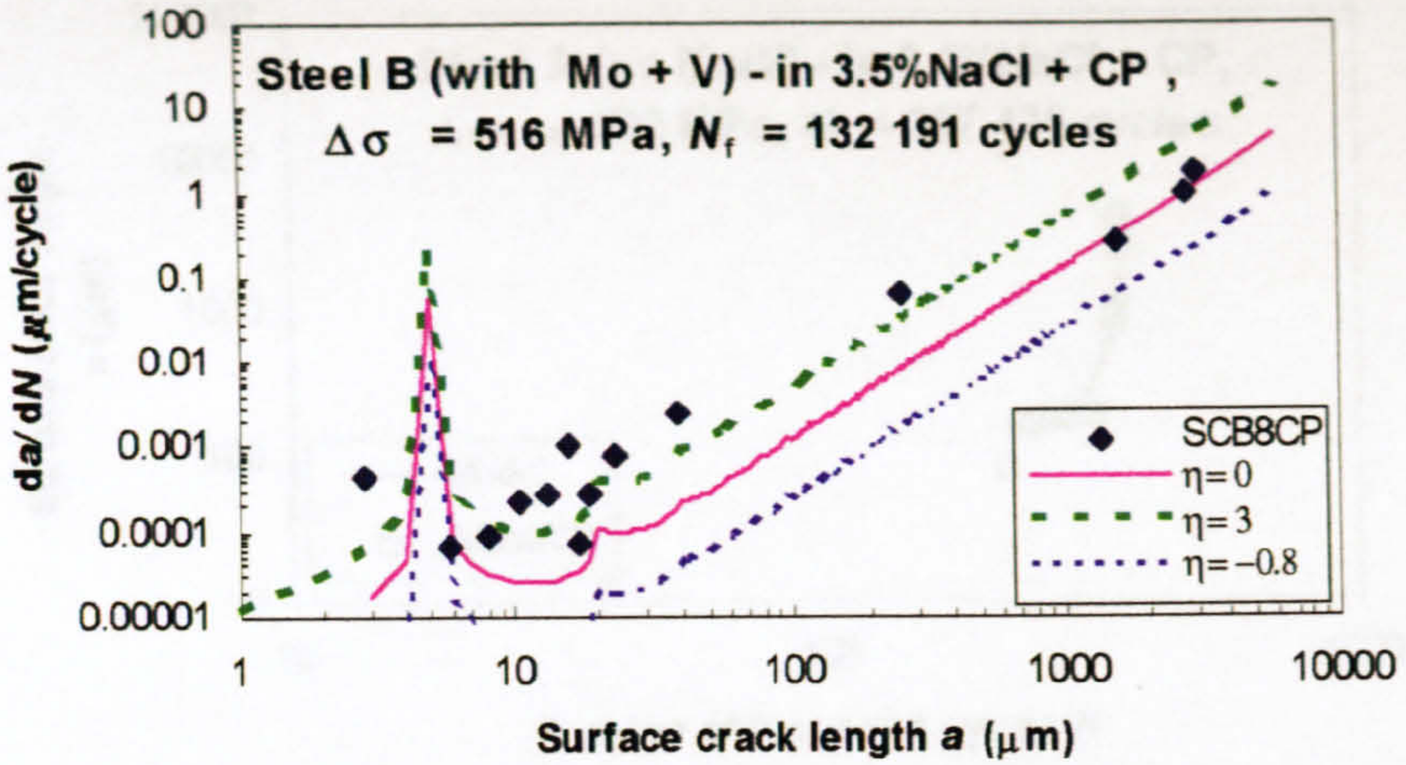

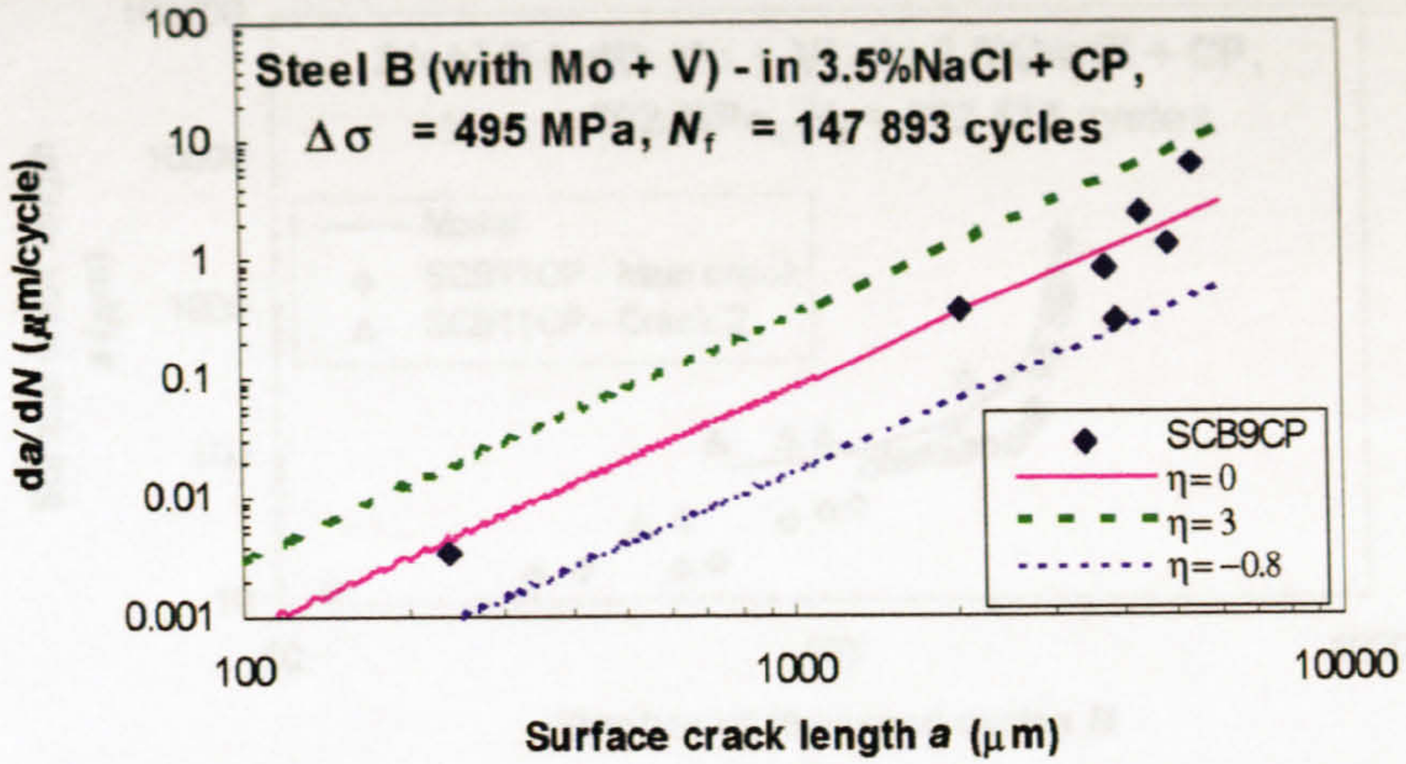

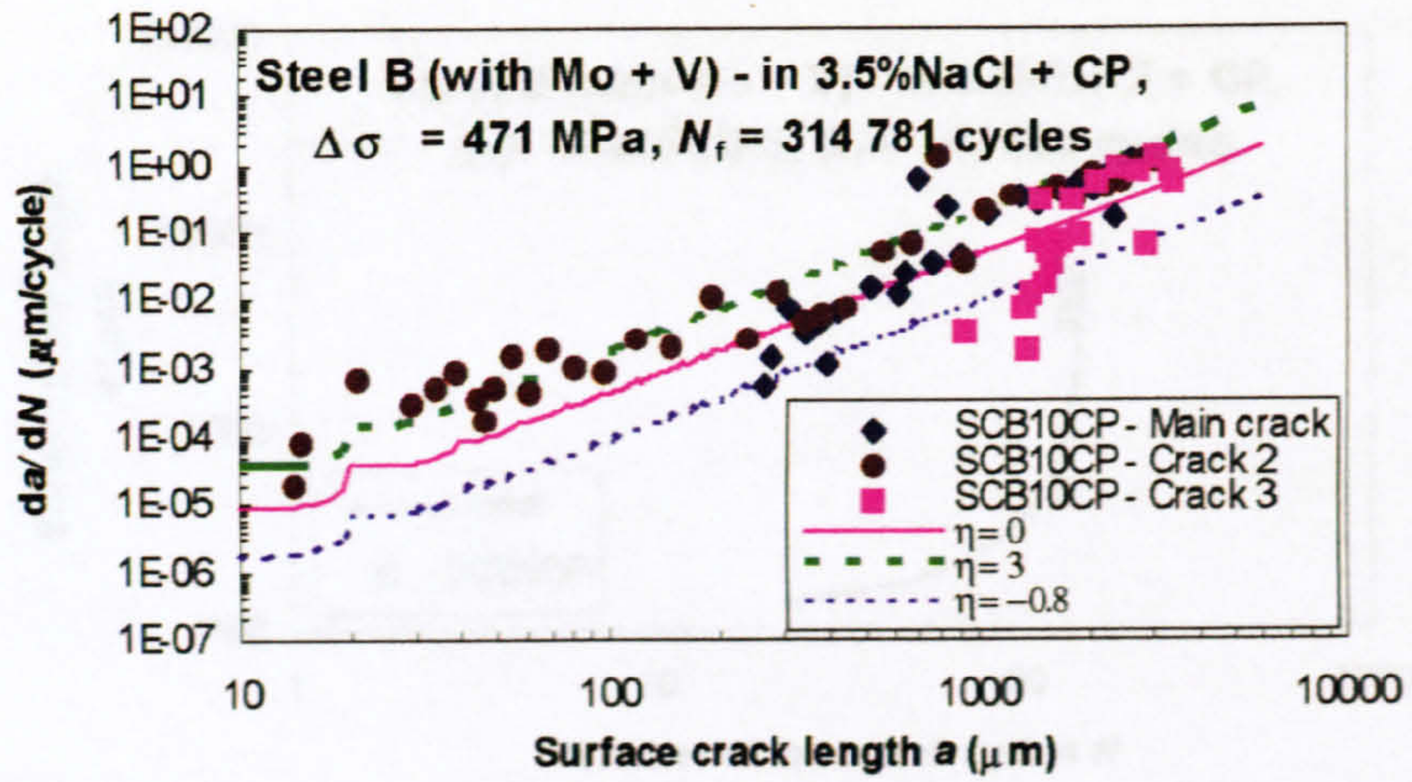

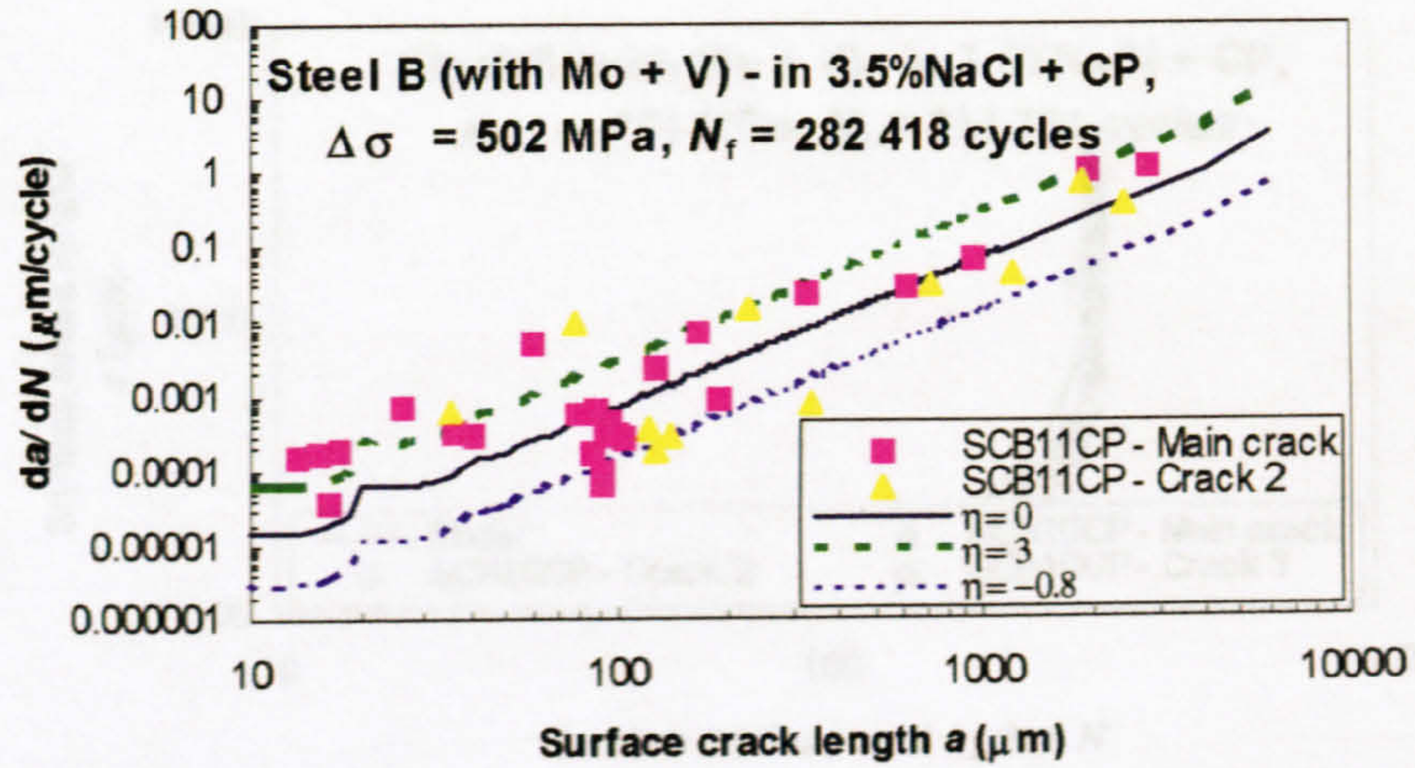

Figure 9.3 **The d*a*/d*N* ~ *N* curve in 3.5%NaCl solution under CP** (-950 mV/SCE) **application for Steel B** (with Mo + V) **obtained from the model**

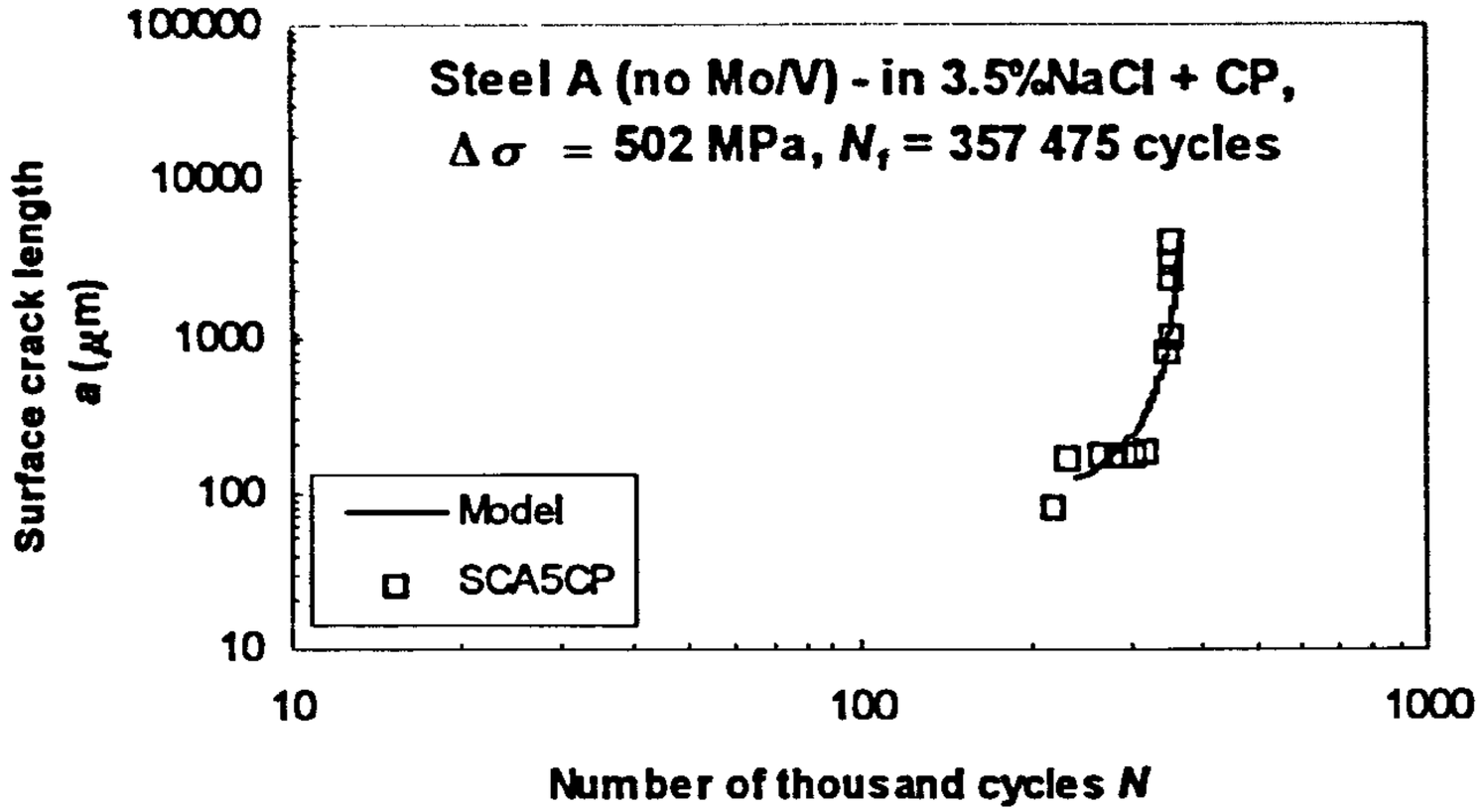

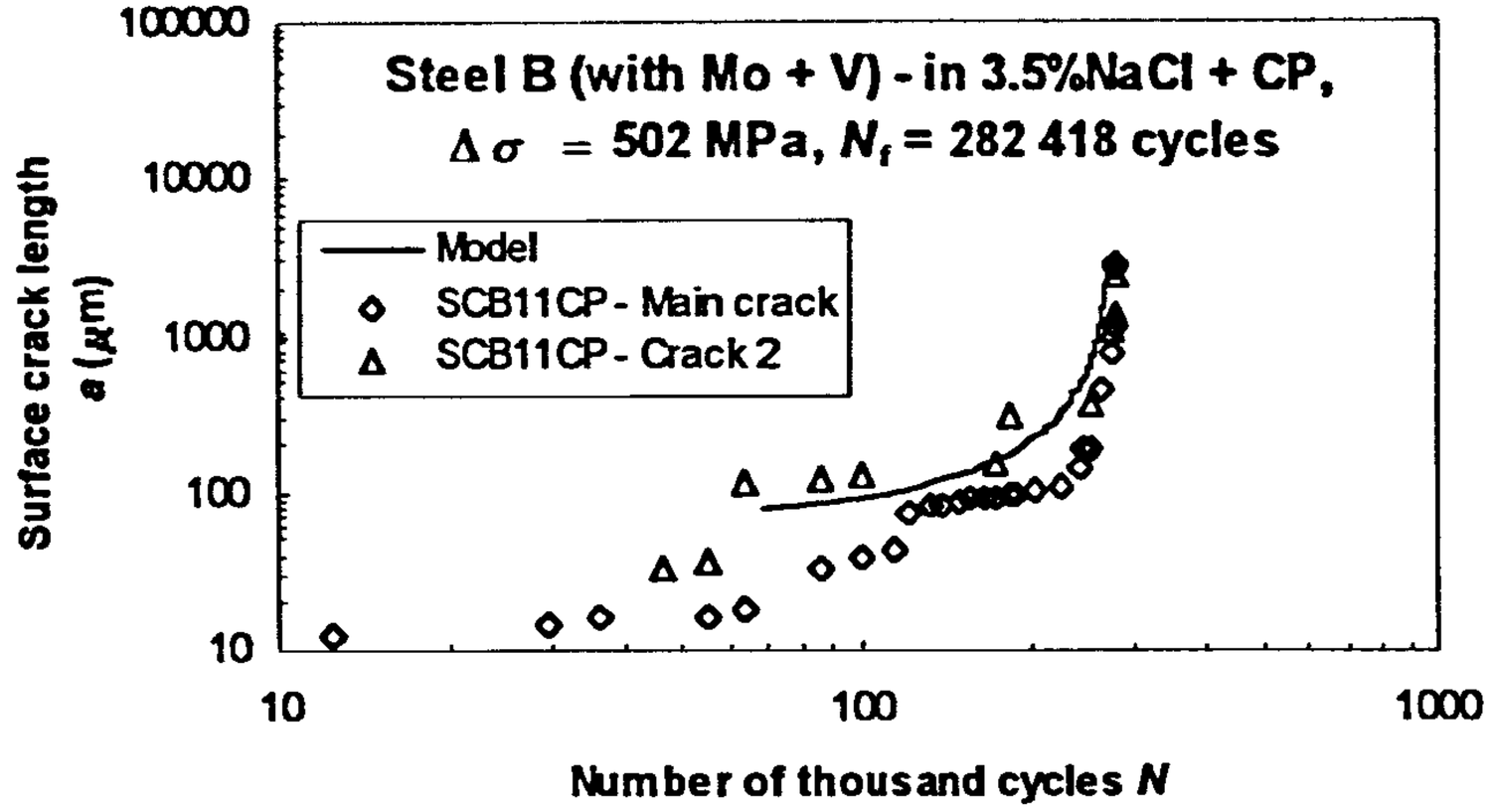

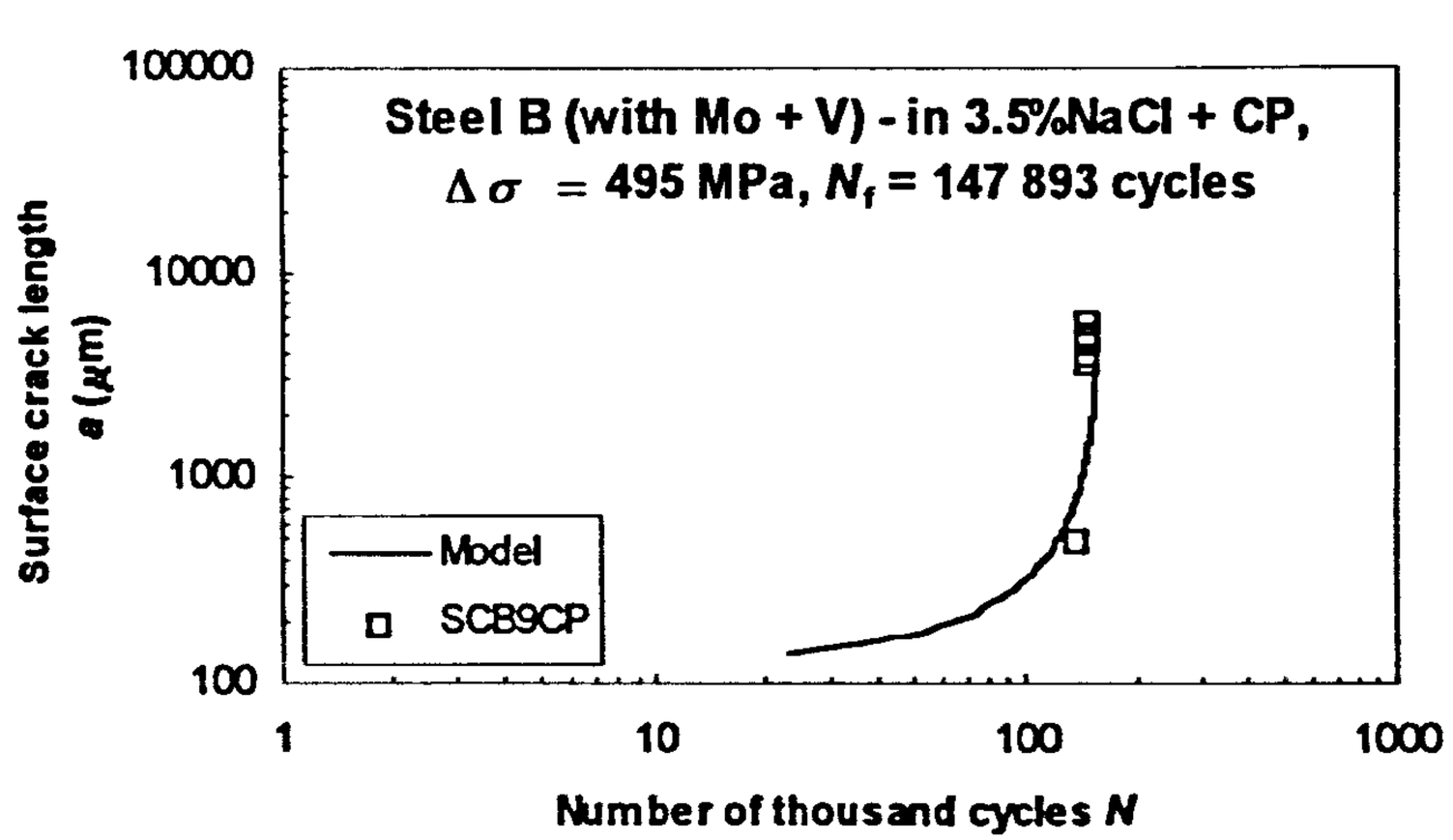

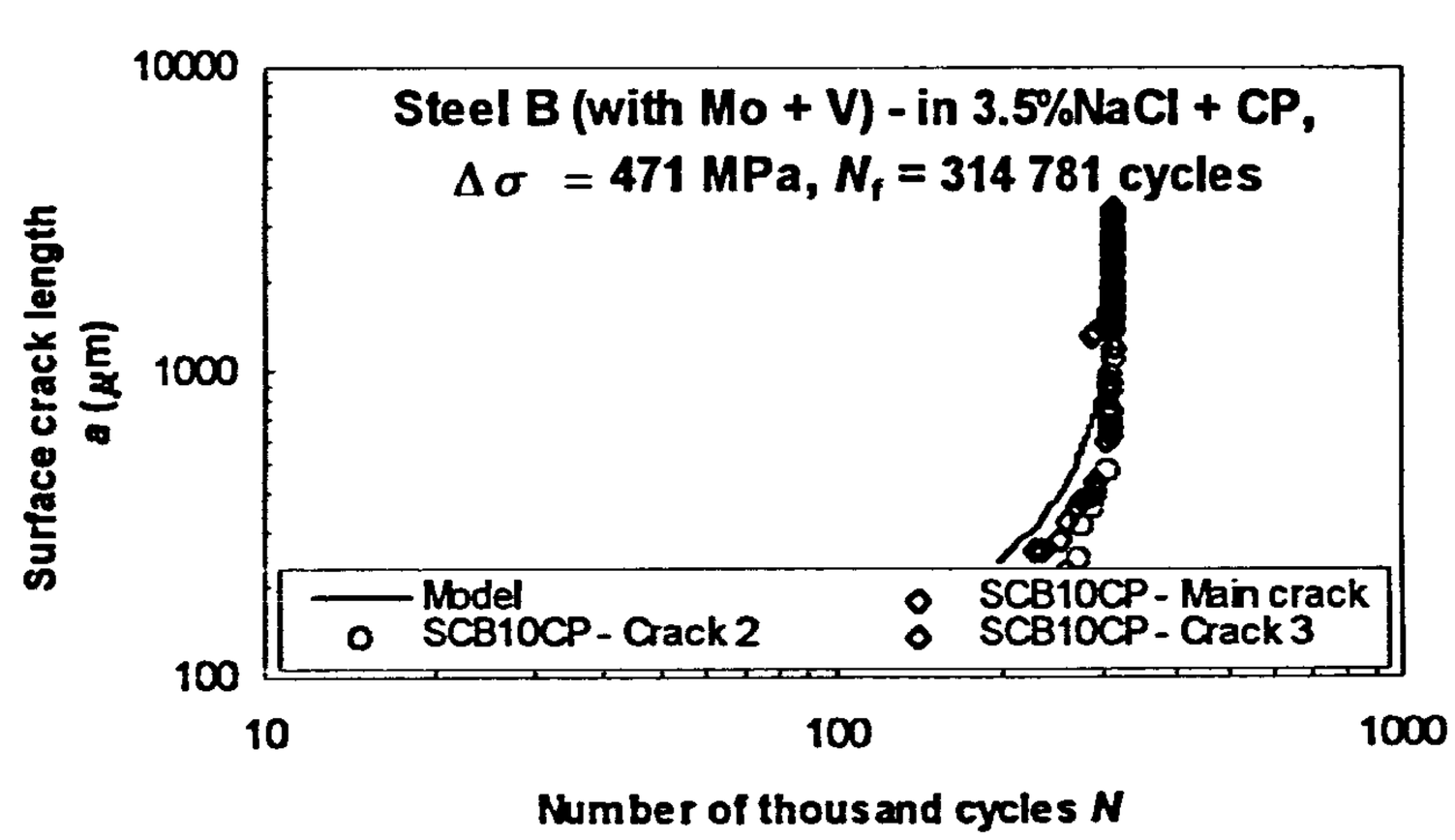

Figure 9.4 The $a \sim N$ curve in 3.5%NaCl solution under applied cathodic polarisation (-950 mV/SCE) obtained from the model

Tables

Table 2.1 Reviews of various mathematical equations for da/dN in literature [69]

Theory of model	Criterion or rate determining requisite	Equation for da/dN
Energy approach (Liu) [70]	Energy balance	$\alpha_1(\frac{\Delta K}{\sigma_{ys}})^2$
Energy approach (Paris) [71]	Energy balance	$\frac{\alpha_2}{l_2}(\frac{\Delta K}{\sigma_{ys}})^4$
Energy approach (Raju) [72]	Energy balance	$\alpha_3\frac{\Delta K^4}{\sigma_{ys}^3(K_{IC}^2-K_{max}^2)}$ $K_{max} << K_1, \alpha_3\frac{\Delta K^4}{\sigma_{ys}^2 K_{IC}^2}$
Energy approach (Cherepanov et al.) [73]	Energy balance	$\alpha_4\frac{\Delta K^4 E}{\sigma_{ys}^3 K_{IC}^2}$
Crack opening displacement (COD) (Rice) [74]	Critical value of cumulative displacement at crack tip	$\frac{\alpha_5}{l_5}(\frac{\Delta K}{\sigma_{ys}})^4$
Continuous dislocation formalism (not crystal dislocation theory) (Weertman) [75]	Critical value of cumulative displacement at crack tip	$\alpha_6\frac{\Delta K^4}{\gamma E\sigma_{ys}^2}$
Continuous dislocation formalism (not crystal dislocation theory) (Weertman et al.) [76, 77]	Critical value of cumulative displacement at crack tip Critical value of plastic work	$\alpha_7\frac{\Delta K^4}{\gamma_p\mu\sigma_n^2}$
COD (Schwalbe) [78]	Critical value of COD	$\alpha_8\frac{\Delta K^2}{E\sigma_{ys}}$
COD (Pook) [79]	Critical value of COD	$\alpha_9(\frac{\Delta K^2}{E})$
Slip band decohesion (Tomkins) [80]	Critical value of COD	$\frac{\pi}{8}(\frac{\Delta K}{\sigma_{ys}})^2(\frac{\Delta\sigma}{\sigma_0})^{1/\beta}$
COD (Donahue) [81]	Critical value of COD	$\alpha_{10}\frac{\Delta K^2}{\mu\sigma_n}$

Table 2.1 (Continued)

Theory of model	Criterion or rate determining requisite	Equation for da/dN
Nucleation rate process approach (kinetic theory) (Yokobori et al.) [82]	Microcrack initiation at crack tip	Elastic-plastic $\alpha_{11}(\frac{\Delta K}{\sqrt{sE}})^{\frac{2\beta}{1+\beta}}(\frac{b\sigma_{cy}^2}{\gamma E})^{\frac{1}{2\xi kT}}$
Dislocations approach (kinetic theory) (Yokobori et al.) [83]	Dynamical emission of dislocation groups from crack tip	Elastic approximation $\alpha_{12}(\frac{\Delta K}{\sqrt{sE}})^{\frac{(m+1)^2}{m+2}}$
Short crack model (Hobson and Brown) [60]		$A(\Delta\varepsilon)^{\alpha}(d-a)$ MSC $B(\Delta\gamma)^{\beta'}a-D$ PSC
Short crack model (dislocation model) (Navarro and de los Rios) [61-63]	Elastic-plastic interface coinciding with a grain boundary	$f'\phi$

Symbols of Table 2.1

A = material constant
a = crack length
B = material constant
b = constant
D = threshold condition
d = distance to the major microstructural barrier affecting crack growth
E = Young's modulus
f' = fraction of dislocations
K_{Ic} = plane strain fracture toughness
K_{max} = maximum stress intensity factor
ΔK = stress intensity factor range
l_i = appropriate measure of length
m = dislocation velocity power exponent
N = number of applied loading cycles
s = appropriate measure of length
α = material constant
α_i = numerical factor
β = cyclic hardening exponent
β' = material constant
γ = specific surface energy
$\Delta\gamma$ = applied shear strain range
γ_p = effective surface energy for fatigue crack growth
ε_{cy} = strain at σ_{cy} in cyclic stress-strain relation, $\sigma_{cy} = E\varepsilon_{cy}$
$\Delta\varepsilon_p$ = cyclic plastic strain range
ϕ = crack tip plastic displacement
μ = shear modulus
σ_u = appropriate measure of strength of alloy
σ_{cy} = initial yield stress for cyclic stress-strain relation, $\Delta\sigma = \sigma_{cy}(\Delta\varepsilon_p/\varepsilon_{cy})^{\beta}$
σ_{ys} = monotonic or static yield strength yield strength
$\Delta\sigma$ = cyclic stress range

Subscripts: i = 1, 2, 3, ... etc.

Table 2.2 Models for environment-assisted fatigue crack growth prediction [85]

Wei/Landes: Superposition model

$$(\frac{da}{dN})_e = (\frac{da}{dN})_{AIR} + \int_{t_1}^{t_2} \frac{da}{dt} k(t) dt$$

Austen/Walker: Process competition model

$$(\frac{da}{dN})_e = \max\{(\frac{da}{dN})_{AIR} (\frac{da}{dt}) \frac{1}{F}$$

Gallagher:

$$(\frac{da}{dN})_e = (\frac{da}{dt})_{env} + (\frac{da}{dN})_{AIR} F$$

Nakasa:

$$(\frac{da}{dN})_e = (\frac{da}{dN})_{AIR} + \beta \int_{t_1}^{t_2} \frac{da}{dt} t dt$$

Wei/Simons: Superposition model

$$(\frac{da}{dN})_e = (\frac{da}{dN})_{AIR} + (\frac{da}{dN})_{CF} + (\frac{da}{dN})_{SCC}$$

Marshall: Superposition model

$$(\frac{da}{dN})_e = (\frac{da}{dN})_{AIR} + (\frac{da}{dN})_{\text{oxide penetr}}$$

Solomon:

$$(\frac{da}{dN})_e = c(\Delta \varepsilon_p) \nu^{k-1}$$

Kawai:

$$(\frac{da}{dN})_e = D(\frac{da}{dN})_{AIR}$$

Table 3.1.1 Composition of RQT501 steels

Steel type	C (%)	Si (%)	Mn (%)	S (%)	P (%)	Cr (%)	Mo (%)	Nb (%)	V (%)	Ti (%)	Ni (%)	Cu (%)	Al (%)	CEV (%)
Steel A (12.5 mm)	0.12	0.30	1.45	0.003	0.011	0.02	0.01	0.003	0.01	0.004	0.02	0.02	0.04	0.38
Steel B (25 mm)	0.10	0.30	1.30	0.003	0.011	0.02	0.17	0.003	0.05	0.004	0.02	0.02	0.03	0.37

Table 3.1.2 Mechanical properties of RQT501 steels

Steel type	Plate thickness (mm)	0.2% Proof stress (MPa)	Reduction of area (%)	Elongation (%)	Tensile strength σ_b (MPa)
Steel A	12.5	508	77	22	608
Steel B	25	515	80	26	600

Table 3.2.1 Results of grain size

Steel A (no Mo/V) (plate thickness - 12.5 mm)		
Overall mean grain size		**8.7 μm**
		Grain size (μm)
(1) LT section (face 1)	Mean	9.2
	Longitudinal direction	9.6
	Transverse direction	8.8
	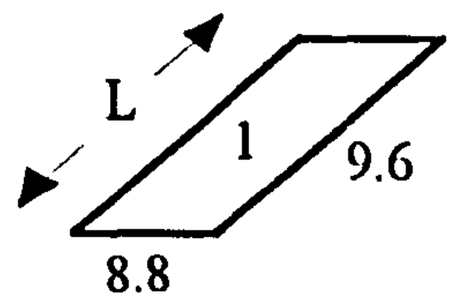	
(2) VL section (face 2)	Mean	8.4
	Longitudinal direction	8.1
	Vertical direction	8.6
	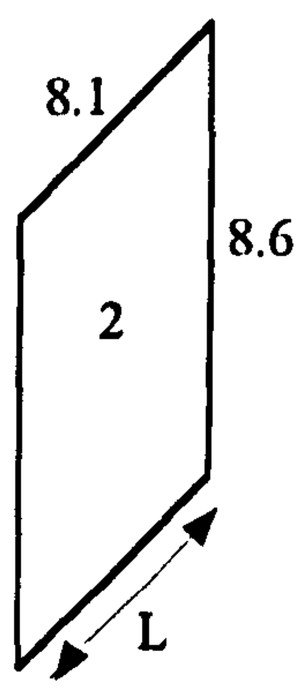	
(3) TV section (face 3)	Mean	8.4
	Vertical direction	8.0
	Transverse direction	8.7
	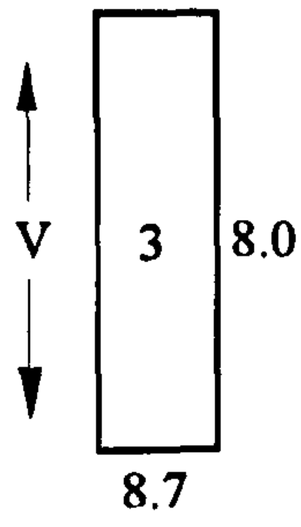	

Table 3.2.1 (Continued)

Steel B (with Mo + V) (plate thickness - 25 mm)		
Overall mean grain size		**10.7 μm**
		Grain size (μm)
(1) LT section	Mean	10.7
(face 1)	Longitudinal direction	11.0
	Transverse direction	10.3
	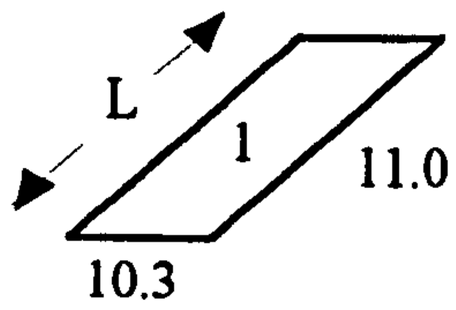	
(2) VL section	Mean	10.5
(face 2)	Longitudinal direction	10.5
	Vertical direction	10.4
	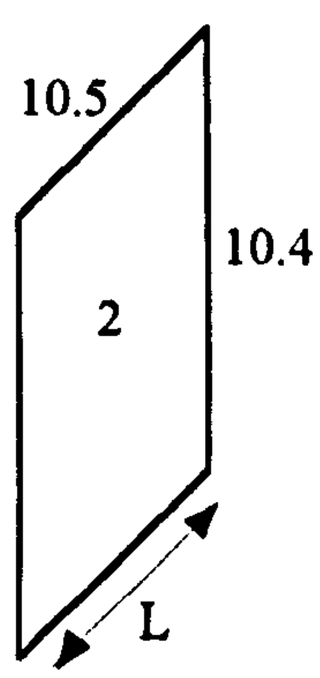	
(3) TV section	Mean	10.9
(face 3)	Vertical direction	11.1
	Transverse direction	10.7
	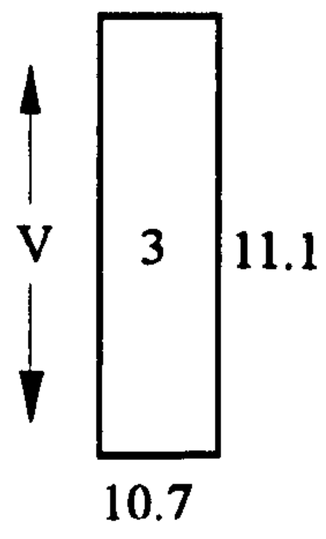	

Table 3.3.1 Feature analysis from VANOX

	Section	Area (μm^2)	Perimeter (μm)	Long. Dims. (μm)	Breadth (μm)	Form Factor
Steel A	LT	47.7	24.5	7.3	5.6	0.59
	LV	84.7	32.6	10.6	6.9	0.59
	VT	57.1	28.6	9.1	5.8	0.57
	Mean	63.5	28.6			0.58
Steel B	LT	57.4	28.8	8.8	7.2	0.64
	LV	116.2	42.4	14.9	8.3	0.61
	VT	74.1	28.1	7.6	5.6	0.49
	Mean	82.6	33.1			0.58

	Section	Horz. Int (μm)	Vert. Int (μm)	*X* feret (μm)	*Y* feret (μm)	$\frac{X \text{ feret} + Y \text{ feret}}{2}$ (μm)
Steel A	LT	6.0	6.7	6.6	5.9	6.3
	VL	8.0	9.6	9.5	7.8	8.7
	VT	8.2	7.0	6.8	8.0	7.4
	Mean					7.5
Steel B	LT	7.7	7.7	7.6	7.7	7.6
	VL	14.3	9.1	8.3	11.5	9.9
	VT	8.7	8.4	6.7	6.7	6.7
	Mean					8.1

Where *X* feret = longest projection in the horizontal axis

Y feret = longest projection in the vertical axis

Form factor = $\frac{4\pi \times \text{Area}}{\text{Perimeter}^2}$ and gives an indication of the roundness of a feature

Table 3.3.2 Field analysis from VANOX

	Section	Area (μm^2)	Perimeter (μm)	Feat. count	End count	Field area (μm^2)
Steel A	LT	608.2	336.9	14.5	15.0	913114.5
	LV	1193.6	362.0	11.1	12.0	913114.5
	VT	962.7	467.6	17.2	18.0	913114.5
	Mean	921.5	388.8	14.3	15.0	913114.5
Steel B	LT	1000.6	409.8	14.4	14.5	913114.5
	LV	2745.7	927.4	27.2	28.6	913114.5
	VT	736.3	288.0	9.1	14.2	913114.5
	Mean	1207.8	465.3	15.6	17.6	913114.5

	Section	Area frac. (%)	Horz. Int (μm)	Vert. Int (μm)	Anisotropy	$\frac{\text{Count}}{\text{Area}}$ (μm^{-2})
Steel A	LT	0.07	91.8	100.8	0.92	1.6E-05
	LV	0.13	101.8	112.2	0.96	1.2E-05
	VT	0.11	148.9	122.7	1.23	1.9E-05
	Mean	0.10			1.04	1.6E-05
Steel B	LT	0.11	117.7	121.0	0.97	1.6E-05
	LV	0.30	297.6	247.6	1.22	3.0E-05
	VT	0.81	90.8	91.7	0.94	1.0E-06
	Mean	0.13			1.04	1.7E-05

	Section	Hz. Int/Area (μm^{-1})	Vt. Int/Area (μm^{-1})
Steel A	LT	1.0E-04	1.1E-04
	LV	1.1E-04	1.2E-04
	VT	1.6E-04	1.3E-04
Steel B	LT	1.3E-04	1.3E-04
	LV	3.3E-04	2.7E-04
	VT	9.9E-05	1.0E-04

Table 3.3.3 Field analysis from Repan

	Section	Mean Area (μm^2)	Area (μm^2)	Field area (μm^2)	Area frac. (%)
Steel A	LT	73.8	738.22	175365.6	0.42
	LV	128.0	770.46	177101.2	0.44
	VT	110.9	628.65	173343.9	0.36
	Mean	104.2	712.44	175270.2	0.41
Steel B	LT	89.19	752.17	174867.8	0.44
	LV	65.59	1080.50	149115.0	0.72
	VT	84.98	715.20	149493.7	0.48
	Mean	79.92	849.29	157825.5	0.55

Table 3.3.4 Summary of inclusion size

Steel A (no Mo/V) (plate thickness - 12.5 mm)			
Overall mean inclusion size			**7.5 μm**
		Inclusion size (μm)	
		Maximum	Mean
(1) LT section	Mean		6.3
(face 1)	Longitudinal direction	49.2	6.6
	Transverse direction	53.4	5.9
(2) VL section	Mean		8.7
(face 2)	Longitudinal direction	53.0	7.8
	Vertical direction	64.0	9.5
(3) TV section	Mean		7.4
(face 3)	Vertical direction	47.7	6.8
	Transverse direction	74.8	8.0

Table 3.2.5 (Continued)

Steel B (with Mo + V) (plate thickness - 25 mm)			
Overall mean inclusion size			**8.1** μm
		Inclusion size (μm)	
		Maximum	Mean
(1) LT section (face 1)	Mean		7.7
	Longitudinal direction	38.5	7.6
	Transverse direction	40.6	7.7
(2) VL section (face 2)	Mean		9.9
	Longitudinal direction	62.0	11.5
	Vertical direction	49.2	8.3
(3) TV section (face 3)	Mean		6.7
	Vertical direction	42.7	6.7
	Transverse direction	59.8	6.7

Table 4.1 Test results of fatigue lifetime of Steel A (no Mo/V)

Sample	$\Delta\sigma$ (MPa)	f (Hz)	Environment	N_f (cycles)	N.B.
SA1*	525	10	Air	389190	etched
SA2*	520	10	Air	615070	etched
SA3*	522	10	Air	690000	etched
SA4	528	10	Air	1820	etched
SA5	529	10	Air	12700	etched
SA6	524	10	Air	18260	etched
SA7*	496	10	Air	6375000	etched/unbroken
SA8*	515	10	Air	7209490	etched/unbroken
SA9*	519	10	Air	4420000	etched/unbroken
SCSA1	516	0.2	Artificial seawater	613	
SCSA2*	516	0.2	Artificial seawater	50455	
SCA1*	495	0.2	3.5%NaCl	77161	etched
SCA2*	396	0.2	3.5%NaCl	355000	
SCA4	516	0.2	3.5%NaCl	5798	
SCA5*	495	0.2	3.5%NaCl	104098	
SCA7*	471	0.2	3.5%NaCl	104868	
SCA8	516	0.2	3.5%NaCl	5140	
SCA9*	516	0.2	3.5%NaCl	78224	
SCA1CP*	495	0.2	3.5%NaCl + CP	723997	unbroken
SCA2CP	517	0.2	3.5%NaCl + CP	960	
SCA3CP	515	0.2	3.5%NaCl + CP	1560	
SCA4CP	510	0.2	3.5%NaCl + CP	7200	
SCA5CP*	502	0.2	3.5%NaCl + CP	357475	

* - the specimens with replicas

Table 4.2 Test results of fatigue lifetime of Steel B (with Mo/V)

Sample	$\Delta\sigma$ (MPa)	f (Hz)	Environment	N_f (cycles)	N.B.
SB1	502	10	Air	547000	
SB2	532	5	Air	14820	etched
SB3*	528	10	Air	141690	etched
SB4*	530	10	Air	205630	etched
SB5*	522	10	Air	214190	etched
SB6*	516	10	Air	339240	etched
SB7*	502	10	Air	505990	etched
SB8*	495	10	Air	1147130	etched
SB9*	474	10	Air	2220000	etched/unbroken
SCSB1*	516	0.2	Artificial seawater	59000	
SCSB2*	495	0.2	Artificial seawater	100000	
SCB1*	VA	0.2	3.5%NaCl	114237	360 MPa/495 MPa
SCB2*	515	0.2	3.5%NaCl	45764	
SCB3	527	0.2	3.5%NaCl	1626	
SCB4*	471	0.2	3.5%NaCl	78321	
SCB5*	471	0.2	3.5%NaCl	65104	
SCB6*	495	0.2	3.5%NaCl	62563	
SCB7*	396	0.2	3.5%NaCl	151913	
SCB8CP*	516	0.2	3.5%NaCl + CP	132191	
SCB9CP*	495	0.2	3.5%NaCl + CP	147893	
SCB10CP*	471	0.2	3.5%NaCl + CP	310000	
SCB11CP*	502	0.2	3.5%NaCl + CP	282418	
SCB12CP*	495	0.2	3.5%NaCl + CP	600000	unbroken
SCB13CP	516	0.2	Artificial seawater + CP	475615	

* - the specimens with replicas

Table 4.3 **Constants for regression equation $\Delta\sigma^{n_1} N_f = n_2$ and fatigue endurance at 10^7 cycles for Steel A (no Mo/ V)**

Environment	n_1	n_2	Std. Dev.	Fatigue Endurance (MPa)
Air	0.0034	1.02	0.9205	516
3.5%NaCl (OCP)				
Region I: $\Delta\sigma \geq$ 511 MPa	0.0058	1.04	0.9346	
Region II: $\Delta\sigma \leq$ 511 MPa	0.1536	3.39	0.9507	240
CP (-950 mV/SCE)	0.0081	1.05	0.9974	480

Table 4.4 **Constants for regression equation $\Delta\sigma^{n_1} N_f = n_2$ and fatigue endurance at 10^7 cycles for Steel B (with Mo + V)**

Environment	n_1	n_2	Std. Dev.	Fatigue endurance (MPa)
Air				
Region I: $\Delta\sigma \geq$ 529 MPa	0.0017	1.01	0.9426	
Region II: $\Delta\sigma \leq$ 529 MPa	0.0359	1.27	0.9083	480
3.5%NaCl (OCP)				
Region I: $\Delta\sigma \geq$ 517 MPa	0.0042	1.03	0.9516	
Region II: $\Delta\sigma \leq$ 517 MPa	0.2208	6.71	0.9656	160
CP (-950 mV/SCE)	0.0598	1.48	0.4776	390

Table 4.5 A summary of pit/crack transition behaviour for Steel A (no Mo/V)

$\Delta\sigma$ (MPa)	$t_{p/c}$ (hrs.)	$a_{p/c}$ (μm)	Average transition time (hrs.)	Average transition pit size (μm)
516	40	93	35	72
	30	73		
	40	63		
	30	59		
495	52	61	52	61
471	53	49	68	59
	76	59		
	76	71		
396	107	67	107	67

Table 4.6 A summary of pit/crack transition behaviour for Steel B (with Mo + V)

$\Delta\sigma$ (MPa)	$t_{p/c}$ (hrs.)	$a_{p/c}$ (μm)	Average transition time (hrs.)	Average transition pit size (μm)
516	27	166	27	163
	27	161		
495	23	138	26	141
495	29	144		
471	57	140	48	106
471	57	96		
471	50	74		
471	28	113		

Table 5.1 Long fatigue crack growth rate test results in different environments

Sample	Environment	*B* (mm)	Mo/V addition	Range of ΔK ($MPa\cdot\sqrt{m}$)	d*C*/d*N* (m/cycle)
LA	Air	11	N	$15.1 \le \Delta K \le 30.1$	$1.1\times10^{-11}\Delta K^{2.77}$
				$30.1 < \Delta K \le 71.6$	$1.2\times10^{-8}\Delta K^{0.71}$
LB	Air	24	Y	$13.3 \le \Delta K \le 25.4$	$7.0\times10^{-13}\Delta K^{3.65}$
				$25.4 < \Delta K \le 70.4$	$2.9\times10^{-10}\Delta K^{1.78}$
LCA	OCP	11	N	$14.8 \le \Delta K \le 21.3$	$5.0\times10^{-14}\Delta K^{4.97}$
				$21.3 < \Delta K \le 69.2$	$5.0\times10^{-10}\Delta K^{1.96}$
LCB	OCP	24	Y	$13.8 \le \Delta K \le 18.1$	$6.0\times10^{-16}\Delta K^{6.51}$
				$18.1 < \Delta K \le 62.9$	$7.0\times10^{-11}\Delta K^{2.48}$
LCPA	CP (-950 mV)	11	N	$13.0 \le \Delta K \le 16.2$	$8.0\times10^{-15}\Delta K^{6.04}$
				$16.2 < \Delta K \le 79.9$	$5.0\times10^{-10}\Delta K^{2.07}$
LCPB	CP (-950 mV)	24	Y	$13.7 \le \Delta K \le 17.3$	$1.3\times10^{-26}\Delta K^{15.97}$
				$17.3 < \Delta K \le 71.8$	$6.0\times10^{-10}\Delta K^{1.91}$

Table 5.2 Long fatigue crack growth rate (FCGR.) (m/cycle) in different environments at ΔK = 20, 30 and 40 $MPa\cdot\sqrt{m}$

Sample	Environment	FCGR. at ΔK = 20 $MPa\cdot\sqrt{m}$	FCGR. at ΔK = 30 $MPa\cdot\sqrt{m}$	FCGR. at ΔK = 40 $MPa\cdot\sqrt{m}$
LA	Air	4.37×10^{-8}	1.34×10^{-7}	1.65×10^{-7}
LB	Air	3.89×10^{-8}	1.25×10^{-7}	2.09×10^{-7}
LCA	OCP	1.46×10^{-7}	3.9×10^{-7}	6.84×10^{-7}
LCB	OCP	1.19×10^{-7}	3.25×10^{-7}	6.63×10^{-7}
LCPA	CP (-950 mV)	2.46×10^{-7}	5.69×10^{-7}	1.03×10^{-6}
LCPB	CP (-950 mV)	1.92×10^{-7}	4.19×10^{-7}	7.29×10^{-7}

Table 6.1 Values of F_1 for Poisson's ratio $\nu = 0.3$ and $C/a = 0.5$ [138, 139]

C/d	0	0.063	0.125	0.188	0.250
F_1	0.660	0.665	0.683	0.714	0.758

Table 6.2 Fatigue crack growth enhancement over OCP for RQT501 steel in 3.5%NaCl solution under CP application

Steel	$\Delta K = 15$ (MPa$\sqrt{m}$)	$\Delta K = 20$ (MPa$\sqrt{m}$)	$\Delta K = 25$ (MPa$\sqrt{m}$)	$\Delta K = 30$ (MPa$\sqrt{m}$)	$\Delta K = 35$ (MPa$\sqrt{m}$)	$\Delta K = 40$ (MPa$\sqrt{m}$)	$\Delta K = 45$ (MPa$\sqrt{m}$)
Steel A (no Mo/V)	2.89	1.68	1.43	1.46	1.48	1.51	1.53
Steel B (with Mo + V)	2.92	1.61	1.43	1.29	1.18	1.10	1.03

Table 7.1 Prediction of fatigue lifetime of Steel A (no Mo/V) from the model

Sample	$\Delta\sigma$ (MPa)	Environment	Fatigue life $N_{f(Test)}$ (cycles)	Fatigue life $N_{f(Model)}$ (cycles)	$\frac{N_{f(Test)} - N_{f(Model)}}{N_{f(Test)}}$ (%)
SA1	525	Air	389190	378392	2.8
SA2	520	Air	615070	636789	7.7
SA3	522	Air	690000	589185	4.2
SCA2	396	3.5%NaCl	380000	396325	-4.3
SCA5	495	3.5%NaCl	104098	111230	-6.9
SCA7	471	3.5%NaCl	104868	181860	-73.4
SCA9	516	3.5%NaCl	78224	69462	11.2
SCA5CP	502	3.5%NaCl + CP	357475	359653	-0.6

Table 7.2 Prediction of fatigue lifetime of Steel B (with Mo + V) from the model

Sample	$\Delta\sigma$ (MPa)	Environment	Fatigue life $N_{f(Test)}$ (cycles)	Fatigue life $N_{f(Model)}$ (cycles)	$\frac{N_{f(Test)} - N_{f(M}}{N_{f(Test)}}$ (%)
SB4	530	Air	205630	199332	3.0
SB5	522	Air	214190	325317	-51.9
SB6	516	Air	339240	371796	-9.6
SB7	502	Air	505990	510460	-0.9
SB8	495	Air	1147130	1163060	-2.3
SCB2	515	3.5%NaCl	45764	39115	14.5
SCB4	471	3.5%NaCl	78321	128869	-64.5
SCB6	495	3.5%NaCl	62563	61025	2.5
SCB7	396	3.5%NaCl	151913	149928	1.3
SCB8CP	516	3.5%NaCl + CP	132191	147733	-10.5
SCB9CP	495	3.5%NaCl + CP	147893	152425	-3.0
SCB10CP	471	3.5%NaCl + CP	310000	319231	-1.4
SCB11CP	502	3.5%NaCl + CP	282418	269242	4.9